Optical and Electrical Optimization by Advanced Characterization of Monolithic Perovskite/Silicon Tandem Solar Cells

vorgelegt von

M. Sc.

Eike Köhnen

ORCID: 0000-0002-3637-4907

an der Fakultät IV - Elektrotechnik und Informatik

der Technischen Universität Berlin

zur Erlangung des akademischen Grades

Doktor der Ingenieurwissenschaften

- Dr.-Ing. -

genehmigte Dissertation

Promotionsausschuss:
Vorsitzender: Prof. Dr. Bernd Szyszka
Gutachter: Prof. Dr. Bernd Rech
                   Prof. Dr. Steve Albrecht
                   Prof. Dr. Stefaan De Wolf

Tag der wissenschaftlichen Aussprache: 05. Juli 2021

Berlin 2021

Abstract

Hybrid metal-halide perovskite solar cells have experienced a tremendous development within a short time period. In 2009 the first perovskite single-junction solar cell with a power conversion efficiency (PCE) of 3.8% was presented. Just eleven years later, in year 2020, a PCE of 25.5% was achieved, which approaches the value of silicon single-junction solar cells. As metal-halide perovskite solar cells can be bandgap-optimized for top cells via compositional tuning, both types of solar cells can be combined into perovskite/silicon tandem solar cells. The synergy can enable higher efficiencies than the single cells alone, while the addition of the perovskite can potentially be done inexpensively, which makes this technology attractive for the photovoltaic market. The first monolithic perovskite/silicon tandem solar cell was presented in 2015 with a PCE of 13.7%. Just two years later, in 2017, when the work on this dissertation started, the PCE was already increased to 23.6%.

This dissertation covers the PCE improvement of monolithic perovskite/silicon tandem solar cells to a world record level above 29% and makes an important contribution to the understanding of the principles of device operation and to the techniques used to analyze these cells.

Despite the transition to an optically advantageous tandem solar cell design, the optical properties in the multi-layer stack with more than ten different films have a significant influence on the photogenerated current density (J_{Ph}) that can be generated in both subcells. Especially high reflection and parasitic absorption reduce the amount of light available for power conversion. In a first study covered by this dissertation, precise adjustments of thickness and deposition conditions of the perovskite layer, selective contact layers and transparent conductive oxide were presented. These optimizations led to an improvement from 25.0% to 26.0% due to reduced reflection and better matching of the photogenerated current densities of the perovskite and silicon subcell. The cumulated photogenerated current density of $39.5\,\mathrm{mA\,cm^{-2}}$ for this tandem cell, which had a flat front side, is today still one of the highest values and even comparable to cells with a textured front side. Although the short-circuit current density (J_{SC}) could be increased by $1.4\,\mathrm{mA\,cm^{-2}}$, the fill factor (FF) decreased by ~2 percentage points when the subcells operate closer to current matching conditions. Thus, we accounted this reduction to the reduced mismatch and analyzed this in more detail: We artificially induced various mismatch conditions by illuminating the tandem solar cell with different LED-based spectra. We found that the FF reached a minimum close to current matching conditions. If current mismatch between both subcells occurs in the tandem solar cell (i.e. either of the subcells generated a lower current density), the fill factor increased. This effect partially compensates the reduction of the J_{SC} induced by current mismatched subcells and makes monolithic tandem solar cells less sensitive to small mismatch conditions. This is highly important for energy yield analysis and has to be incorporated into yield simulations for more precise analysis. We verified the effect of FF enhancement under current mismatch by simulating the tandem solar cell electrically. Although the simulated FF trend could be well reproduced well as a function of the mismatch, the absolute value of the FF was higher when compared to the measured tandem solar cell. This revealed that further investigation and advanced characterization methods are required to reconstruct the tandem solar cell properly, understand the individual subcell characteristics in more detail and to improve the cell to reach the values obtained by electrical simulations.

The second study is linked to the FF losses and addresses the optimization of the FF and open-circuit voltage (V_{OC}) to further improve the PCE further. This was enabled by a self-assembled monolayer (SAM) as a hole-selective contact in the perovskite top cell, which was for the first time utilized in these tandem solar cells. Besides commercially available SAM molecules, which were shown to perform better in single-junction solar cells than the typically used polymer PTAA (poly[bis(4-phenyl)(2,5,6 trimentlyphenyl) amine]), we introduced the molecule Me-4PACz ([4-(3,6-dimethyl-9H-carbazol-9-yl) butyl]phosphonic acid), a new SAM for perovskite-based tandem and single-junction solar cells. In addition to the well-passivated perovskite interface, it enabled a fast hole extraction, which led to high V_{OC} and FF values and an improved photostability for

perovskite compositions with high bromide loading to enable 1.68 eV bandgaps, which typically suffer from halide segregation. In tandem solar cells we found similar benefits. All SAMs enabled higher PCE values compared to cells using PTAA as hole-selective contact. Furthermore, Me-4PACz led to high V_{OC} and FF values of up to 1.92 V and 81%, respectively. Together with a high J_{SC}, which was optimized in the previous study, a certified world record PCE of 29.15% was enabled. To evaluate the long-term stability of tandem solar cells, we specifically designed and fabricated a light source consisting of two types of LED arrays (193 LEDs in total), enabling precise control to match subcell photocurrent generation with AM1.5g conditions over long periods. Non-encapsulated tandem solar cells were measured continuously for 300 hours in air with relative humidity between 30-40%. The tandem solar cell with Me-4PACz showed highest stability, retaining 95.5% of its initial PCE. As evident from the first study, detailed analysis of the subcell is desired. However, typically it is difficult to evaluate the performance of the individual subcells in series connected tandem solar cells. We used injection-dependent absolute electroluminescence measurements to access the performance of the individual subcells. With this method, we were able to reconstruct the subcell current density-voltage characteristics without the influence of series resistances. From these reconstructions the photovoltaic parameters such as the maximum power point or pseudo fill factor could be determined. Furthermore, the parametrized reconstructed current density-voltage curves were used to simulate the tandem solar cell electrically, which revealed that with this tandem structure a PCE of more than 32% is achievable if series resistance losses can be minimized.

The rapid increase in tandem efficiency also increases the need for fast technology transfer into industry. All previously reported high-efficiency tandem solar cells have in common that they are based on >250 μm thick floatzone (FZ) silicon with most of them having a polished front side to enable efficient solution processing of the thin top cell. However, for mass production and thus for economic reasons, it is crucial to use thinner czochralski (CZ) grown wafers, ideally without the need for polishing. Therefore, in the third study, we fabricated tandem solar cells on 100 μm thin CZ silicon based bottom cells with a rough surface and compared the performance to tandem cells fabricated on laboratory-typical bottom cells accompanied by a 1000 hour MPP-track and optical simulations. We found that the median performance of both types was with 27.8% equally high with maximum values of 27.89% and 28.15% for CZ- and FZ-based tandem cells, respectively. However, the individual photovoltaic performance parameters differed: The thinner bottom cell for CZ-based devices enabled higher V_{OC} values due to reduced recombination current density. Furthermore, the photogenerated current density was reduced in the case of thinner silicon subcells, which led to an increased current mismatch. As investigated in the first study, this results in higher FF values of the CZ-based devices. Optical simulations revealed that the reduction of the bottom cell thickness from 280 μm to 100 μm enables to widen the top cell bandgap by ~0.02 eV and hence further increase the PCE, if current matching conditions should be maintained. Interestingly, this widening is independent of the perovskite's thickness. On the one hand the widened bandgap could lead to a higher V_{OC}, on the other hand wider bandgaps typically suffer from reduced stability and strong interface recombination. We found the same results for double-side textured tandem solar cells with conformally deposited perovskite and the findings regarding the optimum top-cell bandgap for industrial perovskite/silicon tandem solar cells are highly important for the future development of these fascinating tandem solar cells.

This dissertation plays an important role in the development of perovskite/silicon tandem solar cells and hence, will hopefully contribute to the expansion of photovoltaics.

Zusammenfassung

Hybride Metallhalogenid Perowskit-Solarzellen haben in sehr kurzer Zeit eine enorme Entwicklung erfahren. Die erste Perowskit-Solarzelle wurde 2009 mit einem Wirkungsgrad von 3.8% veröffentlicht. Nur 11 Jahre später, im Jahr 2020, konnte der Wirkungsgrad auf 25.5% gesteigert werden, welches sich der Effizienz von Silizium-Solarzellen nähert. Da sich die Bandlücke des Perowskits über die chemische Zusammensetzung anpassen und für eine Oberzelle optimieren lässt, können beide Arten von Solarzellen zu sogenannten Perowskit/Silizium Tandem-Solarzellen kombiniert werden. Das Zusammenspiel der beiden Solarzellen ermöglicht einen deutlich höheren Wirkungsgrad als jede Zelle für sich. Es wird davon ausgegangen, dass sich die Perowskit-Oberzelle kostengünstig herstellen lässt, was diese Technologie attraktiv für die Solarindustrie macht. Die erste Perowskit/Silizium-Tandem-Solarzelle wurde 2015 mit einem Wirkungsgrad von 13.7% veröffentlicht. Nur zwei Jahre später, im Jahr 2017, als die Arbeit an dieser Dissertation begann, wurde bereits ein Wirkungsgrad von 23.6% erreicht.

Diese Dissertation behandelt die Verbesserung des Wirkungsgrades von Perowskit/Silizium-Tandem-Solarzellen auf ein Weltrekord-Niveau von über 29% und leistet einen wichtigen Beitrag zum Verständnis, zur Wirkungsweise und zu Analysemethoden dieser Technologie.

Trotz einer Veränderung der Architektur, welche für Tandem-Solarzellen optisch vorteilhaft ist, haben die optischen Eigenschaften in dem Vielschichtsystem, welches aus mehr als zehn verschiedenen Schichten besteht, starken Einfluss auf die in den Teil-Solarzellen generierte Photostromdichte J_{Ph}. Vor allem die hohe Reflexion und parasitäre Absorption reduziert den nutzbaren Anteil des Lichts. In der ersten Studie in dieser Dissertation werden präzise Anpassungen der Schichtdicke und den Abscheidebedingungen vom Perowskit und den selektiven Kontaktschichten vorgenommen, welche die Reflexion verringern und eine bessere Übereinstimmung der Photoströme in den Teil-Solarzellen hervorbringt und somit den Wirkungsgrad von 25.0% auf 26.0% steigern. Die Summe der Photoströme, welche nach Optimierung $39.5\,\mathrm{mA\,cm^{-2}}$ beträgt, ist bis heute einer der höchsten J_{Ph}-Werte für Tandem-Solarzellen mit planarer Vorderseite. Er ist sogar vergleichbar mit beidseitig texturierten Tandem-Solarzellen. Auch wenn die Kurzschlussstromdichte J_{SC} um $1.4\,\mathrm{mA\,cm^{-2}}$ gesteigert werden konnte, ist der Füllfaktor (FF) gleichzeitig um rund zwei Prozentpunkte gesunken, welches wir der verbesserten Übereinstimmung der J_{Ph}-Werte zuschrieben. Um diesen Effekt genauer zu analysieren wurde die Tandem-Solarzelle mittels eines LED-Sonnensimulators unter unterschiedlichen Lichtbedingungen gemessen um künstlich das Ungleichgewicht der J_{Ph}-Werte zu erzeugen. Wir fanden heraus, dass der FF am geringsten ist, wenn die Teil-Solarzellen ungefähr im Stromgleichgewicht sind. Sobald es ein Ungleichgewicht der Ströme gab (d.h., dass entweder die Silizium- oder die Perowskit-Solarzelle weniger Strom generiert), erhöhte sich der FF. Dieser Effekt kompensiert teilweise den durch das Ungleichgewicht reduzierten Kurzschlussstrom und macht die Tandem-Solarzellen weniger empfindlich gegenüber geringen Ungleichgewichten der Photoströme. Das ist ein sehr wichtiger Aspekt, welcher in die Analyse der Solarenergieausbeute berücksichtigt werden muss um präzise Ergebnisse zu erhalten. Wir bestätigten die Erhöhung des FF aufgrund des Stromungleichgewichts mit elektrischen Simulationen. Auch wenn der Verlauf des Füllfaktors in Abhängigkeit vom Stromungleichgewicht nachgestellt werden konnte, war der simulierte FF höher als der experimentell gemessene FF. Das zeigt, dass weitere Untersuchungen und fortgeschrittenere Messmethoden notwendig sind um die Tandem-Solarzellen und die jeweiligen Teil-Solarzellen besser charakterisieren zu können und eine bessere Übereinstimmung von simulierten und experimentellen Ergebnissen zu bekommen. Mit dem daraus gewonnenen Wissen können die Eigenschaften der Tandem-Solarzellen verbessert werden.

Die zweite Studie in dieser Dissertation knüpft an den FF-Verlust an und behandelt die Optimierung des FFs und der Leerlaufspannung V_{OC} um den Wirkungsgrad weiter zu steigern. Dies wurde durch die Nutzung einer selbstorganisierenden Schicht bestehend aus einer einzelnen Lage (engl.: self-assembled monolayer; SAM) als lochselektiver Kontakt ermöglicht, welcher das erste Mal in Tandem-Solarzellen eingesetzt

wurde. Neben den bereits im Handel erhältlichen SAM-Molekülen, welche in Einzel-Solarzellen bereits bessere Eigenschaften ermöglichten als das typischerweise benutzte Polymer PTAA (poly[bis(4-phenyl)(2,5,6 trimentlyphenyl) amine]), haben wir ein neues SAM Molekül Me-4PACz ([4-(3,6-dimethyl-9H-carbazol-9-yl) butyl]phosphonic acid) für perowskitbasierte Einzel- und Tandem-Solarzellen vorgestellt. Zusätzlich zur gut passivierten Perowskit-Grenzfläche ermöglicht das neue Molekül eine schnelle Ladungsträgerextraktion, was zu einem erhöhten V_{OC} und FF führt sowie einer verbesserten Photostabilität, obwohl der Perowskit einen erhöhten Bromanteil aufweist um eine Bandlücke von 1.68 eV zu erhalten. Normalerweise führt der erhöhte Anteil an Brom zur unerwünschten Phasentrennung der Halogenide. Die Vorteile der SAMs übertrugen sich auch in die Leistung der Tandem-Solarzellen. Zum einen zeigten Tandem-Solarzellen, welche SAMs als lochselektiven Kontakt nutzen, einen höheren Wirkungsgrad als das überlicherweise genutzte Polymer PTAA. Zum anderen führte Me-4PACz zu sehr hohem V_{OC} bis zu 1.92 V und einem FF bis zu 81%. Zusammen mit dem durch die vorherige Optimierung hohen J_{SC}, wurde ein von unabhängiger Seite zertifizierter Weltrekord-Wirkungsgrad von 29.15% erreicht. Um die Langzeitstabilität der Tandem-Solarzellen zu bewerten, haben wir eigens eine LED-basierte Lichtquelle entwickelt und hergestellt, welche eine präzise Kontrolle der J_{Ph}-Werte beider Teil-Solarzellen ermöglicht. Dadurch kann eine stabile Beleuchtung gewährleistet werden, welche das AM1.5g Spektrum imitiert. Die unverkapselten Zellen wurden für 300 Stunden an Luft und einer relativen Luftfeuchtigkeit von 30% bis 40% kontinuierlich beleuchtet und gemessen. Die Tandem-Solarzelle mit Me-4PACz zeigt dabei die höchste Stabilität und hatte nach diesen 300 Stunden immernoch 95.5% ihrer Anfangseffizienz. Wie aus der ersten Studie ersichtlich ist, ist es wünschenswert die Teil-Solarzellen genauestens zu analysieren. Durch die Serienverschaltung gestaltet sich das Analysieren der Teil-Solarzellen allerdings üblicherweise als schwierig. Um die Teil-Solarzellen dennoch evaluieren zu können, nutzten wir injektionsabhängige Elektrolumineszenz-Messungen, welche es ermöglichten die Strom-Spannungs-Kennlinie der Teil-Solarzellen ohne den Einfluss von Serienwiderständen zu rekonstruieren. Aus den rekonstruierten Kurven konnten wir die charakteristischen Merkmale wie den Punkt maximaler Leistung oder den Pseudo-Füllfaktor beider Teil-Solarzellen separat extrahieren. Weiterhin konnten wir die rekonstruierten Teil-Solarzellen parametrisieren und für elektrische Simulationen nutzen, welche zeigten, dass ein Wirkungsgrad von über 32% erreichbar ist wenn Verluste durch Serienwiderstände minimiert werden können.

Die schnelle Verbesserung des Wirkungsgrades von Tandem-Solarzellen macht ebenfalls einen schnellen Technologietransfer in die Industrie notwendig. Alle hocheffizienten Perowskit/Silizium-Tandem-Solarzellen die bisher vorgestellt wurden basieren auf >250 μm dickem Silizium, welches aus dem Zonenschmelzverfahren (engl.: floatzone; FZ) gewonnen wird. Die meisten Silizium Teil-Solarzellen haben zusätzlich eine polierte Vorderseite. Für die Massenproduktion und somit aus wirtschaftlichen Gründen, ist es notwendig dünneres Silizium zu nutzen welches mittels Czochralski-Verfahren (CZ) hergestellt wird. Außerdem ist es wünschenswert auf die mechanische Politur der Vorderseite zu verzichten. Desshalb wurden in einer dritten Studie Tandem-Solarzellen, welche auf 100 μm dünnem CZ-Silizium mit rauer Oberfläche basieren, hergestellt und mit labortypischen Tandem-Solarzellen verglichen, begleitet von einem 1000-Stunden Langzeittest sowie optischen Simulationen. Wir konnten zeigen, dass beide Arten von Unterzellen zu Tandem-Solarzellen mit einem Wirkungsgrad von durchschnittlich ~27.8% führten, wobei die höchsten Werte 27.89% für CZ- und 28.15% für FZ-basierte Zellen waren. Obwohl die Effizienz sehr ähnlich war, unterschieden sich die charakteristischen Parameter. Die dünnere Unterzelle führte aufgrund von geringeren Rekombinationsverlusten zu einem höheren V_{OC}. Außerdem war das J_{Ph} geringer wenn das dünnere Silizium genutzt wurde, was zu einem größeren Stromunterschied der beiden Teil-Solarzellen führte. Wie aus der ersten Studie bekannt, erhöhte dieser Stromunterschied den FF der CZ-basierten Tandem-Solarzellen. Mittels optischer Simulationen fanden wir heraus, dass die Reduzierung der Silizium-Schichtdicke von 280 μm auf 100 μm eine Vergrößerung der Bandlücke um ~0.02 eV ermöglicht, wenn ein Stromgleichgewicht bestehen bleiben soll. Interessanterweise ist diese Vergrößerung unabhängig von der Perowskit-Schichtdicke. Auf der einen Seite könnte durch die Vergrößerung der Bandlücke das V_{OC} erhöht werden, was den Wirkungsgrad weiter steigert. Auf der anderen Seite sind Perowskite mit weiteren

Bandlücken typischerweise instabiler und führen zur erhöhten unerwünschten Grenzflächenrekombination. Optische Simulationen mit beidseitig texturierten Tandem-Solarzellen wiesen genau dasselbe Ergebnis auf. Das Finden der optimalen Bandlücke für industrielle Perowskit/Silizium-Tandem-Solarzellen ist sehr wichtig für die weitere Entwicklung dieser faszinierenden Technologie.

Diese Dissertation ist wichtig für den Fortschritt von Perowskit/Silizium-Tandem-Solarzellen und wird hoffentlich zum Ausbau von Photovoltaik beitragen.

Contents

1 Introduction

Anthropogenic greenhouse gas emissions have increased continuously since the pre-industrial era. Concomitantly, the global land and ocean surface temperature increased, the mean sea level rose, the amounts of snow and ice have diminished and the ocean surface water became more acidic.[1] To prevent further worsening and catastrophic environmental cascade reactions, [2] 195 countries signed the Paris agreement in 2015. Its main goal is to keep global warming below 2 °C or preferably below 1.5 °C compared to pre-industrial (1850–1900) levels. To achieve this long-term temperature goal, the emission of greenhouse gases needs to be reduced dramatically.[3] Besides methane (CH_4) and nitrous oxide (N_2O), carbon dioxide (CO_2) is the main driver for climate change. To reduce the emission of CO_2, burning fossil fuels for energy generation needs to be replaced with greenhouse gas neutral energy sources such as photovoltaics.

In 2019, the electricity generation by solar photovoltaic (PV) globally amounted to 720 TWh which is only around 3% of the total generated electricity.[4] To keep global warming below 2 °C at the end of the 21st century, 7.6 TWp installed PV is necessary in 2050, which will cover around 22% of the global electricity demand.[5] To achieve this goal, more photovoltaic devices need to be installed along with an increased capability to convert light into electrical energy. Today, solar energy is already one of the cheapest forms of electricity. [6] Nonetheless it is necessary to continue the development of this technology by increasing the power conversion efficiency (PCE) and further reducing its costs. Around 95% of the installed photovoltaic devices consist of crystalline silicon (c-Si).[5] With a record PCE of 26.7%,[7] single-junction silicon solar cells are approaching their theoretical maximum PCE of 29.4%.[8]

One successful way to improve the PCE is to combine multiple photovoltaic absorber materials into multijunction solar cells. Each absorbing material converts a specific part of the light spectrum into electrical energy, enabling a more efficient utilization of the spectrum. In the case of two absorbing materials, the devices are commonly termed tandem solar cells. With a record PCE of 47.1% for a solar cell comprising six different absorbing materials and using concentrated light, the PCE indeed surpassed the record PCE of single-junction solar cells.[9] However, this technology requires complicated and costly manufacturing processes. A more preferable way to increase the PCE is to combine the well-established silicon solar cell technology with an appropriate low-cost solar cell. A promising candidate is the polycrystalline metal-halide perovskite solar cell. With a PCE improvement from 3.8% in 2009 to 25.5% in 2020 for perovskite single-junction solar cells, this technology has attracted great attention.[9, 10] The outstanding performance is a result of the excellent optoelectronic properties of the perovskite films such as high absorption coefficient[11] and exceptional defect tolerance.[12] Furthermore, its tunable bandgap[13] and potentially low-cost fabrication[14] makes perovskite solar cells a favorable partner for the silicon technology. The perovskite/silicon tandem technology is expected to reduce the levelized cost of electricity (LCOE) by around 11% compared to conventional silicon solar cells.[14] Similar to perovskite single-junction solar cells, monolithic perovskite/silicon tandem solar cells experienced an exceptional PCE improvement from 13.7% in 2015 to 23.6% in 2017, when the work on this dissertation started.[15, 16] Since then, the PCE rapidly improved further to 29.5% in 2020.[9] This surpassed the theoretical PCE limit of silicon single-junction solar cells as well as the overall record PCE for single-junction solar cells (gallium arsenide) with 29.1%.[17] However, these highly efficient tandem solar cells commonly have an active area of 1 cm^2 and do not necessarily give information about long-term stability or outdoor performance. For commercialization, further understanding is needed to improve the PCE, long-term stability, outdoor performance and to increase the size of the devices to an industrially relevant level.

This thesis covers several aspects of monolithic perovskite/silicon tandem solar cells. Cutting-edge characterization techniques enabled detailed analysis of tandem solar cells or parts of the cells such as individual interfaces. Typically, it is difficult to access the performance of the subcell because of the series connection of both cells. However, we were able to access the subcell performance by using advanced characterization methods. Driven by the spectral dependence of the tandem solar cell performance, we designed and fabricated a new setup which allows proper illumination for long-term indoor measurements.

The gained knowledge was used to optimize the tandem solar cells optically and electrically. The improved tandem solar cells reached a certified PCE of 29.15%, a world record at that time and showed improved stability. Furthermore, we successfully demonstrated highly efficient tandem solar cells based on industry compatible silicon bottom cells. Thus, this dissertation plays an important role in attracting further attention, understanding the fundamental principles of operation of these devices and promoting commercialization.

This dissertation is based on three studies. The first study

Eike Köhnen, Marko Jošt, Anna Belen Morales-Vilches, Philipp Tockhorn, Amran Al-Ashouri, Bart Macco, Lukas Kegelmann, Lars Korte, Bernd Rech, Rutger Schlatmann, Bernd Stannowski, and Steve Albrecht. Highly efficient monolithic perovskite silicon tandem solar cells: analyzing the influence of current mismatch on device performance. *Sustainable Energy & Fuels*, 3(8):1995–2005, 2019. doi:10.1039/C9SE00120D,

which is addressed in section 6.1, covers mainly but not only the optical optimization by fine-tuning the thickness and deposition conditions of various layers such as the perovskite itself and the contact layers of the perovskite and silicon bottom cell. The reduced reflection and current mismatch between the subcells enabled an improvement of the current density and hence the PCE. However, the reduced mismatch led to a reduced fill factor. To get more insights into this effect, we measured a tandem solar cell with different illumination spectra to artificially create various mismatch conditions and quantified the change in fill factor as a function of the current mismatch. This behavior is verified by electrical simulations but reveals that further investigation and analysis of the performance of the subcells is needed.

In the second study

Amran Al-Ashouri, Eike Köhnen, Bor Li, Artiom Magomedov, Hannes Hempel, Pietro Caprioglio, José A Márquez, Anna Belen Morales Vilches, Ernestas Kasparavicius, Joel A. Smith, Nga Phung, Dorothee Menzel, Max Grischek, Lukas Kegelmann, Dieter Skroblin, Christian Gollwitzer, Tadas Malinauskas, Marko Jošt, Gašper Matič, Bernd Rech, Rutger Schlatmann, Marko Topič, Lars Korte, Antonio Abate, Bernd Stannowski, Dieter Neher, Martin Stolterfoht, Thomas Unold, Vytautas Getautis, and Steve Albrecht. Monolithic perovskite/silicon tandem solar cell with >29% efficiency by enhanced hole extraction. *Science*, 370(6522):1300–1309, 2020. doi:10.1126/science.abd4016,

which is covered in section 6.2, we used for the first time self-assembled monolayer (SAM) as hole-selective contacts in the perovskite top cell. More importantly, a new SAM, Me-4PACz, was presented which enabled a high level of passivation and fast charge extraction, thoroughly analyzed by advanced characterization methods. We compared the $J - V$ performance as well as the long-term stability of tandem solar cells using SAMs with cells using PTAA as hole-selective layer. All SAMs showed superior properties. The certified efficiency of 29.15% enabled with the newly presented Me-4PACz set a new world record. Furthermore, injection-dependent electroluminescence measurements gave us the possibility to access the performance of the individual subcells, which is otherwise not easy to measure due to the series connection of the top and bottom cell. The extracted subcell performances were used to simulate the tandem solar cells electrically and predict an achievable PCE value of >32% with our layer stack.

In the third study

Eike Köhnen, Philipp Wagner, Felix Lang, Alexandros Cruz, Bor Li, Marcel Roß, Marko Jošt, Anna B. Morales Vilches, Marko Topič, Martin Stolterfoht, Dieter Neher, Lars Korte, Bernd Rech, Rutger Schlatmann, Bernd Stannowski and Steve Albrecht. 27.9% Efficient Monolithic Perovskite/Silicon Tandem Solar Cells on Industry Compatible Bottom Cells. *Solar RRL*, 5:2100244, 2021. doi:10.1002/solr.202100244,

which is covered in section 6.3, we used silicon bottom cells, which are more suitable for industrial production. We demonstrated that tandem solar cells based on industry-compatible bottom cells enable a similarly high efficiency (~27.8%) compared to tandem cells based on laboratory-typical bottom cells. However, the

reduced bottom cell thickness for the industry-compatible devices reduced the photogenerated current density in the silicon bottom cell and hence adjustments are required if current matching conditions should be maintained. Supported by optical simulations we gave a guide how to adjust the thickness and/or bandgap of the perovskite layer to maintain these current matching conditions.

2 Solar Cell Fundamentals

In one hour, the Sun delivers a huge amount of energy to the Earth's surface, which covers the world's energy consumption of one year. Solar cells are electronic devices based on semiconductors, which can convert the radiant energy delivered by the Sun into electrical energy. To do this in an efficient way, multiple photovoltaic active materials can be stacked to multijunction solar cells. In the case of two absorbers, the cells are termed tandem solar cells. In the following, the fundamentals of single-junction and tandem solar cells as well as the efficiency limit of these technologies are reviewed.

2.1 Solar Irradiation

All objects with a temperature higher than $0\,\text{K}$ reflect, absorb and emit light. An ideal theoretical body, called a black body, does not reflect light but absorbs and emits all of the light perfectly. The spectral radiance L_λ of this body as a function of the temperature T is given by

$$L_\lambda(T) = \frac{2hc^2}{\lambda^5} \frac{1}{e^{\frac{hc}{\lambda kT}} - 1} \tag{2.1}$$

where λ is the wavelength, h is the Planck constant, c is the speed of light and k is the Boltzmann constant.[18, 19] The unit of the *spectral radiance* L_λ is [W m^{-3} sr^{-1}]. Thus, to calculate the *spectral irradiance* E_λ, which is given in [W m^{-3}], it is necessary to multiply by the solid angle. For several calculations the photon flux $\Phi_{\text{ph},\lambda}$ is a useful quantity, which is connected to E_λ via

$$\Phi_{\text{ph},\lambda} = E_\lambda \frac{\lambda}{hc} \tag{2.2}$$

Considering the Sun as a black body with a temperature of $5800\,\text{K}$, a spectrum as shown in Figure 1 would reach the Earth. This spectrum is in good agreement with the extraterrestrial spectrum ASTM-E490 (also termed AM0) developed by the American Society for Testing and Materials (ASTM). When the light enters the Earth's atmosphere, gases such as water vapor, carbon dioxide, nitrous oxide methane, oxygen, ozone as well as dust particles alter the spectrum. The absorption increases with the length of the path through the atmosphere, i.e. with the mass of the air. The ratio between the path length through the atmosphere l and the atmosphere's thickness l_0 is called the air-mass coefficient. For this reason, the spectrum outside of the atmosphere is called AM0, whereas the spectrum is called AM1 on the Earth's surface for normal incidence. Over the course of the day, the solar altitude changes and with that the air mass. Hence, the spectrum changes depending on the time of day. An example is shown in Figure 1B for the location of Berlin. Because of the variation of the spectrum, a standardized spectrum is needed to measure solar cell efficiencies. The AM1.5g represents the overall yearly average for mid-latitudes and is therefore used as a standard spectrum. The appended "g" denotes that this refers to a global, hemispherical spectrum within a 2π steradian field of view of the tilted plane. The total irradiance of this spectrum is $1000\,\text{W m}^{-2}$.[20]

2.2 Reflection, Absorption and Transmission

When light falls onto an interface of two materials, three things may happen with the light. It may be reflected from the interface, it may be absorbed by the material or it may be transmitted if the material is totally or partially transparent to the light.[23] In the following, the three processes are explained.
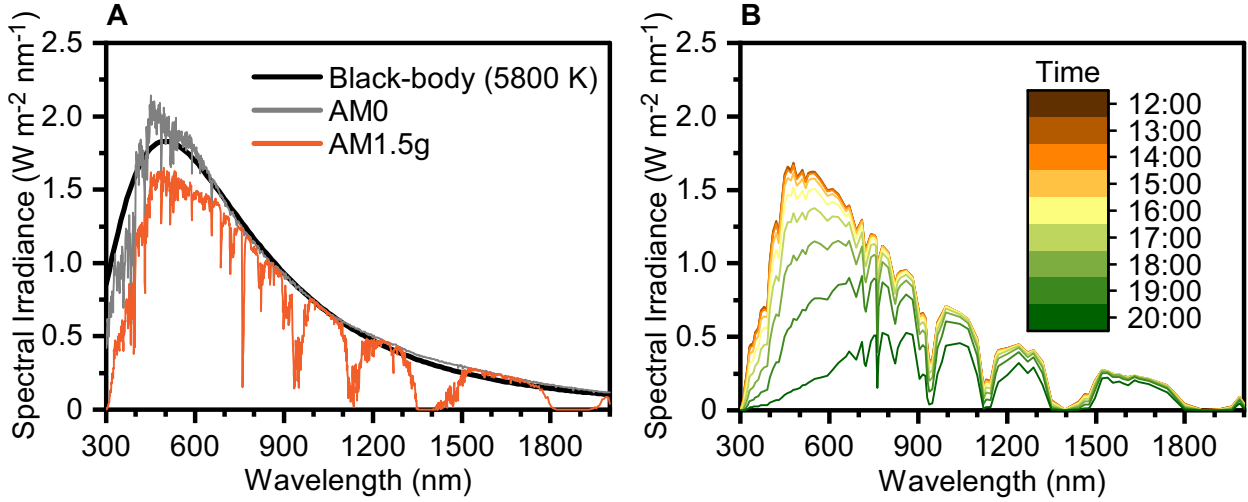
Figure 1: Spectral Irradiance. (A) Spectrum reaching the Earth when assuming the Sun as a black-body with a temperature of 5800 K. The spectrum is calculated according to equation 2.1. Standard spectra ASTM E-490 (AM0) and ASTM G173-03 global tilt (AM1.5g) developed by the American Society for Testing and Materials.[21] (B) Calculated spectra using SPCTRL2 Simple Spectral Model.[22] The spectra are calculated for Berlin at the 150th day of the year (i.e. May 30th) assuming a sun-tracking surface.

Reflection

For the interface of two materials with the refractive indices n_1 and n_2 the incident angle θ_i and angle of reflected light θ_r are equal. The angle of light traversing the interface θ_t is related to θ_i via Snell's law:[18]

$$n_1 \cdot \sin\theta_i = n_2 \cdot \sin\theta_t \tag{2.3}$$

Figure 2 illustrates this equation. The amount of reflected and traversed light is given by the Fresnel equations. In the case of normal incidence, $\theta_i = \theta_r = 0$, the amount of reflected light R is given by [18]

$$R = \left| \frac{n_1 - n_2}{n_1 + n_2} \right|^2 \tag{2.4}$$

Due to conservation of energy, the sum of reflected light R and light traversing the interface T_i must be unity:[18]

$$R + T_i = 1 \tag{2.5}$$

According to equation 2.4, the amount of reflected light increases with increasing difference in refractive indices. At an interface of air ($n_1 = 1$) and indium tin oxide ($n_2 = 2$ at 600 nm), approximately 11% of the incident light is reflected.

In addition to reflection described by the Fresnel equations, thin-film effects can enhance or reduce the amount of reflected light. For films with a thickness d in the range of the impinging wavelength λ, the reflected light at the top interface can interfere with the reflected light from the bottom interface. When the optical path difference OPD is an integer multiple m of λ, the interference of the two waves will be constructive, enhancing reflection. When the the optical path length is an odd number of half wavelengths, destructive interference occurs. These two events are expressed in the following equations: [24]

$$OPD = 2n_2 d \cos\theta_2 \begin{cases} m\lambda & \text{for destructive interference} \\ (m + \frac{1}{2})\lambda & \text{for constructive interference} \end{cases} \tag{2.6}$$
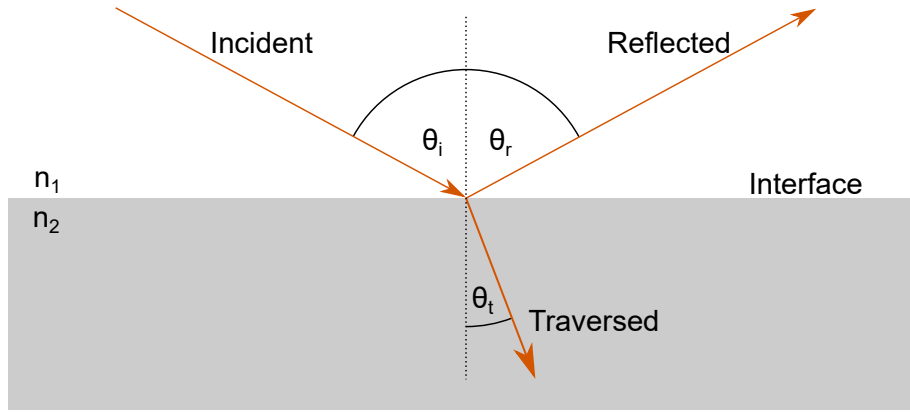
Figure 2: Snell's law. Illustration of Snell's law when a light beam impinges on an interface of two materials with the refractive indices n_1 and n_2. A certain amount of light might get reflected with an angle θ_r equal to the incident angle θ_i. Some light may traverse the interface with an angle θ_t. The angles and refractive indices are related via Snell's law as displayed in equation 2.3

Absorption

The light which is not reflected but traversed the interface and enters the material with n_2 can get absorbed. In a semiconducting material, the valence band is the energetically highest band of energy states, which is at a temperature of $0\,\text{K}$ completely filled with electrons. The top edge of this band is called valence band maximum and the corresponding energy is denoted as E_V. The energetically next higher band of available energy states is called conduction band and at $0\,\text{K}$ it is not populated with electrons. The bottom edge of this band is called conduction band minimum with an energy E_C. The energetic distance $E_C - E_V$ is called bandgap E_G. When the energy $h\nu$ of a photon is equal to or greater than the E_G of the material, the photon can be absorbed by the material and excites an electron into the conduction band, where it is free to move and participates in conduction. Any excess energy ($h\nu - E_G$) will be converted to thermal energy and does not contribute to the conductivity of the material. This loss is called thermalization.

The amount of light being absorbed by a material depends on its absorption coefficient α. The intensity I of the photon flux at any depth x is given as

$$I(x) = I_0 \cdot e^{-\alpha \cdot x} \tag{2.7}$$

with I_0 as the initial intensity. The intensity of the photon flux decreases exponentially with distance through the material. If the absorption coefficient is large, photons are absorbed over a relatively small distance.[25] Consequently, the absorption A is given by

$$A = 1 - e^{-\alpha d} \tag{2.8}$$

To increase the absorption of thin films, a reflector can be placed at the rear side. Photons which are not absorbed will be reflected and will pass the film again, which effectively increases d typically by a factor of 2.

In a real semiconductor, the band edges E_V and E_C depend on the so called k-vector that describes the crystal momentum. If E_V and E_C are at the same momentum in the crystals k-space, the semiconductor has a *direct* bandgap. Electrons can be excited from the E_V to the E_C without the need for additional momentum. If the electron cannot be excited without changing its momentum, it is referred to as an *indirect* bandgap material. The electron can only change its momentum by momentum exchange with the crystal, i.e. by receiving momentum from or giving momentum to vibrations of the crystal lattice. A direct bandgap enables high absorption coefficients with sharp edges near the band edge. Consequently, the required layer thickness to achieve a high absorption of the solar spectrum differs for direct and indirect bandgaps. For crystalline silicon as a material with an indirect bandgap, a thickness of several hundred micrometers is needed to

sufficiently absorb the light. On the contrary, hybrid perovskites with a direct bandgap, only need to be several hundred nanometers thick to absorb a large portion of the incident light.

If an electron is elevated to the conduction band, a vacancy is created in the valence band. This vacancy behaves like a particle with a positive elementary charge and is called hole. The absorption of a photon creates therefore an electron-hole pair.[18]

Transmission

Photons with an energy lower than E_G are not able to excite electrons and thus are not absorbed. Nonetheless, there is also a probability that photons with an energy larger than E_G are not absorbed. According to equation 2.8, the absorption A can be lower than unity, if the absorption coefficient is low or the material is thin. Not absorbed photons will reach the backside of the material, i.e. the next interface, where they can again traverse the interface or get reflected. In the case of reflection at the backside, the photons will travel through the material again. If the photons traversed the interface at the backside of the material, it transmitted the entire material and enters the next material, which can also be air. With T as the portion of transmitted light, all the incident light is reflected (R), absorbed (A) or transmitted:

$$1 = A + R + T \tag{2.9}$$

2.3 Generation of Current Density

The absorption of photons was previously described in section 2.2. Typically, the number of charge carriers which can contribute in conduction is similar to the number of absorbed photons, when neglecting losses such as recombination. Thus, the current density generated by absorption of radiation is given by

$$J = q \int EQE(\lambda) \, \Phi_{\text{ph},\lambda} \mathrm{d}\lambda \tag{2.10}$$

with q as the elementary charge and $\Phi_{\text{ph},\lambda}$ as the photon flux. The external quantum efficiency ($EQE(\lambda)$ or just EQE) is the ratio of the number of carriers extracted from the solar cell to the number of photons of a given wavelength incident on the solar cell. If this current is generated by intentional illumination, it is called *photogenerated current density* J_{Ph}. Assuming that a semiconductor like silicon with a bandgap of 1.12 eV absorbs all photons with energies above the bandgap (EQE = 100%), whereas photons with energies below the bandgap are not absorbed (EQE=0%), the J_{Ph} amounts to 438.1 A m^{-2} or 43.81 mA cm^{-2} if it is illuminated with the AM1.5g spectrum. However, the EQE decreases if the incident photons are partially reflected or transmitted as described in section 2.2. In addition, parasitic absorption in contact layers may reduce the EQE.

2.4 Quasi-Fermi Levels

In a semiconducting material, the probability whether a state in the conduction band or valence band is occupied is given by the Fermi-Dirac statistics

$$f(E) = \frac{1}{e^{\frac{E - E_F}{kT}} + 1} \tag{2.11}$$

where E_F is the Fermi level which is defined as the energy at which the Fermi-Dirac function is 0.5. To calculate the number of electrons in the conduction band, the Fermi-Dirac statistic needs to be multiplied with the density of states $g(E)$:

$$n = \int_{E_C}^{\infty} g(E) f(E) dE = N_C \exp\left(-\frac{E_C - E_F}{kT}\right) \tag{2.12}$$

where N_C is the so-called effective density of states, which is a volume density having the energy dependency of the density of states $g(E)$ already included. Consequently, the occupation probability of holes is $1 - f(E)$, which is due to symmetry of the Fermi-Dirac function equal to $f(-E)$. The hole density p is therefore given as

$$p = \int_{-\infty}^{E_V} g(E)f(-E)dE = N_V \exp\left(-\frac{E_F - E_V}{kT}\right) \tag{2.13}$$

Thus, the product

$$n_0 p_0 = n_i^2 = N_C N_V \exp\left(-\frac{E_G}{kT}\right) \tag{2.14}$$

with n_i as the carrier concentration in the pristine, intrinsic semiconductor, is independent of the position of E_F. Equation 2.14 is valid in thermal equilibrium denoted by the index 0 even if electron and hole densities are not equal for example due to intentional doping. According to equation 2.12 and 2.13, n-doping or p-doping will shift the E_F towards the conduction band or valence band, respectively.

If excess charge carriers are generated for example by absorption of light, n and p will increase and will simultaneously be larger than n_i. In contrast, doping will increase either n or p. If excess charge carriers are generated, the semiconductor is no longer in thermal equilibrium and the Fermi level is no longer strictly defined. The increase in n will shift E_F towards the conduction band. However, the simultaneous increase in p will shift E_F towards the valence band. This can only be fulfilled if two different Fermi levels E_{Fn} and E_{Fp} are present for electrons and holes, respectively. These energy levels are called *quasi-Fermi levels*.[25, 26] Inserting this into equation 2.12 and 2.13 the product is given as

$$n \cdot p = N_C \exp\left(-\frac{E_C - E_{Fn}}{kT}\right) \cdot N_V \exp\left(-\frac{E_{Fp} - E_V}{kT}\right) = n_i^2 \exp\left(\frac{E_{Fn} - E_{Fp}}{kT}\right) \tag{2.15}$$

The maximum open-circuit voltage, which is limited by thermodynamic laws is defined by the quasi-Fermi level splitting (QFLS):[26]

$$qV_{OC}^{max} = E_{Fn} - E_{Fp} = \text{QFLS} \tag{2.16}$$

Thus, according to equation 2.15, the maximum achievable V_{OC} depends on the charge carrier concentration, which again depends on the illumination intensity. Thus, V_{OC}^{max} depends logarithmically on the illumination intensity.

2.5 Charge Separation

Once photons are absorbed, the generated charge carriers (holes and electrons) need to get extracted at distinct locations. The fundamental process to separate charge carriers is the selective transport of electrons and holes to different terminals which is based on different conductivities for electrons and holes.[27] A prerequisite for efficient charge separation is a sufficient diffusion length of the charge carriers to reach the terminals.[26] The charge current of electrons j_e is given by

$$j_e = \frac{\sigma_n}{q} grad\ E_{Fn} \tag{2.17}$$

with σ_n being the conductivity for electrons. Similarly, the charge current of holes is expressed with

$$j_h = \frac{\sigma_p}{q} grad\ E_{Fp} \tag{2.18}$$

with σ_p being the conductivity for holes.

When at one terminal the amount of electrons exceeds the amount of holes, this terminal is named electron contact (also termed n-contact). For the hole contact (or p-contact) it is vice versa: The amount of holes reaching the terminal should exceed the amount of electrons. For the electron contact, j_e should

be high and j_h should be low, while the opposite is desired for the hole contact. The conductivity σ_k is proportional to the product of the mobility μ_k and carrier concentration n_k

$$\sigma_k = q\mu_k n_k \tag{2.19}$$

for the particles k (electrons or holes). Consequently, the charge current can be adjusted by changing n_k and/or μ_k. In traditional silicon homojunction solar cells, the selective contacts are created by changing n_k via doping. In contrast to this, heterojunction solar cells made from silicon (commonly termed silicon heterojunction; SHJ) but also perovskite solar cells utilize selective layers with bandgaps differing from the bulk material to induce energetic offsets. One layer has a large electron (hole) conductivity and small hole (electron) conductivity. This electron (hole) transport layer allows electrons (holes) to flow to the electron (hole) contact, while blocking the holes (electrons). Similar to the homojunction, the difference in conductivities is achieved by doping. However, the large bandgap at both contacts ensures a smaller conductivity of the minority carriers (holes in the electron selective layer and electrons in the hole selective layer), which reduces unfavorable recombination of electrons and holes. Simultaneously, the large bandgap of the selective layers prevents parasitic absorption of light in the contact layers.[26, 27]

2.6 Basic Solar Cell Equations
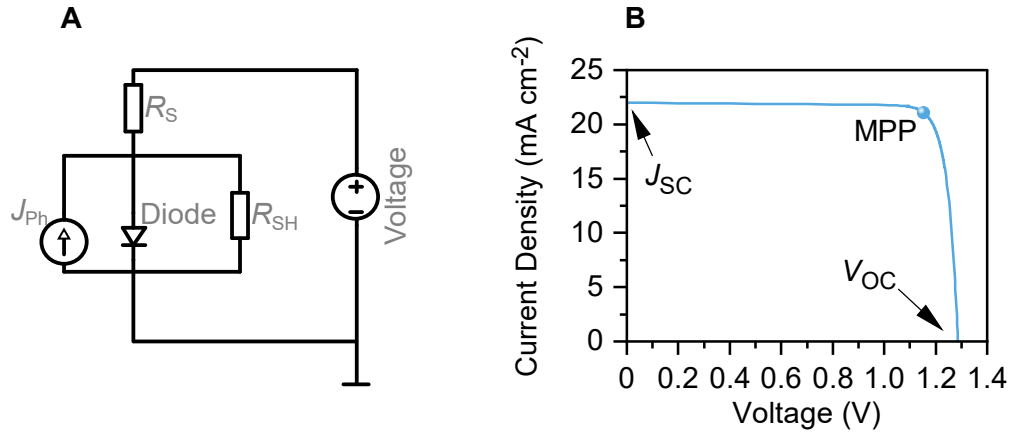
Figure 3: Single-junction solar cells. (A) Equivalent circuit diagram of the one-diode model for single-junction solar cells. R_S is the series resistance, R_SH is the shunt resistance, J_Ph is the photogenerated current density and 'Diode' is the representation of the diode which includes the ideality factor n_ID and reverse saturation current density J_0. (B) Example of a $J-V$ characteristic which follows equation 2.21. The graph includes the most important values: The open-circuit voltage V_OC, short-circuit current density J_SC and the maximum power point MPP.

To describe the electrical behavior of a solar cell, the ideal diode equation as presented by Shockley is commonly used.[28] It describes the current density J as a function of the applied voltage V for an ideal p-n junction in semiconductors. As described in section 2.2, absorbed light generates additional charge carriers and hence, a photogenerated current density J_Ph in the semiconductor. However, recombination losses (as described in section 2.8) reduces the current density depending on the voltage. Thus, the current density - voltage $(J-V)$ characteristic of a solar cell is then given as

$$J(V) = J_\mathrm{Ph} - J_0\left(e^{\frac{qV}{kT}} - 1\right) \tag{2.20}$$

with J_0 as reverse saturation current density (see equation 2.27), q as elementary charge, k as Boltzmann constant and T as temperature.[28]

The equivalent circuit representing $J - V$ characteristics for heterojunction solar cells can become more complicated.[29] However, for the sake of simplicity, we use equation 2.20 to derive commonly used solar cell parameters. In practice, solar cells comprise resistances affecting the $J - V$ characteristics. The most common parasitic resistances are the series resistance R_S, typically occurring in contact layers and the shunt resistance R_{SH}, embodying alternate current paths.[18] Furthermore, in real solar cells the $J - V$ characteristic is additionally affected by non-radiative recombination losses (see Section 2.8). These loss channels can be considered in the diode equation as separate terms [20] or combined into an ideality factor n_{ID}. The implementation of the parasitic resistances and the ideality factor in equation 2.20 gives

$$J(V) = J_{Ph} - J_0 \left(e^{\frac{q(V - J R_S A)}{n_{ID} k T}} - 1 \right) - \frac{V - J R_S A}{R_{SH} A} \tag{2.21}$$

where A is the area of the solar cell. An equivalent circuit diagram following this equation is shown in Figure 3A.

Figure 3B demonstrates a typical $J - V$ curve, which follows equation 2.21. The characteristic points are marked and will be explained next.

The short-circuit current density J_{SC} is the current which flows, when the cell is under short-circuit conditions, i.e. at $V = 0$ (see Figure 3B). It is mainly determined by J_{Ph} but also depends on the R_S. Thus, J_{SC} can be lower than J_{Ph} for high R_S. However, typically the influence of R_S on the J_{SC} can be neglected leading to $J_{SC} = J_{Ph}$ and depends on the amount of absorbed light.

At the open-circuit voltage V_{OC} no current is extracted from the solar cell (see Figure 3B). Inserting $J = 0$ simplifies equation 2.21. Furthermore, the R_{SH} is typically large enough to neglect the last term in equation 2.21. It follows:

$$V_{OC} = \frac{n_{ID} k T}{q} \ln \left(\frac{J_{Ph}}{J_0} + 1 \right) \approx \frac{n_{ID} k T}{q} \ln \left(\frac{J_{Ph}}{J_0} \right) \tag{2.22}$$

where the approximation is justified because $J_{Ph} \gg J_0$. While J_{Ph} typically has a small variation, J_0 has a key influence since this may vary by orders of magnitude depending on the recombination in the solar cell (see section 2.7 and 2.8). Therefore, V_{OC} is a measure of the amount of recombination in the device.[18]

The electrical power density is defined as the product of current density and voltage. The point, where the solar cell generates the maximum power density P_{max} is called maximum power point MPP. The corresponding voltage and current density at this point are labeled V_{MPP} and J_{MPP}, respectively. The power conversion efficiency (PCE) determines how much of the incident radiant power P_{in} can be converted into electrical power:

$$PCE = \frac{P_{max}}{P_{in}} = \frac{V_{MPP} \cdot J_{MPP}}{P_{in}} = \frac{J_{SC} \cdot V_{OC} \cdot FF}{P_{in}} \tag{2.23}$$

where FF is the so called fill factor. It is given by the ratio of the maximum power density to the product of J_{SC} and V_{OC}:

$$FF = \frac{V_{MPP} \cdot J_{MPP}}{J_{SC} \cdot V_{OC}} \tag{2.24}$$

Graphically, the FF is a measure of the "squareness" of the $J - V$ curve.[26]

2.7 Efficiency Limit of Single-Junction Solar Cells

The power conversion efficiency of solar cells is limited due to the laws of thermodynamics. William Shockley and Hans J. Queisser calculated the fundamental efficiency limit (commonly termed *detailed balance limit* or *Shockley-Queisser limit*) of a solar cell comprising a single absorbing material.[30] The main losses in efficiency stem from an incomplete utilization of the spectrum, which can be divided into losses due to thermalization and transmission. Photons with an energy lower than the bandgap E_G (with λ_G as the corresponding wavelength) will not be absorbed. Assuming that all incident photons with energies above E_G are absorbed (EQE=100%), the fraction of absorbed power density can be calculated with

$$p_{abs} = \frac{\text{absorbed power density}}{\text{incident power density}} = \frac{\int_0^{\lambda_G} \frac{hc}{\lambda} \Phi_{ph,\lambda} d\lambda}{\int_0^{\infty} \frac{hc}{\lambda} \Phi_{ph,\lambda} d\lambda} \tag{2.25}$$

where $\Phi_{ph,\lambda}$ is the photon flux as described in section 2.1. For silicon with a bandgap of $1.12\,\text{eV}$ and the AM1.5g standard spectrum ($\sim 1000\,\text{W}\,\text{m}^{-2}$), approximately 81% of the incident power density (=Intensity) is absorbed in the material, meaning that $\sim 19\%$ are not absorbed but transmitted. However, the fraction of the absorbed photon energy exceeding the bandgap energy is lost because of thermalization. It is calculated by

$$p_{\text{thermalization}} = \frac{\text{absorbed power density - usable power power density}}{\text{incident power density}} = \frac{\int_0^{\lambda_G} \frac{hc}{\lambda} \Phi_{ph,\lambda} d\lambda - E_G \int_0^{\lambda_G} \Phi_{ph,\lambda} d\lambda}{\int_0^{\infty} \frac{hc}{\lambda} \Phi_{ph,\lambda} d\lambda} \tag{2.26}$$

In the case of silicon, $\sim 32\%$ of the incident power is lost due to thermalization. Figure 4A presents the AM1.5g spectrum with the fraction of usable power for a silicon absorber. The efficiency, taking just this thermalization and transmission into account is called *ultimate efficiency*.[30] As calculated, the ultimate efficiency for silicon is $\sim 49\%$.

For temperatures above $0\,\text{K}$, the surrounding will emit black-body radiation corresponding to its temperature, which will be absorbed in the solar cell and generate charge carriers. In the dark without applied voltage, the rate of generation must be equal to the rate of recombination. The reverse saturation current density $J_{0,rad}$ is the current density if just radiative recombination is present, which is also referred to as the recombination current density and is calculated from the black-body radiation (equation 2.1) by

$$J_{0,rad} = J_0 = \pi q \int \text{EQE}(\lambda) \cdot L_\lambda(T,\lambda) d\lambda \overset{\text{EQE=1}}{=} \pi q \int_0^{\lambda_G} L_\lambda(T) d\lambda \tag{2.27}$$

where π arises from the Lambert's cosine law. Note that for individual films no EQE spectrum exists. Instead, the absorption $A(\lambda)$ is used to calculate $J_{0,rad}$. It is assumed that a perfect mirror is on the back side of the solar cell. Thus, the cell emits just from the front side. For the emission to both, the front and back side, J_0 will be twice as high.[18, 30] The maximum amount of photogenerated current density J_{Ph} as a function of the bandgap is calculated as described in section 2.3. With calculated values of J_0 and J_{Ph}, the $J-V$ characteristics (equation 2.20) can be calculated including the common parameters PCE, V_{OC}, J_{SC} and FF. Figure 4B shows the detailed balance limit as a function of the bandgap with a temperature of $300\,\text{K}$ and the AM1.5g spectrum. For wider bandgaps, the PCE decreases as the amount of transmission increases. On the contrary, for narrower bandgaps, the amount of transmission decreases but the loss due to thermalization becomes dominating. For silicon with a bandgap of $1.12\,\text{eV}$, the maximum achievable PCE is 33.4%. This value is close to the global maximum appearing at a bandgap of $1.34\,\text{eV}$ and amounts to 33.7%. For perovskite with a bandgap of 1.63, as used in section 6.1, the PCE limit is 30.25%. For wider bandgaps such as the tandem-relevant $1.68\,\text{eV}$, as used later in secion 6.2 and 6.3, the PCE limit decreases to 29.33%.

The above calculated efficiency limit just takes radiative recombination into account. However, further loss mechanisms reduce the efficiency limit. Considering Auger recombination, parasitic free-carrier absorption and bandgap narrowing, Richter *et al.* reassessed the efficiency limit of silicon solar cells.[8] These considerations led to an efficiency limit of 29.43%.

To overcome the efficiency limit of single-junction solar cells, multiple absorbers with different bandgaps can be combined, where each absorber converts a specific part of the spectrum into electrical energy. The more efficient utilization of the spectrum increases the PCE limit, which will be elaborated in section 2.9.

2.8 Recombination

Excited electrons, independent on whether they are generated by illumination or by the nature of thermal processes, drift and diffuse in the semiconductor and may come in close proximity to holes which leads to annihilation of both charge carriers and is also referred to as *recombination*. Besides the beneficial radiative
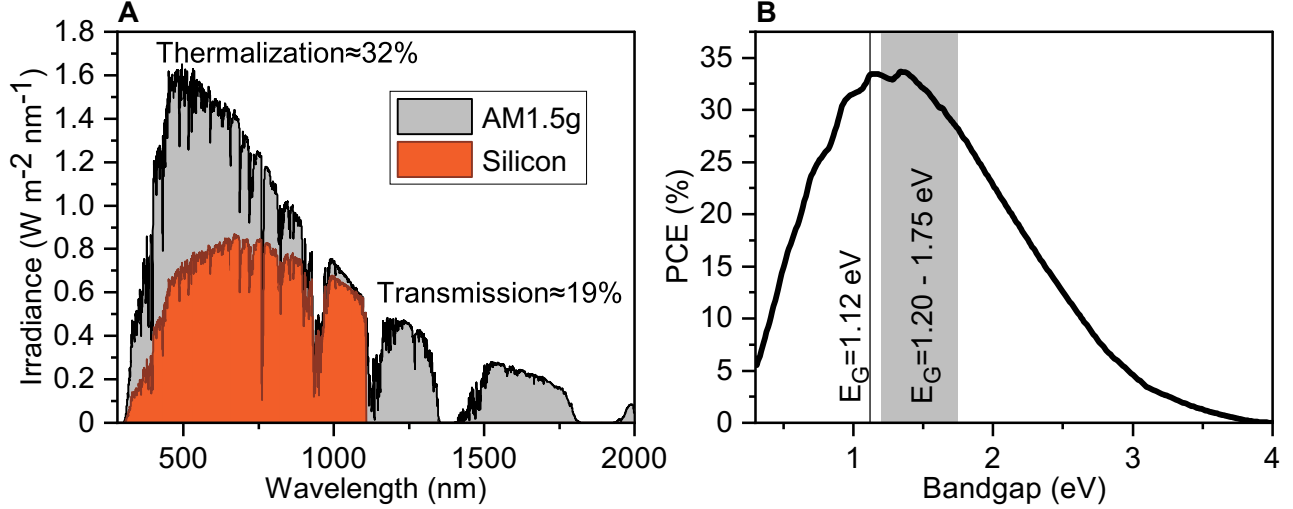
Figure 4: Theoretical efficiency limit. (A) Standard AM1.5g spectrum and the part of the spectrum which can be effectively used in a silicon absorber ($E_G = 1.12\,\text{eV}$). Approximately 19% of the incident power is not absorbed (i.e. transmitted), whereas $\sim 32\%$ is lost due to thermalization. (B) Detailed balance limit as a function of the bandgap calculated with the AM1.5g spectrum and a global temperature of $300\,\text{K}$. The theoretical achievable power conversion efficiency with silicon ($E_G=1.12\,\text{eV}$) as absorbing material is $\sim 33.4\%$ and is close to the global maximum of 33.7% for a bandgap of $1.34\,\text{eV}$. The gray area indicates the bandgap range between $1.20\,\text{eV}$ and $1.75\,\text{eV}$ that is considered for perovskites in single- or multijunction applications.[31]

recombination, there exist different types of adverse non-radiative recombination. The total recombination rate R_{tot} is calculated as the sum of all recombination rates:[25]

$$R_{\text{tot}} = \sum_i R_i \qquad (2.28)$$

For all recombination processes, the recombination rate R_i is defined by the ratio of excess charge carrier density Δn and the charge carrier lifetime τ_i:[25]

$$R_i = \frac{\Delta n}{\tau_i} \qquad (2.29)$$

In the following, the different recombination processes will be described.

Radiative Recombination

Radiative recombination is the inverse process of charge carrier generation by illumination. Excited electrons in the conduction band recombine with holes in the valence band and emit the released energy as photons. As the charge carriers typically recombine from the conduction band minimum and valence band maximum, the energy of the released photons is equal to the bandgap energy. This process is more likely to happen in direct semiconductors. For indirect semiconductors, additional momentum is needed for this recombination type, which makes it unlikely. This process is proportional to the electron density n and hole density p. Taking equation 2.15 into account, the radiative recombination rate is given as

$$R_{\text{rad}} = \beta n p = G_0 \exp\left(\frac{E_{\text{Fn}} - E_{\text{Fp}}}{kT}\right) \qquad (2.30)$$

where β is the radiative recombination constant, which represents a volume rate constant and G_0 is the generation rate in equilibrium.[25, 26] Equation 2.30 demonstrates that radiative recombination increases with larger carrier density ($R_{\text{rad}} \propto n^2$) and thus larger QFLS.[26]

Shockley-Read-Hall Recombination

The bandgap defines an energetic region, where no electronic states should be present and thus available. However, impurities or defects in the material may create electronic states within the bandgap which are called *trap states*. An electron can be trapped at such defect and consequently recombine with a hole that is attracted by the trapped electron. This Shockley-Read-Hall (SRH) recombination is typically non-radiative and the excess energy dissipates into heat.[32, 33] The recombination rate depends on several properties of the defect and material such as trap concentration N_T, capture cross sections σ, thermal velocity v and energetic position of the trap level E_T in the bandgap:

$$R_{SRH} = \frac{np - n_i^2}{\frac{n + N_C \exp(-(E_C - E_T)/(kT))}{N_T \sigma_p v_p} + \frac{p + N_V \exp(-(E_T - E_V)/(kT))}{N_T \sigma_n v_n}} \tag{2.31}$$

While for silicon, it is of great importance to avoid the inclusion of contaminants,[34] hybrid perovskites are rather tolerant against crystal defects and impurities.[12, 35] SRH recombination is also called monomolecular recombination, as a free charge carrier recombines with a localized, trapped charge, and it roughly holds $R_{SRH} \propto n$. [26]

Auger Recombination

Similar to radiative recombination, charge carriers recombine from band edge to band edge. However, the excess energy is transferred to another charge carrier (electron or hole) which is excited to a higher energy level without moving to another energy band. Excited charge carriers can lose their excess energy in thermal vibrations. If the energy is transferred to an electron, one hole and two electrons are involved in this process. The recombination rate R_{eeh} is proportional to n^2 and p. If the excess energy is transferred to a hole, the recombination rate R_{ehh} is proportional to p^2 and n. The overall Auger recombination is then given as the sum of both processes [25]

$$R_{aug} = R_{eeh} + R_{ehh} = C_n(n^2 p) + C_p(np^2) \tag{2.32}$$

where C_n and C_p are Auger capture probabilities that are strongly dependent on the temperature.[25] Since this is a three particle process with R_{aug} being proportional to n^3, this recombination becomes more important in non-equilibrium conditions where the carrier concentration is high.[25]

Interface Recombination

All of the above mentioned recombination types can happen inside of the bulk material. However, the surface of a semiconductor represents a special case as it causes a sudden discontinuation of the crystal structure. Hence, trap states occur, which enhance recombination of charge carriers. Not just the bare surface of a material, but also the interface to adjacent materials such as contact layers can introduce trap states and hence, evoke SHR recombination. Typically, the surface recombination is quantified by the surface recombination velocity S_r.[25] For state-of-the-art perovskite solar cells, this interface recombination dominates the non-radiative loss, which reduces the quasi-Fermi level splitting and open-circuit voltage of these cells.[36]

2.9   Tandem Solar Cells

The power conversion efficiency of single-junction solar cells is limited by the laws of thermodynamics. The maximum achievable PCE with one absorbing material is ~33.7%, as calculated in section 2.7, which is limited by losses due to thermalization and transmission. One way to improve the utilization of the spectrum is to split the spectrum into different energy ranges and convert each part of the spectrum with a solar cell with an appropriate bandgap. It was realized that spectral filtering could be achieved by stacking cells on top of one another. If the various bandgaps are ordered in a descending order with the widest bandgap facing
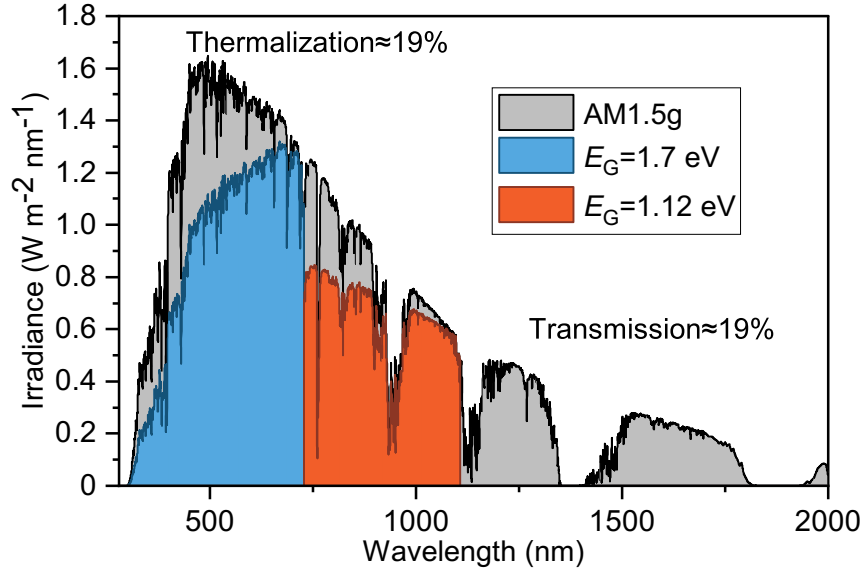
Figure 5: Visualization of the usable energy in a tandem solar cell. (A) AM1.5g spectrum and the part of the spectrum which can be used if a wide bandgap material with $E_G = 1.7\,\text{eV}$ is stacked onto a material with $E_G = 1.12\,\text{eV}$ such as silicon. Compared to a single silicon absorber as shown in Figure 4, the amount of thermalization is reduced to 19%, whereas the transmission loss is the same (19%).

the light source, not absorbed light in the wide bandgap material will be transmitted to the cell with the next narrower bandgap.[37] These devices are commonly termed *multijunction* solar cells. In the specific case of two absorbing materials, the devices are termed *tandem* solar cells.

In the following sections, the efficiency limits of the most prominent tandem solar cell architectures, namely two-terminal and four-terminal tandem solar cells, are calculated. Subsequently, both technologies are briefly contrasted, followed by a section addressing special characteristics of two-terminal tandem solar cells.

2.9.1 Efficiency Limit of Tandem Solar Cells

Similar to the calculations presented in section 2.7, the amount of thermalization and transmission can be calculated for multijunction, or as presented here, tandem solar cells. The first material (i.e. wide bandgap absorber) absorbs all photons in the range of $0 < \lambda < \lambda_{G1}$, where λ_{G1} is the wavelength corresponding the the bandgap of the first material. The second material absorbs all photons in the wavelength range of $\lambda_{G1} < \lambda < \lambda_{G2}$ with λ_{G2} as the wavelength corresponding to the bandgap of the second material. Figure 5 shows the utilizable spectrum if two materials with bandgaps of 1.7 eV and 1.12 eV are used. As the lower bandgap is the same as calculated as an example for single-junction solar cells, the amount of transmission loss is identical to the single-junction cell. However, the high energetic photons which would lead to severe thermalization losses will be absorbed and converted in the wide bandgap material. Hence, the loss due to thermalization is reduced to ~19% as a larger fraction of the incident power density can be used.

Likewise, the detailed balance limit is not just restricted to single-junction solar cells but can be applied to multijunction solar cells. [38–42] Figure 6A shows the detailed balance limit of a tandem solar cell as a function of the top and bottom cell bandgap. It is assumed that each subcell can operate at its individual maximum power point. The power density of the tandem solar cell is then given as

$$P_{4T} = P_1 + P_2 = V_1 J_1 + V_2 J_2 \tag{2.33}$$

with the subscripts 1 and 2 denoting the different subcells. Thus, four terminals would be necessary to contact the tandem solar cell. Therefore, these devices are termed *four-terminal* or 4T tandem solar cells.

The maximum achievable efficiency in this configuration is 46.1% if absorbers with bandgaps of 1.73 eV and 0.93 eV are combined. If silicon with a bandgap of 1.12 eV is used as a bottom cell, the highest efficiency of 45.2% is achieved if the top cell has a bandgap of 1.82 eV. If the subcells are connected in series, e.g. if the tandem cell is fabricated monolithically, the subcells cannot be operated at each individual maximum power point because the same current flows through both subcells. The power of the series connected tandem solar cell is then given as

$$P_{2\mathrm{T}} = (V_1 + V_2)J \tag{2.34}$$

This will be explained in more detail in section 2.9.3. In this case, the PCE of a monolithic tandem solar cell, commonly also named *two-terminal* or 2T tandem solar cell, is more sensitive to variations of the bandgap or more generally to the current-voltage characteristics of the subcells. Although the bandgap window in which high efficiencies can be achieved is smaller compared to a 4T tandem cell, the maximum PCE is with 45.7% similarly high (see Figure 6B). To achieve this, materials with bandgaps of 1.60 eV and 0.94 eV need to be combined. If silicon is used as bottom cell, the highest efficiency of 45.0% is achieved when combining it with a material with $E_\mathrm{G} = 1.73$ eV. There are several effects which may change the optimum combination of bandgaps and the respective maximum achievable PCE. The results presented here assume for example a perfect reflector at the rear side. Thus, photons generated by radiative recombination will be emitted just at the front side of the tandem cell. As described by de Vos *et al.*, the photons emitted by one subcell can get absorbed in the other subcell, enhancing its photogenerated current density. However, these effects will not substantially change the results.[37, 38, 40]

As previously discussed, there are various ways to realize tandem solar cells. The most prominent architectures are the four-terminal and two-terminal tandem solar cells. Recently, also the three-terminal design attracted attention. However, this will not be addressed in this work and the reader is referred to other reports for three-terminal tandem solar cells.[43, 44] In the following section, the advantages and disadvantages of 4T and 2T tandem solar cells will be briefly discussed. For the latter, the fundamental device physics will be addressed in more detail. Most of the fundamentals can be applied generally for series connected multijunction solar cell (i.e. more than two photoactive materials).

The detailed balance limit gets higher if more subcells are combined. As calculated by Martí *et al.* a multijunction solar cell consisting of an infinite number of subcells can reach a PCE of 65.4% with a cell temperature of 300 K and AM1.5 direct normal irradiance. If the light is maximal concentrated, a theoretical PCE of 85.0% is calculated.[45]

2.9.2 Two-Terminal and Four-Terminal Tandem Solar Cells

As described above, there are two prominent ways to realize tandem solar cells: The two-terminal and four-terminal approach.

In the four-terminal configuration, the top and bottom cell are stacked mechanically. This allows to fabricate each subcell individually, hence enabling optimized fabrication processes for each of them. Thus, there are no design or process restrictions when fabricating the subcells. As each subcell can be driven individually, the four-terminal approach gives highest operational flexibility. The PCE of the tandem solar cell can be easily maximized by operating each subcell at their respective maximum power point. For this reason, the bandgap window to achieve high efficiencies is large (see Figure 6). Nonetheless, the individual operation also has its drawback as more peripheral equipment such as cables and inverters are needed, making the four-terminal approach more expensive on the system level. Additionally, four-terminal tandem solar cells require four electrodes of which 3 need to be transparent, i.e. two more transparent electrodes than a two-terminal cell. These additional transparent electrodes will lead to increased parasitic absorption and manufacturing costs.[47–49]

In two-terminal tandem solar cells, the top and bottom cells are fabricated directly on top of each other. Typically, the narrow bandgap bottom cell is fabricated at first and the wide bandgap top cell is added onto this bottom cell. However, it is possible to make it the other way round. Therefore, this architecture has strict process-compatibility requirements as the fabrication of the top cell should not deteriorate the
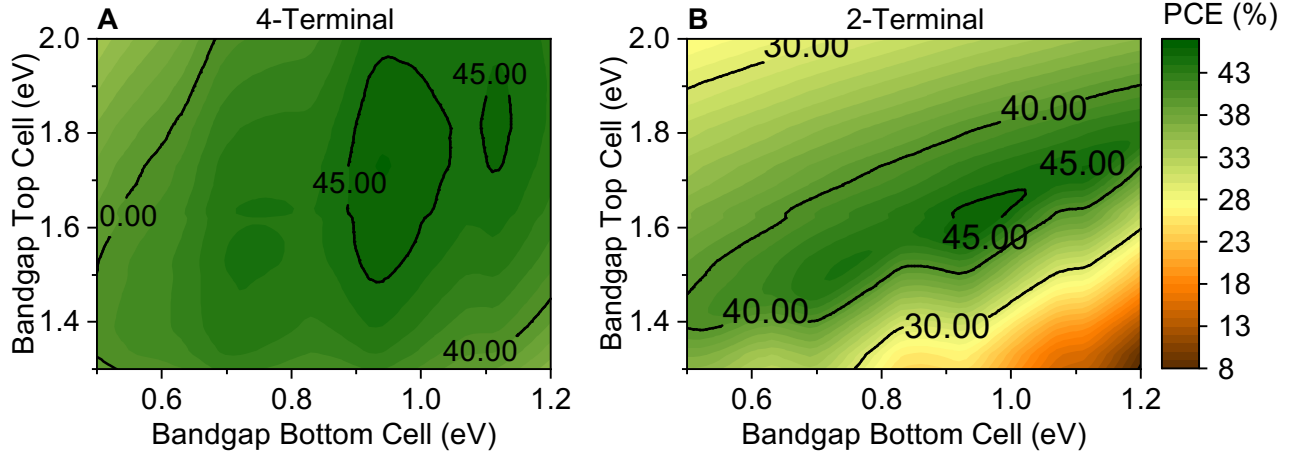
Figure 6: Detailed balance limit of tandem solar cells (A) Power conversion efficiency of a tandem solar cell if both subcells are independently operated at their respective maximum power point (4-Terminal). The generated power density is calculated according to 2.33. (B) Power conversion efficiency limit of a tandem solar cell if both subcells are connected in series (2-Terminal). Consequently, the current density flowing through both subcells is equal. The power density is calculated according to 2.34.

performance of the bottom cell. Among others, this includes the utilization of solvents and restriction in process temperatures. In contrast to the 4T tandem design, the monolithic integration of subcells only requires one transparent conductive electrode, which reduces costs and parasitic absorption losses. On the other hand, the interconnecting layer in the 2T tandem design plays an essential role in charge carrier collection and needs to be designed properly to enable a good contact to both subcells.[50] The monolithic design makes system integration simple because no additional equipment is needed. As the subcells are fabricated on top of each other and only two terminals are present, the subcells are connected in series (see Figure 7). Therefore, the same current flows through both subcells. For optimal operation of two-terminal tandem (or more generally: series connected multijunction) solar cells, the photogenerated currents in the subcells need to be adjusted. As the photogenerated current density in each subcell depends among others on the bandgaps, the bandgap window to achieve high efficiencies is smaller than for the 4T configuration (see Figure 6). More on this current restriction and operation of 2T tandem solar cells will be discussed in section 2.9.3 and section 6.1.

2.9.3 Operation of Two-Terminal Tandem Solar Cells

The optimal operation of two-terminal tandem solar cells is more complicated than in the four-terminal case because of serial connection of the subcells (see Figure 7). As described in section 2.6, a solar cell can be electrically described with a one-diode model. Thus, the simplest way to describe a two-terminal tandem solar cell is to connect two one-diode models in series as shown in Figure 8A.[51] This is valid when assuming that the interconnecting layer does not have any electrical contribution. The same current flows through both subcells. If the amount of generated charge carriers is different between both cells, the subcell with the lower J_{Ph} will guide the J_{SC} of the tandem solar cell. According to Kirchhoff's voltage law,[46] the voltage of the tandem solar cell V_{Tandem} at each given current density J is the sum of the voltage of its subcells V_1 and V_2:

$$V_{2\text{T}}(J) = V_1(J) + V_2(J) \tag{2.35}$$

Following this equation, it is possible that the short-circuit current density J_{SC} of the tandem solar cell can be higher than the minimum photogenerated current density of the subcells. This is preliminary the case when the limiting subcell (i.e. the subcell with lower J_{Ph}) has a low shunt resistance R_{SH}, as for
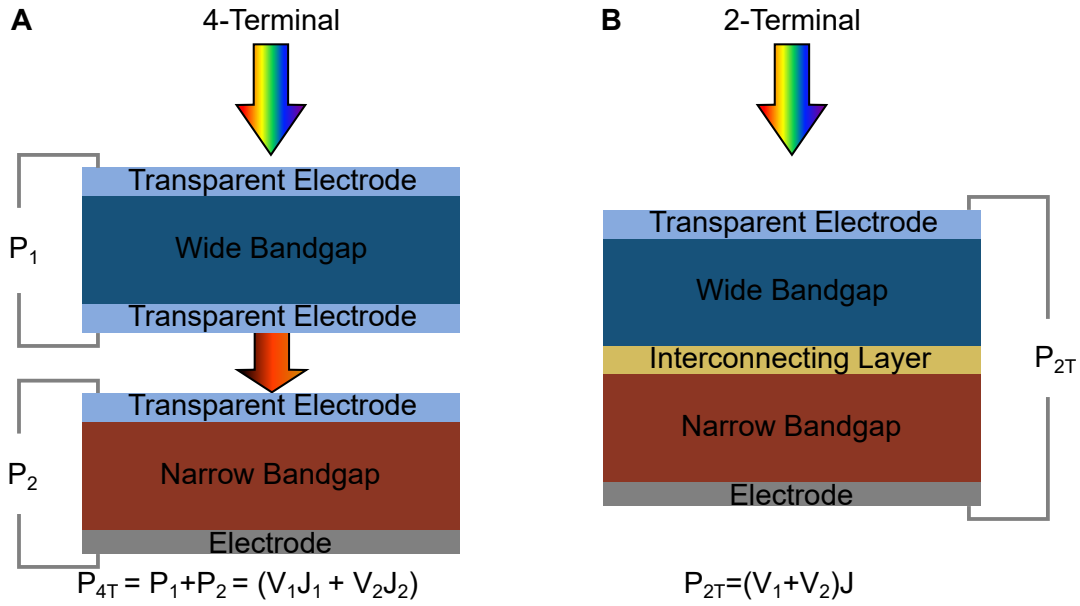
Figure 7: Tandem solar cell architectures (A) Schematic of a four-terminal tandem solar cell. The wide bandgap top cell absorbs the high energetic part of the spectrum, whereas the low energetic part is transmitted to the narrow bandgap bottom cell. Each subcell can be fabricated and operated individually. Thus, the power of the tandem solar cell is the sum of the power generated by the subcells. (B) Schematic structure of a monolithic two-terminal tandem solar cell. The subcells are fabricated on top of each other. Both subcells are connected in series enabling operation with just two terminals. According to Kirchhoff's voltage law,[46] the voltage of the tandem solar cell is the sum of the voltages of both subcells. The subcells are connected via an interconnecting layer.

example presented in Figure 8B. Under short-circuit conditions, the limiting subcell is operated in reverse bias-voltage, whereas the non-limiting subcell is operated with the same value in forward bias-voltage.[52] However, if the R_{SH} of the limiting subcell is sufficiently good, it is valid to assume that the J_{SC} of the tandem solar cell is equal to the J_{Ph} of the limiting subcell, as displayed in Figure 8C.

The power density of a two-terminal tandem solar cell is given by the product of the voltage and current density. Due to the same current flowing through both subcells, the power density is given by

$$P_{\mathrm{2T}} = V_{\mathrm{2T}} \cdot J = (V_1 + V_2)J = V_1 J + V_2 J \tag{2.36}$$

In order to maximize the power density and with that the PCE of the tandem solar cell, it is necessary to maximize both, $V_1 J$ and $V_2 J$. Thus, per definition, both subcells should be operated at their respective maximum power point. With the same current flowing through both subcells, it follows that the maximum power density of the tandem solar cell is achieved if the current of the maximum power point J_{MPP} is equal for both subcells. This condition is called *power matching*.[53] In contrast, *current matching* describes the condition if the photogenerated current densities J_{Ph} of both subcells are equal. Thus, depending on the performance of the subcells, the maximum power of a tandem solar cell may be achieved if a current mismatch (i.e. different J_{Ph} values for the subcells) is present. This is for example shown in Figure 8C, where the J_{MPP} is equal for both subcells but the J_{Ph} values differ.

The inability to measure the performance of the subcells individually, makes it difficult to extract the J_{MPP} values of the subcells. This problem will be addressed later in the publications in section 6.2. However, for good subcells, especially if the R_{SH} values are similarly good, it is valid to assume that current matching conditions simultaneously result in power matching conditions.

Equations 2.35 and 2.36 can be easily extended for multijunction solar cells with more than two absorbing materials.
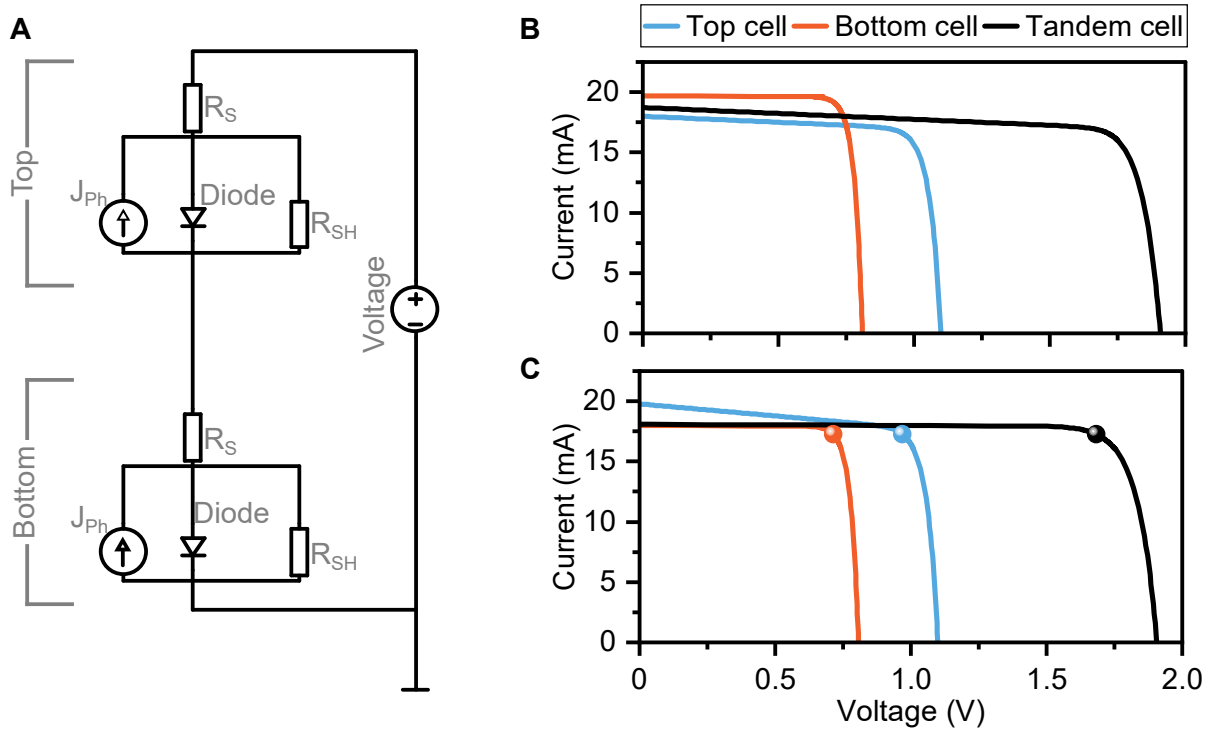
Figure 8: Electrical circuit of tandem solar cells. (A) Equivalent circuit diagram of a two-terminal tandem solar cell using one-diode models for the top and bottom cell, respectively. (B) Simulated tandem solar cell with a low R_{SH} of the bottom cell. This demonstrates that the J_{SC} of the tandem solar cell can be higher than the J_{Ph} of the limiting cell. (C) Simulated tandem solar cell with a low $R_{SH,Top}$ and high $R_{SH,Bottom}$. Consequently, to achieve the same J_{MPP} (indicated as spheres) in both subcells, a mismatch of J_{Ph} is necessary. Furthermore, this simulation demonstrates that the J_{SC} of the tandem solar cell is equal to the J_{Ph} of the limiting cell if its shunt resistance is high.

3 Current Status of Silicon- and Perovskite-based Solar Cells

In this section, the current status of different photovoltaic technologies will be discussed. Firstly, an overview of the well-established crystalline silicon technology with a focus on silicon heterojunction solar cells will be provided. Secondly, metal-halide perovskites will be introduced, followed by an overview of important milestones, achieved during the development of solar cells based on this material. Lastly, this section will cover recent developments of the conjunction of these materials, namely perovskite/silicon tandem solar cells.

3.1 Silicon Solar Cells

In 1839 Alexandre Edmond Becquerel discovered the photovoltaic effect. Since then it took 115 years until 1954, where Chapin, Fuller and Pearson from the Bell Telephone Laboratories presented a silicon solar cell with a PCE of ~ 6% based on a p-n homojunction.[54] Since then, silicon solar cells attracted a lot of interest, which came along with myriads of publications and a thorough understanding of this technology. Compared with other PV materials, crystalline silicon (c-Si) with a bandgap energy of 1.12 eV is one of the most appropriate candidates for building multijunction cells owing to its suitable bandgap, high efficiency, cost competitiveness, non-toxicity, and good stability.[55]

The conventional (c-Si) cell with full area aluminum back surface field (Al-BSF) is still the most common approach due to its simplicity, low cost and high reliability. However, the full area Al-BSF only provides moderate passivation quality of the rear surface limiting the PCE to ~20%.[56] To overcome the disadvantages of the full-area Al-BSF, a rear dielectric passivation scheme is added to the PERC (passivated emitter and rear cell) device followed by the formation of local Al-BSF, which enabled a PCE of ~24.0%.[17, 55] To further improve the PCE, a local diffusion of boron in the rear contact areas, which reduces the minority carrier density in these regions and hence reduces unwanted recombination, was introduced. This enabled the reduction of spacing at the rear contact points and resulted in an improved fill factor. These cells are called 'passivated emitter and rear locally diffused' (PERL) and achieved PCE values of 25%.[55, 57] However, these homojunction solar cells show typically a maximum V_{OC} of 700 mV.[55]

As for series connected tandem solar cells the voltage is a crucial parameter, silicon heterojunction (SHJ) cells may be better suited for the application in tandem solar cells as they can reach high lifetimes of ~10 ms and V_{OC} values of up to 750 mV.[58] The heterojunction contact simultaneously acts as a passivating and contact layer.[59] In the beginning, amorphous silicon (a-Si:H) was used as a contact. The n-type silicon wafer with a p-doped a-Si:H emitter had a performance of 12% with a moderate FF.[60] This was mainly a result of high reverse saturation current caused by interface defect states. The introduction of a thin intrinsic a-Si:H layer between the wafer and doped emitter reduced the amount of interface states[61] and enabled a PCE of 14.5%. Today, SHJ solar cells achieve a PCE of 26.7%,[7] which is the highest efficiency reached with crystalline silicon (non-concentrating).[9, 17]

Usually, short lifetimes in the doped and intrinsic layers of SHJ solar cells lead mostly to parasitic absorption. However, in tandem solar cells, the UV and visible wavelength range is in any case absorbed in the top cell, reducing the relevance for this problem. SHJ cells are typically fabricated at temperatures around 200 °C which reduces energy costs compared to traditional homojunction solar cells. On the other hand, at temperatures above 200 °C the passivation of the intrinsic amorphous layer will deteriorate and reduce the performance of the solar cell. This is an important aspect when this technology will be used for tandem solar cells.

From the 95% market share of c-Si solar cells, most of the silicon solar cells are based on the BSF and PERC/PERL technology. The heterojunction technology holds just a small fraction of the world market share but it is expected that this share will gain a market share of about 10% in 2024 and 17% in 2030.[5]

3.2 Perovskite Solar Cells

A comparably new material class for photovoltaic application belongs to the class of perovskites. The name for this crystal structure was introduced by Gustav Rose in 1839 by, who named it after the Russian mineralogist Lev Perovski.[18, 62] The mineral which was investigated by Rose was $CaTiO_3$. More generally, the perovskite structure is characterized the chemical formula ABX_3. Not all materials with perovskite crystal structure exhibit photovoltaic activities. The first report on a photoactive perovskite from 1978 described the fundamental material properties of hybrid organic-inorganic lead halide perovskites.[63] Nonetheless, it took more than three decades to realize solar cells based on this material. In 2009, Kojima *et al.* reported the first solar cell based on methylammonium lead triiodide ($CH_3NH_3PbI_3$; $MAPbI_3$) with a PCE of 3.8%.[10] Since then, worldwide research activities on perovskite solar cells skyrocketed its PCE within just more then 10 years to 25.5%, approaching the PCE of well-engineered silicon solar cells and surpassing the PCE of other thin film technologies such as CIGS, CdTe, dye sensitized or organic solar cells.[17] Instead of competing with other technologies, the excellent solar cell related properties of perovskite including a tunable bandgap makes this technology suitable for multijunction application.

In the following, the fundamentals of perovskite and perovskite solar cells will be discussed with the focus on bandgap engineering for application as a top cell in tandem solar cells.

Compositional Engineering and Deposition Methods

The general chemical formula of perovskite is ABX_3. If X is a halogen, the A and B sites of the perovskite structure are monovalent and divalent cations, respectively. As described above, originally, $MAPbI_3$ was used to demonstrate a perovskite solar cell. However, other materials can be used to form a perovskite. The formability of various types of perovskite is determined by a dimensionless number called Goldschmidt tolerance factor t,[64] which is an indicant of crystal stability and its structure deformity and is given by

$$t = \frac{r_A + r_X}{\sqrt{2}(r_B + r_X)} \tag{3.1}$$

where r denotes the ionic radii of the cations A and B and the anion X. To form a stable photoactive perovskite structure, the tolerance factor should be between 0.8 and 1.[65]

Over the years, myriads of compositions were predicted, investigated and tested to improve the PCE and/or stability. The most prominent A-site cations are methylammonium (MA), formamidinium (FA), cesium (Cs) and rubidium (Rb). For the B-site, typically lead (Pb) and tin (Sn) are used, whereas the X-site is typically filled with halides such as bromide (Br), iodide (I) and chloride (Cl). It should be noted that each site can be a pure element/molecule or a mixture of different components. The variety of compositions enables to tune the bandgap of the perovskite in a wide range between 1 and 3 eV.[13, 66–68] With respect to the bandgap of $MAPbI_3$ (1.55 eV), the bandgap should be decreased in order to get the single-junction detailed balance maximum at 1.34 eV. On the contrary, as calculated in section 2.9, an optimum bandgap of ~1.7 eV is necessary if the perovskite is used as a top cell in a two-terminal perovskite/silicon tandem solar cell. Besides the bandgap tunability, perovskite layers show excellent charge carrier lifetimes of several microseconds [69] and high defect tolerances[35]. Furthermore, the direct bandgap of commonly used perovskites enable a sharp absorption edge at the bandgap energy. The low absorption coefficient below the bandgap energy and hence the small so-called Urbach energy [70] is a likely reason for the high V_{OC} values which can be achieved in perovskite solar cells. Due to the high absorption coefficient at energies above the bandgap, a thin layer is sufficient to absorb a large amount of light.[11] In opaque single-junction solar cells, a metal on the rear side reflects not absorbed light, which increases the optical path length. Therefore, several hundred nanometer thick perovskite layers are sufficient to absorb a large amount of light. However, in semitransparent and tandem solar cells (with perovskite as wide bandgap subcell), not absorbed light will be transmitted and is lost or absorbed in the narrow bandgap cell, respectively. Thus, the perovskite needs to be thicker to enable sufficient absorption. To still maintain good charge extraction, the diffusion length in the perovskite needs to be large enough that the charge carriers can reach the terminals. Motivated by this problem, Chen *et al.* demonstrated an approach to enable electron diffusion length of up to 2.3 μm.[71] More impressively, a diffusion length of >25 μm was demonstrated in micrometer-thick $MAPbI_3$ films.[72]

Perovskite solar cells are fabricated either in p-i-n or n-i-p configuration. The notation is given by the order of fabrication of the contact layers and perovskite material. In the p-i-n case, first the hole-selective (p) contact is deposited. Subsequently, the intrinsic (i) perovskite and electron-selective (n) contact are deposited. For n-i-p cells, the n-contact is deposited first, followed by the perovskite (i) and the p-contact.[65] Single-junction perovskite solar cells are typically fabricated in *superstrate* configuration, where the light enters the solar cell from the glass (or foil) side. Thus, the light passes the contact which is first deposited (e.g. n-contact in n-i-p configuration) before being absorbed in the perovskite. In monolithic tandem solar cells it is the other way round: Due to the *substrate* configuration, the light will pass the contact which is deposited at last (e.g. p-contact for n-i-p configuration) before being absorbed in the perovskite.

The highest PCE values of perovskite single-junction cells are achieved in the n-i-p configuration.[73, 74] However, with the prospect to use perovskite solar cells as a top cell in tandem solar cells, the n-i-p configuration has two drawbacks: (i) Typically titanium dioxide TiO_2 is used as n-contact. The deposition requires temperatures as high as 500 °C,[74] which makes it impractical if SHJ solar cells are used, which tolerate temperatures below 200 °C. SnO_2 is an efficient alternative and can be deposited at SHJ-suitable temperatures.[73] (ii) For high-efficiency n-i-p solar cells, molecularly doped spiro-OMeTAD is usually used

as p-contact. It is well known, that this material induces high parasitic absorption losses if used in tandem solar cells, thus reducing the J_Ph especially in the perovskite subcell.

Although the PCE values of p-i-n perovskite solar cells are still lower for single-junction cells (maximum PCE: 22.3%)[75] as compared to n-i-p counterparts (25.5%), the p-i-n device polarity shows superior properties in tandem solar cells, as will be discussed in section 3.3.

Although highest efficiencies for single-junction perovskite solar cells are reached with ~1.5 eV bandgaps based on FAPbI$_3$ compositions,[74, 76] wide bandgap compositions with bandgaps larger than ~ 1.65 eV are needed for tandem applications. Such wide bandgap materials were first investigated in 2013 by Noh et $al.$ and Eperon et $al.$ who analyzed MAPb(I$_{1-x}$Br$_x$) and FAPb(I$_{1-x}$Br$_x$), respectively.[13, 67] It was demonstrated that the bandgap could be gradually tuned from 1.5 eV for x=0 (i.e. pure MAPbI$_3$) to 2.3 eV for x=1 (i.e. pure MAPbBr$_3$) and from 1.48 eV for pure FAPbI$_3$ to 2.23 eV for pure FAPbBr$_3$. While the proven bandgap tunability is attractive for tandem solar cells, the PCE suffered from photoinstability. In 2016, McMeekin et $al.$ presented a perovskite using a mixture of Cs and FA as A-site cation enabling higher photostability than compositions containing MA. With a bandgap of 1.74 eV, the perovskite solar cells had a PCE of 17.1%. [77] In the same year, Saliba et $al.$ presented a perovskite composition containing Cs, FA and MA as A-site cations and a halogen mix of Br and I at the X-site. This composition has a slightly lower bandgap of 1.63 eV but showed superior phase stability and a high PCE of 21.1%.[78] Although many different compositions and additives were investigated over the past years, the above described compositions are still widely used and will be labeled as CsFA and CsMAFA (also termed $triple$ $cation$).

While the widening of the perovskite bandgap was demonstrated for example by increasing the bromide content, the V_OC did not follow the bandgap enlargement by the same amount but is capped instead.[79] Thus, the V_OC deficit ($E_\text{G}/q - V_\text{OC}$) increases. On the one hand a low-energy peak was observed in photoluminescence spectroscopy which was explained with a photo-induced phase segregation. Especially the formation of iodine-rich domains leads to a reduction of the V_OC. This effect is commonly termed 'Hoke effect'.[79, 80] However, photoluminescence measurements of wide-bandgap perovskite films, which were never exposed to light showed substantial non-radiative recombination, thus limiting the V_OC. It highlights that the emission from iodide-rich domains is not the dominant factor determining the V_OC but that it is rather the high interfacial defect density in the mixed halide phase.[81]

Originally, the perovskite is deposited from a solution via spin coating. Today, this deposition technique is still the method enabling highest efficiencies and is practical for laboratory devices (i.e. small devices) as it is fast and no complex tools are needed. Therefore, the perovskite is deposited via spin coating for this work. However, different ways were developed or deployed to deposit perovskite films. The main incitement was to find a deposition technique which is able to deposit high-quality perovskite on a large scale. These deposition methods can be divided into two types, solution-based and vapor-based processing. Among the solution-based processing techniques such as inkjet printing, blade coating, slot-die coating and spray coating can be found.[82–84] A challenge for solution-based techniques is the drying of the wet film and the simultaneous crystallization of the perovskite. This can be done by quenching of the wet film, i.e. driving out solvent and thereby initiating crystallization, with vacuum[85], gas[86] or antisolvent[87]. The latter is used in this work. The introduction of the antisolvent onto the precursor solution film deposited on a substrate can induce fast supersaturation and precipitation of the perovskite precursor film by removing the solvent from the precursor solution. To enable this, the antisolvent must not be miscible with the perovskite deposition solvent and an insolubility of the perovskite in the antisolvent is required.[84]

On the other hand, deposition from the vapor-phase does not require utilization of potentially toxic solvents. The perovskite layer is formed by co-evaporation of various materials, which enables advantages such as precise control of the thickness, conformal deposition to cover uneven substrates like textured silicon[88] and homogeneous deposition for large area solar cells.[89] With this method, PCE values above 20% were achieved.[89] However, this was achieved with MAPbI$_3$, which is not suitable for tandem solar cells due to a too low bandgap. The deposition of wide bandgap material is yet rarely reported.

The hybrid deposition which utilizes evaporation of the inorganic components and solution-based deposition of the organic component combines the flexibility of compositional engineering and conformal

deposition on textured substrates.[90, 91] Although the advantage of conformal deposition was presented in multijunction solar cells using textured silicon,[92–94] highest PCE values in perovskite/silicon tandem solar cells to date are still reached via spin coating.

3.3 Two-Terminal Perovskite/Silicon Tandem Solar Cells
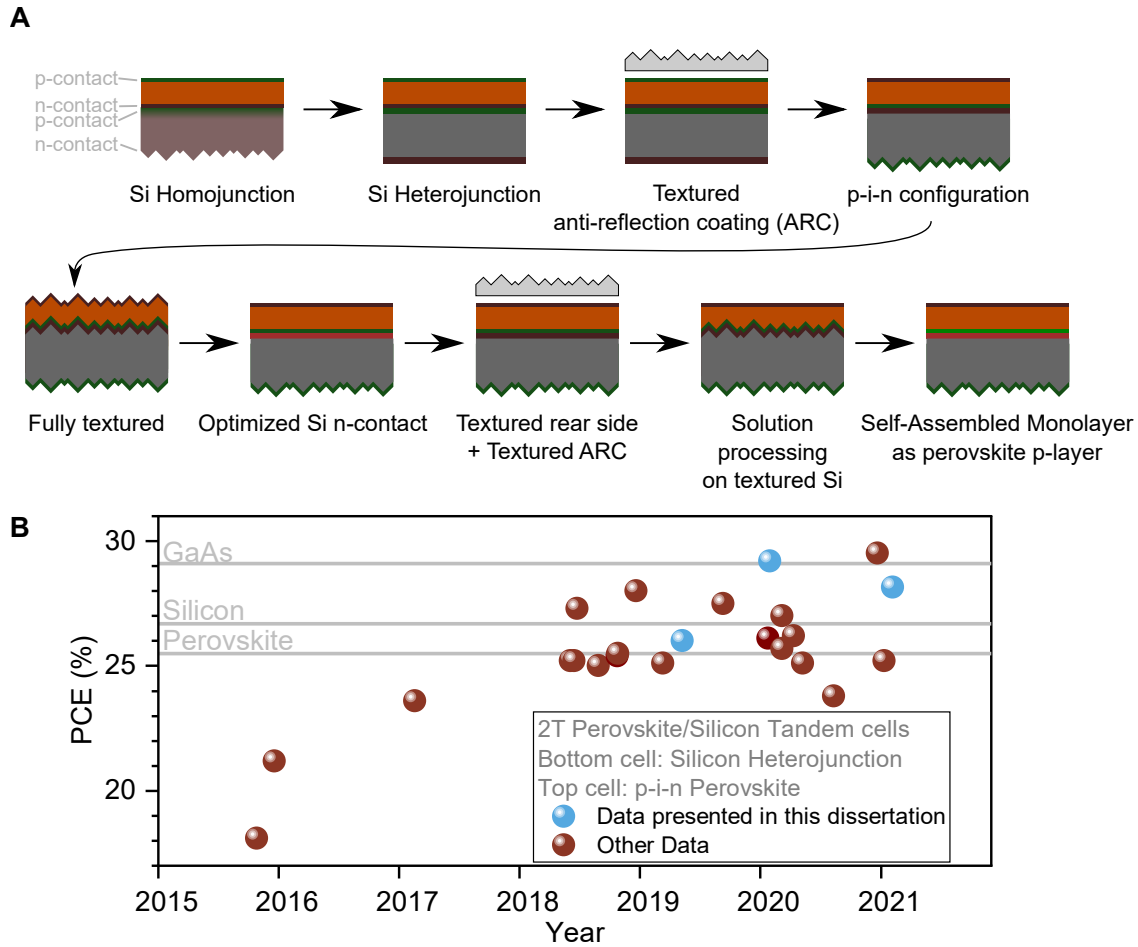
Figure 9: Evolution of two-terminal perovskite/silicon tandem solar cells. (A) Progress of two-terminal tandem solar cells shown as generic structures. The key inventions are given below each cell. (B) Presentation of PCE-development of two-terminal tandem solar cells consisting of p-i-n perovskite top cells and silicon heterojunction bottom cells. The record efficiencies of perovskite (25.5%), silicon (26.7%) and gallium arsenide (29.1%) single-junction solar cells are given as horizontal reference lines.[17] The blue dots represent the work which is presented in this dissertation. The tabulated data can be found in appendix B

As described in the previous sections, perovskite with its superior optoelectronic properties such as high absorption coefficient, sharp absorption edge and low sub-bandgap absorption is an excellent material for multijunction solar cells. The bandgap tunability makes it adjustable to various multijunction technologies. Narrow-bandgap perovskite compositions such as Sn-Pb mixtures with bandgaps of ~1.2 eV can be used as a bottom cell,[95] whereas wide-bandgap perovskites are well-suited for the application as top cells. This ability was experimentally demonstrated for various high efficiency monolithic tandem technologies such as perovskite/perovskite (24.8%)[95], perovskite/CIGS (24.2%)[9] and perovskite/silicon (29.5%)[9].

This section will summarize the development and key inventions of monolithic 2T perovskite/silicon tandem solar cells. Figure 9A illustrates some of these key inventions. The development of the PCE is shown

in Figure 9B.

The first functional 2T tandem solar cell was published by Mailoa *et al.* in 2015. The combination of a standard n-type back surface field (BSF) silicon cell with a perovskite (MAPbI$_3$) top cell in n-i-p configuration enabled a PCE of 13.7%. The high parasitic absorption of the spiro-OMeTAD, which was used as p-contact in the perovskite top cell strongly limited the J_{SC}.[15] Furthermore, the lower voltage of silicon homojunctions compared to SHJ makes them unfavorable for the 2T tandem technology but the high process temperature (500 °C) of the n-type contact, TiO$_2$, in the top cell is not compatible with SHJ, as described in section 3.1.

Later in 2015, Albrecht *et al.* used SnO$_2$ deposited via atomic layer deposition (ALD) as n-contact, which was deposited at temperatures below 120 °C. This allows to fabricate tandem solar cells with SHJ as bottom cells. The so fabricated tandem solar cell improved the PCE to stabilized values of 18.1%.[96] Since this achievement, the majority of highly efficient (>25%) tandem solar cells is fabricated with SHJ solar cells. Therefore, in this section only SHJ solar cells will be considered.

Also in 2015, Werner *et al.* fabricated a tandem solar cell with MAPbI$_3$ as top cell and a SHJ as a bottom cell. The planar surfaces of the silicon bottom cell, which enable solution processing of the perovskite, induce severe interference patterns in the EQE, reducing the J_{SC}. The utilization of a micro-textured anti-reflective foil enhanced the J_{SC} and improved the PCE of the tandem solar cell to 21.2%.[97] The PCE was strongly limited by the parasitic absorption of spiro-OMeTAD, the p-contact of the perovskite top cell.

Optically, the p-i-n configuration is favorable but the n-contact in this configuration, which is typically fabricated using organic materials such as C$_{60}$/BCP (Bathocuproine) or the fullerene derivative PCBM ([6,6]-Phenyl-C61-butyric acid methyl ester), is not able to withstand the subsequent sputtering of the transparent conductive oxide (TCO). Driven by this problem, Bush *et al.* presented a tandem architecture enabling the utilization of a p-i-n top cell in 2017. They added ALD-deposited SnO$_2$ onto the organic n-contact, which serves as a buffer layer to protect from sputter damage when subsequently sputtering a TCO such as indium tin oxide (ITO) on top. The low deposition temperature of the top cell below 120 °C also enabled to use a SHJ bottom cell. With this design, non-encapsulated single-junction solar cells with the CsFA perovskite were stable over 1000 h continuous operation (relative humidity: ~40%, cell temperature: 35 °C). The corresponding tandem solar cell reached a certified PCE of 23.6% and was stable over a 30 minutes MPP-track.[16] Until today, the organic n-contact covered by SnO$_2$ is used in highly efficient tandem solar cells. However, due to the impossibility to deposit ALD SnO$_2$ directly on top of the perovskite,[98] the organic n-contact is still used, which limits the V_{OC} due to induced interface defects.[99, 100] Although ALD enables large area conformal deposition and is already used in industry already, it is time-consuming and may be replaced or quicken for mass production.

Usually, silicon bottom cells have textured surfaces to reduce reflection losses. However, the several micrometer high pyramids are not compatible with solution processing of the perovskite, which is an order of magnitude thinner than these pyramids. Sahli *et al.* presented a deposition method for perovskite, which enables the utilization of silicon bottom cells with textured front sides. First, the inorganic part is deposited via thermal evaporation. Although the organic part is solution processed afterwards, a conformal perovskite film is formed. The reduced reflection enabled high photogenerated current densities in the subcells and with that a high J_{SC} in the tandem solar cell. Furthermore, the utilization of a tunnel recombination junction instead of a TCO recombination layer was demonstrated. The certified 25.2% were published in 2018.[92]

Also in 2018, Mazzarella *et al.* optimized the silicon bottom cell (again with planar front side). As described by the Fresnel equation (equation 2.4) large steps of refractive indices enhance the reflection at the respective interface. To reduce reflection of infrared light at the n-contact of the silicon bottom cell, nanocrystalline silicon oxide (nc-SiO$_x$:H) was introduced used as a n-contact, which allowed for precise tailoring of the thickness and refractive index that gradually increases from around 2 for perovskite to 2.7 for the nc-SiO$_x$:H towards 4 for the crystalline Si. The PCE of the optimized tandem solar cell was independently certified and amounted to 25.2% as well.[101].

At the same time in 2018, Oxford PV announced a certified PCE of 27.3%. However, no details are known about this solar cell.[102]

Instead of using textured silicon bottom cells, Jošt *et al.* used a textured anti-reflective light management

foil to improve the optical performance of tandem solar cells. Besides the experimental realization, which demonstrated a 25.5% efficient tandem solar cell in 2018, optical simulations were performed for tandem solar cells using flat or textured interfaces or a light management foil. Although double side textured tandem solar cells showed highest photocurrents and thus performance in the simulation, a flat front side with a textured light management foil presents a good alternative, especially for high energy yield under non-perpendicular light incidence.[31]

In 2018, Oxford PV surpassed their own record with a certified PCE of 28.0%, again without disclosing any information about the cell.[103]

In 2019, precise adjustments of certain layers such as the thickness of the perovskite, deposition temperature of ALD-deposited SnO_2 and the thicknesses of the TCO as well as the previously mentioned nc-SiO_x:H improved the PCE from 25.0% to 26.0%, as reported by the author of this dissertation. This study came along with a thorough analysis of the performance of the tandem solar cell as a function of the current mismatch.[104] More details will be found in section 6.1 as the publication is part of this dissertation.

To overcome the difficulty of efficient solution processing on top of textured silicon, Chen *et al.* adjusted the silicon surface as well as the perovskite thickness. The optimized texturing process of the silicon front side reduced the pyramid height to the sub micrometer range while maintaining sufficient anti-reflective characteristics. Simultaneously, the blade-coating process to deposit the perovskite is adjusted to obtain thick perovskite layers to cover the pyramids. However, it needs to be thin enough to collect photogenerated charge carriers. As solution-based blade coating is not a conformal process and the film thickness remains larger than the mild texture, the top surface of the perovskite becomes flat. The utilization of an anti-reflective foil further reduced reflection losses yielding a tandem solar cell with a PCE of 26.1% in early 2020.[105]

With a newly designed hole-selective layer for the perovskite top cell, the author of this dissertation achieved a certified PCE of 29.15%, which was announced in January 2020 and thus, set a new world record. It approaches the theoretical limit of silicon solar cells (see section 2.7). The hole-selective layer, a self-assembling monolayer (SAM) enabled reduced non-radiative recombination and fast charge extraction which led to improved FF and V_{OC} values.[99] This publication will be addressed later in this dissertation as a basis of section 6.2.

Instead of optimizing the selective contacts, Xu and Boyd *et al.* focused on improving the perovskite composition, which was published in March 2020. In contrast to other publications, where chlorine was used to improve morphology or surface passivation, this publication demonstrated the incorporation of Cl into the lattice, changing the perovskite's bandgap. With this, the amount of Br in the CsFA perovskite could be reduced by partial substitution with Cl, which improved photostability. The latter is demonstrated with a 1000 h MPP-track of a semitransparent perovskite single-junction at around 60 °C in nitrogen which degraded less than 4%. With the new perovskite composition, commonly also called triple-halide perovskite, a tandem PCE of 27.0% was achieved.[106]

On the same date in March 2020, Hou, Aydin, Bastiani *et al.* demonstrated a perovskite/silicon tandem solar cell on fully textured silicon. The adjusted spin-coating recipe enabled micrometer thick layers which fully covered the pyramids without the need to smoothen the texture. To improve the charge carrier diffusion length and hence enable proper carrier collection, the perovskite was covered by a self-limiting passivant, which -importantly- also suppressed phase segregation. The enhanced stability of the tandem solar cells with a certified PCE of 25.7% was demonstrated with encapsulated cells. Regular $J-V$ measurements of cells stored at 85 °C and cells which were continuously MPP-tracked at 40 °C showed no degradation after 400 h.[107]

In the mean time, the work on tandem solar cells with a silicon homojunction was continued. To circumvent the high absorption of spiro-OMeTAD in the n-i-p configuration, a down-shifting material was used to convert UV light, which is otherwise parasitically absorbed, into green light which can effectively be absorbed in the perovskite. Simultaneously, this material acts as a anti-reflective layer. However, the V_{OC} and J_{SC} is still much lower compared to SHJ-based tandem cells and limits the efficiency to 23.0%.[108]

The impressive improvement of the PCE and stability for perovskite/silicon tandem solar cells is yet unique among all solar cell technologies. However, ultimately these cells need prove their excellent properties

under real conditions i.e. conditions differing from the standard test conditions. This includes effects such as changing illumination spectra as will be discussed in section 6.1 and various cell temperatures. Although the effect of temperature on the performance of perovskite as well as silicon single-junction solar cell were already investigated,[109, 110] the outdoor performance of perovskite/silicon tandem solar cells is yet to be investigated. Therefore, Aydin *et al.* analyzed the performance of tandem solar cells outdoor in a hot sunny climate. The elevated cell temperature in this study reached up to ~60 °C and led to a widening of the bandgap of the perovskite subcell while simultaneously narrowing the bandgap of the silicon subcell. Hence, a current mismatch occurs as the photogenerated current in the perovskite subcell decreases whereas the current in the silicon subcell increases. Thus, the optimum perovskite bandgap will shift towards lower energies for elevated cell temperatures, which relaxes the need for wide-bandgap perovskite compositions.[94]

Another way to reduce the perovskite's bandgap while maintaining current-matching conditions is to fabricate a bifacial perovskite/silicon tandem solar cell. Light reflected from the ground will enter the solar cell from the rear side and thus increase the photogenerated current density in the silicon bottom cell. As reported by Bastiani *et al.*, the optimum perovskite bandgap depends on the amount of additional light entering the solar cell from the rear side. Additional $20 \, \mathrm{mW \, cm^{-2}}$ are sufficient to achieve current matching conditions when a perovskite bandgap of 1.59 eV is used. This is beneficial in terms of long term stability of the perovskite. Besides the laboratory measurements, this study adds thorough outdoor measurements of monofacial and bifacial tandem solar cells with different ground materials. In both cases, outdoor and indoor, the bifacial solar cell outperforms the monofacial configuration.[111]

End of 2020, 11 month after release of our world record, Oxford PV announced a certified tandem solar cell with a PCE of 29.5% which surpassed for the first time the theoretical limit of silicon single-junction solar cells and simultaneously surpassed the highest single-junction solar cell (GaAs).[9]

This impressive improvement in PCE in such a short time attracts increasing attention. However, there are several issues which still need to be addressed to realize commercialization of this technology. The above mentioned high efficiency tandem solar cells have a laboratory-typical active area of $\sim 1 \mathrm{cm^2}$. Thus, upscaling is necessary, ideally without suffering from lower PCE. First attempts are experimentally demonstrated.[112, 113] This will bring new challenges to industry-relevant metallization such as screen printing and tabbing of the wires.

The higher PCE for tandem solar cells compared to single-junction solar cells needs to remain for a long time. Thus, the stability of the perovskite top cells needs to be improved to ultimately pass the IEC tests, which are intended for standardization of solar modules.

Furthermore, most of the tandem solar cells mentioned above use thick floatzone silicon (FZ-Si) bottom cells. This is not compatible with industrial production as the typical industry-relevant thickness much smaller than used in lab-scale devices and czochralski silicon will remain the main method to fabricate silicon ingots.[5] Therefore, tandem solar cells on industry-compatible silicon bottom cells were fabricated and compared to tandem solar cells based on thick FZ-Si. The study will be discussed in section 6.3.

As no perovskite-based solar cells are commercially available yet, the calculation of the economical benefit of perovskite/silicon tandem solar cells is difficult to evaluate. Calculations reveal that the tandem modules need to approach 30% to reduce the levelized cost of electricity by $\sim 11\%$.[14]

Due to the many worldwide activities in the field of perovskite solar cells, the above mentioned challenges are likely to be addressed soon to facilitate commercialization.

4 Sample and Solar Cell Fabrication

The technological development of monolithic perovskite/silicon tandem solar cells from first working tandem cells in the newly established Innovation Lab HySPRINT in 2017 towards the certified world record in early 2020 is a key element of this thesis. Therefore, the fabrication of perovskite single-junction solar cells, silicon bottom cells and the resulting perovskite/silicon tandem solar cell will be described in this section for the baseline fabrication processes. Note that this is the baseline recipe and some of the steps were adjusted in the different publications. The specific changes towards baseline solar cells devices will be declared in the respective sections (alternatively: See original studies in appendix E, F and G) and the proper characterization as well as electrical and optical simulation of the samples will be explained in the next chapter. For several characterization methods, entire solar cell or tandem device stacks were fabricated and developed. For other characterization methods only selected layers were implemented into the device stack as will be described below.

4.1 Perovskite Single-Junction Solar Cells

This section describes the fabrication of baseline p-i-n perovskite single-junction solar cells as used in this work.

Materials

Anhydrous (anh.) DMSO (dimethyl sulfoxide), anh. DMF (dimethylformamide), anh. anisole, ethylacetate, PTAA (poly[bis(4-phenyl)(2,5,6-trimentlyphenyl)amine]) and LiF (lithium fluoride; purity$\geqslant$99.99%) were purchased from Sigma Aldrich. C_{60} (sublimed) was bought from CreaPhys GmbH. FAI (formamidinium iodide) and MABr (methylammonium bromide) were purchased from Dyenamo. PbI_2 and $PbBr_2$ were provided by Tokyo Chemical Industry Co., Ltd. (TCI). CsI (cesium iodide; 99.999%) was purchased from abcr GmbH. The ceramic 2-inch IZO target ($90\%_{wt}$ In_2O_3 and $10\%_{wt}$ ZnO was purchased from FHR Anlagenbau GmbH. The self-assembled monolayer (SAM) MeO-2PACz ([2-(3,6-dimethoxy-9H-carbazol-9-yl)ethyl]phosphonic acid) and 2PACz ([2-(9H-carbazol-9-yl)ethyl]phosphonic acid) were synthesized by TCI. Me-4PACz ([4-(3,6-dimethyl-9H-carbazol-9-yl)butyl]phosphonic acid) is synthesized at Kaunas University of technology and detailed described in the publication of Al-Ashouri and Köhnen *et al.*[99] ethanol (anh.) for the SAMs was bought from VWR. TDMASn (Tetrakis(dimethylamino)tin(IV); precursor for SnO_2, 99.99% Sn) was purchased from STREM Chemicals, Inc.

Solar Cell Fabrication

The perovskite solar cell was deposited on indium tin oxide (ITO)-covered glass (Automated Research GmbH, 15 Ohm sq^{-1} sheet resistance), which was cleaned with Mucasol (Schülke; 2% in DI-water), DI-water, acetone and isopropanol, each for 15 minutes in an ultrasonic bath. Afterwards the substrates were cleaned 10-15 minutes in an UVOH 150 LAB (FHR) tabletop UV-ozone cleaner. The single-junction cell configuration is ITO/HSL/Perovskite/(LiF)/C_{60}/SnO_2/Ag, where the hole-selective layer (HSL) is PTAA, MeO-2PACz, 2PACz or Me-4PACz, the optional LiF is lithium fluoride, SnO_2 is tin oxide and Ag is silver. All the spin-coating layer deposition steps were conducted in a nitrogen atmosphere. The hole-transport material PTAA (2 mg ml^{-1} in toluene) was deposited using spin coating (5000 rpm for 30 s, 5 s acceleration), followed by heating for 10 min at 100 °C. The rotation was reduced for the SAM-solutions to 3000 rpm (used concentration of the SAM solutions=1 mmol l^{-1}, or ~0.3 mg ml^{-1} in anhydrous ethanol). The perovskite was prepared following the typical triple cation process.[78] In short, 1.5 M nominal PbI_2 and $PbBr_2$ in DMF:DMSO = 4:1 volume were first prepared as stock solutions (shook overnight at 60 °C) and then added to FAI and MABr with 9% PbX_2 excess, respectively (X = I or Br). The so obtained $FAPbI_3$ and $MAPbBr_3$ with a nominal concentration of 1.24 mol l^{-1} were then mixed in 83:17 volume ratio to obtain the baseline perovskite (E_G =1.63 eV). For the

wide bandgap (E_G =1.68 eV) a volume ratio for FAPbI$_3$ to MAPbBr$_3$ of 77:23 was used. Finally, 5%$_{vol}$ of 1.5 M nominal CsI in DMSO was added to the perovskite precursor. 100 µl of perovskite solution was then spread on the substrate and spun with a SC-210 (MBraun) spin coater using one step spin-coating process (4000 rpm for 35 s, 5 s acceleration). 25 s after starting the program, 500 µl ethylacetate (for section 6.1 and 6.3) or 250 µl anisole (for section 6.2) as the antisolvent was dripped on the film. The films were then annealed at 100 °C for 60 min (section 6.1) or 20 min (section 6.2 and 6.3) on a PZ28-2 hotplate (Präzitherm). Afterwards, 20 nm of C$_{60}$ were thermally evaporated with a ProVap T5 or EcoVap (MBraun) at a rate of 0.15 Å s^{-1} onto the perovskite film. Optionally, as indicated, a 1 nm thick LiF interlayer was deposited between C$_{60}$ and perovskite, evaporated at a rate of 0.05 Å s^{-1}, within the same vacuum run as the C$_{60}$ layer. 20 nm of SnO$_2$ were then deposited by thermal ALD in an Arradiance GEMStar reactor. Tetrakis(dimethylamino)tin(IV) (TDMASn) was used as the Sn precursor and was held at 60 °C in a stainless-steel container. Water was used as an oxidant, and was delivered from a stainless-steel container without active heating, whereas the precursor delivery manifold was heated to 115 °C. Initially, the depositions were done at 120 °C (see section 6.1). However, after reduction to 80 °C, the TDMASn/purge1/H$_2$O/purge2 times were 1 s/10 s/0.2 s/15 s with corresponding nitrogen flows of 30 sccm/90 sccm/90 sccm/90 sccm. With this, 140 cycles lead to 20 nm tin oxide. Finally, 100 nm Ag films were deposited by thermal evaporation in a ProVap T5 or EcoVap (MBraun) at a rate of 1 Å s^{-1}. The substrates were designed in a way that 6 electrical independent solar cells with an active area of 0.16 cm^2 are fabricated on one substrate. The schematic stack and device layout is shown in Figure 10A and B.

4.2 Monolithic Perovskite/Silicon Tandem Solar Cells

In this section, the fabrication of monolithic perovskite/silicon tandem solar cells is described.

4.2.1 Silicon Bottom Cell

For the studies described in 6.1, 6.2 and 6.3, the silicon heterojunction (SHJ)-bottom cell was fabricated from a 280 µm thick, ~3 Ω cm polished FZ <100> n-type crystalline silicon (c-Si) wafer in a rear-junction configuration. Additionally, for the results in section 6.3, <100>-oriented 130 µm thick (as-cut) n-type CZ silicon with saw damage etched front side was used. The front surface of the wafer was left unchanged by capping with a PECVD deposited SiO$_2$ prior to wet texturing to obtain random pyramids with <111> facets. After removal of the capping in HF another final RCA clean and HF dip (1% dilution in water) were done and an approx. 5 nm thick, intrinsic (i) amorphous silicon (a-Si:H) layer stack was grown on both sides of the c-Si wafer in order to passivate the c-Si surface. On the textured rear-side, an approx. 5 nm thick, p-doped a-Si:H layer stack was deposited to form the hole contact (junction). On the polished front side, a 20 nm thick, n-doped nanocrystalline silicon oxide layer (nc-SiO$_x$:H) with a refractive index, n, of 2.7 at 633 nm was used as the electron contact of the SHJ bottom cell and the optical intermediate layer between the top and the bottom cells. Note that after a first optimization in section 6.1 the thickness was increased to 90 nm. The a- and nc-Si layers were deposited with an Applied Materials (AKT1600) plasma enhanced chemical vapor deposition (PECVD) cluster tool. In order to contact the bottom cell a ZnO:Al/Ag layer stack was deposited on the textured rear side and a 20 nm (70 nm thick for single-junction references) thick ITO layer was deposited on the polished front side on top of the nc-SiO$_x$:H interlayer. Both depositions were DC-sputtered in an in-line sputter tool from Leybold Optics using Ar/O$_2$ gas mixtures. For the ITO a tube target with 95/5 doping ratio and for the AZO a tube target with 1% Al$_2$O$_3$ in ZnO was used. The ITO on the front side as well as the AZO/Ag on the rear side were deposited using aligned shadow masks with an opening of 1.0 cm×1.0 cm (2 cm×2 cm for single-junction reference cells). Note that this changed to 1.13 cm×1.13 cm after the first publication in section 6.1 to obtain a larger active area for certified and acknowledged tandem solar cells. For single-junction reference cells with an aperture area of 2 cm×2 cm, an Ag grid was screen-printed on top of the front ITO. For single-junction silicon solar cells in section 6.1, a IZO layer is deposited on top of the ITO to obtain a thick TCO and hence better series resistance. Subsequently,

a metal frame for charge collection is evaporated as described in the next section. For the top cell fabrication, the wafers were laser-cut into 2.5 cm×2.5 cm pieces

4.2.2 Perovskite Top Cell

The as-fabricated bottom cells were blown with N_2 and ethanol was spin coated at 3000 rpm to remove dust particles. Subsequently, the bottom cells were UV-O_3-treated for 15 minutes. The same HSL, perovskite, (LiF), C_{60} and SnO_2 deposition as described above was conducted on the silicon bottom cells. Subsequently, before any optimization, 130 nm IZO (Roth&Rau MicroSys 200 PVD) were deposited by sputtering. After optimization in section 6.1, the thickness was reduced to 90. At a RF-power of 70 W the cells oscillated with an angle of ±15° under the target to have a uniform deposition. After initial optimization (section 6.1), the amount of oxygen in the chamber was set to $0.2\%_{vol}$. A 100 nm silver frame was thermally evaporated through a shadow mask to collect the charge carriers without a need of grid fingers. Lastly, 100 nm LiF were evaporated as an anti-reflective coating by thermal evaporation. The cell area was defined by the inner metal frame and is ~ $0.78\,cm^2$ for the first publication in section 6.1 and ~ $1\,cm^2$ for all other publications (section 6.2 and 6.3).

However, as the evaporation mask consisting of one part can not create a complete ring in a single evaporation process but a split ring-type busbar as shown in Figure 10D, the illumination area is not perfectly defined by the metal. Two solutions were used to designate the active area. Either, a laser-cut black paper mask (also shown in Figure 10D) was used, just smaller as the inner metal frame to define the illumination area or two evaporation runs were carried out with the masks being rotated by 90° to obtain a complete ring (see Figure 10E). The latter approach took longer for fabrication but did not require precise alignment of the aperture mask to cover the part of the substrate outside of the metal frame. The active area was then measured with a digital optical microscope.
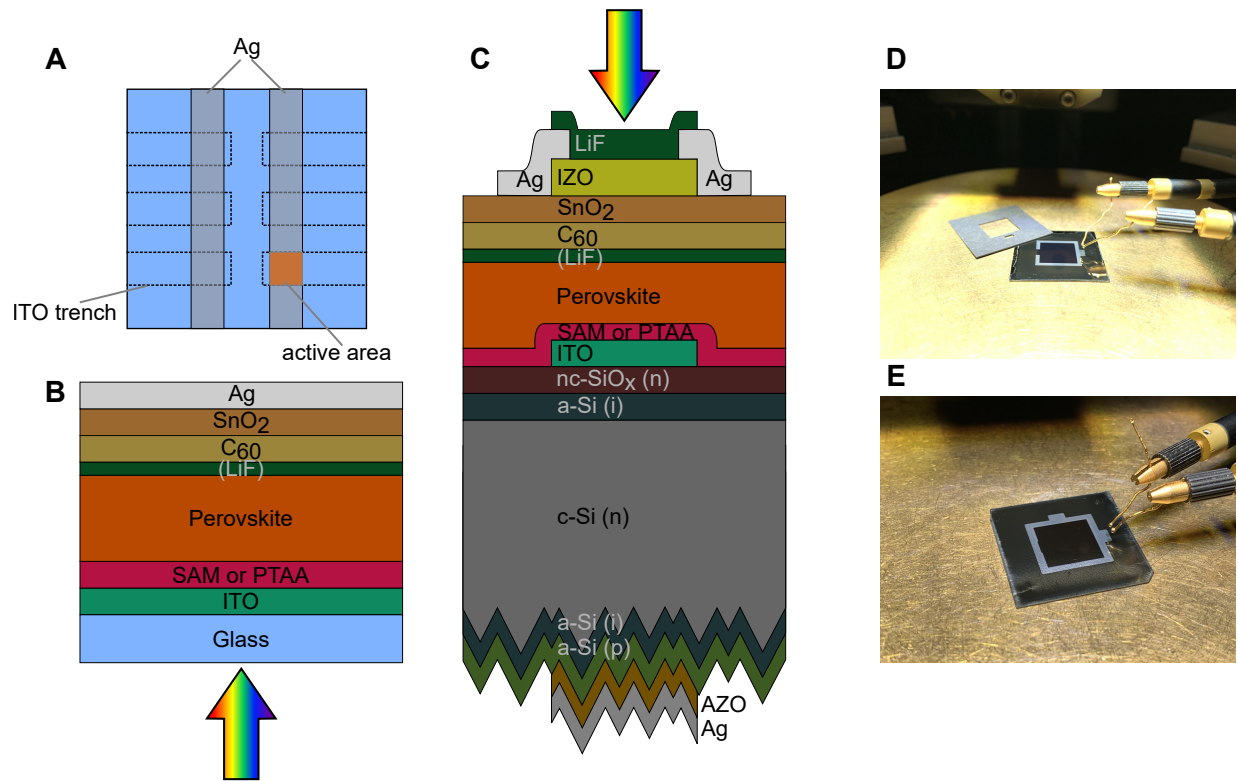
Figure 10: Single-junction and tandem solar cells (A) Schematic device layout of perovskite single-junction solar cells used in this work. The device design enables 6 independent solar cells on one substrate. The active area is defined by the overlap of the separated ITO area and silver stripe. (B) Schematic stack of perovskite single-junction solar cells used in this work. (C) Schematic stack of the tandem solar cells used in this work. (D) Tandem solar cell placed on a brass chuck in the light of the solar simulator. Two gold needles with sphere-shaped tips are used to contact the front side. (E) Tandem solar cell with a complete metal frame which defines the active area precisely.

5 Characterization and Simulation

To develop and optimize solar cells, advanced characterization methods are necessary to understand the loss mechanisms and fundamental principles of the device operation. Especially for two-terminal tandem solar cells, where the individual subcell properties are not easily accessible, these methods are of highest importance. The gained knowledge from the detailed characterization can be used for electrical and optical simulations to thoroughly understand the device physics. This section will address the characterization methods to analyze single-junction and tandem solar cells. In addition, the fundamentals of electrical and optical simulations are covered.

5.1 External Quantum Efficiency

The external quantum efficiency (EQE) spectra of a solar cell gives information about the optical performance of the solar cell as a function of the incident wavelength. It gives information about how efficiently photons are converted into electron-hole pairs. An EQE of 1 (or 100%) means that every incident photon at that specific wavelength generates an electron-hole pair and that these charges can be collected at the electrodes and the given bias condition (typically short-circuit). Thus, as previously already addressed, it is connected to the photogenerated current density J_{Ph}, which can be calculated according to equation 2.10. In combination with the spectrally resolved reflection it is possible to disentangle losses stemming from reflection, parasitic absorption (e.g. in contact layers) or ineffective charge collection.[20] As typically the J_{SC} of a single-junction is close to the J_{Ph} (see section 2.6), this characterization can give a verification of correct measurement settings such as active area and/or illumination intensity. The EQE is also necessary to establish accurate power conversion efficiencies, because it determines the spectral mismatch between light from the solar simulator and tabulated AM1.5g spectrum.[52] More details to this procedure will be found in section 5.2. The method is especially important for monolithic multijunction solar cells to separately measure the photogenerated current densities of the subcells. However, to measure multijunction solar cells, a slightly advanced setup is needed.[52] Metrologically, the spectral response (SR) is measured,[20] which is given as the ratio of current extracted from the solar cell to the power incident on the solar cell. The SR and EQE are connected via

$$\mathrm{EQE}(\lambda) = \mathrm{SR}(\lambda)\frac{hc}{q\lambda} \tag{5.1}$$

In the following two sections, the method to characterize single-junction solar cells and tandem solar cells are covered separately.

5.1.1 Perovskite Single-Junction Solar Cells

EQE spectra of perovskite single-junction solar cells were recorded with an Oriel Instruments QEPVSI-b system with a Newport 300 W xenon arc lamp, controlled by TracQ-Basic software. The light was chopped at a frequency of 78 Hz and a Newport Cornerstone 260 monochromator was used to generate monochromatic light. The increment amounted to 10 nm. The system is calibrated using a silicon reference cell with known spectral response before every measurement session. The electrical response of the device under test is measured with a Stanford Research SR830 Lock-In amplifier and evaluated in TracQ software. All measurements were conducted in nitrogen atmosphere.

5.1.2 Tandem Solar Cells

Measuring the EQE spectra of series-connected tandem solar cells becomes more difficult as the cell is only able to pass current properly when both, wide-bandgap top cell and narrow-bandgap bottom cell are simultaneously excited with light. As described previously (section 2.9.3), the extracted current is determined by the subcell with a lower current generation. Hence, the subcell under investigation needs

to be current limiting in the entire wavelength range. To achieve this, bias light with proper wavelength is used to generate charge carriers in either the top cell or the bottom cell (in the following termed *flooded cell*) and no or very low amount of charge carriers in the non-biased cell (in the following termed *cell under investigation*). The choice of bias light depends on the absorption characteristics of the subcells.[52] To flood the silicon bottom cell (but not the perovskite top cell), we use an LED with a peak emission wavelength of 850 nm (corresponding to a photon energy below the bandgap of the perovskite top cell). For the selective illumination of the perovskite top cell, an LED with a wavelength of 455 nm is chosen (corresponding to a photon energy well above the bandgap of the perovskite top cell).

Usually, the EQE is measured at short-circuit conditions. However, if one subcell (e.g. silicon) is illuminated to measure the response of the cell under investigation (e.g. perovskite), the flooded cell will generate a photovoltage. As the outer terminals will be kept at a fixed bias, i.e. short-circuit, the cell under investigation will operate at approximately $-V_{OC}$ of the flooded cell. The amount of photovoltage generated by the flooded cell from bias illumination depends on the cell type but also on the intensity of the illumination. Note that, as the V_{OC} scales logartihmically with intensity (see equation 2.22) and the bias light needs to be intense to fulfill flooding, the photovoltage approaches V_{OC} close to values under AM1.5g illumination conditions. Depending on the performance of the subcell under investigation (especially on the characteristics around $V = 0$) this can lead to overestimation of the EQE. To compensate this voltage, an electrical bias-voltage is necessary in order to measure the EQE at short-circuit conditions for the cell under investigation. Gilot *et al.* gives a guide how to determine the amount of voltage that has to be applied to compensate for this effect.[52] In our case, the voltage is chosen to be 80-90% of the V_{OC} expected under 1-sun AM1.5g illumination. Thus, if the perovskite subcell is investigated, the silicon bottom cell is flooded with near-infrared (NIR) light and an additional voltage of 0.6 V is applied. To measure the EQE of the silicon bottom cell, the perovskite subcell is flooded with blue light and the bias-voltage amounts to 0.9-1 V.

Note that, as the photocurrent of the silicon and perovskite sub-cells are rather linear with intensity in the flooding regime, no light intensity correction was applied.[52] All measurements were done in ambient conditions.

5.2 Solar Simulator Calibration and Mismatch Correction

The correct illumination of solar cells is a crucial requirement to evaluate the performance correctly. As the light generated from solar simulators typically differs from the AM1.5g standard spectrum, corrections need to be applied in order to simulate AM1.5g conditions and thus, correctly measure the solar cells. These mismatch corrections can be different for single-junction and tandem solar cells.

For single-junction solar cells, a calibrated reference solar cell is used to calibrate the intensity of the light source. With the knowledge of the spectral response of the reference cell and of the cell under investigation, as well as the knowledge of the reference AM1.5g spectrum and the spectrum emitted by the solar simulator, the spectral mismatch factor can be calculated.[114]

In our case, a Oriel LCS-100 light source is used to illuminate the single-junction solar cells. As the reference cell, a KG3 filtered silicon cell calibrated by Fraunhofer ISE CalLab, provides almost the same spectral response as the perovskite cells under investigation, the mismatch factor is with 0.997 close to unity and thus, the intensity was simply calibrated to the reference cell.

For tandem solar cells, the spectral mismatch correction becomes more difficult but also more important as not just the J_{SC} depends on the illumination, but also the FF is affected by the current mismatch (see Emery *et al.*[115] and section 6.1). Although it is possible to apply the same mismatch correction for each subcell as is done for single-junction solar cells, this method is time-consuming. Thus, Meusel *et al.* proposed a faster way to perform spectral mismatch correction.[116] To do so, a multi-source solar simulator is necessary to adjust the spectrum in different wavelength ranges. For tandem solar cells, it is sufficient to have two individual adjustable light sources. Ideally, the light sources are chosen such that the current generation in each subcell is mainly caused by one of the light sources. Additionally, at least one reference cell which covers the spectral sensitivity range of both subcells is needed. To reduce uncertainty, it is

beneficial to use two reference cells with spectral sensitivities matching with the subcells of the tandem solar cell. For the mismatch calibration it is necessary to know the relative spectra of the two light sources as well as the relative spectral responses of each subcell and reference cell. Ultimately, the short-circuit current densities of the reference cells are calculated and corrected by the mismatch factor calculation[114] and the corresponding light sources are set to obtain the correct illumination for the tandem solar cell.[116]

Under certain circumstances it is possible to simplify the calibration process without the need to know the exact spectrum and use calibrated reference solar cells. For sufficiently high shunt resistances of the subcells, the tandem J_{SC} is determined by the photogenerated current density of the limiting subcell. If light sources which can tune the photogenerated current density of one subcell without changing the J_{Ph} of the other subcell, are available, the correct J_{Ph} values of both subcells can be obtained by the following procedure.

If we assume a perovskite/silicon tandem solar cell with silicon as the limiting subcell, we expect the J_{SC} of the tandem solar cell to be equal to the J_{Ph} of the silicon subcell obtained by integration of the EQE spectrum according to equation 2.10. To access the J_{Ph} of the perovskite subcell, the LED intensity in the infrared wavelength range is increased until the tandem solar cell J_{SC} is perovskite limited. Thus, then the J_{SC} is determined by the perovskite subcell. Now, the intensity in the visible wavelength range can be adjusted until the tandem J_{SC} is equal to the J_{Ph} of the perovskite top cell, obtained from the EQE integration (and AM1.5g illumination). Subsequently, the intensity of the visible wavelength range is fixed and in the infrared range decreased again until silicon bottom cell is the limiting subcell and the J_{SC} of the tandem solar cell matches with the J_{Ph} of the silicon obtained from EQE integration. Similarly, this can be done for perovskite limited or current matched tandem cells.

It is of highest importance that the last step (in this example: changing the NIR intensity) will not affect the current in the perovskite subcell, i.e. the intensity in the visible range. Hence, a light source with a wavelength range should be chosen where the EQE of the perovskite subcell is zero.

To reduce uncertainties, the initial spectrum should be close to the AM1.5g spectrum.

For the $J-V$ measurements conducted for tandem solar cells in this dissertation, a Wavelabs Sinus-70 solar simulator is used, which is rated class AAA and exceeds the spectral class A significantly. The 21 spectrally different LED types enable the previously mentioned calibration method. To obtain the initial spectrum, which is close to the AM1.5g spectrum, the internal spectrometer including the feedback loop is utilized.

5.3   Current Density - Voltage Characteristics

To measure the current density - voltage ($J-V$) characteristic of a perovskite single-junction solar cells, the light is calibrated as described in section 5.2. The $J-V$ curve is then recorded using a Keithley 2400 source-measure unit, controlled by a custom LabView program. $J-V$ scans and MPP-tracks were performed in a nitrogen filled glovebox using two-wire sensing. The typical step size was 20 mV, with an integration time of 20 ms and settling time of 20 ms (250 mV s^{-1}). MPP-tracks were recorded using voltage perturbation.

To measure the $J-V$ characteristics and MPP-tracks of tandem solar cells in air, the solar simulator was calibrated as described in section 5.2. The backside of the cell was contacted with a metal vacuum chuck at 25 °C, whereas the front side was contacted with two Au probes. A black laser-cut aperture mask covered the substrate outside of the active area. The typical voltage step size was 20 mV, with an integration time of 20 ms and settling time of 20 ms (250 mV s^{-1}). MPP-tracks were recorded using voltage perturbation.

5.4   Reflection, Transmission and Absorption

The spectrally resolved reflection and transmission measurements were conducted with a Perkin Elmer Lambda $-$ 1050 UV/vis/NIR spectrophotometer using an integrating sphere. Reflection and transmission were measured as a function of wavelength from 300 to 1200 nm with an increment of 10 nm. The instrument

was calibrated with a white spectralon reflection standard. The absorption can be calculated according to equation 2.9

5.5 Photoluminescence and Electroluminescence

In the following, three methods will be described which are used to measure the radiative recombination and thus, the QFLS.

5.5.1 Absolute Photoluminescence

Photoluminescence of the perovskite top and the silicon bottom cell was recorded under selective excitation using a 445 nm or 808 nm CW laser from Insaneware (for the measurements on tandem solar cells presented in section 6.3). For the measurements of perovskite single-junction solar cells, a 520 nm laser from Insaneware is used. The lasers were coupled through an optical fiber into an integrating sphere. The intensity of the lasers was adjusted to a one sun equivalent intensity, which matched the current density generated within each subcell. The photoluminescence was then detected via a second optical fiber that coupled the output of the integrating sphere to an Andor SR393i-B spectrometer equipped with an Andor iDus silicon CCD camera and an iDus InGaAs (1.7 μm) detector array. Photoluminescence from the perovskite was then measured with the silicon CCD, while the silicon bottom cell PL was measured with the InGaAs detector. The system was calibrated using a calibrated halogen lamp with specified spectral irradiance, which was directed into the integrating sphere. For each detector array, a spectral correction factor was calculated to match the detector's spectral output to the calibrated spectral irradiance of the lamp. The spectral photon density was obtained from the corrected detector signal (spectral irradiance) by division through the photon energy ($h\nu$), and the photon numbers of the excitation and emission obtained from numerical integration using Matlab. We corroborated the accuracy of derived PLQY values for the Si detector by measuring three fluorescent test samples with high specified PLQY (~70%) supplied from Hamamatsu Photonics, where the specified value could be accurately reproduced within a small relative error of <5%. The accuracy of PLQY values measured with the InGaAs detector was double-checked with the Si detector.

The QFLS was then calculated in the individual subcells by using the Shockley-Queisser equation, which links the radiative recombination current density of free charges (J_{rad}) with the chemical potential per free electron-hole pair (μ) or the quasi-Fermi level splitting (QFLS) in the respective active material.[28, 117]

$$J_{\text{rad}} = J_{0,\text{rad}} \cdot e^{\left(\frac{\text{QFLS}}{kT}\right)} \tag{5.2}$$

with $J_{0,\text{rad}}$ calculated as in equation 2.27. If radiative recombination comes only from free charges, the radiative recombination current is identical to the photoluminescence yield times the elementary charge, that is $J_{\text{rad}} = \phi_{PL}$. Moreover, we can define the photoluminescence quantum yield (PLQY) as the ratio of radiative to total recombination ($J_{R,tot}$) current density.[25] At open-circuit conditions, no net current is flowing and thus the total recombination current density equals the photogenerated current density:

$$\text{PLQY} = \frac{J_{\text{rad}}}{J_{\text{R,tot}}} = \frac{J_{\text{rad}}}{J_{\text{Ph}}} \tag{5.3}$$

The QFLS is then given by

$$\text{QFLS} = kT \ln\left(\text{PLQY}\frac{J_{\text{Ph}}}{J_{0,\text{rad}}}\right) \tag{5.4}$$

with $T = 300\,\text{K}$ and J_{Ph} approximated with the photogenerated current density of a complete solar cell under AM1.5g illumination. Equation 5.3 is only valid if the spectral dependence of J_{rad} is identical to $J_{0,\text{rad}}$, meaning recombination goes through the same channels regardless of the QFLS.

5.5.2 Hyperspectral Absolute Photoluminescence Imaging

Absolute PL imaging measurements of tandem solar cells were performed with two 450 nm LEDs for the perovskite subcell and with an 850 nm LED for the excitation of the silicon subcell. The excitation intensities for both measurements were set to $1.4 \times 10^{21}\,\mathrm{m^{-2}\,s^{-1}}$. The photoluminescence image detection was performed with a charge-coupled device (CCD) camera (Allied Vision) for the perovskite subcell and with an InGaAs based camera for the Si subcell. Both cameras were coupled with a liquid crystal tunable filter unit. The systems were calibrated to absolute photon numbers.

The QFLS was then calculated by fitting the high-energy wing of the PL emission spectra.[118]

5.5.3 Hyperspectral Absolute Electroluminescence Imaging

Quantitative electroluminescence (EL) imaging in section 6.2 was performed by sweeping a voltage between 1.4 and 2.0 V with a 2 mV voltage step and 0.5 s dwell time. The dark current J_{dark} was recorded for the sweeps. To avoid large data collection a luminescence image at every step for every subcell was recorded at the energy of maximum emission. The intensity of the images was scaled to absolute photon numbers with a full hyperspectral image collected at a given injection. This results in a data set containing the electroluminescence yield of each subcell (i) $\phi_{\mathrm{EL}}^{\mathrm{i}}(J_{\mathrm{dark}})$ as a function of the injected current density. The radiative current density of every subcell $J_{\mathrm{rad}}^{\mathrm{i}}$ is calculated by $q\,\phi_{\mathrm{EL}}^{\mathrm{i}}(J_{\mathrm{dark}})$. Finally, the QFLS values of the subcells are calculated with

$$\mathrm{QFLS^i} = kT\ln\left(\frac{J_{\mathrm{rad}}^{i} + J_{0,\mathrm{rad}}^{\mathrm{i}}}{J_{0,\mathrm{rad}}^{\mathrm{i}}}\right) \tag{5.5}$$

5.6 Variable Angle Spectral Ellipsometry

The optical constants n and k, so the complex refractive index, was determined by variable angle spectral ellipsometry. Measurements were performed in air using a Sentech SE 850 DUV ellipsometer. For IZO a triple Tauc-Lorentz oscillator with a Drude term was used as proposed in [119]. For SnO_2, a double Tauc-Lorentz and Cauchy for the native oxide underneath was used. To extract the optical properties of a perovskite, a film deposited directly on a fused quartz substrate was measured at 35-70° with 5° steps. Fitting was performed point-by-point, without using dispersion models. The film and surface roughness thicknesses were determined by minimizing the sum of all errors for each wavelength. The procedure is described in detail in [120].

5.7 X-Ray Diffraction

For the X-Ray diffraction patterns a Bruker D8 diffractometer in Bragg-Brentano geometry was used. The X-Ray tube was operated at 40 mA and 40 kV acceleration voltage, emitting Cu K-alpha radiation. All X-Ray diffraction patterns were recorded at room temperature using a self-constructed nitrogen filled sample holder.

5.8 Scanning Electron Microscopy

Scanning electron microscopy (SEM) is a practical method to obtain images from thin films.[118] In this method, an electron beam is focused on the surface of the sample from which a part of the electrons are reflected elastically and another part of them releases secondary electrons from the material of the sample. The reflected as well as the released electrons are perceived at their respective detector and the system processes their intensities to yield brightness levels. When the whole sample has been scanned with the electron beam, a two dimensional image of the scanned surface can be developed.

The measurements were carried out in a MERLIN microscopy system by Zeiss.

5.9 Electrical Simulation

5.9.1 SPICE Simulation

To simulate the electrical behavior of solar cells, a equivalent circuit diagram is created via SPICE (Simulation Program with Integrated Circuit Emphasis) with the simulation tool LTspice.[121] The electrical simulations for section 6.1 were done as follows:

For the electrical parametrization, single-junction silicon and perovskite solar cells were fabricated with comparable contact design as used in the tandem stack; both cells are then measured at different intensities to extract the ideality factors n_{ID}. This is done by plotting V_{OC} against $\ln(J_{\mathrm{SC}})$ and calculating the slope. The saturation current J_0 is adjusted in a way that the experimental and simulated V_{OC} coincide. The series and shunt resistances R_{S} and R_{SH} are adjusted in a way that the slope around $V = V_{\mathrm{OC}}$ and $V = 0$ of the simulated $J - V$ curves fit to the experimental results. To simulate the tandem $J - V$ curves, both parameterized reference subcells are connected in series. As the V_{OC} of the monolithic tandem solar cell is slightly lower than the sum of the single-junction solar cells, which most likely stems from a lower V_{OC} of the perovskite sub-cell, the J_0 of the perovskite is slightly adjusted until the simulated and experimentally measured tandem V_{OC} matched.

The SPICE simulations were conducted similarly for the study discussed in section 6.2. However, to access the parameter for the perovskite and silicon subcell, the reconstructed subcell $J - V$ curves were fitted using a one-diode model. Subsequently, the tandem solar cell was again constructed by series connection of both one-diode equivalent circuits.

5.9.2 Quokka Simulation

To simulate the $J - V$ parameters of the silicon heterojunction solar cells used for bottom devices in section 6.3, the Quokka3 simulation tool was utilized.[122] Most parameters are equal for CZ and FZ wafers in this case except for the wafer resistivity which was acquired via quasi steady-state photo conductance decay (QSSPC) measurements from the experimental wafers using a WCT-120 tester by Sinton Instruments. A short flash pulse creates excess electron-hole pairs in the silicon bulk generating photo induced conductance. From the measured photo conductance decay, the effective minority carrier lifetime can be extracted.[123] The obtained wafer resistivities (ρW) were 7 and $3\,\Omega\,\mathrm{cm}$ for the CZ and the FZ wafer, respectively. Apart from this parameter, the wafers differ on their electron and hole lifetime (τ_{n}, τ_{p}) which were set to 3000 and 6000 μs for the CZ and the FZ wafer, respectively. The wafer thickness was varied from 100 to 340 μm to highlight the behavior of the $J - V$ parameters of the bottom cells in dependence of this parameter.

5.10 Optical Simulations

Optical simulations were performed using the Matlab based software GenPro4. It is based on the extended net-radiation method in which ray optics and wave optics are combined in a computationally efficient way.[124] The first and last layers are set to be incoherent (i.e. thick compared to the coherence length of the incident sunlight of ~1 μm) infinitely-thick air. Additionally, the silicon wafer is treated incoherently, as the thickness of several hundred μm exceeds the coherence length of the sunlight, too. All other layers were treated coherently (i.e. interference does play a role). Just as in the manufactured devices, the rear side of the silicon bottom cell, including all layers deposited on the rear side of the silicon wafer, is textured using an AFM measured topography image as input. All other interfaces were considered to be optically flat. The refractive indices n and extinction coefficients k are obtained either by spectral ellipsometry measurements (IZO, SnO_2, C_{60}, ITO, nc-SiO_x and AZO) or taken from standard literature. For the results presented in section 6.1, the optical data for the perovskite was taken from literature[125] but adjusted in n and k to match with the correct bandgap, as it was previously used by Albrecht *et al.*[126]

For the results in section 6.3, the optical parameters of the perovskite were extracted from in-house fabricated triple-cation ($Cs_{0.05}(MA_{0.17}FA_{0.83})Pb(Br_{0.17}I_{0.83})_3$) perovskite layers and subsequently shifted in

n and k around the absorption onset to cover a perovskite bandgap range of $1.63\,\text{eV}$ to $1.78\,\text{eV}$.

From the absorption spectra A_i obtained from the GenPro4 simulations, the photogenerated current density absorbed in each layer (i) is calculated with

$$J_{\text{Ph,i}} = q \int A_i(\lambda) \Phi_{\text{ph},\lambda} d\lambda \tag{5.6}$$

Without substantial charge collection losses, the absorption in the perovskite and silicon will be equal to the their respective EQE spectra. Hence, equation 5.6 and 2.10 will be equal.

6 Results

This section will introduce several innovations and thorough investigations related to perovskite/silicon tandem solar cells. It is divided into three parts based on the three studies which were published in peer-reviewed journals.

1. The first publication addresses the optical optimization of two-terminal monolithic perovskite/silicon tandem solar cells. The improved deposition processes increased the PCE from certified 25.0% to 26.0%. However, the improved current-mismatch conditions reduced the FF of the optimized solar cell. A thorough analysis of the current-mismatch conditions on the performance of tandem solar cells is presented, which includes the measurement of tandem solar cells with various illumination spectra and continuative electrical simulations.

   The publication can be found in appendix E.

   - Publication:
     Eike Köhnen, Marko Jošt, Anna Belen Morales-Vilches, Philipp Tockhorn, Amran Al-Ashouri, Bart Macco, Lukas Kegelmann, Lars Korte, Bernd Rech, Rutger Schlatmann, Bernd Stannowski, and Steve Albrecht. Highly efficient monolithic perovskite silicon tandem solar cells: analyzing the influence of current mismatch on device performance. *Sustainable Energy & Fuels*, 3(8):1995–2005, 2019. https://doi.org/10.1039/C9SE00120D.

   - Author contribution:
     E.K., M.J., P.T., A.A. and Lu.K. developed and optimized the perovskite solar cell fabrication process; E.K. fabricated the perovskite top cell, performed the *J-V*, EQE, Hall and UV-Vis measurements and optimized the top contact; A.B.M.V., La.K. and B.S. developed and optimized the silicon-heterojunction solar cell fabrication process and fabricated bottom cells; B.M. and E.K. optimized the SnO_2 process and performed and analyzed spectroscopic ellipsometry measurements; E.K., P.T. and A.A. performed the optical and electrical simulations; E.K. drafted the manuscript; All authors participated in proofreading and correcting; B.R., R.S., B.S. and S.A. initiated and supervised the project.

2. The second publication presents a newly designed hole-selective layer (HSL) for p-i-n perovskite solar cells. The combination of an excellent interface, which enables high V_{OC} values and fast charge extraction leading to high FF values and improved photostability makes the self-assembled monolayer *Me-4PACz* advantageous compared to other HSL. The utilization in tandem solar cells enabled PCE values up to certified 29.15%, which was a world record at that time. The presentation of high PCE values is accompanied by long-term MPP-tracks of tandem solar cells using various HSL. Furthermore, detailed analysis using hyperspectral absolute electroluminescence imaging enabled the reconstruction and evaluation of the individual subcell performances. The extracted parameters are used to simulate the tandem solar cell electrically and reveal its PCE potential.

   The accepted version can be found in appendix F.

   - Publication:
     Amran Al-Ashouri, Eike Köhnen, Bor Li, Artiom Magomedov, Hannes Hempel, Pietro Caprioglio, José A Márquez, Anna Belen Morales Vilches, Ernestas Kasparavicius, Joel A. Smith, Nga Phung, Dorothee Menzel, Max Grischek, Lukas Kegelmann, Dieter Skroblin, Christian Gollwitzer, Tadas Malinauskas, Marko Jošt, Gašper Matič, Bernd Rech, Rutger Schlatmann, Marko Topič, Lars Korte, Antonio Abate, Bernd Stannowski, Dieter Neher, Martin Stolterfoht, Thomas Unold, Vytautas Getautis, and Steve Albrecht. Monolithic perovskite/silicon tandem solar cell with >29% efficiency by enhanced hole extraction. *Science*, 370(6522):1300–1309, 2020. https://doi.org/10.1126/science.abd4016.

- Author contribution:
  A.A.-A. and Ei.K. contributed equally, A.A.-A., Ei.K., and S.A. planned the experiments, coordinated the work and prepared the figures; Er.K., A.M., and T.M. designed and synthesized the Me-4PACz SAM and the (Me-)nPACz series; A.A.-A. and B.L. processed the single-junction cells and optimized the SAM deposition; A.B.M.V. processed the Si bottom cells and measured Si single-junction solar cells; Ei.K. and B.L. processed the perovskite top cells; Ei.K. planned the analysis of the tandem solar cells, measured $J - V$, EQE and reflection of all tandem solar cells and performed short-term (incl. elevated temperature) MPP-tracking; A.A.-A., H.H., and J.A.M. conducted and analyzed the PL experiments; Ei.K., J.A.M. and A.A.-A. conducted and analyzed the EL studies; Ei.K. performed the subcell fitting and electrical simulations; H.H. recorded the terahertz measurements and performed the data analysis; P.C., M.G., and M.S. conducted the pseudo–$J - V$ and FF-V_{OC} loss analysis (intensity-dependent V_{OC} and QFLS) of films and single-junction solar cells; D.M. performed the photoelectron spectroscopy; J.A.S., D.S., and N.P. performed crystallographic analysis; G.M., M.J., B.L., and Ei.K. designed and built the tandem aging setup and recorded the long-term MPP-tracks; All authors contributed to data interpretation; Ei.K and A.A.-A. drafted the manuscript; All authors participated in proofreading and correcting; S.A., V.G., M.S., T.U., T.M., C.G., R.S., M.T., La.K., A.A., D.N., B.S., and B.R. supervised the projects.

3. The third study presents the utilization of industry-compatible silicon bottom cells. Especially, the reduced thickness compared to bottom cells which are typically used in laboratory cells affects the performance of the tandem solar cells. The high PCE values of up to 27.9% are just below 28.15% enabled on standardly used bottom cells. The reduction of the bottom cell thickness requires changing the perovskite bandgap if current matching should be maintained. We quantify the required bandgap change by optical simulations. The exact perovskite bandgap for industrial-compatible tandem solar cells will be higher as previously utilized and this has a strong influence towards further improvements and understanding as the compositional tuning to achieve this higher bandgap has to consider halide segregation and contact optimization further.

The publication can be found in appendix G.

- Publication:
  <u>Eike Köhnen</u>, Philipp Wagner, Felix Lang, Alexandros Cruz, Bor Li, Marcel Roß, Marko Jošt, Anna B. Morales Vilches, Marko Topič, Martin Stolterfoht, Dieter Neher, Lars Korte, Bernd Rech, Rutger Schlatmann, Bernd Stannowski and Steve Albrecht. 27.9% Efficient Monolithic Perovskite/Silicon Tandem Solar Cells on Industry Compatible Bottom Cells. *Solar RRL*, 5:2100244, 2021. https://doi.org/10.1002/solr.202100244.

- Author contribution:
  E.K. fabricated the perovskite top cell, measured the EQE, $J - V$ and UV-Vis and performed the optical simulations; P.W., A.B.M.V., L.K. and B.S. developed and fabricated the silicon bottom cell; E.K., A.B.M.V., P.W., B.S. and S.A. planned the experiments. E.K. and F.L. conducted and analyzed the PL measurements; A.C. performed the silicon single-junction solar cell simulations; M.R. conducted and analyzed the XRD measurements; E.K., M.J. ,B.L. and M.T. designed fabricated and built-up the tandem aging setup; E.K. drafted the manuscript; All authors participated in proofreading and correcting; M.T., D.N., L.K., B.R., R.S., B.S. and S.A. supervised the projects.

6.1 Highly efficient monolithic perovskite silicon tandem solar cells: analyzing the influence of current mismatch on device performance

This section is based on the work '**Highly efficient monolithic perovskite silicon tandem solar cells: analyzing the influence of current mismatch on device performance**' published by Eike Köhnen, Marko Jošt, Anna Belen Morales-Vilches, Philipp Tockhorn, Amran Al-Ashouri, Bart Macco, Lukas Kegelmann, Lars Korte, Bernd Rech, Rutger Schlatmann, Bernd Stannowski, and Steve Albrecht in *Sustainable Energy & Fuels*, 3(8):1995–2005, 2019. doi: 10.1039/C9SE00120D.

In this study we thoroughly address the optical but also electrical optimization of our tandem solar cells, which reduces not just the amount of reflected light but redistributes the photogenerated current densities to enable reduced current mismatch.

As the optimized tandem solar cell shows a reduced fill factor, we analyze the effect of the mismatch on the fill factor by illuminating the tandem solar cell with various spectra to induce various mismatch conditions.

Ultimately, we verify our findings with electrical simulations and give an outlook which PCE values are potentially achievable based on the realistic experimental input parameters collected before.

With that we have triggered the first report about current versus maximum power point matching and a more precise understanding of monolithic perovskite/silicon tandem solar cells.

6.1.1 Introduction

To overcome the theoretical limit of silicon single-junction solar cells of 29.4%,[8] silicon and perovskite solar cells can be combined to monolithic tandem solar cells with a theoretical limit of ~45% (see section 2.9). As a bottom cell, silicon heterojunction (SHJ) solar cells are suited due to their well-passivated c-Si surface enabling high V_{OC} values. Furthermore, the top layer of this architecture is a transparent conductive oxide (TCO), which makes the deposition of the perovskite top cell simple as perovskite single-junction solar cells are fabricated on TCOs, too. Tandem solar cells with a p-i-n perovskite top cell has proven to be advantageous as the n-type window layer is much more transparent compared to the p-type window layer in n-i-p architecture.[16, 127] At the time of this publication, the certified record PCE for monolithic perovskite/silicon tandem solar cells was 28% achieved by Oxford PV.[103] No further details are acquainted as this value was announced in a press release instead of an scientific article. Therefore, the best performing tandem solar cell published in a scientific article had a PCE of 25.5%, which was enabled by Jošt *et al.* utilizing a light management foil to reduce reflection losses.[31]

Although optically a textured front side would be beneficial, the perovskite deposition on textures remains still challenging. Devices with a flat front side still suffer from immense losses due to high reflection. We optimized preliminarily the optical properties of our tandem solar cells which enhanced the PCE from certified 25.0% to 26.0%. Further optical improvement enabled a cumulative photogenerated current density of more than $40\,\mathrm{mA\,cm^{-2}}$ and is thus comparable to textured devices. However, the high photogenerated current density was achieved with thin front contact layers that reduced electrical performance to a PCE of 25.3%. The highest efficiency of 26.0% was realized by a trade-off between optical and electrical properties of the front contact stack to achieve almost current matching between both subcells but simultaneously the fill factor (FF) decreased, which is already known from other tandem technologies.[116, 128] To analyze the origin of the reduced FF, the optimized tandem solar cell is measured under various illumination spectra based on an LED solar simulator to artificially change the current mismatch. The result strongly suggests that the change in FF stems from the reduced current mismatch.

To verify our results, we performed electrical simulations. These electrical simulations revealed the PCE limit which can be achieved with this tandem solar cell design. However, a difference between the simulations and measurements demonstrated that further investigation is needed to get a better matching between experiment and simulation and hence gain knowledge about the device operation.

6.1.2 Optimization of Tandem Solar Cells

One crucial layer in monolithic perovskite/silicon tandem solar cells, especially in the p-i-n top cell polarity, for the FF as well as for the J_{Ph} is the top TCO in which the generated charge carriers are collected and transported laterally to e.g. the metal grid or busbar (here a ring-type metal frame is utilized). The typical tandem device structure used in this work is shown in Figure 10. The top TCO layer should be as transparent as possible while enabling low resistive losses. By adding oxygen to the sputtering chamber during deposition of the TCO, the amount of oxygen vacancies and with that the transparency and electrical conductivity of the layer can be tuned. These vacancies typically contribute two electrons per defect. The added oxygen will occupy these vacancies.[129, 130] The lower carrier density leads to a reduction of the free carrier absorption especially in the NIR, but also to narrowing of the optical bandgap due to the Burstein-Moss effect.[129] Hall measurements verified these theories (Figure 11A). Simultaneously, the mobility increases with an increasing amount of oxygen, most likely due to structural changes in the film, as explained by Martins *et al*.[131] We found that the resulting resistivity is almost constant if the fraction x of the oxygen in the argon/oxygen mixture ranges from 0.05 to 0.25 volume percent. Therefore the optimum amount of oxygen was chosen by the lowest absorption in the relvant wavelength range from 300 to 1200 nm. We found the best value for x=0.2% where just $1.18\,\text{mA}\,\text{cm}^{-2}$ are lost due to parasitic absorption when integrating the absorption spectra multiplied with the AM1.5g spectrum over the wavelength range (see equation 5.6).
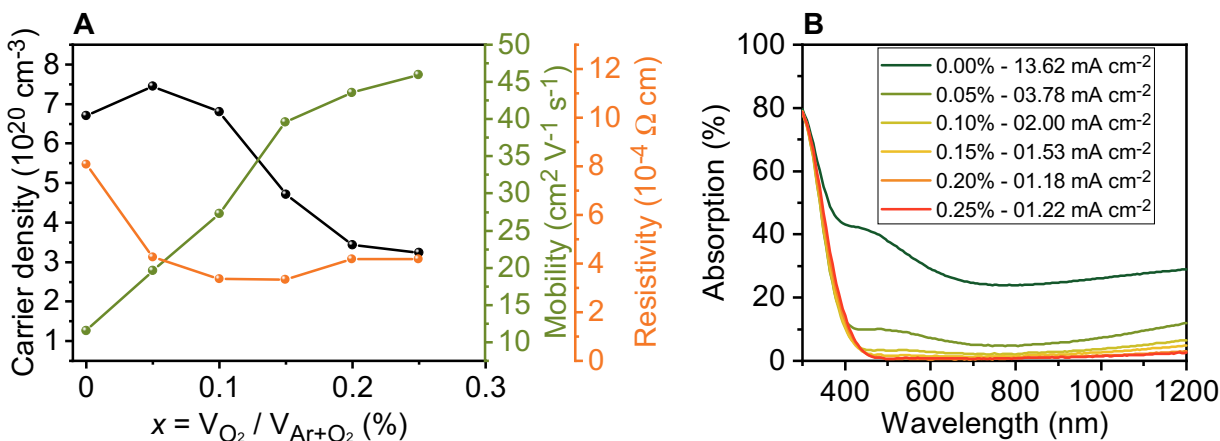
Figure 11: Optimization of the front transparent conductive oxide, here indium zink oxide (IZO). (A) Carrier density, mobility and resistivity of IZO layers deposited on glass with various fractions (given in volume percent) of oxygen added to the sputter chamber. The values are obtained from hall measurements. (B) Absorption of equally thick IZO layers deposited on glass obtained by absorption and reflection spectroscopy. The equivalent current density which is lost due to parasitic absorption is calculated using equation 5.6 and AM1.5g illumination. This figure is adapted with permission from [104] - Published by The Royal Society of Chemistry.

Using the optimized IZO layer to enable the best trade-off between sheet resistance and parasitic absoprtion, together with a tin oxide (SnO_2) buffer layer, which is deposited via atomic layer deposition, it forms a transparent n-type contact. A tandem solar cell PCE of 25.0% was achieved, which was independently certified by the calibration laboratory at Fraunhofer ISE (CalLab) and is shown in Figure 13C. The certificate can be found in appendix C. Although the FF of this device was as high as 78.6%, the low short-circuit current density (J_{SC}) of just $17.8\,\text{mA}\,\text{cm}^{-2}$ strongly limited the PCE. This low J_{SC} was a result of highly mismatched subcells, as shown in Figure 13A. With a photogenerated current density (J_{Ph}) of $17.85\,\text{mA}\,\text{cm}^{-2}$ and $20.69\,\text{mA}\,\text{cm}^{-2}$ in the silicon and perovskite subcell, respectively, the mismatch was more than $2.8\,\text{mA}\,\text{cm}^{-2}$. The major reason for the low cumulative J_{Ph} of $38.54\,\text{mA}\,\text{cm}^{-2}$ was the immense reflection in the infrared wavelength range. The current loss due to reflection amounted to $4.65\,\text{mA}\,\text{cm}^{-2}$. As the J_{SC} of a monolithic tandem solar cell is guided by the minimum photogenerated current density (J_{Ph}) of the both cells (see

section 2.9.3), it is desirable to achieve approximately short-circuit current matching conditions.

In order to enable better current matching conditions and less reflection losses, further optimizations were performed. The 20 nm nc-SiO$_x$:H which is the n-type contact of the bottom cell was previously optimized for silicon single-junction solar cells.[132] For tandem solar cells, however, just the long wavelengths are important for the silicon bottom cell. Hence, the thickness was increased to around ~90 nm in order to improve the infrared response of the silicon bottom cell and with that increase its J_{Ph}.[101]

Additionally, the front TCO has a significant impact on the parasitic absorption especially in the UV and infrared wavelength range (see Figure 11). Thus, optically a very thin TCO is desired to minimize the parasitic absorption. Optical simulations revealed a gain of 0.32 mA cm when reducing the thickness from the used 130 nm to 90 nm. However, further reduction would increase the resistance of the TCO and worsen the electrical performance of the solar cell. Thus, 90 nm were used in the optimized cell. To precisely determine the optimum between optical and electrical properties, optoelectronical simulations would be necessary but are not conducted here. To redistribute the J_{Ph} of the subcells more advantageously, the perovskite thickness was adjusted by changing the spin-coating speed. The faster spinning led to thinner perovskite layers making it more transparent especially in the range with a lower absorption coefficient, i.e. above ~500 nm. Consequently, more light is transmitted to the silicon bottom cell. The faster speed enabled a reduction of the perovskite thickness from 580 to 460 nm.
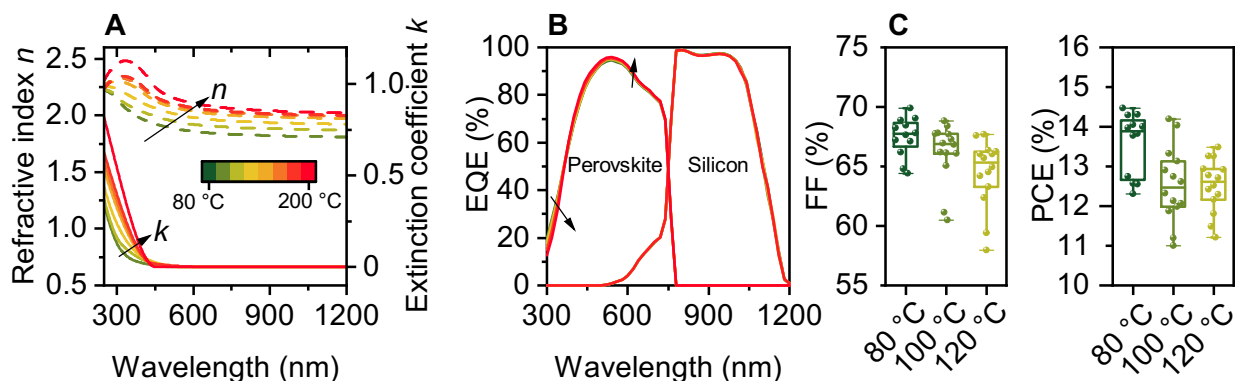
Figure 12: Optimization of tin oxide (SnO$_2$) depostied via atomic layer deposition. (A) Refractive index n and extinction coefficient k of SnO$_2$ deposited at temperatures ranging from 80 °C to 200 °C in 20 °C steps. The data were extracted from ellipsometry measurements. The arrows indicate the direction for increasing temperature. (B) Simulated EQE spectra of monoltihic perovskite/silicon tandem solar cells using optical data of SnO$_2$ displayed in (A). All other layers in the tandem stack were kept the same. The arrows indicate the direction for increasing temperature. (C) Fill factor and power converion efficiency of opaque perovskite single-junction solar cells with SnO$_2$ deposited at 80, 100 and 120 °C. This Figure is adapted with permission from [104] - Published by The Royal Society of Chemistry.

During the deposition of 20 nm SnO$_2$, the perovskite is exposed to 100 °C for about 1 hour, which might reduce the performance of the top cell. Hence, SnO$_2$ layers deposited at various temperatures were analyzed optically. Figure 12A shows that higher SnO$_2$ deposition temperatures increase the absorption in the UV range, whereas the refractive index n is increased in the entire wavelength range. Optical simulations shown in Figure 12B demonstrate that the J_{Ph} of the perovskite and silicon subcell are barely affected within the temperature range of 80 to 200 °C for the SnO$_2$ deposition and resulting changes in the optical properties of SnO$_2$. This is because the EQE of the perovskite above 370 nm increases with higher temperature, whereas the higher absorption coefficient below 370 nm reduces the EQE. Due to the temperature sensitivity of perovskite solar cells, we decided to fabricate perovskite single-junction solar cells with SnO$_2$ being deposited at temperatures between 80 and 120 °C. Figure 12C highlights that the lower temperature enabled higher PCE values mainly due to an increased FF. The reduced refractive indices for lower deposition temperatures indicate a lower density. However, as described by Elam *et al.*, this leads to an increase in resistivity.[133]

Thus, this cannot explain the improved FF. As described by Mullings *et al.*, the deposition temperature has an effect on the bandgap of the SnO_2.[134] The band alignment for layers deposited at lower temperatures might be beneficial for this application. However, the improved properties may not be related to a difference in the SnO_2 itself but can be an effect of the reduced temperature to which the perovskite layer is exposed, namely there is a trade-off between optoeletric properties of SnO_2 and perovskite degradation at higher reaction temperatures.

All above mentioned optimizations were implemented into tandem solar cells. The EQE (incl. reflection) is shown in Figure 13B, as well as the resulting $J-V$ in Figure 13C. As intended, the loss due to reflection decreased by approximately $1\,mA\,cm^{-2}$, enhancing also the cumulative J_{Ph} by the same amount to $39.46\,mA\,cm^{-2}$. Till today this cumulative J_{Ph} is one of the highest value for tandem solar cells with a planar front side. It is even comparable to the values achieved by tandem solar cells using solution processed perovskite on top of textured silicon,[105, 107] and approaches the values of some cells using textured silicon with conformally deposited perovskite.[94, 135] However, the impressive value of $40.4\,mA\,cm^{-2}$ achieved by Sahli *et al.* with a conformally deposited perovskite on textured silicon demonstrates that this approach can be beneficial in terms of optical properties.
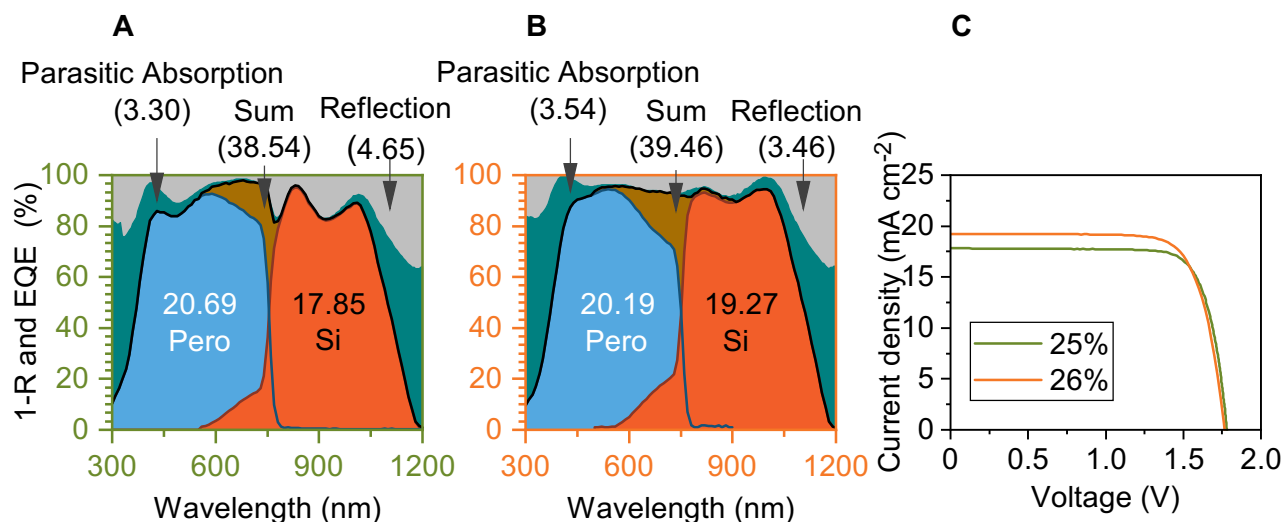
Figure 13: Performance of the initial and optimized tandem solar cell. (A-B) In-house measured EQE and reflection (denoted as 1-R) of the initial (A) and optimized (B) tandem solar cell. The J_{Ph} values and their respective sum, parasitic absorption, and loss due to reflection are given in $mA\,cm^{-2}$ for AM1.5g illumination. (C) Corresponding $J-V$ curves of the initial and optimized tandem solar cell with certified 25% and in-house measured 26%, respectively. This Figure is adapted with permission from [104] - Published by The Royal Society of Chemistry.

In addition to the improvement of the cumulative J_{Ph}, the J_{Ph} values of the subcells were successfully redistributed. The increased J_{Ph} of the silicon subcell reduced the mismatch between the subcells to $0.9\,mA\,cm^{-2}$. Thus, the subcells are still not perfectly current matched. Ideally the bandgap of the perovskite can be widened to reduce the $J_{Ph,Perovskite}$ while increasing $J_{Ph,Silicon}$. Simultaneously, the wider bandgap should enable higher V_{OC} values. However, wider bandgaps are usually achieved by increasing the amount of bromide, which can result in unwanted halide segregation.[136] We will address the topic of wider bandgaps in section 6.2.

Nonetheless, the reduced mismatch increased the J_{SC} of the tandem solar cell by about $1.4\,mA\,cm^{-2}$ to $19.22\,mA\,cm^{-2}$. Together with a FF of 76.6% and V_{OC} of 1.77 V this cell had a PCE of 26.0%. At that time, this value was the highest PCE giving all scientific details in a peer reviewed journal.

Guided by optical simulations, further reduction of the IZO thickness enabled a cumulative current density of $40\,mA\,cm^{-2}$, which is a remarkable value for devices with a planar front side and comparable to the

above mentioned experimentally realized double-side textured devices presented by Sahli *et al.*[92] However, the reduced TCO thickness increased the series resistive losses and deteriorated the overall performance. This device reached a stabilized PCE of just 25.3%, which is nonetheless higher than achieved with fully textured devices.[92, 94, 135]

The long-term stability of a tandem device with the design which enabled 26% was measured using a glass-glass encapsulation with a UV-curable edge-sealant. During 1000 hours, the device was stored in ambient conditions and regularly MPP-tracked for at least 30 minutes. The performance was remarkably stable with relative PCE drop of less than 1% for the last measurement after 1000 hours.

Obviously, the tandem solar cells need to perform on a high level when being in continuous operation. However, as we will describe in more detail in section 6.2, a proper light source is necessary to correctly measure the tandem solar cells as the performance can depend on the current mismatch. The latter effect will be investigated in more detail in the next section.

6.1.3 Influence of the Current Mismatch on the Solar Cell Performance

Comparing the FF values of the initial and optimized tandem cells, the latter shows a reduced FF by more than two percentage points. As reported for other tandem technologies, the mismatch conditions can affect the FF of the solar cells.[53, 116, 128, 137, 138] As a thorough understanding of the influence of non-current matching conditions is important for device understanding and energy yield analysis, the influence of the mismatch conditions on the performance of perovskite/silicon tandem solar cells was analyzed. The optimized tandem cell was illuminated with various spectra. By changing the intensity of the blue wavelength range, the J_{Ph} of the perovskite subcell was changed, whereas the J_{Ph} of the silicon subcell was kept constant. With this, the mismatch conditions were changed artificially and for each condition, the performance of the tandem solar cell was recorded. The utilized spectra as well as the AM1.5g standard spectrum are shown in Figure 14A. With these spectra and the spectral responses of the subcells, the J_{Ph} values of the subcells were calculated according to equation 2.10.

For the case of a very high J_{Ph} in the perovskite, the silicon subcell was limiting and the J_{SC} of the tandem solar cell was constant. For reduced J_{Ph} in the perovskite subcell, the tandem solar cell became perovskite limited and the J_{SC} started to decrease (see Figure 14B). It is typically reported that the FF is lowest when the tandem solar cell is operated close to the current matching point.[53, 128, 137] However, it is not necessarily exactly at the current matching point and depends on the performance of the individual subcells.[138] In this study, the FF reached its minimum when the silicon subcell is slightly limiting (see Figure 14C). To verify that the change in FF after optimization stems solely from a reduced current mismatch, the slope on the left side of the FF minimum was calculated and amounts to -1.31% FF per $\mathrm{mA\,cm^{-2}}$. Thus, with a current mismatch of $-2.8\,\mathrm{mA\,cm^{-2}}$, as obtained from the certified cell, a FF of ~79% is expected. This predicted FF is in very good agreement with the value of the certified cell, strongly indicating that the change in FF arose from the change in mismatch conditions. The benefit of ALD optimization (increased FF) and enhanced resistive losses from thinner front IZO seemed to counterbalance here. On the right side of the FF minimum, the slope amounts to 0.93% FF per $\mathrm{mA\,cm^{-2}}$.

Even though the J_{SC} decreases, the simultaneous increase of the FF partially compensates a loss in PCE. Therefore, the PCE of monolithic tandem solar cells are barely sensitive to small changes in current-mismatch conditions. The low sensitivity is reflected in a broad peak around the PCE maximum in Figure 14D. If the currents would be equally distributed (i.e. current matching conditions), the PCE would amount to 26.34%.

The described characteristic is important for energy yield analysis especially when comparing two-terminal and four-terminal tandem solar cells. One of the arguments in favor for four-terminal tandem solar cells is to avoid decrease in performance due to current reduction if current mismatch occurs. This mismatch can occur for example over the course of the day, when the intensity of the blue light is reduced in the morning and evening due to Rayleigh scattering, as shown in Figure 1.[139] To estimate the amount of current mismatch happening during the day we simulated an EQE with $J_{\mathrm{Ph,Silicon}}$ and $J_{\mathrm{Ph,Perovskite}}$ values at
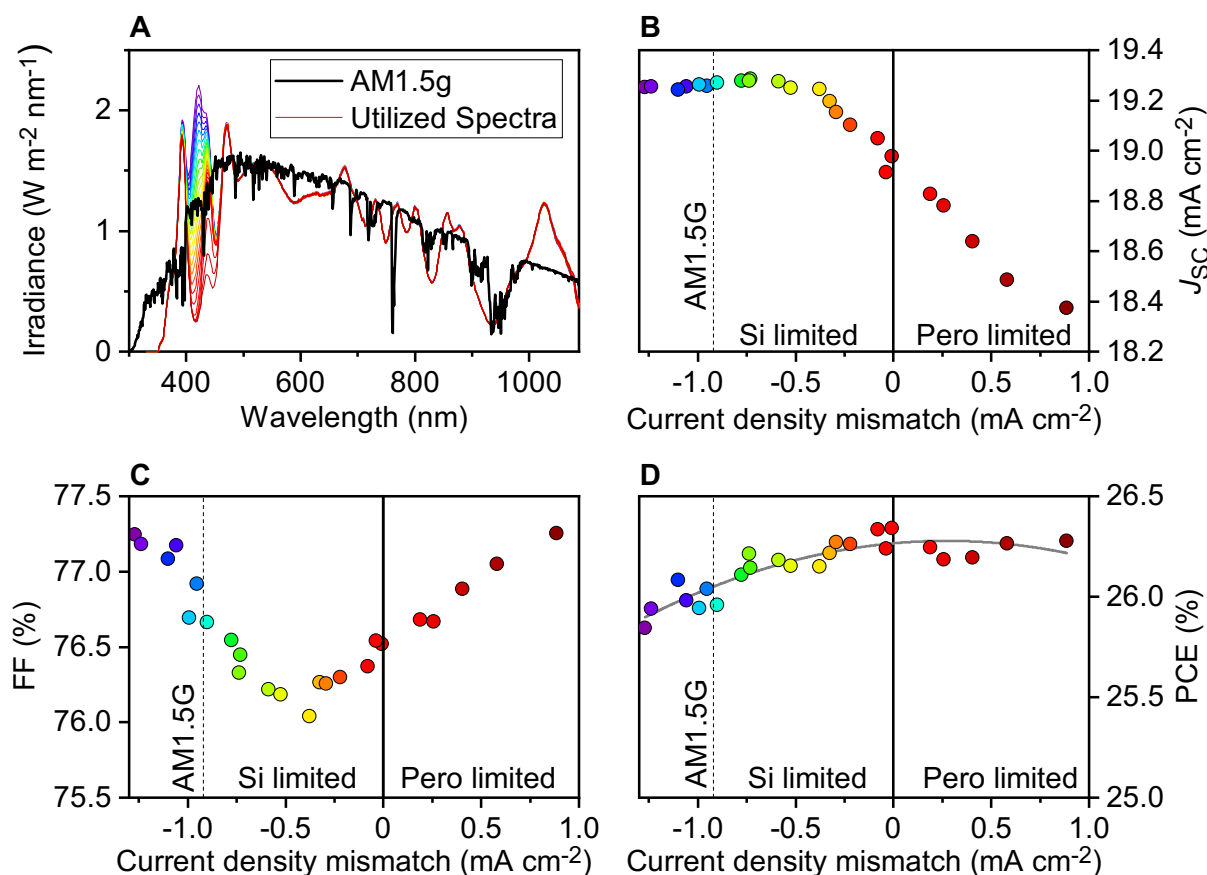
Figure 14: Performance of monolithic perovskite/silicon tandem solar cells as a function of the current mismatch between the subcells. (A) Utilized spectra to change the current density mismatch between the perovskite and silicon subcell. The change in blue intensity alters the photogenerated current density in the perovskite, whereas it stays constant for the silicon subcell. (B) Short-circuit current density, (C) fill factor and (D) power conversion efficiency of the tandem solar cell as a function of the current density mismatch ($J_{\mathrm{Ph,Silicon}} - J_{\mathrm{Ph,Perovskite}}$). This figure is adapted with permission from [104] - Published by The Royal Society of Chemistry.

AM1.5g illumination of 19.61 and 19.67 mA cm^{-2}, respectively. When using the spectra shown in Figure 1B, the silicon subcell generates 0.78 mA cm^{-2} less than the perovskite subcell at 12:00. In the evening at 19:00 the perovskite subcell is limiting by 4.7 mA cm^{-2} due to the strongly reduced intensity in the visible wavelength range. However, as demonstrated by Aydin *et al.*, the J_{Ph} values are furthermore affected by the cell temperature.[94] Typically, the cells are warmer during noon. Towards evening, the temperature decreases which leads to a reduction of the $J_{\mathrm{Ph,Silicon}}$ and a increase in $J_{\mathrm{Ph,Perovskite}}$. Consequently, the above mentioned mismatch in the evening will be reduced due to reduced cell temperature.

6.1.4 Electrical Simulations

To validate the experimental results, electrical simulations were performed using the electronic design automation software LTspice.[121] As discussed in section 2.9.3, the simplest way to describe a tandem solar cell is to connect two one-diode models representing the top and bottom cell in series. To access the electrical parameters for the subcells, perovskite and silicon single-junction solar cells were fabricated and measured at various intensities. From the intensity dependent V_{OC} values, the ideality factor n_{ID} and reverse saturation current density J_0 were extracted. The series resistance values R_{S} and shunt resistance values R_{SH} were extracted from the slope around $V = V_{\mathrm{OC}}$ and $V = 0$, respectively.
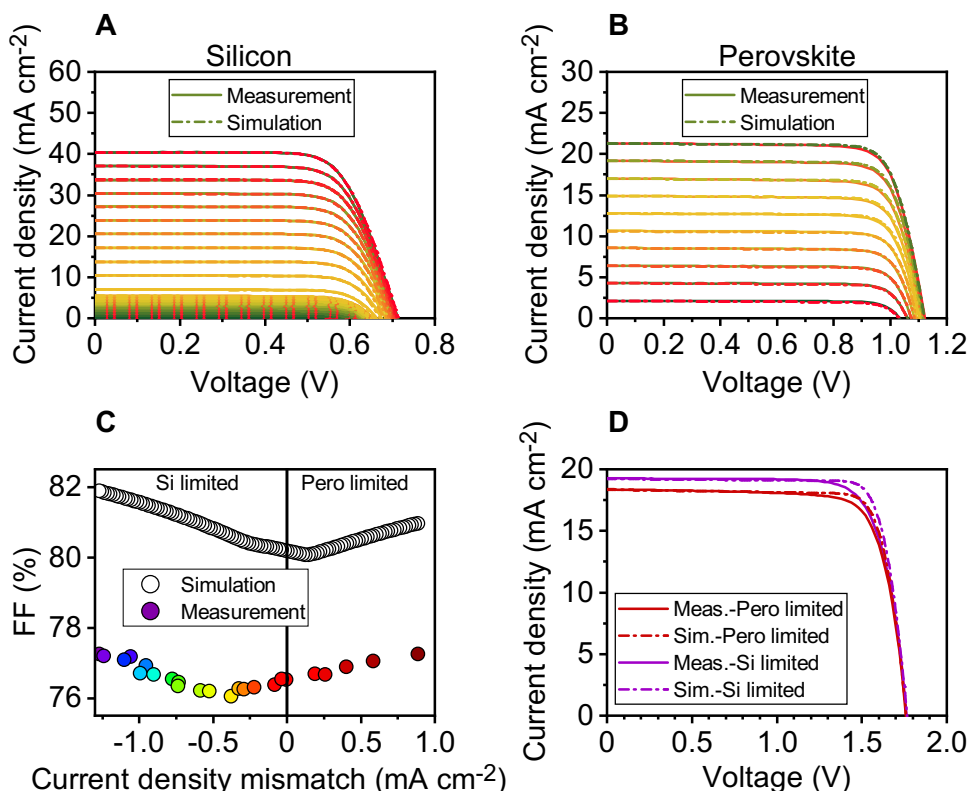
Figure 15: Verification of electrical simulations for tandem solar cells. (A) Measured and simulated silicon single-junction solar cell at various intensities. The experimental data were fitted using a one-diode model. (B) Measured and simulated perovskite single-junction solar cell at various intensities. The experimental data were fitted using a one-diode model. (C) Experimental and simulated fill factor of a tandem solar cell as a function of the current density mismatch. The tandem solar cell is simulated by connecting the one-diode models of the perovskite and silicon cells in series. The white circles are the simulated FF values, whereas the colored circles are the measured FF values as shown in Figure 14C. (D) Simulated and measured $J - V$ characteristics for the highly perovskite and highly silicon limited case (i.e. the very left and very right data points in (C)). This figure is adapted with permission from [104] - Published by The Royal Society of Chemistry.

Due to different geometries and hence different series resistances, the R_S value in the tandem solar cell was adjusted in a way that the slopes around $V = V_{OC}$ of the simulated and measured tandem solar cell matched. In addition, the sum of the V_{OC} values of the single-junction solar cells was slightly lower than the V_{OC} measured in the tandem solar cell, which we accounted to a difference in the perovskite top cell. Thus, the J_0 value was slightly adjusted until the measured and simulated V_{OC} values matched.

For the simulated tandem solar cell, the same J_{Ph} values were used as in the measured tandem solar cell. We found the same V_{OC} and J_{SC} bahaviour as for the measured tandem solar cell. For the FF values, which are shown in Figure 15C, we found a similar shape as for the measured tandem solar cell, verifying our experimental data. However, the values for the simulated tandem solar cell were much higher than the measured values. The individual $J - V$ curves revealed that the main difference between simulated and measured curves appeared around the MPP (see Figure 15D) although this behavior is not present in the single-junction solar cells.

One possible explanation is that the recombination layer might behave in a non-ohmic manner, thus another electrical component such as a diode needs to be implemented in the simulation to achieve a good matching between simulation and measurement. However, for the single-junction solar cells the same

contact stack is present. In the silicon subcell as well as in the silicon single-junction cell, the electrons will be extracted via the nc-SiOx:H(n)/ITO interface, which forms a low resistive contact.[50] Also the extraction of the holes from the perovskite is the same in perovskite single-junction cells and the perovskite subcells in the tandems. Another possible explanation may be the difference between the semitransparent perovskite top cell in the tandem solar cell and the opaque perovskite single-junction cell. The sputtering of the TCO for the semitransparent cells might alter the perovskite performance.[140–142] In addition the size of the active area was just $0.16\,cm^2$ for the single-junction cells, whereas it was $0.78\,cm^2$ for the tandem solar cell, which may led to an increased number of pinholes and non-uniformities of the spin-coated perovskite layer.[47] These pinholes (i.e. direct contact of the hole- and electron-selective contact) can lead to non-linear diode-like behavior and thus affect the maximum power point while not affecting the low-voltage range.[143]

Further investigation is needed to exactly reconstruct the monolithic tandem solar cell in an electrical simulation and with this, gain knowledge about the device physics and ideally improve the PCE.

If the difficulties with the reduced FF can be solved, a PCE of 27.6% under AM1.5g illumination is achievable. If the series resistance can be optimized, for example by implementation of grid fingers and negligence of bulk an contact resistance, the maximum achievable PCE increases to 29.0%.

6.1.5 Conclusion

In this work, we optimized monolithic perovskite/silicon tandem solar cells especially optically. The initial PCE of 25.0% was certified independently by the Fraunhofer ISE CalLab. The current mismatch of more than $2.8\,mA\,cm^{-2}$ of the subcells enabled a high FF of 78.6% but a low short-circuit current density of just $17.8\,mA\,cm^{-2}$. The latter was also low because of high reflection. To increase the J_{SC}, we reduced the amount of reflected light from ~4.7 to ~$3.5\,mA\,cm^{-2}$ as well as the mismatch of the J_{Ph} values from ~2.8 to ~$0.9\,mA\,cm^{-2}$. This was enabled by increasing the thickness of the nc-SiOx:H layer, reducing the thickness of the IZO and reducing the thickness of the perovskite absorber. Furthermore, the SnO_2 deposition temperature was reduced from 100 to 80 °C which improved the FF in single-junction devices, likely by reduction of process-induced degradation.

The optimized tandem solar cell reached a PCE of 26.0%. Although the J_{SC} indeed increased, we found a reduction in the FF.

To analyze this in more detail, we measured the tandem solar cell with different illumination spectra to achieve different mismatch conditions. The FF changed strongly with the mismatch. A minimum of 76% appeared close to current matching conditions, whereas it increased when the mismatch increased. This effect partially compensates the reduced J_{SC} if the subcells are mismatched. Consequently, the tandem solar cells are barely sensitive against small mismatch conditions.

To validate this, we performed electrical simulations. Although the simulated single-junction solar cells match very well with the measured cells at different illumination conditions, the resulting tandem solar cell showed a higher FF. The larger area for the tandem solar cell in comparison to the perovskite single-junction utilized for extraction of diode model paramters may have increased the amount of pinholes inducing a non-ohmic current path and thus lowering the top cell FF in the tandem solar cell.

However, if the reduced power extraction around MPP could be eliminated, a PCE of 27.6% should be achievable. By additional optimization of the series resistance (i.e. $R_S = 0$) we simulated a PCE of 29.0%.

More sophisticated characterization methods are needed to analyze the single-junction solar cells or even better the subcells in order to understand and solve the mismatch between simulations and experiment.

6.2 Monolithic perovskite/silicon tandem solar cell with >29% efficiency by enhanced hole extraction

This section is based on the work '**Monolithic perovskite/silicon tandem solar cell with >29% efficiency by enhanced hole extraction**' published by Amran Al-Ashouri, Eike Köhnen, Bor Li, Artiom Magomedov, Hannes Hempel, Pietro Caprioglio, José A Márquez, Anna Belen Morales Vilches, Ernestas Kasparavicius, Joel A. Smith, Nga Phung, Dorothee Menzel, Max Grischek, Lukas Kegelmann, Dieter Skroblin, Christian Gollwitzer, Tadas Malinauskas, Marko Jošt, Gašper Matič, Bernd Rech, Rutger Schlatmann, Marko Topič, Lars Korte, Antonio Abate, Bernd Stannowski, Dieter Neher, Martin Stolterfoht, Thomas Unold, Vytautas Getautis, and Steve Albrecht in *Science*, 370(6522):1300–1309, 2020. doi: 10.1126/science.abd4016.

In this study, we present a new hole-selective self-assembled monolayer (SAM) material with the nomenclature Me-4PACz ([4-(3,6-dimethyl-9H-carbazol-9-yl)butyl]phosphonic acid). We use advanced characterization techniques to analyze the properties of perovskite films deposited on top of this SAM and correlate these film and charge carrier dynamic properties to the performance of single-junction devices with different hole-selective layers (HSL).

For the first time, we use SAMs in perovskite/silicon tandem solar cells. The advantages of the new SAM such as fast hole extraction, proper passivation and thereby enabling photostability of a 1.68 eV wide-bandgap perovskite could be transferred effectively into tandem solar cells. That enabled a certified PCE of 29.15%, a world record at that time.

To measure the long-term stability of the tandem solar cells, we used a newly designed setup which enables precise control of the photogenerated current densities in the subcells to properly imitate AM1.5g matching conditions.

Driven by the problem to evaluate the performance of the individual subcells in monolithic tandem solar cells, we used injection-dependent electroluminescence to access the subcell $J-V$ characteristics. With the extracted subcell properties we simulated the tandem solar cells used in this publication and calculated its efficiency potential.

6.2.1 Introduction

Previously in section 6.1, we precisely optimized the deposition of several layers. Especially the optical properties were improved enabling high cumulative J_{Ph} values of $39.46\,\mathrm{mA\,cm^{-2}}$ and J_{SC} values of $19.22\,\mathrm{mA\,cm^{-2}}$. Despite the improved optical properties, there is still room for improvement of the PCE due to moderate V_{OC} and FF values.

A lot of effort is done to passivate the interfaces between the perovskite and contact layers to reduce non-radiative recombination and hence, increase the V_{OC}. For p-i-n perovskite solar cells, Al-Ashouri *et al.* presented self-assembled monolayer (SAM) which enabled low non-radiative recombination resulting in high V_{OC} values. Compared to the typically used polymer PTAA (poly[bis(4-phenyl) (2,5,6-trimentlyphenyl) amine]), the utilization of the SAM 2PACz ([2-(9H-carbazol-9-yl)ethyl]phosphonic acid) enhanced the V_{OC} by more than 60 mV. Due to the self-assembling nature of the material, it enables conformal coverage of rough surfaces, too, which was demonstrated with the application on rough CIGS bottom cells to fabricate perovskite/CIGS tandem solar cells. The certified tandem solar cell PCE of 23.26% was a world record at that time.[144] By further improvement, a higher certified record of 24.2% was achieved.[17] Using these hole-selective self-organized monolayers for perovskite solar cells was patented by HZB together with the Kaunas University of Technology (see appendix A). Moreover, the SAMs 2PACz and MeO-2PACz ([2-(3,6-dimethoxy-9H-carbazol-9-yl)ethyl]phosphonic acid) used in the above mentioned publication were made available by commercialization.[145, 146] Although the superior V_{OC} improves the efficiency, the FF of p-i-n perovskite solar cells are still far below the theoretically achievable values calculated with the detailed balance limit and as shown in the previous chapter, below expectations from electrical simulations.

Here we present a newly designed SAM molecule which combines an equally high level of passivation but a faster charge extraction and thus, enabling an increased FF and reduced phase segregation. This can

still be realized by using $Cs_{0.05}(MA_{0.23}FA_{0.77})Pb(Br_{0.23}I_{0.77})_3$ perovskite composition with increased amount of bromide to obtain a tandem relevant bandgap of 1.68 eV. The benefits are demonstrated in single-junction and tandem solar cells, which were compared to devices with other hole-selective layers such as other SAMs or the standardly used polymer PTAA. To measure the long-term stability of tandem solar cells, we designed a new setup which enables proper illumination. The tracked tandem solar cells comprising different HSL demonstrates the superior stability of the new SAM. Ultimately, we analyze the performance of the subcells using injection-dependent electroluminescence.

6.2.2   Stabilization of wide-bandgap perovskite with the hole-selective layer

As described in section 2.9.1, the theoretical ideal top cell bandgap in combination with a silicon bottom cell is 1.73 eV. However, practically due to non-perfect absorption edges and parasitic absorption, a bandgap of 1.68 to 1.7 eV is desired to achieve high V_{OC} values while maintaining power matching conditions (see section 2.9.3).[31] These wide bandgaps often feature a Br/I ratio of >20%, which can lead to phase instabilities caused by light-induced phase segregation, most strikingly evident from photoluminescence (PL) spectra that show a double-peak formation under continuous illumination.[80, 147]

We show that both fast charge extraction and good passivation at the selective contacts can effectively suppress this double-peak formation while simultaneously enabling high V_{OC} and FF values.

Instead of optimizing the perovskite composition, we used the well-known "triple cation" perovskite consisting of cesium, formamidinium (FA) and methylammonium (MA) as monovalent cations, lead as divalent cation and a halogen mix of iodide and bromide.[78] Typically, a bandgap of ~1.63 eV is enabled with ~17% Br, which we used for the results in section 6.1. However, with this compsition, we obtained a silicon limiting tandem solar cell with a moderate V_{OC}. To address these problems, we widened the bandgap to 1.68 eV by increasing the fraction of Br to 23%. Thus, the nominal composition is $Cs_{0.05}(MA_{0.23}FA_{0.77})Pb(Br_{0.23}I_{0.77})_3$.

First, we compare the QFLS values of the perovskite deposited on quarz glass and various HSL using absolute PL with a 1-sun illumination.

In recently published high-PCE p-i-n single-junction and tandem solar cells, PTAA or the comparable polyTPD (poly[N,N'-bis(4-butylphenyl)-N,N'-bis(phenyl)-benzidine]) is typically used.[75, 106, 148, 149] Alternatively, SAMs based on carbazole, such as MeO-2PACz and 2PACz, can form passivated interfaces while allowing for low transport losses because they are ultra thin (<1 nm).[144]

The introduction of a methyl-group (Me) substitution to the already presented 2PACz led to a optimized energy alignment with the valence band of the perovskite and with a similar dipole moment (~ 1.7 D). The aliphatic chain length (n) was optimized in actual solar cells. For nPACz and Me-nPACz an optimum of n=2 and n=4 was found, respectively. Hence, for the rest of this study, Me-4PACz is analyzed and compared to the commercially available SAMs 2PACz and MeO-2PACz as well as the standardly used PTAA.

The QFLS values of the bare perovskite deposited on glass/ITO/HSL shows that the perovskite on Me-4PACz and 2PACz enables the same high values of 1.25 eV as on quartz glass, which is commonly regarded as a perfectly passivated substrate.[150] In contrast, PTAA and MeO-2PACz show a lower QFLS suggesting a lower level of passivation with higher losses from surface recombination.

Perovskite compositions with high bromide content typically segregate into iodide-rich phases indicated by increased PL intensity at lower photon energies, here at a wavelength of 780 nm.[80] The emergence of this additional signal is for example shown in Figure 16A, where the perovskite is deposited on glass/ITO/PTAA, and measured for 10 minutes. The same evolution is visible on MeO-2PACz. In contrast, the perovskite deposited on Me-4PACz, shown in Figure 16B, and 2PACz do not show this behavior.

To create more harsh conditions, the excitation flux was increased to a 30-suns equivalent illumination. Under these conditions, also 2PACz shows signs of segregation, whereas the perovskite on Me-4PACz remains stable.

We experimentally demonstrate that the phase segregation is inhibited if both, fast charge extraction and a high level of passivation is present by comparing the PL spectra of the Me-4PACz/perovskite deposited on either a insulating or conductive substrate. Despite the good passivation of Me-4PACz, a signal around
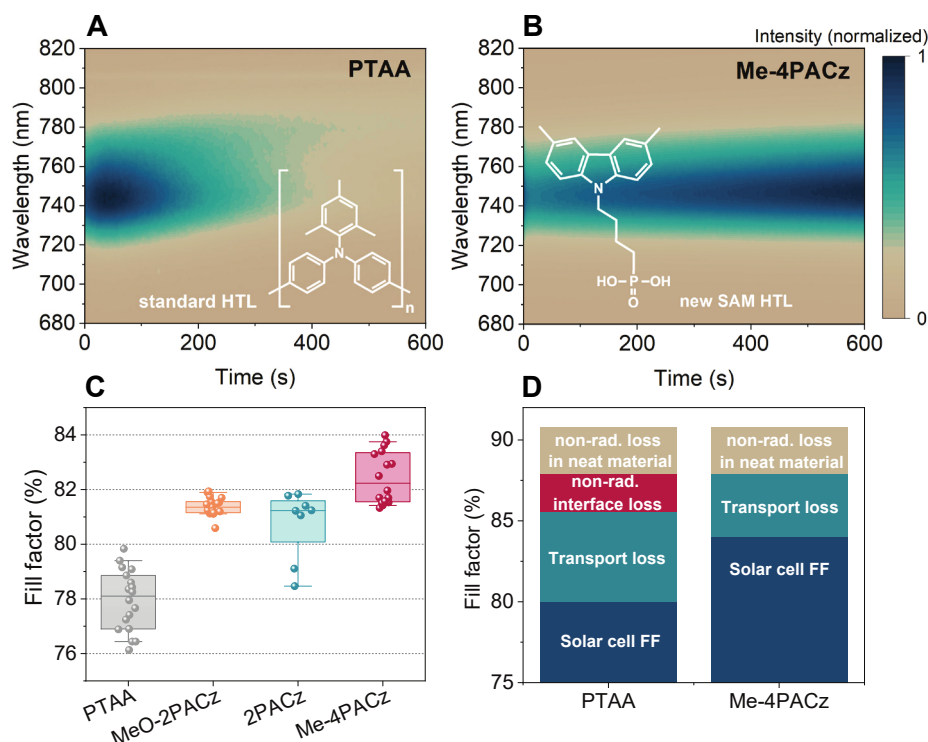
Figure 16: Analysis of various hole-selective layers for phase stability and various recombination losses. (A-B) Time-dependent photoluminescence spectra of the perovskite ($E_G = 1.68\,\text{eV}$) deposited on glass/ITO/PTAA (A) and glass/ITO/Me-4PACz (B). (C) Comparison of fill factor values of perovskite solar cells with the stack glass/ITO/HSL/perovskite/C_{60}/SnO$_2$/Ag, where the perovskite is a triple-cation perovskite absorber with 1.68 eV bandgap. All data are from cells made from the same perovskite precursor and contact processing batch. The boxes indicate the 25/75 percentiles; the whiskers indicate the 10/90 percentiles. (D) Distribution of loss mechanisms lowering the cell's FF below the detailed balance limit, comparing PTAA and Me-4PACz cells. From [99]. Reprinted with permission from AAAS.

780 nm (iodide-rich domains) appears in the case of the insulating substrate. In contrast, the PL spectrum on the conductive substrate shows a sharp peak at 740 nm (neat perovskite).

To analyze the charge extraction speed, we used transient photoluminescence (TrPL). The full decay is governed by nonradiative, trap-assisted surface/bulk recombination (mostly monoexponential decay), radiative recombination ("bimolecular," second-order decay), and charge transfer effects, which can be disentangled if these time constants differ sufficiently from each other.[151]

With MeO-2PACz and PTAA it was not possible to clearly differentiate between charge extraction and trap-assisted recombination because the nonradiative recombination was high (as evidenced by lower QFLS values relative to quartz glass) and because transients did not saturate toward one process. Comparing the TrPL measuremnts on 2PACz and Me-4PACz we found that the latter one demonstrates faster charge extraction.

As solar cells also comprise a electron-selective contact, it is improtant to know the properties of the perovskite/C_{60} interface. To extract the electron extraction speed at the perovskite/C_{60} interface, we combined time-resolved terahertz photoconductivity measurements with TrPL measurements. We found a electron transfer time of ~1 ns, substentially faster than the hole transfer at the hole-selective interface.

6.2.3 Performance of Perovskite Single-Junction Solar Cells

The advantage of this new SAM shall be evaluated in perovskite single-junction solar cells. Therefore, we fabricated standard p-i-n solar cells in the following configuration: ITO/HSL/Perovskite/C_{60}/SnO$_2$/Ag. As

the charge extraction on the electron selective interface is much faster, we expect that the difference in hole-extraction speed will be visible in the single-junction devices.

With the standardly used PTAA, a maximum FF of 80% was achieved (see Figure 16C). 2PACz and MeO-2PACz enabled a maximum value of 82%, whereas the top values are achieved with Me-4PACz and amount to 84%, which we account for the fast hole-extraction speed as well as the high level of passivation.

To analyze the FF values in more detail and without the influence of the series resistance, we measured the V_{OC} of complete devices as a function of the illumination intensity (Suns-V_{OC}) and the QFLS of the neat perovskite on the different HSL as a function of the illumination intensity (Suns-PL).[100] From these measurements we were able to disentangle different loss mechanisms. The comparison between cells with PTAA or Me-4PACz is shown in Figure 16D. We found no loss due to non-radiative recombination at the interface and a lower transport loss when using Me-4PACz as HSL.

Furthermore, from intensity dependent V_{OC} measurements, the ideality factor n_{ID} was extracted. For PTAA the ideality factor amounts to 1.55, which is in agreement with values reported for similar device architectures.[100] For MeO-2PACz the n_{ID} is 1.51. For the other SAMS the n_{ID} decreases to 1.42 in the case of 2PACz and impressive 1.26 for Me-4PACz.

6.2.4 Integration into Tandem Solar Cells
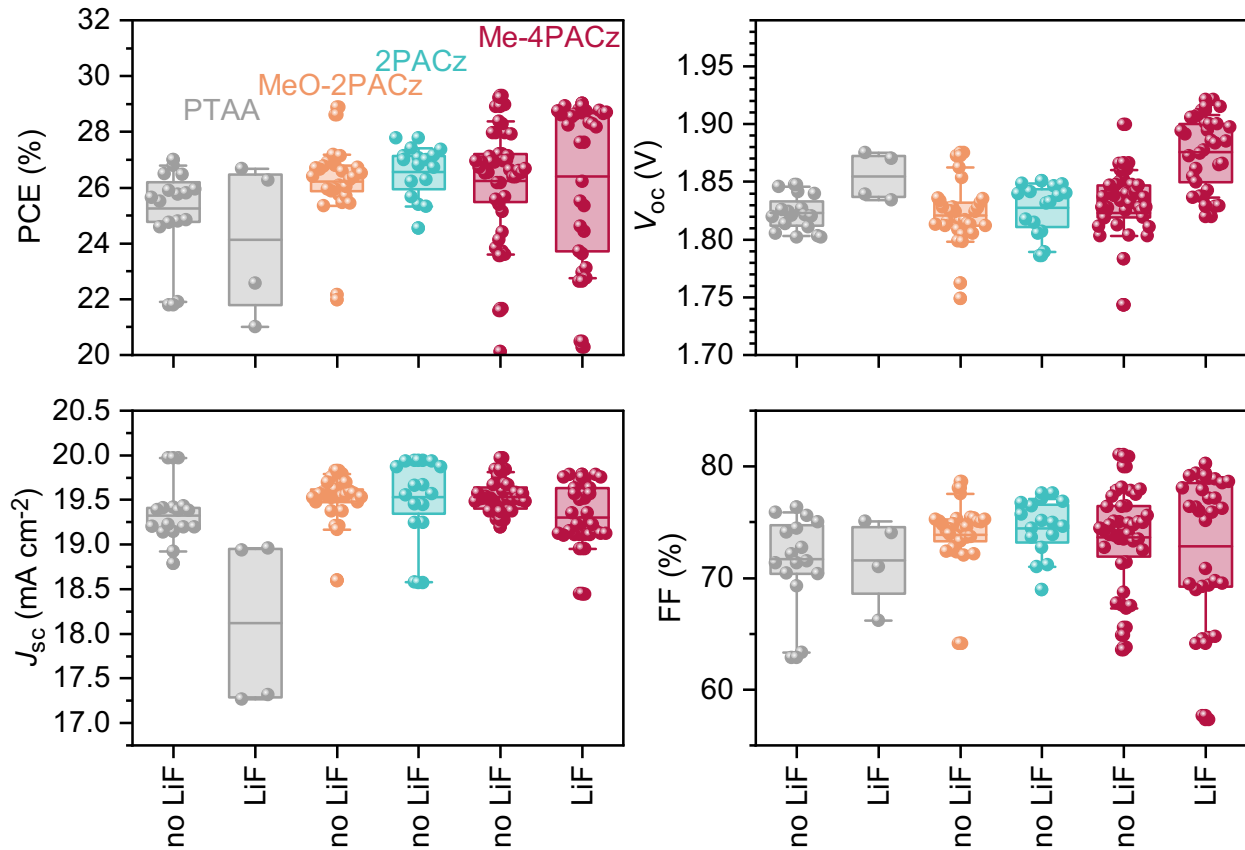
Figure 17: Performance of tandem solar cells for various hole-selective contacts and lithium-fluoride interlayers. Performance metrics of tandem solar cells using hole-selective layers as indicated in the top left graph. Tandem solar cells with and without LiF interlayer were fabricated when PTAA or Me-4PACz were used as HSL. The graphs include parameters from forward and reverse measurements. The boxes indicate the 25/75 percentiles and the whiskers mark the 10/90 percentiles. The line in the plots mark the respective average value. From [99]. Reprinted with permission from AAAS.

Efficient passivation in combination with fast hole extraction of Me-4PACz in perovskite single-junctions could be transferred into monolithic tandem solar cells, which led to higher FF, V_{OC}, and stability.

The performance of tandem solar cells using different hole-selective layers is shown in Figure 17. The arithmetic mean value, indicated by the horizontal line, reveals a similar FF behavior as for the single-junction solar cells shown in Figure 16C. With PTAA the lowest FF values are achieved, whereas MeO-2PACz and 2PACz lead to almost the same FF values. For Me-4PACz higher FF values are expected. However, as can be seen from the boxplot, the spread of the FF values is larger compared to the other HSL. This stems mostly from a poorer wetting of the perovskite on Me-4PACz, which leads to an increased spread of the performance metrics of tandem solar cells. However, the maximum achievable FF is with ~81% higher than for the other HSL despite almost all cells being perovskite limited. Because the shape of the $J-V$, especially for voltages below V_{MPP}, is mostly determined by the limiting subcell, the high FF highlights the good performance of the perovskite top cell. The average values for the J_{SC} and V_{OC} are very similar for all variations. Consequently, the PCE follows the same pattern as the FF: PTAA leads to the lowest PCE with an average value of 25.3%. It should be noted that the highest PCE with PTAA, 27.0%, is on the same level as the best scientifically published tandem solar cell.[106] For tandem solar cells with MeO-2PACz, 2PACz and Me-4PACz, the average PCE values are similar and amount to 26.2%, 26.6% and 26.3%. However, the highest PCE values are achieved with Me-4PACz.

To improve the PCE further, it is reported that a LiF interlayer between the perovskite and C_{60} is beneficial and should increase the V_{OC}.[36] Thus, we additionally fabricated tandem solar cells using this LiF interlayer for PTAA- and Me-4PACz-based tandem solar cells (denoted as 'LiF' in Figure 17). It indeed increases the V_{OC} strongly. For cells with PTAA, the average V_{OC} increased from 1.82 V to 1.85 V. Unfortunately, cells with LiF and PTAA tend to degrade faster leading to a reduced J_{SC} and PCE. We will discuss this later in more detail. For Me-4PACz the interlayer improves the V_{OC} strongly. The average values increase from 1.82 V to 1.88 V with a maximum V_{OC} of 1.92 V. In contrast, the FF and the J_{SC} decreases slightly, leading in the end to a similar PCE distribution as without LiF. However, as mentioned before the interlayer induces instabilities which will be shown later.

The best tandem solar cell at that time, which was a cell with Me-4PACz and LiF interlayer, was sent to Fraunhofer ISE CalLab for independent certification. With a V_{OC} of 1.9 V, FF of 79.4% and a J_{SC} of 19.23 mA cm^{-2} the cell had a PCE of 29.01%, similar to our in-house $J-V$ measurements. The certified value, which is defined by the MPP-track of the cell, amounts to 29.15% and was a world record from January 2020 to December 2020. This value entered the well-known "Best Research-Cell Efficiency Chart" by the National Renewable Energy Laboratory (NREL) as well as the "Solar cell efficiency tables".[9, 17] The certificate can be found in appendix D. This PCE is on par with the highest single-junction solar cell (GaAs) with the same area of ~1 cm^2 and approaches the theoretical limit of silicon single-junction solar cells.[8] Figure 18A shows the $J-V$ measured at Fraunofer ISE CalLab and for comparison the best $J-V$ achieved with PTAA (i.e. without LiF interlayer).

The photogenerated current densities, extracted from EQE measurements (Figure 18B), reveal that the cell is perovskite limited with $J_{Ph,Perovskite} = 19.41$ mA cm^{-2} and $J_{Ph,Silicon} = 20.18$ mA cm^{-2}. However, as described in section 6.1, the loss in PCE due to the reduced J_{SC} is partially compensated by a higher FF. The high cumulative current density of 39.59 mA cm^{-2} and low reflection loss of 2.57 mA cm^{-2} is a result of the optical optimization thoroughly described in section 6.1.
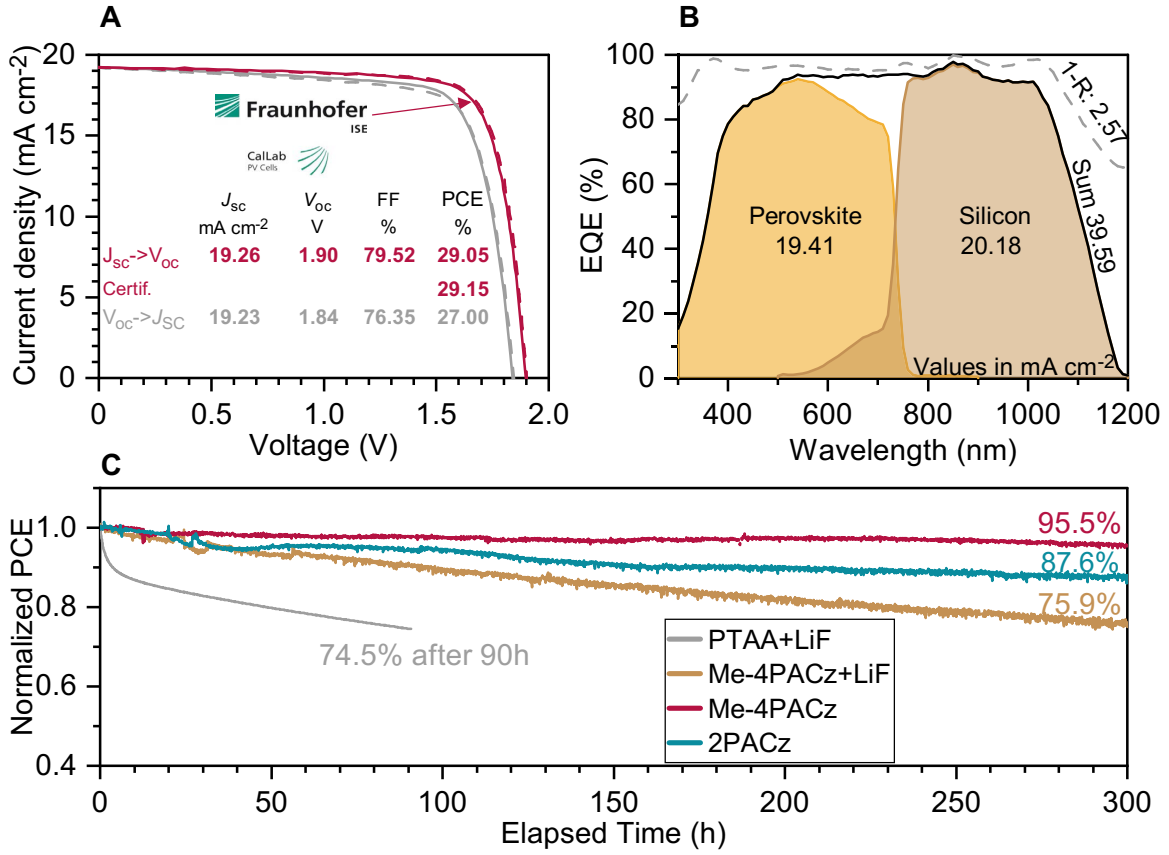
Figure 18: Performance and operational stability of tandem solar cells. (A) $J-V$ curve of the best tandem solar cell with PTAA and Me-4PACz(+LiF). The latter was measured at Fraunhofer ISE. (B) External quantum efficiency spectrum of the certified tandem solar cell including the reflection (denoted as 1-R). The values given in $\mathrm{mA\,cm^{-2}}$ are calculated using AM15g illumination. (C) Long-term MPP-track of non-encapsulated tandem solar cells measured in air. The given numbers denote the efficiency after $300\,\mathrm{h}$ or $90\,\mathrm{h}$ (for PTAA+LiF). From [99]. Reprinted with permission from AAAS.

After certification we continued fabricating devices and achieved a slightly higher PCE with Me-4PACz without LiF interlayer. As expected, the V_{OC} of $1.87\,\mathrm{V}$ is lower without the LiF interlayer but the high FF of 81% enabled a stabilized efficiency of 29.32% (see Figure 17). Thus the record efficiency (though yet not certified) could also be realized without the LiF interlayer.

As described above, we found stable PL spectra if the perovskite is deposited on 2PACz and Me-4PACz, whereas the latter shows a stable spectrum even at high intensities. To evaluate whether the stability of the film can be transferred to a higher operational stability of tandem solar cells, we measured the performance of different tandem solar cells for 300 hours. In order to measure the long-term stability of tandem solar cells, a proper light source is necessary. However, typical setups make use of single white light sources, which do not represent the AM1.5g spectrum sufficiently. Although we elaborated in section 6.1 that the PCE is not too sensitive to current-mismatch conditions, for stability measurements it is important to have the correct and stable conditions over the long period of tracking to ensure similar mismatch conditions. Elsewise, the wrong subcell might be limiting, which can affect the long-term stability. In the worst case, a usually (under perfect AM1.5g illumination) perovskite limited tandem solar cell would be tracked by illuminating the cell with a light source with low NIR intensity, rendering the silicon cell limiting. Thus, a degradation of the perovskite might be underestimated and could lead to wrong conclusions. With the single white light sources, it is not possible to adjust the photogenerated current density in the subcells to imitate AM1.5g illumination. To address this problem, we, in corporation with the University Ljubljana, developed a

bichromatic LED light source to enable full control of the illumination spectrum. The light source consists of two different LED types. Blue LEDs with a peak emission wavelength of 470 nm will generate charge carriers in the perovskite without affecting the silicon subcell. NIR LEDs with a peak emission wavelength of 940 nm will generate a photocurrent in the silicon subcell without affecting the perovskite subcell. To enable homogeneous illumination over an area of 7.5 cm×7.5 cm, an LED array of 144 blue and 49 NIR LEDs were simulated, designed and fabricated. The intensity can be controlled individually and is set as described in section 5.2. To account for any intensity fluctuations, the intensity is measured for each LED type with selective photodiodes.

The non-encapsulated tandem solar cells are placed in ambient conditions on a vacuum copper block which is cooled to 25 °C. The maximum power point was tracked using voltage perturbation and is recorded every 5 minutes. However, to account for measurement noise, the following PCE values are average values over 60 minutes (i.e. initial values are the average values of 0 min to 60 min, whereas the values after 300 h are the average values of the points recorded between 299 h and 300 h). The relative humidity was tracked as well and amounted to 30% to 40%.

As described previously, tandem solar cells with PTAA and LiF interlayer degrade fast, which is also represented in this MPP-track. After only 90 h the PCE decreased to 74.5% of its initial value. With 2PACz, the tandem solar cell operated after 300 h still at 87.6% of its initial PCE. As expected, the tandem solar cell with Me-4PACz shows the best stability after 300 h with still 95.5% of the initial PCE. Comparing this result to state-of-the-art stability tests of non-encapsulated tandem solar cells in ambient conditions, where the cells retained 90% of initial PCE after 61 hours[92] and 92% after 100 hours[105], our Me-4PACz tandem solar cell showed a superior operational stability. However, there are some reports demonstrating excellent tandem stability of encapsulated tandem solar cells even under harsh conditions such as elevated temperatures or high relative humidity.[92, 107]

Additionally, we tracked a tandem solar cell with Me-4PACz and LiF interlayer. Unambiguously, the LiF interlayer worsens the long-term stability. As described in other reports, the decrease in stability might be caused by deterioration of the electrodes and C_{60} interface upon migration of Li^+ and F^- ions.[152–155]

In addition to the long-term MPP-tracks, we tracked a tandem solar cell with Me-4PACz (without LiF interlayer) at elevated temperatures. Following the procedure carried out by Jošt $et\ al.$, the temperature was successively increased from 25 °C to 85 °C and back to 25 °C in 15 °C steps. At each temperature the cell was held for at least 15 minutes. After this procedure, which took approx. 200 min, the cell had the same PCE as before, despite the increased Br content in the perovskite.

6.2.5   Extraction of Subcell Performance

One downside of monolithic tandem solar cells is that the subcells are not individually measurable. Thus, it is difficult to give information about the performance of the subcells, especially in the exact tandem configuration with e.g. fixed bottom cell surface topography. EQE spectra are the only measurement disclosing information about the subcells which is used in nearly all multijunction publications. In addition, we used hyperspectral absolute photoluminescence imaging to access the QFLS of the individual subcells.[156] The evaluation of the PL spectra reveals that the silicon and perovskite subcell delivers a QFLS of 0.72 eV and 1.18 eV, respectively. This is in excellent agreement with the V_{OC} of 1.90 V obtained by a $J-V$ measurement. Figure 19A and B show the integrated photon flux of the perovskite and silicon subcell under 1-sun illumination using excitation wavelengths of 455 nm and 850 nm for the perovskite and silicon subcell, respectively.

Although this gives slightly more insight into the performance of the subcells, the maximum power point and FF for example are still unknown. Ideally the FF values of both subcells are equally high to have simultaneously current matching an power matching (cf. section 2.9.3). Hence, it is desirable to measure the J_{MPP}.

To evaluate the performance of the subcells in more detail, we measured injection-dependent electroluminescence (EL). The injected current, which flows equally through both subcells, cause radiative
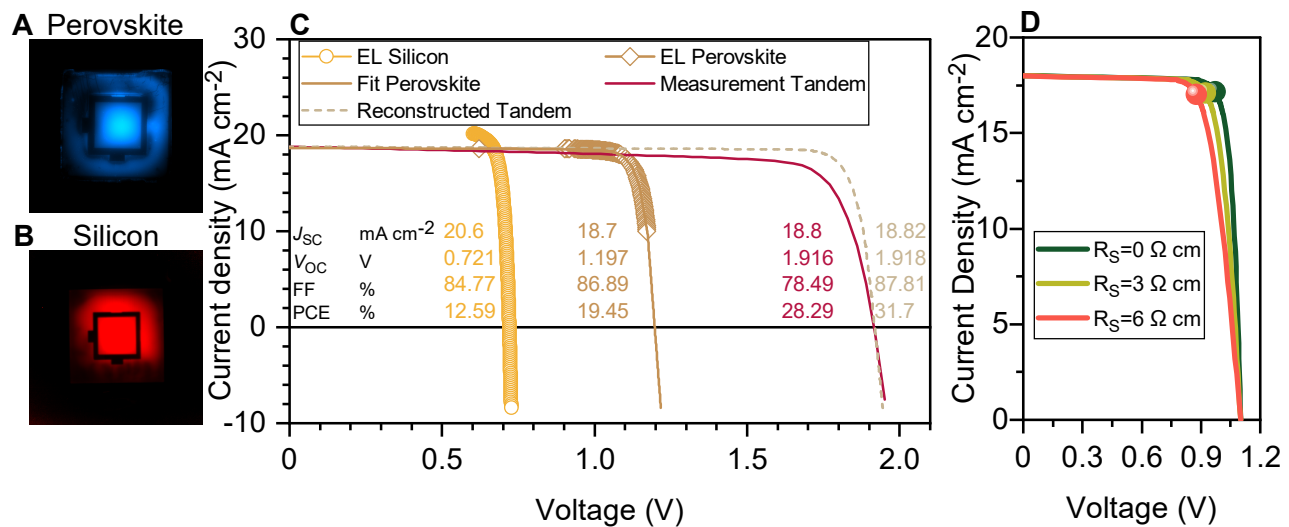
Figure 19: Subcell analysis by photoluminescence and injection-dependent electroluminescence
(A-B) Integrated photon flux from photoluminescence imaging of the perovskite (A) and silicon (B) subcell at 1-sun intensity. The excitation wavelengths are 455 nm and 850 nm for the perovskite and silicon subcell, respectively. (C) Reconstructed subcell $J - V$ characteristics generated from injection-dependent electroluminescence measurements. To cover the entire voltage range, the perovskite subcell was fitted using a one-diode model. Furthermore, the reconstructed and measured tandem $J - V$ curve is shown. The parameters of each curve are given. (D) Simulated $J - V$ curves according to equation 2.21 with different series resistance values as given in the legend. The circles represent the maximum power points. (A-C) From [99]. Reprinted with permission from AAAS.

recombination from which the QFLS (corresponds to the voltage) can be calculated. This was done for a series of injected currents. The so generated current density - voltage pairs assemble reconstructed dark $J - V$ curves for the perovskite and silicon subcell. Reconstructed light $J - V_{rec}$ curves were then generated by shifting the dark $J - V$ curves of the perovskite and silicon subcell by the respective J_{Ph}. Caution needs to be taken as a series resistance will generate a difference between the shifted dark $J - V$ and the $J - V$ curve measured under illumination.[157] Especially the V_{OC} of the shifted dark $J - V$ will be overestimated then. However, the performed method to reconstruct the dark $J - V$ does not include the series resistance as the internal voltage is used instead of the external voltage. The reconstructed subcell $J - V_{rec}$ curves are shown in Figure 19C as open symbols. To access the entire range, the perovskite subcell was fitted with a one-diode model using the ideality factor $n_{ID} = 1.26$ as extracted from the Suns-V_{OC} measurements described above. With this, we are able to access the performance of the individual subcells excluding the series resistance. The reconstructed tandem $J - V$ is generated by adding the voltages of the subcells for each current density (as explained in section 2.9.3). The comparison of the reconstructed and under the solar simulator measured tandem $J - V$ curve shows mainly two differences: (i) The reconstructed curve shows a slightly higher shunt resistance. On the one hand this might be an effect of very small pinholes which affect the measured $J - V$ curve differently than the injection dependent EL measurements. In the EL images these tiny shunts might not be visible and therefore they would not affect the reconstructed $J - V$. On the other hand, the curve at voltages below V_{MPP} is reconstructed by injecting low currents (reminder: the curve was generated by shifting the dark $J - V$). The low current leads to a low amount of emitted photons and thus, to a larger measurement error. Additionally, metrologically induced fluctuations in the injected current may occur, increasing the measurement error as well. (ii) In the measured $J - V$, the series resistance is included, whereas it is not included in the reconstructed curve. Therefore, the PCE of 31.7% and FF of 87.8% for the reconstructed curve can be seen as the maximum value which can be achieved if the series resistance can be optimized until it does not have a substantial contribution anymore.

As the series resistance does not have a major effect on the J_{MPP} (see Figure 19D; For comparison: The slope around $V = V_{OC}$ of the measured tandem solar cell is ~5 Ω cm), it is possible to extract the J_{MPP} for the subcells with sufficient precision. The J_{MPP} values of the perovskite and silicon subcell amount to 17.99 and 19.31 mA cm^{-2}. Hence, adjustments such as increasing the current density in the perovskite while decreasing the current density in the silicon are necessary to enable the same J_{MPP}.

Although there might be a small error for the J_{MPP} values due to the difference in the shunt resistance between the measured and reconstructed tandem $J - V$ curve, the error should be small enough to get sufficient precision.

To estimate the PCE potential, we conducted SPICE (Simulation Program with Integrated Circuit Emphasis) simulations with one-diode models for each subcell as we have done in section 6.1. The parameters were extracted by fitting the reconstructed subcell $J - V$ curves.

Assuming the same cumulative current density of 39.3 mA cm^{-2} as obtained by EQE and AM1.5g illumination, we found a maximum PCE of 32.43% if the subcells are current matched. However, as elaborated in section 6.1 and apparent from these simulations, the PCE is not too sensitive to small mismatch conditions. Even if the mismatch amounts to ± 1.2 mA cm^{-2}, the PCE is still above 32%.
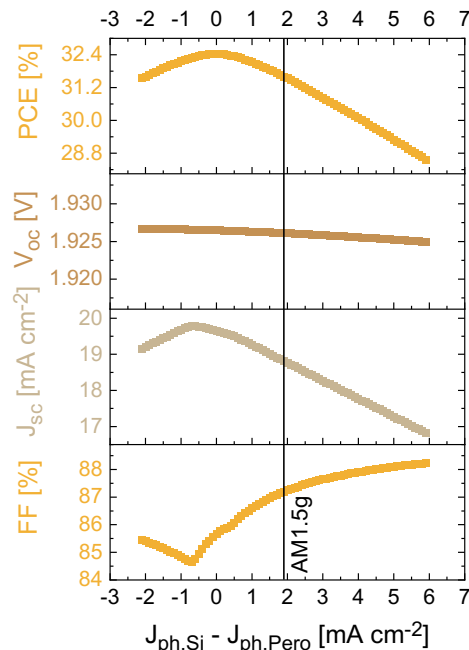
Figure 20: Electrical simulation to identify optimum performance conditions. Simulations are based on Simulation Program with Integrated Circuit Emphasis (SPICE) and two one-diode models were connected in series to create the tandem solar cell model. The parameters for the subcells were extracted by fitting the subcell $J - V$ curves shown in Figure 19C. The ideality factor for the perovskite was fixed to 1.26, obtained by Suns-V_{OC} measurements described previously. From [99]. Reprinted with permission from AAAS.

6.2.6 Conclusion

In summary we presented Me-4PACz, a new superior self-assembled monolayer molecule which shows a high level of interface passivation leading to a high PLQY and thus V_{OC} and a fast hole-extraction speed enabling high FF values. The new hole-selective contact provides improved phase stability demonstrated with prolonged photoluminescence measurements at high illumination intensities, despite using a wide-bandgap perovskite (E_G=1.68 eV) with increased amount of bromide.

These advantages are transferred to into monolithic perovskite/silicon tandem solar cells, where different hole-selective layers are compared. As expected from the superior properties in single-junction solar cells, also in tandem solar cells, Me-4PACz leads to highest efficiencies. We achieved high FF values of up to 81% and high V_{OC} values up to 1.92 V. Consequently, with a certified PCE of 29.15% we set a new world record for this kind of solar cell.

We demonstrated the improved phase stability using a newly designed aging setup to properly measure long-term MPP-tracks of tandem solar cells. The non-encapsulated tandem solar cell with Me-4PACz retained 95.5% of its initial PCE after 300 hours continuous operation.

To evaluate the performance of the individual subcells, we used injection-dependent electroluminescence. This advanced characterization method enables us to reconstruct and analyze the subcell $J - V$ curves without the influence of the series resistance. To validate the method, we calculated the tandem $J - V$ from the reconstructed subcell $J - V$ curves and found good agreement between the measured and reconstructed tandem solar cell. However, a slight difference of the reconstructed and measured curve in the range of $1 < V < 1.7$ occurs which leaves some room for improvement of this characterization method.

Ultimately we used the reconstructed subcell $J - V$ curves to estimate the potential of this tandem solar cell design. Electrical simulations using the parameters extracted from the reconstructed subcell curves reveal that a PCE of 32.43% is achievable in the absence of serial losses for the herein used material and layer stack.

6.3 27.9% Efficient Monolithic Perovskite/Silicon Tandems on Industry Compatible Bottom Cells

This section is based on the work '**27.9% Efficient Monolithic Perovskite/Silicon Tandem Solar Cells on Industry Compatible Bottom Cells**' published by Eike Köhnen, Philipp Wagner, Felix Lang, Alexandros Cruz, Bor Li, Marcel Roß, Marko Jošt, Anna B. Morales Vilches, Marko Topič, Martin Stolterfoht, Dieter Neher, Lars Korte, Bernd Rech, Rutger Schlatmann, Bernd Stannowski and Steve Albrecht in *Solar RRL*, 5:2100244, 2021. doi:10.1002/solr.202100244.

In this study, we demonstrate monolithic perovskite/silicon tandem solar cells on bottom cells which are more compatible to industrial production. These bottom cells are based on czochralski silicon, are ~3-fold thinner compared to typical laboratory cells and have a rough front side as no chemical-mechanical polishing is applied. We compare the results of these bottom cells to laboratory-typical bottom cells. The thinner bottom cells necessitate to change the bandgap or thickness of the top cell if current matching conditions should be maintained. On the one hand, a wider bandgap can enable higher V_{OC} values. On the other hand, widening the perovskite's bandgap comes typically along with reduced stability due to halide segregation. Systematic optical simulations reveal the optimum balance of perovskite thickness, bandgap and bottom cell thickness to enable maximum J_{SC} values for flat and textured front sides.

6.3.1 Introduction

As described in section 3.3 and demonstrated in section 6.1 and 6.2, perovskite/silicon tandem solar cells have experienced an excellent improvement of the PCE in a very short time. Nonetheless, this technology is not commercially available, yet. There are well-known hurdles which are addressed with an increasing interest such as upscaling and long-term stability. However, all in section 3.3 listed tandem solar cells (where data is available), make use of silicon bottom cells which are not relevant for industrial production. The bottom cells used in these laboratory tandem cells are made from floatzone (FZ) silicon with mostly mechanically polished front sides and thicknesses above 250 µm which is not industry relevant for three reasons: (i) FZ silicon is not used in industry. Instead, the czochralski method will remain the main method for growing silicon ingots.[5] (ii) Chemical-mechanical polishing (CMP) to planarize the front side is time consuming and expensive. Hence, this step should be omitted by using saw damage etched or textured surfaces. The latter is favorable due to optical advantages and is addressed in a couple of publications.[92, 94, 107, 111] However, typical spin-coated devices (which is not compatible with regular texture) enable still higher PCE values (see section 3.3 and 6.2). (iii) The absorption of silicon for photon energies just above the bandgap, i.e. in the infrared (IR) part of the spectrum, is relatively poor. For tandem cells however, where the top cell will absorb most of the higher energy photons, the IR response of the bottom cells is crucial.[101, 158] Hence, the bottom cell thickness in most publications on perovskite/silicon tandem solar cells is 260 µm to 300 µm, whereas according to current market forecasts, the industry-relevant thickness for n-type monocrystalline silicon is just 140 µm to 150 µm (as cut) in 2022.[5]

Therefore, we demonstrate monolithic perovskite/silicon tandem solar cells based on thin non-polished n-type CZ silicon. More precisely, we used (100)-oriented 130 µm thick (as-cut) saw damage etched n-type CZ-silicon wafers with a specified resistivity of ~5 Ω cm (in the following termed ´CZ-based´). As a reference, we use (100)-oriented 280±20 µm thick FZ wafers with a CMP front side and a resistivity of ~3 Ω cm (in the following termed ´FZ-based´). The complete FZ and CZ-based bottom cells had thicknesses of 280 µm and 100 µm, respectively. See section 4 for more details.

6.3.2 Tandem Solar Cells with Different Bottom Cells

The topography of the bottom cells was measured using confocal 3D laser scanning microscope (CLSM) for the CZ bottom cell to aquire a large area. Because of the very flat surface for the FZ-based bottom cell, the CLSM leads to visual artifacts. Hence, we used atomic force microscopy to analyze the surface of the

FZ-based bottom cells. The root mean square roughness values amount to 1 nm and 736 nm, whereas the maximum height values are 9 nm and 7.7 μm for the polished FZ and non-polished CZ based bottom cell, respectively. Although the maximum height of 7.7 μm is more than 10 times higher than the thickness of the perovskite absorber (500-700 nm), the lateral dimension of the features is large enough (typically several 10 to 100 μm) to enable complete coverage during spin coating.

Because of higher reproducibility (see section 6.2), we used 2PACz as hole-selective layer. The perovskite with a nominal composition of $Cs_{0.05}(MA_{0.23}FA_{0.77})Pb(Br_{0.23}I_{0.77})_3$ has a bandgap of 1.68 eV. As the tandem solar cells have been perovskite limited in the study presented in section 6.2, we increased the thickness of the perovskite by using ethylacetate instead of anisole as antisolvent. To achieve highest V_{OC} values, we utilized a LiF interlayer between the perovskite and C_{60}. The top cell is fabricated identically on both types of bottom cells. More details on the fabrication can be found in section 4. The generic stack of the complete tandem cell is shown in Figure 10C.

To monitor the process, opaque perovskite single-junction solar cells with an active area of $0.16\,cm^2$ were fabricated together with the tandem solar cells. The median performance values (10 devices) for opaque perovskite single-junctions are 78.5% for the fill factor (FF), $20.3\,mA\,cm^{-2}$ for the short-circuit current density (J_{SC}), 1.2 V for the open-circuit voltage (V_{OC}) and 19.3% for the PCE. A maximum efficiency of 19.9% with a V_{OC} of 1.21 V was obtained in this p-i-n type configuration, which is among the highest PCE and V_{OC} values for perovskite cells typically used as top cells in two-terminal perovskite/silicon tandem solar cells.[159]
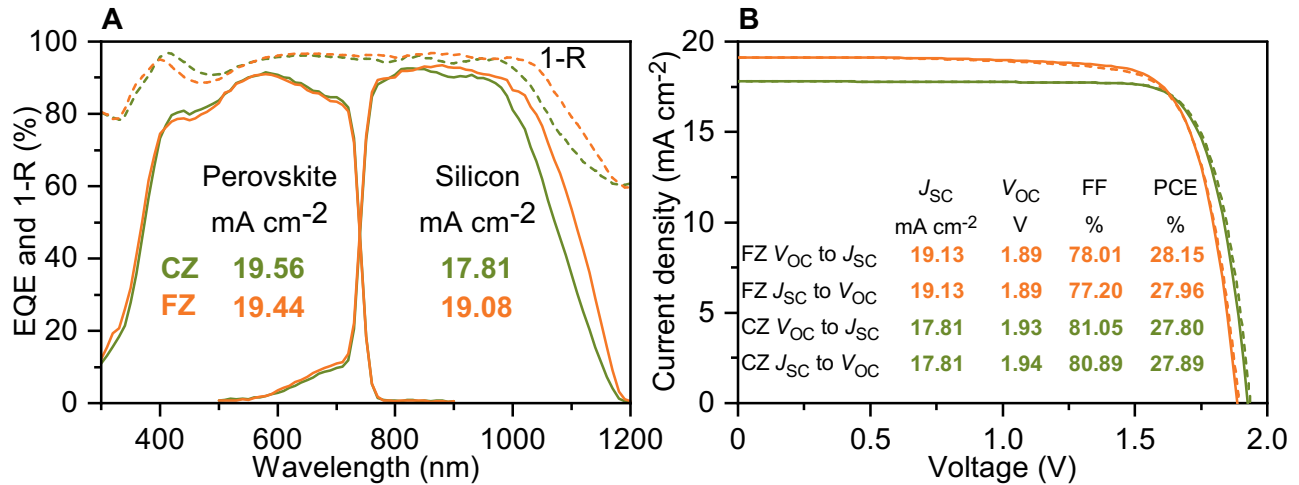
Figure 21: Tandem solar cells based on czochralski and floatzone silicon (A) External quantum efficiency (EQE) and reflection (denoted as 1-R) spectra of the best tandem solar cells utilizing floatzone (FZ) and czochralski (CZ) silicon for the bottom cells. The perovskite top cell is fabricated identically on both types of bottom cells. Furthermore, photogenerated current densities J_{Ph} calculated with AM1.5g illumination are given. (B) $J-V$ characteristics of the respective tandem solar cells under AM1.5g illumination including the PV parameter for $J-V$ scanning in both bias directions.

The EQE spectra in Figure 21A shows an identical response for the perovskite subcell on both types of bottom cells. Hence, the $J_{Ph,Perovskite}$ values of 19.56 and $19.44\,mA\,cm^{-2}$ for the CZ- and FZ-based devices are almost the same. In contrast, the utilization of a thinner bottom cell reduces the response in the near-infrared wavelength range. As a result, the $J_{Ph,Silicon}$ of the CZ-based device is with $17.81\,mA\,cm^{-2}$ lower than the value for the FZ-based device ($19.08\,mA\,cm^{-2}$).[i] Consequently, the expected J_{SC} will be lower for the CZ-based device. The lower absorption of NIR light in the thin silicon bottom cell increases the amount of light which is reflected at the rear side of the tandem cell. As elaborated in section 6.1, the

---

[i]These J_{Ph} values differ from the values presented in section 6.2, because a new IZO target was used which was not optimized when the samples were fabricated.

increased current mismatch will increase the FF. Furthermore, thinner silicon wafers lead to higher V_{OC} values due to a decreasing total recombination current density.[8]

To quantify the gain in V_{OC} due to thinner silicon bottom cells, we simulated silicon single-junction solar cells with both types of utilized wafers with the program Quokka3. The J_{Ph} is used as typically achieved in tandem solar cells. The simulated improvement in V_{OC} amounts to 17 mV when using thinner CZ-based bottom cells. Even though the FF is also affected by the thickness and grow method, based on the simulations the configurations used in this study should deliver the same FF of 82.5% to 83%, .

Summarizing, the tandem solar cells with CZ-based bottom cells are expected to have lower J_{SC} due to thinner wafer and lower NIR response, higher V_{OC} due to lower recombination current density and higher FF due to increased current mismatch.

The $J-V$ characteristics of the best devices (in terms of PCE) shown in Figure 21B verify our expectations. The reference cell based on FZ-Si has a J_{SC} of 19.13 mA cm^{-2}, V_{OC} of 1.89 V, and FF up to 78.0% and as a result a PCE of 28.15%. The tandem solar cell based on thin CZ-Si shows a high FF value of 80.89%, which partially compensates the lower J_{SC} of 17.81 mA cm^{-2}. Together with an increased V_{OC} which amounts up to 1.94 V, the CZ-based tandem solar cell has a PCE of 27.89%. Thus, this value is just 0.26 percentage points below the reference cell. The maximum FF achieved with the CZ-based tandem solar cell is 81.15%, which is to the best of our knowledge the highest reported value for this tandem technology. Three CZ- and four FZ-based tandem solar cells reveal the same median PCE of 27.8% for both types.

The V_{OC} difference of 30 to 40 mV for the devices shown in Figure 21B is slightly higher than expected from the simulations of the silicon bottom cells. To analyze the V_{OC} in more detail, we measured absolute PL and extracted the QFLS for the perovskite and silicon subcells. The intensity of the laser which selectively illuminates the top or bottom cell was set to match with the J_{Ph} values of the respective subcell. The perovskite subcell delivers the same QFLS on both bottom cell types and amount to 1.20 eV, which is consistent with the V_{OC} of the perovskite single-junction reference cells. The QFLS of the silicon subcell in the FZ-based device is ~690 meV. The resulting sum of the perovskite and silicon subcell amounts to 1.89 eV, which matches well with the V_{OC} of 1.90 V to 1.91 V measured for this specific sample. The QFLS of the silicon bottom cell in the CZ-based device is ~710 eV. The enhancement of ~20 meV agrees well with the simulated increase of 17 mV. The cumulative QFLS of ~1.91 eV matches with the measured V_{OC} of 1.92 to 1.92 V. Therefore, we account the previously mentioned improvement of up to 40 mV to a sample-to-sample variation. To elaborate more on this, a larger amount of cells would be needed to improve the statistical evaluation but this will not be covered in thus study.

To exclude any structural changes in the perovskite due to different surface topographies of the bottom cells, X-Ray diffraction (XRD) measurements were conducted. The XRD patterns acquired for the HSL/perovskite stack deposited on the different bottom cells reveal similar crystallization of the perovskite films on both surfaces. A minor difference appears around 32.8°, which we attribute to the In$_2$O$_3$ recombination layer instead of the perovskite layer.

To analyze the improvement in FF for the CZ-based devices in more detail, we measured both, FZ- and CZ-based devices with the exactly same mismatch. To enable this, the intensity in the near-infrared wavelength range for the CZ-based device was increased to enhance the $J_{Ph,Silicon}$. Thus, the $J_{Ph,Perovskite}$ and $J_{Ph,Silicon}$ for the CZ-based device match with the values from the FZ-based device obtained by EQE (and AM1.5g illumination). The similar FF values for both device types under the same mismatch conditions strongly suggests that the enhancement in FF under AM1.5g illumination mostly stems from the difference in mismatch conditions.

An advanced way to analyze the subcells in more detail was presented in section 6.2 using injection-dependent EL. However, this would be beyond the scope of this study as the combination of the EQE and PL is sufficient (for this work) to gain knowledge about the subcell performance.

We tracked the long-term stability of one CZ- and two FZ-based devices for 1000 h using the home-built tandem aging setup as described in section 6.2. Initially, the PCE values were 27.6% (CZ), 28.15%(FZ) and 27.4% (FZ). As all cells are initially perovskite photocurrent-limited and we assume that mainly the perovskite is degrading, we expect that all cells will behave similarly. Besides the J_{MPP} and V_{MPP} from

	J_{sc}	V_{oc}	FF	PCE
	mA cm^{-2}	V	%	%
FZ V_{oc} to J_{sc}	19.13	1.89	78.01	28.15
FZ J_{sc} to V_{oc}	19.13	1.89	77.20	27.96
CZ adj. Spectrum V_{oc} to J_{sc}	19.09	1.92	77.42	28.38
CZ adj. Spectrum J_{sc} to V_{oc}	19.09	1.93	76.29	28.11
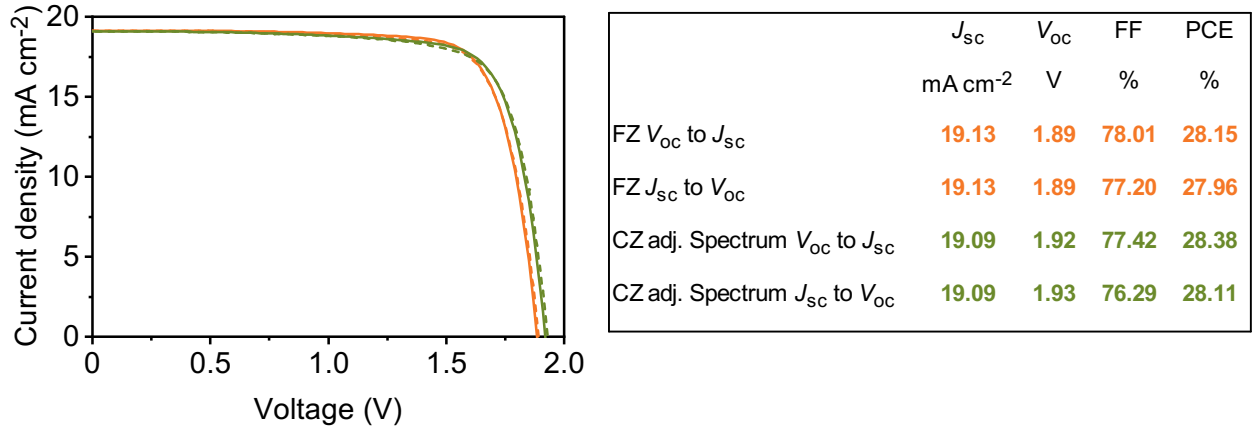
Figure 22: Performance of tandem solar cells under same mismatch conditions. (A) $J - V$ characteristics of CZ- and FZ-based tandem solar cells under the same mismatch conditions. The FZ-based tandem solar cells is illuminated with the standard AM1.5g spectrum (i.e. same curve as in Figure 21B). The CZ-based tandem solar cell is illuminated with a NIR-enhanced spectrum to achieve the same $J_{Ph,Silicon}$ as in the FZ-based device. Hence, the $J_{Ph,Silicon}$ and $J_{Ph,Perovskite}$ values in both cells are ~19.1 and ~19.5 mA cm^{-2}.

which we calculated the absolute PCE and normalized PCE, we added the measured cell temperature as well as the measured relative humidity (RH). After 1000 h the cells operated at 67% (CZ), 70% (FZ) and 67% (FZ) of their respective initial PCE values. As previously described in section 6.2, the LiF interlayer which increases the V_{OC} is not beneficial for long-term stability. The long-term stability could be enhanced using MA-free perovskite compositions and/or incorporating chloride, as presented by Xu and Boyd *et al.*[106] Interestingly, all tandem solar cells regardless of the bottom cell type seem to stabilize after ~500 h, mainly because of a steady J_{MPP}. Although these values do not represent the best stability, this is to date the longest MPP-track for perovskite/silicon tandem solar cells. Additionally, this track should be a good example of reporting long-term MPP-Tracks as it includes the cell temperature and RH. In the ideal case, the intensity of the different LED types (blue and NIR) will be provided. Yet, there are challenges which need to be addressed but in the near future we will be able to add the intensity of each LED type to have a measure for the mismatch.

6.3.3 Optical Simulations

The reduced $J_{Ph,Silicon}$ for thinner bottom cells necessitates adjustments if current matching (or power matching) should be maintained. Although we demonstrated in this study and in section 6.1 that the PCE is not too sensitive to small mismatch conditions, it makes sense to keep current matching under standard test conditions (STC). On the one hand, reducing the mismatch by increasing the perovskite's bandgap will ideally increase the PCE due to increased V_{OC} leading in the end eventually to the exactly same PCE for thin and thick bottom cells. On the other hand, as demonstrated by Aydin *et al.*, the temperature of the solar cell will alter the mismatch conditions, too. Hence, if the cell will be mismatched under STC, the mismatch might increase further for elevated cell temperatures, reducing the PCE

To achieve these matching conditions, the thickness of the perovskite can be reduced to enable more light being transmitted to the silicon subcell. Efficiency-wise the more favorable way is to increase the perovskite's bandgap as this would simultaneously result in higher V_{OC} values. However, caution needs to be exercised as the wider bandgap typically leads to reduced stability due to phase segregation.[80, 136] To quantify the needed bandgap and/or thickness, we performed optical simulations for 100 μm and 280 μm thick silicon bottom cells. The optical parameters for the perovskite were extracted from spectral ellipsometry for a perovskite composition with a bandgap of 1.63 eV. To cover a bandgap range from 1.63 eV to 1.78 eV, the
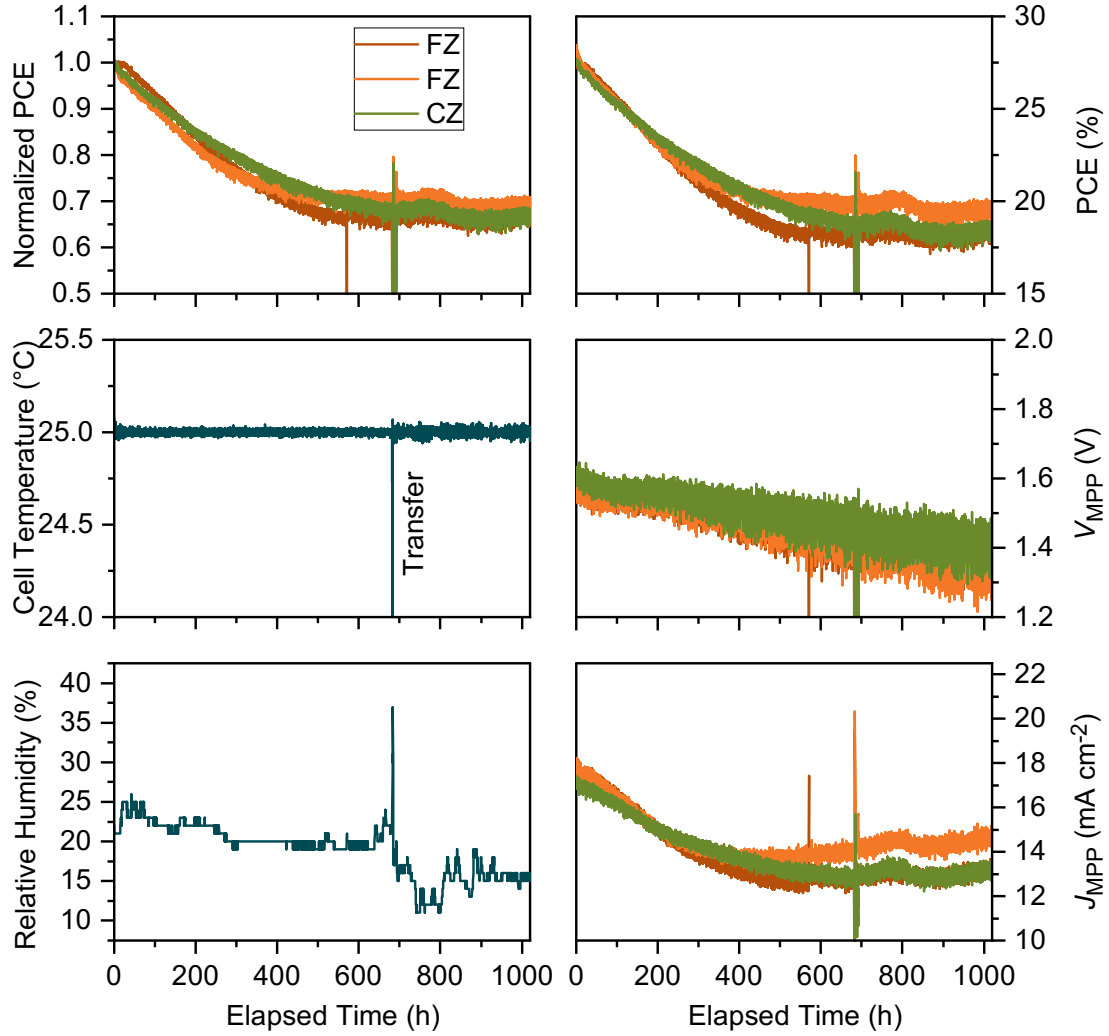
Figure 23: Long-term MPP track. Performance of FZ- and CZ-based tandem solar cells tracked for 1000 hours. The cells were continuously illuminated and tracked using the tandem ageing setup described in section 6.2. Besides the performance of the tandem solar cells, the tracked cell temperature and relative humidity is given. During the measurement, the setup had to be stopped for 10 min and moved, which caused the data noise around 680 h (labeled with 'Transfer').

refractive index n and extinction coefficient k were shifted along the wavelength axis as it was done in previous publications.[126, 127] For each bandgap, the thickness was varied between 700 and 1500 nm as the perovskite thickness should be thick enough to enable current matching with wide bandgaps and with that high V_{OC} values. Highly efficient solar cells with such thick perovskite layers have already been reported.[72, 105, 107, 160]

Figure 24 shows which top cell bandgap is needed to obtain current matching conditions as a function of the perovskite thickness and bottom cell thickness. If the perovskite's thickness is increased from 700 to 1500 nm, the top cell bandgap needs to be widened by 0.047 eV for both bottom cell thicknesses. Additionally, we found that a reduction of the bottom cell thickness from 280 µm to 100 µm, as experimentally presented in this study, requires to widen the perovskite's bandgap by 0.02 eV, regardless of the perovskite thickness. Simultaneously, the $J_{Ph,matched}$, which is equal in the top and bottom cell, is reduced from 19.64 to 19.14 mA cm^{-2}, independent of the perovskite thickness. This means for example that the perovskite's bandgap (if its thickness is 700 nm) needs to increase from 1.69 eV to 1.71 eV if the thinner bottom cell is used. The higher V_{OC} from both, bottom and top cell (40 to 50 mV) will exactly compensate the reduced
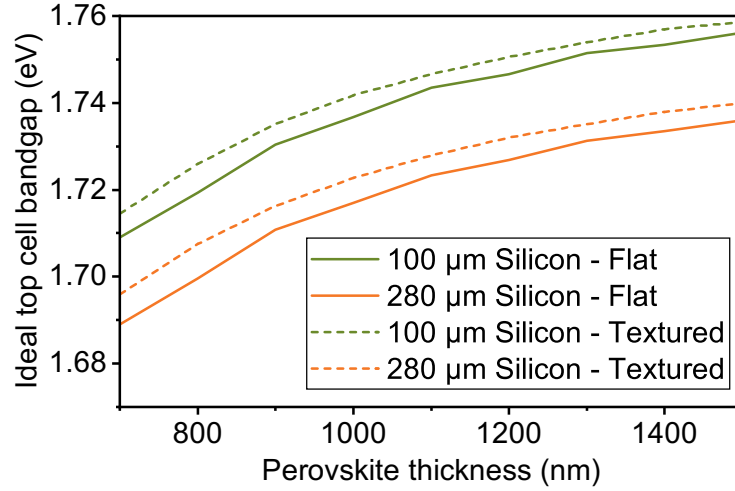
Figure 24: Optical simulation of tandem solar cells. Ideal perovskite bandgap which is needed to obtain current matching conditions as a function of the perovskite thickness. The simulations were performed for 100 μm and 280 μm thick silicon.

J_{SC} (when assuming that $J_{Ph,matched} = J_{SC}$). To maintain the same PCE, the FF needs to stay constant regardless of the perovskite's thickness. Ultimately, a trade-off between high J_{SC} (thick silicon, low top cell bandgap) and high V_{OC} (thin silicon, high top cell bandgap) needs to be made. Finding the optimum bottom cell thickness will be subject for future work.

We performed the same simulations using double-side textured silicon with a conformally deposited top cell. As previously simulated and experimentally demonstrated,[31, 92, 94, 135] the additional front-side texture reduces reflection and removes interference patterns, enabling higher J_{Ph} and J_{SC} values. The exact same pattern was found, as shown in Figure 24: The utilization of 100 μm silicon instead of 280 μm requires to widen the top cell bandgap by ~0.02 eV while the J_{SC} will decrease from ~20.44 to 19.95 mA cm^{-2}.

6.3.4 Conclusion

We demonstrated perovskite/silicon tandem solar cells based on industry-relevant silicon bottom cells, namely 100 μm thin CZ-wafers with a saw damage etched front side (i.e. without chemical-mechanical polishing) and a textured rear side. For comparison, we fabricated tandem cells based on 280 μm thick FZ-wafers with a chemical-mechanical polished front side, which are commonly used in laboratory-scale tandem devices. The CZ-based tandem cells have PCE values of up to 27.89%, which is just slightly below the maximum value of 28.15% for FZ-based tandem cells. However, the median PCE of 27.8% indicates equal performance for both bottom cell types. The median V_{OC} increases from 1.89 V (max. 1.91 V) for the FZ-based cells to 1.92 V (max. 1.94 V) for the CZ-based cells, explained by the higher V_{OC} of the thin CZ bottom cell. Simultaneously, thinner silicon bottom cells present a lower EQE in the infrared region, leading to a lower photogenerated current density and, thus, a lower J_{SC} (19.1 vs. 17.8 mA cm^{-2}). The increased mismatch, when using an identical top cell, results in improved FF values (77.2 vs. 80.9%) with a maximum FF of 81.15%.

Long-term MPP-tracking demonstrates that the non-encapsulated tandem solar cells perform at 67% (CZ) and 67 to 70% (FZ) of their initial PCE values after 1000 h. Although this is not the highest stability, it is the first MPP-track of perovskite/silicon tandem solar cells which lasted for 1000 h in air and sets a first benchmark. We performed optical simulations to find current matching conditions for the 100 μm and 280 μm silicon bottom cells with planar and textured front sides. The perovskite bandgap needs to be widened by ~0.02 eV when using a 100 μm thin silicon wafer instead of the commonly used thickness of 280 μm. Simultaneously, the expected J_{SC} reduces by ~0.5 mA cm^{-2}. The higher V_{OC} from both top and

bottom cell together (40 to 50 mV) will exactly compensate the reduction in J_{SC}.

Although we give a guide for the design of the perovskite thickness and bandgap depending on the thickness of the silicon bottom cell, there exist other effects, which alter the practical optimum top cell bandgap. On the one hand, a highly luminescent perovskite top cell will emit photons due to radiative recombination, which will be absorbed in the silicon bottom cell enhancing the $J_{Ph,Silicon}$ and leads to a relaxed requirement for current-matching conditions.[161] Furthermore, in outdoor application, the temperature of the tandem solar cell will differ from the 25 °C used as standard test condition (STC). The optical bandgap of both perovskite and silicon will change depending on the temperature. It was found that a lower top cell bandgap (at STC) is required if the cell operates at elevated temperatures.[94] Another effect which decreases the perovskite's bandgap is the transition from a monofacial to a bifacial solar cell. The additional light which enters the solar cell from the rear side, will be absorbed in the silicon bottom cell enhancing its J_{Ph}. Thus, every bit of additional light will decrease the optimum top cell bandgap.[111]

Hence, we cannot give a general optimum perovskite bandgap as it depends on several conditions. However, here we give a further effect which needs to be taken into account with care when designing monolithic perovskite/silicon tandem solar cells.

7   Summary & Outlook

This thesis was motivated by the emergence of perovskite solar cells, which explored an impressive improvement in PCE but also in scalability and stability since the first publication in 2009 with a PCE of 3.8%. Just 11 years later, in 2020, the PCE increased to 25.5% in laboratory scale, approaching the same level as the silicon technology.

Instead of competing with well-developed silicon solar cells, perovskite, with its excellent optoelectronic properties such as the tunable bandgap can be combined with silicon to tandem solar cells. These tandem solar cells can surpass the fundamental efficiency limit of single-junction solar cells. As the perovskite cell can potentially be fabricated inexpensively, this technology gives the oportunity to reduce the levelized cost of electricity and makes photovoltaic even cheaper and more attractive.

In 2015, the first perovskite/silicon tandem solar cell was presented with a PCE of 13.7%. Two years later, in 2017, when the work on this dissertation started, the PCE was already increased to 23.6%.

In this dissertation the PCE of monolithic perovskite/silicon tandem solar cell using a p-i-n perovskite top cell and a silicon heterojunction bottom cell was further improved to a world record level and on the way, the stability was improved, too. To enable this, advanced characterization methods were used to thoroughly analyze complete tandem solar cells, single-junction solar cells or just parts of a solar cell such as individual interfaces. To measure long-term stability of tandem solar cells properly, a new setup was designed and fabricated.

In the following, the main conclusions of the studies will be presented and discussed. The last section will address the prospective of this technology and will give a brief overview on what needs to be addressed to improve the technology further and enable commercialization.

7.1   Summary

In section 6.1, we presented thoroughly the optical optimization of tandem solar cells with a p-i-n perovskite top cell and a front-side polished silicon heterojunction bottom cell. The initial efficiency of 25.0% was certified independently. However, the PCE was limited by a low J_{SC} because of high reflection and substential mismatch of the subcell current densities. The nanocrystalline silicon oxide, the n-type contact of the silicon bottom cell, was initially optimized for silicon single-junction solar cells. However, as in tandem solar cells just the near infrared part of the spectrum is absorbed in the silicon bottom cell, we adjusted the thickness of the layer to improve the response in the tandem-relevant wavelength range. To reduce the parasitic absorption and with that increase the amount of light which can be absorbed in the photoactive materials, we reduced the thickness of the front TCO. However, to maintain good conductivity, the thickness must stay above a certain value to ensure the necessary sheet resistance. By adjusting the spin-coating speed, we were able to reduce the photogenerated current density in the perovskite while increasing it in the silicon subcell. With that we reduced the current mismatch. Lastly, the deposition temperature of the tin oxide was reduced to enable less harmful conditions for the perovskite. Implementing all optimizations enabled a PCE of 26.0% with a high cumulative photogenerated current density of $39.5\,\mathrm{mA\,cm^{-2}}$, which approached the value of double-side textured tandem solar cells. While the J_{SC} indeed increased due to reduced reflection and current mismatch, the fill factor was reduced substantially, too. To analyze this in more detail, we illuminated the optimized tandem solar cell with various spectra using an LED based solar simulator to enable different current-matching conditions. We found that the FF had a minimum close to current-matching conditions. Hence, mismatched subcells reduced the J_{SC} but the increased FF partially compensated the loss in PCE, which made these devices less sensitive to small current mismatches. We validated our findings by electrical simulations. Although we found a good agreement between simulated and experimental data for perovskite and silicon single-junction solar cells, the simulated tandem solar cell revealed a higher FF compared to the measured tandem solar cell. More sophisticated characterization methods are needed to analyze the performance of the subcells in tandem solar cells and to simulate these

devices properly. However, if the tandem solar cell can be optimized to follow the simulations, a PCE of 29.0% is achievable under current-matching conditions and negligence of losses due to series resistance.

While we developed tandem solar cells with high cumulative current densities, we further focused on improving the FF and V_{OC}. Instead of optimizing the perovskite itself, we worked in section 6.2 on an improved hole-selective contact. Hence, we used the typical triple-cation perovskite but increased the bandgap from 1.63 eV to 1.68 eV by increasing the bromide fraction. The wider bandgap enabled higher V_{OC} values. First we measured and compared properties of the interface between the perovskite and hole-selective layer using various hole-selective layers. Self-assembling monolayer molecules such as MeO-2PACz and 2PACz enabled superior properties. which led to higher FF and V_{OC} values compared to the typically used PTAA. Additionally, we implemented a new SAM, Me-4PACz, with longer chain between anchor group and conjugated fragment that contains a methyl functional unit. It enabled the same high level of passivation as the previously reported 2PACz but allowed faster hole extraction and hence, led to improved FF values of up to 84% in single-junction solar cells. Despite the increased amount of bromide, the good passivation and fast charge extraction inhibited phase segregation. These properties were analyzed in detail using cutting edge characterization methods. We compared all three SAMs and PTAA in tandem solar cells. As expected, 2PACz and MeO-2PACz performed better in terms of PCE than PTAA. However, due to the superior properties of Me-4PACz, tandem solar cells with this hole-selective layer achieved highest PCE values. To validate our measurements, one of the cells was sent for independent certification. The certified PCE of 29.15% set a new world record for this tandem technology at the time of certification in early 2020. To evaluate the improved stability, we specifically designed and fabricated a new setup which enabled proper illumination of the tandem solar cells for long-term stability tests. After 300 hours, the non-encapsulated tandem solar cell with Me-4PACz as hole-selective layer had still 95.5% of its initial efficiency, while all other types of tandem solar cells experienced more degradation. Driven by the difficulty to measure the performance of the subcells independently in a monolithic tandem stack, we used an advanced characterization to analyze the subcells. With injection-dependent absolute electroluminescence, we were able to reconstruct the subcell $J - V$ curves. Lastly, electrical simulations using parameters extracted from the reconstructed subcells revealed that our device design is able to achieve a PCE of 32.43% if the series resistance can be reduced and current matching can be achieved.

All reported pervoskite/silicon tandem solar cells are based on thick bottom cells fabricated from floatzone (FZ) silicon. Additionally, most of the devices have a chemical-mechanical polished (CMP) surface to enable spin coating. Although these bottom cells enable high PCE values, they are not compatible with industry production. In section 6.3 we fabricated tandem solar cells with bottom cells which are more compatible to industry. The bottom cells were fabricated from the much thinner czochralski (CZ) grown silicon with a non-CMP (i.e. rough but not textured) front side. The thinner silicon bottom cell increased the V_{OC} while the reduced spectral response in the near infrared wavelength range reduced the photogenerated current density in the silicon bottom cell. Hence, the mismatch increased which led to an elevated FF, as studied previously. A PCE of 27.89% achieved with the CZ-based tandem solar cells was just below the 28.15% enabled on laboratory typical bottom cells using thick FZ silicon with highly planarized front-side surfaces. The reduced spectral response of the silicon bottom cell when using thin CZ silicon can be further compensated by increasing the top cell's bandgap, which in the ideal case leads to an increases V_{OC}. Systematic optical simulations revealed that the bandgap needs to be widened by 0.02 eV if the bottom cell thickness is reduced from 280 μm to 100 μm and current-matching conditions should be maintained. This has a very important implication for the development towards optimized top cell bandgaps as higher bandgaps typically suffer from halide segregation and strong interface recombination. Therefore, the study gave important guidelines next to other factors such as luminescent coupling and operation temperature influenced bandgaps, on the proper bandgap. Consequently, the industry compatible bottom cells can potentially enable the same high PCE values as the laboratory typical bottom cells.

7.2 Outlook

Perovskite/silicon tandem solar cells experienced an impressive development. From the first demonstration in 2015 with a PCE of 13.7% it took just 5 years until in 2020 the theoretical silicon single-junction solar cell limit was surpassed with an certified tandem efficiency of 29.5%.

Although this high PCE attracts a lot of attention, several issues need to be addressed before this technology might enter the market with commercial applications. On the one hand, as identified here with various approximations and simulations, the experimental realized PCE is still lower than predicted values. Although the detailed balance limit is ~46%, setting a fundamental PCE limit for tandem solar cells, a practical limit of 35% within the next years is expected.

A lot of work was done in optimizing the J_{SC} as well as the V_{OC}. Despite highly efficient tandem solar cells with a planar front side can achieve high J_{SC} values, tandem solar cells with textured bottom cells and conformally deposited perovskite layers are desired as they show superior optical performance in outdoor application where the cells are illuminated from various angles. Some of these devices were realized using a hybrid deposition method. However, the moderate fill factor of the perovskite top cell limits the PCE of the tandem solar cells. Also co-evaporation is a promising method which enables conformal deposition of the perovskite. Despite the demonstration of highly efficient single-junction solar cells on planar surfaces, the deposition on textured surfaces still remains challenging. Further investigation is needed to understand the properties of the perovskite on textured surfaces in more detail and ultimately optimize the perovskite deposition to enable highly efficient fully textured tandem solar cells.

Furthermore, investigations of the fill factor in tandem solar cells are scarce. As demonstrated in this dissertation, especially the region around the maximum power point does not follow the electrical simulations. Continued research is needed identify the losses leading to a reduced fill factor. Advanced characterization methods to analyze the subcells of tandem solar cells, as demonstrated in this dissertation could help determining this loss. On the one hand this understanding could help reduce this loss and hence improve the PCE, on the other hand it would enable proper electrical simulations which is highly important for detailed analysis.

Figure 25 shows the last 201 tandem solar cells fabricated by the author of this dissertation as a scatter plot. For the impact of the short-circuit current density J_{SC}, open-circuit voltage V_{OC} and fill factor on the PCE a linear fit is shown from which the coefficient of determination R^2 is calculated. The values reveal that the fill factor strongly determines the the PCE, which highlights that in the future the optimization of the fill factor should be intensified to enable higher tandem PCE values.

Although the concept of multijunction solar cells itself reaches higher PCE values than single-junction solar cells, these cells can be combined with other concepts like up- and down-conversion, hot carriers or the generation of multiple electron-hole pairs per photon to further increase the PCE.

Besides the improvement of the PCE, there are other aspects which need to be addressed before commencing industrial production of perovskite/silicon tandem solar cells. Highly efficient tandem solar cells have typically an area of ~1 cm². For the compatibility with conventional silicon wafer sizes, the large-area depositions of the perovskite top cell needs to be enabled. Obviously, a sufficient long-term stability needs to be provided. Furthermore, for real-world application, the device design will change. First, the larger area will require a proper metallization to collect the charge carriers. In small laboratory devices, the metal is typically deposited via thermal evaporation and does not necessarily comprise grid fingers. However, in industry-scale applications, the metal grid is usually screen-printed. Hence, a perovskite-compatible screen printing process needs to be provided, which includes chemical as well as thermal compatibility. As tandem solar cells will deliver just ~50% of the current density of silicon single-junction solar cells, the grid design can be adjusted. For instance an increased finger spacing will reduce the consumption of metal as well as losses due to shading. Lastly, encapsulation is required to protect the solar cells from environmental impacts such as humidity but also mechanical stress. Besides the required compatibility of this process with the tandem solar cells, the addition of an encapsulation will alter the impinging spectrum and hence, requires one to readjust the optical performance of the entire stack including the encapsulation.
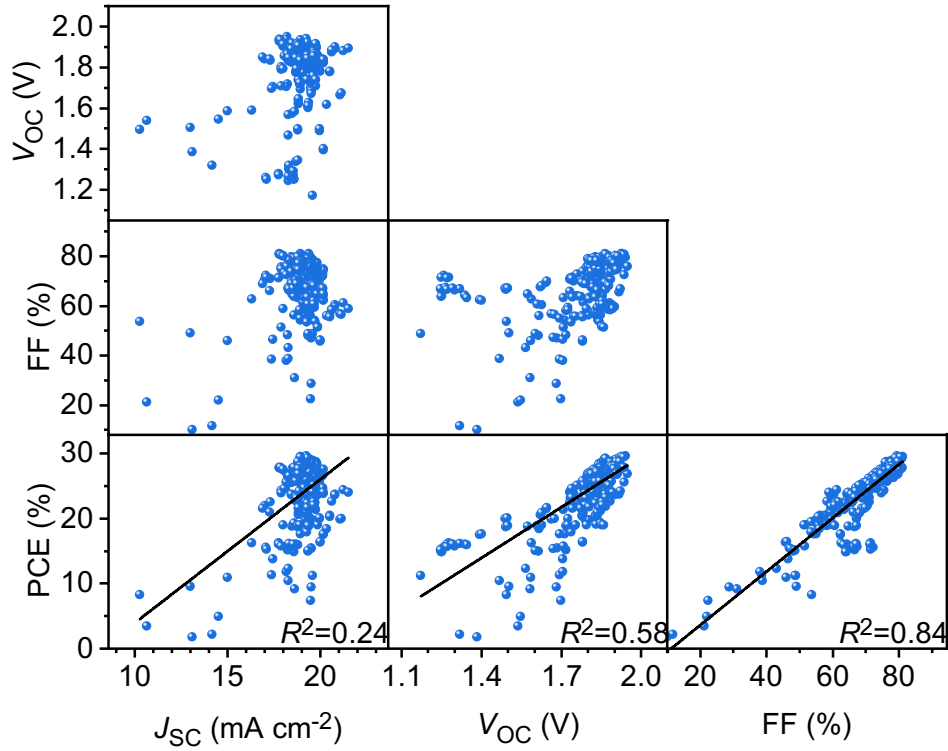
Figure 25: Tandem performance displayed as scatter plot. Scatter plot of all tandem solar cells fabricated by the author of this dissertation since July 2019. The 402 data points include the parameters extracted from $J-V$ scans in both bias directions (i.e. 201 devices). For the influence of the short-circuit current density (J_{SC}), open-circuit voltage (V_{OC}) and fill factor (FF) on the power conversion efficiency (PCE), a linear fit is shown from which the coefficient of determination (R^2) is calculated. Note that these tandem solar cells include diverse variations like the perovskite bandgap, perovskite composition, antisolvent, bottom cell type, etc.

Although there are other tandem technologies which already enable higher PCE values, the required materials for perovskites solar cells are cheap and the process temperatures are comparably low, making the combination of perovskite and silicon a potential candidate to reduce the levelized cost of electricity of photoviltaics.

Bibliography

[1] R.K. Pachauri and L.A. Meyer (eds). IPCC, 2014: Climate Change 2014: Synthesis Report. Contribution of Working Groups I, II and III to the Fifth Assessment Report of the Intergovernmental Panel on Climate Change. Technical report, IPCC, Geneva, Swizerland, 2014. URL https://www.ipcc.ch/report/ar5/syr/.

[2] Will Steffen, Johan Rockström, Katherine Richardson, Timothy M. Lenton, Carl Folke, Diana Liverman, Colin P. Summerhayes, Anthony D. Barnosky, Sarah E. Cornell, Michel Crucifix, Jonathan F. Donges, Ingo Fetzer, Steven J. Lade, Marten Scheffer, Ricarda Winkelmann, and Hans Joachim Schellnhuber. Trajectories of the Earth System in the Anthropocene. *Proceedings of the National Academy of Sciences*, 115(33):8252–8259, 2018. doi: 10.1073/pnas.1810141115. URL http://www.pnas.org/lookup/doi/10.1073/pnas.1810141115.

[3] UNITED NATIONS. PARIS AGREEMENT, 2015. URL https://unfccc.int/process-and-meetings/the-paris-agreement/the-paris-agreement. [Accessed on: 2021-01-05].

[4] International Energy Agency. Solar PV - Analysis. URL https://www.iea.org/reports/solar-pv. [Accessed on: 2021-02-25].

[5] ITRPV. International Technology Roadmap for Photovoltaic (ITRPV) 11th Edition, 2019. URL https://itrpv.vdma.org/en/ueber-uns.

[6] Christoph Kost, Shivenes Shammugam, Verena Jülich, Tran Nguyen, Huyen, and Thomas Schlegl. Levelized Cost of Electricity Renawable Energy Technologies. 2018. URL https://www.ise.fraunhofer.de/content/dam/ise/en/documents/publications/studies/EN2018_Fraunhofer-ISE_LCOE_Renewable_Energy_Technologies.pdf.

[7] Kunta Yoshikawa, Hayato Kawasaki, Wataru Yoshida, Toru Irie, Katsunori Konishi, Kunihiro Nakano, Toshihiko Uto, Daisuke Adachi, Masanori Kanematsu, Hisashi Uzu, and Kenji Yamamoto. Silicon heterojunction solar cell with interdigitated back contacts for a photoconversion efficiency over 26%. *Nature Energy*, 2(5):17032, 2017. doi: 10.1038/nenergy.2017.32. URL http://www.nature.com/articles/nenergy201732.

[8] Armin Richter, Martin Hermle, and Stefan W Glunz. Reassessment of the Limiting Efficiency for Crystalline Silicon Solar Cells. *IEEE Journal of Photovoltaics*, 3(4):1184–1191, 2013. doi: 10.1109/JPHOTOV.2013.2270351. URL http://ieeexplore.ieee.org/document/6557081/.

[9] National Renewable Energy Laboratory, "Best Research-Cell Efficiency Chart", 2021. URL https://www.nrel.gov/pv/cell-efficiency.html. [Accessed on: 2021-01-05].

[10] Akihiro Kojima, Kenjiro Teshima, Yasuo Shirai, and Tsutomu Miyasaka. Organometal Halide Perovskites as Visible-Light Sensitizers for Photovoltaic Cells. *Journal of the American Chemical Society*, 131(17):6050–6051, 2009. doi: 10.1021/ja809598r. URL https://pubs.acs.org/doi/10.1021/ja809598r.

[11] Stefaan De Wolf, Jakub Holovsky, Soo-Jin Moon, Philipp Löper, Bjoern Niesen, Martin Ledinsky, Franz-Josef Haug, Jun-Ho Yum, and Christophe Ballif. Organometallic Halide Perovskites: Sharp Optical Absorption Edge and Its Relation to Photovoltaic Performance. *The Journal of Physical Chemistry Letters*, 5(6):1035–1039, 2014. doi: 10.1021/jz500279b. URL https://pubs.acs.org/doi/10.1021/jz500279b.

[12] Wan-Jian Yin, Tingting Shi, and Yanfa Yan. Unusual defect physics in CH 3 NH 3 PbI 3 perovskite solar cell absorber. *Applied Physics Letters*, 104(6):063903, 2014. doi: 10.1063/1.4864778. URL http://aip.scitation.org/doi/10.1063/1.4864778.

[13] Jun Hong Noh, Sang Hyuk Im, Jin Hyuck Heo, Tarak N Mandal, and Sang Il Seok. Chemical Management for Colorful, Efficient, and Stable Inorganic–Organic Hybrid Nanostructured Solar Cells. *Nano Letters*, 13(4):1764–1769, 2013. doi: 10.1021/nl400349b. URL https://pubs.acs.org/doi/10.1021/nl400349b.

[14] Christoph Messmer, Baljeet S. Goraya, Sebastian Nold, Patricia S.C. Schulze, Volker Sittinger, Jonas Schön, Jan Christoph Goldschmidt, Martin Bivour, Stefan W. Glunz, and Martin Hermle. The race for the best silicon bottom cell: Efficiency and cost evaluation of perovskite–silicon tandem solar cells. *Progress in Photovoltaics: Research and Applications*, 29(7):744–759, 2021. doi: 10.1002/pip.3372. URL https://onlinelibrary.wiley.com/doi/10.1002/pip.3372.

[15] Jonathan P. Mailoa, Colin D. Bailie, Eric C. Johlin, Eric T. Hoke, Austin J. Akey, William H. Nguyen, Michael D. McGehee, and Tonio Buonassisi. A 2-terminal perovskite/silicon multijunction solar cell enabled by a silicon tunnel junction. *Applied Physics Letters*, 106(12):121105, 2015. doi: 10.1063/1.4914179. URL http://aip.scitation.org/doi/10.1063/1.4914179.

[16] Kevin A. Bush, Axel F. Palmstrom, Zhengshan J. Yu, Mathieu Boccard, Rongrong Cheacharoen, Jonathan P. Mailoa, David P. McMeekin, Robert L. Z. Hoye, Colin D. Bailie, Tomas Leijtens, Ian Marius Peters, Maxmillian C. Minichetti, Nicholas Rolston, Rohit Prasanna, Sarah Sofia, Duncan Harwood, Wen Ma, Farhad Moghadam, Henry J. Snaith, Tonio Buonassisi, Zachary C. Holman, Stacey F. Bent, and Michael D. McGehee. 23.6%-efficient monolithic perovskite/silicon tandem solar cells with improved stability. *Nature Energy*, 2(4):17009, 2017. doi: 10.1038/nenergy.2017.9. URL http://www.nature.com/articles/nenergy20179.

[17] Martin Green, Ewan Dunlop, Jochen Hohl-Ebinger, Masahiro Yoshita, Nikos Kopidakis, and Xiaojing Hao. Solar cell efficiency tables (version 57). *Progress in Photovoltaics: Research and Applications*, 29 (1):3–15, 2021. doi: 10.1002/pip.3371. URL https://onlinelibrary.wiley.com/doi/10.1002/pip.3371.

[18] A. Smets, K. Jäger, O. Isabella, R. van Swaaij, and M. Zeman. *Solar Energy: The Physics and Engineering of Photovoltaic Conversion, Technologies and Systems*. UIT Cambridge, 2016. ISBN 9781906860325. URL https://books.google.de/books?id=vTkdjgEACAAJ.

[19] Max Planck. Ueber das Gesetz der Energieverteilung im Normalspectrum. *Annalen der Physik*, 309(3): 553–563, 1901. doi: 10.1002/andp.19013090310. URL http://doi.wiley.com/10.1002/andp.19013090310.

[20] P. Würfel and U. Würfel. *Physics of Solar Cells: From Basic Principles to Advanced Concepts, 3rd Edition*. Wiley-VCH Verlag GmbH & Co. KGaA, 2019.

[21] NREL Solar Spectra, 2020. URL https://www.nrel.gov/grid/solar-resource/spectra.html. [Accessed on: 2021-01-08].

[22] Richard E. Bird and Carol Riordan. Simple Solar Spectral Model for Direct and Diffuse Irradiance on Horizontal and Tilted Planes at the Earth's Surface for Cloudless Atmospheres. *Journal of Climate and Applied Meteorology*, 25(1):87–97, 1986. doi: 10.1175/1520-0450(1986)025<0087:SSSMFD>2.0.CO;2. URL http://journals.ametsoc.org/doi/10.1175/1520-0450(1986)025%3C0087:SSSMFD%3E2.0.CO;2.

[23] Otwin Breitenstein and Martin Langenkamp. *Lock-in Thermography*, volume 10 of *Springer Series in Advanced Microelectronics*. Springer Berlin Heidelberg, Berlin, Heidelberg, 2003. ISBN 978-3-642-07785-2. doi: 10.1007/978-3-662-08396-3. URL http://link.springer.com/10.1007/978-3-662-08396-3.

[24] M Bass, Optical Society of America Staff, Optical Society of America, E W Van Stryland, W L Wolfe, and D R Williams. *Handbook of Optics: Fundamentals, techniques, and design*. Handbook of Optics. McGraw-Hill, 1995. ISBN 9780070477407. URL https://books.google.de/books?id=ggc6AQAAIAAJ.

[25] D.A. Neamen. *Semiconductor Physics and Devices: Basic Principles*. McGraw-Hill, 2011. ISBN 978-0-07-352958-5.

[26] Wolfgang Tress. *Organic Solar Cells*, volume 208 of *Springer Series in Materials Science*. Springer International Publishing, Cham, 2014. ISBN 978-3-319-10096-8. doi: 10.1007/978-3-319-10097-5. URL http://link.springer.com/10.1007/978-3-319-10097-5.

[27] Uli Wurfel, Andres Cuevas, and Peter Wurfel. Charge Carrier Separation in Solar Cells. *IEEE Journal of Photovoltaics*, 5(1):461–469, 2015. doi: 10.1109/JPHOTOV.2014.2363550. URL https://ieeexplore.ieee.org/document/6960066.

[28] W. Shockley. The Theory of p-n Junctions in Semiconductors and p-n Junction Transistors. *Bell System Technical Journal*, 28(3):435–489, 1949. doi: 10.1002/j.1538-7305.1949.tb03645.x. URL https://ieeexplore.ieee.org/document/6773080.

[29] T. F. Schulze, L. Korte, E. Conrad, M. Schmidt, and B. Rech. Electrical transport mechanisms in a-Si:H/c-Si heterojunction solar cells. *Journal of Applied Physics*, 107(2):023711, 2010. doi: 10.1063/1.3267316. URL http://aip.scitation.org/doi/10.1063/1.3267316.

[30] William Shockley and Hans J. Queisser. Detailed balance limit of efficiency of p-n junction solar cells. *Journal of Applied Physics*, 32(3):510–519, 1961. doi: 10.1063/1.1736034.

[31] Marko Jošt, Eike Köhnen, Anna Belen Morales-Vilches, Benjamin Lipovšek, Klaus Jäger, Bart Macco, Amran Al-Ashouri, Janez Krč, Lars Korte, Bernd Rech, Rutger Schlatmann, Marko Topič, Bernd Stannowski, and Steve Albrecht. Textured interfaces in monolithic perovskite/silicon tandem solar cells: advanced light management for improved efficiency and energy yield. *Energy & Environmental Science*, 11(12):3511–3523, 2018. doi: 10.1039/C8EE02469C. URL http://xlink.rsc.org/?DOI=C8EE02469C.

[32] W. Shockley and W. T. Read. Statistics of the Recombinations of Holes and Electrons. *Physical Review*, 87(5):835–842, 1952. doi: 10.1103/PhysRev.87.835. URL https://link.aps.org/doi/10.1103/PhysRev.87.835.

[33] R. N. Hall. Electron-Hole Recombination in Germanium. *Physical Review*, 87(2):387–387, 1952. doi: 10.1103/PhysRev.87.387. URL https://link.aps.org/doi/10.1103/PhysRev.87.387.

[34] J.R. Davis, Ajeet Rohatgi, R.H. Hopkins, P.D. Blais, P. Rai-Choudhury, J.R. McCormick, and H.C. Mollenkopf. Impurities in silicon solar cells. *IEEE Transactions on Electron Devices*, 27(4):677–687, 1980. doi: 10.1109/T-ED.1980.19922. URL http://ieeexplore.ieee.org/document/1480715/.

[35] K. Xerxes Steirer, Philip Schulz, Glenn Teeter, Vladan Stevanovic, Mengjin Yang, Kai Zhu, and Joseph J. Berry. Defect Tolerance in Methylammonium Lead Triiodide Perovskite. *ACS Energy Letters*, 1(2):360–366, 2016. doi: 10.1021/acsenergylett.6b00196. URL https://pubs.acs.org/doi/10.1021/acsenergylett.6b00196.

[36] Martin Stolterfoht, Christian M Wolff, José A Márquez, Shanshan Zhang, Charles J Hages, Daniel Rothhardt, Steve Albrecht, Paul L Burn, Paul Meredith, Thomas Unold, and Dieter Neher. Visualization and suppression of interfacial recombination for high-efficiency large-area pin perovskite solar cells. *Nature Energy*, 3(10):847–854, 2018. doi: 10.1038/s41560-018-0219-8. URL http://www.nature.com/articles/s41560-018-0219-8.

[37] Martin Green. *Third Generation Photovoltaics*, volume 12 of *Springer series in photonics*. Springer Berlin Heidelberg, 2006. ISBN 978-3-540-26562-7. doi: 10.1007/b137807. URL http://link.springer.com/10.1007/b137807.

[38] Sven Rühle. The detailed balance limit of perovskite/silicon and perovskite/CdTe tandem solar cells. *physica status solidi (a)*, 214(5):1600955, 2017. doi: 10.1002/pssa.201600955. URL http://doi.wiley.com/10.1002/pssa.201600955.

[39] Mohammad I. Hossain, Wayesh Qarony, Sainan Ma, Longhui Zeng, Dietmar Knipp, and Yuen Hong Tsang. Perovskite/Silicon Tandem Solar Cells: From Detailed Balance Limit Calculations to Photon Management. *Nano-Micro Letters*, 11(1):58, 2019. doi: 10.1007/s40820-019-0287-8. URL http://link.springer.com/10.1007/s40820-019-0287-8.

[40] A De Vos. Detailed balance limit of the efficiency of tandem solar cells. *Journal of Physics D: Applied Physics*, 13(5):839–846, 1980. doi: 10.1088/0022-3727/13/5/018. URL http://stacks.iop.org/0022-3727/13/i=5/a=018?key=crossref.52c973ed3027bb6aad7a763a45b7f68a.

[41] Moritz H. Futscher and Bruno Ehrler. Efficiency Limit of Perovskite/Si Tandem Solar Cells. *ACS Energy Letters*, 1(4):863–868, 2016. doi: 10.1021/acsenergylett.6b00405. URL http://pubs.acs.org/doi/abs/10.1021/acsenergylett.6b00405.

[42] Andrew S. Brown and Martin A. Green. Detailed balance limit for the series constrained two terminal tandem solar cell. *Physica E: Low-dimensional Systems and Nanostructures*, 14(1-2):96–100, 2002. doi: 10.1016/S1386-9477(02)00364-8. URL https://linkinghub.elsevier.com/retrieve/pii/S1386947702003648.

[43] Philipp Tockhorn. *Minimising Optical and Electrical Losses in Perovskite Solar Cells - From Single-Junctions to Advanced Tandem Designs*. Dissertation, Technical University Berlin, 2020.

[44] Emily L. Warren, William E. McMahon, Michael Rienäcker, Kaitlyn T. VanSant, Riley C. Whitehead, Robby Peibst, and Adele C. Tamboli. A Taxonomy for Three-Terminal Tandem Solar Cells. *ACS Energy Letters*, 5(4):1233–1242, 2020. doi: 10.1021/acsenergylett.0c00068. URL https://pubs.acs.org/doi/10.1021/acsenergylett.0c00068.

[45] Antonio Martí and Gerardo L. Araújo. Limiting efficiencies for photovoltaic energy conversion in multigap systems. *Solar Energy Materials and Solar Cells*, 43(2):203–222, 1996. doi: 10.1016/0927-0248(96)00015-3. URL https://linkinghub.elsevier.com/retrieve/pii/0927024896000153.

[46] Studiosus Kirchhoff. Ueber den Durchgang eines elektrischen Stromes durch eine Ebene, insbesondere durch eine kreisförmige. *Annalen der Physik und Chemie*, 140(4):497–514, 1845. doi: 10.1002/andp.18451400402. URL http://doi.wiley.com/10.1002/andp.18451400402.

[47] Zhihao Zhang, Zicheng Li, Lingyi Meng, Shui-Yang Lien, and Peng Gao. Perovskite-Based Tandem Solar Cells: Get the Most Out of the Sun. *Advanced Functional Materials*, 2001904:2001904, 2020. doi: 10.1002/adfm.202001904. URL https://onlinelibrary.wiley.com/doi/abs/10.1002/adfm.202001904.

[48] Niraj N. Lal, Yasmina Dkhissi, Wei Li, Qicheng Hou, Yi-Bing Cheng, and Udo Bach. Perovskite Tandem Solar Cells. *Advanced Energy Materials*, 7(18):1602761, 2017. doi: 10.1002/aenm.201602761. URL http://doi.wiley.com/10.1002/aenm.201602761.

[49] Henning Schulte-Huxel, Daniel J. Friedman, and Adele C. Tamboli. String-Level Modeling of Two, Three, and Four Terminal Si-Based Tandem Modules. *IEEE Journal of Photovoltaics*, 8(5):1370–1375, 2018. doi: 10.1109/JPHOTOV.2018.2855104. URL https://ieeexplore.ieee.org/document/8421224/.

[50] Michele De Bastiani, Anand S. Subbiah, Erkan Aydin, Furkan H. Isikgor, Thomas G. Allen, and Stefaan De Wolf. Recombination junctions for efficient monolithic perovskite-based tandem solar cells: physical principles, properties, processing and prospects. *Materials Horizons*, 7(11):2791–2809, 2020. doi: 10.1039/D0MH00990C. URL http://xlink.rsc.org/?DOI=D0MH00990Chttp://pubs.rsc.org/en/Content/ArticleLanding/2020/MH/D0MH00990C.

[51] Jonathan Lehr, Malte Langenhorst, Raphael Schmager, Simon Kirner, Uli Lemmer, Bryce S. Richards, Chris Case, and Ulrich W. Paetzold. Energy yield modelling of perovskite/silicon two-terminal tandem PV modules with flat and textured interfaces. *Sustainable Energy & Fuels*, 2(12):2754–2761, 2018. doi: 10.1039/C8SE00465J. URL http://xlink.rsc.org/?DOI=C8SE00465J.

[52] Jan Gilot, Martijn M. Wienk, and René A. J. Janssen. Measuring the External Quantum Efficiency of Two-Terminal Polymer Tandem Solar Cells. *Advanced Functional Materials*, 20(22):3904–3911, 2010. doi: 10.1002/adfm.201001167. URL http://doi.wiley.com/10.1002/adfm.201001167.

[53] C. Ulbrich, C. Zahren, A. Gerber, B. Blank, T. Merdzhanova, A. Gordijn, and U. Rau. Matching of Silicon Thin-Film Tandem Solar Cells for Maximum Power Output. *International Journal of Photoenergy*, 2013:1–7, 2013. doi: 10.1155/2013/314097. URL http://www.hindawi.com/journals/ijp/2013/314097/.

[54] D. M. Chapin, C. S. Fuller, and G. L. Pearson. A New Silicon p-n Junction Photocell for Converting Solar Radiation into Electrical Power. *Journal of Applied Physics*, 25(5):676–677, 1954. doi: 10.1063/1.1721711. URL http://aip.scitation.org/doi/10.1063/1.1721711.

[55] L.L. Yan, C. Han, B. Shi, Y. Zhao, and X.D. Zhang. A review on the crystalline silicon bottom cell for monolithic perovskite/silicon tandem solar cells. *Materials Today Nano*, 7:100045, 2019. doi: 10.1016/j.mtnano.2019.100045. URL https://doi.org/10.1016/j.mtnano.2019.100045https://linkinghub.elsevier.com/retrieve/pii/S2588842019301142.

[56] Quntao Tang, Hanyu Yao, Binbin Xu, and Jiawei Ge. Enhanced energy conversion efficiency of Al-BSF c-Si solar cell by a novel hierarchical structure composed of inverted pyramids with different sizes. *Solar Energy*, 208(July):1–9, 2020. doi: 10.1016/j.solener.2020.07.073. URL https://linkinghub.elsevier.com/retrieve/pii/S0038092X20308057.

[57] Martin A. Green. The path to 25% silicon solar cell efficiency: History of silicon cell evolution. *Progress in Photovoltaics: Research and Applications*, 17(3):183–189, 2009. doi: 10.1002/pip.892. URL http://doi.wiley.com/10.1002/pip.892.

[58] Mikio Taguchi, Ayumu Yano, Satoshi Tohoda, Kenta Matsuyama, Yuya Nakamura, Takeshi Nishiwaki, Kazunori Fujita, and Eiji Maruyama. 24.7% Record Efficiency HIT Solar Cell on Thin Silicon Wafer. *IEEE Journal of Photovoltaics*, 4(1):96–99, 2014. doi: 10.1109/JPHOTOV.2013.2282737. URL http://ieeexplore.ieee.org/document/6620960/.

[59] E. Yablonovitch, T. Gmitter, R. M. Swanson, and Y. H. Kwark. A 720 mV open circuit voltage SiO x : c -Si:SiO x double heterostructure solar cell. *Applied Physics Letters*, 47(11):1211–1213, 1985. doi: 10.1063/1.96331. URL http://aip.scitation.org/doi/10.1063/1.96331.

[60] Stefaan De Wolf, Antoine Descoeudres, Zachary C. Holman, and Christophe Ballif. High-efficiency Silicon Heterojunction Solar Cells: A Review. *green*, 2(1):7–24, 2012. doi: 10.1515/green-2011-0018. URL https://www.degruyter.com/view/j/green.2012.2.issue-1/green-2011-0018/green-2011-0018.xml.

[61] J. I. Pankove and M. L. Tarng. Amorphous silicon as a passivant for crystalline silicon. *Applied Physics Letters*, 34(2):156–157, 1979. doi: 10.1063/1.90711. URL http://aip.scitation.org/doi/10.1063/1.90711.

[62] Gustav Rose. Ueber einige neue Mineralien des Urals. *Journal für Praktische Chemie*, 19(1):459–468, 1840. doi: 10.1002/prac.18400190179. URL http://doi.wiley.com/10.1002/prac.18400190179.

[63] Dieter Weber. CH3NH3PbX3, ein Pb(II)-System mit kubischer Perowskitstruktur / CH3NH3PbX3, a Pb(II)-System with Cubic Perovskite Structure. *Zeitschrift für Naturforschung B*, 33(12):1443–1445, 1978. doi: 10.1515/znb-1978-1214. URL https://www.degruyter.com/view/journals/znb/33/12/article-p1443.xml.

[64] V. M. Goldschmidt. Die Gesetze der Krystallochemie. *Die Naturwissenschaften*, 14(21):477–485, 1926. doi: 10.1007/BF01507527. URL http://link.springer.com/10.1007/BF01507527.

[65] Juan-Pablo Correa-Baena, Michael Saliba, Tonio Buonassisi, Michael Grätzel, Antonio Abate, Wolfgang Tress, and Anders Hagfeldt. Promises and challenges of perovskite solar cells. *Science*, 358 (6364):739–744, 2017. doi: 10.1126/science.aam6323. URL https://www.sciencemag.org/lookup/doi/10.1126/science.aam6323.

[66] Zhaoning Song, Cong Chen, Chongwen Li, Rasha A Awni, Dewei Zhao, and Yanfa Yan. Wide-bandgap, low-bandgap, and tandem perovskite solar cells. *Semiconductor Science and Technology*, 34(9):093001, 2019. doi: 10.1088/1361-6641/ab27f7. URL https://iopscience.iop.org/article/10.1088/1361-6641/ab27f7.

[67] Giles E. Eperon, Samuel D. Stranks, Christopher Menelaou, Michael B. Johnston, Laura M. Herz, and Henry J. Snaith. Formamidinium lead trihalide: a broadly tunable perovskite for efficient planar heterojunction solar cells. *Energy & Environmental Science*, 7(3):982, 2014. doi: 10.1039/c3ee43822h. URL http://xlink.rsc.org/?DOI=c3ee43822h.

[68] Michael Saliba, Juan-Pablo Correa-Baena, Michael Grätzel, Anders Hagfeldt, and Antonio Abate. Perovskite Solar Cells: From the Atomic Level to Film Quality and Device Performance. *Angewandte Chemie International Edition*, 57(10):2554–2569, 2018. doi: 10.1002/anie.201703226. URL http://doi.wiley.com/10.1002/anie.201703226.

[69] Emilio Gutierrez-Partida, Hannes Hempel, Sebastián Caicedo-Dávila, Meysam Raoufi, Francisco Peña-Camargo, Max Grischek, René Gunder, Jonas Diekmann, Pietro Caprioglio, Kai O. Brinkmann, Hans Köbler, Steve Albrecht, Thomas Riedl, Antonio Abate, Daniel Abou-Ras, Thomas Unold, Dieter Neher, and Martin Stolterfoht. Large-Grain Double Cation Perovskites with 18 μs Lifetime and High Luminescence Yield for Efficient Inverted Perovskite Solar Cells. *ACS Energy Letters*, pages 1045–1054, 2021. doi: 10.1021/acsenergylett.0c02642. URL https://pubs.acs.org/doi/10.1021/acsenergylett.0c02642.

[70] Franz Urbach. The Long-Wavelength Edge of Photographic Sensitivity and of the Electronic Absorption of Solids. *Physical Review*, 92(5):1324–1324, 1953. doi: 10.1103/PhysRev.92.1324. URL https://link.aps.org/doi/10.1103/PhysRev.92.1324.

[71] Bin Chen, Se-woong Baek, Yi Hou, Erkan Aydin, Michele De Bastiani, Benjamin Scheffel, Andrew Proppe, Ziru Huang, Mingyang Wei, Ya-kun Wang, Eui-hyuk Jung, Thomas G Allen, Emmanuel Van Kerschaver, F. Pelayo García de Arquer, Makhsud I Saidaminov, Sjoerd Hoogland, Stefaan De Wolf, and Edward H Sargent. Enhanced optical path and electron diffusion length enable high-efficiency perovskite tandems. *Nature Communications*, 11(1):1257, 2020. doi: 10.1038/s41467-020-15077-3. URL http://dx.doi.org/10.1038/s41467-020-15077-3http://www.nature.com/articles/s41467-020-15077-3.

[72] Fuzong Xu, Jiang Liu, Anand S. Subbiah, Wenzhu Liu, Jingxuan Kang, George T. Harrison, Xinbo Yang, Furkan H. Isikgor, Erkan Aydin, Michele De Bastiani, and Stefaan De Wolf. Potassium Thiocyanate-Assisted Enhancement of Slot-Die-Coated Perovskite Films for High-Performance Solar Cells. *Small Science*, 2000044:2000044, 2021. doi: 10.1002/smsc.202000044. URL https://onlinelibrary.wiley.com/doi/10.1002/smsc.202000044.

[73] Qi Jiang, Yang Zhao, Xingwang Zhang, Xiaolei Yang, Yong Chen, Zema Chu, Qiufeng Ye, Xingxing Li, Zhigang Yin, and Jingbi You. Surface passivation of perovskite film for efficient solar cells. *Nature Photonics*, 2019. doi: 10.1038/s41566-019-0398-2. URL http://www.nature.com/articles/s41566-019-0398-2.

[74] Hanul Min, Maengsuk Kim, Seung-Un Lee, Hyeonwoo Kim, Gwisu Kim, Keunsu Choi, Jun Hee Lee, and Sang Il Seok. Efficient, stable solar cells by using inherent bandgap of α-phase formamidinium

lead iodide. *Science*, 366(6466):749–753, 2019. doi: 10.1126/science.aay7044. URL https://www.sciencemag.org/lookup/doi/10.1126/science.aay7044.

[75] Xiaopeng Zheng, Yi Hou, Chunxiong Bao, Jun Yin, Fanglong Yuan, Ziru Huang, Kepeng Song, Jiakai Liu, Joel Troughton, Nicola Gasparini, Chun Zhou, Yuanbao Lin, Ding-Jiang Xue, Bin Chen, Andrew K. Johnston, Nini Wei, Mohamed Nejib Hedhili, Mingyang Wei, Abdullah Y. Alsalloum, Partha Maity, Bekir Turedi, Chen Yang, Derya Baran, Thomas D. Anthopoulos, Yu Han, Zheng-Hong Lu, Omar F. Mohammed, Feng Gao, Edward H. Sargent, and Osman M. Bakr. Managing grains and interfaces via ligand anchoring enables 22.3%-efficiency inverted perovskite solar cells. *Nature Energy*, 5(2):131–140, 2020. doi: 10.1038/s41560-019-0538-4. URL http://dx.doi.org/10.1038/s41560-019-0538-4http://www.nature.com/articles/s41560-019-0538-4.

[76] Jason J Yoo, Gabkyung Seo, Matthew R Chua, Tae Gwan Park, Yongli Lu, Fabian Rotermund, Young-ki Kim, Chan Su Moon, Nam Joong Jeon, Juan-Pablo Correa-Baena, Vladimir Bulović, Seong Sik Shin, Moungi G Bawendi, and Jangwon Seo. Efficient perovskite solar cells via improved carrier management. *Nature*, 590(7847):587–593, 2021. doi: 10.1038/s41586-021-03285-w. URL http://www.nature.com/articles/s41586-021-03285-w.

[77] D. P. McMeekin, G. Sadoughi, W. Rehman, G. E. Eperon, M. Saliba, M. T. Horantner, A. Haghighirad, N. Sakai, L. Korte, B. Rech, M. B. Johnston, L. M. Herz, and H. J. Snaith. A mixed-cation lead mixed-halide perovskite absorber for tandem solar cells. *Science*, 351(6269):151–155, 2016. doi: 10.1126/science.aad5845. URL http://www.sciencemag.org/cgi/doi/10.1126/science.aad5845.

[78] Michael Saliba, Taisuke Matsui, Ji-Youn Seo, Konrad Domanski, Juan-Pablo Correa-Baena, Moham-mad Khaja Nazeeruddin, Shaik M. Zakeeruddin, Wolfgang Tress, Antonio Abate, Anders Hagfeldt, and Michael Grätzel. Cesium-containing triple cation perovskite solar cells: improved stability, reproducibility and high efficiency. *Energy & Environmental Science*, 9(6):1989–1997, 2016. doi: 10.1039/C5EE03874J. URL http://xlink.rsc.org/?DOI=C5EE03874Jhttp://arxiv.org/abs/1408.1149.

[79] E. L. Unger, L. Kegelmann, K. Suchan, D. Sörell, L. Korte, and S. Albrecht. Roadmap and roadblocks for the band gap tunability of metal halide perovskites. *Journal of Materials Chemistry A*, 5(23):11401–11409, 2017. doi: 10.1039/C7TA00404D. URL http://xlink.rsc.org/?DOI=C7TA00404D.

[80] Eric T. Hoke, Daniel J. Slotcavage, Emma R. Dohner, Andrea R. Bowring, Hemamala I. Karunadasa, and Michael D. McGehee. Reversible photo-induced trap formation in mixed-halide hybrid perovskites for photovoltaics. *Chemical Science*, 6(1):613–617, 2015. doi: 10.1039/C4SC03141E. URL http://xlink.rsc.org/?DOI=C4SC03141E.

[81] Francisco Peña-Camargo, Pietro Caprioglio, Fengshuo Zu, Emilio Gutierrez-Partida, Christian M. Wolff, Kai Brinkmann, Steve Albrecht, Thomas Riedl, Norbert Koch, Dieter Neher, and Martin Stolter-foht. Halide Segregation versus Interfacial Recombination in Bromide-Rich Wide-Gap Perovskite Solar Cells. *ACS Energy Letters*, 5(8):2728–2736, 2020. doi: 10.1021/acsenergylett.0c01104. URL https://pubs.acs.org/doi/10.1021/acsenergylett.0c01104.

[82] Florian Mathies, Emil J. W. List-Kratochvil, and Eva L. Unger. Advances in Inkjet-Printed Metal Halide Perovskite Photovoltaic and Optoelectronic Devices. *Energy Technology*, 8(4):1900991, 2020. doi: 10.1002/ente.201900991. URL https://onlinelibrary.wiley.com/doi/abs/10.1002/ente.201900991.

[83] Richard Swartwout, Maximilian T. Hoerantner, and V. Bulović. Scalable Deposition Methods for Large-area Production of Perovskite Thin Films. *ENERGY & ENVIRONMENTAL MATERIALS*, 2(2):119–145, 2019. doi: 10.1002/eem2.12043. URL https://onlinelibrary.wiley.com/doi/abs/10.1002/eem2.12043.

[84] Minsu Jung, Sang-Geun Ji, Gwisu Kim, and Sang Il Seok. Perovskite precursor solution chemistry: from fundamentals to photovoltaic applications. *Chemical Society Reviews*, 48(7):2011–2038, 2019. doi: 10.1039/C8CS00656C. URL http://xlink.rsc.org/?DOI=C8CS00656C.

[85] Feng Xian Xie, Di Zhang, Huimin Su, Xingang Ren, Kam Sing Wong, Michael Grätzel, and Wallace C. H. Choy. Vacuum-Assisted Thermal Annealing of CH 3 NH 3 PbI 3 for Highly Stable and Efficient Perovskite Solar Cells. *ACS Nano*, 9(1):639–646, 2015. doi: 10.1021/nn505978r. URL https://pubs.acs.org/doi/10.1021/nn505978r.

[86] Fuzhi Huang, Yasmina Dkhissi, Wenchao Huang, Manda Xiao, Iacopo Benesperi, Sergey Rubanov, Ye Zhu, Xiongfeng Lin, Liangcong Jiang, Yecheng Zhou, Angus Gray-Weale, Joanne Etheridge, Christopher R. McNeill, Rachel A. Caruso, Udo Bach, Leone Spiccia, and Yi-Bing Cheng. Gas-assisted preparation of lead iodide perovskite films consisting of a monolayer of single crystalline grains for high efficiency planar solar cells. *Nano Energy*, 10:10–18, 2014. doi: 10.1016/j.nanoen.2014.08.015. URL https://linkinghub.elsevier.com/retrieve/pii/S2211285514202278.

[87] Manda Xiao, Fuzhi Huang, Wenchao Huang, Yasmina Dkhissi, Ye Zhu, Joanne Etheridge, Angus Gray-Weale, Udo Bach, Yi-Bing Cheng, and Leone Spiccia. A Fast Deposition-Crystallization Procedure for Highly Efficient Lead Iodide Perovskite Thin-Film Solar Cells. *Angewandte Chemie*, 126(37): 10056–10061, 2014. doi: 10.1002/ange.201405334. URL http://doi.wiley.com/10.1002/ange.201405334.

[88] Lidón Gil-Escrig, Marcel Roß, Johannes Sutter, Amran Al-Ashouri, Christiane Becker, and Steve Albrecht. Fully Vacuum-Processed Perovskite Solar Cells on Pyramidal Microtextures. *Solar RRL*, 2000553:2000553, 2020. doi: 10.1002/solr.202000553. URL https://onlinelibrary.wiley.com/doi/10.1002/solr.202000553.

[89] Marcel Roß, Lidón Gil-Escrig, Amran Al-Ashouri, Philipp Tockhorn, Marko Jošt, Bernd Rech, and Steve Albrecht. Co-Evaporated p-i-n Perovskite Solar Cells beyond 20% Efficiency: Impact of Substrate Temperature and Hole-Transport Layer. *ACS Applied Materials & Interfaces*, 12(35):39261–39272, 2020. doi: 10.1021/acsami.0c10898. URL https://pubs.acs.org/doi/10.1021/acsami.0c10898.

[90] Patricia S.C. Schulze, Karl Wienands, Alexander J. Bett, Saeid Rafizadeh, Laura E. Mundt, Ludmila Cojocaru, Martin Hermle, Stefan W. Glunz, Harald Hillebrecht, and Jan Christoph Goldschmidt. Perovskite hybrid evaporation/ spin coating method: From band gap tuning to thin film deposition on textures. *Thin Solid Films*, 704:137970, 2020. doi: 10.1016/j.tsf.2020.137970. URL https://linkinghub.elsevier.com/retrieve/pii/S004060902030184X.

[91] Fan Fu, Stefano Pisoni, Thomas P. Weiss, Thomas Feurer, Aneliia Wäckerlin, Peter Fuchs, Shiro Nishiwaki, Lukas Zortea, Ayodhya N. Tiwari, and Stephan Buecheler. Compositionally Graded Absorber for Efficient and Stable Near-Infrared-Transparent Perovskite Solar Cells. *Advanced Science*, 5(3):1700675, 2018. doi: 10.1002/advs.201700675. URL http://doi.wiley.com/10.1002/advs.201700675.

[92] Florent Sahli, Jérémie Werner, Brett A. Kamino, Matthias Bräuninger, Raphaël Monnard, Bertrand Paviet-Salomon, Loris Barraud, Laura Ding, Juan J. Diaz Leon, Davide Sacchetto, Gianluca Cattaneo, Matthieu Despeisse, Mathieu Boccard, Sylvain Nicolay, Quentin Jeangros, Bjoern Niesen, and Christophe Ballif. Fully textured monolithic perovskite/silicon tandem solar cells with 25.2% power conversion efficiency. *Nature Materials*, 17(9):820–826, 2018. doi: 10.1038/s41563-018-0115-4. URL http://www.nature.com/articles/s41563-018-0115-4.

[93] Jérémie Werner, Florent Sahli, Fan Fu, Juan J. Diaz Leon, Arnaud Walter, Brett A. Kamino, Bjoern Niesen, Sylvain Nicolay, Quentin Jeangros, and Christophe Ballif. Perovskite/Perovskite/Silicon Monolithic Triple-Junction Solar Cells with a Fully Textured Design. *ACS Energy Letters*, 3(9):2052–2058, 2018. doi: 10.1021/acsenergylett.8b01165. URL http://pubs.acs.org/doi/10.1021/acsenergylett.8b01165.

[94] Erkan Aydin, Thomas G Allen, Michele De Bastiani, Lujia Xu, Jorge Ávila, Michael Salvador, Emmanuel Van Kerschaver, and Stefaan De Wolf. Interplay between temperature and bandgap energies on the outdoor performance of perovskite/silicon tandem solar cells. *Nature Energy*, 2020. doi: 10.1038/s41560-020-00687-4. URL http://www.nature.com/articles/s41560-020-00687-4.

[95] Renxing Lin, Ke Xiao, Zhengyuan Qin, Qiaolei Han, Chunfeng Zhang, Mingyang Wei, Makhsud I Saidaminov, Yuan Gao, Jun Xu, Min Xiao, Aidong Li, Jia Zhu, Edward H Sargent, and Hairen Tan. Monolithic all-perovskite tandem solar cells with 24.8% efficiency exploiting comproportionation to suppress Sn(ii) oxidation in precursor ink. *Nature Energy*, 2019. doi: 10.1038/s41560-019-0466-3. URL http://dx.doi.org/10.1038/s41560-019-0466-3http://www.nature.com/articles/s41560-019-0466-3.

[96] Steve Albrecht, Michael Saliba, Juan Pablo Correa Baena, Felix Lang, Lukas Kegelmann, Mathias Mews, Ludmilla Steier, Antonio Abate, Jörg Rappich, Lars Korte, Rutger Schlatmann, Mohammad Khaja Nazeeruddin, Anders Hagfeldt, Michael Grätzel, and Bernd Rech. Monolithic perovskite/silicon-heterojunction tandem solar cells processed at low temperature. *Energy & Environmental Science*, 9(1):81–88, 2016. doi: 10.1039/C5EE02965A. URL http://xlink.rsc.org/?DOI=C5EE02965A.

[97] Jérémie Werner, Ching-Hsun Weng, Arnaud Walter, Luc Fesquet, Johannes Peter Seif, Stefaan De Wolf, Bjoern Niesen, and Christophe Ballif. Efficient Monolithic Perovskite/Silicon Tandem Solar Cell with Cell Area >1 cm 2. *The Journal of Physical Chemistry Letters*, 7(1):161–166, 2016. doi: 10.1021/acs.jpclett.5b02686. URL http://pubs.acs.org/doi/10.1021/acs.jpclett.5b02686.

[98] Axel F. Palmstrom, James A. Raiford, Rohit Prasanna, Kevin A. Bush, Melany Sponseller, Rongrong Cheacharoen, Maxmillian C. Minichetti, David S. Bergsman, Tomas Leijtens, Hsin-Ping Wang, Vladimir Bulović, Michael D. McGehee, and Stacey F. Bent. Interfacial Effects of Tin Oxide Atomic Layer Deposition in Metal Halide Perovskite Photovoltaics. *Advanced Energy Materials*, 8(23):1800591, 2018. doi: 10.1002/aenm.201800591. URL http://doi.wiley.com/10.1002/aenm.201800591.

[99] Amran Al-Ashouri, Eike Köhnen, Bor Li, Artiom Magomedov, Hannes Hempel, Pietro Caprioglio, José A Márquez, Anna Belen Morales Vilches, Ernestas Kasparavicius, Joel A. Smith, Nga Phung, Dorothee Menzel, Max Grischek, Lukas Kegelmann, Dieter Skroblin, Christian Gollwitzer, Tadas Malinauskas, Marko Jošt, Gašper Matič, Bernd Rech, Rutger Schlatmann, Marko Topič, Lars Korte, Antonio Abate, Bernd Stannowski, Dieter Neher, Martin Stolterfoht, Thomas Unold, Vytautas Getautis, and Steve Albrecht. Monolithic perovskite/silicon tandem solar cell with >29% efficiency by enhanced hole extraction. *Science*, 370(6522):1300–1309, 2020. doi: 10.1126/science.abd4016. URL https://www.sciencemag.org/lookup/doi/10.1126/science.abd4016.

[100] Martin Stolterfoht, Max Grischek, Pietro Caprioglio, Christian M. Wolff, Emilio Gutierrez-Partida, Francisco Peña-Camargo, Daniel Rothhardt, Shanshan Zhang, Meysam Raoufi, Jakob Wolansky, Mojtaba Abdi-Jalebi, Samuel D. Stranks, Steve Albrecht, Thomas Kirchartz, and Dieter Neher. How To Quantify the Efficiency Potential of Neat Perovskite Films: Perovskite Semiconductors with an Implied Efficiency Exceeding 28%. *Advanced Materials*, 32(17):2000080, 2020. doi: 10.1002/adma.202000080. URL https://onlinelibrary.wiley.com/doi/abs/10.1002/adma.202000080.

[101] Luana Mazzarella, Yen-Hung Lin, Simon Kirner, Anna B. Morales-Vilches, Lars Korte, Steve Albrecht, Ed Crossland, Bernd Stannowski, Chris Case, Henry J. Snaith, and Rutger Schlatmann. Infrared Light Management Using a Nanocrystalline Silicon Oxide Interlayer in Monolithic Perovskite/Silicon Heterojunction Tandem Solar Cells with Efficiency above 25%. *Advanced Energy Materials*, 9(14):1803241, 2019. doi: 10.1002/aenm.201803241. URL http://doi.wiley.com/10.1002/aenm.201803241.

[102] Oxford PV. Oxford PV sets world record for perovskite solar cell, 2018. URL https://www.oxfordpv.com/news/oxford-pv-sets-world-record-perovskite-solar-cell. [Accessed on: 2018-09-18].

[103] OxfordPV. Oxford PV perovskite solar cell achieves 28% efficiency, 2019. URL https://www.oxfordpv.com/news/oxford-pv-perovskite-solar-cell-achieves-28-efficiency. [Accessed on: 2019-02-05].

[104] Eike Köhnen, Marko Jošt, Anna Belen Morales-Vilches, Philipp Tockhorn, Amran Al-Ashouri, Bart Macco, Lukas Kegelmann, Lars Korte, Bernd Rech, Rutger Schlatmann, Bernd Stannowski, and Steve Albrecht. Highly efficient monolithic perovskite silicon tandem solar cells: analyzing the influence of current mismatch on device performance. *Sustainable Energy & Fuels*, 3(8):1995–2005, 2019. doi: 10.1039/C9SE00120D. URL http://pubs.rsc.org/en/Content/ArticleLanding/2019/SE/C9SE00120D.

[105] Bo Chen, Zhengshan J. Yu, Salman Manzoor, Shen Wang, William Weigand, Zhenhua Yu, Guang Yang, Zhenyi Ni, Xuezeng Dai, Zachary C Holman, and Jinsong Huang. Blade-Coated Perovskites on Textured Silicon for 26%-Efficient Monolithic Perovskite/Silicon Tandem Solar Cells. *Joule*, 4(4):850–864, 2020. doi: 10.1016/j.joule.2020.01.008. URL https://linkinghub.elsevier.com/retrieve/pii/S2542435120300350.

[106] Jixian Xu, Caleb C Boyd, Zhengshan J Yu, Axel F Palmstrom, Daniel J Witter, Bryon W Larson, Ryan M France, Jérémie Werner, Steven P Harvey, Eli J Wolf, William Weigand, Salman Manzoor, Maikel F. A. M. van Hest, Joseph J Berry, Joseph M Luther, Zachary C Holman, and Michael D. McGehee. Triple-halide wide–band gap perovskites with suppressed phase segregation for efficient tandems. *Science*, 367(6482):1097–1104, 2020. doi: 10.1126/science.aaz5074. URL https://www.sciencemag.org/lookup/doi/10.1126/science.aaz5074.

[107] Yi Hou, Erkan Aydin, Michele De Bastiani, Chuanxiao Xiao, Furkan H Isikgor, Ding-jiang Xue, Bin Chen, Hao Chen, Behzad Bahrami, Ashraful H. Chowdhury, Andrew Johnston, Se-woong Baek, Ziru Huang, Mingyang Wei, Yitong Dong, Joel Troughton, Rawan Jalmood, Alessandro J Mirabelli, Thomas G Allen, Emmanuel Van Kerschaver, Makhsud I Saidaminov, Derya Baran, Qiquan Qiao, Kai Zhu, Stefaan De Wolf, and Edward H Sargent. Efficient tandem solar cells with solution-processed perovskite on textured crystalline silicon. *Science*, 367(6482):1135–1140, 2020. doi: 10.1126/science.aaz3691. URL https://www.sciencemag.org/lookup/doi/10.1126/science.aaz3691.

[108] Jianghui Zheng, Hamid Mehrvarz, Chwenhaw Liao, Jueming Bing, Xin Cui, Yang Li, Vinicius R. Gonçales, Cho Fai Jonathan Lau, Da Seul Lee, Yong Li, Meng Zhang, Jincheol Kim, Yongyoon Cho, Laura Granados Caro, Shi Tang, Chao Chen, Shujuan Huang, and Anita W. Y. Ho-Baillie. Large-Area 23%-Efficient Monolithic Perovskite/Homojunction-Silicon Tandem Solar Cell with Enhanced UV Stability Using Down-Shifting Material. *ACS Energy Letters*, 4(11):2623–2631, 2019. doi: 10.1021/acsenergylett.9b01783. URL https://pubs.acs.org/doi/10.1021/acsenergylett.9b01783.

[109] N.D. Arora and J.R. Hauser. Temperature dependence of silicon solar cell characteristics. *Solar Energy Materials*, 6(2):151–158, 1982. doi: 10.1016/0165-1633(82)90016-8. URL https://linkinghub.elsevier.com/retrieve/pii/0165163382900168.

[110] Marko Jošt, Benjamin Lipovšek, Boštjan Glažar, Amran Al-Ashouri, Kristijan Brecl, Gašper Matič, Artiom Magomedov, Vytautas Getautis, Marko Topič, and Steve Albrecht. Perovskite Solar Cells go Outdoors: Field Testing and Temperature Effects on Energy Yield. *Advanced Energy Materials*, page 2000454, 2020. doi: 10.1002/aenm.202000454. URL https://onlinelibrary.wiley.com/doi/abs/10.1002/aenm.202000454.

[111] Michele De Bastiani, Alessandro J Mirabelli, Yi Hou, Fabrizio Gota, Erkan Aydin, Thomas G Allen, Joel Troughton, Anand S Subbiah, Furkan H Isikgor, Jiang Liu, Lujia Xu, Bin Chen, Emmanuel Van Kerschaver, Derya Baran, Beatrice Fraboni, Michael F Salvador, Ulrich W Paetzold, Edward H Sargent, and Stefaan De Wolf. Efficient bifacial monolithic perovskite/silicon tandem solar cells via bandgap engineering. *Nature Energy*, 2021. doi: 10.1038/s41560-020-00756-8. URL http://www.nature.com/articles/s41560-020-00756-8.

[112] Brett A. Kamino, Bertrand Paviet-Salomon, Soo-Jin Moon, Nicolas Badel, Jacques Levrat, Gabriel Christmann, Arnaud Walter, Antonin Faes, Laura Ding, Juan J. Diaz Leon, Adriana Paracchino, Matthieu Despeisse, Christophe Ballif, and Sylvain Nicolay. Low-Temperature Screen-Printed Metallization for the Scale-Up of Two-Terminal Perovskite–Silicon Tandems. *ACS Applied Energy Materials*, 2(5):3815–3821, 2019. doi: 10.1021/acsaem.9b00502. URL http://pubs.acs.org/doi/10.1021/acsaem.9b00502.

[113] Eike Köhnen, Amran Al-Ashouri, Artiom Magomedov, Marcel Roß, Ernestas Kasparavičius, Jose A. Marquez, Pietro Caprioglio, Martin Stolterfoht, Anna Belen Morales-Vilches, Bor Li, Bernd Rech, Rutger Schlatmann, Lars Korte, Dieter Neher, Thomas Unold, Tadas Malinauskas, Vytautas Getautis, Bernd Stannowski, and Steve Albrecht. Perovskite/silicon tandem cells: Self-assembled monolayer as HTL for 29.2% efficiency and progress in upscaling to large areas. In *37th EU PVSEC*, 2020.

[114] K. A. Emery, C. R. Osterwald, T. W. Cannon, D. R. Myers, J. Burdick, T. Glatfelter, W. Czubatyj, and J. Yang. Methods for Measuring Solar Cell Efficiency Independent of Reference Cell or Light Source. In *Conference Record of the IEEE Photovoltaic Specialists Conference*, pages 623–628, 1985.

[115] K. Emery, C.R. Osterwald, T. Glatfelter, J. Burdick, and G. Virshup. A comparison of the errors in determining the conversion efficiency of multijunction solar cells by various methods. *Solar Cells*, 24 (3-4):371–380, 1988. doi: 10.1016/0379-6787(88)90089-0. URL https://linkinghub.elsevier.com/retrieve/pii/0379678788900890.

[116] M. Meusel, R. Adelhelm, F. Dimroth, A.W. Bett, and W. Warta. Spectral mismatch correction and spectrometric characterization of monolithic III-V multi-junction solar cells. *Progress in Photovoltaics: Research and Applications*, 10(4):243–255, 2002. doi: 10.1002/pip.407. URL http://doi.wiley.com/10.1002/pip.407.

[117] P. Wurfel. The chemical potential of radiation. *Journal of Physics C: Solid State Physics*, 15(18): 3967–3985, 1982. doi: 10.1088/0022-3719/15/18/012. URL https://iopscience.iop.org/article/10.1088/0022-3719/15/18/012.

[118] Daniel Abou-ras, Thomas Kirchartz, and Uwe Rau. *Advanced Characterization Techniques for Thin Film Solar Cells*. Wiley-VCH Verlag GmbH & Co. KGaA, Weinheim, Germany, 2011. ISBN 9783527636280. doi: 10.1002/9783527636280. URL http://doi.wiley.com/10.1002/9783527636280.

[119] Andreas Pflug, Volker Sittinger, Florian Ruske, Bernd Szyszka, and Georg Dittmar. Optical characterization of aluminum-doped zinc oxide films by advanced dispersion theories. *Thin Solid Films*, 455-456:201–206, 2004. doi: 10.1016/j.tsf.2004.01.006. URL https://linkinghub.elsevier.com/retrieve/pii/S0040609004000070.

[120] J. A. Guerra, A. Tejada, L. Korte, L. Kegelmann, J. A. Töfflinger, S. Albrecht, B. Rech, and R. Weingärtner. Determination of the complex refractive index and optical bandgap of CH 3 NH 3 PbI 3 thin films. *Journal of Applied Physics*, 121(17):173104, 2017. doi: 10.1063/1.4982894. URL http://aip.scitation.org/doi/10.1063/1.4982894.

[121] Linear Technology. LTspice, 2019. URL https://www.analog.com/en/design-center/design-tools-and-calculators/ltspice-simulator.html.

[122] Andreas Fell. A Free and Fast Three-Dimensional/Two-Dimensional Solar Cell Simulator Featuring Conductive Boundary and Quasi-Neutrality Approximations. *IEEE Transactions on Electron Devices*, 60(2):733–738, 2013. doi: 10.1109/TED.2012.2231415. URL http://ieeexplore.ieee.org/document/6387589/.

[123] Ronald A. Sinton and Andres Cuevas. Contactless determination of current–voltage characteristics and minority-carrier lifetimes in semiconductors from quasi-steady-state photoconductance data. *Applied Physics Letters*, 69(17):2510–2512, 1996. doi: 10.1063/1.117723. URL http://aip.scitation.org/doi/10.1063/1.117723.

[124] Rudi Santbergen, Tomomi Meguro, Takashi Suezaki, Gensuke Koizumi, Kenji Yamamoto, and Miro Zeman. GenPro4 Optical Model for Solar Cell Simulation and Its Application to Multijunction Solar Cells. *IEEE Journal of Photovoltaics*, 7(3):919–926, 2017. doi: 10.1109/JPHOTOV.2017.2669640. URL http://ieeexplore.ieee.org/document/7866819/.

[125] Philipp Löper, Michael Stuckelberger, Bjoern Niesen, Jérémie Werner, Miha Filipič, Soo-Jin Moon, Jun-Ho Yum, Marko Topič, Stefaan De Wolf, and Christophe Ballif. Complex Refractive Index Spectra of CH 3 NH 3 PbI 3 Perovskite Thin Films Determined by Spectroscopic Ellipsometry and Spectrophotometry. *The Journal of Physical Chemistry Letters*, 6(1):66–71, 2015. doi: 10.1021/jz502471h. URL http://pubs.acs.org/doi/10.1021/jz502471h.

[126] Steve Albrecht, Michael Saliba, Juan-Pablo Correa-Baena, Klaus Jäger, Lars Korte, Anders Hagfeldt, Michael Grätzel, and Bernd Rech. Towards optical optimization of planar monolithic perovskite/silicon-heterojunction tandem solar cells. *Journal of Optics*, 18(6):064012, 2016. doi: 10.1088/2040-8978/18/6/064012. URL http://stacks.iop.org/2040-8986/18/i=6/a=064012?key=crossref.45a23b6f71c5ad46179d135f7142c4db.

[127] Klaus Jäger, Lars Korte, Bernd Rech, and Steve Albrecht. Numerical optical optimization of monolithic planar perovskite-silicon tandem solar cells with regular and inverted device architectures. *Optics Express*, 25(12):A473, 2017. doi: 10.1364/OE.25.00A473. URL https://www.osapublishing.org/abstract.cfm?URI=oe-25-12-A473.

[128] W. E. McMahon, K. E. Emery, D. J. Friedman, L. Ottoson, M. S. Young, J. S. Ward, C. M. Kramer, A. Duda, and Sarah Kurtz. Fill factor as a probe of current-matching for GaInP 2 /GaAs tandem cells in a concentrator system during outdoor operation. *Progress in Photovoltaics: Research and Applications*, 16(3):213–224, 2008. doi: 10.1002/pip.798. URL http://doi.wiley.com/10.1002/pip.798.

[129] David S. Ginley. *Handbook of Transparent Conductors*. Springer US, Boston, MA, 2011. ISBN 978-1-4419-1637-2. doi: 10.1007/978-1-4419-1638-9. URL http://link.springer.com/10.1007/978-1-4419-1638-9.

[130] H. Kim, C. M. Gilmore, A. Piqué, J. S. Horwitz, H. Mattoussi, H. Murata, Z. H. Kafafi, and D. B. Chrisey. Electrical, optical, and structural properties of indium–tin–oxide thin films for organic light-emitting devices. *Journal of Applied Physics*, 86(11):6451–6461, 1999. doi: 10.1063/1.371708. URL http://aip.scitation.org/doi/10.1063/1.371708.

[131] R. Martins, P. Barquinha, A. Pimentel, L. Pereira, and E. Fortunato. Transport in high mobility amorphous wide band gap indium zinc oxide films. *physica status solidi (a)*, 202(9):R95–R97, 2005. doi: 10.1002/pssa.200521020. URL http://doi.wiley.com/10.1002/pssa.200521020.

[132] Luana Mazzarella, Matteo Werth, Klaus Jäger, Marko Jošt, Lars Korte, Steve Albrecht, Rutger Schlatmann, and Bernd Stannowski. Infrared photocurrent management in monolithic perovskite/silicon heterojunction tandem solar cells by using a nanocrystalline silicon oxide interlayer. *Optics Express*, 26(10):A487, 2018. doi: 10.1364/OE.26.00A487. URL https://www.osapublishing.org/abstract.cfm?URI=oe-26-10-A487.

[133] Jeffrey W. Elam, David A. Baker, Alexander J. Hryn, Alex B. F. Martinson, Michael J. Pellin, and Joseph T. Hupp. Atomic layer deposition of tin oxide films using tetrakis(dimethylamino) tin. *Journal*

of Vacuum Science & Technology A: Vacuum, Surfaces, and Films, 26(2):244–252, 2008. doi: 10.1116/1. 2835087. URL http://avs.scitation.org/doi/10.1116/1.2835087.

[134] Marja N. Mullings, Carl Hägglund, and Stacey F. Bent. Tin oxide atomic layer deposition from tetrakis(dimethylamino)tin and water. *Journal of Vacuum Science & Technology A: Vacuum, Surfaces, and Films*, 31(6):061503, 2013. doi: 10.1116/1.4812717. URL http://avs.scitation.org/doi/10.1116/1.4812717.

[135] G. Nogay, F. Sahli, J. Werner, R. Monnard, M. Boccard, M. Despeisse, F-J. Haug, Q. Jeangros, A. Ingenito, and C. Ballif. 25.1%-Efficient Monolithic Perovskite/Silicon Tandem Solar Cell Based on a p -type Monocrystalline Textured Silicon Wafer and High-Temperature Passivating Contacts. *ACS Energy Letters*, 4(4):844–845, 2019. doi: 10.1021/acsenergylett.9b00377. URL https://pubs.acs.org/doi/10.1021/acsenergylett.9b00377.

[136] Rachel E Beal, Nanna Zhou Hagström, Julien Barrier, Aryeh Gold-Parker, Rohit Prasanna, Kevin A Bush, Donata Passarello, Laura T. Schelhas, Karsten Brüning, Christopher J. Tassone, Hans-Georg Steinrück, Michael D McGehee, Michael F Toney, and Ana Flávia Nogueira. Structural Origins of Light-Induced Phase Segregation in Organic-Inorganic Halide Perovskite Photovoltaic Materials. *Matter*, 01:1–13, 2019. doi: 10.1016/j.matt.2019.11.001. URL https://linkinghub.elsevier.com/retrieve/pii/S2590238519303376.

[137] Steve Reynolds and Vladimir Smirnov. Modelling Performance of Two- And Four-terminal Thin-film Silicon Tandem Solar Cells under Varying Spectral Conditions. *Energy Procedia*, 84(0):251–260, 2015. doi: 10.1016/j.egypro.2015.12.321. URL https://linkinghub.elsevier.com/retrieve/pii/S1876610215029860.

[138] M. Bonnet-Eymard, M. Boccard, G. Bugnon, F. Sculati-Meillaud, M. Despeisse, and C. Ballif. Optimized short-circuit current mismatch in multi-junction solar cells. *Solar Energy Materials and Solar Cells*, 117:120–125, 2013. doi: 10.1016/j.solmat.2013.05.046. URL https://linkinghub.elsevier.com/retrieve/pii/S0927024813002699.

[139] J.W. Strutt. XV. On the light from the sky, its polarization and colour. *The London, Edinburgh, and Dublin Philosophical Magazine and Journal of Science*, 41(271):107–120, 1871. doi: 10.1080/14786447108640452. URL https://www.tandfonline.com/doi/full/10.1080/14786447108640452.

[140] Tina Wahl, Jonas Hanisch, Sven Meier, Moritz Schultes, and Erik Ahlswede. Sputtered indium zinc oxide rear electrodes for inverted semitransparent perovskite solar cells without using a protective buffer layer. *Organic Electronics*, 54(September 2017):48–53, 2018. doi: 10.1016/j.orgel.2017.12.020. URL https://doi.org/10.1016/j.orgel.2017.12.020http://linkinghub.elsevier.com/retrieve/pii/S156611991730616X.

[141] Jérémie Werner, Guy Dubuis, Arnaud Walter, Philipp Löper, Soo-jin Moon, Sylvain Nicolay, Monica Morales-Masis, Stefaan De Wolf, Bjoern Niesen, and Christophe Ballif. Sputtered rear electrode with broadband transparency for perovskite solar cells. *Solar Energy Materials and Solar Cells*, 141: 407–413, 2015. doi: 10.1016/j.solmat.2015.06.024. URL https://linkinghub.elsevier.com/retrieve/pii/S0927024815002937.

[142] Marlene Härtel. *Soft growth of TCOs for application in Tandem-Perovskite Solar Cells*. Master thesis, Technical University Berlin, 2017.

[143] Pascal Kaienburg, Paula Hartnagel, Bart E. Pieters, Jiaoxian Yu, David Grabowski, Zhifa Liu, Jinane Haddad, Uwe Rau, and Thomas Kirchartz. How Contact Layers Control Shunting Losses from Pinholes in Thin-Film Solar Cells. *The Journal of Physical Chemistry C*, 122:acs.jpcc.8b09400, 2018. doi: 10.1021/acs.jpcc.8b09400. URL http://pubs.acs.org/doi/10.1021/acs.jpcc.8b09400.

[144] Amran Al-Ashouri, Artiom Magomedov, Marcel Roß, Marko Jošt, Martynas Talaikis, Ganna Chisti-akova, Tobias Bertram, José A. Márquez, Eike Köhnen, Ernestas Kasparavičius, Sergiu Levcenco, Lidón Gil-Escrig, Charles J Hages, Rutger Schlatmann, Bernd Rech, Tadas Malinauskas, Thomas Unold, Christian A. Kaufmann, Lars Korte, Gediminas Niaura, Vytautas Getautis, and Steve Albrecht. Conformal monolayer contacts with lossless interfaces for perovskite single junction and monolithic tandem solar cells. *Energy & Environmental Science*, 12(11):3356–3369, 2019. doi: 10.1039/C9EE02268F. URL http://xlink.rsc.org/?DOI=C9EE02268F.

[145] Tokyo Chemical Industry Co. MeO-2PACz, . URL https://www.tcichemicals.com/OF/en/p/D5798. [Accessed on: 2021-02-12].

[146] Tokyo Chemical Industry Co. 2PACz, . URL https://www.tcichemicals.com/DE/en/p/C3663. [Accessed on: 2021-02-12].

[147] Daniel J. Slotcavage, Hemamala I. Karunadasa, and Michael D. McGehee. Light-Induced Phase Segregation in Halide-Perovskite Absorbers. *ACS Energy Letters*, 1(6):1199–1205, 2016. doi: 10.1021/acsenergylett.6b00495. URL https://pubs.acs.org/doi/10.1021/acsenergylett.6b00495.

[148] Daehan Kim, Hee Joon Jung, Ik Jae Park, Bryon W Larson, Sean P Dunfield, Chuanxiao Xiao, Jekyung Kim, Jinhui Tong, Passarut Boonmongkolras, Su Geun Ji, Fei Zhang, Seong Ryul Pae, Minkyu Kim, Seok Beom Kang, Vinayak Dravid, Joseph J. Berry, Jin Young Kim, Kai Zhu, Dong Hoe Kim, and Byungha Shin. Efficient, stable silicon tandem cells enabled by anion-engineered wide-bandgap perovskites. *Science*, 368(6487):155–160, 2020. doi: 10.1126/science.aba3433. URL https://www.sciencemag.org/lookup/doi/10.1126/science.aba3433.

[149] Martin Stolterfoht, Pietro Caprioglio, Christian M. Wolff, José A. Márquez, Joleik Nordmann, Shan-shan Zhang, Daniel Rothhardt, Ulrich Hörmann, Yohai Amir, Alex Redinger, Lukas Kegelmann, Fengshuo Zu, Steve Albrecht, Norbert Koch, Thomas Kirchartz, Michael Saliba, Thomas Unold, and Dieter Neher. The impact of energy alignment and interfacial recombination on the internal and external open-circuit voltage of perovskite solar cells. *Energy & Environmental Science*, 12(9):2778–2788, 2019. doi: 10.1039/C9EE02020A. URL http://xlink.rsc.org/?DOI=C9EE02020A.

[150] Ian L. Braly, Dane W. DeQuilettes, Luis M. Pazos-Outón, Sven Burke, Mark E. Ziffer, David S. Ginger, and Hugh W. Hillhouse. Hybrid perovskite films approaching the radiative limit with over 90% photoluminescence quantum efficiency. *Nature Photonics*, 12(6):355–361, 2018. doi: 10.1038/s41566-018-0154-z. URL http://www.nature.com/articles/s41566-018-0154-z.

[151] Thomas Kirchartz, José A. Márquez, Martin Stolterfoht, and Thomas Unold. Photoluminescence-Based Characterization of Halide Perovskites for Photovoltaics. *Advanced Energy Materials*, 10(26):1904134, 2020. doi: 10.1002/aenm.201904134. URL https://onlinelibrary.wiley.com/doi/abs/10.1002/aenm.201904134.

[152] Rafael Quintero-Bermudez, Jeffrey Kirman, Dongxin Ma, Edward H Sargent, and Rafael Quintero-Torres. Mechanisms of LiF Interlayer Enhancements of Perovskite Light-Emitting Diodes. *The Journal of Physical Chemistry Letters*, 11(10):4213–4220, 2020. doi: 10.1021/acs.jpclett.0c00757. URL https://pubs.acs.org/doi/10.1021/acs.jpclett.0c00757.

[153] Zhen Li, Chuanxiao Xiao, Ye Yang, Steven P. Harvey, Dong Hoe Kim, Jeffrey A. Christians, Mengjin Yang, Philip Schulz, Sanjini U. Nanayakkara, Chun-Sheng Jiang, Joseph M. Luther, Joseph J. Berry, Matthew C. Beard, Mowafak M. Al-Jassim, and Kai Zhu. Extrinsic ion migration in perovskite solar cells. *Energy & Environmental Science*, 10(5):1234–1242, 2017. doi: 10.1039/C7EE00358G. URL http://xlink.rsc.org/?DOI=C7EE00358G.

[154] Su-Mi Bang, Seong Sik Shin, Nam Joong Jeon, Young Yun Kim, Geunjin Kim, Tae-Youl Yang, and Jangwon Seo. Defect-Tolerant Sodium-Based Dopant in Charge Transport Layers for Highly Efficient and Stable Perovskite Solar Cells. *ACS Energy Letters*, 5(4):1198–1205, 2020. doi: 10.1021/acsenergylett.0c00514. URL https://pubs.acs.org/doi/10.1021/acsenergylett.0c00514.

[155] Severin N. Habisreutinger, Tomas Leijtens, Giles E. Eperon, Samuel D. Stranks, Robin J. Nicholas, and Henry J. Snaith. Carbon Nanotube/Polymer Composites as a Highly Stable Hole Collection Layer in Perovskite Solar Cells. *Nano Letters*, 14(10):5561–5568, 2014. doi: 10.1021/nl501982b. URL https://pubs.acs.org/doi/10.1021/nl501982b.

[156] Marko Jošt, Tobias Bertram, Dibyashree Koushik, J.A. Jose A. Marquez, Marcel A. M.A. Verheijen, M.D. Marc Daniel Heinemann, Eike Köhnen, Amran Al-Ashouri, Steffen Braunger, Felix Lang, Bernd Rech, Thomas Unold, Mariadriana Creatore, Iver Lauermann, Christian A. C.A. Kaufmann, Rutger Schlatmann, and Steve Albrecht. 21.6%-Efficient Monolithic Perovskite/Cu(In,Ga)Se 2 Tandem Solar Cells with Thin Conformal Hole Transport Layers for Integration on Rough Bottom Cell Surfaces. *ACS Energy Letters*, 4(2):583–590, 2019. doi: 10.1021/acsenergylett.9b00135. URL http://pubs.acs.org/doi/10.1021/acsenergylett.9b00135.

[157] D. Pysch, A. Mette, and S.W. Glunz. A review and comparison of different methods to determine the series resistance of solar cells. *Solar Energy Materials and Solar Cells*, 91(18):1698–1706, 2007. doi: 10.1016/j.solmat.2007.05.026. URL http://linkinghub.elsevier.com/retrieve/pii/S0927024807002255.

[158] Rudi Santbergen, Ryota Mishima, Tomomi Meguro, Masashi Hino, Hisashi Uzu, Johan Blanker, Kenji Yamamoto, and Miro Zeman. Minimizing optical losses in monolithic perovskite/c-Si tandem solar cells with a flat top cell. *Optics Express*, 24(18):A1288, 2016. doi: 10.1364/OE.24.0A1288. URL https://www.osapublishing.org/abstract.cfm?URI=oe-24-18-A1288.

[159] Jinhui Tong, Qi Jiang, Fei Zhang, Seok Beom Kang, Dong Hoe Kim, and Kai Zhu. Wide-Bandgap Metal Halide Perovskites for Tandem Solar Cells. *ACS Energy Letters*, 6(1):232–248, 2021. doi: 10.1021/acsenergylett.0c02105. URL https://pubs.acs.org/doi/10.1021/acsenergylett.0c02105.

[160] Abdullah Y Alsalloum, Bekir Turedi, Khulud Almasabi, Xiaopeng Zheng, Rounak Naphade, Samuel D Stranks, Omar F. Mohammed, and Osman M. Bakr. 22.8%-Efficient single-crystal mixed-cation inverted perovskite solar cells with a near-optimal bandgap. *Energy & Environmental Science*, 14 (4):2263–2268, 2021. doi: 10.1039/D0EE03839C. URL http://pubs.rsc.org/en/Content/ArticleLanding/2021/EE/D0EE03839Chttp://xlink.rsc.org/?DOI=D0EE03839C.

[161] Alan R Bowman, Felix Lang, Yu-hsien Chiang, Alberto Jiménez-Solano, Kyle Frohna, Giles E Eperon, Edoardo Ruggeri, Mojtaba Abdi-Jalebi, Miguel Anaya, Bettina V Lotsch, and Samuel D Stranks. Relaxed Current Matching Requirements in Highly Luminescent Perovskite Tandem Solar Cells and Their Fundamental Efficiency Limits. *ACS Energy Letters*, 6(2):612–620, 2021. doi: 10.1021/acsenergylett.0c02481. URL https://pubs.acs.org/doi/10.1021/acsenergylett.0c02481.

[162] Kevin A. Bush, Salman Manzoor, Kyle Frohna, Zhengshan Jason Yu, James A. Raiford, Axel F. Palmstrom, Hsin-Ping Wang, Rohit Prasanna, Stacey F. Bent, Zachary C Holman, and Michael D. McGehee. Minimizing Current and Voltage Losses to Reach 25% Efficient Monolithic Two-Terminal Perovskite–Silicon Tandem Solar Cells. *ACS Energy Letters*, 3(9):2173–2180, 2018. doi: 10.1021/acsenergylett.8b01201. URL http://pubs.acs.org/doi/10.1021/acsenergylett.8b01201.

[163] Bo Chen, Zhengshan Yu, Kong Liu, Xiaopeng Zheng, Ye Liu, Jianwei Shi, Derrek Spronk, Peter N. Rudd, Zachary Holman, and Jinsong Huang. Grain Engineering for Perovskite/Silicon Monolithic Tandem Solar Cells with Efficiency of 25.4%. *Joule*, 3(1):177–190, 2019. doi: 10.1016/j.joule.2018.10.003. URL https://linkinghub.elsevier.com/retrieve/pii/S2542435118304653.

[164] Patricia S. C. Schulze, Alexander J. Bett, Martin Bivour, Pietro Caprioglio, Fabian M. Gerspacher, Özde Ş. Kabaklı, Armin Richter, Martin Stolterfoht, Qinxin Zhang, Dieter Neher, Martin Hermle, Harald Hillebrecht, Stefan W. Glunz, and Jan Christoph Goldschmidt. 25.1% High-Efficiency Monolithic Perovskite Silicon Tandem Solar Cell with a High Bandgap Perovskite Absorber. *Solar RRL*, 4(7): 2000152, 2020. doi: 10.1002/solr.202000152. URL https://onlinelibrary.wiley.com/doi/abs/10.1002/solr.202000152.

[165] Anand Selvin Subbiah, Furkan H. Isikgor, Calvyn T. Howells, Michele De Bastiani, Jiang Liu, Erkan Aydin, Francesco Furlan, Thomas G. Allen, Fuzong Xu, Shynggys Zhumagali, Sjoerd Hoogland, Edward H. Sargent, Iain McCulloch, and Stefaan De Wolf. High-Performance Perovskite Single-Junction and Textured Perovskite/Silicon Tandem Solar Cells via Slot-Die-Coating. *ACS Energy Letters*, 5(9):3034–3040, 2020. doi: 10.1021/acsenergylett.0c01297. URL https://pubs.acs.org/doi/10.1021/acsenergylett.0c01297.

[166] OxfordPV. Oxford PV hits new world record for solar cell, 2020. URL https://www.oxfordpv.com/news/oxford-pv-hits-new-world-record-solar-cell. [Accessed on: 2021-02-23].

[167] Eike Köhnen, Philipp Wagner, Felix Lang, Alexandros Cruz, Bor Li, Marcel Roß, Marko Jošt, Anna B. Morales-Vilches, Marko Topič, Martin Stolterfoht, Dieter Neher, Lars Korte, Bernd Rech, Rutger Schlatmann, Bernd Stannowski, and Steve Albrecht. 27.9% Efficient Monolithic Perovskite/Silicon Tandem Solar Cells on Industry Compatible Bottom Cells. *Solar RRL*, 5(7):2100244, 2021. doi: 10.1002/solr.202100244. URL https://onlinelibrary.wiley.com/doi/10.1002/solr.202100244.

Appendices

A Publications and Patents

A.1 Publications

- Marko Jošt, <u>Eike Köhnen</u>, Anna Belen Morales-Vilches, Benjamin Lipovšek, Klaus Jäger, Bart Macco, Amran Al-Ashouri, Janez Krč, Lars Korte, Bernd Rech, Rutger Schlatmann, Marko Topič, Bernd Stannowski, and Steve Albrecht. Textured interfaces in monolithic perovskite/silicon tandem solar cells: advanced light management for improved efficiency and energy yield. *Energy & Environmental Science*, 11(12):3511–3523, 2018. doi: 10.1039/C8EE02469C. URL http://xlink.rsc.org/?DOI=C8EE02469C.

- <u>Eike Köhnen</u>, Marko Jošt, Anna Belen Morales-Vilches, Philipp Tockhorn, Amran Al-Ashouri, Bart Macco, Lukas Kegelmann, Lars Korte, Bernd Rech, Rutger Schlatmann, Bernd Stannowski, and Steve Albrecht. Highly efficient monolithic perovskite silicon tandem solar cells: analyzing the influence of current mismatch on device performance. *Sustainable Energy & Fuels*, 3(8):1995–2005, 2019. doi: 10.1039/C9SE00120D. http://pubs.rsc.org/en/Content/ArticleLanding/2019/SE/C9SE00120D

- Amran Al-Ashouri, <u>Eike Köhnen</u>, Bor Li, Artiom Magomedov, Hannes Hempel, Pietro Caprioglio, José A Márquez, Anna Belen Morales Vilches, Ernestas Kasparavicius, Joel A. Smith, Nga Phung, Dorothee Menzel, Max Grischek, Lukas Kegelmann, Dieter Skroblin, Christian Gollwitzer, Tadas Malinauskas, Marko Jošt, Gašper Matič, Bernd Rech, Rutger Schlatmann, Marko Topič, Lars Korte, Antonio Abate, Bernd Stannowski, Dieter Neher, Martin Stolterfoht, Thomas Unold, Vytautas Getautis, and Steve Albrecht. Monolithic perovskite/silicon tandem solar cell with >29% efficiency by enhanced hole extraction. *Science*, 370(6522):1300–1309, 2020. doi: 10.1126/science.abd4016. https://www.sciencemag.org/lookup/doi/10.1126/science.abd4016

- Marko Jošt, Tobias Bertram, Dibyashree Koushik, J.A. Jose A. Marquez, Marcel A. M.A. Verheijen, M.D. Marc Daniel Heinemann, <u>Eike Köhnen</u>, Amran Al-Ashouri, Steffen Braunger, Felix Lang, Bernd Rech, Thomas Unold, Mariadriana Creatore, Iver Lauermann, Christian A. C.A. Kaufmann, Rutger Schlatmann and Steve Albrecht. 21.6%-Efficient Monolithic Perovskite/Cu(In,Ga)Se$_2$ Tandem Solar Cells with Thin Conformal Hole Transport Layers for Integration on Rough Bottom Cell Surfaces. *ACS Energy Letters*, 4(2):583–590, 2019. doi: 10.1021/acsenergylett.9b00135. http://pubs.acs.org/doi/10.1021/acsenergylett.9b00135

- Amran Al-Ashouri, Artiom Magomedov, Marcel Roß, Marko Jošt, Martynas Talaikis, Ganna Chistiakova, Tobias Bertram, José A. Márquez, <u>Eike Köhnen</u>, Ernestas Kasparavičius, Sergiu Levcenco, Lidón Gil-Escrig, Charles J. Hages, Rutger Schlatmann, Bernd Rech, Tadas Malinauskas, Thomas Unold, Christian A. Kaufmann, Lars Korte, Gediminas Niaura, Vytautas Getautis, and Steve Albrecht. Conformal monolayer contacts with lossless interfaces for perovskite single junction and monolithic tandem solar cells. *Energy & Environmental Science*, 12(11):3356–3369, 2019. doi: 10.1039/C9EE02268F. http://xlink.rsc.org/?DOI=C9EE02268F

- Felix Lang, Marko Jošt, Kyle Frohna, <u>Eike Köhnen</u>, Amran Al-Ashouri, Alan R. Bowman, Tobias Bertram, Anna Belen Morales-Vilches, Dibyashree Koushik, Elizabeth M. Tennyson, Krzysztof Galkowski, Giovanni Landi, Mariadriana Creatore, Bernd Stannowski, Christian A. Kaufmann, Jürgen Bundesmann, Jörg Rappich, Bernd Rech, Andrea Denker, Steve Albrecht, Heinz-Christoph Neitzert, Norbert H. Nickel, and Samuel D. Stranks. Proton Radiation Hardness of Perovskite Tandem Photovoltaics. *Joule*, 4(5):1054–1069, 2020. doi: 10.1016/j.joule.2020.03.006. https://linkinghub.elsevier.com/retrieve/pii/S2542435120300982

- <u>Eike Köhnen</u>, Philipp Wagner, Felix Lang, Alexandros Cruz, Bor Li, Marcel Roß, Marko Jošt, Anna B. Morales Vilches, Marko Topič, Martin Stolterfoht, Dieter Neher, Lars Korte, Bernd Rech, Rutger Schlatmann, Bernd Stannowski and Steve Albrecht. 27.9% Efficient Monolithic Perovskite/Silicon Tandem Solar Cells on Industry Compatible Bottom Cells. *Solar RRL*, 5:2100244, 2021. doi:10.1002/solr.202100244. https://onlinelibrary.wiley.com/doi/10.1002/solr.202100244

A.2 Patents

- "Verbindung und Verfahren zur Bildung von selbstorganisierten Monolagen auf TCO-Substraten zur Verwendung in Perowskit-Solarzellen in invertierter Architektur ".
  Artiom Magomediv, Amran Al-Ashouri, Ernestas Kasparavičius, Steve Albrecht, Vytautas Getautis, Marko Jošt, Tadas Malinauskas, Lukas Kegelmann, <u>Eike Köhnen</u>
  DE 10 2018 115 379 B3 2019.10.10.
  Applied 26.06.2018. Issued 10.10.2019

  - International follow-up application of item above: "Hole-transporting Self-organized Monolayer for Perovskite Solar Cells".
    PCT/EP2019/060586, 25.04.2019, pending

- "Perowskit-Mehrfachsolarzelle mit Multischichtsystem als Verbindungsschicht".
  Amran Al-Ashouri, Steve Albrecht, <u>Eike Köhnen</u>, Marcel Roß, Marko Jošt, Lukas Kegelmann, Artiom Magomedov, Vytautas Getautis, Tadas Malinauskas.
  DE 10 2019 116 851 B3 2020.11.05.
  Applied 21.06.2019. Issued 05.11.2020

  - International follow-up application of item above: "Perovskite Multi-Junction Solar Cell Having Multi-Layer System as Connection Layer".
    PCT/EP2020/067252, 19.06.2020, pending

B Evolution of two-terminal perovskite/silicon tandem solar cells

Date (publication or announcement)	PCE (%)	First author	Literature
24.03.2015	13.7	Mailoa	[15]
27.10.2015	18.1	Albrecht	[96]
19.12.2015	21.2	Werner	[97]
17.02.2017	23.6	Bush, Palmstrom	[16]
11.06.2018	25.2	Sahli	[92]
15.06.2018	25.2	Mazzarella	[101] (anounced)
25.06.2018	27.3	OxfordPV	[102]
28.08.2018	25.0	Bush	[162]
24.10.2018	25.4	Chen	[163]
25.10.2018	25.5	Jost	[31]
20.12.2018	28.0	OxfordPV	[103]
12.03.2019	25.1	Nogay, Sahli	[135]
10.05.2019	26.0	Köhnen	[104]
09.09.2019	27.5	Albrecht	announced at EUPVSEC 2019
24.01.2020	26.1	Chen, Yu	[105]
29.01.2020	29.2	Al-Ashouri, Köhnen	[99] (anounced)
06.03.2020	25.7	Hou, Aydin, De Bastiani	[107]
06.03.2020	27.0	Xu, Boyd	[106]
10.04.2020	26.2	Kim, Jung, Park	[148]
08.05.2020	25.1	Schulze	[164]
11.08.2020	23.8	Subbiah, Isikgor	[165]
14.09.2020	25.1	Aydin	[94]
21.12.2020	29.5	OxfordPV	[166]
11.01.2021	25.2	De Bastiani	[111]
21.04.2021	28.2	Köhnen	[167]

C   Certificate 24.97%

Fraunhofer ISE CalLab PV Cells

Heidenhofstr.2

79110 Freiburg

Werkskalibrierschein
Proprietary calibration report

| 10003085HMI0418 |

Gegenstand *Object*	**solar cell**
Hersteller *Manufacturer*	**Helmholtz Zentrum Berlin**
Typ *Type*	**Perovskite/Silicon Tandem**
Fabrikat/Serien-Nr. *Serial number*	**EKTa07 / HMI003**
Auftraggeber *Customer*	**Helmholtz-Center Berlin** **Young Investigator Group Perovskite Tandem Solar Cells** **Kekuléstr. 5** **12489 Berlin** **Germany**
Auftragsnummer *Order No.*	**085HMI0418**
Anzahl der Seiten *Number of pages*	**6**
Datum der Kalibrierung *Date of calibration*	**18.05.2018**

Kalibrierscheine ohne Unterschrift haben keine Gültigkeit. *Calibration certificates without signature are not valid.*

Datum *Date*	Leiter des Kalibrierlaboratoriums *Head of the calibration laboratory*	Bearbeiter *Person in charge*
18.05.2018		
	Jochen Hohl-Ebinger	*Astrid Semeraro*

Fraunhofer
ISE

CalLab
PV Cells

1. Beschreibung des Kalibriergegenstandes

Description of the calibrated object
Das Messobjekt ist eine Tandem-Solarzelle . Typ: Perowskit/Silicium.
The device under test is a perovskite-silicon tandem solar cell.

2. Messverfahren

Measurement procedure

Die Kalibrierung des Kalibrierobjektes wird gemäß /1/ mit einem Zweilampen-DC-Sonnensimulator durchgeführt. Die Einstrahlung wird mit Hilfe einer Monitorzelle während der gesamten Messdauer aufgenommen und deren Schwankungen bezüglich der Messung korrigiert. Die Divergenz der Randstrahlen ist < 5°. Die Solarzelle wird auf einem Vakuumprobentisch thermisch stabilisiert.
The calibration of the test sample was performed at Standard Testing Conditions (STC) with a dual light steady-state solar simulator according to /1/. The irradiance is controlled with a monitor cell during the measurement in order to correct fluctuations. The divergence of the peripheral beams is < 5°. The solar cell is kept at a constant temperature on

Rückführung der Referenzsolarzellen/*Traceability of the reference solar cells* :

Identitäts-Nr. / *Identity-Nr.* :	Kalibrierschein-Nr./ *Certificate-Nr.* :	Rückführung/ *Traceability* :
007-2012	47149-PTB-17	PTB
011-2012	47146-PTB-17	PTB

Die Korrektur der spektralen Fehlanpassung (Mismatch), die durch die Abweichung der spektralen Verteilung des Sonnen Simulators vom Standard-Spektrum AM1.5G /3/ in Kombination mit den verschiedenen spektralen Empfindlichkeiten von Referenzzelle und Messobjekt entsteht /4/, wurde durch eine erweiterte Mismatchberechnung /4/ - wie in /2/ beschrieben - korrigiert.
Dazu wurde die spektrale Verteilung der Bestrahlung (Sonnensimulator) mit einem Spektralradiometer und die spektrale Empfindlichkeit des Messobjektes mit einem laserbasierten Messplatz /5/ gemessen (s. Kalibrierschein Nr: 9003085HMI0418).
The spectral mismatch - caused by the deviation of the simulator spectrum from the standard spectrum AM1.5G /3/ in combination with the difference between the spectral response of the reference cell and that of the device under test (DUT) – is calculated by a generalized mismatch correction /3/ as described in /2/.
For the spectral mismatch correction the spectral distribution of the solar simulator is measured with a spectroradiometer, the spectral response of the DUT is measured with a laser-based setup according to /5/ (cf. Calibration Mark: 9003085HMI0418).

Der P_{MPP} wurde durch MPP-Tracking über 420s bestimmt. Der angegebene P_{MPP} ist der Mittelwert der letzten 300s dieser stabilisierten Messung. Anschließend wurde die IV-Kennlinie in zwei Richtungen (V_{OC} -> I_{SC} und I_{SC} -> V_{OC}) aufgenommen.
The P_{MPP} was determined by MPP-Tracking for 420s. The reported P_{MPP} represents the average value of the last 300s of this stabilized measurement. Afterwards, the IV-curve was determined with a scan in both directions (V_{OC} -> I_{SC} and I_{SC} -> V_{OC}).

Fraunhofer
ISE

CalLab
PV Cells

Die Rückführung der Spektralmessung auf SI-Einheiten erfolgte über den Vergleich mit einer Standardlampe.
The traceability of the measurement of the spectral distribution to SI-Units is achieved using a standard lamp for the calibration of the spectroradiometer.

Identitäts-Nr. / *Identity-Nr.* :	Kalibrierschein-Nr./ *Certificate-Nr.* :	Rückführung/ *Traceability* :
BN-9101-451	40002-14-PTB	PTB

3. Messbedingungen
Measurement conditions

Standardtestbedingungen (STC) / *Standard Testing Conditions (STC)* :

Absolute Bestrahlungsstärke / *Total irradiance* : 1000 W/m²

Temperatur des Messobjektes / *Temperature of the DUT* : 25 °C

Spektrale Bestrahlungsstärke / *Spectral irradiance distribution* : AM1.5G Ed.2 (2008)

Die Messung der IV-Kennlinie (Strom-Spannungs-Kennlinie) des Messobjektes erfolgt mit Hilfe eines Vierquadranten-Netzteiles und eines Kalibrierwiderstandes.
The measurement of the IV-curve is performed with a 4-quadrant power amplifier and a calibration resistor.

4. Messergebnis
Measurement results

Fläche / *Area* (da)[1]:   =   (0.7709   ±   0.013   ) cm²

[1] : (t) = total area, (ap) = aperture area, (da) = designated illumination area /7/

Kennlinienparameter des Messobjektes unter Standardtestbedingungen (STC) / *IV-curve parameter under Standard Testing Conditions (STC)* :

		Vorwärtsrichtung / *forwards scan direction*		Rückwärtsrichtung / *reverse scan direction*		MPP-Tracking / *MPP-Tracking*
V_{oc}	=	(1780.8 ± 11.9) mV		(1777.9 ± 11.9) mV		
I_{SC} (Ed.2 - 2008)	=	(13.73 ± 0.26) mA		(13.73 ± 0.26) mA		
I_{MPP}	=	12.92 mA		12.91 mA		(12.89 ± 0.33) mA
V_{MPP}	=	1488.2 mV		1481.9 mV		(1494.0 ± 25.2) mV
P_{MPP}	=	19.24 mW		19.14 mW		(19.25 ± 0.51) mW
FF	=	78.64 %		78.36 %		
η	=	24.95 %		24.82 %		(24.97 ± 0.73) %

Angegeben ist jeweils die erweiterte Messunsicherheit, die sich aus der Standardmessunsicherheit durch Multiplikation mit dem Faktor k=2 ergibt. Sie wurde gemäß dem "Guide to the expression of Uncertainty in Measurement" ermittelt. Sie entspricht bei einer Normalverteilung der Abweichungen vom Messwert einer Überdeckungswahrscheinlichkeit von 95%.

The expanded measurement uncertainty resulting from the standard measurement uncertainty multiplied with a factor k=2 is specified. The calculation was carried out according to the "Guide to the expression of Uncertainty in Measurement". The value corresponds to a Gaussian distribution denoting the deviations of the measurement value within a probability of 95%.

5. Zusatzinformationen

Additional information

Fraunhofer
ISE

CalLab
PV Cells

steady state MPP

6. Literatur

Literature

/1/ IEC 60904-1-Ed.2:2006, *Photovoltaic devices - Part 1: Measurement of photovoltaic current-voltage characteristics*

/2/ M. Meusel, R. Adelhelm, F. Dimroth, A.W. Bett, W. Warta Spectral Mismatch Correction and Spectrometric Characterization of Monolithic III–V Multi-junction Solar Cells Prog. Photovolt: Res. Appl. 10 (2002) p. 243–255

/3/ IEC 60904-3-Ed.2:2008, *Photovoltaic devices - Part 3: Measurement principles for terrestrial photovoltaic (PV) solar devices with reference spectral irradiance data*

/4/ IEC 60904-7-Ed.3:2008, *Photovoltaic devices - Part 7: Computation of the spectral mismatch error introduced in the testing of a photovoltaic device*

/5/ IEC 60904-8-Ed.3:2014*, Photovoltaic devices - Part 8: Measurement of the spectral responsivity of a photovoltaic (PV) device*

/6/ IEC 60904-9-Ed.2:2010, *Photovoltaic devices - Part 9: Solar simulator performance requirements*

/7/ M.A. Green, K. Emery, Y. Hishikawa, W. Warta, and E. D. Dunlop, *Solar cell efficiency tables (version 39)*. Progress in Photovoltaics: Research and Applications, 2012. 20: p. 12-20.

D   Certificate 29.15%

Fraunhofer ISE CalLab PV Cells

Heidenhofstr.2

79110 Freiburg

Werkskalibrierschein
Proprietary calibration report

| 10003155HMI0919 |

Gegenstand *Object*	**solar cell**
Hersteller *Manufacturer*	**Helmholtz-Center Berlin**
Typ *Type*	**Perovskite/Silicon Tandem**
Fabrikat/Serien-Nr. *Serial number*	**HMI003 / EKTb84**
Auftraggeber *Customer*	**Helmholtz-Center Berlin** **Young Investigator Group Perovskite Tandem Solar Cells** **Kekuléstr. 5** **12489 Berlin** **Germany**
Auftragsnummer *Order No.*	**155HMI0919**
Anzahl der Seiten *Number of pages*	**6**
Datum der Kalibrierung *Date of calibration*	**22.01.2020**

Kalibrierscheine ohne Unterschrift haben keine Gültigkeit. *Calibration certificates without signature are not valid.*

Datum *Date*	Leiter des Kalibrierlaboratoriums *Head of the calibration laboratory*	Bearbeiter *Person in charge*
24.01.2020		
	Jochen Hohl-Ebinger	*Astrid Semeraro*

93

Fraunhofer
ISE

CalLab
PV Cells

1. Beschreibung des Kalibriergegenstandes

Description of the calibrated object
Das Messobjekt ist eine Tandem-Solarzelle . Typ: Perowskit/Silicium.
The device under test is a perovskite-silicon tandem solar cell.

2. Messverfahren

Measurement procedure

Die Kalibrierung des Kalibrierobjektes wird gemäß /1/ mit einem Zweilampen-DC-Sonnensimulator durchgeführt. Die Einstrahlung wird mit Hilfe einer Monitorzelle während der gesamten Messdauer aufgenommen und deren Schwankungen bezüglich der Messung korrigiert. Die Divergenz der Randstrahlen ist < 5°. Die Solarzelle wird auf einem Vakuumprobentisch thermisch stabilisiert.
The calibration of the test sample was performed at Standard Testing Conditions (STC) with a dual light steady-state solar simulator according to /1/. The irradiance is controlled with a monitor cell during the measurement in order to correct fluctuations. The divergence of the peripheral beams is < 5°. The solar cell is kept at a constant temperature

Rückführung der Referenzsolarzellen/*Traceability of the reference solar cells* :

Identitäts-Nr. / *Identity-Nr.* :	Kalibrierschein-Nr./ *Certificate-Nr.* :	Rückführung/ *Traceability* :
040-2002	47115-PTB-18	PTB
022-2012	47114-PTB-18	PTB

Die Korrektur der spektralen Fehlanpassung (Mismatch), die durch die Abweichung der spektralen Verteilung des Sonnen Simulators vom Standard-Spektrum AM1.5G /3/ in Kombination mit den verschiedenen spektralen Empfindlichkeiten von Referenzzelle und Messobjekt entsteht /4/, wurde durch eine erweiterte Mismatchberechnung /4/ - wie in /2/ beschrieben - korrigiert.
Dazu wurde die spektrale Verteilung der Bestrahlung (Sonnensimulator) mit einem Spektralradiometer und die spektrale Empfindlichkeit des Messobjektes mit einem laserbasierten Messplatz /5/ gemessen (s. Kalibrierschein Nr: 9003155HMI0919).
The spectral mismatch - caused by the deviation of the simulator spectrum from the standard spectrum AM1.5G /3/ in combination with the difference between the spectral response of the reference cell and that of the device under test (DUT) – is calculated by a generalized mismatch correction /3/ as described in /2/.
For the spectral mismatch correction the spectral distribution of the solar simulator is measured with a spectroradiometer, the spectral response of the DUT is measured with a laser-based setup according to /5/ (cf.

Der P_{MPP} wurde durch MPP-Tracking über 300s bestimmt. Der angegebene P_{MPP} ist der Mittelwert von 325-625s dieser stabilisierten Messung. Anschließend wurde die IV-Kennlinie in zwei Richtungen (V_{OC} -> I_{SC} und I_{SC} -> V_{OC}) aufgenommen.
The P_{MPP} was determined by MPP-Tracking for 300s. The reported P_{MPP} represents the average value of the range 325-625s of this stabilized measurement. Afterwards, the IV-curve was determined with a scan in both directions (V_{OC} -> I_{SC} and I_{SC} -> V_{OC}).

94

Fraunhofer
ISE

CalLab
PV Cells

Die Rückführung der Spektralmessung auf SI-Einheiten erfolgte über den Vergleich mit einer Standardlampe.
The traceability of the measurement of the spectral distribution to SI-Units is achieved using a standard lamp for the calibration of the spectroradiometer.

Identitäts-Nr. / *Identity-Nr.* :	Kalibrierschein-Nr./ *Certificate-Nr.* :	Rückführung/ *Traceability* :
BN-9101-451	40002-14-PTB	PTB

3. Messbedingungen
Measurement conditions

Standardtestbedingungen (STC) / *Standard Testing Conditions (STC)* :

Absolute Bestrahlungsstärke /
Total irradiance :   1000   W/m²

Temperatur des Messobjektes /
Temperature of the DUT :   25   °C

Spektrale Bestrahlungsstärke /
Spectral irradiance distribution :   AM1.5G Ed.2 (2008)

Die Messung der IV-Kennlinie (Strom-Spannungs-Kennlinie) des Messobjektes erfolgt mit Hilfe eines Vierquadranten-Netzteiles und eines Kalibrierwiderstandes.
The measurement of the IV-curve is performed with a 4-quadrant power amplifier and a calibration resistor.

4. Messergebnis
Measurement results

Fläche / *Area* (da)[1]:   =   (1.0599   ±   0.0066   ) cm²
[1] : (t) = total area, (ap) = aperture area, (da) = designated illumination area /7/

Kennlinienparameter des Messobjektes unter Standardtestbedingungen (STC) / *IV-curve parameter under Standard Testing Conditions (STC)* :

		Vorwärtsrichtung / *forwards scan direction*		Rückwärtsrichtung / *reverse scan direction*		steady state MPP	
V_{oc}	=	(1900.3 ± 12.7) mV		(1894.6 ± 12.7) mV			
I_{SC} (Ed.2 - 2008)	=	(20.38 ± 0.39) mA		(20.40 ± 0.39) mA			
I_{MPP}	=	18.83	mA	18.75	mA	(19.11 ± 0.40) mA	
V_{MPP}	=	1633.0	mV	1625.3	mV	(1616.6 ± 36.6) mV	
P_{MPP}	=	30.74	mW	30.47	mW	(30.90 ± 0.85) mW	
FF	=	79.40	%	78.85	%		
η	=					(29.15 ± 0.82) %	

95

Angegeben ist jeweils die erweiterte Messunsicherheit, die sich aus der Standardmessunsicherheit durch Multiplikation mit dem Faktor *k*=2 ergibt. Sie wurde gemäß dem "Guide to the expression of Uncertainty in Measurement" ermittelt. Sie entspricht bei einer Normalverteilung der Abweichungen vom Messwert einer Überdeckungswahrscheinlichkeit von 95%.

The expanded measurement uncertainty resulting from the standard measurement uncertainty multiplied with a factor k=2 is specified. The calculation was carried out according to the "Guide to the expression of Uncertainty in Measurement". The value corresponds to a Gaussian distribution denoting the deviations of the measurement value within a probability of 95%.

5. Zusatzinformationen

Additional information

Fraunhofer
ISE

CalLab
PV Cells

Steady State Pmpp

97

6.Literatur
Literature

/1/ IEC 60904-1-Ed.2:2006, *Photovoltaic devices - Part 1: Measurement of photovoltaic current-voltage characteristics*

/2/ M. Meusel, R. Adelhelm, F. Dimroth, A.W. Bett, W. Warta Spectral Mismatch Correction and Spectrometric Characterization of Monolithic III–V Multi-junction Solar Cells Prog. Photovolt: Res. Appl. 10 (2002) p. 243–255

/3/ IEC 60904-3-Ed.2:2008, *Photovoltaic devices - Part 3: Measurement principles for terrestrial photovoltaic (PV) solar devices with reference spectral irradiance data*

/4/ IEC 60904-7-Ed.3:2008, *Photovoltaic devices - Part 7: Computation of the spectral mismatch error introduced in the testing of a photovoltaic device*

/5/ IEC 60904-8-Ed.3:2014*, Photovoltaic devices - Part 8: Measurement of the spectral responsivity of a photovoltaic (PV) device*

/6/ IEC 60904-9-Ed.2:2010, *Photovoltaic devices - Part 9: Solar simulator performance requirements*

/7/ M.A. Green, K. Emery, Y. Hishikawa, W. Warta, and E. D. Dunlop, *Solar cell efficiency tables (version 39).* Progress in Photovoltaics: Research and Applications, 2012. 20: p. 12-20.

E Publication: Highly efficient monolithic perovskite silicon tandem solar cells: analyzing the influence of current mismatch on device performance

The following pages contain the publication addressed in section 6.1.

- Publication:
  Eike Köhnen, Marko Jošt, Anna Belen Morales-Vilches, Philipp Tockhorn, Amran Al-Ashouri, Bart Macco, Lukas Kegelmann, Lars Korte, Bernd Rech, Rutger Schlatmann, Bernd Stannowski, and Steve Albrecht. Highly efficient monolithic perovskite silicon tandem solar cells: analyzing the influence of current mismatch on device performance. *Sustainable Energy & Fuels*, 3(8):1995–2005, 2019.

  https://doi.org/10.1039/C9SE00120D

- Author contribution:
  E.K., M.J., P.T., A.A. and Lu.K. developed and optimized the perovskite solar cell fabrication process; E.K. fabricated the tandem devices, performed the *J-V*, EQE, Hall and UV-Vis measurements and optimized the top contact; A.B.M.V., La.K. and B.S. developed and optimized the silicon-heterojunction solar cell fabrication process and fabricated bottom cells; B.M. and E.K. optimized the SnO_2 process and performed and analyzed spectroscopic ellipsometry measurements; E.K., P.T. and A.A. performed the optical and electrical simulations; E.K. drafted the manuscript; All authors participated in proofreading and correcting; B.R., R.S., B.S. and S.A. initiated and supervised the project.

Showcasing research from Professor Albrecht's laboratory, the HySPRINT Innovation Lab at Helmholtz-Center Berlin, Germany.

Highly efficient monolithic perovskite silicon tandem solar cells: analyzing the influence of current mismatch on device performance

Metal halide perovskites show great promise to enable highly efficient and low cost tandem solar cells when being combined with silicon. By careful optimization of the tandem design, Köhnen and coworkers enabled the highest yet scientifically published efficiency of 26.0% for monolithic perovskite / silicon tandem solar cells. In addition, the team also measured tandem current voltage characteristics and extracted the fill factor (FF) under various illumination spectra, to imitate the illumination over the course of the day. Interestingly, the reduction in photocurrent for spectral changes occurring during the course of a day is partially compensated by an enhancement of the FF, compensating the otherwise reduced efficiency.

Copyright Tim Beyer, Mitrostudios.com, Potsdam, Germany

ROYAL SOCIETY OF CHEMISTRY | Celebrating IYPT 2019

rsc.li/sustainable-energy

Registered charity number: 207890

PAPER

Highly efficient monolithic perovskite silicon tandem solar cells: analyzing the influence of current mismatch on device performance†

Eike Köhnen, [ID] *[a] Marko Jošt, [ID] [a] Anna Belen Morales-Vilches, [ID] [b] Philipp Tockhorn,[a] Amran Al-Ashouri, [ID] [a] Bart Macco, [ID] [cd] Lukas Kegelmann, [ID] [a] Lars Korte, [ID] [d] Bernd Rech, [ID] [de] Rutger Schlatmann, [ID] [b] Bernd Stannowski [ID] [b] and Steve Albrecht *[ae]

Metal halide perovskites show great promise to enable highly efficient and low cost tandem solar cells when being combined with silicon. Here, we combine rear junction silicon heterojunction bottom cells with p–i–n perovskite top cells into highly efficient monolithic tandem solar cells with a certified power conversion efficiency (PCE) of 25.0%. Further improvements are reached by reducing the current mismatch of the certified device. The top contact and perovskite thickness optimization allowed increasing the J_{SC} above 19.5 mA cm^{-2}, enabling a remarkable tandem PCE of 26.0%, however with a slightly limited fill factor (FF). To test the dependency of the FF on the current mismatch between the sub-cells, the tandems' J–V curves are measured under various illumination spectra. Interestingly, the reduced J_{SC} in unmatched conditions is partially compensated by an enhancement of the FF. This finding is confirmed by electrical simulations based on input parameters from reference single junction devices. The simulations reveal that especially the FF in the experiment is below the expected value and show that with improved design we could reach 29% PCE for our monolithic perovskite/silicon tandem device and 31% PCE if record perovskite and silicon cell single junctions could be combined in tandem solar cells.

Introduction

The well-established technology of silicon solar cells dominates the photovoltaic market. With a current record power conversion efficiency (PCE) of 26.7% on interdigitated back contacted silicon heterojunction solar cells (SHJ),[1,2] silicon solar cells are approaching their theoretical efficiency limit of 29.4%.[3] To exceed this limit significantly, multiple absorbers with different band gaps can be combined into a multijunction solar cell architecture to exploit the solar light more efficiently than a single junction. Due to excellent optoelectronic quality in polycrystalline films, tunable optical band gap and potentially low-cost fabrication, metal halide perovskites are promising candidates for tandem applications.[4–7] Besides low band gap Sn-based perovskites[8,9] and Cu(In,Ga)Se$_2$ (CIGS),[10–12] crystalline silicon cells are well suited for tandem integration with perovskite absorbers. The latter combination is the most extensively studied perovskite-based tandem technology, with several groups reporting power conversion efficiencies above 25%,[1,4–7] a certified record PCE of 28%,[13] and predicted efficiencies above 30%.[14–18]

The monolithic integration of a perovskite top cell on a silicon bottom cell is challenging due to material and processing restrictions. So far, mostly silicon heterojunction (SHJ) bottom cells are utilized due to the well-passivated c-Si wafer surface which leads to high open circuit voltages (V_{OC}s).[4,5,7,19,20] Recently, the p–i–n architecture for perovskite top-cells prevailed over the n–i–p architecture, especially due to temperature limitations of the SHJ cell (200 °C), which prevents the use of high temperature process, such as sintering of mesoporous TiO$_2$.[21–23] Although there are possibilities to deposit the n-type contact at lower temperatures,[24] and use temperature stable bottom cells,[25,26] strong absorption of the p-type top contacts was reported for n–i–p architectures.[14,27] An efficient device design was presented by Bush et al., who mitigated these losses

^{a}Helmholtz-Zentrum Berlin für Materialien und Energie GmbH, Young Investigator Group Perovskite Silicon Tandem Solar Cells, 12489 Berlin, Germany. E-mail: eike.koehnen@helmholtz-berlin.de; steve.albrecht@helmholtz-berlin.de

^{b}Helmholtz-Zentrum Berlin für Materialien und Energie, PVcomB, 12489 Berlin, Germany

^{c}Department of Applied Physics, Eindhoven University of Technology, P.O. Box 513, 5600 MB Eindhoven, The Netherlands

^{d}Helmholtz-Zentrum Berlin für Materialien und Energie GmbH, Institute for Silicon Photovoltaics, 12489 Berlin, Germany

^{e}Technical University Berlin, Faculty IV – Electrical Engineering and Computer Science, 10587 Berlin, Germany

† Electronic supplementary information (ESI) available. See DOI: 10.1039/c9se00120d

by utilizing a p–i–n top cell architecture with reduced parasitic absorption in the n-type top contact. By implementing an ALD SnO_2 buffer layer in the top contact, the sensitive underlying layers were protected from damage induced by the subsequent sputter deposition of the top electrode, enabling a PCE of 23.6%.[28] Later on, Sahli et al. used the same polarity and a similar top contact and demonstrated the use of a hybrid sequential fabrication enabling a conformal growth of the perovskite on top of a textured silicon bottom cell. The reduced reflection in the tandem solar cell led to a short circuit current density (J_{SC}) of 19.5 mA cm^{-2} and a certified PCE of 25.2%.[1,4] At the same time, a tandem cell with planar front side was certified with similar PCE of 25.2%, also using p–i–n top cells and implementing a n-type nc-SiO_x:H interlayer that increases light in-coupling into the Si bottom cell, resulting in a J_{SC} above 19 mA cm^{-2}.[1,29] By grain engineering and additionally adjusting the band gap of the perovskite absorber, a PCE of 25.4% was achieved in the p–i–n top cell configuration by Chen et al. in 2018.[5] A PCE of 25.5% was published along with detailed analysis of the influence of textured interfaces, depending on their position in the cell stack, using a well-developed tandem solar cell and an anti-reflective foil attached on top of the cell.[6] Recently, Oxford PV disclosed a certified PCE of 28% for perovskite/silicon tandem solar cell, however, without giving any details about the materials and the structure used.[13]

Despite these impressive efficiency improvements of monolithic perovskite/silicon tandem solar cells, the experimentally realized efficiencies are still far behind the predicted maximum values.[6,14,15] In addition, there is still insufficient insight into how the individual sub-cells influence each other. One example is dependency of the fill factor (FF) on the difference between the J_{SC}s of the sub-cells (in the following: mismatch m). This effect has already been investigated for other tandem technologies, such as $GaInP_2$/GaAs a-Si:H/μc-Si:H or a-Si:H/a-Si:H, showing a mismatch dependent FF and emphasizing the need of power matching (i.e. same J_{MPP} for both sub-cells) instead of current matching (i.e. same J_{SC} for both sub-cells).[30–33] The issue was also theoretically addressed for perovskite/silicon tandem cells,[18] but for this device layout, detailed investigations and experimental results are lacking. Despite the difference between power and current matching conditions, the latter can be used as a first approximation for maximum power and is easier to extract from standard EQE measurements. The current matching conditions can be affected during outdoor operation by temporal and weather spectral changes. A tandem cell being current matched at AM1.5G illumination does not necessarily lead to the highest energy yield over time.[30] Furthermore, different degradation of the sub-cells could lead to a varying mismatch over time. Therefore, it is important to analyze and understand the performance of a monolithic tandem solar cell as a function of the current mismatch.

Results and discussion

In this work, the development of an optically and electrically optimized n-type front contact with reduced reflection and parasitic absorption is demonstrated. This is achieved by the following adjustments: first, a good balance between conductivity and transparency of the indium zinc oxide (IZO) top electrode is found by fine-tuning the oxygen concentration during sputtering. Second, a SnO_2 buffer layer that is deposited via ALD, enables a good electron-selective contact for the p–i–n top cell. This top contact optimization leads to a certified PCE of 25.0% at a high FF approaching 80%, but with highly unmatched current densities of the sub-cells. In order to enable tandem solar cells with improved current matching, the tandem solar cells are further optimized optically: the thicknesses of the nc-SiO_x:H, the perovskite absorber, and the IZO front electrode are fine-tuned to achieve photocurrents well above 19 mA cm^{-2}. In addition, reducing the ALD processing temperature increases the FF in the perovskite top cell. With both optimizations, a stabilized PCE of 26.0% is achieved which is higher than the highest reported two-side contacted c-Si single junction PCE.[1,34] Further reduction of the front IZO thickness enabled a J_{SC} of 19.77 mA cm^{-2} for the limiting sub-cell and a cumulative photocurrent $J_{Pero+Si}$ > 40 mA cm^{-2}, even for planar front sides. In addition, we investigate the behavior of the highly efficient monolithic tandem solar cell as a function of current mismatch. Varying the incident spectrum using a LED based sun simulator, we show that the FF of the tandem solar cell is significantly affected by the current mismatch when reducing or enhancing the intensity of the blue wavelength range of incident light. The FF reaches its minimum when the sub-cells are close to current matching. This is highly important for precise energy yield analysis as the FF enhancement under nonmatching conditions mitigates the PCE loss that would be expected on the basis of J_{SC} loss.[18] Electrical simulations validate the change in FF by using parametrized single junction reference parameters with a single diode equivalent circuit. The simulations predict a higher FF than obtained experimentally in our tandem solar cell, which highlights that further understanding and optimization of the recombination contact is needed to achieve higher efficiencies. In our case, the ideal series connection would lead to a PCE of 29%. In addition, over 31% could be realized if performance metrics from record perovskite and silicon cells single junctions could be combined in a tandem solar cell.

Fig. 1a and b display a stack of a typical monolithic perovskite/silicon tandem solar cell used in this work. The cross sectional SEM image shows the textured backside of the bottom cell (lower panel) and the top cell (upper right panel) recorded with the in-lens detector. The image obtained with the energy selective backscattered (ESB) detector (upper left panel) especially highlights the PTAA layer, which is not resolvable with the in-lens detector. As bottom cell, a rear-junction SHJ solar cell with a textured rear side and a planar front side is used. To improve light in-coupling into the bottom cell, n-doped nc-SiO_x:H is utilized to create an electron-selective contact with proper refractive index interfacing with a 20 nm thin indium tin oxide (ITO) as recombination layer to interconnect both subcells. The perovskite top cell with p–i–n architecture is utilized in the following layer sequence with the light entering the top cell from the LiF side: ITO/PTAA/perovskite/C_{60}/SnO_2/IZO/LiF. Both charge-selective contacts, poly[bis(4-phenyl)(2,4,6-trimethylphenyl)

102
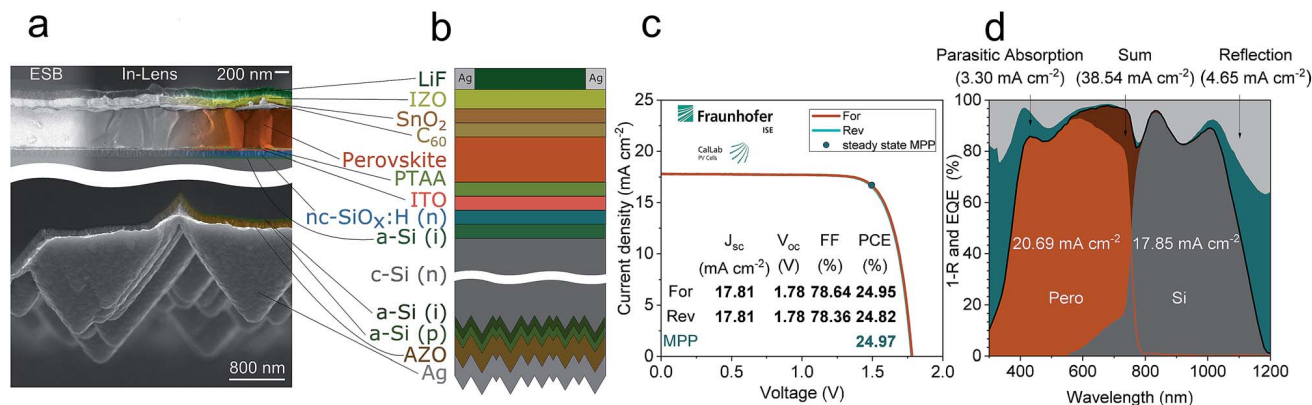
Fig. 1 (a) Colored cross sectional SEM image of the top cell (upper panel) and back side of the bottom cell (lower panel) of a typical monolithic tandem solar cell used in this work. The left side of the top cell is recorded with an energy selective backscattered (ESB) detector, the right side with an in lens detector. Note that scale bars in the top and bottom panel are different as indicated; (b) schematic device layout of the tandem architecture utilized in this work. (c) Certified current density–voltage (J–V)-characteristics measured by Fraunhofer Institute for Solar Energy Systems (ISE) with the certified performance parameters as displayed in the inset table. Steady state efficiency from 400 second maximum power point (MPP)-tracking was 24.97%, see Fig. S3.† (d) Measured external quantum efficiency and reflection spectra of the certified tandem solar cell with integrated current densities and their sum as indicated. Additionally, the loss in current density due to parasitic absorption (as the difference between sum of the EQE and 1-reflectance) and reflection are shown.

amine] (PTAA) and C_{60} for holes and electrons, respectively, were previously shown to be efficient in single-junction and tandem devices,[5,35,36] however, with a V_{OC} limited due to non-radiative recombination losses.[37] A perovskite absorber with a so called "triple cation" composition with mixed cations and mixed halides: $Cs_{0.05}(MA_{0.83}FA_{0.17})Pb(I_{0.83}Br_{0.17})_3$ was deposited *via* the anti-solvent route.[38] For semitransparent top cell integration, a 20 nm ALD SnO_2 is deposited at 100 °C. Instead of using the pulsed CVD-mode, as reported recently,[28] we are using a true ALD mode in order to benefit from ALD merits such as large-area uniformity and conformality. SnO_2 was implemented to the top contact as a barrier and buffer layer. It prevents both moisture and oxygen penetration into the solar cell, and decomposition products of the perovskite like MAI from leaving the layer,[39,40] In addition, SnO_2 protects the underlying layers from sputter damage.[28] As a transparent conductive oxide (TCO) that forms the transparent top electrode, sputtered IZO is implemented. For current collection, a thermally evaporated silver metal frame around the 9×9 mm^2 cell area is forming the busbar without grid fingers. Finally, thermally evaporated LiF serves as an anti-reflective coating. Fig. S2† shows a schematic top view of the tandem solar cell. The use of a quadratic aperture mask slightly decreases the active area to 0.7709 cm^2.

To ensure a high FF, the top TCO needs to be highly conductive. At the same time, the near infrared absorption needs to be mitigated, so that the light can be absorbed in the bottom cell. Adding 0.2%$_{vol}$ oxygen during the sputter process of IZO results in a good balance between transparency, conductivity and the optical band gap and is therefore used in our optimized process. More details can be found in ESI note 1.†

The resulting tandem device, containing a 20 nm thick n-type nc-SiO_x:H and SnO_2 processed at 100 °C deposition temperature, was sent for independent certification to CalLab, Fraunhofer Institute for Solar Energy Systems (ISE). Fig. 1c displays the J–V characteristics reported by the certification lab;

a PCE of 25.0% was measured, stable during 400 seconds of maximum power point tracking (see Fig. S3†). The device exhibits virtually no hysteresis and the deviation between the maximum power point parameters obtained from MPP tracking and those from J–V measurement is negligible. The V_{OC} of 1.78 V is close to the cumulative sub-cell V_{OC}s as expected from single junction devices and to the V_{OC}s found recently with similar device architectures.[4,6,7] A FF of 78.6% is one of the highest measured for a perovskite/silicon tandem solar cell and will be discussed in more detail below. On the other hand, a J_{SC} of 17.81 mA cm^{-2} indicates one of the limiting factors of the certified tandem solar cell. This is further confirmed by the EQE measurements, presented in Fig. 1d along with the total reflectance of the device presented as 1-R. The photocurrent densities are $J_{Pero} = 20.69$ mA cm^{-2} and $J_{Si} = 17.85$ mA cm^{-2} for the perovskite top and silicon bottom cell, respectively. This shows that the certified tandem device is strongly current-mismatched with the silicon sub-cell being the limiting one. Although the J_{SC} of a tandem solar cell can be higher than the minimum J_{SC} of the sub-cells,[41,42] for state of the art solar cells the tandem J_{SC} is expected to be very close to the minimum J_{SC} of the sub-cells (limiting sub-cell). This is valid when the limiting sub-cell (here: silicon) has a high shunt resistance. Assuming this, the integrated current density J_{Si} of 17.85 mA cm^{-2} measured in-house is in very good agreement with the certified J_{SC} of 17.81 mA cm^{-2} measured at Fraunhofer ISE. The mismatch m between J_{Pero} and J_{Si} is more than 2.8 mA cm^{-2}, which needs to be reduced in order to achieve higher PCEs. Fig. 1d displays the sum of the EQEs (black line) and the parasitic losses as the blue area between the sum and 1-R. The parasitic losses are high in the UV and near infrared (NIR) wavelength range and are below 1% on average between 550 nm and 1000 nm. The integrated reflection losses amount to an equivalent photocurrent of 4.65 mA cm^{-2} in the complete wavelength regime; between 750 nm and 1050 nm, there are

distinct reflection features with 1.9 mA cm^{-2} reflection losses only in this region. In order to extract parasitic losses for each individual layer, an optical simulation was carried out using GenPro4 (Fig. S4†).[43] We find, that in the UV region, mostly IZO, SnO$_2$ and C$_{60}$ absorb light, whereas in the infrared region the photons are absorbed by the IZO at the front side, by the ITO connecting the sub-cells and by the aluminum doped zinc oxide (AZO) and silver (Ag) at the backside of the cell. The rather high reflection losses and the strong current mismatch indicate that further optical optimizations are required.

In order to further improve the tandem solar cell, a lower temperature of the ALD SnO$_2$ process was first considered. Exposing the perovskite for 1 h to 100 °C (in addition to the perovskite annealing) might reduce the perovskite top cell performance, thus limiting the tandem efficiency.[44,45] Therefore, we analyze the SnO$_2$ layer in terms of optical properties as a function of deposition temperature. Fig. 2a shows that changing the deposition temperature has an effect on the optical properties of the deposited layer, as evidenced by the shift in extinction coefficient and refractive index. At higher temperatures, a higher absorption in the UV is measured and the absorption onset becomes steeper. Simultaneously, the refractive index increases. However, using optical simulations including the measured differences in optical data, we find that changing the deposition temperature in the range of 80 °C to 200 °C does not have a major effect on J_{Pero} and J_{Si} in our tandem device (Fig. S5a†). For higher deposition temperatures, the EQE of the perovskite improves for wavelengths above 370 nm but also reduces below 370 nm as the absorption of the SnO$_2$ increases in that wavelength range. Overall, the cumulated current density $J_{Pero+Si}$ is constant in the practically relevant range of 80 °C to 120 °C (Fig. S5b†). More importantly, changing the deposition temperature can have a strong effect on the electrical performance. Therefore, semitransparent perovskite solar cells with SnO$_2$ deposited at moderate temperatures of 80 °C, 100 °C and 120 °C are fabricated and analyzed. The results, depicted in Fig. 2b and c, indeed show a beneficial effect on the FF by reducing the temperature from 120 °C to 80 °C, which directly transfers to the change in PCE. The V_{OC} and J_{SC}, however, are hardly affected by the different deposition temperatures of the ALD SnO$_2$ (see Fig. S6a and b†).

Additionally, the thickness of the top TCO in the tandem stack, here IZO, has a significant influence on parasitic absorption throughout the entire wavelength range. To analyze the impact of top electrode thickness, an optical simulation of the tandem stack with thicknesses of IZO between 60 nm and 130 nm in 10 nm steps is performed. Fig. S7† shows the simulated gain in current density, which amounts to ~0.32 mA cm^{-2} when reducing the thickness from 130 nm to 90 nm. Further reducing the IZO thickness would be ideal to increase J_{Pero} and J_{Si}. However, reducing the thickness also leads to a higher sheet resistance and might have a negative impact on the cell performance, especially reduction of FF. Therefore, 90 nm was used in the optimized device.

Apart from being the electron-selective contact layer for the bottom SHJ solar cell the use of n-type nc-SiO$_x$:H between the perovskite and silicon absorber has two benefits: first, the refractive index at 633 nm of around 2.7 is in between those of the neighboring layers, which reduces reflection; second, this reflection can be spectrally tuned when the layer thickness is adapted for destructive interference in a particular wavelength range. For the n-type nc-SiO$_x$:H, a thickness of around 95 nm was found both in simulations and experimental results to be ideal for monolithic perovskite/silicon tandem solar cells.[15,29] Thus, this thickness is implemented in the further development.

Finally, the thickness of the perovskite absorber is fine-tuned by adjusting the spin coating speed to enable conditions closer to current matching.[4,7] Fig. S8† presents optical simulations with varying perovskite thickness between 390 nm and 520 nm. While $J_{Pero+Si}$ hardly changes, a thinner perovskite absorber layer will transmit more light into the silicon bottom cell, enhancing the J_{Si}. As the sub-cell with the lower current approximately determines the J_{SC} of the tandem cell, a maximum tandem J_{SC} is expected for a perovskite thickness of around 470 nm for our design.

All above described optimizations are implemented into tandem solar cell devices and the results are shown in Fig. 3. Indeed, the optical losses are reduced and the sub-cells enable short circuit current densities closer to current matching. The J_{SC} improved by 1.4 mA cm^{-2} to a value of 19.22 mA cm^{-2}. The V_{OC} remained almost unchanged (1.77 V) while the FF is slightly lower (76.6%). Overall, a stabilized PCE of 26.0% is achieved, confirmed by a 5 minute MPP-track as shown in Fig. 3a. Fig. 3b highlights the EQE spectra together with total reflectance depicted as 1-R for the optimized tandem design. Due to improved optics, interference patterns in the 800 nm to 1050 nm wavelength range are smoothened, reducing reflection by more than 1 mA cm^{-2} and increasing J_{Si}. Compared to the device shown in Fig. 1c and d, the improved device is much closer to current matching, with only 0.9 mA cm^{-2} mismatch. In Fig. S9,† EQE spectra of similarly fabricated single junction silicon and perovskite cells are shown.
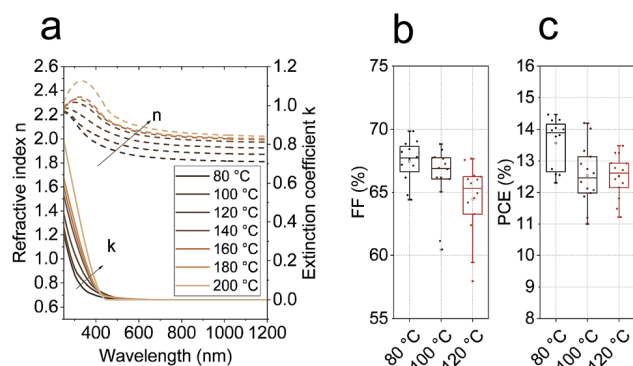
Fig. 2 (a) Optical properties of SnO$_2$ deposited via ALD at temperatures from 80 °C to 200 °C. The refractive index (n, left axis) and extinction coefficient (k, right axis) are extracted from spectroscopic ellipsometry measurements using Tauc−Lorentz oscillators. (b and c) FF and PCE for semitransparent perovskite solar cells with ALD SnO$_2$ deposited at 80 °C, 100 °C and 120 °C. The cells have the same architecture as the tandem cell without a LiF anti-reflective coating and are illuminated through the IZO side. The corresponding V_{OC} and J_{SC} values are shown in ESI Fig. S6.†
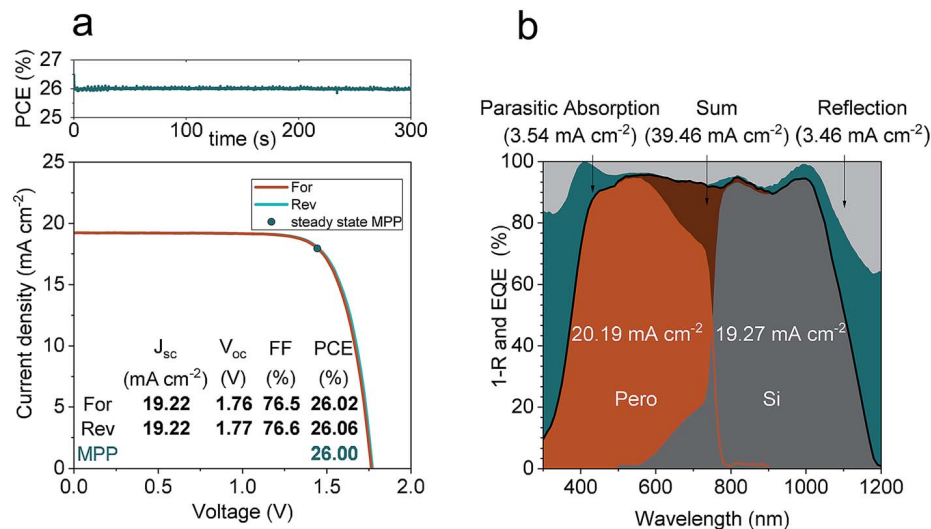
Fig. 3 (a) *J*–*V*-characteristics of the optimized tandem solar cell with the performance metrics and a 5 min. MPP-track. (b) External quantum efficiency (EQE) and 1-reflectance (1-*R*) spectra of the same device. The integrated current densities are 20.19 mA cm^{-2} and 19.27 mA cm^{-2} for the perovskite and silicon cell sub-cells, respectively. Additionally, the integrated loss currents from parasitic absorption and 1-*R* are shown.

To test the stability of these optimized tandem devices, a similar tandem solar cell with comparable performance as shown in Fig. 3 was glass/glass encapsulated with edge-sealant and stored in ambient conditions. Due to different optics after encapsulation, the PCE dropped from 26.0% to 24.6% mostly because of additional reflection from the air/glass interface, as compared to air/LiF. During 1000 h, the device was stored in ambient air and light conditions (*i.e.* 19–21 °C and 50–90% RH) and regularly MPP-tracked for at least 30 min at each data point. The measurements were performed at 25 °C, ambient humidity and under simulated full 1 sun AM1.5G illumination. The exact spectrum is shown later in Fig. 4a. The PCE as function of time is presented in Fig. S10† and found to be remarkably stable with a relative PCE drop of less than 1% for the last measurement after 1000 h of ambient storage.

As the optimized tandem device in Fig. 3 still shows current mismatch and the $J_{Pero+Si}$ stays below 40 mA cm^{-2}, the optical benefit of further reducing the front IZO thickness is tested. As described above, Fig. S7† shows simulation results for thinner front IZO. A $J_{Pero+Si}$ above 40 mA cm^{-2} is only realized with IZO thicknesses of around 60 nm. Consequently, a tandem solar cell with this thin IZO layer is fabricated and the experimental results are presented in Fig. S11.† Integrated current densities from the EQE spectra up to 20.27 mA cm^{-2} for the top and 19.77 mA cm^{-2} for the bottom cell are measured, which indeed results in a $J_{Pero+Si}$ of more than 40 mA cm^{-2}. This current density is comparable to values reported by Sahli *et al.*[4] for a fully textured tandem cell but is still lower than the best J_{SC} of silicon single junction cells (42.87 mA cm^{-2}).[1] If the $J_{Pero+Si}$ would be equally distributed between J_{Pero} and J_{Si}, the tandem cell with thin IZO would exceed a J_{SC} of 20 mA cm^{-2}, a remarkable result for a planar front side tandem design. Due to a lower FF, which is mainly a result of lower shunt resistance and slightly higher series resistance – the latter due to higher ohmic losses in thinner IZO – the stabilized PCE during MPP-tracking

is only 25.3% (see Fig. S11†). For the optimal performance with thin IZO, metal fingers are necessary and to optimize the resistive *versus* shading losses, opto-electrical simulations are required,[46] which is a subject of future work.

Comparing the two tandem solar cells, presented in Fig. 1 and 3, we observe a lower FF for the device that operates closer to current matching. Besides the possibility of a cell-to-cell variation, operating the sub-cells under strong non-matching conditions should improve the tandem FF, as reported for other tandem technologies.[18,30,33] As a thorough understanding of the influence of non-current matching conditions is important for (a) device understanding and (b) energy yield analysis, the FF of the best performing tandem solar cell shown in Fig. 3 is measured here for various illumination spectra, leading to non-matching conditions. Using a LED-based sun simulator, the intensity of individual LEDs can be adjusted while leaving the others unchanged. Thus, the device can be measured under different non-matching conditions *m*. As basis, the simulated AM1.5G spectrum is used. To increase or decrease the irradiance in the blue region, the intensities of two blue LEDs (emission peaks centered at 420 nm and 440 nm) are changed, while leaving all other LEDs constant to simulate the AM1.5G spectrum. This way, only the current generation in the perovskite top cell is affected. Fig. 4a shows the utilized spectra including the AM1.5G reference spectrum. The measurement series starts with the highest intensity of blue light well above the blue intensity in the AM1.5G spectrum. Then the intensities of the two blue LEDs are decreased and a tandem *J*–*V*-curve for each spectrum is measured. The raw data of the 26 measurements are presented in Fig. S12,† plotted against the spectrum (measurement) number. The first and last *J*–*V* curve in the series are measured under AM1.5G illumination and ensure that there is no degradation of the cell and no drift of the spectrum during the course of the series. As the intensity of the blue light (*i.e.* current generation in the perovskite) decreases, the
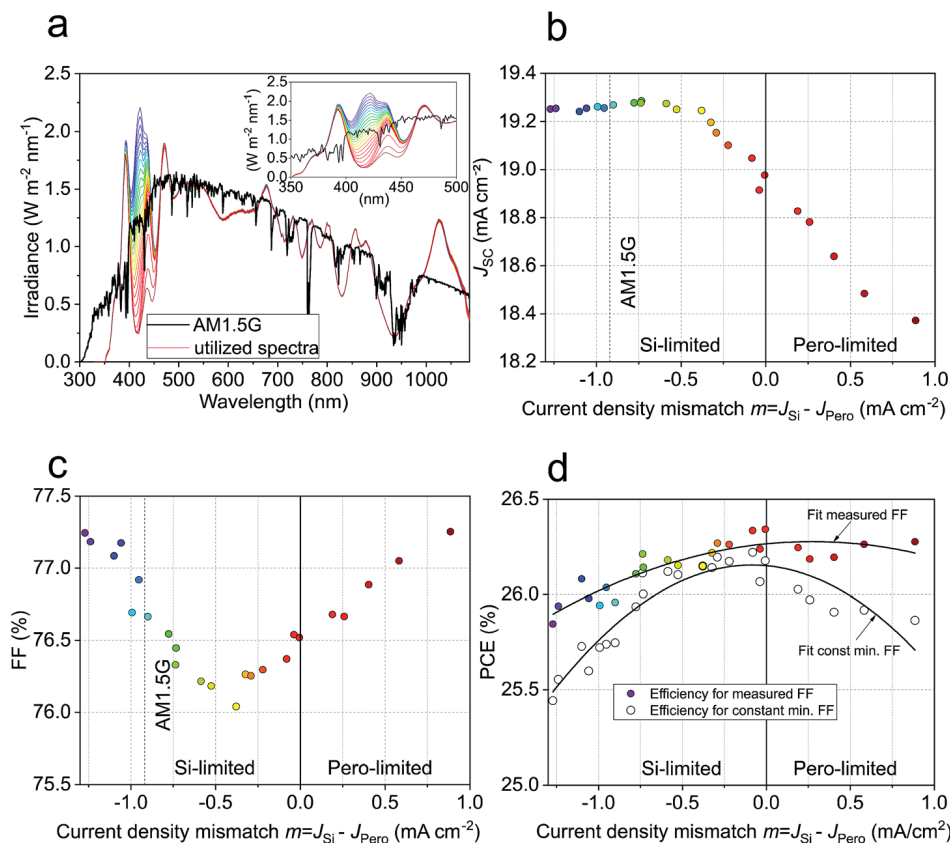
Fig. 4 (a) Utilized spectra of the LED–based sun simulator. The illumination intensities of two selected LEDs emitting in the blue part of the spectrum are adjusted in order to get a spectrum with a higher or lower intensity in the blue wavelength range, as compared to the AM1.5G. (b–d) Short circuit current density, fill factor and PCE of the tandem solar cell from Fig. 4 as a function of the mismatch in calculated photogeneration currents between the sub–cells. Additionally, the power density is shown when assuming that the FF = FF$_{min}$ and does not change with changing mismatch.

hysteresis of the tandem cell starts increasing, revealing that the hysteresis of the perovskite sub-cell is influenced by current mismatch. Interestingly, the hysteresis is decreased after the series is done. However, in the following, only the V_{OC} to J_{SC} (reverse scan) measurements will be considered. The currents of the sub-cells are calculated by integrating the sub-cell EQE multiplied by the measured spectra. From these, the mismatch $m = J_{Si} - J_{Pero}$ is calculated as the difference between J_{Si} and J_{Pero}. Fig. 4b–d show the tandem J_{SC}, FF and PCE as a function of mismatch. Due to the logarithmic dependence on J_{SC}, the V_{OC} is only marginally affected by the changing spectrum (Fig. S12†). As can be seen from the comparison of Fig. 4a and b, a stronger photogeneration in the blue wavelength range, *i.e.* a higher J_{Pero}, does not affect the tandem J_{SC}, as this metric is limited by the unchanged bottom cell current. This confirms that the silicon sub-cell is limiting for the AM1.5G illumination conditions (see Fig. 4b) and high intensities of blue light, as seen in the EQE measurement shown in Fig. 3b. Once the blue intensity is lower than in the AM1.5G spectrum, the tandem cell becomes top cell limited, where the J_{SC} is reduced in accordance to the reduced intensity (see positive current density mismatch values $m = J_{Si} - J_{Pero}$ in Fig. 4b).

Changing the spectrum and therefore changing the mismatch does not only have an effect on the current density,

but also on the FF (Fig. 4c). It is typically reported that the FF is lowest when the tandem solar cell is operated close to the current matching point,[30,33,47] but this is not necessarily exactly at the matching point and depends on the individual performance of the sub-cells.[31] Interestingly, the FF minimum occurs here when the silicon bottom cell is the limiting sub-cell. With a slope of −1.31% FF per mA cm^{-2} mismatch, a FF of 79% is expected for a mismatch of −2.8 mA cm^{-2}, which is the mismatch value of the certified tandem cell discussed above. As this mismatch-predicted FF value is close to the FF of the certified cell, it strongly supports the assumption that the reduced FF after decreasing the photocurrent mismatch is mainly due to the device physics instead of a cell-to-cell variation. The benefit of ALD optimization and enhanced resistive losses from thinner front IZO counterbalance here. Although, the FF can change with the photocurrent due to *e.g.* reduced collection losses, we can exclude this effect to be dominant in our tandem solar cell as the FF of a similar fabricated cell does not vary with J_{SC} in the relevant photocurrent range utilized for mismatch analysis.[6]

Fig. 4d shows the PCE of the tandem solar cell as a function of the current density mismatch. The intensity of each spectrum is calculated as stated in ESI note 3.† Although the J_{SC} decreases for a mismatch $m > -0.3$ mA cm^{-2}, the PCE increases due to the

increasing FF (colored data points). The quadratic fit of the PCE calculated with the measured FF reveals a maximum PCE of 26.3% close to current matching. Furthermore, the PCE is calculated assuming the measured J_{SC} and V_{OC}, but a constant FF = FF_{min} with FF_{min} being the minimum FF measured in the series (white data points). The comparison between the constant and non-constant FF highlights that the changing FF mostly compensates the drop in J_{SC}, thus leading to a broader peak around the maximum PCE. For a mismatch of $m = 1$ mA cm^{-2}, the PCE-difference between both curves is 0.49% while for $m = -1$ mA cm^{-2} the PCEs differ by 0.26%. The PCE of a slightly mismatched monolithic tandem solar cells suffers only marginally from the decreased J_{SC}. This is highly important for energy yield analysis, especially when comparing monolithic 2-terminal with 4-terminal tandem solar cells. One of the arguments in favor of 4-terminal devices is to avoid decrease in performance due to current reduction if current mismatch occurs. However, we show that in 2-terminal, monolithic devices the FF increases with mismatch (see colored data points in Fig. 4c). Thus, the drop in J_{SC} is mostly compensated, leading to a PCE which is less sensitive to current density mismatch. Assuming an ideal current redistribution with $J_{SC,matched} = 0.5 J_{Pero+Si} = 19.73$ mA cm^{-2} for both sub-cells in Fig. 3b, using the measured values for $FF_{matched}$, and $V_{OC,matched}$ extracted for $m = 0$, a PCE of 26.6% would be reached.

To validate the experimental results in Fig. 4c, we perform electrical simulations using the electronic design automation software LTspice (for more details and parameters see ESI note 4†).[48] An equivalent circuit diagram consisting of two series connected single diode models was built as shown in Fig. S14a.† In the first step, we prove that the FF minimum is not necessarily at the current matching point for any kind of monolithic tandem solar cell. For this, two identical solar cells are connected in series in this simulation. When sweeping the J_{Top} and J_{Bottom} while maintaining a constant $J_{Top+Bottom}$, the FF indeed changes as a function of current mismatch (see Fig. S14b,† upper graph) with a FF minimum for current matching conditions. The same procedure is carried out for a reduced shunt resistance R_{Sh} of either the top or the bottom cell. Now, the FF minimum is not in the current matching point anymore but shifts to the bottom cell limited side for a low $R_{Sh,Bottom}$ and to the top cell limited side for a low $R_{Sh,Top}$ (Fig. S14b†). Although the experimentally detected FF minimum is present for silicon limiting illumination conditions (Fig. 4c), we do not expect to have a lower R_{Sh} in the silicon bottom cell compared to the perovskite top cell. The difference between the simulation and experiment is discussed below. The bottom graph in Fig. S14b† shows that a mismatch between J_{Pero} and J_{Si} might be necessary for achieving the highest PCE. As stated earlier in this paper, the highest power is achieved if both sub-cells have the same J_{MPP}. The necessity of current matching depends on the shunt resistance and with that overall of the individual sub-cells (i.e. the difference between J_{SC} and J_{MPP}). If the difference between J_{SC} and J_{MPP} of both sub-cells is similar, J_{SC}-matching leads to the highest power output. If the difference between J_{SC} and J_{MPP} is unequal for both sub-cells, a J_{SC}-mismatch is needed to achieve

J_{MPP}-matching and with that, the highest power output. In a second step, we attempt to reconstruct the measured tandem J–V-characteristics using electrical simulations. For this, single junction silicon and perovskite (opaque) cells are fabricated with similar device layout as in our tandem solar cell and parametrized using a single diode model. Fig. S15a and b† show the measured J–Vs at different intensities of the single junction solar cells as well as the simulated J–Vs. We use the parameters of the fitted single junction cells to reconstruct the tandem solar cell and simulate the experiment. Solely the series resistance R_s and saturation current of the perovskite $J_{0,Pero}$ are adjusted slightly to match the tandem conditions (see ESI note 4†). The simulated J_{SC} and FF as a function of mismatch m are shown in Fig. S15c and d† and reveal a higher and shifted FF minimum but a similar variation of J_{SC}. Using the FF, V_{OC} and J_{SC} from simulated results would lead to a PCE of 27.6% for AM1.5G illumination for the tandem device presented in see Fig. 3, mostly due to higher FF in simulation. Comparing the J–Vs with most negative and most positive mismatch, the difference between the simulated and experimentally measured J–Vs appears to be just around the MPP (Fig. S15e†). For unmatched sub-cells, charge carriers accumulate at the recombination contact. This could affect the recombination behavior. Moreover, the electric fields and with this, the charge collection of the sub-cells is affected by the charge accumulation. This might also be the reason for the dependency of the hysteresis on the mismatch. Additionally, the recombination layer might behave non-ohmic, thus another electrical component needs to be implemented in the simulation. Further investigation is needed to understand the device physics in more detail, to exactly reconstruct the monolithic tandem solar cell in an electrical simulation and with this, increase the PCE. If we assume an ideal contact design in the tandem solar cell for example by implementing grid fingers, leading to a series resistance of $R_S = 0$ Ω cm^2 (for this, we additionally assume a negligible series resistance of the bulk and vanishing contact resistance), the simulated tandem device could reach a PCE of 29% (Fig. S16b†). Here the $J_{Pero+Si}$ is maintained constant at 39.46 mA cm^{-2}, the same $J_{Pero+Si}$ as for the device shown in Fig. 3. Furthermore, we simulate a monolithic tandem solar cell by using electrical parameters from record p–i–n perovskite[49] and both side contacted c-Si cells.[34,50] By neglecting the series resistance, which mostly stems from the perovskite sub-cell, the FF increases and therefore a maximum PCE of 31.0% is expected due to improved V_{OC} (Fig. S14d†).

Conclusions

In summary, we implemented a transparent n-type top contact layer stack in monolithic silicon/perovskite tandem solar cells in order to achieve a certified PCE of 25.0% at highly unmatched photocurrents. Further improvements of the rear junction silicon bottom cell with adjusted n-type nc-SiO$_x$:H layer thickness, the n-type top cell contact with proper ALD SnO$_2$ deposition temperature and IZO thickness, as well as adjusted perovskite thickness led to a remarkable tandem PCE of 26.0%. Further reducing the front IZO thickness allowed J_{SC}s over 19.7 mA cm^{-2} and

cumulative current densities $J_{Pero+Si}$ over 40 mA cm^{-2} in tandem cells with a planar front side. As the FF was found to depend on the mismatch condition $m = J_{Si} - J_{Pero}$, the sub-cell mismatch for the best tandem device was analyzed by varying the illumination spectrum. We show that the FF improves under unmatched current conditions of the tandem solar cell and that the loss in tandem PCE due to lower J_{SC} at unmatched conditions is less pronounced than it would be with a constant FF. This dependence is highly important for energy yield analysis, especially when comparing 2-terminal and 4-terminal tandem solar cells. Electrical simulations based on input parameters from reference single junction devices parametrized with a single diode model confirmed the increasing FF for unmatched monolithic tandem solar cells. The simulation of the tandem performance shows that the FF in our experimentally realized device is lower than the FF expected from simulations, leaving room for improvement. An ideal series resistance can lead to a PCE of 29% for our tandem architecture. The simulation of a monolithic tandem solar cell with record perovskite and silicon cells from literature and a negligible series resistance reveals a PCE of 31%. Therefore, our work provides a detailed device understanding under different current matching conditions. This is mandatory to improve the PCE potential of silicon/perovskite tandem solar cells to predicted values above 30%.

Materials and methods

Perovskite materials

Anhydrous DMSO (dimethyl sulfoxide), DMF (dimethylformamide), and toluene were purchased from Sigma Aldrich. PTAA (poly [bis(4-phenyl)(2,5,6-trimentlyphenyl)amine]), C_{60} (purity = 99.9%) and lithium fluoride (purity $\geq$ 99.99%) were purchased from Sigma Aldrich. FAI (formamidinium iodide) and MABr (methylammonium bromide) were purchased from Dyenamo. PbI_2 and $PbBr_2$ were bought from TCI. CsI was purchased from abcr GmbH. The ceramic 2 inch IZO target was purchased from FHR Anlagenbau GmbH.

Perovskite solar cell preparation on silicon bottom cell

The fabricated perovskite sub-cell has an inverted (p–i–n) planar structure and a layer configuration of Si bottom cell (incl. ITO)/ PTAA/perovskite/C_{60}/SnO$_2$/IZO, where IZO is zinc doped indium oxide. The silicon substrates were blown with nitrogen before use. All the spin-coating layer deposition steps were conducted in a nitrogen atmosphere. The hole transport material PTAA (2mg ml^{-1} in toluene) was deposited using spin-coating (4000 rpm for 30 s) and annealed for 10 min at 100 °C, leading to a 10 nm to 15 nm thick layer. The perovskite was prepared following the typical triple cation process.[38,51] In short, 1.5 M nominal PbI$_2$ and PbBr$_2$ in DMF : DMSO = 4 : 1 volume were first prepared as stock solutions and then added to FAI and MABr with 10% PbX$_2$ excess, respectively (X = I or Br). The so obtained FAPbI$_3$ and MAPbBr$_3$ were then mixed in 5 : 1 volume ratio to obtain the "double cation" perovskite. Finally, 5% volume of 1.5 M nominal CsI in DMSO was added to form the "triple cation" perovskite. 120 μl of perovskite solution was then spread on the substrate and spun using one step spin-coating process (4000 rpm or 5000 rpm for 35 s). 25 s after the start of a spinning, 500 μl ethyl acetate anti-solvent drop was utilized. The films were annealed at 100 °C for 1 h. The perovskite thickness is around 580 nm and 460 nm for 4000 rpm and 5000 rpm. Afterwards, 15 nm C_{60} was thermally evaporated at a rate of 0.15 Å s^{-1} at 400 °C. 20 nm SnO$_2$ were prepared by thermal ALD in an Arradiance GEMStar reactor. Tetrakis(dimethylamino)tin(IV) (TDMASn) was used as the Sn precursor and was held at 60 °C in a stainless steel container. Water was used as oxidant, and was delivered from a stainless steel container without intentional heating, whereas the precursor delivery manifold was heated to 115 °C. For the deposition at 100 °C, the TDMASn/purge1/H$_2$O/purge2 times are 1 s/7.5 s/0.2 s/10 s with corresponding nitrogen flows of 30 sccm/90 sccm/90 sccm/90 sccm. With this, 167 cycles leads to 20 nm tin oxide. For the deposition at the lower temperature of 80 °C, the purging times were slightly increased (i.e. times of 1 s/10 s/0.2 s/15 s) to account for less efficient purging of reactants and their reaction products at lower temperatures. 140 cycles were needed to deposit 20 nm at 80 °C. IZO was sputtered in a Roth&Rau MicroSys 200 PVD. The 2 inch ceramic target consisted of 90%$_{wt}$. In$_2$O$_3$ and 10%$_{wt}$. ZnO. At a RF-power of 70 W, the cells oscillated under the target to have a uniform deposition. To add additional oxygen to the deposition chamber, a mix of Ar and O$_2$ is added. The added amount of oxygen ranges from 0.0%$_{vol}$ to 0.25%$_{vol}$ while the total gas flow is the same for all depositions. A 150 nm thick Ag metal frame was evaporated through a shadow mask as a top contact. Finally, 100 nm LiF was evaporated to serve as an anti-reflective coating.

Silicon solar cell preparation

The silicon heterojunction (SHJ)-bottom cell was fabricated on a 260 μm thick polished FZ ⟨100⟩ n-type crystalline silicon (c-Si) wafer in a rear junction configuration. The front surface of the wafer was left polished in order to facilitate the perovskite top cell deposition, while the rear surface of the wafer was wet-chemically textured to obtain random pyramid with ⟨111⟩ facets in order to improve the optical response of the bottom cell in the NIR region. After a final RCA clean and a 3 minute HF dip (1% dilution in water) to strip the SiO$_2$ of the surface, a 5 nm thick, intrinsic (i) amorphous silicon (a-Si:H) layer was grown on both sides of the c-Si wafer in order to passivate the c-Si surface. On the textured back-side, a 5 nm thick, p-doped a-Si:H was deposited on the rear passivating layer to form the junction of the SHJ cell. On the polished front-side, a 20 nm thick, n-doped nanocrystalline silicon oxide layer (nc-SiO$_x$:H) with a refractive index, n, of 2.7 at 633 nm was used as a front surface field (FSF) of the SHJ bottom cell and intermediate layer between the top and the bottom cells. For the second optimization, this thickness was increased to 95 nm. All the a- and nc-Si layers were deposited with an Applied Materials (AKT1600) plasma enhanced chemical vapor deposition (PECVD) tool. In order to contact the bottom cell a ZnO:Al/Ag layer stack was deposited on the textured back-side and a 20 nm thick ITO layer was deposited on the polished front-side on top of the nc-SiO$_x$:H

interlayer, both depositions were DC-sputtered in an in-line sputtering tool from Leybold Optics. The contact layers of the silicon were deposited using shadow masks with an opening of 1×1 cm^2.

Silicon single junction solar cell preparation

To fabricate a silicon single junction, 80 nm IZO is additionally deposited on the 20 nm ITO of the bottom cell in order to reduce the sheet resistance. As for the tandem solar cell, a metal frame is evaporated as a top contact.

Semitransparent perovskite single junction solar cell preparation

The semitransparent solar cells are manufactured as described in the section of the perovskite solar cell preparation on silicon bottom cells. Instead of the silicon bottom cell, an ITO coated glass substrate (25×25 mm, 15 Ω sq^{-1}, patterned by Automatic Research GmbH) was used and cleaned sequentially for 15 min with Acetone, Mucasol ($2\%_{vol}$ in water), DI-water and isopropanol in an ultrasonic bath. Before the deposition of the HTM, the samples were treated in an UV-ozone cleaner for 15 min.

Tin oxide layers for optical characterization

For optical characterization, tin oxide was deposited on a silicon wafer coated with 450 nm silicon oxide. For the deposition temperature of 80 °C, the parameters are mentioned in the section "perovskite solar cell fabrication". For all other temperatures, the pulse- and purge times and nitrogen flows are equal to the deposition of tin oxide at 100 °C.

Device characterization

The current density–voltage (J–V) measurements were performed under standard test conditions (25 °C, LED based sun simulator from Wavelabs, class AAA), adjusted with a non-filtered calibrated silicon reference cell (Fraunhofer ISE). The scan rate was 0.25 V s^{-1} with a voltage increment of 20 mV. The external quantum efficiency (EQE) was measured as a function of wavelength from 300 nm to 1200 nm with a step of 10 nm using a home built small spot EQE system. The beam size is 2×5 mm^2, thus smaller than the active area. When measuring perovskite top cell, infrared (850 nm) bias light was applied along with 0.6 V bias voltage to ensure a measurement in short circuit conditions. Additionally, the cell is slightly illuminated with blue (455 nm) light that partially increases the signal to noise ratio. When measuring silicon bottom cell, blue (455 nm) bias light was applied. The EQE of the silicon bottom cell is not affected by bias voltage, as the shunt resistance of the silicon cell is very high. Reflection was measured as a function of wavelength from 300 nm to 1200 nm with a step of 5 nm using an integrating sphere with a PerkinElmer Lambda – 1050 UV/VIS/NIR spectrophotometer, calibrated with a white Spectralon. The optical properties of ALD SnO$_2$ were evaluated by spectroscopic ellipsometry. Measurements were performed using a Sentech SE 850 at angles of incidence 50°, 60° and 70°.

The dielectric function was modeled using Tauc–Lorentz oscillators to account for the absorption for energies above the band gap.

Author contributions

Conflicts of interest

There are no conflicts to declare.

Acknowledgements

References

1 M. A. Green, Y. Hishikawa, E. D. Dunlop, D. H. Levi, J. Hohl-Ebinger and A. W. Y. Ho-Baillie, *Prog. Photovoltaics*, 2018, **26**, 427–436.

2 K. Yoshikawa, H. Kawasaki, W. Yoshida, T. Irie, K. Konishi, K. Nakano, T. Uto, D. Adachi, M. Kanematsu, H. Uzu and K. Yamamoto, *Nat. Energy*, 2017, **2**, 17032.

3 A. Richter, M. Hermle and S. W. Glunz, *IEEE J. Photovolt.*, 2013, **3**, 1184–1191.

4 F. Sahli, J. Werner, B. A. Kamino, M. Bräuninger, R. Monnard, B. Paviet-Salomon, L. Barraud, L. Ding, J. J. Diaz Leon, D. Sacchetto, G. Cattaneo, M. Despeisse, M. Boccard, S. Nicolay, Q. Jeangros, B. Niesen and C. Ballif, *Nat. Mater.*, 2018, **17**, 820–826.

5 B. Chen, Z. Yu, K. Liu, X. Zheng, Y. Liu, J. Shi, D. Spronk, P. N. Rudd, Z. Holman and J. Huang, *Joule*, 2018, 1–14.

109

6 M. Jošt, E. Köhnen, A. B. Morales-Vilches, B. Lipovšek, K. Jäger, B. Macco, A. Al-Ashouri, J. Krč, L. Korte, B. Rech, R. Schlatmann, M. Topič, B. Stannowski and S. Albrecht, *Energy Environ. Sci.*, 2018, **11**, 3511–3523.

7 K. A. Bush, S. Manzoor, K. Frohna, Z. J. Yu, J. A. Raiford, A. F. Palmstrom, H.-P. Wang, R. Prasanna, S. F. Bent, Z. C. Holman and M. D. McGehee, *ACS Energy Lett.*, 2018, **3**, 2173–2180.

8 D. Zhao, Y. Yu, C. Wang, W. Liao, N. Shrestha, C. R. Grice, A. J. Cimaroli, L. Guan, R. J. Ellingson, K. Zhu, X. Zhao, R.-G. Xiong and Y. Yan, *Nat. Energy*, 2017, **2**, 17018.

9 T. Leijtens, R. Prasanna, K. A. Bush, G. E. Eperon, J. A. Raiford, A. Gold-Parker, E. J. Wolf, S. A. Swifter, C. C. Boyd, H.-P. Wang, M. F. Toney, S. F. Bent and M. D. McGehee, *Sustainable Energy Fuels*, 2018, **2**, 2450–2459.

10 T. Todorov, T. Gershon, O. Gunawan, Y. S. Lee, C. Sturdevant, L. Y. Chang and S. Guha, *Adv. Energy Mater.*, 2015, **5**, 1–6.

11 Q. Han, Y.-T. Hsieh, L. Meng, J.-L. Wu, P. Sun, E.-P. Yao, S.-Y. Chang, S.-H. Bae, T. Kato, V. Bermudez and Y. Yang, *Science*, 2018, **361**, 904–908.

12 M. Jošt, T. Bertram, D. Koushik, J. A. Marquez, M. A. Verheijen, M. D. Heinemann, E. Köhnen, A. Al-Ashouri, S. Braunger, F. Lang, B. Rech, T. Unold, M. Creatore, I. Lauermann, C. A. Kaufmann, R. Schlatmann and S. Albrecht, *ACS Energy Lett.*, 2019, 583–590.

13 OxfordPV, Oxford PV perovskite solar cell achieves 28% efficiency, https://www.oxfordpv.com/news/oxford-pv-perovskite-solar-cell-achieves-28-efficiency, accessed 5 February 2019.

14 K. Jäger, L. Korte, B. Rech and S. Albrecht, *Opt. Express*, 2017, **25**, A473.

15 L. Mazzarella, M. Werth, K. Jäger, M. Jošt, L. Korte, S. Albrecht, R. Schlatmann and B. Stannowski, *Opt. Express*, 2018, **26**, A487.

16 M. H. Futscher and B. Ehrler, *ACS Energy Lett.*, 2016, **1**, 863–868.

17 T. Leijtens, K. A. Bush, R. Prasanna and M. D. McGehee, *Nat. Energy*, 2018, **3**, 828–838.

18 M. T. Hörantner and H. J. Snaith, *Energy Environ. Sci.*, 2017, **10**, 1983–1993.

19 B. Chen, X. Zheng, Y. Bai, N. P. Padture and J. Huang, *Adv. Energy Mater.*, 2017, **7**, 1602400.

20 J. Werner, F. Sahli, F. Fu, J. J. Diaz Leon, A. Walter, B. A. Kamino, B. Niesen, S. Nicolay, Q. Jeangros and C. Ballif, *ACS Energy Lett.*, 2018, **3**, 2052–2058.

21 J. H. Heo, S. H. Im, J. H. Noh, T. N. Mandal, C.-S. Lim, J. A. Chang, Y. H. Lee, H. Kim, A. Sarkar, M. K. Nazeeruddin, M. Grätzel and S. Il Seok, *Nat. Photonics*, 2013, **7**, 486–491.

22 W. S. Yang, B.-W. Park, E. H. Jung, N. J. Jeon, Y. C. Kim, D. U. Lee, S. S. Shin, J. Seo, E. K. Kim, J. H. Noh and S. Il Seok, *Science*, 2017, **356**, 1376–1379.

23 W. S. Yang, J. H. Noh, N. J. Jeon, Y. C. Kim, S. Ryu, J. Seo and S. I. Seok, *Science*, 2015, **348**, 1234–1237.

24 Q. Jiang, Z. Chu, P. Wang, X. Yang, H. Liu, Y. Wang, Z. Yin, J. Wu, X. Zhang and J. You, *Adv. Mater.*, 2017, **1703852**, 1–7.

25 H. Shen, S. T. Omelchenko, D. A. Jacobs, S. Yalamanchili, Y. Wan, D. Yan, P. Phang, T. Duong, Y. Wu, Y. Yin, C. Samundsett, J. Peng, N. Wu, T. P. White, G. G. Andersson, N. S. Lewis and K. R. Catchpole, *Sci. Adv.*, 2018, **4**, eaau9711.

26 Y. Wu, D. Yan, J. Peng, T. Duong, Y. Wan, S. P. Phang, H. Shen, N. Wu, C. Barugkin, X. Fu, S. Surve, D. Grant, D. Walter, T. P. White, K. R. Catchpole and K. J. Weber, *Energy Environ. Sci.*, 2017, **10**, 2472–2479.

27 S. Altazin, L. Stepanova, J. Werner, B. Niesen, C. Ballif and B. Ruhstaller, *Opt. Express*, 2018, **26**, A579.

28 K. A. Bush, A. F. Palmstrom, Z. J. Yu, M. Boccard, R. Cheacharoen, J. P. Mailoa, D. P. McMeekin, R. L. Z. Hoye, C. D. Bailie, T. Leijtens, I. M. Peters, M. C. Minichetti, N. Rolston, R. Prasanna, S. Sofia, D. Harwood, W. Ma, F. Moghadam, H. J. Snaith, T. Buonassisi, Z. C. Holman, S. F. Bent and M. D. McGehee, *Nat. Energy*, 2017, **2**, 1–7.

29 L. Mazzarella, Y.-H. Lin, S. Kirner, A. B. Morales-Vilches, L. Korte, S. Albrecht, E. Crossland, B. Stannowski, C. Case, H. J. Snaith and R. Schlatmann, *Adv. Energy Mater.*, 2019, **1803241**, 1803241.

30 W. E. McMahon, K. E. Emery, D. J. Friedman, L. Ottoson, M. S. Young, J. S. Ward, C. M. Kramer, A. Duda and S. Kurtz, *Prog. Photovoltaics*, 2008, **16**, 213–224.

31 M. Bonnet-Eymard, M. Boccard, G. Bugnon, F. Sculati-Meillaud, M. Despeisse and C. Ballif, *Sol. Energy Mater. Sol. Cells*, 2013, **117**, 120–125.

32 M. Zeman, J. A. Willemen, L. L. A. Vosteen, G. Tao and J. W. Metselaar, *Sol. Energy Mater. Sol. Cells*, 1997, **46**, 81–99.

33 C. Ulbrich, C. Zahren, A. Gerber, B. Blank, T. Merdzhanova, A. Gordijn and U. Rau, *Int. J. Photoenergy*, 2013, **2013**, 1–7.

34 A. Richter, J. Benick, F. Feldmann, A. Fell, M. Hermle and S. W. Glunz, *Sol. Energy Mater. Sol. Cells*, 2017, **173**, 96–105.

35 A. Magomedov, A. Al-Ashouri, E. Kasparavičius, S. Strazdaite, G. Niaura, M. Jošt, T. Malinauskas, S. Albrecht and V. Getautis, *Adv. Energy Mater.*, 2018, **8**, 1801892.

36 M. Stolterfoht, C. M. Wolff, Y. Amir, A. Paulke, L. Perdigón-Toro, P. Caprioglio and D. Neher, *Energy Environ. Sci.*, 2017, **10**, 1530–1539.

37 M. Stolterfoht, C. M. Wolff, J. A. Márquez, S. Zhang, C. J. Hages, D. Rothhardt, S. Albrecht, P. L. Burn, P. Meredith, T. Unold and D. Neher, *Nat. Energy*, 2018, **3**, 847–854.

38 M. Saliba, J.-P. Correa-Baena, C. M. Wolff, M. Stolterfoht, N. Phung, S. Albrecht, D. Neher and A. Abate, *Chem. Mater.*, 2018, **30**, 4193–4201.

39 K. O. Brinkmann, J. Zhao, N. Pourdavoud, T. Becker, T. Hu, S. Olthof, K. Meerholz, L. Hoffmann, T. Gahlmann, R. Heiderhoff, M. F. Oszajca, N. A. Luechinger, D. Rogalla, Y. Chen, B. Cheng and T. Riedl, *Nat. Commun.*, 2017, **8**, 1–9.

40 L. Hoffmann, D. Theirich, D. Schlamm, T. Hasselmann, S. Pack, K. O. Brinkmann, D. Rogalla, S. Peters, A. Räupke, H. Gargouri and T. Riedl, *J. Vac. Sci. Technol., A*, 2018, **36**, 01A112.

110

41 J. Gilot, M. M. Wienk and R. A. J. Janssen, *Adv. Mater.*, 2010, **22**, E67–E71.

42 J. Gilot, M. M. Wienk and R. A. J. Janssen, *Adv. Funct. Mater.*, 2010, **20**, 3904–3911.

43 R. Santbergen, T. Meguro, T. Suezaki, G. Koizumi, K. Yamamoto and M. Zeman, *IEEE J. Photovolt.*, 2017, **7**, 919–926.

44 A. Dualeh, P. Gao, S. Il Seok, M. K. Nazeeruddin and M. Grätzel, *Chem. Mater.*, 2014, **26**, 6160–6164.

45 B. Conings, J. Drijkoningen, N. Gauquelin, A. Babayigit, J. D'Haen, L. D'Olieslaeger, A. Ethirajan, J. Verbeeck, J. Manca, E. Mosconi, F. De Angelis and H.-G. Boyen, *Adv. Energy Mater.*, 2015, **5**, 1500477.

46 T. Fellmeth, F. Clement and D. Biro, *IEEE J. Photovolt.*, 2014, **4**, 504–513.

47 S. Reynolds and V. Smirnov, *Energy Procedia*, 2015, **84**, 251–260.

48 Linear Technology, LTspice, https://www.analog.com/en/design-center/design-tools-and-calculators/ltspice-simulator.html.

49 D. Luo, W. Yang, Z. Wang, A. Sadhanala, Q. Hu, R. Su, R. Shivanna, G. F. Trindade, J. F. Watts, Z. Xu, T. Liu, K. Chen, F. Ye, P. Wu, L. Zhao, J. Wu, Y. Tu, Y. Zhang, X. Yang, W. Zhang, R. H. Friend, Q. Gong, H. J. Snaith and R. Zhu, *Science*, 2018, **360**, 1442–1446.

50 M. A. Green, Y. Hishikawa, E. D. Dunlop, D. H. Levi, J. Hohl-Ebinger and A. W. Y. Ho-Baillie, *Prog. Photovoltaics*, 2018, **26**, 3–12.

51 M. Saliba, T. Matsui, J.-Y. Seo, K. Domanski, J.-P. Correa-Baena, M. K. Nazeeruddin, S. M. Zakeeruddin, W. Tress, A. Abate, A. Hagfeldt and M. Grätzel, *Energy Environ. Sci.*, 2016, **9**, 1989–1997.

111

Electronic Supplementary Information

Highly Efficient Monolithic Perovskite Silicon Tandem Solar Cells: Analyzing the Influence of Current Mismatch on Device Performance

Eike Köhnen[a], Marko Jošt[a], Anna Belen Morales-Vilches[b], Philipp Tockhorn[a], Amran Al-Ashouri[a], Bart Macco[cd], Lukas Kegelmann[a], Lars Korte[d], Bernd Rech[d], Rutger Schlatmann[b], Bernd Stannowski[b] and Steve Albrecht[ae]

[a.] Helmholtz-Zentrum Berlin für Materialien und Energie GmbH, Young investigator group Perovskite Silicon Tandem Solar Cells, 12489 Berlin, Germany
[b.] Helmholtz-Zentrum Berlin für Materialien und Energie, PVcomB, 12489 Berlin, Germany
[c.] Department of Applied Physics, Eindhoven University of Technology, P.O. Box 513, 5600 MB Eindhoven, The Netherlands.
[d.] Helmholtz-Zentrum Berlin für Materialien und Energie GmbH, Institute for Silicon Photovoltaics, 12489 Berlin, Germany
[e.] Technical University Berlin, Faculty IV– Electrical Engineering and Computer Science, 10587 Berlin, Germany

1. Measured optical and electrical properties of IZO

Supplementary note 1

As a front contact, IZO was recently used in perovskite/silicon tandem solar cells.[1,2] In comparison to ITO, it already has superior optoelectrical properties when being deposited at room temperature and does not need to be annealed above 200 °C,[3,4] which would harm both the perovskite and SHJ solar cells. Besides the deposition temperature, IZO layer properties can be tuned by adding oxygen gas during the process. This leads to a reduction of oxygen vacancies, affecting conductivity and transparency as depicted in Figure S1. By adding oxygen, the vacancies, which contribute two electrons per defect,[5,6] are occupied. The lower carrier density leads to a reduction of the free carrier absorption especially in the NIR, but also to narrowing of the optical band gap due to the Burstein-Moss effect. Additionally, the mobility increases up to $46 \, cm^2 \, V^{-1} \, s^{-1}$, when adding up to $0.25 \, \%_{vol}$ oxygen. As the resistivity, the inverse product of mobility and carrier density, is rather constant in this range, the optical properties are the decisive factor. The current density loss due to the absorption of IZO is calculated and displayed in the legend of Figure S1. As a minimum loss of $1.18 \, mA \, cm^{-2}$ is achieved for $0.20 \, \%_{abs}$ (grey line in Figure S1b) oxygen and 100 nm, we decided this to be an optimum for our design.

a)

b)
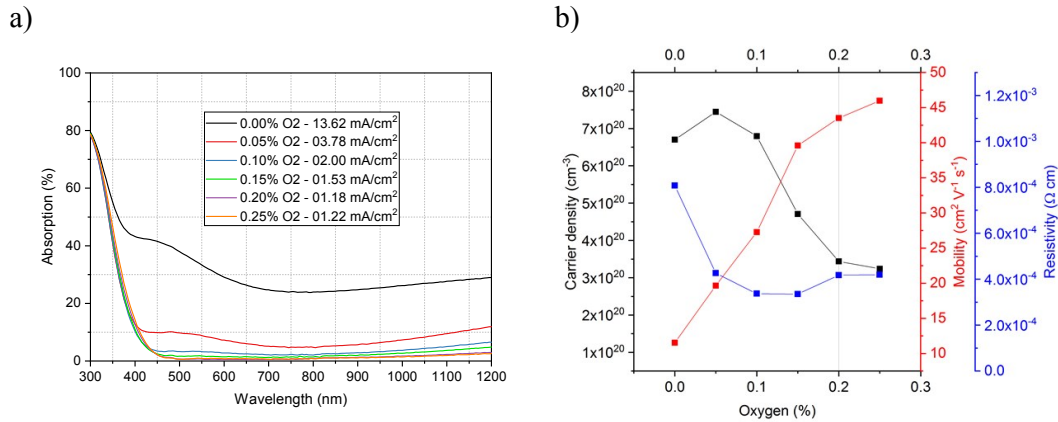
Figure S1: a) Absorption spectra of IZO films deposited on glass at room temperature with nominal thickness of 100 nm and different amounts of oxygen gas added into the sputter chamber. b) Carrier density, mobility and resistivity extracted from Hall-measurements for the IZO films shown in a). For the tandem solar cell, $0.2 \, \%_{vol}$ oxygen (grey line) is added to the sputter chamber.

2. Schematic design of the tandem solar cell
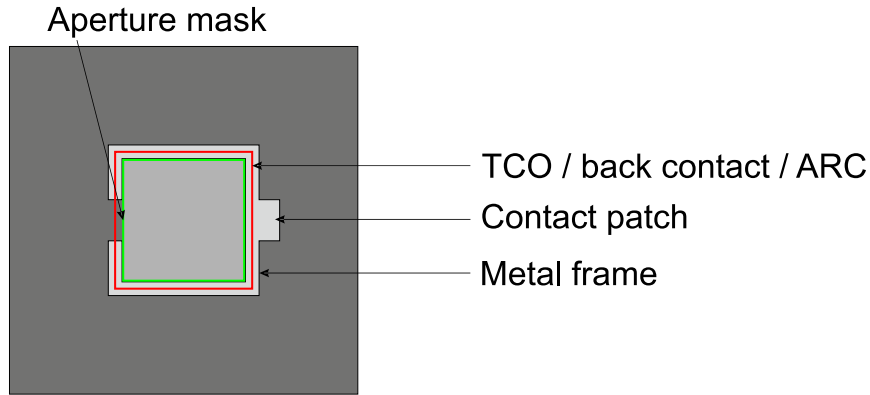
Figure S2: Schematic design of a tandem solar cell on a 25.0 x 25.0 cm^2 silicon substrate used in this study. The back contact, TCO between the sub-cells, front TCO and antireflective coating is deposited partially with an area of 1 x 1 cm^2 as indicated by the red square. To extract the carriers, the front metal frame needs to be in contact with the TCO and therefore it needs to be partially inside of the TCO-square. The inner square of the metal frame is 0.9 x 0.9 cm^2. The aperture mask (green square), used for measuring the JVs, reduced the size of illuminated area to 0.7709 cm^2

3. Further certification results including MPP track

		Vorwärtsrichtung / forwards scan direction			Rückwärtsrichtung / reverse scan direction			MPP-Tracking / MPP-Tracking			
V_{oc}	=	(1780.8 ±	11.9) mV		(1777.9 ±	11.9) mV					
I_{SC} (Ed.2 - 2008)	=	(13.73 ±	0.26) mA		(13.73 ±	0.26) mA					
I_{MPP}	=	12.92	mA		12.91	mA		(12.89 ±	0.33) mA		
V_{MPP}	=	1488.2	mV		1481.9	mV		(1494.0 ±	25.2) mV		
P_{MPP}	=	19.24	mW		19.14	mW		(19.25 ±	0.51) mW		
FF	=	78.64	%		78.36	%					
η	=	24.95	%		24.82	%		(24.97 ±	0.73) %		

Figure S3 MPP track of a monolithic perovskite/silicon tandem solar cell, measured and certified by Fraunhofer ISE. With an area of 0.7709 cm^2, the stabilized efficiency is 24.97 % (average value of the last 300 s), as can be seen in the table below. Additionally it has to be highlighted that the forward and reverse scan direction show very similar performances indicating virtually hysteresis-free characteristics.

4. Optical simulation of the stack used for certified tandem cell
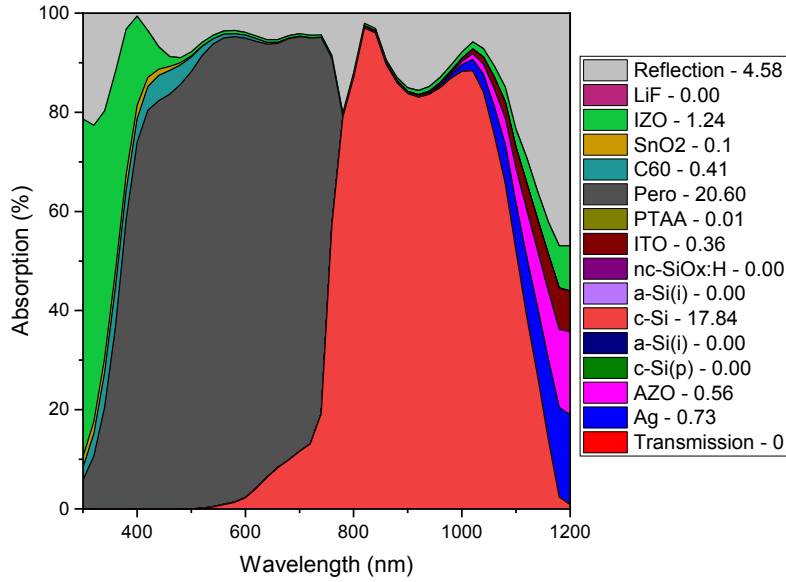
Figure S4: Simulated absorption and reflection spectra of the monolithic perovskite/silicon tandem solar cell from Figure 2 in the main text. The legend includes the current density (mA cm^{-2}), which is generated in the perovskite and silicon sub cell or lost due to reflection and parasitic absorption in each layer assuming AM1.5G incident illumination. The simulation is done with GenPro4[7] with n/k data sets as reported previously[8] and thicknesses determined via SEM, profilometry or spectroscopic ellipsometry.

5. Optical simulation for different ALD deposition temperatures of SnO$_2$

a)

b)
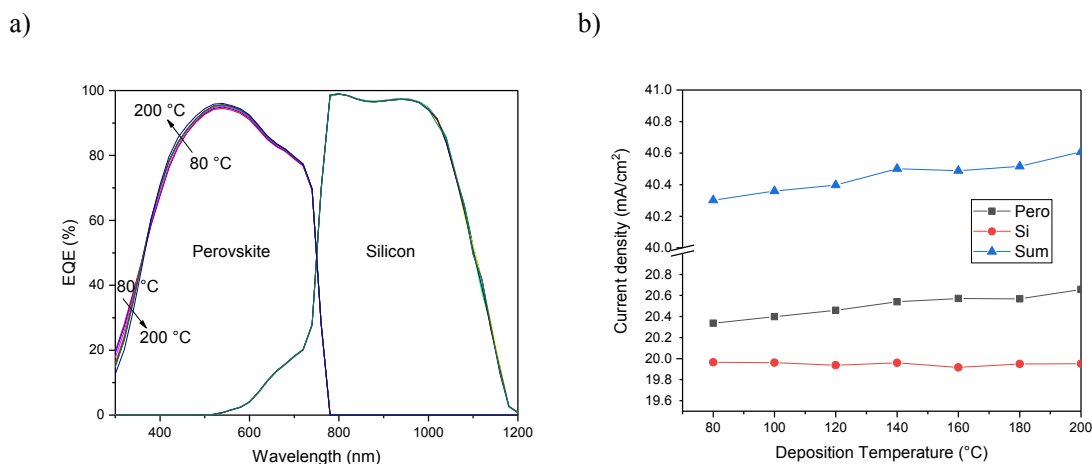
Figure S5: Simulation of a monolithic perovskite/silicon tandem solar cell with GenPro4.[7] The optical parameters of SnO$_2$, deposited at temperatures at 80 °C to 200 °C were changed, whereas all other optical parameters and thicknesses are constant. A lower deposition temperature leads to a higher EQE in the UV-range but simultaneously lowers the EQE above 370 nm (a). In the practical relevant range from 80 °C to 120 °C the sum increases just by 0.1 mA cm^{-2} (b). Sharing this to the sub-cells, this would lead to a current density increase of just 0.05 mA cm^{-2}.

6. Measured influence of the ALD temperature of SnO_2 for semitransparent perovskite top cells

a)

b)
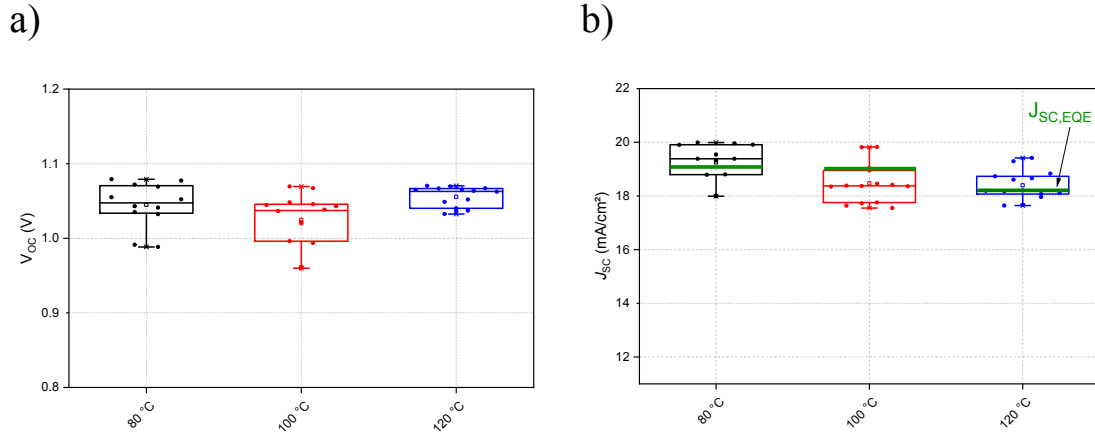
Figure S6: V_{OC} (a) and J_{SC} (b) of semitransparent p-i-n perovskite solar cells with SnO_2 deposited at temperatures ranging from 80 °C to 120 °C. The cell architecture is equal to the top cell of a tandem cell without the anti-reflection coating. The cells are illuminated through the IZO layer. The green bars in b) indicate the J_{SC} calculated from the measured EQE for AM1.5G illumination.

7. Optical simulation for different front IZO thicknesses

a)
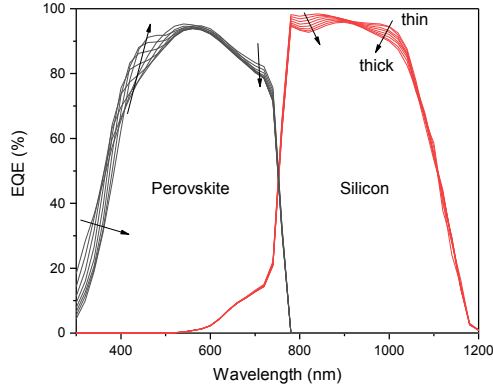
b)
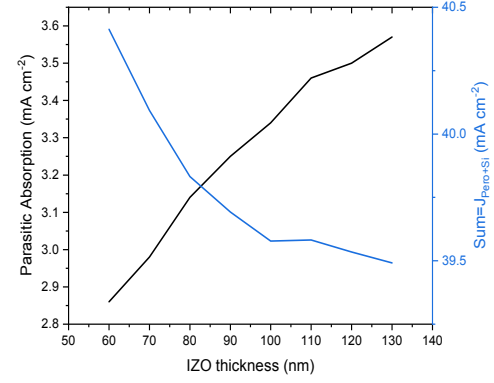
Figure S7: Simulation of a perovskite/silicon tandem solar cell with varying thickness of the IZO layer. a) Simulated absorption of the light in the perovskite and the silicon sub cells varying the IZO thicknesses from 60 nm to 130 nm. The arrows show the trend from thin to thick IZO. b) Calculated parasitic absorption and cumulative currents $J_{\text{Pero+Si}}$ of the sub cells. Reducing the thickness leads to a reduced parasitic absorption and therefore a higher $J_{\text{Pero+Si}}$.

8. Optical simulation for different perovskite thicknesses

a)
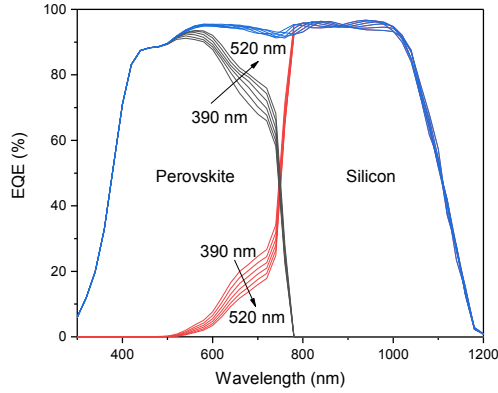
b)
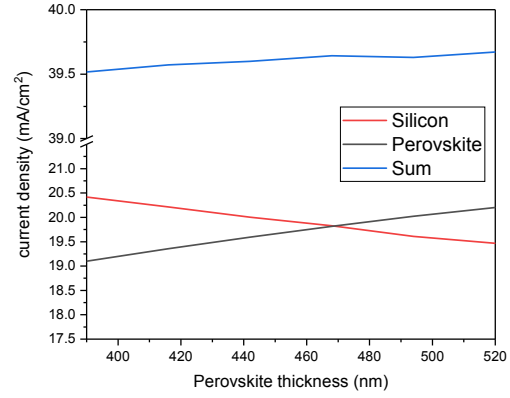
Figure S8: Simulation of a tandem solar cell with varying perovskite thickness. With changing the thickness (between 390 nm and 520 nm), the generated currents in the sub cells can be adjusted. a) Simulated absorption in the perovskite (black) and silicon (red) sub cells. Also the sum (blue) of the sub cells is shown, which hardly changes with the perovskite thickness. b) Calculated photogenerated current density in the sub-cells using the AM1.5G illumination. As the lowest current density approximately determines the J_{SC} in the total tandem cell, a maximum J_{SC} is expected for a perovskite thickness of around 470 nm.

9. EQE spectra of the individual single junction solar cells
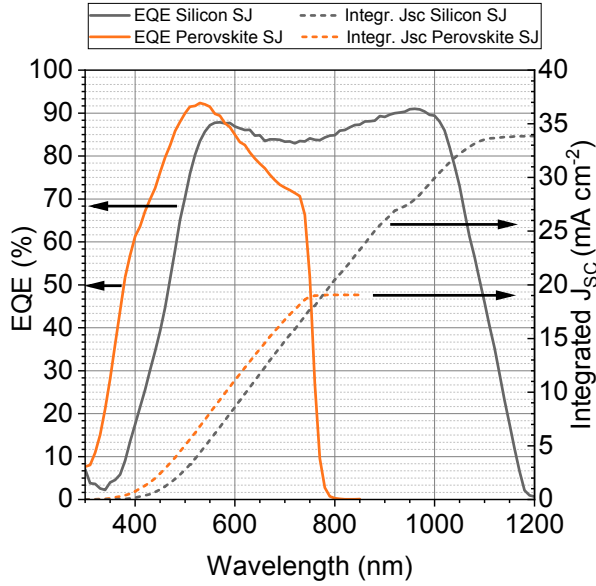
Figure 9: EQE spectra of single junction perovskite and silicon solar cells including integrated Jsc for AM1.5G illumination. The perovskite solar cell is a semitransparent cell with IZO as top layer, i.e. no antireflective coating is utilized. The EQE is measured through the IZO-side in substrate configuration as it is done in the tandem solar cell. A similar but opaque perovskite single junction solar cell is already published by Magomedov *et al.*[9]. The herein utilized silicon single junction solar cell is similar to the bottom cell used in our tandem stack. Only the nc-SiOx:H is 80 nm instead of 95 nm thick, which does not have a major impact on the overall performance. A similar silicon single junction solar cell was published by Mazzarella *et al.*[10]. Note, that for both, the perovskite and silicon cell, neither an antireflective coating is used nor the optical properties reflect that of the tandem integrated sub-cells as different absorption and interference features occur.

10.   Stability analysis of the tandem solar cell
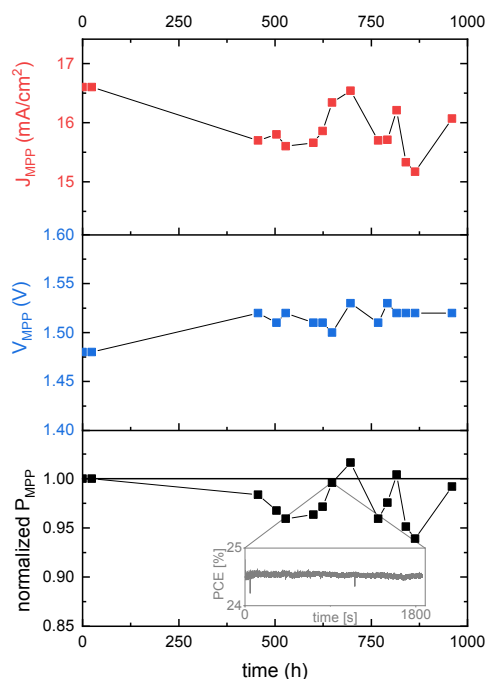
Figure S10: Stability study of an encapsulated monolithic tandem solar cell at 25 °C, ambient humidity and AM1.5G illumination. The initial values are V_{MPP} = 1.48 V, J_{MPP} = 16.6 mA cm^{-2}, PCE = 24.6 %. The PCE or power density follows the fluctuation of J_{MPP}, which is most likely a result of a fluctuating intensity. Nevertheless, the PCE did not drop below 93 % of its initial value after 1000 h. The inset shows the MPP tracking on day 27 after encapsulation. More details can be found below in Supplementary note 2.

Supplementary note 2

For stability measurements, we encapsulated a tandem solar cell, which was fabricated 23 days before and measured several times in ambient conditions. Before encapsulation, the stabilized efficiency was 26 % with V_{MPP} = 1.45 V and J_{MPP} = 17.88 mA cm^{-2}. It is encapsulated between two glasses and edge-sealed with an UV curable glue. Two copper stripes are used to connect the front and rear contact, respectively. Between the 30 minutes MPP tracks measured under standard test conditions, the sample was stored in ambient conditions. Summing up all measurements, the cell was measured for about 9.4 h. While the individual MPP tracks are stable (shown as an inset), the power has some variation unfortunately. This stems most likely from a fluctuating intensity of the sun simulator on different days (despite being calibrated) leading to fluctuating J_{MPP}. When taking the lowest measured value, the power density did not drop below 93 % after 1000 h. The last measured value is above 99 % of the initial performance.

11.   Experimental tandem results for reduced front IZO thickness

a)

b)
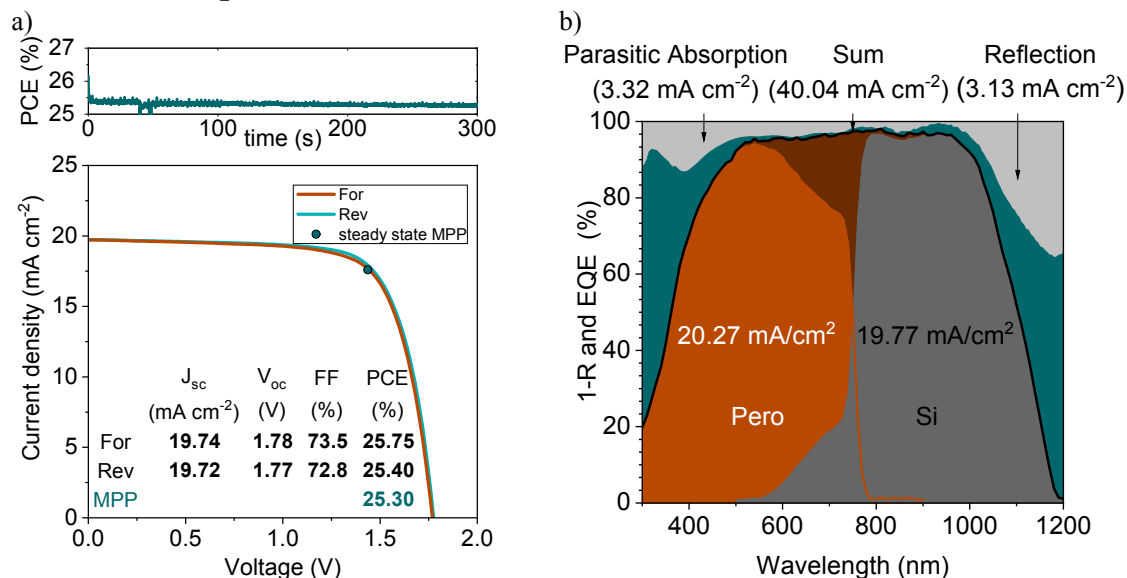
Figure S11: a) JV curve of an optimized monolithic perovskite/silicon tandem solar cell. This cell has the highest J_{SC}, measured within this work. b) EQE measurement of an optimized tandem solar cell gives a very high current density $J_{SC,EQE}$ of 19.77 mA cm^{-2}. This is comparable to the best tandem solar cell on textured silicon.[1] The sum already exceeds 40 mA cm^{-2}.

12. Measured tandem performance as function of current mismatch
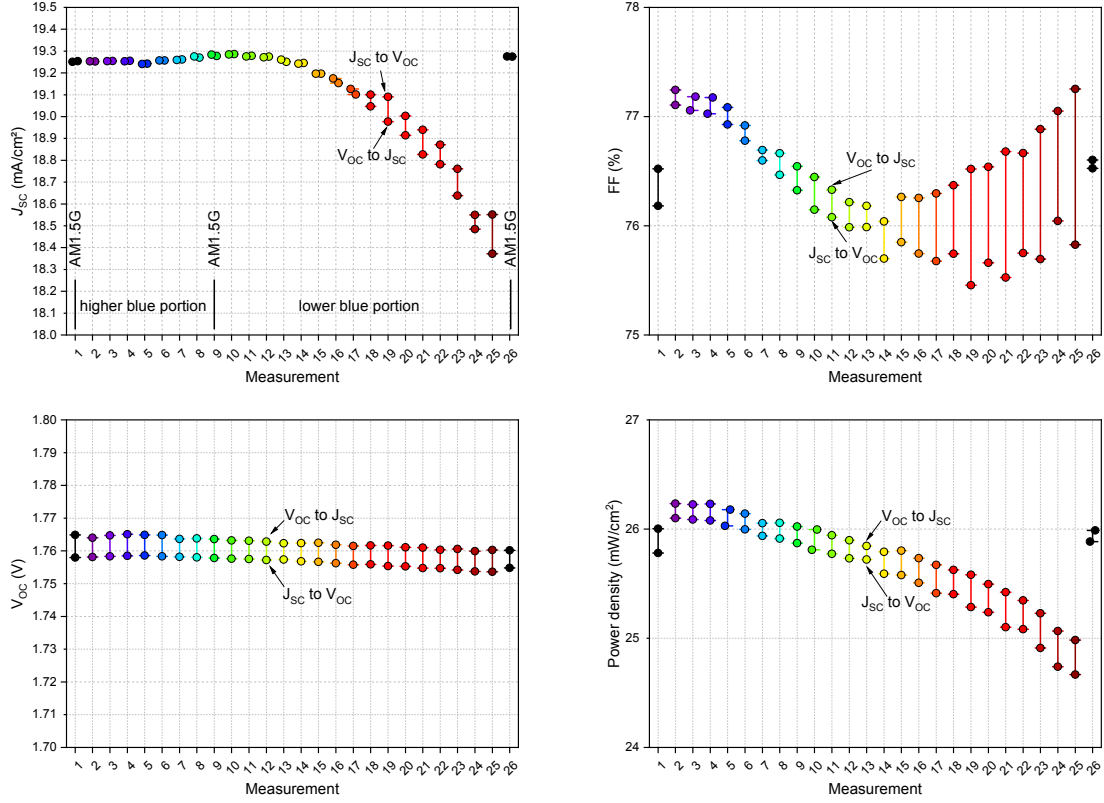
Figure S12: Parameters of a tandem solar cell illuminated with different spectra. By changing the intensity of two blue LEDs, we changed current generation in the perovskite sub cell. Starting from measurement no. 2 with the highest portion of blue light, the blue light is continuously decreased passing the AM1.5G at measurement no. 9 and decreased further until measurement no. 25. Before and after this series, a *J-V* was recorded under AM1.5G illumination to ensure that neither the cell degraded nor the spectrum shifted (measurement no. 1 and 26). In the main text in Figure 5 only the V_{OC} to J_{SC} (reverse scan) measurements are shown.

13. Calculating the integrated intensity of the measured spectra

Supplementary note 3

As the utilized LED spectra are recorded just between 330 nm and 1087 nm, they need to be extended in order to calculate the integrated intensity (input power) and therefore the efficiency in Figure 5d in the main text. As measurement no. 1 in the series is measured close to AM1.5G conditions, the recorded spectrum no. 1 is used as a reference. Each other spectrum used, with more or less blue light, is then divided by spectrum no. 1 leading to a correction factor for each wavelength (factor function). Figure S13 shows the spectrum no. 1, spectrum no. 2 and the factor function for spectrum no. 2. Below 330 nm and above 1087 nm, the factor is set to 1. Each factor function is multiplied with the correct AM1.5G (ASTM G173-03) spectrum. The integrated intensity is then calculated by integrating the new spectrum and used as input power for the resulting efficiency.
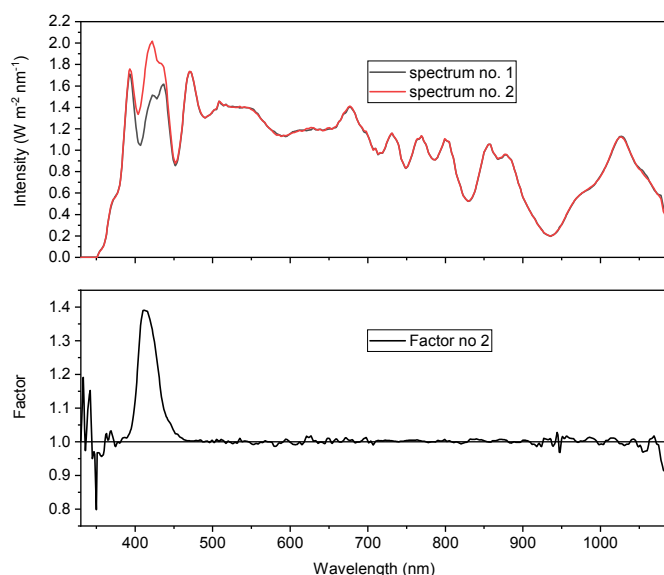
Figure S13: Spectrum recorded for measurement no. 1 and 2, respectively. The factor no. 2 is calculated by dividing spectrum no. 2 by spectrum no. 1.

14. Electrical simulations and comparison to experimental results

a)
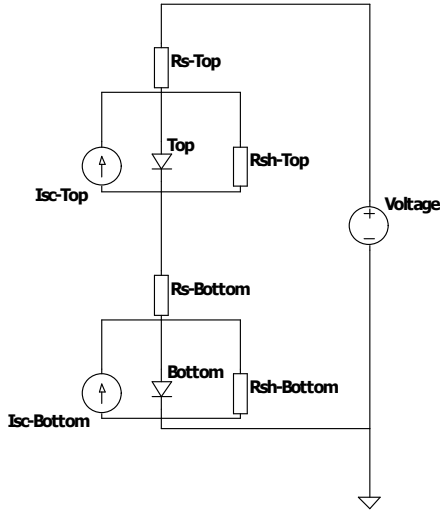
b)
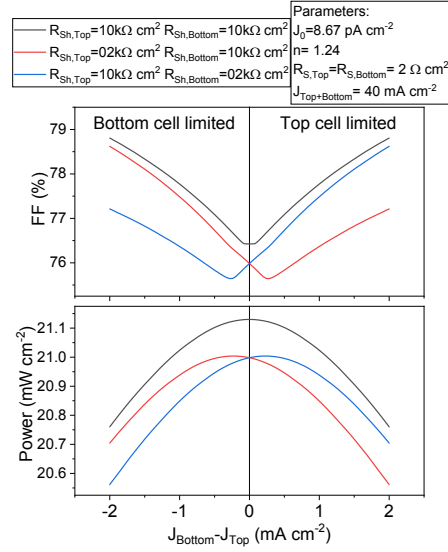
Figure S14: a) Equivalent circuit diagram utilized to describe a tandem solar cell using the simulation tool LTspice. The top and bottom cell, each consisting of a single diode model, are connected in series. b) Simulated FF and generated power as a function of the current density mismatch ($m = J_{Bottom}$-J_{Top}) for identical and asymmetric sub-cells. For the simulation of asymmetric sub-cells the shunt resistance R_{Sh} of the top and bottom cell is changed, as stated in the legend.

a)

b)

c)

d)

e)
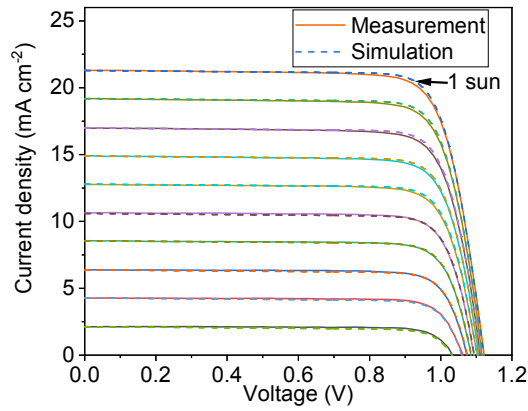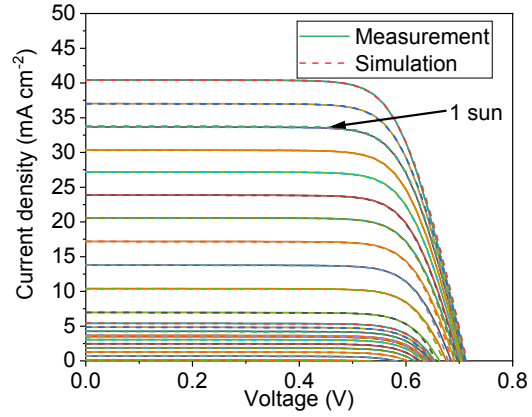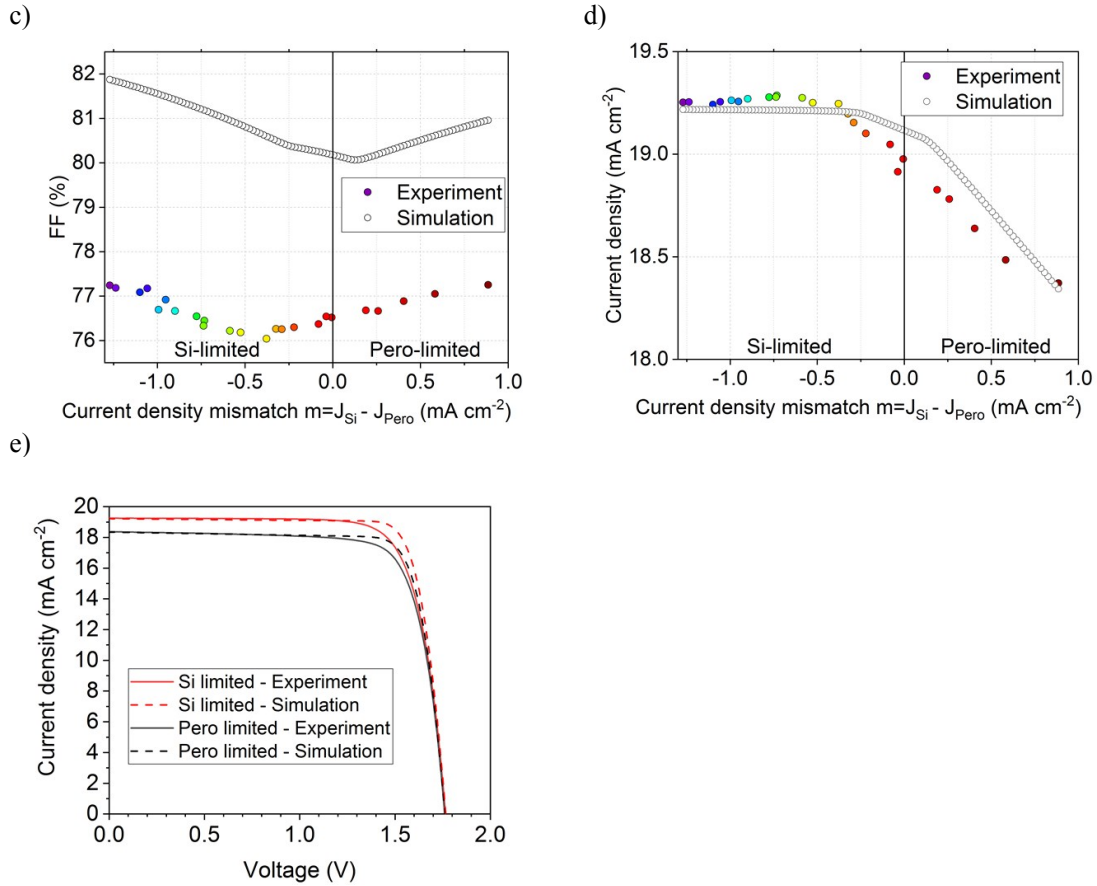
Figure S15: a) Opaque perovskite single junction solar cell measured at different intensities to extract electrical parameters for the single diode model. As this cell is opaque (i.e. a metal is used instead of a TCO), the series resistance due to the sheet resistance of the TCO is not included in this measurement and simulation. The corresponding fitting from electrical parametrization is also shown and the agreement is very good for the used range of intensities. b) Silicon single junction solar cell measured at different intensities to extract electrical parameters for the single diode equation. The corresponding fitting from electrical parametrization is also shown and is in very good agreement for the used range of intensities. c) FF as a function of the sub-cell current density mismatch from the experiment and simulation, respectively, using the electrical data from parametrized single junction solar cells as shown in Figure S15 a and b. Detailed information can be found in Supplementary note 4. d) Simulated and experimental short circuit current of the monolithic tandem solar cell as a function of current density mismatch. e) Simulated and experimental *J-V*s of the tandem solar cell measured at the most negative and most positive current mismatch *m* within this series.

Supplementary note 4

To simulate the FF dependency of a monolithic tandem solar cell in Figure S14b, two identical solar cells are connected in series with parameters displayed in the graphic. The shunt resistance is varied as stated in Figure S14b, while the top cell current is changed from $19\,\text{mA cm}^{-2}$ to $21\,\text{mA cm}^{-2}$ and the bottom cell current is adjusted in a way that the sum of the top and bottom cell is constantly at $40\,\text{mA cm}^{-2}$.

For the electrical parametrization, single junction silicon and perovskite solar cells were fabricated with comparable contact design as used in the tandem stack; both cells are then measured at different intensities to extract the ideality factors. This is done by plotting V_{OC} against $\ln(J_{SC})$ and calculating the slope. This method results in ideality factors of $n_{Pero} = 1.46$ and $n_{Si} = 1.24$. The ideality factor agrees reasonably well for the perovskite[11] and is slightly higher as typically reported values for silicon[12] which we attribute to the contact design with a significant amount of electrically connected but not illuminated area. The saturation current J_0 is adjusted in a way that the experimental and simulated V_{oc} coincide: $J_{0,Silicon} = 8.6743$ pA cm^{-2}, $J_{0,Pero} = 26.78$ fA cm^{-2}. The series and shunt resistances R_S and R_{Sh} are adjusted in a way that the slope around V_{OC} and J_{SC} of the simulated J-Vs fit to the experimental results. This leads to the following values: $R_{S,Pero} = 2.976$ Ω cm^2, $R_{Sh,Pero} = 4800$ Ω cm^2, $R_{S,Si} = 2.08$ Ω cm^2 and $R_{Sh,Si} = 9250$ Ω cm^2. As no grid fingers are used, the high series resistances might be attributed to the sheet resistance of the front TCO. All values are additionally summarized in Table S1

To simulate the tandem J-V curves, both parameterized reference sub-cells are connected in series. As the V_{OC} of the monolithic tandem solar cell is slightly lower than the sum of the single junctions, which most likely stems from a lower V_{OC} of the perovskite sub-cell, the $J_{0,Pero}$ is changed to $J_{0,Pero} = 8.5$ fA cm^{-2}. Furthermore, the R_s is adjusted to the slope around V_{OC}, resulting in a sum of $R_{S,Si} + R_{S,Pero} = 3$ Ω cm^2.

Table S1: Summarized parameters for the simulation with LTspice

	Perovskite as SJ (HZB)	Perovskite in Tandem (HZB)	Perovskite as SJ (PKU)[13]	Si as SJ and Tandem (HZB)	Si as SJ and Tandem (ISE)[14,15]
n	1.46	1.46	1.86	1.24	1.125
R_S	2.976 Ω cm^2	$R_{S,Si}+R_{S,Pero}=3$ Ω cm^2	3 Ω cm^2	2.08 Ω cm^2	0.001 Ω cm^2
R_{Sh}	4800 Ω cm^2	4800 Ω cm^2	20 kΩ cm^2	9250 Ω cm^2	9000 Ω cm^2
J_0	2.678 fA cm^{-2}	8.5 fA cm^{-2}	0.407 pA cm^{-2}	8.6743 pA cm^{-2}	0.665 pA cm^{-2}
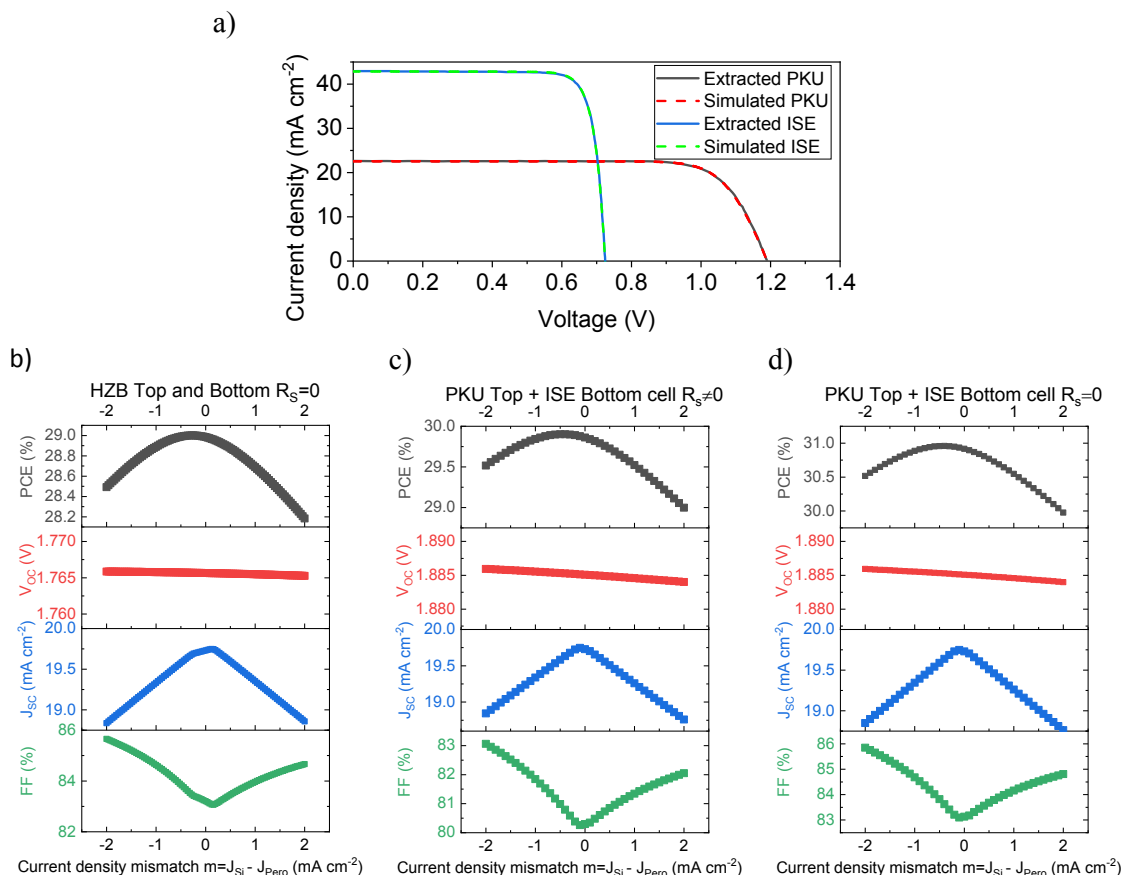
Figure S16: a) Extracted and simulated *J-V*s of a record p-i-n single junction perovskite[11] and both side contacted c-Si cell.[14,15] The parameters are displayed in Table S1. b) Simulation of the monolithic tandem solar cell shown in Figure S15 c-d with a series resistance of $R_s = 0\,\Omega\,cm^2$ and a constant cumulative photogenerated current density $J_{\text{Pero+Si}}$ of 39.46 mA cm^{-2}. c) Simulation of a monolithic tandem solar cell using the parametrized record cell shown in a); The parameters used for the electrical simulation are shown in Table S1. A cumulative photogenerated current density of 39.46 mA cm^{-2} is assumed. d) Simulation of the same tandem solar cell as in c) but with a series resistance of $R_s = 0\,\Omega\,cm^2$

Supporting Bibliography

1   F. Sahli, J. Werner, B. A. Kamino, M. Bräuninger, R. Monnard, B. Paviet-Salomon, L. Barraud, L. Ding, J. J. Diaz Leon, D. Sacchetto, G. Cattaneo, M. Despeisse, M. Boccard, S. Nicolay, Q. Jeangros, B. Niesen and C. Ballif, *Nat. Mater.*, 2018, **17**, 820–826.

2   J. Werner, F. Sahli, F. Fu, J. J. Diaz Leon, A. Walter, B. A. Kamino, B. Niesen, S. Nicolay, Q. Jeangros and C. Ballif, *ACS Energy Lett.*, 2018, **3**, 2052–2058.

3   H. Hosono and K. Ueda, *Springer Handbook of Electronic and Photonic Materials*, Springer US, Boston, MA, 2007.

4   M. Morales-Masis, S. De Wolf, R. Woods-Robinson, J. W. Ager and C. Ballif, *Adv. Electron. Mater.*, 2017, **3**, 1600529.

5   D. S. Ginley, *Handbook of Transparent Conductors*, Springer US, Boston, MA, 2011.

6   H. Kim, C. M. Gilmore, A. Piqué, J. S. Horwitz, H. Mattoussi, H. Murata, Z. H. Kafafi and D. B. Chrisey, *J. Appl. Phys.*, 1999, **86**, 6451–6461.

7   R. Santbergen, T. Meguro, T. Suezaki, G. Koizumi, K. Yamamoto and M. Zeman, *IEEE J. Photovoltaics*, 2017, **7**, 919–926.

8   M. Jošt, E. Köhnen, A. B. Morales-Vilches, B. Lipovšek, K. Jäger, B. Macco, A. Al-Ashouri, J. Krč, L. Korte, B. Rech, R. Schlatmann, M. Topič, B. Stannowski and S. Albrecht, *Energy Environ. Sci.*, 2018, **11**, 3511–3523.

9   A. Magomedov, A. Al-Ashouri, E. Kasparavičius, S. Strazdaite, G. Niaura, M. Jošt, T. Malinauskas, S. Albrecht and V. Getautis, *Adv. Energy Mater.*, 2018, **8**, 1801892.

10   L. Mazzarella, Y.-H. Lin, S. Kirner, A. B. Morales-Vilches, L. Korte, S. Albrecht, E. Crossland, B. Stannowski, C. Case, H. J. Snaith and R. Schlatmann, *Adv. Energy Mater.*, 2019, **1803241**, 1803241.

11   M. Stolterfoht, C. M. Wolff, Y. Amir, A. Paulke, L. Perdigón-Toro, P. Caprioglio and D. Neher, *Energy Environ. Sci.*, 2017, **10**, 1530–1539.

12   K. Yoshikawa, H. Kawasaki, W. Yoshida, T. Irie, K. Konishi, K. Nakano, T. Uto, D. Adachi, M. Kanematsu, H. Uzu and K. Yamamoto, *Nat. Energy*, 2017, **2**, 17032.

13   D. Luo, W. Yang, Z. Wang, A. Sadhanala, Q. Hu, R. Su, R. Shivanna, G. F. Trindade, J. F. Watts, Z. Xu, T. Liu, K. Chen, F. Ye, P. Wu, L. Zhao, J. Wu, Y. Tu, Y. Zhang, X. Yang, W. Zhang, R. H. Friend, Q. Gong, H. J. Snaith and R. Zhu, *Science (80-.).*, 2018, **360**, 1442–1446.

14   M. A. Green, Y. Hishikawa, E. D. Dunlop, D. H. Levi, J. Hohl-Ebinger and A. W. Y. Ho-Baillie, *Prog. Photovoltaics Res. Appl.*, 2018, **26**, 3–12.

15   A. Richter, J. Benick, F. Feldmann, A. Fell, M. Hermle and S. W. Glunz, *Sol. Energy Mater. Sol. Cells*, 2017, **173**, 96–105.

F Publication: Monolithic perovskite/silicon tandem solar cell with >29% efficiency by enhanced hole extraction

The following pages contain the publication addressed in section 6.2. For copyright reasons the accepted version is be reproduced here.

- Publication:

- Author contribution:
  A.A.-A. and Ei.K. contributed equally, A.A.-A., Ei.K., and S.A. planned the experiments, coordinated the work and prepared the figures; Er.K., A.M., and T.M. designed and synthesized the Me-4PACz SAM and the (Me-)nPACz series; A.A.-A. and B.L. processed the single-junction cells and optimized the SAM deposition; A.B.M.V. processed the Si bottom cells and measured Si single-junction solar cells; Ei.K. and B.L. processed the perovskite top cells; Ei.K. planned the analysis of the tandem solar cells, measured $J-V$, EQE and reflection of all tandem solar cells and performed short-term (incl. elevated temperature) MPP-tracking; A.A.-A., H.H., and J.A.M. conducted and analyzed the PL experiments; Ei.K., J.A.M. and A.A.-A. conducted and analyzed the EL studies; Ei.K. performed the subcell fitting and electrical simulations; H.H. recorded the terahertz measurements and performed the data analysis; P.C., M.G., and M.S. conducted the pseudo–$J-V$ and FF-V_{OC} loss analysis (intensity-dependent V_{OC} and QFLS) of films and single-junction solar cells; D.M. performed the photoelectron spectroscopy; J.A.S., D.S., and N.P. performed crystallographic analysis; G.M., M.J., B.L., and Ei.K. designed and built the tandem aging setup and recorded the long-term MPP-tracks; All authors contributed to data interpretation; Ei.K and A.A.-A. drafted the manuscript; All authors participated in proofreading and correcting; S.A., V.G., M.S., T.U., T.M., C.G., R.S., M.T., La.K., A.A., D.N., B.S., and B.R. supervised the projects.

Title: Monolithic Perovskite/Silicon Tandem Solar Cell with >29% Efficiency by Enhanced Hole Extraction

Authors: Amran Al-Ashouri*,[a], Eike Köhnen*,[a], Bor Li[a], Artiom Magomedov[b], Hannes Hempel[c], Pietro Caprioglio[a,f], José A. Márquez[c], Anna Belen Morales-Vilches[e], Ernestas Kasparavicius[b], Joel A. Smith[g,j], Nga Phung[g], Dorothee Menzel[a], Max Grischek[a,f], Lukas Kegelmann[a], Dieter Skroblin[h], Christian Gollwitzer[h], Tadas Malinauskas[b], Marko Jošt[a,i], Gašper Matič[i], Bernd Rech[d,k], Rutger Schlatmann[e,k], Marko Topič[i], Lars Korte[a], Antonio Abate[g], Bernd Stannowski[e], Dieter Neher[f], Martin Stolterfoht[f], Thomas Unold[c], Vytautas Getautis[b], Steve Albrecht[a,l,§]

Affiliations:
a Young Investigator Group Perovskite Tandem Solar Cells, Helmholtz-Zentrum Berlin, Kekuléstraße 5, 12489 Berlin, Germany.
b Department of Organic Chemistry, Kaunas University of Technology, Radvilenu pl. 19, Kaunas LT-50254, Lithuania.
c Department of Structure and Dynamics of Energy Materials, Helmholtz-Zentrum-Berlin für Materialien und Energie GmbH, Hahn-Meitner Platz 1, 14109 Berlin, Germany
d Helmholtz-Zentrum Berlin, Scientific Management, 12489 Berlin, Germany
e PVcomB, Helmholtz Zentrum Berlin, Schwarzschildstr. 3, 12489 Berlin, Germany
f Institute of Physics and Astronomy, University of Potsdam, 14476 Potsdam, Germany
g Young Investigator Group Active Materials and Interfaces for Stable Perovskite Solar Cells, Kekuléstraße 5, 12489 Berlin, Germany
h Physikalisch-Technische Bundesanstalt (PTB), Abbestraße 2-12, 10587 Berlin, Germany
i University of Ljubljana, Faculty of Electrical Engineering, Tržaška 25, 1000 Ljubljana, Slovenia
j Department of Physics & Astronomy, University of Sheffield, Hicks Building, Hounsfield Road, Sheffield, S3 7RH, U.K.
k HTW Berlin – University of Applied Sciences, Wilhelminenhofstr. 75a, 12459 Berlin, Germany
l Faculty of Electrical Engineering and Computer Science, Technical University Berlin, Marchstraße 23, 10587 Berlin, Germany
* contributed equally, § corresponding author

Abstract

Tandem solar cells that pair silicon with metal-halide perovskite are a promising option for surpassing the single-cell efficiency limit. We report a certified record monolithic perovskite/silicon tandem with a power conversion efficiency of 29.15%. The perovskite absorber with 1.68 eV bandgap remained phase-stable under illumination through a combination of fast hole extraction and minimized non-radiative recombination at the hole-selective interface. Key was a self-assembled, methyl-substituted carbazole monolayer as hole-selective layer in the perovskite cell. The accelerated hole extraction was linked to a low ideality factor of 1.26 and single-junction fill factors of up to 84%, while enabling the yet highest tandem open-circuit voltage of up to 1.92 volts. In air, without encapsulation, a tandem retained 95% of its initial efficiency after 300 hours of operation.

One Sentence Summary: Combining interface passivation with fast charge extraction for stable, highly efficient perovskite/silicon tandem solar cells

Main text:

A tandem solar cell with a silicon cell overlaid by a perovskite solar cell (PSC) (*1*) could increase efficiencies of commercial mass market photovoltaics beyond the single-junction cell limit (*1*, *2*) without adding substantial costs (*3*, *4*). The power conversion efficiency (PCE) of PSCs has reached up to 25.2% for single-junction solar cells (at an area of ~0.1 cm²) (*5*), 24.2% for perovskite/CIGSe (copper-indium-gallium-selenide) tandem cells (~1 cm²) (*5–7*), 24.8% for all-perovskite tandem cells (0.05 cm²) (*8*, *9*) and 26.2% for the highest openly published perovskite/silicon tandem efficiency (~1 cm^2) (*10*, *11*). Perovskite/silicon tandem cells have additionally undergone technological advances in both stability

1

and compatibility with textured silicon substrates (*11–13*). However, there is still room for improvement for these perovskite-based tandem solar cells, as practical limits for all these tandem technologies are well above 30% (*14*, *15*).

The increase in PSC efficiency has been driven in part by advances in physical and chemical understanding of the defect and recombination mechanisms. Some reports presented near-perfect passivation of surfaces and grain boundaries with photoluminescence quantum yields (PLQYs) approaching theoretical limits (*16–18*). Consequently, PSCs were reported with open-circuit voltage (V_{OC}) values of only a few 10 meV below their radiative limit (*19–23*). These values surpass those reached with crystalline silicon absorbers and are comparable with solar cells based on epitaxially grown GaAs (*23*, *24*). However, perovskite compositions with a wider bandgap that are needed for high-efficiency tandem solar cells still show considerable V_{OC} losses (*14*, *25*). The main reasons include comparably low PLQYs of the absorber material itself, an unsuitable choice of selective contacts and phase instabilities. Even state-of-the-art perovskite/silicon tandem cells still have V_{OC}s well below 1.9 V.

We present a strategy to overcome these issues simultaneously, demonstrated on a 1.68 eV bandgap triple-cation perovskite composition, which enables photostable tandem devices with a V_{OC} of 1.92 V. We note that the charge extraction efficiency, and with that, the fill factor (FF) of PSCs, is still poorly understood. Although reported PSCs usually feature a small active area (~0.1 cm²) with small absolute photocurrents (a few milliamperes), and thus small series resistance losses at the contacts, usual FFs of high-efficiency devices generally range from 79 to 82%. However, based on the detailed balance limit, PSCs should be able to deliver a FF of 90.6% at a bandgap of 1.6 eV. Wider bandgap perovskite compositions near 1.7 eV seem especially prone to low FFs, resulting in tandem cell FF values commonly below 77%, near current-matching conditions (*11*, *12*, *26*). In optimized perovskite single-junction devices, the FFs only recently exceeded 80%, with a maximum value of 84.8% (*27*).

One reason for the low FF might be that there are only few techniques for quantifying and analyzing the FF losses in PSCs. We show that intensity-dependent transient and absolute photoluminescence is a viable technique. A main FF limitation of high-efficiency PSCs is the ideality factor n_{ID}, with typical values of 1.4 to 1.8 for high-V_{OC} devices (*28*), while established solar cell technologies reach values of 1 to 1.3 (*29*). Thus, an important goal for perovskite photovoltaics is to lower the ideality factor while minimizing nonradiative interface recombination to achieve a high V_{OC} (*28*). We designed a self-assembled monolayer (SAM) with methyl group substitution as a hole-selective layer, dubbed Me-4PACz ([4-(3,6-dimethyl-9H-carbazol-9-yl)butyl]phosphonic acid) and show that a fast hole extraction led to a lower ideality factor. Thus, FFs of up to 84% in *p-i-n* single-junction PSCs and >80% in tandem devices were achieved.

The SAM provided both fast extraction and efficient passivation at the hole-selective interface. This combination slowed down light-induced halide segregation of a tandem-relevant perovskite composition with 1.68 eV bandgap, allowed a PLQY as high as on quartz glass and led to high single-junction device V_{OC}s > 1.23 V. The single-junction improvements transferred into tandem devices, which allowed us to fabricate perovskite/silicon tandem solar cells with a certified PCE of 29.15%. This value surpasses the best silicon single-junction cell (26.7%) and is comparable to the best GaAs solar cell (*27*) at the same area of 1 cm². Under maximum power point tracking (MPP) in ambient air without encapsulation, a Me-4PACz tandem cell retained 95% of its initial efficiency after 300 h. Furthermore, we used injection-dependent, absolute electroluminescence spectroscopy to reconstruct the individual subcell current-voltage curves without the influence of series resistance (pseudo-*J-V* curves), demonstrating that the tandem device design that features only a standard perovskite film without additional bulk passivation could in principle realize PCE values up to 32.4%.

2

Stabilization of wide-bandgap perovskite with the hole-selective layer

The ideal top cell bandgap for perovskite absorbers in conjunction with CIGSe and Si bottom cells is ~1.68 eV (*30–32*). These wider bandgap compositions often feature a Br to I ratio >20%, which can lead to phase instabilities caused by light-induced halide segregation, most strikingly evident from photoluminescence (PL) spectra that show a double-peak formation under continuous illumination (*33, 34*). Upon generation of charge carriers in the perovskite film, iodide-rich clusters can form that are highly luminescent as they serve as charge carrier sinks given their lower bandgap compared to the surrounding material (*35*). As quantified by Mahesh et al., although some portion of the V_{OC} loss is related to halide segregation, the dominant source of V_{OC} loss is likely the generally low optoelectronic quality of the Br-rich mixed halide perovskite absorbers itself, or high non-radiative recombination rates at their interfaces (*35*). Hence, in order to unambiguously determine the limitations and potentials of wide bandgap compositions, it is necessary to find suitable charge-selective contacts that do not introduce further losses or instabilities.

We show that fast charge extraction paired with surface passivation can effectively suppress the formation of a double-peak emission in the PL, indicative of phase stabilization, and simultaneously enable a high quasi Fermi level splitting (QFLS) and device performance. Rather than optimizing the perovskite composition or passivating the film, we chose a variant of the widely used Cs-, FA- and MA-containing "triple-cation" perovskite (*36*) that is highly reproducible and focused on preparing an optimal charge-selective contact on which the perovskite film was deposited. We shifted the bandgap upward by increasing of the Br to I ratio to obtain a 1.68 eV (23% Br) absorber instead of the commonly used 1.6-1.63 eV (~17% Br), yielding a nominal precursor composition of $Cs_{0.05}(FA_{0.77}MA_{0.23})_{0.95}Pb(I_{0.77}Br_{0.23})_3$.

3
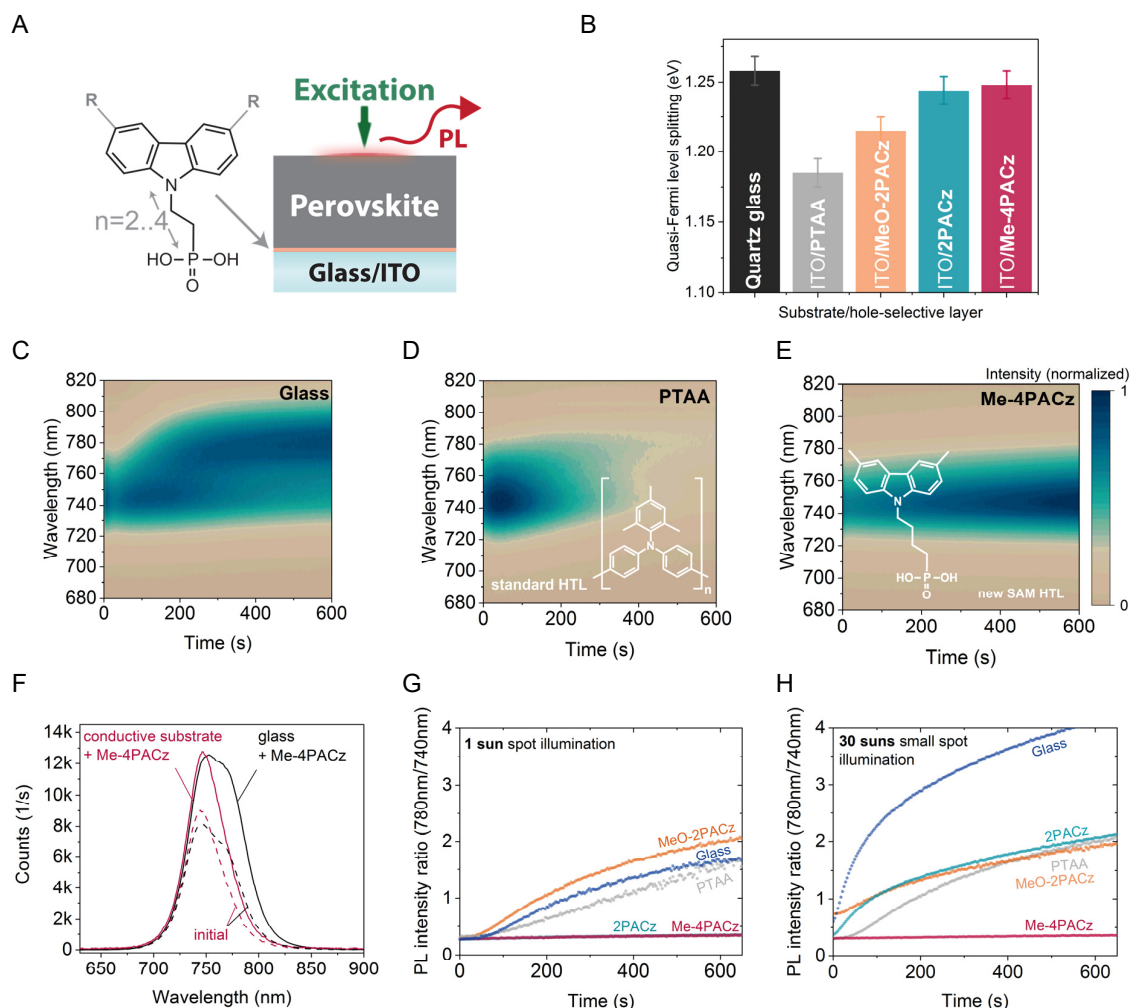
Fig. 1 Photoluminescence properties and stability assessment of perovskite films on different substrates. (**A**) schematic description of the photoluminescence (PL) experiment and chemical structure of a general carbazole-based SAM, with R denoting a substitution (or "termination"), which in this work is either nothing (2PACz), a methoxy group (MeO-2PACz) or a methyl group (Me-4PACz). The number 2 or 4 denotes the number of the linear C-atoms between the phosphonic acid anchor group and the conjugated carbazole main fragment. (**B**) Quasi Fermi level splitting (QFLS) values of non-segregated 1.68 eV bandgap perovskite films on a bare glass substrate and different hole-selective layers on the transparent and conductive indium tin oxide (ITO). (**C-E**), Time-dependent photoluminescence spectra analyzing phase stability of perovskite absorbers with 1.68 eV bandgap. The perovskite films were deposited either on glass (C) or on ITO substrates with different hole-selective layers (D, E). (**F**) PL spectra before (dashed lines) and after 600 s of light-soaking (solid lines) under 1-sun equivalent illumination flux in air, comparing the perovskite grown on Me-4PACz that was deposited on either a glass substrate or conductive ITO substrate. (**G**) As figure of merit for stability, the ratio of PL intensities at 780 nm and 740 nm is shown, from the PL evolutions in (C), (D), (E), and two other hole-selective layers (shown in SI, illumination spot size ~0.12 cm²). (**H**) Same as for (G), but at higher illumination intensity through decrease of the excitation spot size to 0.4 mm².

A schematic of the device stack and the used hole-selective layers (commonly abbreviated as HTLs, "hole transporting layers") used for PL measurements is shown in **Fig. 1**. We first compared the QFLS measured by absolute PL and then the PL stability of this perovskite composition prepared on indium tin oxide (ITO) substrates covered by the HTLs. In recently published high-PCE p-i-n ("inverted") single-junction and tandem PSCs, the polymer bis(4-phenyl)(2,4,6-trime-thylphenyl)amine] (PTAA) or the comparable Poly(N,N'-bis-4-butylphenyl-N,N'-bisphenyl)benzidine (polyTPD) are standardly used (*10*, *11*, *37*, *38*). Alternatively, self-assembled monolayers (SAMs) based on carbazole such as MeO-2PACz and 2PACz can form passivated interfaces while allowing for low transport losses due to their ultrathin thickness (<1 nm) (*7*). The introduction of a methyl-group substitution to the "lossless" hole-selective interface created by 2PACz (*7*) lead to a more optimized alignment with the perovskite valence band edge (see energetic band edge diagram in Figure S1) with a similar dipole moment (~1.7 D) and resulted in faster charge extraction. The supplementary materials contain the synthesis scheme of the

4

herein used SAMs. In literature of the n-i-p configuration of PSCs, methoxy substituents were prevalently used in HTLs, with some works reporting a possible passivation function at the perovskite interface (*39–42*). For the p-i-n configuration however, the standard high-performance HTLs PTAA and polyTPD contain alkyl substituents. In the present study, we directly compared methoxy and methyl substituents in p-i-n cells with MeO-2PACz and Me-4PACz, with the results showing advantages for the methyl substitution regarding both passivation and hole extraction. We tested the influence of the aliphatic chain length (n) in carbazole SAMs without (nPACz) and with methyl substitution (Me-nPACz) on PSC performance and found an optimum FF at n = 2 for nPACz and at n = 4 for Me-nPACz (see Figure S23). For n = 6, both SAMs lead to current-voltage hysteresis.

The QFLS values of bare perovskite films (**Fig. 1B**) deposited on 2PACz and Me-4PACz were similar to that on quartz glass, commonly regarded as a perfectly passivated substrate (*16*). Perovskite compositions with high Br content typically segregate into I-rich phases indicated by increased PL intensity at lower photon energies, here at a wavelength of 780 nm (*33*). Pristine regions of the non-segregated perovskite film emitted photons at a peak wavelength of around 740 nm for perovskite deposited on glass (**Fig. 1C**) or ITO/PTAA (**Fig. 1D**), and a similar response was seen for the SAM MeO-2PACz (Figure S3) on ITO. However, the perovskite emission was more stable over time on ITO/2PACz and ITO/Me-4PACz substrates (**Fig. 1E** and Figure S3). The raw spectra are shown in Figure S4.

Among the studied HTLs, phase segregation was only inhibited if the perovskite was grown on a substrate that fulfilled the requirements of both fast charge extraction and good passivation; **Fig. 1F** demonstrates that passivation alone was insufficient. The black curve shows a PL spectrum of the perovskite film on an insulating glass substrate that was covered by Me-4PACz, after 10 min of continuous spot illumination with 1-sun equivalent photon flux. The illuminated film showed signs of I-rich phases emitting at a center wavelength of ~780 nm. The glass substrate ensured that no hole transfer out of the perovskite bulk occurred. In contrast, a conductive ITO substrate that allowed hole transmission in combination with Me-4PACz increased the PL stability, as evidenced by the sharp peak with emission centered at ~740 nm even after 10 min of spot illumination.

A bare ITO substrate seemed to prevent charge accumulation as well, allowing a stable PL peak position at 1-sun intensity (0.12 cm² spot size, see Figure S6). The connection between charge accumulation in the perovskite and phase instability was reported in previous studies in which a reduced density of carriers increased the activation energy of mobile ion species and allowed the film to remain in its initial form (*43*, *44*). Spot illumination (0.12 cm² with 1-sun photon flux) represented increased stress testing on phase stability compared to full illumination because it created an outward driving force for ions from the illuminated area (*45*). Consequently, a smaller illumination spot (i.e., larger edge-to-area ratio) at the same illumination intensity showed a faster PL redshift (see Figure S5 & Figure S6). To compare the degree of PL redshift and double-peak formation, we evaluated the ratio of the two emission center intensities at 740 and 780 nm for two different excitation fluences equivalent to 1-sun and 30-suns illumination, in **Fig. 1G** and **H,** respectively. At 1-sun-equivalent intensity, only 2PACz and Me-4PACz on ITO had a stable ratio. However, upon increasing the intensity and thus charge carrier generation rate 30-fold, a Me-4PACz-covered ITO substrate differed from the 2PACz-covered by still displaying a similarly stable PL intensity ratio.
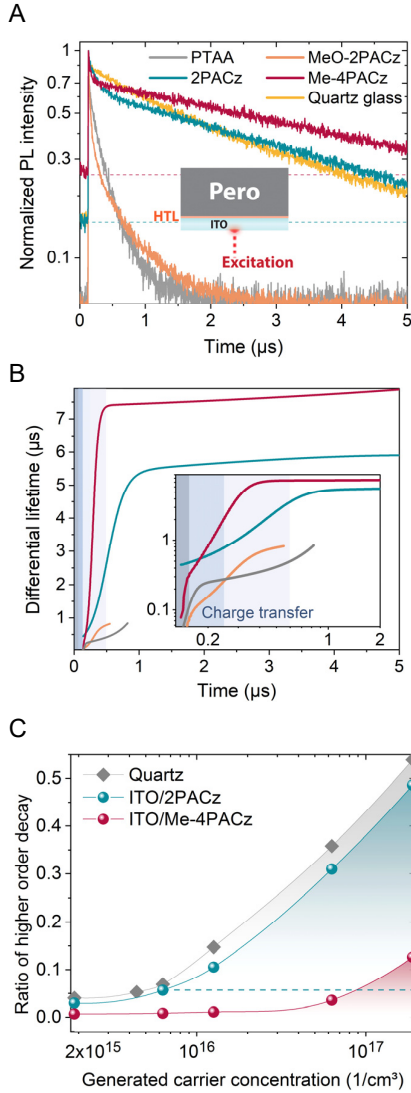
Fig. 2 Role of charge transfer on transient photoluminescence (TrPL). (**A**) PL transients of perovskite on ITO/hole-selective layer substrates. The dashed lines indicate the background levels. (**B**) Computed differential lifetimes from fits to the transients in (A), showing the single-exponential decay time at each time of the transient, with early times shown in the inset. The inset highlights the region of the Me-4PACz and 2PACz transients that is governed by hole transfer into the ITO. Excitation density is similar to 1-sun conditions (fluence of ~30 nJ/cm², 2-3 x 10^{15} cm^{-3}). (**C**) Ratio of higher-order processes to mono-exponential decay in the TrPL transients, revealing that Me-4PACz not only extracts holes faster (inset in B), but also with a ~10 times higher efficiency compared to 2PACz, since the Me-4PACz transient shows the same magnitude of radiative recombination only at a ~10 times higher charge carrier generation (comparison along the dashed line, see Figure S10 for details).

We used transient photoluminescence (TrPL) to analyze charge carrier transfer into adjacent charge-selective layers (*46*). The full decay is governed by non-radiative, trap-assisted surface/bulk recombination (mostly mono-exponential decay), radiative recombination ("bimolecular", second-order differential equation) and charge transfer effects, which can be disentangled if these time constants differ sufficiently from each other (*18*). **Fig. 2A** presents PL transients of 1.68 eV-bandgap perovskite films on ITO/HTL substrates. With MeO-2PACz and PTAA, it is not possible to clearly differentiate between charge extraction and trap-assisted recombination because both the nonradiative recombination is high (as evidenced by lower QFLS values compared to quartz glass, **Fig. 1B**) and the transients did not saturate towards one process. In contrast, the PL transients for 2PACz and Me-4PACz showed a clear mono-exponential decay at later times, indicating Shockley-Read-Hall recombination (*47*). Fits to the TrPL transients (Figure S8) were used to compute the differential lifetime $\tau = -\left(\mathrm{dln}(\phi(t))/\mathrm{dt}\right)^{-1}$ (**Fig. 2B**), with $\phi(t)$ being the time-dependent PL photon flux. In this representation, the processes that reduce the PL counts over time are separable and the transient decay time (or "lifetime") is directly readable at each time point (*46*).

The high, asymptotically reached TrPL lifetimes of >5 µs for both 2PACz and Me-4PACz suggested that there were minimal non-radiative recombination losses at the SAM interfaces. The charge transfer process at early times (until ~1 µs) led to a sharp rise of τ, resembling simulated curves by Krogmeier

6

et al. (*46*). The transition from increasing lifetime to the plateau marks when the charge transfer ends, and non-radiative first-order recombination becomes dominant. Because PLQY measurements of films on 2PACz and Me-4PACz indicated a similar level of interface recombination and charge generation conditions are the same (see also Figure S9), the steepness of this rise was influenced by the charge transfer speed. The observed gradient for Me-4PACz implied a faster hole transfer to the underlying ITO compared to 2PACz, with the saturation starting after ~300 ns as compared to ~1 µs.

In the charge carrier generation regime of this experiment (~1-sun, ~$3 \cdot 10^{15}$ cm^{-3}), trap-assisted recombination dominated with the PL flux scaling proportionally to the density of photogenerated carriers n, as evidenced by intensity-dependent TrPL shown in Figure S9. Figure S9 further demonstrates that at higher generation conditions, the PL flux scaled proportionally to n^2, where transients usually show a multi-exponential signature, as seen with 2PACz and quartz (see Figure S10). Nevertheless, in this regime the Me-4PACz transients remained mono-exponential until generation densities exceeded ~35-suns-equivalent. We interpret this as a consequence of a large hole-extraction flux, which causes first-order recombination to dominate even in this injection regime.

We quantified this phenomenon of persisting domination of first-order recombination in **Fig. 2C** by displaying the ratio of higher-order to first-order recombination for the different generation conditions (see Supp. Note 1a for the evaluation method). The comparison of Me-4PACz to 2PACz indicated that Me-4PACz had a >10 times larger hole-extraction flux, because the curvature of the TrPL transient only began to resemble that of 2PACz at a >10 times higher generation density (indicated by the blue dashed line in **Fig. 2C**).

The carrier mobilities determined by optical-pump-terahertz-probe measurements (Figure S12) were similar between perovskite films grown on the different HTLs. To also exclude differences in perovskite composition and crystal orientation due to possible growth differences, we probed the effect of the HTL on these properties by grazing-incidence wide-angle x-ray scattering (GIWAXS) at the four crystal monochromator beamline of the Physikalisch-Technische Bundesanstalt (*48*). Azimuthally integrated diffraction patterns collected on a movable PILATUS detector module (*49*) showed comparable composition in each case (Figure S13), with marginally increased PbI$_2$ scattering intensity on PTAA as we observed in our previous work (*7*). Comparing azimuthal intensity profiles for perovskite scattering features (Figure S14), we found negligible difference in crystallographic orientation between the samples.

Our complete solar cells were capped by C$_{60}$ as the electron-selective contact. The electron extraction speed was not limiting the cell operation, as demonstrated by a time-resolved Terahertz photoconductivity measurement combined with TrPL on a quartz/perovskite/C$_{60}$ sample (Figure S11). We compared the decays of free charge carriers after interface-near carrier generation on both sample sides and found an electron transfer time constant of roughly 1 ns, significantly faster than hole transfer at the hole-selective layer (~100 ns range). The extraction velocity into the C$_{60}$ in our model was $1.6 \cdot 10^4$ cm/s (see Figure S11 for details), a similar value to earlier reported velocities (*46*).

Performance of perovskite single-junction solar cells

For the analysis on solar cell level, we focused on the simple single-junction device stack glass/ITO/HTL/perovskite/C_{60}/SnO_2/Ag, with the SnO_2 serving as a buffer layer for indium zinc oxide (IZO) sputtering in the fabrication of tandem solar cells (*50*). We show that the combination of fast charge extraction and passivated interface not only mitigated phase instability (re **Fig. 1**) but was also linked to an increased FF of solar cell devices, mainly by a decreased diode ideality factor of the PSCs. The FF is the major remaining parameter for which PSCs have not yet come close to the values of established solar cell technologies (*24, 51*) (see Figure S16 for FF comparisons), with the ideality factor being one of the main properties that limit high-efficiency PSCs (*29*). MeO-2PACz and 2PACz lead to FFs of up to 82% (**Fig. 3A**), while with Me-4PACz, the values ranged to up to 84%, representing ~93% of the radiative limit.

Fig. 3B shows *J-V* curves recorded at simulated AM1.5G illumination conditions, comparing champion PTAA and Me-4PACz cells of the same batch and showing the superior performance of the SAM. The ideality factors n_{ID} for PSCs with different HTLs (**Fig. 3C**) were about 1.26 for Me-4PACz, 1.42 for 2PACz, 1.51 for MeO-2PACz, and 1.55 for PTAA cells. Figure S20 compares the V_{OC} values achieved with the different HTLs. Despite the large differences in passivation at the hole-selective interface, the differences in V_{OC} were not as large (average difference of 30 mV between PTAA and Me-4PACz), due to the limiting non-radiative recombination at the C_{60} interface. However, as reasoned above, the C_{60} layer did not limit charge extraction, thus the different extraction speeds invoked by the HTLs directly influenced the FF values. The high FF with Me-4PACz was accompanied by high V_{OC} values of up to 1.16 V and up to 1.234 V with a LiF interlayer between the perovskite and C_{60} (*52, 53*) (see **Fig. 3D** and Figure S20). The combination of a high V_{OC} with low n_{ID} was previously considered as challenging for PSCs (*28*) and it allowed us to fabricate a perovskite single-junction with a PCE of 20.8% with Me-4PACz (Figure S18) at 1.68 eV bandgap.

To investigate the FF values without the influence of series resistance losses, we measured intensity-dependent absolute PL spectra and computed the QFLS values (or implied V_{OC}, iV_{OC}) at each carrier generation condition. The derived data pairs of generation currents and iV_{OC} values allowed the reconstruction of hypothetical, so-called pseudo-*J-V* curves, as recently shown in ref. (*54*) (**Fig. 3D**). The extracted FF and pseudo-FF values (FF in absence of transport losses) of bare perovskite films grown on different HTLs are summarized in **Table 1**, line 1. Both 2PACz and Me-4PACz enabled high "pseudo-FF" values of ~88%, which is 96.8% of the detailed balance limit and similar to the value achieved on a bare quartz substrate. PTAA allowed for a pFF of only 85.6%.

This analysis highlights how the SAMs formed a practically lossless interface between ITO and perovskite. Interestingly, when including a C_{60} layer on top of the perovskite film, no differences between the studied HTLs for the iV_{OC} and pseudo-FF were apparent (dashed lines in **Fig. 3D, Table 1**, line 2), as the C_{60} layer sets a iV_{OC} limitation through high non-radiative recombination rates (*53*). This limitation was only overcome with a counter electrode on the C_{60} (**Fig. 3E** and full devices), which underlines the role of the dipoles that Me-4PACz and 2PACz created at the ITO surface. The calculated molecular dipole value of the hole-transporting fragment is ~0.2 D for MeO-2PACz, ~1.7 D for Me-4PACz and ~2 D for 2PACz. The positive dipoles shifted the work function of the ITO towards higher absolute numbers (Figure S2a), which presumably resulted in a higher built-in potential throughout the device (*55, 56*). A well-defined built-in potential can exist with the presence of a second electrode countering the ITO; in this case Ag or Cu. Thus, when reconstructing the *J-V*s from the suns-V_{OC} measurement on full devices in **Fig. 3C** to extract the pFF (**Table 1**, line 3), both 2PACz and Me-4PACz overcame the pFF and iV_{OC} limitations imposed by the C_{60} layer (**Fig. 3E**).
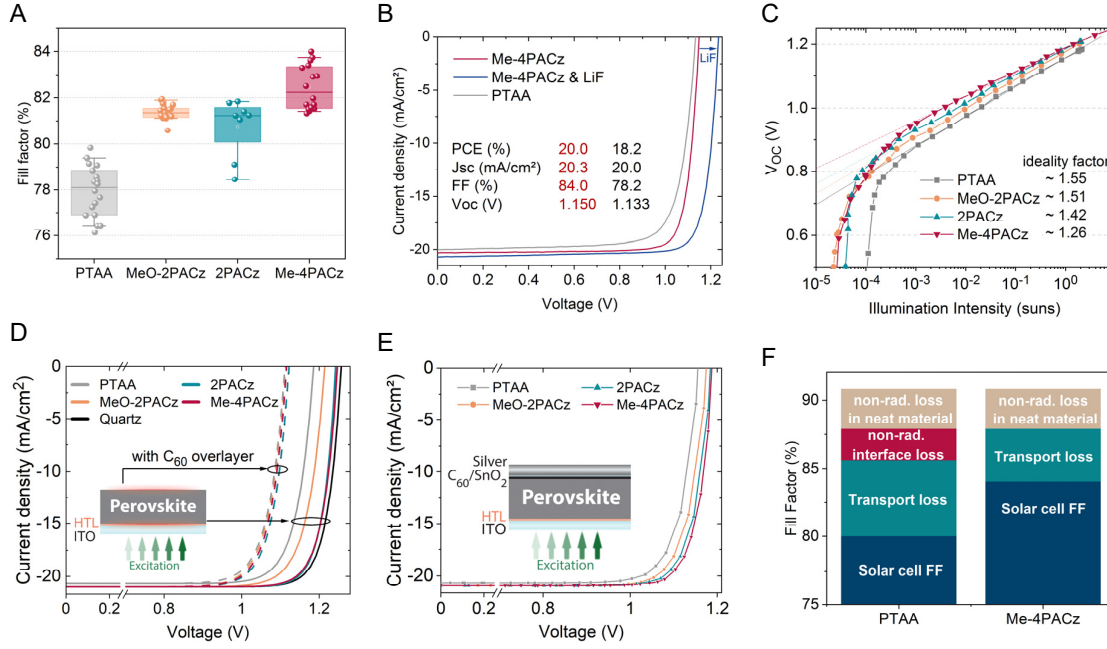
Fig. 3 Performance and fill factor loss analysis of *p-i-n* solar cells with different hole-selective layers. (**A**) Comparison of fill factor values of PSCs with the stack glass/ITO/HTL/perovskite/C$_{60}$/SnO$_2$/Ag, triple-cation perovskite absorber with 1.68 eV bandgap. All shown cells are made from the same perovskite precursor and contact processing batch. (**B**) *J-V* curves of the best cells of the batch in (A), and a *J-V* curve of a Me-4PACz cell from another batch with LiF interlayer between C$_{60}$ and perovskite, reaching a V_{OC} of 1.234 V. (**C**) Intensity-dependent open-circuit voltage with linear fits (dashed lines). (**D**) Pseudo-*J-V* curves reconstructed from intensity-dependent absolute PL measurements on the illustrated sample stack. The 2PACz and Me-4PACz curves almost coincide; the dashed lines represent pseudo-*J-V* curves from the sample variations including the electron-selective C$_{60}$ layer, with which all curves are comparable due to the limiting non-radiative recombination at the C$_{60}$ interface. (**E**) Pseudo-*J-V* curves reconstructed from the measurements in (C). Table 1 summarizes the FF values extracted from the pseudo-*J-V* curves. (**F**) Repartition of loss mechanisms lowering the cell's FF below the detailed balance limit, comparing PTAA and Me-4PACz cells.

Table 1 Comparison of "pseudo" fill factors (pFF) and implied open-circuit voltages (iV_{OC}). The values were derived from suns-PL and suns-V_{OC} measurements for our perovskite film on all studied hole-selective layers and on quartz glass. The table also shows the maximum FF attained in *J-V* measurements (max FF) (see also **Fig. 3**). "Half cell" refers to substrate/HTM/absorber, whereas "full cell" denotes the complete solar cell including C$_{60}$, SnO$_2$ and Ag metal electrode.

	Quartz	PTAA	MeO-2PACz	2PACz	Me-4PACz
pFF (%), half cell (suns-PL)	87.9	85.6	85.5	88.3	87.5
pFF (%), half cell + C$_{60}$ (suns-PL)	85.3	85.3	85.3	85.3	85.3
pFF (%), full cell (suns-Voc)		85.8	85.9	86.9	87.9
max FF (%), full cell (*J-V*)		79.8	81.9	81.8	84.0
iV_{OC} (V), half cell (absolute PL)	1.258	1.185	1.215	1.244	1.248
n$_{ID}$, full cell (suns-V_{OC})		1.55	1.51	1.42	1.26

The differences between the electrical *J-V* curves (max. FF 84%) in **Fig. 3B** and pseudo-*J-V* curves (max. FF ~88%) arose from transport losses caused by the finite mobility of the C$_{60}$, non-optimized sample design, ITO sheet resistance and from the measurement setup. **Fig. 3F** summarizes a comparison of the different contributions to FF losses for PTAA and Me-4PACz, derived from comparisons of the pseudo-*J-V* curves to the electrical ones and radiative limits, as previously reported by Stolterfoht *et al.* (*54*). In addition to non-radiative losses at the PTAA interface (red), the film thickness (~10 nm as

9

compared to <1 nm with a SAM) and low conductivity of the PTAA led to greater transport losses than with Me-4PACz.

Integration into monolithic perovskite/silicon tandem solar cells

Efficient passivation in combination with fast hole extraction of Me-4PACz in perovskite single-junctions transferred into monolithic tandem solar cells, which led to significantly higher FF, V_{OC} and stability. A schematic stack of this solar cell is shown in **Fig. 4A**. We use a silicon heterojunction (SHJ) solar cell as the bottom cell (26), based on a 260 µm thick n-type float-zone Si wafer processed as described in the methods. The textured rear side enhanced the near-infrared absorption, whereas the polished front side enabled the deposition of spin-coated perovskite. The 20 nm ITO recombination layer also served as the anchoring oxide for the SAMs (7). The top cell, with the same 1.68 eV perovskite band gap and nominal precursor composition $Cs_{0.05}(FA_{0.77}MA_{0.23})_{0.95}Pb(I_{0.77}Br_{0.23})_3$ as analyzed above, resembled the single-junction stack of ITO/HTL/Perovskite/(LiF)/C_{60}/SnO$_2$/IZO/Ag/LiF. **Fig. 4B** shows a scanning electron microscope cross-section image of a part of the tandem solar cell; no obvious differences were observed between perovskite films on the different HTLs (Figure S24). The molecular SAM cannot be resolved with the SEM. A photograph and layout of the tandem device is shown in Figure S25.

Fig. 4C compares the PCE of tandem solar cells based on PTAA, MeO-2PACz, 2PACz and Me-4PACz, with and without a LiF interlayer at the perovskite/C_{60} interface. With PTAA, the LiF interlayer lead to rapid degradation of the cells (see Figure S26 for individual parameters). Without the interlayer, we achieved an average PCE of 25.25%. In contrast, the average efficiency of MeO-2PACz and 2PACz was 26.21% and 26.56%, respectively. The utilization of a LiF interlayer for Me-4PACz cells increased the V_{OC} but reduced the FF. Thus, both configurations reached a similar average PCE of 26.25% and 26.41%, respectively. However, with Me-4PACz the maximum PCEs are with >29% higher than cells with 2PACz, mainly because of higher FF of up to 81%. These high FF were achieved despite almost all cells being perovskite limited (Table S27). The statistics of all photovoltaic parameters are shown in Figure S26. The *J-V* measurements of the champion cells of each configuration are shown in Figure S28and the PV parameters are summarized in

S29.

The tandem solar cells did not reach FF values as in single-junction cells due to the larger active area (1 cm^2) and a TCO without grid fingers, leading to increased series resistance. The cells showed very high V_{OC}s of up to 1.92 V (Figure S30). With a V_{OC} of ~715 mV from the bottom cell at half illumination (Figure S31), the contribution of the perovskite subcell was ~1.2 V. **Fig. 4D** shows a direct comparison between champion PTAA and Me-4PACz tandem cells, emphasizing that besides the 50 mV improvement in V_{OC}, the enhanced hole extraction boosted the FF by ~4% absolute.
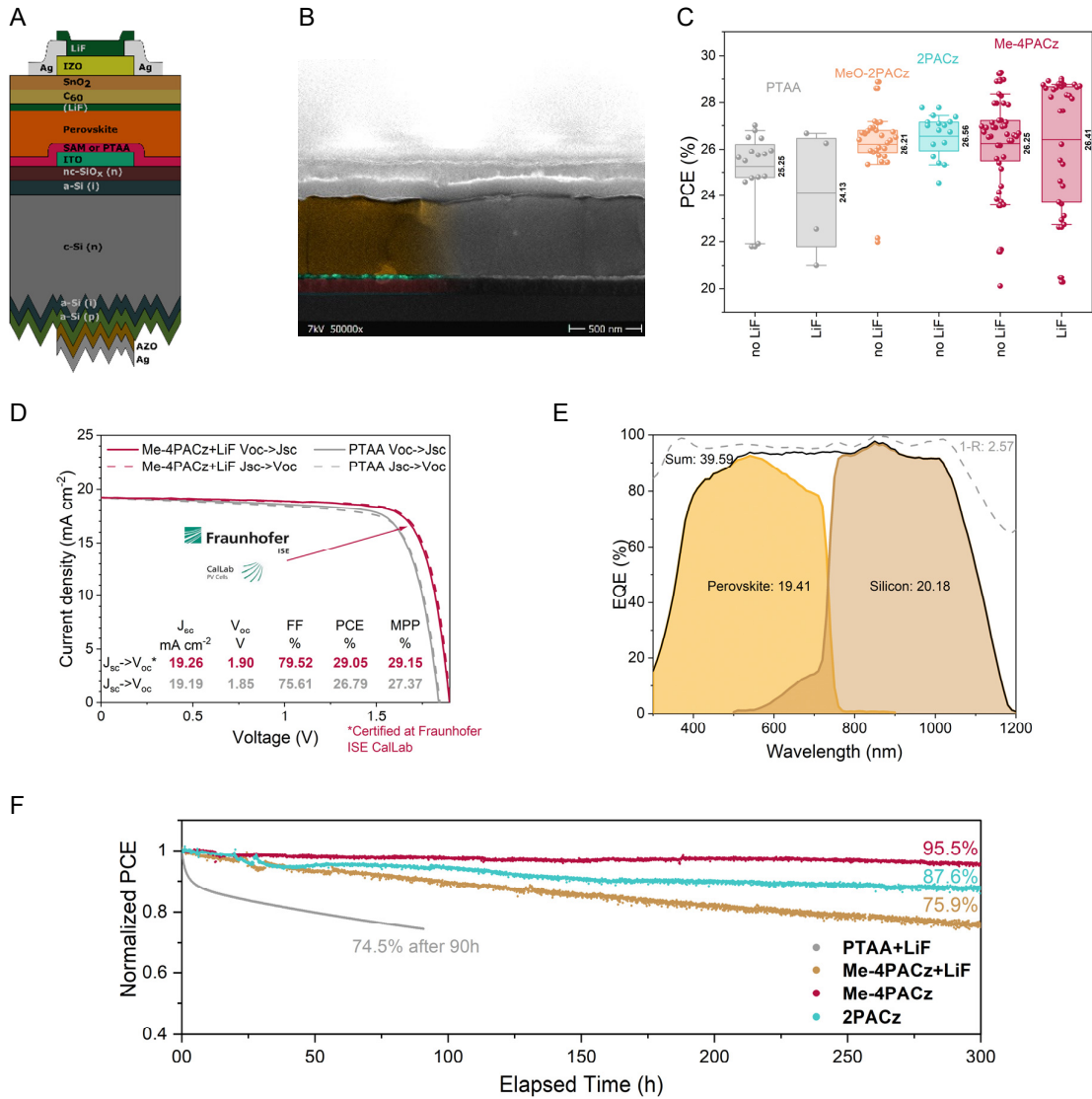
Fig. 4: **Characteristics of monolithic perovskite/silicon tandem solar cells utilizing various HTLs.** (**A**) Schematic stack of the monolithic perovskite/silicon tandem solar cell. (**B**) Scanning electron microscope (SEM) image of a tandem cross-section with Me-4PACz as HTL. (**C**) Statistics of the PCE of several PTAA, MeO-2PACz, 2PACz and Me-4PACz tandem solar cells from *J-V*-scan. (**D**) Certified *J-V* curve conducted at Fraunhofer ISE including the MPP and the device parameters (red) in comparison to a tandem cell with PTAA (gray) as HTL measured in-house. (**E**) External quantum efficiency (EQE) and 1-reflection of the certified tandem cell measured in-house. The AM1.5G-equivalent current densities are given in the legend in mA cm^{-2}. (**F**) Long term MPP-track using a dichromatic LED illumination of non-encapsulated solar cells in air at a controlled temperature of 25 °C and relative humidity of 30 to 40%. The data are normalized to the MPP average of the first 60 minutes of each individual track to account for measurement noise. Due to the fast degradation, the MPP-track of the PTAA+LiF cell is normalized to the first recorded value. The legend shows which HTL and whether the LiF interlayer was used.

We sent a tandem cell with Me-4PACz and LiF interlayer to Fraunhofer ISE CalLab for independent certification (**Fig. 4D**; see Figure S32 for certificate). With a V_{OC} of 1.90 V, FF of 79.4% and J_{SC} of 19.23 mA cm^{-2}, the cell had a PCE of 29.01% when measuring from J_{SC} to V_{OC}, similar to our in-house measurement (Figure S33), and was certified at the MPP with a PCE of 29.15% with a designated area of 1.064 cm². This PCE surpasses other monolithic (*10, 27*) and four-terminal perovskite-based tandem solar cells (*57*), and is on par with the best GaAs single cell at the same active area (*27*).

Fig. 4E shows the external quantum efficiency (EQE) of the certified tandem cell. Under AM1.5G-equivalent illumination conditions, the photogenerated current density J_{ph} in the perovskite and silicon

11

subcells were 19.41 mA cm^{-2} and 20.18 mA cm^{-2}, respectively, which agreed with the measured J_{SC} of 19.23 mA cm^{-2}. The tandem solar cell exhibited a non-ideal current mismatch of 0.77 mA cm^{-2}, and although the perovskite cell sets the tandem shunt resistance, the cell reached an FF of 79.5%. The cumulative photogenerated current density and loss caused by reflection were 39.59 mA cm^{-2} and 2.57 mA cm^{-2}, respectively. A comparison of EQEs and reflection losses between a cell of this work (planar front side) and a fully textured cell by Sahli *et al.* is shown in Figure S34.

After the certification, we fabricated more Me-4PACz tandem solar cells without LiF interlayer (Figure S26), which showed similar average performance as with LiF. The champion cell showed a higher FF of 81% and lower V_{OC} of 1.87 V than without LiF. Together with a J_{SC} of 19.37 mA cm^{-2} this lead to a PCE of 29.29% and a stabilized efficiency of 29.32% (Figure S35).

We measured the stability of different non-encapsulated tandem solar cells (**Fig. 4F**). To track the degradation induced by either the top- or the bottom cell more carefully, we developed a dichromatic LED setup using LEDs with 470 nm and 940 nm center emission wavelengths (Figure S36) and independent intensity calibration and recording. We adjusted the mismatch so that the J_{ph} in the individual subcells was equal to that measured under AM1.5G-equivalent illumination to maintain proper stability tracking of monolithic tandem solar cells (see below and Note S37). The devices were measured under continuous MPP load (using voltage perturbation), at 25 °C and in ambient air with 30-40% relative humidity. The photogenerated current densities of the subcells are given in Table S38 and set which subcell is limiting. The degradation for a perovskite-limited tandem cell with Me-4PACz+LiF showed 75.9% of its initial efficiency (29.13%) after 300 hours. Substituting the Me-4PACz with PTAA (perovskite-limited), the PCE decreased to 74.5% of its initial PCE (25.9%) after only 90 hours.
We additionally tracked a cell with Me-4PACz as HTL without a LiF interlayer to test the intrinsic stability of the HTL/perovskite combination. After 300 hours, the cell still operated at 95.5% of its initial PCE. Although the cells were current-matched, this track monitored a degradation of the perovskite as it directly translates into the performance of the tandem cell and no degradation of the Silicon subcell is expected within these timescales. Our comparison strongly suggests that the utilization of a LiF interlayer reduced the stability. As described in other works (*58–61*), the decrease in stability might be caused by deterioration of the electrodes and C$_{60}$ interface upon migration of Li$^+$ and F$^-$ ions. We would like to note that it is important to declare the mismatch-conditions because the utilization of a NIR-poor spectrum would lead to a silicon limited cell and thus to a higher stability (Note S37). Comparing this result to state-of-the-art stability tests of non-encapsulated tandem solar cells in ambient conditions, where the cells retained and 90% after 61 hours (*62*) and 92% after 100 hours (*13*), our Me-4PACz tandem solar cell showed a superior operational stability.

Beside the long-term stability measurements at 25°C, we conducted an MPP track of a Me-4PACz tandem cell at elevated temperatures. Following the procedure of Jost *et al.*, the temperature was successively increased from 25°C to 85°C and back to 25°C (*63*). There was no loss in PCE after this 200 minutes procedure, despite the increased methylammonium and Br amount of the herein used wide band gap perovskite (Figure S39).

Subcell *J-V* characteristics of a monolithic tandem solar cell

One downside of monolithic multijunction solar cells is that the subcell characteristics are barely accessible. External quantum efficiency measurements are the only subcell-resolved measurements presented in almost all publications reporting multijunction solar cells. Here, we used absolute photoluminescence measurements in each subcell of a representative tandem solar cell (Me-4PACz + LiF). With this, we could estimate the QFLS, and thus the V_{OC} was accessible for both subcells independently. Instead of local excitation and evaluation, we used hyperspectral imaging under 1-sun equivalent excitation fluence (spectra and images shown in **Fig. 5A**).

From the high-energy slope of the absolute PL spectra of the subcells, the individual implied V_{OC}s were calculated, 1.18 V and 0.72 V for the perovskite and silicon subcell, respectively (*18*, *64*). From the PL

spectra, we calculated the PLQY of both subcells yielding values of 1.5% for Si and 0.02% for the perovskite. PLQY values exceeding 5% have been already demonstrated in perovskite single-junction devices for lower band gaps (*19*).

To estimate the pseudo-*J-V* curves of the subcells, we performed absolute electroluminescence (EL) imaging, where the excess charge carriers are generated electrically to access the subcell characteristics (*65–68*). For each injected current, an EL image was recorded, from which the voltage of the subcells can be calculated from an average over the active area (Figure S40). With the reconstructed pseudo-*J-V* curves from injection current-dependent EL imaging, we analyzed the maximum possible efficiency of this cell stack with minimized charge transport losses (see methods and note S3 for more details). We reconstructed both subcell *J-V* curves by calculating the implied voltage at each injected current, yielding a "pseudo" light-*J-V* (JV_{EL}) for each subcell after shifting it by the respective photogenerated current density J_{ph} being calculated from EQE measurements and amount to 18.7 and 20.6 mA cm^{-2} for the top and bottom cell, respectively. The open symbols in **Fig. 5B** show the measured EL data points averaged over the perovskite and silicon subcell and shifted by their respective J_{ph}.

For the perovskite, we additionally fitted the data with a single-diode model to display the *J-V* curve in the whole range, which was otherwise not accessible during the EL measurement. To obtain the tandem JV_{EL}, the voltages of the subcells were summed up for each current density. The dashed line shows the result. The reconstructed curve deviated from the electrically measured *J-V* curve under a solar simulator. This is mainly because EL gave access only to the internal voltage, whereas an electrical *J-V* curve displayed the current density versus external voltage (which is the internal voltage minus the voltage lost at series resistances); more details can be found in Note S41. Hence, a high FF (87.8%) of the JV_{EL} can be regarded as the maximum achievable value for this particular tandem cell if the electrodes and all charge selective layers would pose zero series resistance losses. This would give a PCE of 31.7%, surpassing the theoretical PCE maximum of a silicon single cell (29.4%) (*69*). Thus, this cell stack has the capacity to overcome the 30% barrier through technical optimization of the contacts alone. However, by adjusting the mismatch conditions, even higher efficiencies are achievable.

To find the requirements for the highest efficiency, we fit the silicon subcell with a single-diode model. We conducted SPICE simulations to sweep the photogenerated current densities in the subcell. The single-diode models of the silicon and perovskite subcells were connected in series (schematically shown in Figure S42a) and the cumulative current density was fixed to 39.3 mA cm^{-2} (as it is for AM1.5G-equivalent illumination). Figure S42b shows the photovoltaic parameters as a function of the mismatch ($J_{ph,Si}$-$J_{ph,Pero}$). As shown in a previous publication, the V_{oc} is almost independent of the mismatch, whereas the FF is affected by it (*26*). A minimum FF occurs when the $J_{ph,Si}$ is 0.7 mA cm^{-2} below the $J_{ph,Pero}$. However, simultaneously the J_{SC} is highest under this condition. Here, the highest efficiency is 32.43% in a current matching situation.
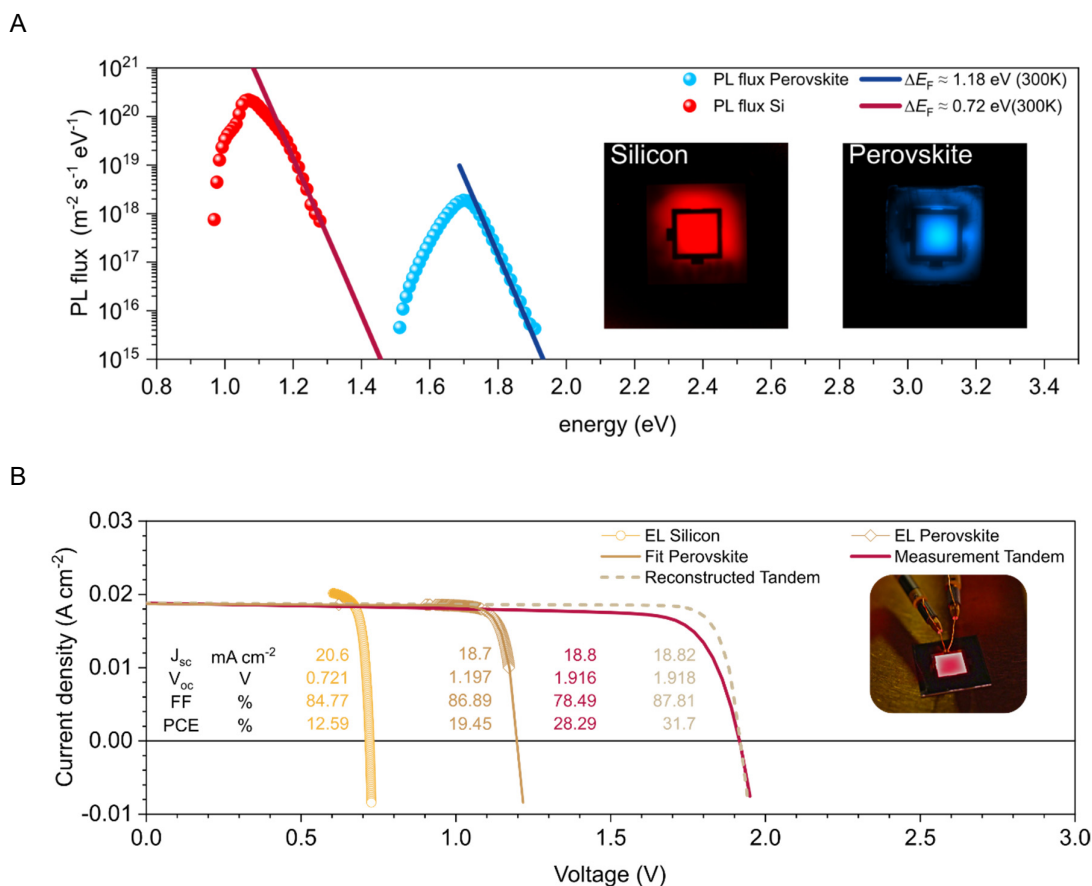
Fig. 5 Luminescence subcell analysis of a tandem solar cell with Me-4PACz and LiF interlayer. (**A**) Absolute PL spectra of the subcells recorded under 1-sun equivalent illumination. The exciting wavelength are 455 nm and 850 nm for the perovskite and silicon subcell, respectively. Additionally, PL images, constructed of the integrated PL fluxes are shown. (**B**) Reconstructed *J-V* curves calculated from injection-dependent electroluminescence measurements (open symbols) and shifting by the photogenerated current density. Furthermore, the perovskite subcell is fitted with a single diode model (solid brown line). The reconstructed tandem *J-V* (dashed line) was calculated by adding the voltages of the subcells for each current density. The *J-V* measurement under simulated 1-sun illumination of this cell is shown as a solid red line. Furthermore, a photo of the tandem solar cell at high injection current is shown. Due to a bandgap of 1.68 eV, the subcell emits light in the visible wavelength range and thus, the emission is visible by eye and with a regular digital camera.

Conclusion

We have demonstrated monolithic perovskite/silicon tandem solar cells with a certified record power conversion efficiency of 29.15%. We elucidated that the combination of efficient passivation at the hole-selective interface and enhanced hole-extraction speed stabilize a perovskite absorber with tandem-relevant bandgap of 1.68 eV. This was revealed by accelerated tests investigating light-induced phase segregation via spot-illumination at 30-suns excitation intensity. Although the electron-selective C_{60} layer in solar cell devices limited the open-circuit voltage, the fill factor was limited by the hole-selective interface. Improved fill factors and photostability were achieved by a new methyl-substituted, carbazole-based self-assembled monolayer (Me-4PACz) that bonds to the transparent conductive oxide of the perovskite cell. With intensity-dependent transient photoluminescence analysis we presented a method to assess charge transfer effects that are relevant for device operation. The faster hole extraction was linked to a low ideality factor of 1.26 for the perovskite subcell, while allowing a high V_{OC} of up to 1.23 V. Fill factors of up to 84% were achieved, and a maximum pseudo-fill factor of 88% was measured by intensity-dependent absolute PL (suns-PL) and suns-V_{OC} measurements. A non-encapsulated tandem

cell with Me-4PACz retained 95.5% of its initial efficiency after 300 h of continuous maximum power point tracking in ambient air, under precise control of the subcell photocurrents to match 1-sun-equivalent conditions. Furthermore, we examined the subcell characteristics without the influence of parasitic resistances by measuring injection-dependent electroluminescence, allowing us to reconstruct the subcell-*J-V* curves. We thereby estimated that upon technical improvements a maximum efficiency of 32.4% for the presented device stack is possible.

Materials and Methods

Single-junction perovskite solar cells were fabricated on glass/ITO substrates. First, the hole-selective layer (PTAA, MeO-2PACz, 2PACz or Me-4PACz) was deposited by spin-coating followed by the one-step spin-coating deposition of the perovskite precursor solution using the antisolvent method. The precursor had a nominal concentration of 1.24 mol/l. Afterwards, layers of C_{60} and SnO_2 were deposited via thermal evaporation and atomic layer deposition. Finally, a layer of silver was deposited via thermal evaporation.

To analyze the quasi-fermi-level splitting, glass/ITO/HTL/perovskite samples were fabricated. The samples were illuminated from the perovskite site with a photon flux equivalent to 1-sun illumination.

Transient photoluminescence was measured by pulsed excitation with 660 nm wavelength and time-correlated single photon counting. The fluence was set to 1-sun equivalent charge generation.

Suns-V_{OC} was measured by illuminating solar cells with varying intensities. For each intensity the stabilized open-circuit voltage was measured. Similarly, suns-PL is measured by illuminating the indicated sample stacks with different intensities. For each intensity (corresponding to a "pseudo" injection current) the quasi-fermi level splitting was calculated.

Tandem solar cells were fabricated by depositing the p-i-n perovskite top cell with various hole-selective layers on a silicon heterojunction solar cell with a textured rear side and polished front side. *J-V* measurements were conducted at simulated AM1.5G illumination in air at 25°C. For long term stability measurements, a custom-built setup with an LED array emitting at 470 nm and 940 nm was designed. This enabled a stable illumination at simulated AM1.5G-equivalent charge carrier generation conditions of the solar cells, which were tracked in air at 25°C. For analyzing the subcells of the tandem solar cell we measured hyperspectral absolute photoluminescence by illuminating the tandem cell with 450 nm light for excitation of the perovskite subcell and an 850 nm wavelength source for the excitation of the silicon subcell. To reconstruct the subcell *J-V*, absolute electroluminescence imaging was conducted at scanned bias voltage.

A detailed description of the fabrication and measurement techniques can be found in the Supplementary Materials.

Acknowledgements

Supplementary Materials:

Materials, Processing and Methods

Figures S1-S43

Table S27, S29, S38

Notes S1, S37, S41

References (70 - 85)

References

1. A. De Vos, Detailed balance limit of the efficiency of tandem solar cells. *J. Phys. D. Appl. Phys.* **13**, 839–846 (1980).

2. W. Shockley, H. J. Queisser, Detailed Balance Limit of Efficiency of p-n Junction Solar Cells. *J. Appl. Phys.* **32**, 510–519 (1961).

3. S. E. Sofia, H. Wang, A. Bruno, J. L. Cruz-Campa, T. Buonassisi, I. M. Peters, Roadmap for cost-effective, commercially-viable perovskite silicon tandems for the current and future PV market. *Sustain. Energy Fuels.* **4**, 852–862 (2020).

4. Z. Li, Y. Zhao, X. Wang, Y. Sun, Z. Zhao, Y. Li, H. Zhou, Q. Chen, Cost Analysis of Perovskite Tandem Photovoltaics. *Joule.* **2**, 1559–1572 (2018).

5. National Renewable Energy Laboratory, "Best Research-Cell Efficiency Chart" (2020), (available at www.nrel.gov/pv/cell-efficiency.html).

6. T. Todorov, T. Gershon, O. Gunawan, Y. S. Lee, C. Sturdevant, L.-Y. Chang, S. Guha, Monolithic Perovskite-CIGS Tandem Solar Cells via In Situ Band Gap Engineering. *Adv. Energy Mater.* **5**, 1500799 (2015).

7. A. Al-Ashouri, A. Magomedov, M. Roß, M. Jošt, M. Talaikis, G. Chistiakova, T. Bertram, J. A. Márquez, E. Köhnen, E. Kasparavičius, S. Levcenco, L. Gil-Escrig, C. J. Hages, R. Schlatmann, B. Rech, T. Malinauskas, T. Unold, C. A. Kaufmann, L. Korte, G. Niaura, V. Getautis, S. Albrecht, Conformal monolayer contacts with lossless interfaces for perovskite single junction and monolithic tandem solar cells. *Energy Environ. Sci.* **12**, 3356–3369 (2019).

8. R. Lin, K. Xiao, Z. Qin, Q. Han, C. Zhang, M. Wei, M. I. Saidaminov, Y. Gao, J. Xu, M. Xiao, A. Li, J. Zhu, E. H. Sargent, H. Tan, Monolithic all-perovskite tandem solar cells with 24.8% efficiency exploiting comproportionation to suppress Sn(ii) oxidation in precursor ink. *Nat. Energy.* **4**, 864–873 (2019).

9. G. E. Eperon, T. Leijtens, K. A. Bush, R. Prasanna, T. Green, J. T.-W. Wang, D. P. McMeekin, G. Volonakis, R. L. Milot, R. May, A. Palmstrom, D. J. Slotcavage, R. A. Belisle, J. B. Patel, E. S. Parrott, R. J. Sutton, W. Ma, F. Moghadam, B. Conings, A. Babayigit, H.-G. Boyen, S. Bent, F. Giustino, L. M. Herz, M. B. Johnston, M. D. McGehee, H. J. Snaith, Perovskite-perovskite tandem photovoltaics with optimized band gaps. *Science (80-.).* **354**, 861–865 (2016).

10. D. Kim, H. J. Jung, I. J. Park, B. W. Larson, S. P. Dunfield, C. Xiao, J. Kim, J. Tong, P. Boonmongkolras, S. G. Ji, F. Zhang, S. R. Pae, M. Kim, S. B. Kang, V. Dravid, J. J. Berry, J. Y. Kim, K. Zhu, D. H. Kim, B. Shin, Efficient, stable silicon tandem cells enabled by anion-engineered wide-bandgap perovskites. *Science (80-.).* **368**, 155–160 (2020).

11. J. Xu, C. C. Boyd, Z. J. Yu, A. F. Palmstrom, D. J. Witter, B. W. Larson, R. M. France, J. Werner, S. P. Harvey, E. J. Wolf, W. Weigand, S. Manzoor, M. F. A. M. van Hest, J. J. Berry, J. M. Luther, Z. C. Holman, M. D. McGehee, Triple-halide wide–band gap perovskites with suppressed phase segregation for efficient tandems. *Science (80-.).* **367**, 1097–1104 (2020).

12. Y. Hou, E. Aydin, M. De Bastiani, C. Xiao, F. H. Isikgor, D.-J. Xue, B. Chen, H. Chen, B. Bahrami, A. H. Chowdhury, A. Johnston, S.-W. Baek, Z. Huang, M. Wei, Y. Dong, J. Troughton, R. Jalmood, A. J. Mirabelli, T. G. Allen, E. Van Kerschaver, M. I. Saidaminov, D. Baran, Q. Qiao, K. Zhu, S. De Wolf, E. H. Sargent, Efficient tandem solar cells with solution-processed perovskite on textured crystalline silicon. *Science (80-.).* **367**, 1135–1140 (2020).

13. B. Chen, Z. J. Yu, S. Manzoor, S. Wang, W. Weigand, Z. Yu, G. Yang, Z. Ni, X. Dai, Z. C. Holman, J. Huang, Blade-Coated Perovskites on Textured Silicon for 26%-Efficient

Monolithic Perovskite/Silicon Tandem Solar Cells. *Joule*. **4**, 850–864 (2020).

14. M. Jošt, L. Kegelmann, L. Korte, S. Albrecht, Monolithic Perovskite Tandem Solar Cells: A Review of the Present Status and Advanced Characterization Methods Toward 30% Efficiency. *Adv. Energy Mater.* **10**, 1904102 (2020).

15. Y. Jiang, I. Almansouri, S. Huang, T. Young, Y. Li, Y. Peng, Q. Hou, L. Spiccia, U. Bach, Y.-B. Cheng, M. A. Green, A. Ho-Baillie, Optical analysis of perovskite/silicon tandem solar cells. *J. Mater. Chem. C*. **4**, 5679–5689 (2016).

16. I. L. Braly, D. W. DeQuilettes, L. M. Pazos-Outón, S. Burke, M. E. Ziffer, D. S. Ginger, H. W. Hillhouse, Hybrid perovskite films approaching the radiative limit with over 90% photoluminescence quantum efficiency. *Nat. Photonics*. **12**, 355–361 (2018).

17. D. W. deQuilettes, S. Koch, S. Burke, R. K. Paranji, A. J. Shropshire, M. E. Ziffer, D. S. Ginger, Photoluminescence Lifetimes Exceeding 8 μs and Quantum Yields Exceeding 30% in Hybrid Perovskite Thin Films by Ligand Passivation. *ACS Energy Lett.* **1**, 438–444 (2016).

18. T. Kirchartz, J. A. Márquez, M. Stolterfoht, T. Unold, Photoluminescence-Based Characterization of Halide Perovskites for Photovoltaics. *Adv. Energy Mater.* **10**, 1904134 (2020).

19. Z. Liu, L. Krückemeier, B. Krogmeier, B. Klingebiel, J. A. Márquez, S. Levcenko, S. Öz, S. Mathur, U. Rau, T. Unold, T. Kirchartz, Open-Circuit Voltages Exceeding 1.26 V in Planar Methylammonium Lead Iodide Perovskite Solar Cells. *ACS Energy Lett.* **4**, 110–117 (2019).

20. P. Caprioglio, F. Zu, C. M. Wolff, J. A. Márquez Prieto, M. Stolterfoht, P. Becker, N. Koch, T. Unold, B. Rech, S. Albrecht, D. Neher, High open circuit voltages in pin-type perovskite solar cells through strontium addition. *Sustain. Energy Fuels*. **3**, 550–563 (2019).

21. Q. Jiang, Y. Zhao, X. Zhang, X. Yang, Y. Chen, Z. Chu, Q. Ye, X. Li, Z. Yin, J. You, Surface passivation of perovskite film for efficient solar cells. *Nat. Photonics*. **13**, 460–466 (2019).

22. S. Yang, J. Dai, Z. Yu, Y. Shao, Y. Zhou, X. Xiao, X. C. Zeng, J. Huang, Tailoring Passivation Molecular Structures for Extremely Small Open-Circuit Voltage Loss in Perovskite Solar Cells. *J. Am. Chem. Soc.* **141**, 5781–5787 (2019).

23. L. Krückemeier, U. Rau, M. Stolterfoht, T. Kirchartz, How to Report Record Open-Circuit Voltages in Lead-Halide Perovskite Solar Cells. *Adv. Energy Mater.* **10**, 1902573 (2020).

24. P. K. Nayak, S. Mahesh, H. J. Snaith, D. Cahen, Photovoltaic solar cell technologies: analysing the state of the art. *Nat. Rev. Mater.* **4**, 269–285 (2019).

25. A. Rajagopal, R. J. Stoddard, S. B. Jo, H. W. Hillhouse, A. K. Y. Jen, Overcoming the Photovoltage Plateau in Large Bandgap Perovskite Photovoltaics. *Nano Lett.* **18**, 3985–3993 (2018).

26. E. Köhnen, M. Jošt, A. B. Morales-Vilches, P. Tockhorn, A. Al-Ashouri, B. Macco, L. Kegelmann, L. Korte, B. Rech, R. Schlatmann, B. Stannowski, S. Albrecht, Highly efficient monolithic perovskite silicon tandem solar cells: analyzing the influence of current mismatch on device performance. *Sustain. Energy Fuels*. **3**, 1995–2005 (2019).

27. M. A. Green, E. D. Dunlop, J. Hohl-Ebinger, M. Yoshita, N. Kopidakis, A. W. Y. Ho-Baillie, Solar cell efficiency tables (Version 55). *Prog. Photovoltaics Res. Appl.* **28**, 3–15 (2020).

28. P. Caprioglio, C. M. Wolff, O. J. Sandberg, A. Armin, B. Rech, S. Albrecht, D. Neher, M. Stolterfoht, On the Origin of the Ideality Factor in Perovskite Solar Cells. *Adv. Energy Mater.* **10**, 2000502 (2020).

29. M. A. Green, A. W. Y. Ho-Baillie, Pushing to the Limit: Radiative Efficiencies of Recent Mainstream and Emerging Solar Cells. *ACS Energy Lett.* **4**, 1639–1644 (2019).

30. K. Jäger, L. Korte, B. Rech, S. Albrecht, Numerical optical optimization of monolithic planar perovskite-silicon tandem solar cells with regular and inverted device architectures. *Opt. Express*. **25**, A473 (2017).

31. M. Jošt, E. Köhnen, A. B. Morales-Vilches, B. Lipovšek, K. Jäger, B. Macco, A. Al-Ashouri, J. Krč, L. Korte, B. Rech, R. Schlatmann, M. Topič, B. Stannowski, S. Albrecht, Textured interfaces in monolithic perovskite/silicon tandem solar cells: advanced light management for improved efficiency and energy yield. *Energy Environ. Sci.* **11**, 3511–3523 (2018).

32. T. Leijtens, K. A. Bush, R. Prasanna, M. D. McGehee, Opportunities and challenges for tandem solar cells using metal halide perovskite semiconductors. *Nat. Energy*. **3**, 828–838 (2018).

33. E. T. Hoke, D. J. Slotcavage, E. R. Dohner, A. R. Bowring, H. I. Karunadasa, M. D. McGehee, Reversible photo-induced trap formation in mixed-halide hybrid perovskites for photovoltaics. *Chem. Sci.* **6**, 613–617 (2015).

34. D. J. Slotcavage, H. I. Karunadasa, M. D. McGehee, Light-Induced Phase Segregation in Halide-Perovskite Absorbers. *ACS Energy Lett.* **1**, 1199–1205 (2016).

35. S. Mahesh, J. M. Ball, R. D. J. Oliver, D. P. McMeekin, P. K. Nayak, M. B. Johnston, H. J. Snaith, Revealing the origin of voltage loss in mixed-halide perovskite solar cells. *Energy Environ. Sci.* **13**, 258–267 (2020).

36. M. Saliba, T. Matsui, J.-Y. Seo, K. Domanski, J.-P. Correa-Baena, M. K. Nazeeruddin, S. M. Zakeeruddin, W. Tress, A. Abate, A. Hagfeldt, M. Grätzel, Cesium-containing triple cation perovskite solar cells: improved stability, reproducibility and high efficiency. *Energy Environ. Sci.* **9**, 1989–1997 (2016).

37. M. Stolterfoht, P. Caprioglio, C. M. Wolff, J. A. Márquez, J. Nordmann, S. Zhang, D. Rothhardt, U. Hörmann, Y. Amir, A. Redinger, L. Kegelmann, F. Zu, S. Albrecht, N. Koch, T. Kirchartz, M. Saliba, T. Unold, D. Neher, The impact of energy alignment and interfacial recombination on the internal and external open-circuit voltage of perovskite solar cells. *Energy Environ. Sci.* **12**, 2778–2788 (2019).

38. D. Luo, W. Yang, Z. Wang, A. Sadhanala, Q. Hu, R. Su, R. Shivanna, G. F. Trindade, J. F. Watts, Z. Xu, T. Liu, K. Chen, F. Ye, P. Wu, L. Zhao, J. Wu, Y. Tu, Y. Zhang, X. Yang, W. Zhang, R. H. Friend, Q. Gong, H. J. Snaith, R. Zhu, Enhanced photovoltage for inverted planar heterojunction perovskite solar cells. *Science (80-.)*. **360**, 1442–1446 (2018).

39. Q. Wang, E. Mosconi, C. Wolff, J. Li, D. Neher, F. De Angelis, G. P. Suranna, R. Grisorio, A. Abate, Rationalizing the Molecular Design of Hole-Selective Contacts to Improve Charge Extraction in Perovskite Solar Cells. *Adv. Energy Mater.* **9**, 1900990 (2019).

40. C. Huang, W. Fu, C.-Z. Li, Z. Zhang, W. Qiu, M. Shi, P. Heremans, A. K. Y. Jen, H. Chen, Dopant-Free Hole-Transporting Material with a C 3 h Symmetrical Truxene Core for Highly Efficient Perovskite Solar Cells. *J. Am. Chem. Soc.* **138**, 2528–2531 (2016).

41. A. Torres, L. G. C. Rego, Surface Effects and Adsorption of Methoxy Anchors on Hybrid Lead Iodide Perovskites: Insights for Spiro-MeOTAD Attachment. *J. Phys. Chem. C*. **118**, 26947–26954 (2014).

42. M. Saliba, S. Orlandi, T. Matsui, S. Aghazada, M. Cavazzini, J.-P. Correa-Baena, P. Gao, R. Scopelliti, E. Mosconi, K.-H. Dahmen, F. De Angelis, A. Abate, A. Hagfeldt, G. Pozzi, M. Graetzel, M. K. Nazeeruddin, A molecularly engineered hole-transporting material for efficient perovskite solar cells. *Nat. Energy*. **1**, 15017 (2016).

43. Y. Lin, B. Chen, Y. Fang, J. Zhao, C. Bao, Z. Yu, Y. Deng, P. N. Rudd, Y. Yan, Y. Yuan, J. Huang, Excess charge-carrier induced instability of hybrid perovskites. *Nat. Commun.* **9**, 4981 (2018).

44. B. Chen, J. Song, X. Dai, Y. Liu, P. N. Rudd, X. Hong, J. Huang, Synergistic Effect of Elevated Device Temperature and Excess Charge Carriers on the Rapid Light-Induced Degradation of Perovskite Solar Cells. *Adv. Mater.* **31**, 1902413 (2019).

45. N. Phung, A. Al-Ashouri, S. Meloni, A. Mattoni, S. Albrecht, E. L. Unger, A. Merdasa, A. Abate, The Role of Grain Boundaries on Ionic Defect Migration in Metal Halide Perovskites. *Adv. Energy Mater.* **10**, 1903735 (2020).

46. B. Krogmeier, F. Staub, D. Grabowski, U. Rau, T. Kirchartz, Quantitative analysis of the transient photoluminescence of CH 3 NH 3 PbI 3 /PC 61 BM heterojunctions by numerical simulations. *Sustain. Energy Fuels*. **2**, 1027–1034 (2018).

47. F. Staub, H. Hempel, J.-C. Hebig, J. Mock, U. W. Paetzold, U. Rau, T. Unold, T. Kirchartz, Beyond Bulk Lifetimes: Insights into Lead Halide Perovskite Films from Time-Resolved Photoluminescence. *Phys. Rev. Appl.* **6**, 044017 (2016).

48. M. Krumrey, G. Ulm, High-accuracy detector calibration at the PTB four-crystal monochromator beamline. *Nucl. Instruments Methods Phys. Res. Sect. A Accel. Spectrometers, Detect. Assoc. Equip.* **467**–**468**, 1175–1178 (2001).

49. D. Skroblin, A. Schavkan, M. Pflüger, N. Pilet, B. Lüthi, M. Krumrey, Vacuum-compatible photon-counting hybrid pixel detector for wide-angle x-ray scattering, x-ray diffraction, and x-ray reflectometry in the tender x-ray range. *Rev. Sci. Instrum.* **91**, 023102 (2020).

50. K. A. Bush, A. F. Palmstrom, Z. J. Yu, M. Boccard, R. Cheacharoen, J. P. Mailoa, D. P. McMeekin, R. L. Z. Z. Hoye, C. D. Bailie, T. Leijtens, I. M. Peters, M. C. Minichetti, N. Rolston, R. Prasanna, S. Sofia, D. Harwood, W. Ma, F. Moghadam, H. J. Snaith, T. Buonassisi, Z. C. Holman, S. F. Bent, M. D. McGehee, 23.6%-efficient monolithic perovskite/silicon tandem solar cells with improved stability. *Nat. Energy*. **2**, 17009 (2017).

51. J.-F. Guillemoles, T. Kirchartz, D. Cahen, U. Rau, Guide for the perplexed to the Shockley–Queisser model for solar cells. *Nat. Photonics*. **13**, 501–505 (2019).

52. J. Seo, S. Park, Y. Chan Kim, N. J. Jeon, J. H. Noh, S. C. Yoon, S. Il Seok, Benefits of very thin PCBM and LiF layers for solution-processed p-i-n perovskite solar cells. *Energy Environ. Sci.* **7**, 2642–2646 (2014).

53. M. Stolterfoht, C. M. Wolff, J. A. Márquez, S. Zhang, C. J. Hages, D. Rothhardt, S. Albrecht, P. L. Burn, P. Meredith, T. Unold, D. Neher, Visualization and suppression of interfacial recombination for high-efficiency large-area pin perovskite solar cells. *Nat. Energy*. **3**, 847–854 (2018).

54. M. Stolterfoht, M. Grischek, P. Caprioglio, C. M. Wolff, E. Gutierrez-Partida, F. Peña-Camargo, D. Rothhardt, S. Zhang, M. Raoufi, J. Wolansky, M. Abdi-Jalebi, S. D. Stranks, S. Albrecht, T. Kirchartz, D. Neher, How To Quantify the Efficiency Potential of Neat Perovskite Films: Perovskite Semiconductors with an Implied Efficiency Exceeding 28%. *Adv. Mater.* **32**, 2000080 (2020).

55. N. Tessler, Y. Vaynzof, Insights from Device Modeling of Perovskite Solar Cells. *ACS Energy Lett.* **5**, 1260–1270 (2020).

56. W. Wang, P. Chen, C. Chiang, T. Guo, C. Wu, S. Feng, Synergistic Reinforcement of Built-In Electric Fields for Highly Efficient and Stable Perovskite Photovoltaics. *Adv. Funct. Mater.* **30**, 1909755 (2020).

57. B. Chen, S.-W. Baek, Y. Hou, E. Aydin, M. De Bastiani, B. Scheffel, A. Proppe, Z. Huang, M. Wei, Y.-K. Wang, E.-H. Jung, T. G. Allen, E. Van Kerschaver, F. P. García de Arquer, M. I. Saidaminov, S. Hoogland, S. De Wolf, E. H. Sargent, Enhanced optical path and electron diffusion length enable high-efficiency perovskite tandems. *Nat. Commun.* **11**, 1257 (2020).

58. R. Quintero-Bermudez, J. Kirman, D. Ma, E. H. Sargent, R. Quintero-Torres, Mechanisms of

LiF Interlayer Enhancements of Perovskite Light-Emitting Diodes. *J. Phys. Chem. Lett.* **11**, 4213–4220 (2020).

59. Z. Li, C. Xiao, Y. Yang, S. P. Harvey, D. H. Kim, J. A. Christians, M. Yang, P. Schulz, S. U. Nanayakkara, C.-S. Jiang, J. M. Luther, J. J. Berry, M. C. Beard, M. M. Al-Jassim, K. Zhu, Extrinsic ion migration in perovskite solar cells. *Energy Environ. Sci.* **10**, 1234–1242 (2017).

60. S.-M. Bang, S. S. Shin, N. J. Jeon, Y. Y. Kim, G. Kim, T.-Y. Yang, J. Seo, Defect-Tolerant Sodium-Based Dopant in Charge Transport Layers for Highly Efficient and Stable Perovskite Solar Cells. *ACS Energy Lett.* **5**, 1198–1205 (2020).

61. S. N. Habisreutinger, T. Leijtens, G. E. Eperon, S. D. Stranks, R. J. Nicholas, H. J. Snaith, Carbon Nanotube/Polymer Composites as a Highly Stable Hole Collection Layer in Perovskite Solar Cells. *Nano Lett.* **14**, 5561–5568 (2014).

62. F. Sahli, J. Werner, B. A. Kamino, M. Bräuninger, R. Monnard, B. Paviet-Salomon, L. Barraud, L. Ding, J. J. Diaz Leon, D. Sacchetto, G. Cattaneo, M. Despeisse, M. Boccard, S. Nicolay, Q. Jeangros, B. Niesen, C. Ballif, Fully textured monolithic perovskite/silicon tandem solar cells with 25.2% power conversion efficiency. *Nat. Mater.* **17**, 820–826 (2018).

63. M. Jošt, B. Lipovšek, B. Glažar, A. Al-Ashouri, K. Brecl, G. Matič, A. Magomedov, V. Getautis, M. Topič, S. Albrecht, Perovskite Solar Cells go Outdoors: Field Testing and Temperature Effects on Energy Yield. *Adv. Energy Mater.* **10**, 2000454 (2020).

64. T. Unold, L. Gütay, in *Advanced Characterization Techniques for Thin Film Solar Cells* (Wiley-VCH Verlag GmbH & Co. KGaA, Weinheim, Germany, 2011), pp. 151–175.

65. S. Chen, L. Zhu, M. Yoshita, T. Mochizuki, C. Kim, H. Akiyama, M. Imaizumi, Y. Kanemitsu, Thorough subcells diagnosis in a multi-junction solar cell via absolute electroluminescence-efficiency measurements. *Sci. Rep.* **5**, 7836 (2015).

66. D. Alonso-Alvarez, N. Ekins-Daukes, Photoluminescence-Based Current–Voltage Characterization of Individual Subcells in Multijunction Devices. *IEEE J. Photovoltaics*. **6**, 1004–1011 (2016).

67. S. Roensch, R. Hoheisel, F. Dimroth, A. W. Bett, Subcell I-V characteristic analysis of GaInP/GaInAs/Ge solar cells using electroluminescence measurements. *Appl. Phys. Lett.* **98**, 251113 (2011).

68. D. Hinken, K. Ramspeck, K. Bothe, B. Fischer, R. Brendel, Series resistance imaging of solar cells by voltage dependent electroluminescence. *Appl. Phys. Lett.* **91**, 182104 (2007).

69. A. Richter, M. Hermle, S. W. Glunz, Reassessment of the Limiting Efficiency for Crystalline Silicon Solar Cells. *IEEE J. Photovoltaics*. **3**, 1184–1191 (2013).

70. L. Mazzarella, Y. Lin, S. Kirner, A. B. Morales-Vilches, L. Korte, S. Albrecht, E. Crossland, B. Stannowski, C. Case, H. J. Snaith, R. Schlatmann, Infrared Light Management Using a Nanocrystalline Silicon Oxide Interlayer in Monolithic Perovskite/Silicon Heterojunction Tandem Solar Cells with Efficiency above 25%. *Adv. Energy Mater.* **9**, 1803241 (2019).

71. U. Rau, Reciprocity relation between photovoltaic quantum efficiency and electroluminescent emission of solar cells. *Phys. Rev. B*. **76**, 085303 (2007).

72. H. Hempel, T. Unold, R. Eichberger, Measurement of charge carrier mobilities in thin films on metal substrates by reflection time resolved terahertz spectroscopy. *Opt. Express*. **25**, 17227 (2017).

73. M. Meusel, R. Adelhelm, F. Dimroth, A. W. Bett, W. Warta, Spectral mismatch correction and spectrometric characterization of monolithic III-V multi-junction solar cells. *Prog. Photovoltaics Res. Appl.* **10**, 243–255 (2002).

74. G. Ashiotis, A. Deschildre, Z. Nawaz, J. P. Wright, D. Karkoulis, F. E. Picca, J. Kieffer, The

fast azimuthal integration Python library: pyFAI. *J. Appl. Crystallogr.* **48**, 510–519 (2015).

75. Z. Ni, C. Bao, Y. Liu, Q. Jiang, W.-Q. Wu, S. Chen, X. Dai, B. Chen, B. Hartweg, Z. Yu, Z. Holman, J. Huang, Resolving spatial and energetic distributions of trap states in metal halide perovskite solar cells. *Science (80-.).* **367**, 1352–1358 (2020).

76. C. M. Wolff, F. Zu, A. Paulke, L. P. Toro, N. Koch, D. Neher, Reduced Interface-Mediated Recombination for High Open-Circuit Voltages in CH 3 NH 3 PbI 3 Solar Cells. *Adv. Mater.* **29**, 1700159 (2017).

77. H. Hempel, C. J. Hages, R. Eichberger, I. Repins, T. Unold, Minority and Majority Charge Carrier Mobility in Cu2ZnSnSe4 revealed by Terahertz Spectroscopy. *Sci. Rep.* **8**, 14476 (2018).

78. H. Hempel, A. Redinger, I. Repins, C. Moisan, G. Larramona, G. Dennler, M. Handwerg, S. F. Fischer, R. Eichberger, T. Unold, Intragrain charge transport in kesterite thin films—Limits arising from carrier localization. *J. Appl. Phys.* **120**, 175302 (2016).

79. F. Peña-Camargo, P. Caprioglio, F. Zu, E. Gutierrez-Partida, C. M. Wolff, K. Brinkmann, S. Albrecht, T. Riedl, N. Koch, D. Neher, M. Stolterfoht, Halide Segregation versus Interfacial Recombination in Bromide-Rich Wide-Gap Perovskite Solar Cells. *ACS Energy Lett.* **5**, 2728–2736 (2020).

80. J. A. Bardecker, H. Ma, T. Kim, F. Huang, M. S. Liu, Y.-J. Cheng, G. Ting, A. K.-Y. Jen, Self-assembled Electroactive Phosphonic Acids on ITO: Maximizing Hole-Injection in Polymer Light-Emitting Diodes. *Adv. Funct. Mater.* **18**, 3964–3971 (2008).

81. P. N. Dickerson, A. M. Hibberd, N. Oncel, S. L. Bernasek, Hydrogen-Bonding versus van der Waals Interactions in Self-Assembled Monolayers of Substituted Isophthalic Acids. *Langmuir.* **26**, 18155–18161 (2010).

82. N. Nerngchamnong, L. Yuan, D.-C. Qi, J. Li, D. Thompson, C. A. Nijhuis, The role of van der Waals forces in the performance of molecular diodes. *Nat. Nanotechnol.* **8**, 113–118 (2013).

83. R.-F. Dou, X.-C. Ma, L. Xi, H. L. Yip, K. Y. Wong, W. M. Lau, J.-F. Jia, Q.-K. Xue, W.-S. Yang, H. Ma, A. K. Y. Jen, Self-Assembled Monolayers of Aromatic Thiols Stabilized by Parallel-Displaced π−π Stacking Interactions. *Langmuir.* **22**, 3049–3056 (2006).

84. M. Boccard, C. Ballif, Influence of the Subcell Properties on the Fill Factor of Two-Terminal Perovskite–Silicon Tandem Solar Cells. *ACS Energy Lett.* **5**, 1077–1082 (2020).

85. P. Caprioglio, M. Stolterfoht, C. M. Wolff, T. Unold, B. Rech, S. Albrecht, D. Neher, On the Relation between the Open-Circuit Voltage and Quasi-Fermi Level Splitting in Efficient Perovskite Solar Cells. *Adv. Energy Mater.* **9**, 1901631 (2019).

Supplementary Materials

Contents

Materials and Methods

Materials for perovskite cell preparation

Anhydrous DMSO (dimethyl sulfoxide), anh. DMF (dimethylformamide), anh. Anisole, PTAA (poly [bis (4-phenyl) (2,5,6-trimentlyphenyl) amine]) and lithium fluoride (purity $\geq 99.99\,\%$) were purchased from Sigma Aldrich. C_{60} (sublimed) was bought from CreaPhys GmbH. FAI (formamidinium iodide) and MABr (methylammonium bromide) were purchased from Dyenamo. PbI_2 and $PbBr_2$ were bought from TCI. CsI was purchased from abcr GmbH. The ceramic 2-inch IZO target was purchased from FHR Anlagenbau GmbH. The SAMs MeO-2PACz and 2PACz were synthesized by TCI. The synthesis of Me-4PACz and the (Me-)nPACz series by us is described in the synthesis section at the end of this document. Ethanol (anh.) for the SAMs was bought from VWR (no difference was observed when using Ethanol from other suppliers, independent of the water content).

Perovskite single-junction preparation

The perovskite solar cell has an inverted (*p-i-n*) planar structure and is deposited on ITO-covered glass (Automated Research GmbH, both 7 Ohm/sq and 15 Ohm/sq sheet conductivities were used in this study), which was cleaned with Mucasol (2% in DI-water, substrates were brushed), DI-water, acetone and isopropanol, each for 15 minutes in an ultrasonic bath. Afterwards the surface was "activated" for 10-15 minutes in an UV-O_3 cleaner (FHR UVOH 150 Lab), which is a crucial step before SAM functionalization (for the tandem cells as well). The single-junction cell configuration is ITO/HTL/Perovskite/(LiF)/C_{60}/SnO_2/Ag, where the HTL is PTAA, MeO-2PACz, 2PACz or Me-4PACz. All the spin-coating layer deposition steps were conducted in a nitrogen atmosphere. The hole transport material PTAA (2 mg ml^{-1} in toluene) was deposited using spin-coating (5000 rpm for 30 s, 5 s acceleration), followed by heating for 10 min at 100 °C. The rotation was reduced for the SAM-solutions to 3000 rpm (used concentration of the SAM solutions = 1 mmol/l, or ~0.3 mg/ml). The perovskite was prepared following the typical triple cation process. In short, 1.5 M nominal PbI_2 and $PbBr_2$ in DMF:DMSO = 4:1 volume were first prepared as stock solutions (shaken overnight at 60 °C) and then added to FAI and MABr with 9 % PbX_2 excess, respectively (X = I or Br) (typical amounts were 0.3 g FAI and 0.06 g of MABr). The so obtained $FAPbI_3$ and $MAPbBr_3$ were then mixed in 77:23 volume ratio to obtain the "double cation" perovskite. Finally, 5 vol-% of 1.5 M nominal CsI in DMSO was added to the perovskite precursor (stock solution prepared one day before, typically ~50 mg

23

powder). 100 µl of perovskite solution was then spread on the substrate and spun using one step spin-coating process (3500 for 35 s, 5 s acceleration). 10-13 s before the end of the program, 300 µl of Anisole as the anti-solvent was dripped on the film. The films were then annealed at 100 °C for 15-30 min. Afterwards, 20 nm of C_{60} was thermally evaporated at a rate of 0.15 Å s^{-1} onto the perovskite film. Optionally, as indicated, a 1 nm-thick LiF interlayer was deposited between C_{60} and perovskite, evaporated at a rate of 0.05 Å s^{-1}, within the same vacuum run as the C_{60} layer. 20 nm of SnO_2 were then deposited by thermal ALD in an Arradiance GEMStar reactor. Tetrakis(dimethylamino)tin(IV) (TDMASn) was used as the Sn precursor and was held at 60 °C in a stainless-steel container. Water was used as oxidant, and was delivered from a stainless-steel container without active heating, whereas the precursor delivery manifold was heated to 115 °C. For the deposition at 80 °C, the TDMASn/purge1/H_2O/purge2 times were 1s/10s/0.2s/15s with corresponding nitrogen flows of 30sccm/90sccm/90sccm/90sccm. With this, 140 cycles lead to 20 nm tin oxide. More details can be found in a previous publication (*26*). We noticed a beneficial effect when letting the TDMASn bottle cool down to room temperature when not in use. Finally, 100 nm Ag were deposited by thermal evaporation at a rate of 1 Å s^{-1}.

Silicon solar cell preparation

The silicon heterojunction (SHJ)-bottom cell was fabricated from a 260 µm thick, ~3 Ω cm^{-1} polished FZ <100> n-type crystalline silicon (c-Si) wafer in a rear junction configuration. The front surface of the wafer was left polished by capping with a PECVD deposited SiO_2 prior to wet texturing to obtain random pyramids with <111> facets. After removal of the capping in HF another final RCA clean and HF dip (1 % dilution in water) were done and an approx. 5 nm thick, intrinsic (i) amorphous silicon (a-Si:H) layer stack was grown on both sides of the c-Si wafer in order to passivate the c-Si surface. On the textured rear-side, an approx. -5-nm thick, p-doped a-Si:H layer stack was deposited to form the hole contact (junction). On the polished front-side, a 95-nm thick (20-nm thick for single-junction reference cells), n-doped nanocrystalline silicon oxide layer (nc-SiO$_x$:H) with a refractive index, n, of 2.7 at 633 nm was used as the electron contact of the SHJ bottom cell and the optical intermediate layer between the top and the bottom cells (*70*). The a- and nc-Si layers were deposited with an Applied Materials (AKT1600) plasma enhanced chemical vapor deposition (PECVD) cluster tool. In order to contact the bottom cell a ZnO:Al/Ag layer stack was deposited on the textured rear-side and a 20 nm (70-nm thick for single-junction references) thick ITO layer was deposited on the polished front-side on top of the nc-SiO$_x$:H interlayer. Both depositions were DC-sputtered in an in-line sputter tool from Leybold Optics using Ar/O_2 gas mixtures. For the ITO a tube target with 95/5 doping ratio and for the AZO a tube target with 1% Al_2O_3 in ZnO was used. Both contact-layer stack of the silicon were deposited using aligned shadow masks with an opening of 1.13 x 1.13 cm^2 (2 x 2 cm^2 for single-junction reference). For single-junction reference cells with an aperture area of 2 x 2 cm^2, an Ag grid was screen-printed on top of the front ITO.

Preparation of tandem solar cells

The bottom cells were blown clean with N_2 and UV-O_3-treated for 15 minutes. The same HTL, perovskite, (LiF), C_{60} and SnO_2 deposition as described above was conducted on the silicon bottom cells. Subsequently, 100 nm IZO (Roth&Rau MicroSys 200 PVD, ceramic target purchased from FHR Anlagenbau GmbH) are deposited by sputtering. The 2-inch ceramic target consisted of 90 %wt. In_2O_3 and 10 %wt. ZnO. At a RF-power of 70 W the cells oscillated under the target to have a uniform deposition. 0.2%$_{vol}$ O_2 was added to the chamber. The previously optimized layer (*26*) has a mobility, carrier density and resistivity of 43.5 cm^2 V^{-1} s^{-1}, 3.4·10^{20} cm^{-3} and 4.2·10^{-4} Ω cm, respectively. A 100 nm silver frame was thermally evaporated through a shadow mask to collect the charge carriers without a need of grid fingers. Lastly, 100 nm LiF is evaporated as an antireflective coating by thermal evaporation. The active area is defined by the metal frame and is slightly larger than 1 cm^2. A photo and schematic of a monolithic tandem solar cell is shown in Figure S25.

Luminescence spectroscopy techniques

Time-dependent steady-state photoluminescence

Time-dependent steady state absolute photoluminescence measurements were performed on a home-built setup using an integrating sphere, where the samples were placed at the edge of the sphere. The PL was collected with a fiber connected to a CCD-array spectrometer (Ocean Optics). The samples were excited with a continuous-wave laser at 532 nm emission wavelength, a photon flux of ~1.2E16 photons/s and a spot size on the sample of 0.12 cm² (around 1-sun-equivalent excitation fluence, calibrated with a certified silicon reference cell). The 30-suns case was realized by a focusing lens to reduce the spot size to 0.4 mm². The spot size was measured by fitting a Gaussian curve to the beam profile extracted from CCD imaging the laser spot. The 1-sun 0.4 mm² case was realized by a focusing lens and appropriate ND filters. Non-absorbed laser light and emitted photoluminescence fluxes were simultaneously detected by the spectrometer, of which the spectral sensitivity was calibrated using a NIST-traceable halogen lamp. The spectral time evolutions of the perovskite films were recorded with an integration time of 300 ms and delay of 2-3 s between each recording. Measurements were carried out in air; the samples were measured promptly after they were taken out from the N2-filled glovebox.

Absolute PL and pseudo-*J-V*s

Excitation for the PL imaging measurements was performed with a 520 nm CW laser (Insaneware) through an optical fibre into an integrating sphere. The intensity of the laser was adjusted to a 1 sun equivalent intensity by illuminating a 1 cm²-sized perovskite solar cell under short-circuit and matching the current density to the J_{SC} under the sun simulator (e.g. ~22.0 mA cm^{-2} at 100 mW cm^{-2}, or 1.375x10^{21} photons m^{-2} s^{-1}). A second optical fiber was used from the output of the integrating sphere to an Andor SR393i-B spectrometer equipped with a silicon CCD camera (DU420A-BR-DD, iDus). The system was calibrated by using a halogen lamp with known spectral irradiance, which was shone into to integrating sphere. A spectral correction factor was established to match the spectral output of the detector to the calibrated spectral irradiance of the lamp. The spectral photon density was obtained from the corrected detector signal (spectral irradiance) by division through the photon energy (hf), and the photon numbers of the excitation and emission were obtained from numerical integration using Matlab. In a last step, three fluorescent test samples with high specified PLQY supplied from Hamamatsu Photonics where measured where the specified value could be accurately reproduced within a small relative error of less than 5%.

The samples were illuminated in the integrating sphere using the same 520 nm CW laser (Insaneware) as described above. A continuously variable neutral density filter wheel (ThorLabs) was used to attenuate the laser power to measure at different intensities which was monitored using an additional Si photodetector. The samples were illuminated at a given intensity for a variable illumination time using an electrical shutter. After an illumination time of 1 second, the PL spectra were recorded by averaging 30 spectra taken using a detector exposure time of 30 µs. The electrical shutter was then closed and the filter wheel was moved to the next position and the steps were repeated. A custom-built Labview code was written to automate the measurement, and a Matlab code to automate the data evaluation.

Pseudo-*J-V*s

The pseudo-*J-V*s were deduced from the intensity-dependent QFLS or V_{OC} measurements as recently demonstrated in ref. (*54*). This was done by calculating the dark-current density from the generated current density at a given light intensity in equivalent suns. E.g. 1 sun corresponds to 22.0 mA cm^{-2}, 1% of a sun to 0.220 mA cm^{-2}. The obtained dark current was then plotted against the measured QFLS or V_{OC} at the given light intensity to create a transport/series resistance-free dark *J-V*-curve. This curve was then shifted to the J_{SC} in the *J-V*-measurement to create the pseudo-*J-V* curve allowing to read of the pseudo- (or implied) FF and V_{OC} of the measured partial cell stack (e.g. the neat film, or perovskite/transport layer junction) or the complete cell. We note, that the implied FF is only impacted

25

156

by the non-radiative (and radiative) recombination processes in the studied sample but not by charge transport or resistive losses that are induced by the active layer or the transport layers, and resistances (e.g. the ITO sheet resistance).

Intensity-dependent V_{OC} measurements

Steady-state intensity dependent V_{OC} measurements were obtained with a 520 nm continuous wave laser (Insaneware) providing a power of 1 W. A continuously variable neutral density filterwheel (ThorLabs) was used to attenuate the laser power (up to OD 6). The light intensity was thereby simultaneously measured with a silicon photodetector and a Keithley 485 to improve the accuracy of the measurement. The measurement was performed by measuring the V_{OC} after a 1 second illumination at a given light intensity and then the J_{SC} after 1 second illumination before the filterwheel rotated to the next position. A custom-built LabView code was written to automate the measurement.

Transient photoluminescence

TrPL measurements were carried out in a home-built setup using 660 nm excitation laser light from a supercontinuum light source (SuperK) with a 25-35 μm spot size. The samples were excited from the glass side to avoid increased reflection stray light, however, no significant difference in decay times was observed between excitation from both sides. We chose the longer wavelength excitation to avoid effects of charge diffusion from a high to low carrier density region. The excitation pulse had a repetition rate of 150 kHz and the PL emission was collected panchromatically through a photomultiplier and time-correlated single photon counting technique. The fluence was controlled with a tuneable neutral density filter and monitored with a power meter.

Absolute photo and electroluminescence imaging of tandems

Absolute PL imaging measurements were performed with two 450 nm LEDs for the perovskite subcell and with an 850 nm LED for the excitation of the silicon subcell. The excitation intensities for both measurements was set to 1.4×10^{21} photons m^{-2} s^{-1}. The photoluminescence image detection was performed with a charge-coupled device (CCD) camera (Allied Vision) for the perovskite subcell and with an InGaAs based camera for the Si subcell. Both cameras were coupled with a liquid crystal tunable filter unit. The systems were calibrated to absolute photon numbers.

Quantitative electroluminescence imaging was performed by sweeping a voltage between 1.4 and 2.0 V with a 2 mV voltage step and 0.5 s dwell time. The dark current J_{dark} was recorded for the sweeps. To avoid large data collection a luminescence image at every step for every subcell was recorded at the maximum energy of the luminescence. The intensity of the images was scaled to absolute photon numbers with a full hyperspectral image collected at a given injection. This results in a data set containing the electroluminescence yield of each subcell (j) $Y_{EL}^{j}(J_{dark})$ as a function of the injected current J_{dark}. The radiative current of every subcell J_{rad}^{j} is calculated by multiplying the $Y_{EL}^{j}(J_{dark})$ by the elementary charge. Finally, the voltage of the subcells V^{j} is calculated with:

$$V^{j} = kT \ln\left(\frac{J_{rad}^{j} + J_{0,rad}^{j}}{J_{0,rad}^{j}}\right).$$

Here, $J_{0,rad}^{j}$ is calculated from the EQE of the individual subcells following the reciprocity theorem (*71*):

$$J_{0,rad}^{j} = q \int EQE^{j}(E)\phi_{bb}(E)dE.$$

26

157

Terahertz-Probe (OPTP) spectroscopy

Optical-Pump Terahertz-Probe (OPTP) spectroscopy can measure the transient photo-excited sheet conductivity $\Delta\sigma_S$ and sum mobility $\mu_\Sigma = \mu_e + \mu_h$ of the electron mobility μ_e and the hole mobility μ_h. The terahertz pulses are generated by optical rectification of 800 nm pulses in a ZnTe crystal. These terahertz pulses are guided through the perovskite sample and the transmitted terahertz field T is measured by electro-optical sampling in a second ZnTe crystal. Additionally, the perovskite samples can be photo-excited by pump pulses with a wavelength of 400 nm and a pulse length of $\approx$150 fs. These charge carriers alter the transmission of the terahertz probe pulse by ΔT, which is also detected. The derived pump-induced change in THz transmission $\Delta T/T$ is analyzed by the thin-film approximation in equation (S5) for the photo-excited sheet conductivity $\Delta\sigma_S$, which is the integral of the induced photoconductivity $\Delta\sigma$ over the sample thickness d. The parameters are the speed of light c, the permittivity of the vacuum ε_0, and the terahertz refractive index of the substrates n_{sub}, which is 1.95 for the used quartz glass substrate.

$$\Delta\sigma_s = \int_{x=0}^{d} \Delta\sigma \, dx = -\varepsilon_0 c (1 + n_{sub}) \frac{\frac{\Delta T}{T}}{1 + \frac{\Delta T}{T}} \quad (1)$$

The transient of the photo-excited sheet conductivity is measured by scanning the delay of the pump pulse by an optical delay line. In this case, the terahertz pulse is sampled at its maximum. Additionally, the full terahertz pulse was scanned by a second delay line at a pump delay time of 10 ps. After both ΔT and T are Fourier-transformed, the photo-excited sheet conductivity spectrum is derived by Equation (1). The sum mobility spectrum is obtained by Equation (2) from the photo-excited sheet conductivity, the flux of the pump beam of 7 x 10^{11} photons/pulse/cm^2, and the reflectance of the pump beam at 400 nm of 25%. The quantum yield of exciton dissociation in such mixed halide perovskites is approximately 1 at room temperature.

$$\Sigma\mu = \mu_e(f,t) + \mu_h(f,t) = \frac{\Delta\sigma_s}{q\varphi_{pump}(1-R)} \quad (2)$$

The gained sum mobility is a spectrum at the frequencies from 0.5 to 3 THz, which constitute the terahertz probe pulse. The observed flat frequency-dependence in fig. 1 indicates no significant difference between the measured terahertz mobilities and the DC-value, which is relevant for the device operation or carrier diffusion.

Further details on the OPTP measurement can be found in (*72*).

Single junction solar cell characterization (Current-Voltage curves, EQE)

The *J-V* curves of single-junction cells were recorded in nitrogen atmosphere with a solar simulator (Oriel LCS-100) and Keithley 2400 source-measure unit, controlled by a custom LabView program. The intensity was calibrated to AM1.5G 1-sun-equivalent with a filtered KG3 Silicon reference solar cell, calibrated by Fraunhofer ISE (spectral mismatch is around 0.997, within the measurement error, thus no correction was applied). *J-V* scans were as performed in a 2-point-probe configuration. The typical step size was 20 mV, with an integration time of 20 ms and settling time of 20 ms (250 mV/s). The cells did not experience any preconditioning. Shunted or partially shunted devices (mostly due to scratches and not perfectly clean substrates) were not considered in the analysis.

EQE spectra were recorded with an Oriel Instruments QEPVSI-b system with a Newport 300 W xenon arc lamp, controlled by TracQ-Basic software. The system is calibrated using a Si reference cell with known spectral response before every measurement. The electrical response of the device under test is measured with a Stanford Research SR830 Lock-In amplifier (time constant of 0.3 s) and evaluated in TracQ. The typical short-circuit current mismatch between integrated external quantum efficiency (EQE) times AM1.5G irradiance and values from *J-V* scans is around 1% if the area of the cell precisely known (considering shadowing through the mask during metal evaporation).

27

Tandem solar cell characterization (Current-Voltage curves, EQE)

The tandem solar cells were measured in air under AM1.5G (1 sun) equivalent illumination with a Wavelabs Sinus-70 LED class AAA sun simulator. The cells did not experience any preconditioning. For calibration we used a slightly modified calibration route compared to Meusel *et al.* (*73*). We adjusted the spectrum such that for both subcells it led to the photogenerated current densities obtained by EQE measurements. Thus, for a perovskite-limited cell, we first increased the intensity of the blue light in order to get a silicon-limited cell. Subsequently, the NIR region was adjusted until the J_{SC} of the silicon-limited tandem solar cell was equal to the $J_{ph,Si}$ (calculated from EQE and AM1.5G spectrum). Finally, the intensity of the blue light was decreased until the tandem solar cell was perovskite-limited again and the J_{SC} was equal to the $J_{ph,Pero}$. For a silicon-limited cell it is done vice versa. The backside of the cell was contacted with a metal vacuum chuck at 25°C, whereas the front side was contacted with two Au probes. A black laser-cut aperture mask covered the substrate outside of the active area. The *J-V* measurements and MPP tracks were recorded using a home-built LabView software. The EQE spectra were recorded with a home-built setup using chopped (79 Hz) monochromatic light from a Xe and He lamp, respectively. To measure the EQE of the perovskite subcell, the silicon subcell was saturated using an LED with 850 nm peak emission. To maintain short circuit conditions, a bias voltage of 0.6 V was applied. The silicon subcell was measured by saturating the perovskite subcell with blue light from a LED (455 nm) and applying a bias voltage of 1 V.

The boxes in the PV parameter boxplots indicate the 25/75 percentiles and the whiskers mark the 10/90 percentiles. The line in the plots mark the respective average value.

Helium Ultra-Violet Photoelectron Spectroscopy

Helium ultra-violet photoelectron spectroscopy (He-UPS) with an excitation energy of 21.2 eV was applied to investigate the secondary electron cutoff (SECO) and the valence band onset. Four different layer stacks were investigated: i) ITO-covered glass substrate, two different SAMs ii) Me-4PACz and iii) 2PACz on an ITO-covered substrate and iv) ITO/PTAA/Perovskite (1.68 eV band gap). All samples were transferred from the glovebox to the vacuum system in a portable chamber in nitrogen atmosphere. The measurements were conducted using a step width of 0.05 eV and a dwell time of 3 seconds. Between the sample, contacted via the ITO, and the electron analyzer a bias voltage of 7 V was applied. Both, the SECO and the valence band onset (E_F-E_V), were determined by the intersection of the linear fit of the data with the linear background. Considering the excitation energy of He I, (21.2 eV - SECO) leads directly to the work function (E_{Vak}-E_F) of the material.

X-ray diffraction

Grazing-incidence wide-angle X-ray scattering (GIWAXS) data were acquired at the four crystal monochromator beamline of the Physikalisch-Technische Bundesanstalt at the synchrotron radiation facility BESSY II (*48*). Under high vacuum, X-rays with 8 keV photon energy ($\lambda = 1.5498$ Å) were incident on 1 cm^2 samples prepared with stack silicon/ITO/HTL/perovskite/C$_{60}$ to mimic growth conditions in devices, and with C$_{60}$ to prevent any material changes under vacuum. Grazing incidence angles from 1.5° to 6.5° were used to probe different depths in the film and at high angles the broadening due to the beam footprint on the sample is reduced. Scattering was detected with a vacuum-compatible version of the PILATUS3 X 100K hybrid photon-counting detector (DECTRIS) (*49*). This detector was rotated around the sample center in 4.5° steps through 16 positions at a sample-to-detector distance of 206 mm with 30 s acquisition at each detector angle. The photon flux was approximately 1.82 x 10^8 s^{-1} with 80 μm beam height. Data was reduced and corrected using *PyFAI* (*74*).

Further 1D X-ray diffraction measurements were acquired using a PANalytical X'Pert Pro MPD (multi-purpose diffractometer) in grazing incidence geometry (GI-XRD). Diffraction patterns were collected with a step size of 0.02 degree, for 6 seconds at each step and at a grazing angle of 1°, with the measurement conducted in air.

Long term stability measurement

Monolithic tandem solar cells were tracked over 300 h at the maximum power point (MPP) with a self-constructed ageing setup in collaboration with the University of Ljubljana (with them providing the LED-array and measurement components). To guarantee homogenous illumination the LED-array consists of 193 LEDs, 144 of which are blue LEDs and 49 are near-infrared LEDs with a wavelength of 470 nm and 940 nm, respectively. The normalized spectra are given in Figure S36. With an independent tunability of both intensities via two potentiometers, the photocurrent of the top and bottom cell can be adjusted to increase or decrease the current mismatch as intended. The bottom cell is electrically connected to a copper block on the backside, whereas the top cell is connected with 2 pogo-pins. Under ambient conditions (relative humidity of 30-40%, measured with a calibrated humidity tracker) the measurement took place in a closed housing at a stable 25°C, while the cells were kept in place with a diaphragm pump. While monitoring the current and voltage of each cell at MPP (using voltage perturbation) the intensity of a blue and infrared reference diode was logged to account for any drops/fluctuation of illumination.

Ultraviolet photoelectron spectroscopy
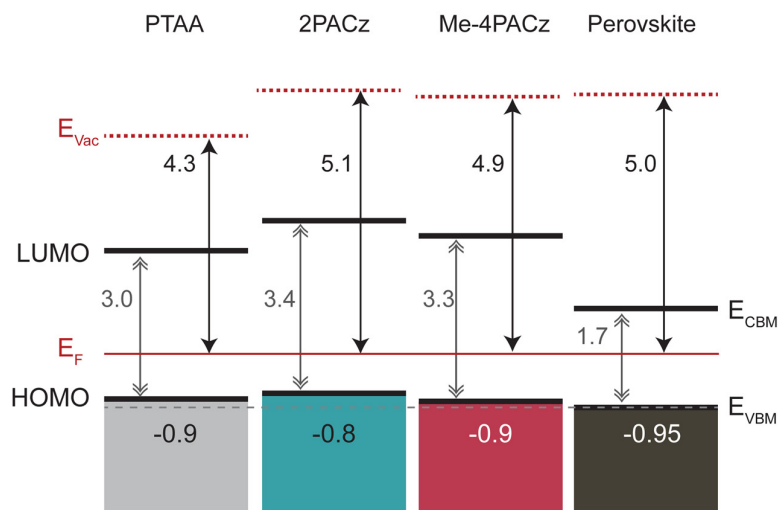
Figure S1 Energetic diagram comparing the alignment between perovskite valence band edge and the HOMO levels of the studied hole-selective layers. A correlation is apparent between fill factor and how close the alignment between perovskite valence band edge and HOMO level of the hole-selective layers is; considering that PTAA has a low conductivity but significant thickness (~10 nm), which adds series resistance that influences the FF as well. The absorption onset in Figure S43 was used to estimate the "bandgap" of the SAMs. The data for PTAA is from ref. (7) (measured at another UPS setup).
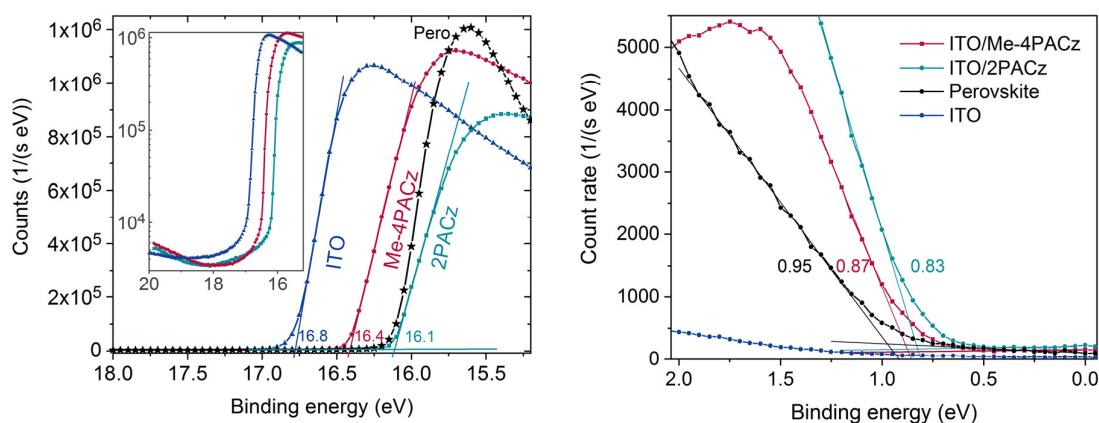
Figure S2 ITO work function shift by the HTLs. Helium ultra-violet photoelectron spectroscopy comparing ITO substrates covered by Me-4PACz or 2PACz, or PTAA/Perovskite (1.68 eV bandgap). The energy scale is relative to the Fermi level. The left panel shows the secondary electron cutoff region and the right panel shows the valence band onset. Both were fitted with a linear function and the intersection with the linear background was read as the work function and the valence band onset, respectively.

Additional photoluminescence data
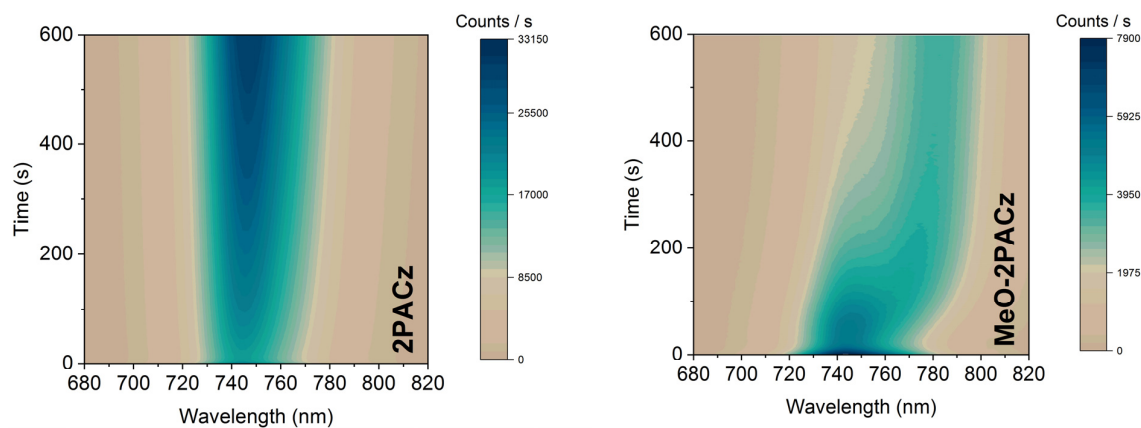
Figure S3 Photoluminescence time evolution of 1.68 eV bandgap perovskite on ITO/2PACz and ITO/MeO-2PACz, complementing Figure 1 of the main text.
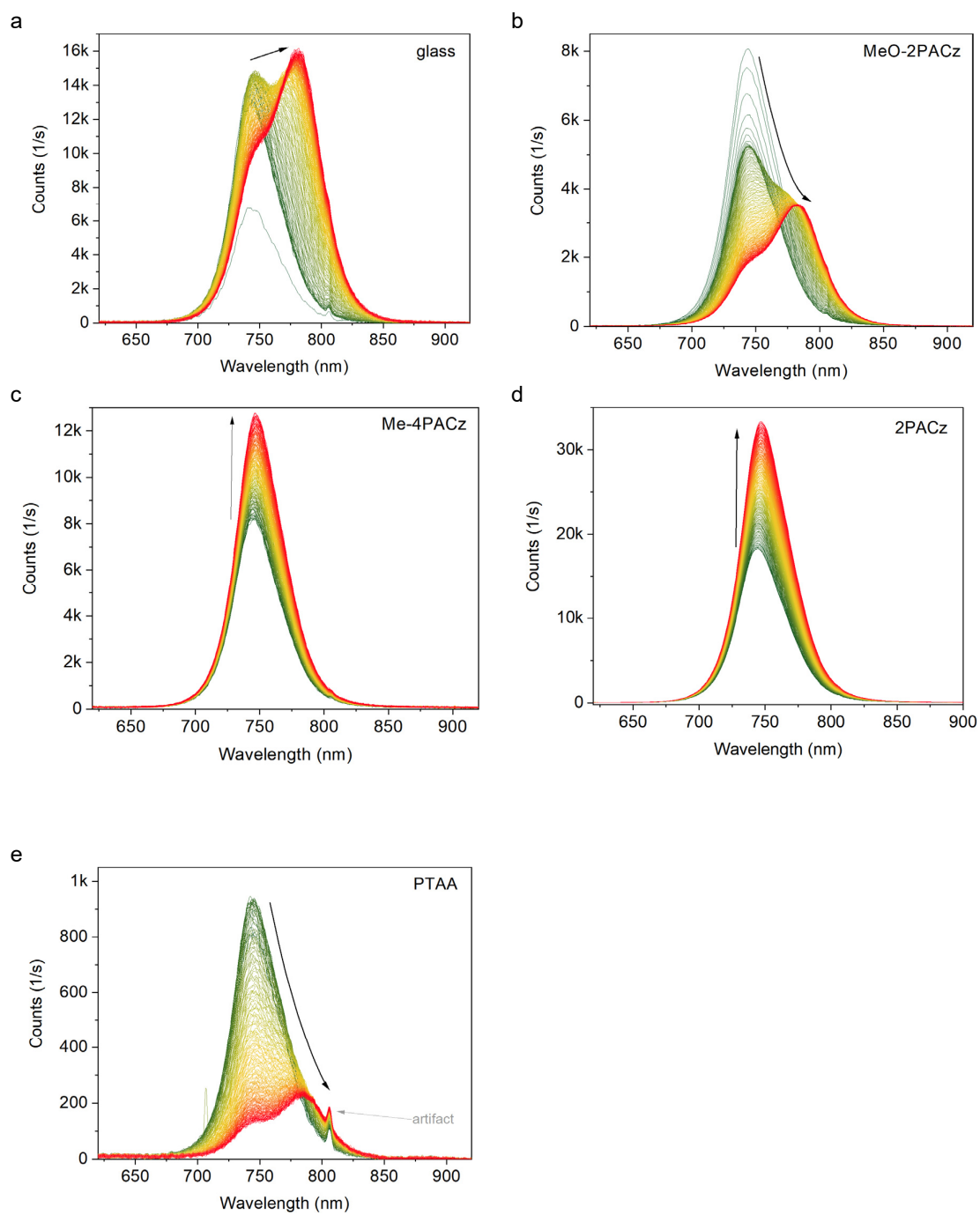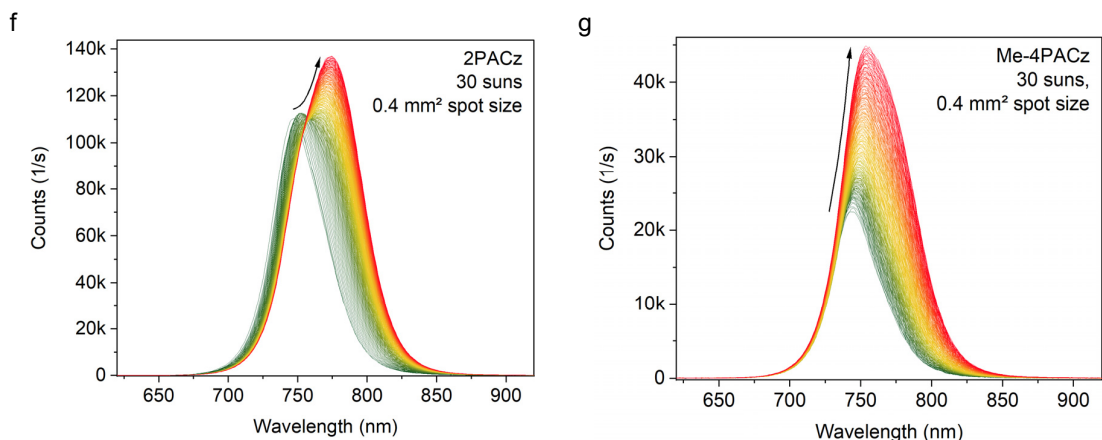
Figure S4 Photoluminescence spectra over time (10 min) under spot-illumination at 1-sun-equivalent excitation fluence. **a-e** show the spectra used for the plots Fig. 1 and Fig. S3. **f-g** show the spectra upon 30-suns fluence and smaller spot illumination.
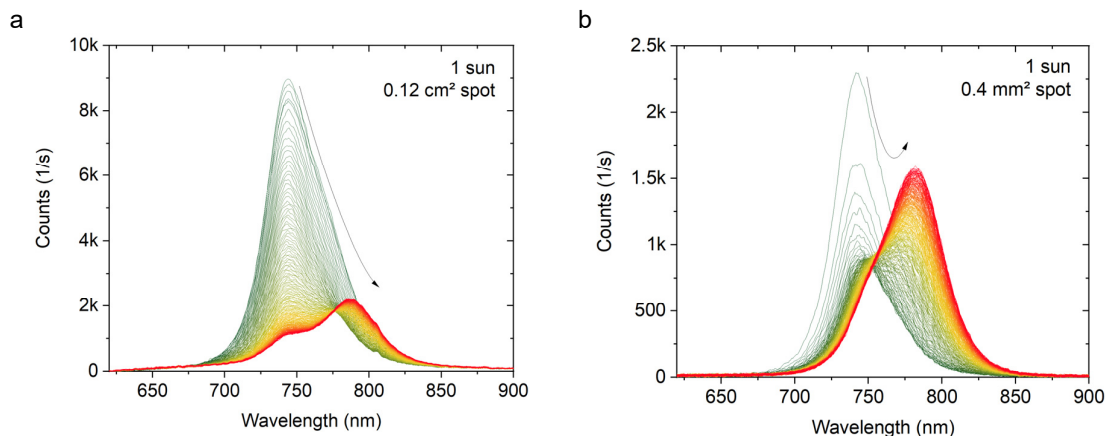
Figure S5 Photoluminescence spectra over time (10 min) of a perovskite film on ITO/MeO-2PACz. The same sample was measured with two different spot sizes: 0.12 cm² (a) and 0.4 mm² (b), each at different positions on the sample – but the excitation fluence was kept the same by placing additional ND1+ND0.4 filters into the beam for the 0.4 mm² case. This demonstrates that a smaller spot, i.e. steeper charge carrier gradient and larger spot edge-to-area ratio, causes a quicker rise of PL of segregated low-bandgap regions (*45*) (which are more emissive than Br-rich phases). The same behavior was observed for all studied substrate/HTL configurations.

33
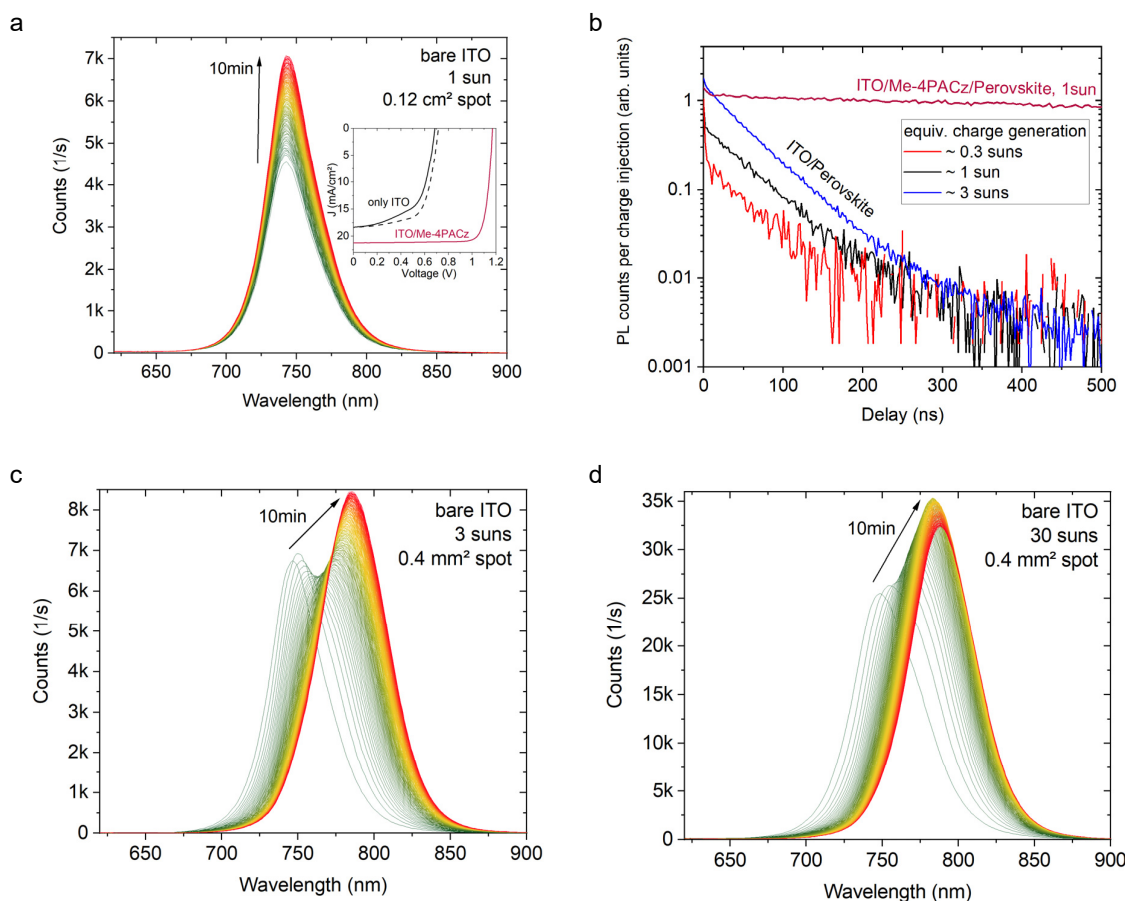
Figure S6 PL on a bare glass/ITO substrate (cleaned and O3-treated like the HTL-covered substrates). **a**, PL evolution in the same experiment as for Figure S4, showing that the conductive substrate could mitigate charge accumulation and thus suppress a double-peak formation. However, due to the ITO being not hole-selective enough, it is not suitable for efficient device operation with the herein used perovskite (inset). **b**, TrPL transients on a bare ITO/perovskite sample for three different excitation fluences. A mono-exponential fit to the 1-sun transient between 50 and 150 ns yielded a decay time of 70 ns. For comparison, the Me-4PACz transient as shown in the main text is included. **c**, Same experiment as in a, but with a smaller illumination spot size. **d**, same spot size as in c, but with 10-times higher intensity.
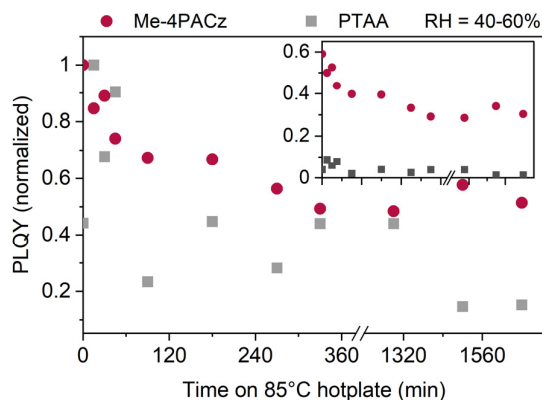
Figure S7 Photoluminescence quantum yield under 85°C in air of perovskite films on Si substrates covered with PTAA and Me-4PACz. The inset shows the non-normalized values. The samples were left on a hotplate in air (relative humidity 40-60 %) and cooled to room temperature before every PL measurement. The PLQY of the PTAA sample fell to almost background-noise level after 90 min. The PL was measured in air under 1-sun equivalent generation with spot illumination (532 nm excitation, 0.12 cm² spot size).
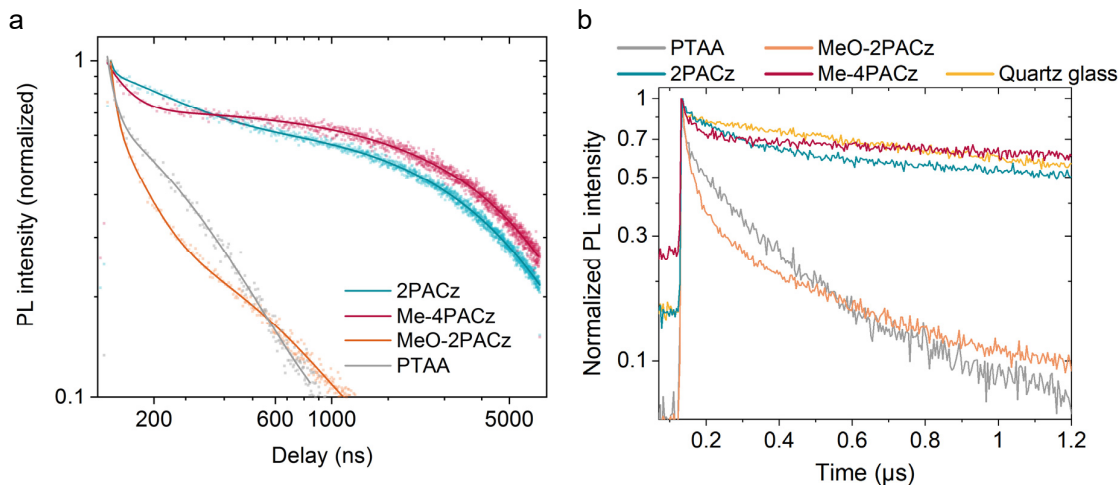
Figure S8 a, Fits to the TrPL transients shown in Figure 2 of the main text. The fits are triple-exponential functions (no physical model, arbitrary choice to fit the data to help with the differential lifetime evaluation) with offsets and are used to compute the derivative of the transients (or differential lifetimes) to avoid high noise levels arising from differentiating the raw experimental data. **b**, Zoom-in to Fig. 2A of the main text.

Note S1

The ratio of higher-order to first-order recombination from the TrPL transients was extracted by first fitting a mono-exponential function to the linear part in logarithmic scale and extrapolating it until t=0. Thus, we could identify the part of the transient corresponding to higher order processes, including radiative recombination (see Figure S10). Integrating the higher-order part of the transient and dividing it by the total area under the transient gives the ratio. Doing this for all investigated generation conditions yielded Figure 2C of the main text.
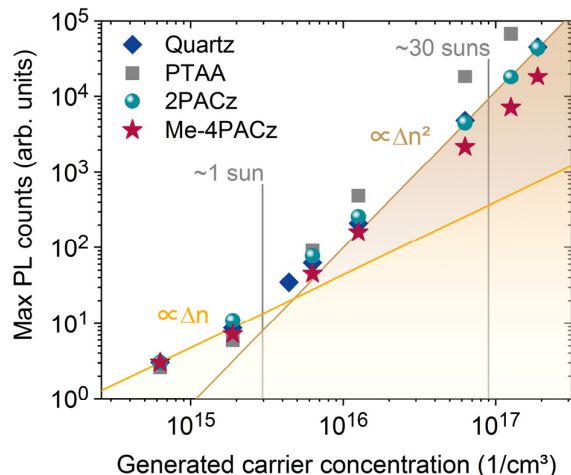
Figure S9 Charge generation regimes in TrPL. Maximum PL intensity for a series of excitation conditions. The transition from linear to quadratic dependence marks the carrier concentration above the background concentration or at which radiative recombination dominates. Although above 1-sun-equivalent carrier generation, Me-4PACz and 2PACz are in this regime, the Me-4PACz transients still showed mostly mono-exponential decay (Figure S10).
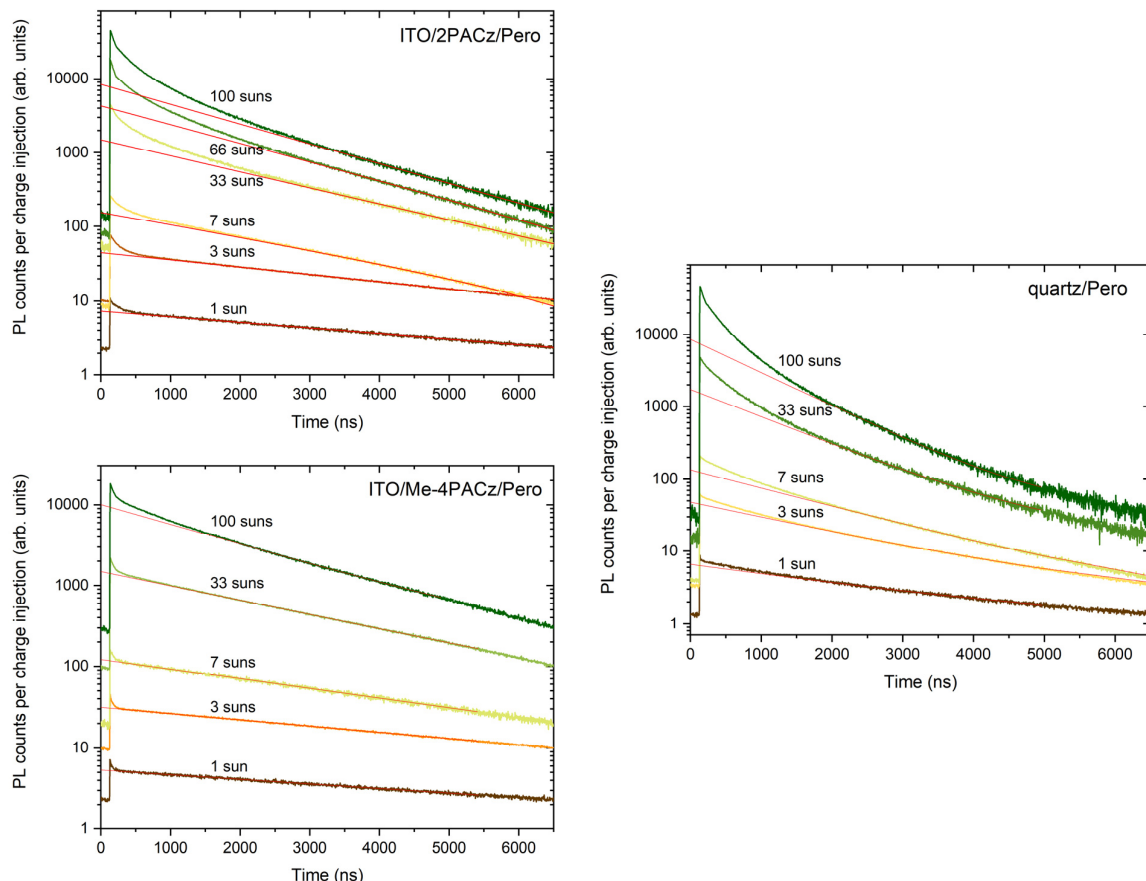
Figure S10 TrPL transients at different excitation fluences of perovskite absorbers on quartz, 2PACz and Me-4PACz. The red lines are linear fits to the mono-exponential tails of the transients. The area under the transients, the area under the linear fit and between linear fit and transient were used for the calculation of Figure 2C of the main text. Only the Me-4PACz transient shows little to no deviation from mono-exponential decay after the charge transfer process.
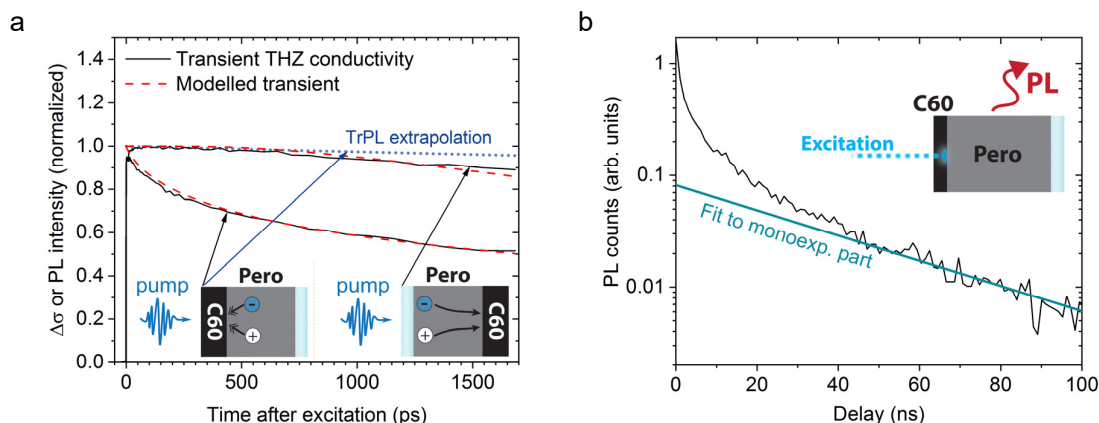
Figure S11 Speed of electron extraction into the C60 layer. a, Terahertz conductivity transients of perovskite films on quartz glass covered by the electron-selective C60 layer. Notably, the decay is considerably slower when the pump pulse hits the quartz side first. A fast decay is visible when the blue pump pulse hits the C_{60} side first since the majority of charge carriers are excited at the C_{60}-near perovskite surface and fast extraction to the C_{60} layer or non-radiative recombination occurs at/in the C_{60} layer (*53*, *75*, *76*). Assuming negligible non-radiative recombination at the quartz interface, the comparison to the C60-side illumination hints that charge carriers diffuse through the perovskite film with a transition time of ~2.3 ns (eq-S1). In order to differentiate whether electron extraction or non-radiative recombination decays the transient, the plot shows an extrapolation of the mono-

exponential part of a TrPL transient on the same sample (b), where trap-assisted recombination dominates, showing that trap-assisted non-radiative recombination would be too slow to be assigned as the underlying cause of the fast decay. Hence, it can be assigned to electron transfer into the C60, happening with a time constant of roughly 1 ns, significantly faster than hole transfer as indicated in Figure 2B (~300 ns). The C60 transients can be modeled by the ambipolar diffusion of the charge carriers to the contact layers with an ambipolar diffusion coefficient D_{am} of 0.5 cm^2/s and their extraction with an extraction velocity S of 1.6 x 10^{4}cm/s. To this end, the continuity equation with S as a boundary condition is used (eq-S2 & eq-S3).

$$\tau_{Transition} \approx \frac{d^2}{\pi^2 D_{am}} + \frac{d}{2S}$$

(eq-S1)

$$\frac{d}{dt}\Delta n = D_{am}\frac{d^2}{dx^2}\Delta n$$

(eq-S2)

$$D_{am}\frac{d}{dx}\Delta n|_{x=0} = -S\Delta n$$

(eq-S3)

$$D_{am} = 2\frac{k_B T}{e}\frac{\mu_e \mu_h}{\mu_e + \mu_h}$$

(eq-S4)

Equation (eq-S2) describes diffusion through the perovskite film, with d being the film thickness and D_{am} denoting the ambipolar diffusion coefficient. (eq-S3) describes recombination at the surface with a recombination velocity S. The ambipolar diffusion coefficient is connected in high injection to the individual mobilities of electrons and holes by (eq-S4). The combination of the ambipolar diffusion coefficient and the sum mobility $\mu_\Sigma = \mu_e + \mu_h$ can be used to gain to the individual mobilities of electrons and holes (77). For the sum mobility μ_Σ of 30 cm^2/Vs, electron and hole mobilities of 6 cm^2/Vs and 24 cm^2/Vs are derived. However, it cannot be clarified whether electrons or holes have the higher value.
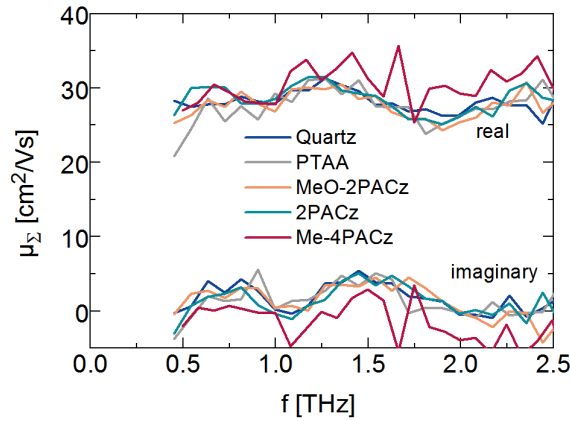
Figure S12 Terahertz (intragrain) mobilities of perovskite films deposited on the studies hole-selective layers and quartz. Growing perovskite on quartz, PTAA, MeO-2PACz, 2PACz or Me-4PACz has no effect on the terahertz mobility in the perovskite film. Such mobilities can be attributed to intra-grain transport for grain sizes above >100 nm (78). Therefore, we conclude that the intra-grain transport in the perovskite thin films is not altered by growing on SAMs and that the gain in fill factor is not caused by improved intra-grain transport.

X-ray diffraction study
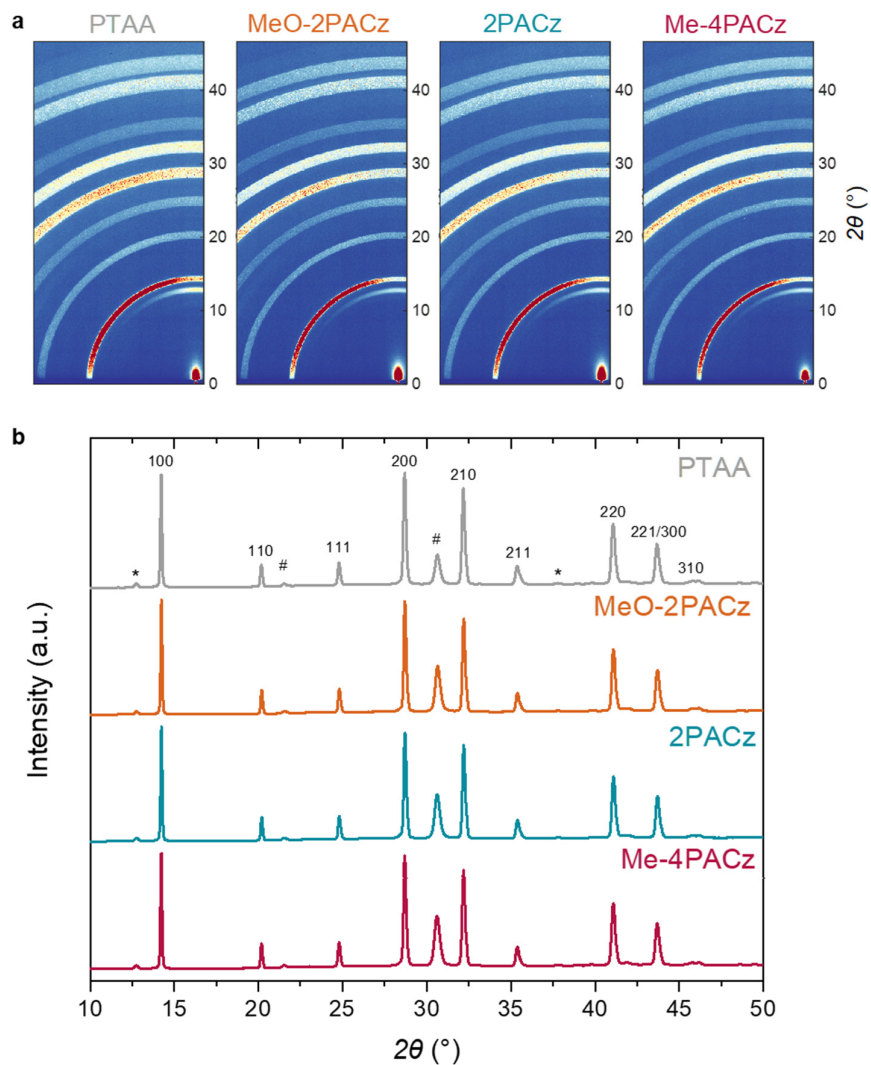
Figure S13 Absence of an effect of HTL on perovskite crystal orientation. a, Combined GIWAXS detector images at a grazing incidence angle of 0.5° and **b**, X-ray diffraction patterns generated by azimuthal integration of GIWAXS images acquired at 6.5° for perovskite grown on the four HTLs (with stack glass/ITO/HTL/Perovskite). Reflections from the pseudo-cubic perovskite are denoted by their Miller index and additional marked scattering features are reflections from ITO (#) and PbI_2 (*). Scattering data shown in part a) are uncorrected images with the scale indicating the detector rotation about the sample.
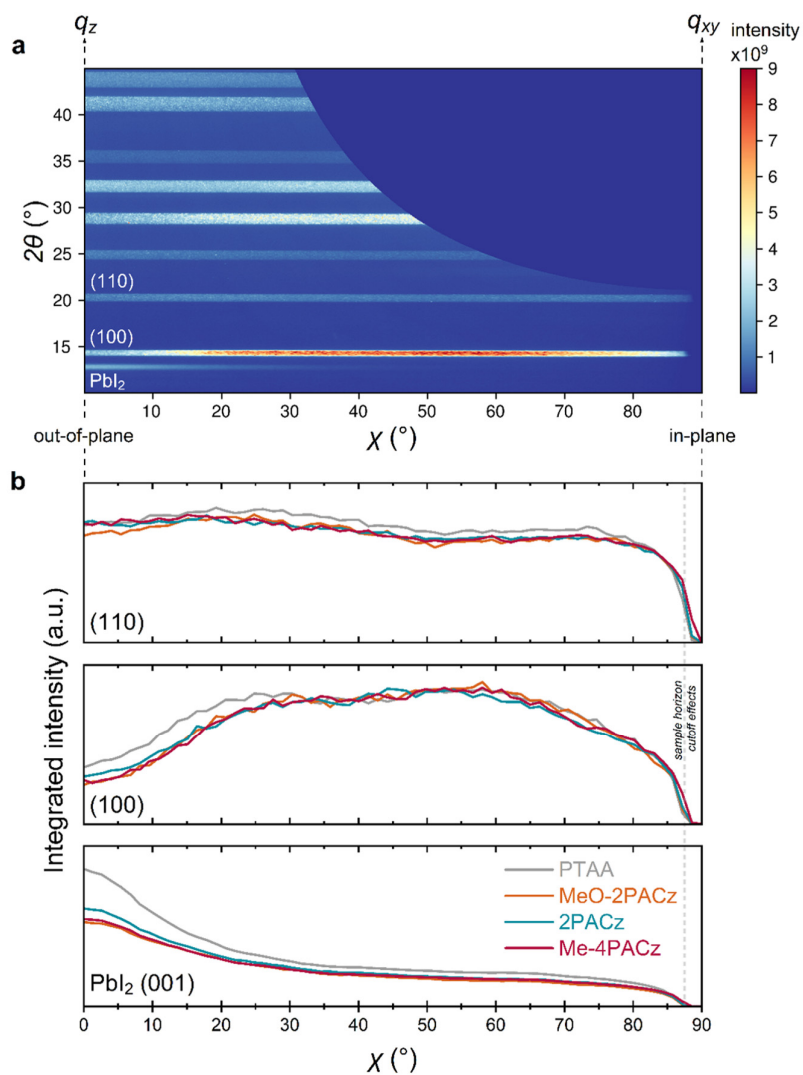
Figure S14 a) Typical remapped 2D scattering intensity data (Me-4PACz shown), plotted as χ (azimuthal scattering angle) vs. 2θ, with (100) and (110) perovskite reflections and PbI$_2$ marked. b) Azimuthal intensity profiles showing orientation distribution for the radially integrated (100) and (110) scattering features and PbI$_2$ for all samples. All data was acquired at a grazing incidence angle of 0.5°.
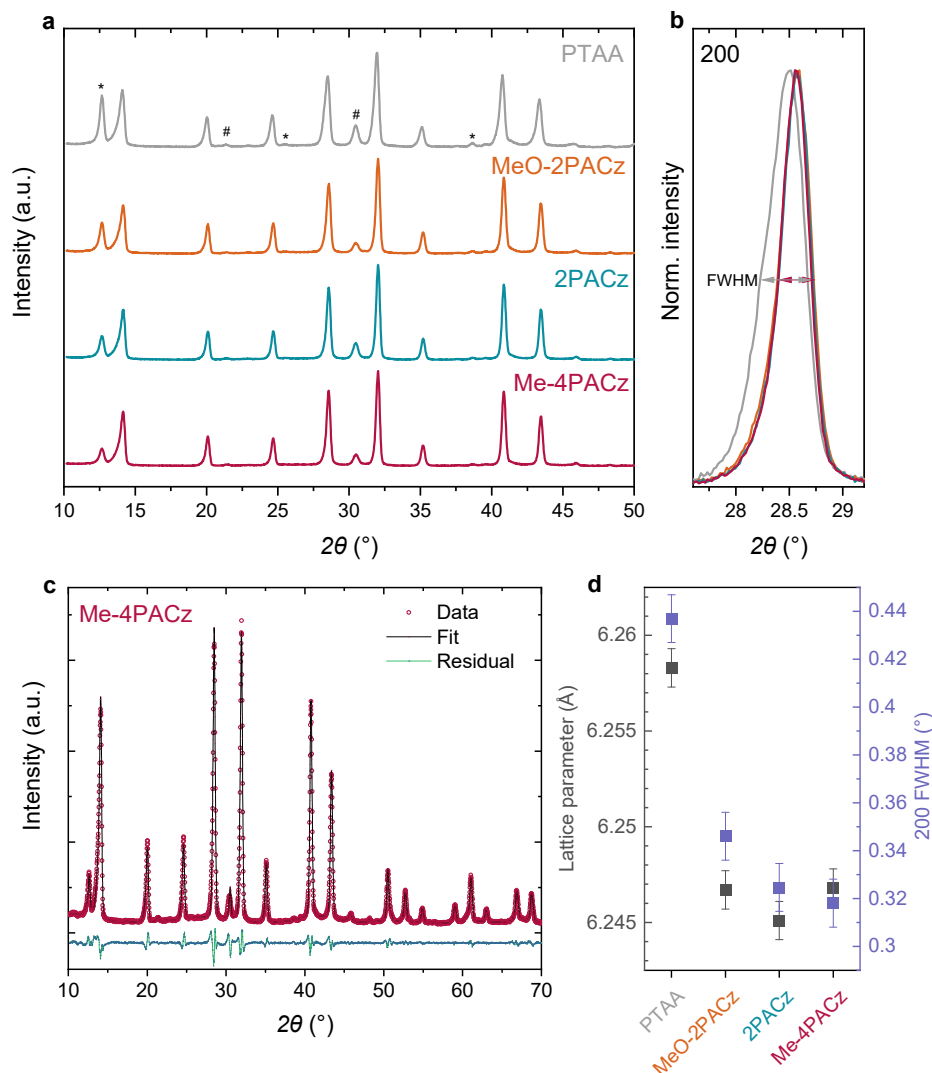
Figure S15 Grazing-incidence X-ray diffraction acquired with a rotating 1D detector (GI-XRD) at an incidence angle of 1°. Prior to measurement, samples were stored for ~2 weeks under N2 and measured in air, so may have undergone partial degradation. **a,** Diffraction patterns from the perovskite thin films with additional marked scattering features from ITO (#) and PbI_2 (*). Here the PbI2 scattering intensity is exaggerated with respect to the perovskite by the 1D detector geometry and out-of-plane texture of this phase, as observed in the GIWAXS measurements (Figure S13). **b**, Highlighted perovskite 200 reflection, showing shift and broadening of the scattering for the PTAA sample. **c**, Example Le Bail structural refinement of the Me-4PACz pattern with cubic Pm-3m perovskite, PbI2 and ITO phases present. **d**, Le Bail refined cubic perovskite lattice parameters and Pseudo-Voigt fitted full width at half maximum (FWHM) of the 200 reflections shown in part b). The differences in peak broadening between SAMs and PTAA might be over-estimated due to possible degradation of the PTAA sample (increased PbI2 peak), which was less pronounced in the 1D scans extracted from the GIWAXS data.

Additional single-junction device data
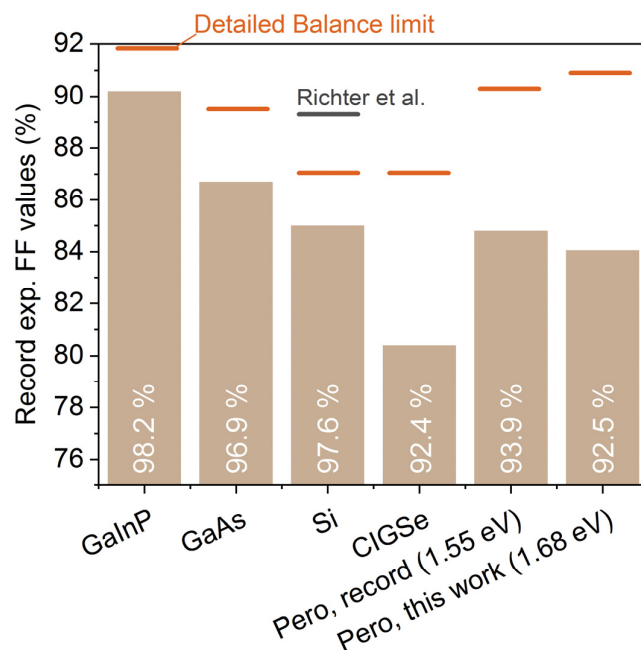
Figure S16 Comparison of experimentally achieved FF values of single-junction cells with different solar materials (*27*). The numbers inside the bars are the percentages with regard to the respective detailed balance limit. For Silicon, the large Auger recombination rate reduces the ideality factor to below 1, thus higher FFs than the detailed balance limit are possible (*69*).
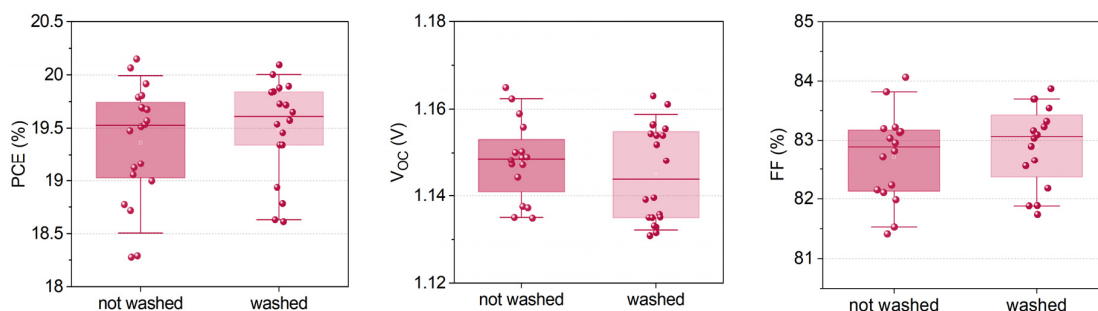
Figure S17 Influence of SAM washing on devices. Performance parameters of single-junction devices (without LiF interlayer) in which the ITO substrate was washed with EtOH after Me-4PACz spin-coating or not. The absence of a difference is characteristic for SAM-covered ITO substrates and in line with our previous findings demonstrating with 2PACz that spin-coating of a dilute solution (~0.3 mg/ml) already yielded a substrate-covering monolayer (*7*).
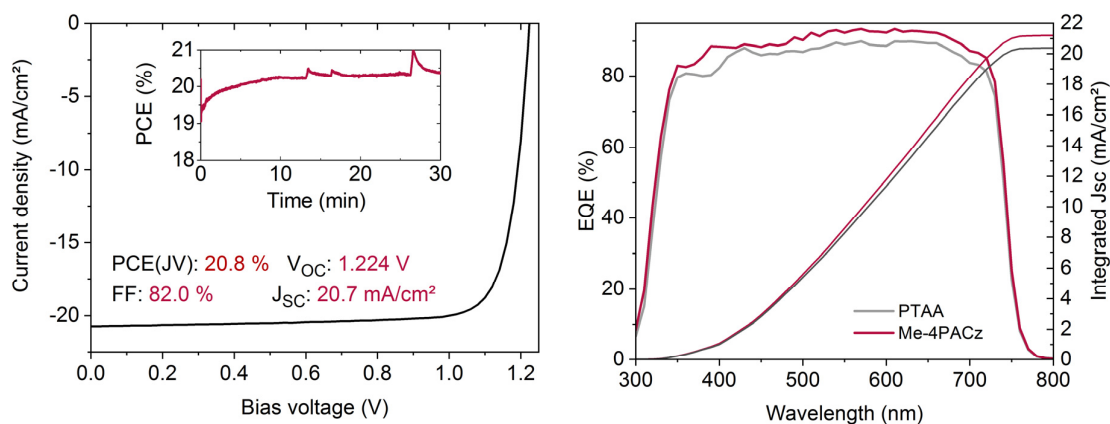
Figure S18 Left: *J-V* curve of the champion single-junction cell based on Me-4PACz as the hole-selective layer and LiF/C_{60}/SnO_2 on the electron-selective side, with the perovskite absorber bandgap being 1.68 eV. The inset shows a MPP track of that cell (spikes are from the unstable halogen lamp). Right: Representative EQE spectra of Me-4PACz and PTAA cells.
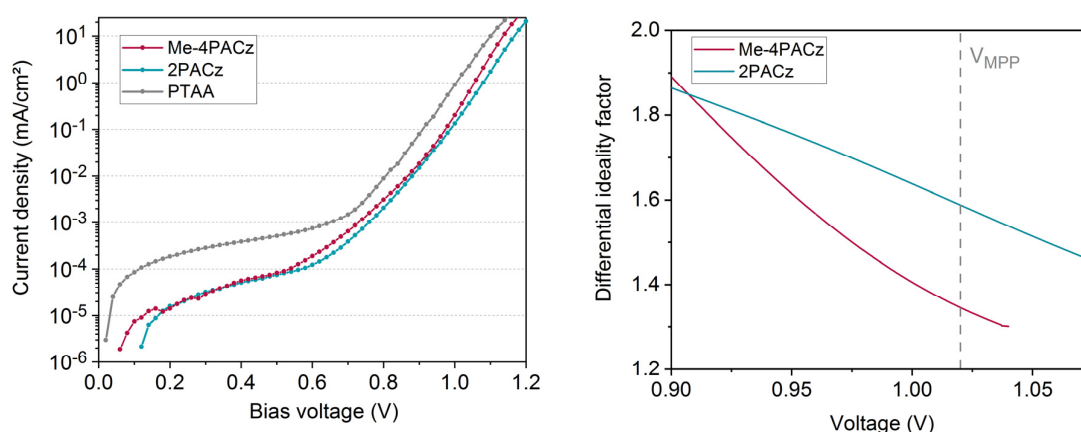
Figure S19 Difference in ideality factor from dark-*J-V* curves. Representative dark-*J-V* curves (left) of single-junction cells (no LiF) and ideality factor extracted from a fit on the data, of which the inverse of the derivative of the logarithm, divided by the thermal energy (25.8 meV) is plotted on the right. In line with the previous findings, the lower ideality factor with Me-4PACz is also visible in the dark curve as a steeper slope of the dark current. However, the suns-Voc method as shown in the main text is the more accurate way of determining the value of the ideality factor.
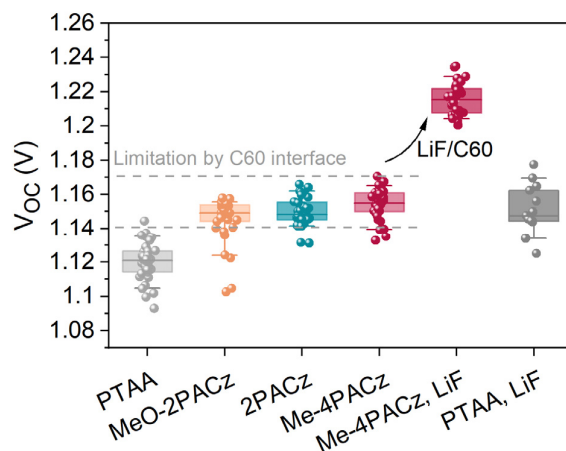
Figure S20 Open-circuit voltages of perovskite solar cells (single-junctions) with the studied hole-selective layers, with and without LiF interlayer between the perovskite and C60 layer. The full V_{OC} potential is only visible upon suppression of non-radiative recombination at the C60 interface, which we here demonstrated by an LiF interlayer. PTAA-based devices are limited by the PTAA interface to ~1.18 V (fitting to the QFLS of bare perovskite on PTAA).
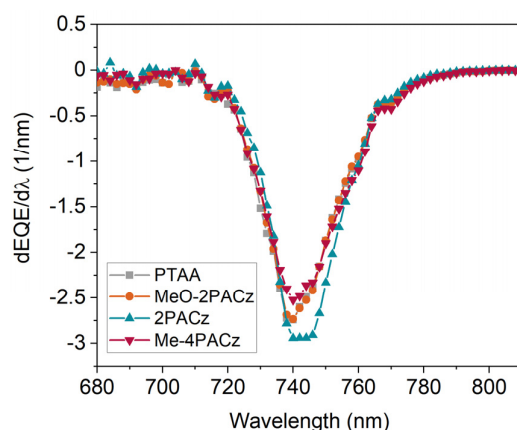
Figure S21 Derivative of the external quantum efficiency of single-junction PSCs based on the compared hole-selective layers. The derivative, or inflection point (*23*), lies at 740 nm, the same wavelength as the PL peaks of pristine perovskite films.
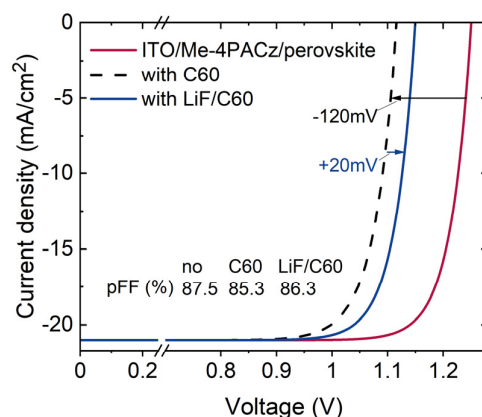
Figure S22 Addition to Figure 3D of the main text, showing the influence of LiF between perovskite and C60 on the intensity-dependent PL measurements for determination of the pFF values. The passivation effect of LiF on the perovskite surface is only minor (20 meV gain in QFLS), hinting that the large gain in V_{OC} by introduction of the LiF interlayer (see Figure S20) cannot be explained by surface passivation alone. We speculate that it might again be connected to differences in built-in potential across the full device and a hole-blocking nature of LiF (*79*).
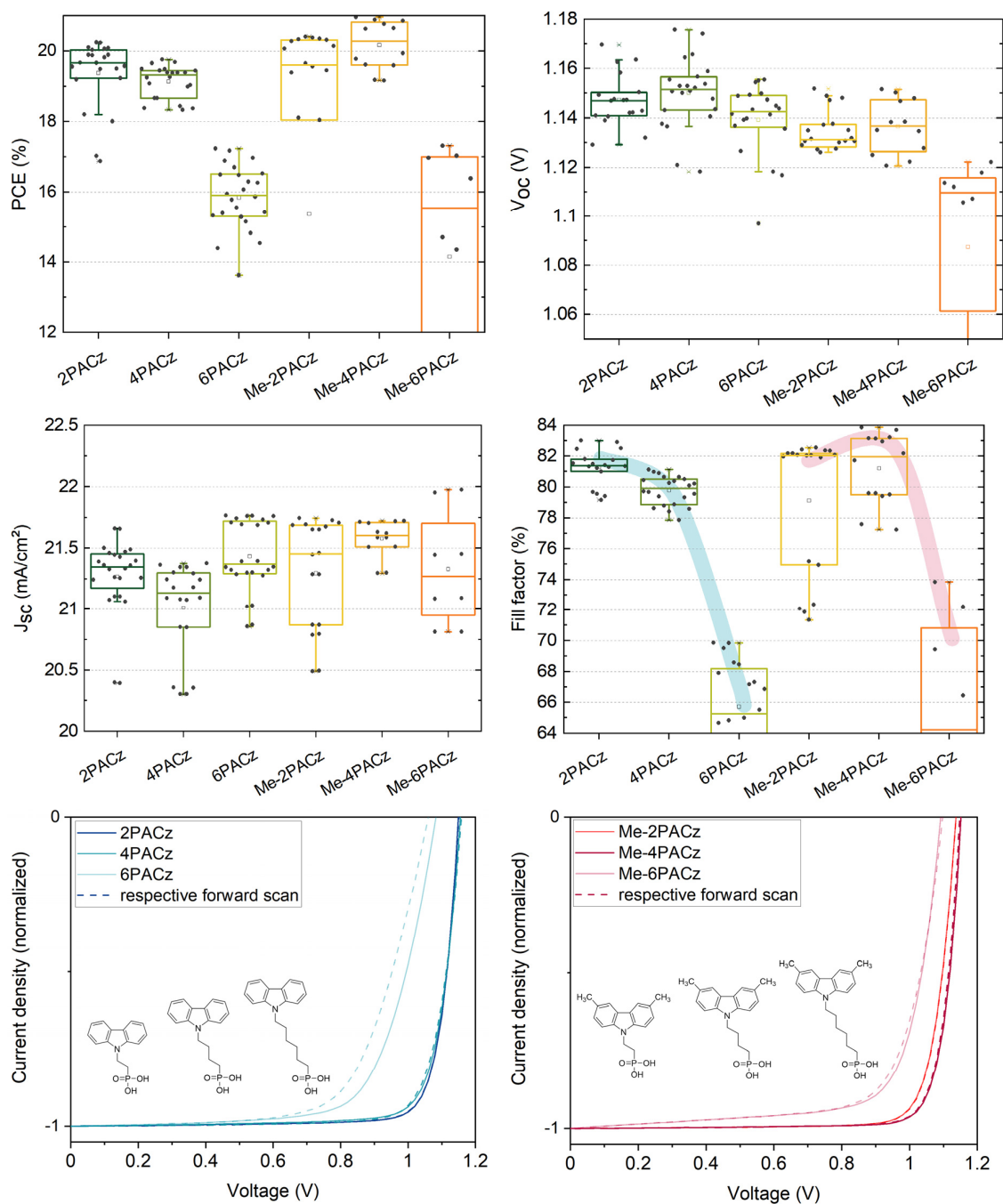
Figure S23 Influence of aliphatic chain length with bare and methyl-substituted carbazole SAMs on perovskite single-junction performance (no LiF). Mainly the FF was affected (J_{SC} values are likely slightly over-estimated, compared to EQE in **Figure S18**). The bottom panels show normalized *J-V* curves of the best-FF devices of each variation. For larger lengths of the isolating, non-conjugated SAM part (aliphatic chains containing 4 and 6 hydrocarbon segments), the fill factor decreases due to higher series resistance and ideality factor. The hampered hole extraction lead to current-voltage hysteresis in n=6 devices. For the methyl-substituted SAM, the optimum FF was reached with a chain length of n=4, while for nPACz, the highest FF was enabled by n=2. Possibly, self-assembly of the bare carbazole SAM nPACz is stabilized by pi-pi interactions of the carbazole fragments, whereas for the Me-substituted SAM an interplay between steric repulsion between the methyl fragments and van der Waals interaction between the hydrocarbon chains controls the SAM ordering and thus interface quality (*80–83*). This might cause the different optimum aliphatic chain lengths for the two different SAM types. Further investigations are needed to clarify the exact role of molecular orientation and effective dipole moment.

PTAA | MeO-2PACz

2PACz | Me-4PACz

500 nm

b

PTAA | MeO-2PACz

2PACz | Me-4PACz

500 nm
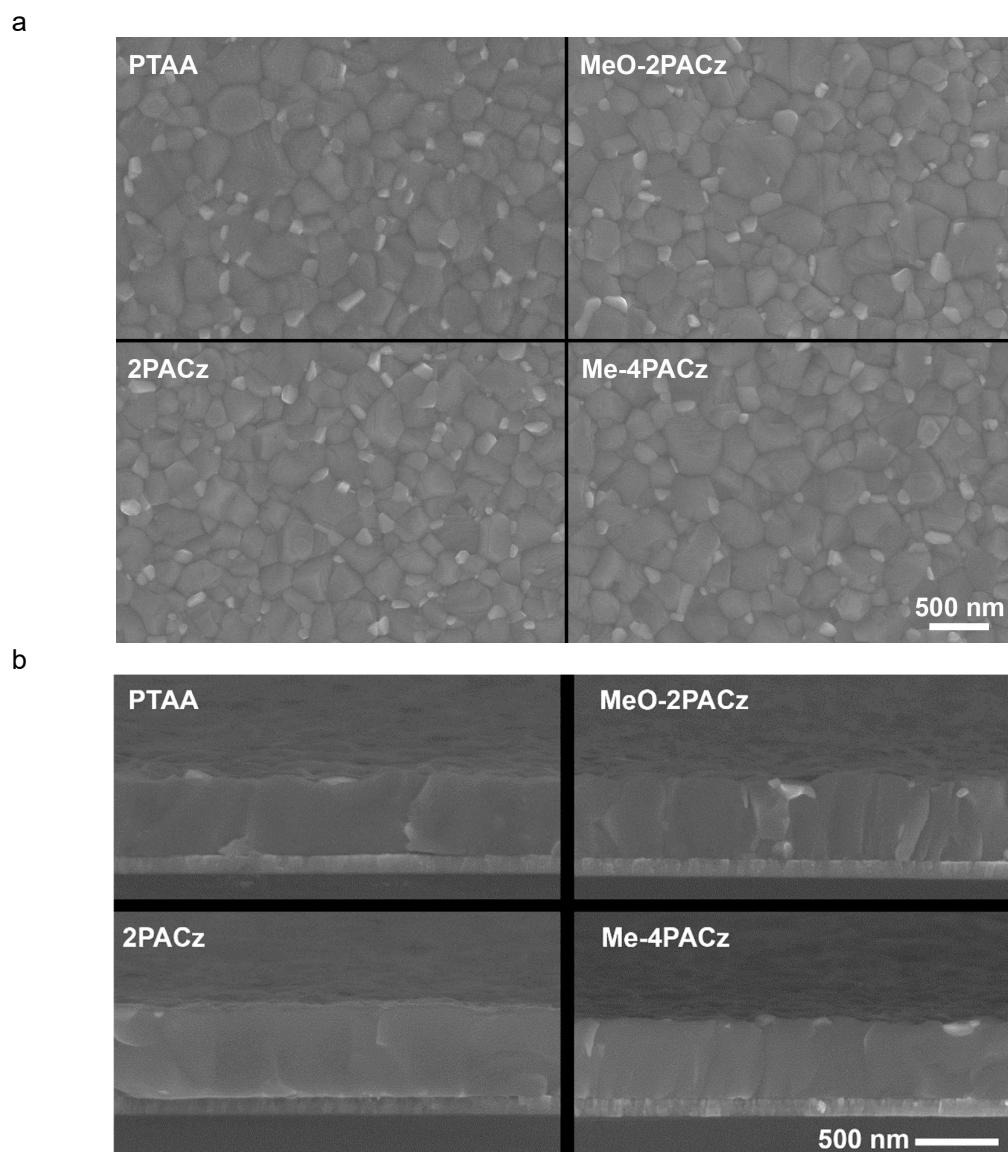
Figure S24 Scanning electron microscopy images of perovskite on the studied HTLs. **a**, top view. **b**, cross-section.

Additional data on tandem devices
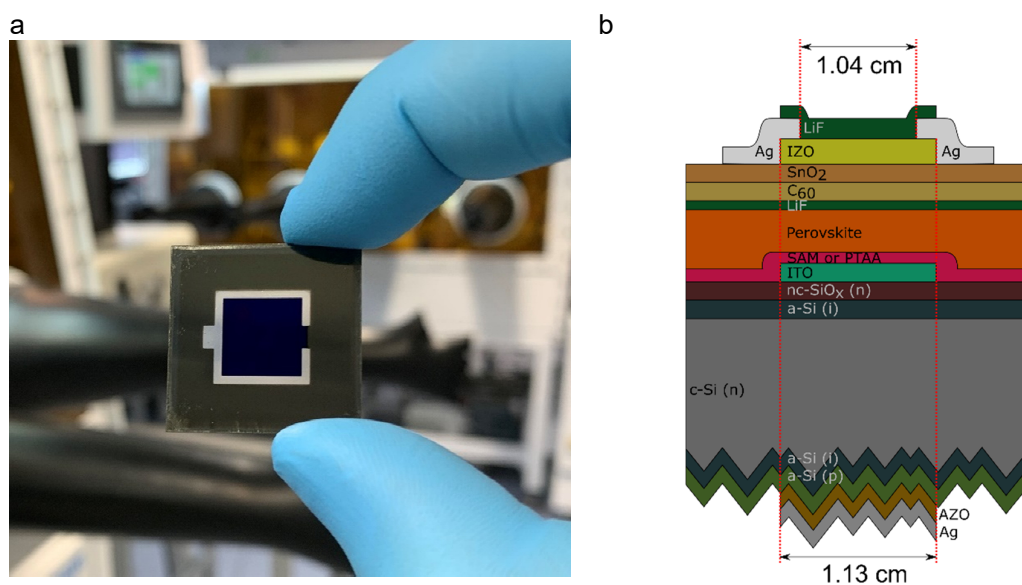
Figure S25 a) Photograph of a monolithic perovskite/silicon tandem solar cell. b) Layout of the tandem solar cells used in this work.
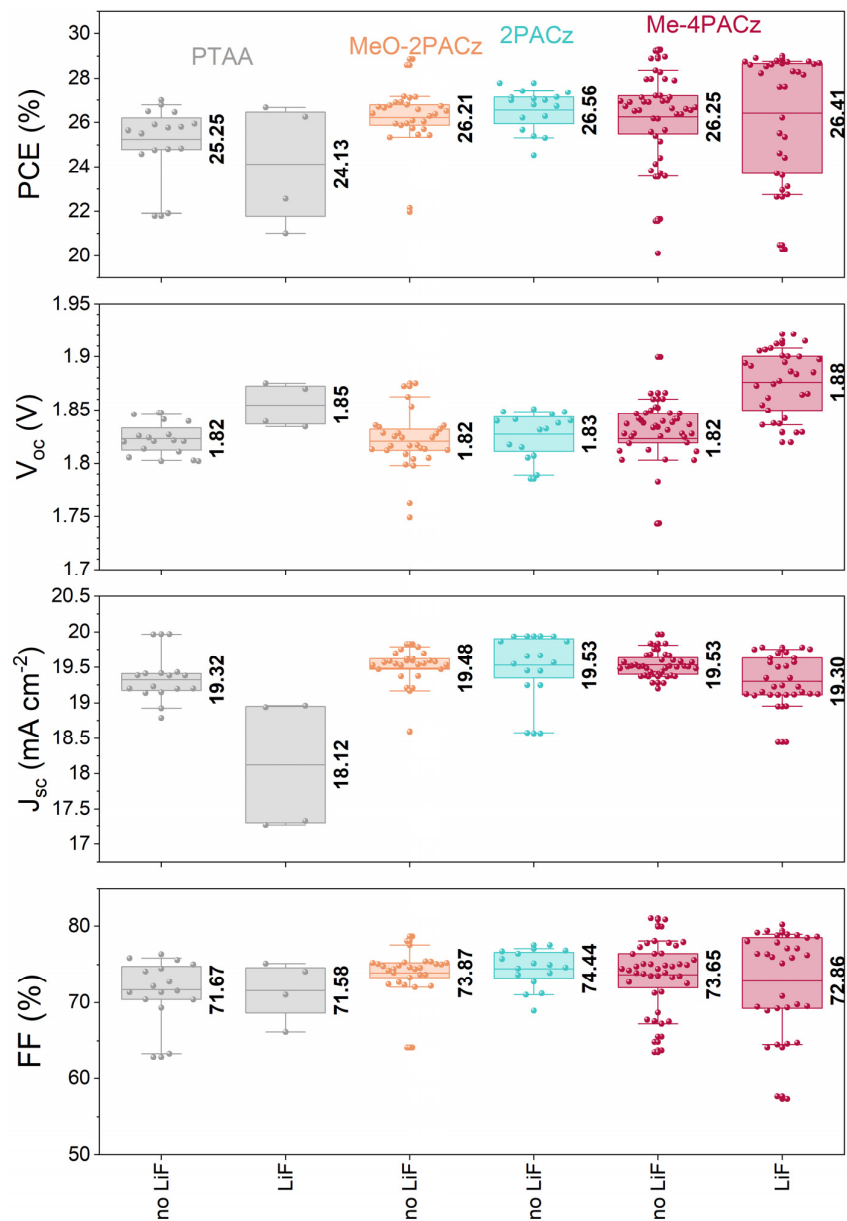
Figure S26 Tandem cell performance parameters from *J-V* curves under 1-sun equivalent illumination, comparing the different hole-selective layers with and without a 1 nm LiF interlayer between C_{60} and perovskite. The arithmetic mean is given for each parameter and HTL.

Table S27 Subcell photogenerated current densities (J_{ph}) values of the tandem cells with Me-4PACz presented in Figure S26 showing that for almost all cells, the perovskite top cell was limiting. This table includes cells with and without LiF interlayer where EQE data was available.

Silicon J_{ph} (mA/cm²)	Perovskite J_{ph} (mA/cm²)	Mismatch: $J_{ph,Silicon}$-$J_{ph,Perovskite}$ (mA/cm²)
19.87	19.42	0.45
19.63	19.39	0.24
20.18	19.58	0.6
19.94	19.51	0.43
20.2	19.51	0.69
20.22	19.52	0.7
19.89	19.05	0.84
20.18	19.41	0.77
20.73	18.76	1.97
20.6	18.7	1.9
20.47	18.98	1.49
19.94	19.24	0.7
19.56	19.31	0.25
19.38	19.41	-0.03
19.6	19.63	-0.03
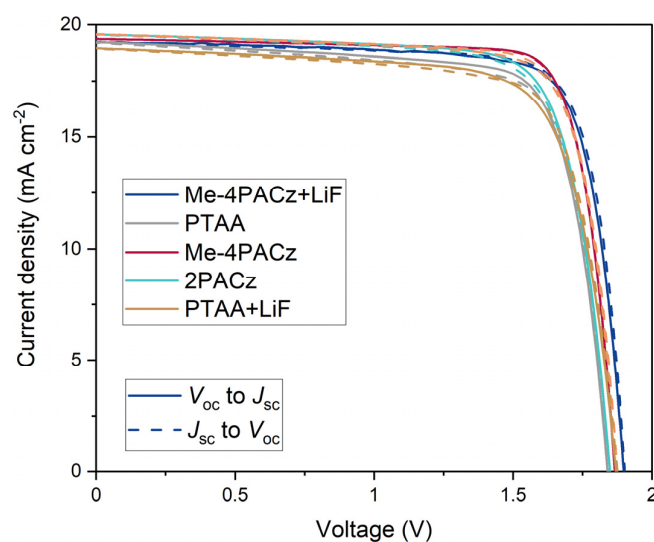
Figure S28 *J-V* curves of the champion tandem solar cells with various HTLs. The parameters are given in S29.

S29 Photovoltaic parameters of the champion cells using PTAA, MeO-2PACz, 2PACz and Me-4PACz as HTL. Additionally, we distinguished between cells with and without LiF interlayer.

Configuration	Direction	J_{sc} in mA cm^{-2}	V_{oc} in V	FF in %	PCE in %
PTAA	J_{sc} to V_{oc}	19.19	1.85	75.6	26.79
PTAA	V_{oc} to J_{sc}	19.23	1.84	76.3	27.00
PTAA - LiF	J_{sc} to V_{oc}	18.94	1.88	75.10	26.67
PTAA - LiF	V_{oc} to J_{sc}	18.96	1.87	74.04	26.25
MeO-2PACz	J_{sc} to V_{oc}	19.57	1.88	78.07	28.60
MeO-2PACz	V_{oc} to J_{sc}	19.58	1.88	78.66	28.88
2PACz	J_{sc} to V_{oc}	19.55	1.85	75.73	27.36
2PACz	V_{oc} to J_{sc}	19.57	1.85	76.83	27.79
Me-4PACz	J_{sc} to V_{oc}	19.37	1.87	80.89	29.23
Me-4PACz	V_{oc} to J_{sc}	19.37	1.87	81.06	29.29
Me-4PACz – LiF (certified values)	J_{sc} to V_{oc}	19.23	1.90	79.40	29.00
Me-4PACz – LiF (certified values)	V_{oc} to J_{sc}	19.24	1.89	78.85	28.75
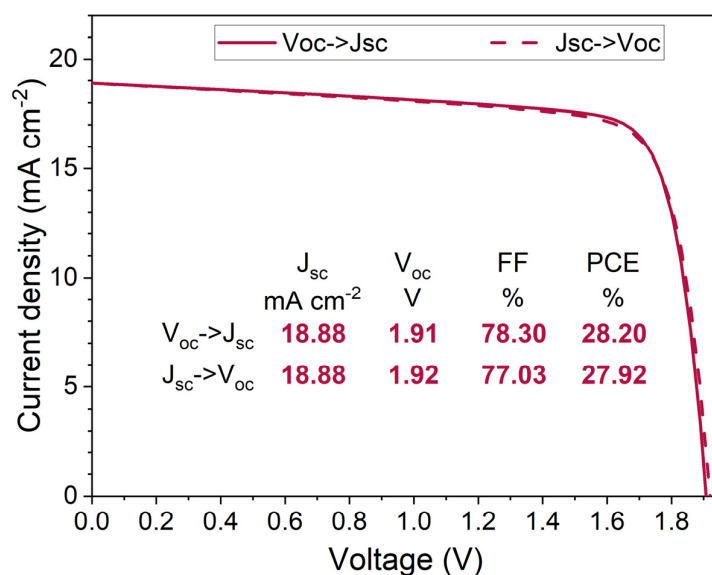
Figure S30 *J-V* of the monolithic perovskite silicon tandem solar cell with the new HTL Me-4PACz and LiF interlayer, showing a record *V*$_{OC}$ of 1.92 eV, featuring a 1.68 eV bandgap perovskite absorber.
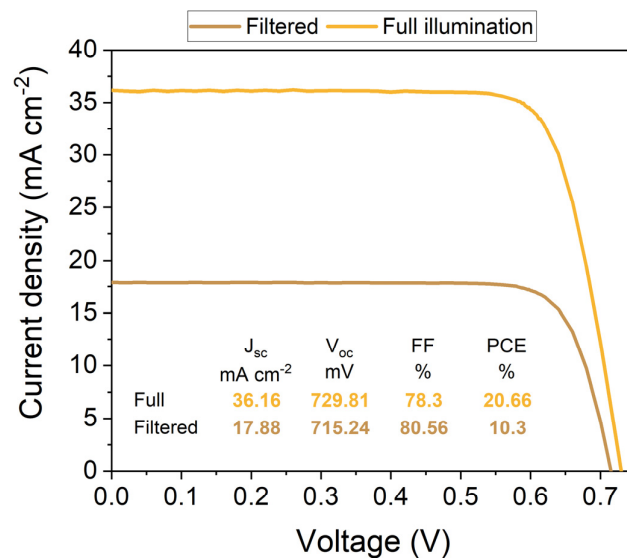
Figure S31 *J-V* curves of a representative silicon single-junction reference cell measured under full 1-sun-equivalent illumination and under filtered light, roughly as transmitted by a perovskite cell. As described in the methods, instead of 95 nm nc-SiO$_x$:H and 20 nm ITO on the front side (which becomes the recombination layer in a tandem solar cell), this reference cell comprises 20 nm nc-SiO$_x$:H and 70 nm ITO. To extract the charges from the 2 x 2 cm^2 active area, a screen-printed Ag grid is used.

Certification

Fraunhofer
ISE

CalLab
PV Cells

10003155HMI0919

Die Rückführung der Spektralmessung auf SI-Einheiten erfolgte über den Vergleich mit einer Standardlampe.
The traceability of the measurement of the spectral distribution to SI-Units is achieved using a standard lamp for the calibration of the spectroradiometer.

Identitäts-Nr. / Identity-Nr. :	Kalibrierschein-Nr./ Certificate-Nr. :	Rückführung/ Traceability :
BN-9101-451	40002-14-PTB	PTB

3. Messbedingungen
Measurement conditions

Standardtestbedingungen (STC) / *Standard Testing Conditions (STC)* :

Absolute Bestrahlungsstärke / *Total irradiance* :	1000	W/m²
Temperatur des Messobjektes / *Temperature of the DUT* :	25	°C
Spektrale Bestrahlungsstärke / *Spectral irradiance distribution* :	AM1.5G Ed.2 (2008)	

Die Messung der IV-Kennlinie (Strom-Spannungs-Kennlinie) des Messobjektes erfolgt mit Hilfe eines Vierquadranten-Netzteiles und eines Kalibrierwiderstandes.
The measurement of the IV-curve is performed with a 4-quadrant power amplifier and a calibration resistor.

4. Messergebnis
Measurement results

Fläche / *Area* (da)[1]: = (1.0599 ± 0.0066) cm²

[1] : (t) = total area, (ap) = aperture area, (da) = designated illumination area /7/

Kennlinienparameter des Messobjektes unter Standardtestbedingungen (STC) / *IV-curve parameter under Standard Testing Conditions (STC)* :

		Vorwärtsrichtung / forwards scan direction			Rückwärtsrichtung / reverse scan direction			steady state MPP		
V_{oc}	=	(1900.3 ±	12.7) mV	(	1894.6 ±	12.7) mV				
I_{SC} (Ed.2 - 2008)	=	(20.38 ±	0.39) mA	(	20.40 ±	0.39) mA				
I_{MPP}	=	18.83	mA		18.75	mA	(	19.11 ±	0.40) mA	
V_{MPP}	=	1633.0	mV		1625.3	mV	(	1616.6 ±	36.6) mV	
P_{MPP}	=	30.74	mW		30.47	mW	(	30.90 ±	0.85) mW	
FF	=	79.40	%		78.85	%				
η	=						(	29.15 ±	0.82) %	

51

Fraunhofer
ISE

CalLab
PV Cells

Angegeben ist jeweils die erweiterte Messunsicherheit, die sich aus der Standardmessunsicherheit durch Multiplikation mit dem Faktor *k*=2 ergibt. Sie wurde gemäß dem "Guide to the expression of Uncertainty in Measurement" ermittelt. Sie entspricht bei einer Normalverteilung der Abweichungen vom Messwert einer Überdeckungswahrscheinlichkeit von 95%.

The expanded measurement uncertainty resulting from the standard measurement uncertainty multiplied with a factor k=2 is specified. The calculation was carried out according to the "Guide to the expression of Uncertainty in Measurement". The value corresponds to a Gaussian distribution denoting the deviations of the measurement value within a probability of 95%.

5. Zusatzinformationen
Additional information

Fraunhofer
ISE

CalLab
PV Cells

Figure S32: Certification report from Fraunhofer ISE for a monolithic perovskite silicon tandem solar cell with Me-4PACz as HTL and LiF interlayer.

53
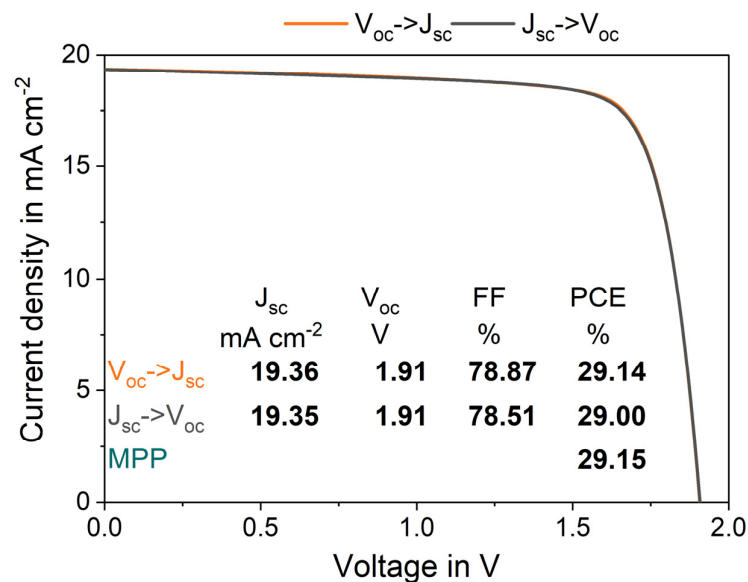
Figure S33 *J-V* curve under 1-sun-equivalent illumination of the certified Me-4PACz+LiF tandem solar cell, measured in-house, yielding almost the same results as the certified measurement shown in the main text.
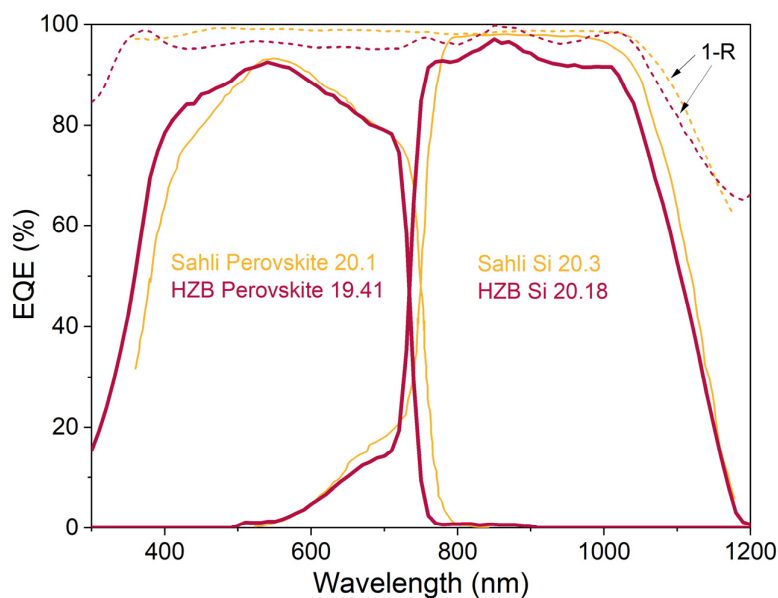
Figure S34 External quantum efficiencies of the certified champion device in this publication (measured in-house) and of the publication from Sahli *et al.* (*62*). The latter shows that the textured front side can increase the photogenerated current density by reduced reflection. This led to a cumulative current density of 40.4 mA cm^{-2}, whereas the flat front side of this publication led to 39.59 mA cm^{-2}. Additionally, the dashed lines show the reflection (1-R) of the respective cell.
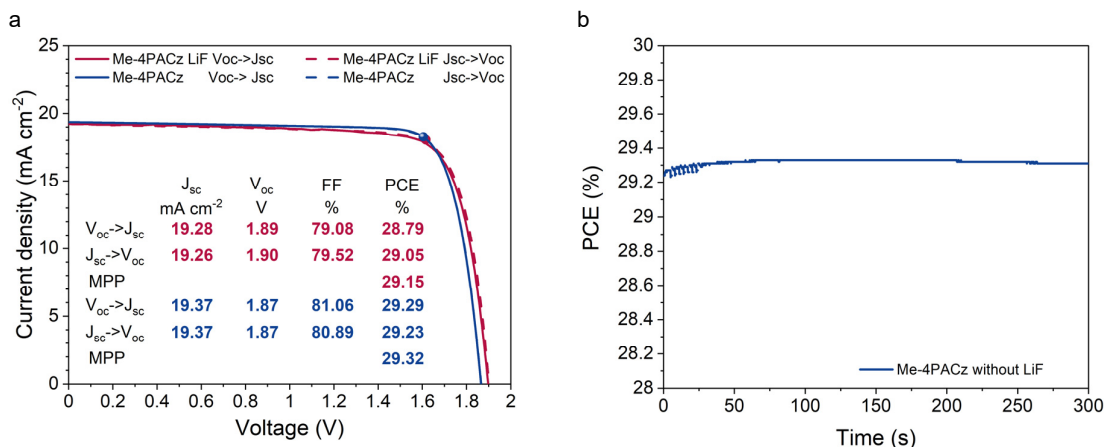
Figure S35 a) Comparison of champion monolithic perovskite silicon tandem solar cells (Me-4PACz) with and without LiF interlayer. The *J-V* of the cell with LiF interlayer was certified at Fraunhofer ISE. The higher V_{oc} but lower FF for cells with LiF interlayer is clearly visible. b) 5 minutes MPP-track of the champion cell without LiF interlayer with an average value of 29.32%
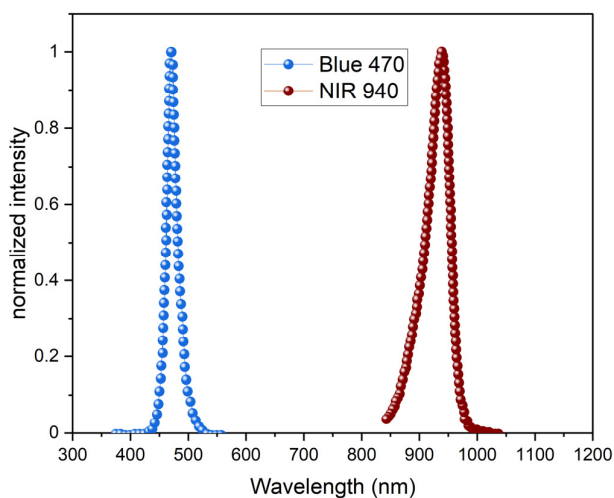
Figure S36 Normalized spectra of the LEDs used for long term MPP-tracks of tandem solar cells. The spectra are given by the manufacturer. For the MPP-tracks, the intensities were adjusted such that in the subcells the same charge carrier densities are generated as derived from the respective EQE measurements.

Note S37: Light sources for long term stability tests of tandem solar cells

Typically, low-class lamp spectra provide less NIR light and thus the photogenerated current density of the silicon bottom cell will be reduced, leading potentially to a silicon-limited tandem solar cell. Silicon-limited tandem solar cells would show higher stability as the degradation of the perovskite subcell barely affects the performance of the tandem until a certain threshold is reached. Therefore, the subcell limitation will also affect operational stability, depending on the degree of mismatch and type of degradation. A detailed analysis of the influence of the subcell properties on the tandem solar cell is given by Boccard and Ballif (*84*).

Table S38 Photogenerated current of tandem solar cells. The photogenerated current densities were extracted by measuring the short circuit current under one or the other limitation. We assume that the short circuit current is equal to the photogenerated current of the limiting subcell. The limitation is artificially created by enhancing the sun simulator intensity in the spectral region that only the non-limiting cell absorbs (i.e., increased NIR intensity for perovskite limitation and increased blue intensity for silicon limitation).

	$I_{ph,Pero}$ (mA)	$I_{ph,Si}$ (mA)
PTAA LiF	18.88	20.05
Me-4PACz LiF	19.57	19.86
2PACz	19.04	19.5
Me-4PACz	20.10	20.06
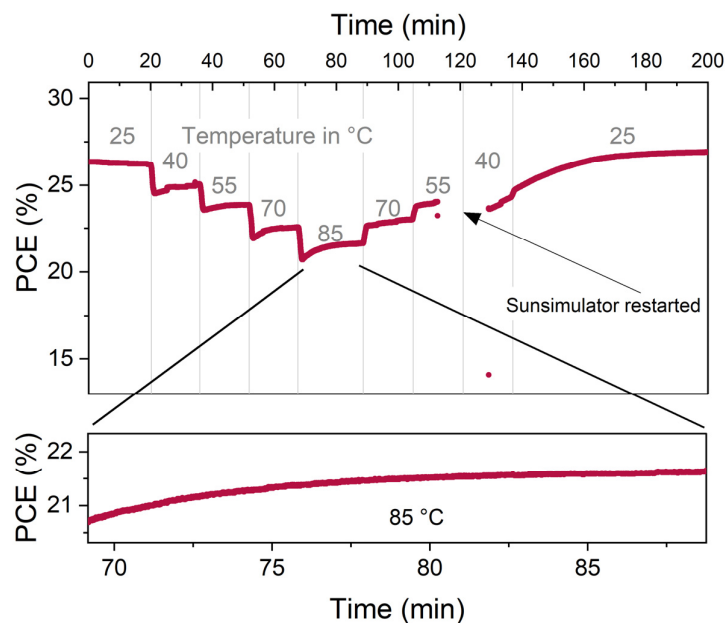
Figure S39 MPP track of a tandem solar cell with Me-4PACz as HTL (without LiF interlayer). The cell was illuminated with an AM1.5G spectrum (calibrated with a KG-3 filtered silicon reference cell, certified at Fraunhofer ISE). Following the procedure of Jošt *et al.*(*63*), the cell was held for 15 minutes at 40 °C, 55 °C and 70 °C and for 20 minutes at 85 °C. Due to a technical issue, the sun simulator needed to be restarted. However, the cell was still exposed to the elevated temperature.

56
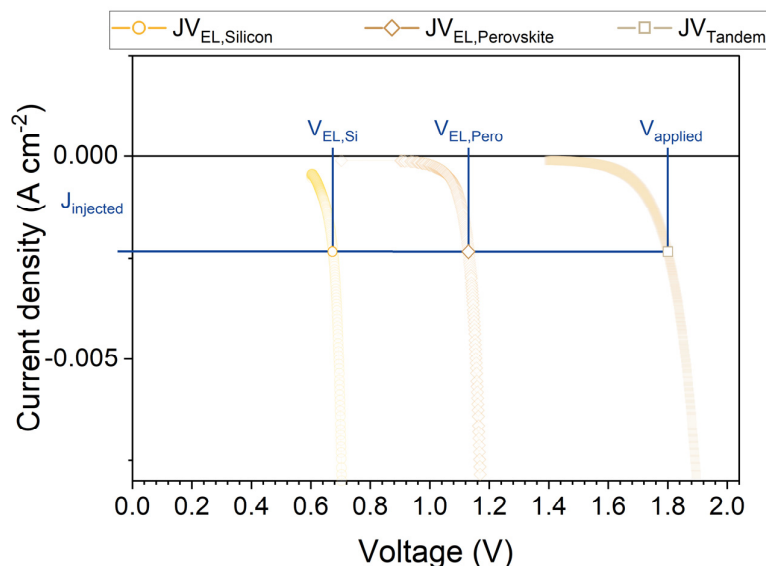
Figure S40 Injection dependent EL measurements of a monolithic tandem solar cell using Me-4PACz as HTL and LiF interlayer. By applying a voltage to the solar cell, we inject a current, which flows through both subcells. From the EL measurement, we extract the QFLS at each injected current and can reconstruct a dark *J-V*.

Note S41: *J-V* reconstructed from EL measurements

When comparing the reconstructed *J-V* obtained from EL measurements (JV_{EL}) to the *J-V* measured under a solar simulator (JV_{Sunsim}), we first notice a slightly higher shunt resistance R_{Sh} for the $JV_{\text{EL,Tandem}}$. We attribute this to pinholes in the perovskite top cell (e.g., direct contact between C_{60} and ITO), which are electrically active and lead to leakage currents in the JV_{Sunsim}. However, these pinholes are not visible in the EL images due to limited camera resolution and pixel bleeding of the luminescence intensity. Thus, the reconstructed perovskite subcell $JV_{\text{EL,Pero}}$ is a representation of a top cell processed under perfect substrate and precursor cleanliness, pinhole-free wetting etc. Secondly, the reconstructed JV_{EL} curve does not feature any series resistance, because the EL gives access only to the *internal* voltage, whereas an electrical *J-V* curve displays the current density versus *external* voltage. The external voltage at a given current is smaller than the internal one for example due to voltage drops at series resistances (*85*). Additionally, in the EL reconstruction, a larger current is flowing at the reconstructed V_{OC} as compared to the reconstructed V_{MPP}, since 1-sun equivalent electrical current injection corresponds to the reconstructed V_{OC}. In contrast, under electrical *J-V*-sweeping, a higher net current flows at V_{MPP} compared to V_{OC}. Since in a solar cell diode equation the series resistance appears in the product $R_{\text{s}} \times I$, the JV_{EL} thus simulates a *J-V* curve under small net current flow.
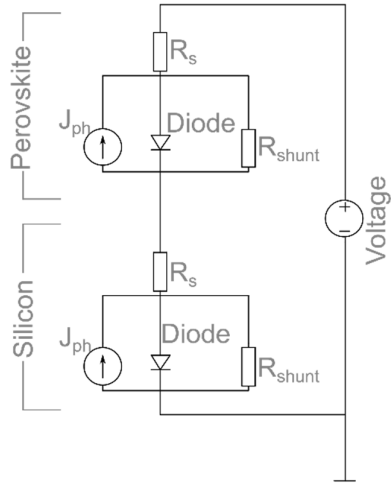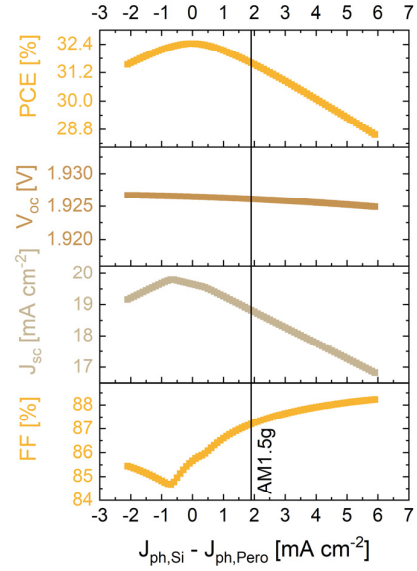
Figure S42 a, Schematic of the SPICE simulation. For the top and bottom cell a single diode model is used consisting of a current source J_{ph}, series resistance R_s, parallel resistance R_{shunt} and the diode. In this case, the Rs was set to 0. **b**, result of the simulation using the parameter extracted from the JV_{EL} of the individual subcells. The J_{ph} of the subcells were changed while maintaining a constant cumulative current density of 39.3 mA cm^{-2} as it is the case for AM1.5G-equivalent illumination (calculated by EQE). Thus, the individual parameters are a function of the mismatch of the subcells. A FF minimum occurs at a mismatch of -0.7 mA cm^{-2}, whereas it is simultaneously the point of maximum J_{sc}. Thus, a tradeoff needs to be done. Here, the maximum PCE of 32.43% is reached when both subcells have the same J_{ph} (i.e. mismatch=0).

Synthesis of the new SAMs
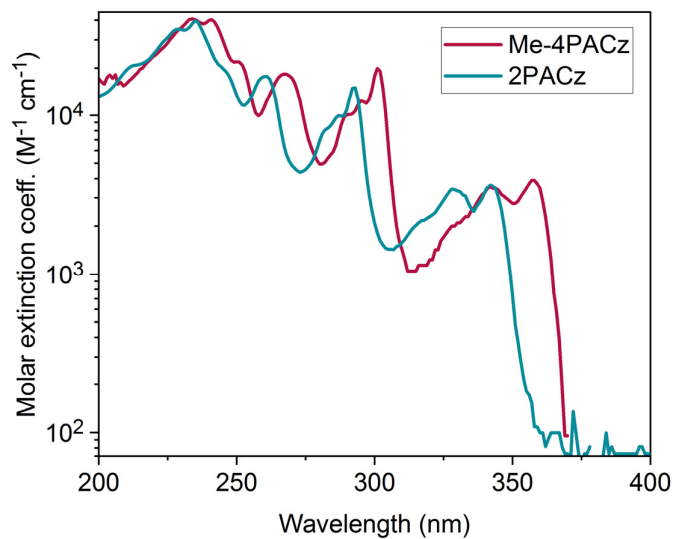
Figure S43 Molar extinction coefficient of 2PACz and Me-4PACz dissolved in THF (10^{-4} M). UV/Vis spectra were recorded on a PerkinElmer Lambda 35 spectrometer.

Me-nPACz (n = 2,4,6)

Materials used for the synthesis were purchased from Sigma-Aldrich or TCI Europe and were used as received without further purification.

The ^{1}H and ^{13}C NMR spectra were taken on Bruker Avance III (400 MHz) spectrometer at room temperature. Chemical shifts are reported in parts per million (δ, ppm) downfield from tetramethylsilane standard and are referenced to residual signal of the solvent. The course of the reactions products was monitored by TLC on ALUGRAM SIL G/UV254 plates and developed with UV light. Silica gel (grade 9385, 230–400 mesh, 60 Å, Aldrich) was used for column chromatography. Elemental analysis was performed with an Exeter Analytical CE-440 elemental analyzer, Model 440 C/H/N/.
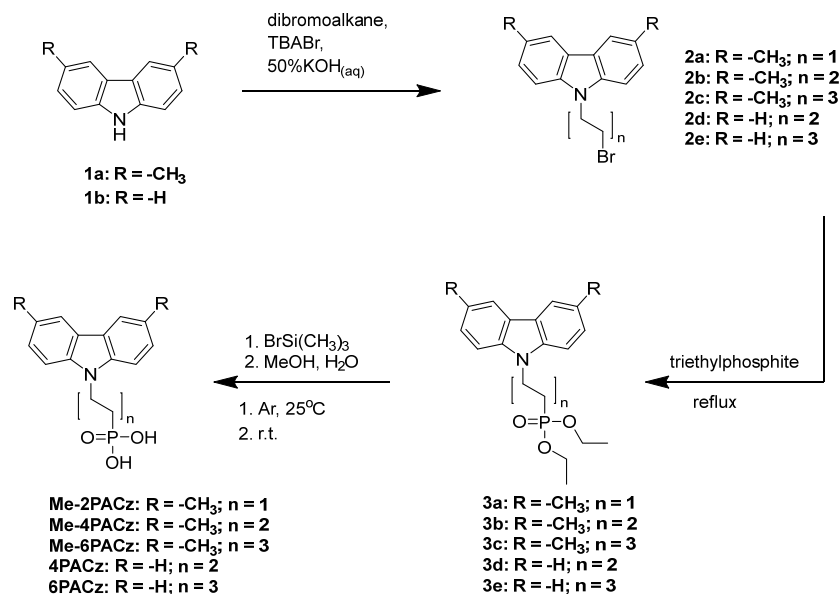
Figure S44 Synthesis scheme of the new materials **(Me)-nPACz** (n = 2, 4, 6).
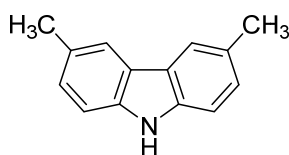
(3,6-Dimethyl-9H-carbazole) (1a). 3,6-Dibromocarbazole (10 g, 30.77 mmol) and 1,3-bis-(diphenylphosphino)dichloronickel(II) (Ni(dppp)$_2$Cl$_2$) (2.5g, 4.62 mmol) were dissolved in 700 ml of absolute diethyl ether under argon atmosphere. After 15 min, 40.9 mL of a 3 M CH$_3$MgBr solution in diethyl ether (123.08 mmol) was added over a period of 60 min to the purple red suspension, yielding a brown and clear solution. Afterwards reaction mixture was refluxed for 5 h, cooled to room temperature, and quenched with 100 mL of saturated aqueous NH$_4$Cl solution. Organic phase was separated and extracted three times with 200 mL of saturated aqueous Na$_2$CO$_3$ solution, three times with 200 mL of water, and finally three times with 200 mL of saturated aqueous NaCl solution. The organic layer was dried over anhydrous Na$_2$SO$_4$ and the solvent was distilled off under reduced pressure. The crude product was purified by column chromatography (acetone n-hexane 1:24 v/v) to give 3.5 g (58 %) of white crystalline powder.

^{1}H NMR (400 MHz, (CD$_3$)$_2$SO): δ 10.95 (s, 1H), 7.84 (s, 2H), 7.35 (d, J = 8.1 Hz, 2H), 7.18 (d, J = 8.0 Hz, 2H), 2.46 (s, 6H).

¹³C NMR (100 MHz, (CD₃)₂SO): δ 138.3, 126.8, 126.6, 122.4, 119.8, 110.6, 21.1.

Anal. calcd for $C_{14}H_{13}N$, %: C 86.12, H 6.71, N 7.17, found, %: C 85.91, H 6.82, N 7.27.
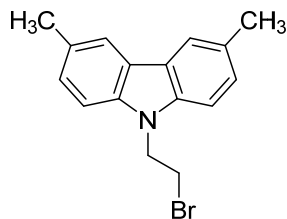
**9-(2-Bromoethyl)-3,6-dimethyl-9*H*-carbazole (2a)**: **1a** (0.6 g, 3.07 mmol) was dissolved in 1,2-dibromoethane (7 ml, 81.23 mmol), tetrabuthylammonium bromide (0.148 g, 0.46 mmol) and 50% KOH aqueous solution (0.86 ml, 15.35 mmol) were added subsequently. Reaction was stirred at 50°C for two days (TLC, acetone: *n*-hexane 2:23 *v/v*) after each 24h tetrabuthylammonium bromide (0.1 g, 0,31 mmol) and 0.5 ml of 50% aqueous KOH solution were added. After completion of the reaction, extraction was done with dichloromethane. The organic layer was dried over anhydrous Na_2SO_4 and the solvent was distilled off under reduced pressure. The crude product was purified by column chromatography (acetone: *n*-hexane 1:23 *v/v*) to give 0.52 g (47%) of colourless solid.

¹H NMR (400 MHz, CDCl₃): δ 7.82 (s, 2H), 7.27 – 7.22 (m, 4H), 4.57 (t, *J* = 7.5 Hz, 2H), 3.58 (t, J = 7.5 Hz, 2H), 2.50 (s, 6H).

¹³C NMR (100 MHz, CDCl₃): δ 138.6, 128.8, 127.2, 123.2, 120.6, 108.2, 44.8, 28.4, 21.5.

Anal. calcd for $C_{16}H_{16}BrN$, %: C 63.59, H 5.34, N 4.63, found, %: C 63.72, H 5.52, N 4.77.
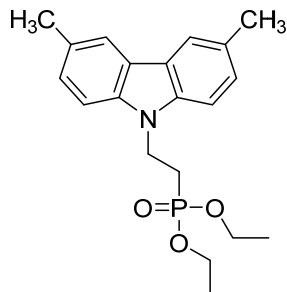
Diethyl [2-(3,6-dimethyl-9*H*-carbazol-9-yl)ethyl]phosphonate (3a): **2a** (0.4 g, 1.32 mmol) was dissolved in triethyl phosphite (6 ml, 34.99 mmol) and the reaction mixture was heated at reflux for 19 h. After reaction completion (TLC, acetone: *n*-hexane 8:17 *v/v*) the solvent was distilled off under reduced pressure. The crude product was purified by column chromatography (acetone: *n*-hexane 1:4 *v/v*) to give 0.46g (97%) of yellowish resin.

¹H NMR (400 MHz, CDCl₃): δ 7.84 (s, 2H), 7.30 – 7.23 (m, 4H), 4.55 (q, *J* = 8.5 Hz, 2H), 4.08 (quint, *J* = 7.1 Hz, 4H), 2.52 (s, 6H), 2.28 – 2.16 (m, 2H), 1.28 (t, *J* = 7.0 Hz, 6H).

¹³C NMR (100 MHz, CDCl₃): δ 138.3, 128.4, 127.1, 123.2, 120.5, 108.2, 62.0, 61.9, 37.1, 26.0, 24.6, 21.5, 16.54, 16.48.

Anal. calcd for $C_{20}H_{26}NO_3P$, %: C 66.84, H 7.29, N 3.90, found, %: C 67.01, H 7.09, N 4.08.

61
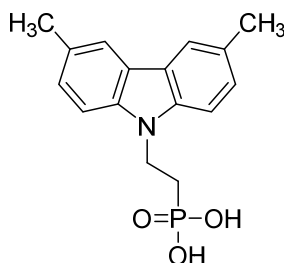
[2-(3,6-dimethyl-9*H*-carbazol-9-yl)ethyl]phosphonic acid (Me-2PACz): **3a** (0.47 g, 1.31 mmol) was dissolved in anhydrous 1,4-dioxane (15 ml) under argon atmosphere and bromotrimethylsilane (1.73 ml, 13.07 mmol) was added dropwise. Reaction was stirred for 22 h at 25 °C under argon atmosphere. Afterwards, methanol (3 ml) was added and stirring continued for 3h. Finally, distilled water was added dropwise (10 ml), until solution became opaque, and it was stirred overnight. Product was filtered off, washed with water, dissolved in tetrahydrofuran (1 ml) and precipitated into *n*-hexane (12 ml). The product was filtered off and washed with *n*-hexane, to give 0.360 g (91 %) of white powder.

^{1}H NMR (400 MHz, (CD$_3$)$_2$SO): δ 9.59 (br s, 2H), 7.88 (s, 2H), 7.38 (d, *J* = 8.3 Hz, 2H), 7.25 (d, *J* = 8.3 Hz, 2H), 4.59 – 4.40 (m, 2H), 2.46 (s, 6H), 2.09 – 1.90 (m, 2H).

^{13}C NMR (100 MHz, (CD$_3$)$_2$SO): δ 138.0, 127.4, 126.9, 122.3, 120.2, 108.6, 37.4, 28.0, 26.7, 21.0.

Anal. calcd for C$_{16}$H$_{18}$NO$_3$P, %: C 63.36, H 5.98, N 4.62, found, %: C 63.53, H 5.81, N 4.76.
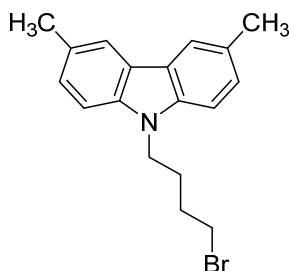
9-(4-bromobutyl)-3,6-dimethyl-9*H*-carbazole (2b): **1a** (0.6 g, 3.07 mmol) was dissolved in 1,4-dibromobutane (9.1 ml, 76.75 mmol), tetrabuthylammonium bromide (0.148 g, 0.46 mmol) and 50% KOH aqueous solution (0.86 ml, 15.35 mmol) were added subsequently. Reaction was stirred at 60°C overnight (TLC, acetone:*n*-hexane, 1:24, v:v). After completion of the reaction, extraction was done with dichloromethane. The organic layer was dried over anhydrous Na$_2$SO$_4$ and the solvent was distilled off under reduced pressure. The crude product was purified by column chromatography (acetone *n*-hexane 1:124 v/v) to give 0.91 g (90 %) of white crystalline solid.

^{1}H NMR (400 MHz, CDCl$_3$): δ 7.85 (s, 2H), 7.29 – 7.20 (m, 4H), 4.27 (t, *J* = 6.8 Hz, 2H), 3.33 (t, *J* = 6.5 Hz, 2H), 2.52 (s, 6H), 2.01 (quint, *J* = 7.1 Hz, 2H), 1.86 (quint, *J* = 6.4 Hz, 2H).

^{13}C NMR (100 MHz, CDCl$_3$): δ 139.0, 128.1, 127.0, 123.0, 120.5, 108.3, 42.3, 33.4, 30.4, 27.8, 21.5.

Anal. calcd for C$_{18}$H$_{20}$BrN, %: C 65.46, H 6.10, N 4.24, found, %: C 65.31, H 6.34, N 4.39.
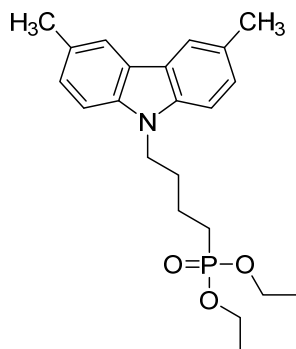
Diethyl [4-(3,6-dimethyl-9*H*-carbazol-9-yl)butyl]phosphonate (3b): **2b** (0.8 g, 2.42 mmol) was dissolved in triethyl phosphite (9 ml, 52.49 mmol) and the reaction mixture was heated at reflux overnight. After reaction completion (TLC, acetone: *n*-hexane, 6:19, v:v) the solvent was distilled off under reduced pressure. The crude product was purified by column chromatography (acetone/*n*-hexane 1:4 v/v) to give 0.89g (95%) of yellowish resin.

^{1}H NMR (400 MHz, CDCl$_3$): δ 7.84 (s, 2H), 7.25 – 7.22 (m, 4H), 4.24 (t, J = 7.0 Hz, 2H), 4.00 (quint, J = 7.3 Hz, 4H), 2.51 (s, 6H), 1.93 (quint, J = 7.5 Hz, 2H), 1.75 – 1.58 (m, 4H), 1.24 (t, J = 7.0 Hz, 6H).

^{13}C NMR (100 MHz, CDCl$_3$): δ 139.0, 127.9, 126.9, 122.9, 120.4, 108.3, 61.62, 61.56, 42.6, 29.92, 29.77, 26.2, 24.8, 21.5, 20.54, 20.49, 16.53, 16.47.

Anal. calcd for C$_{22}$H$_{30}$NO$_3$P, %: C 68.20, H 7.80, N 3.62, found, %: C 68.03, H 7.98, N 3.79.
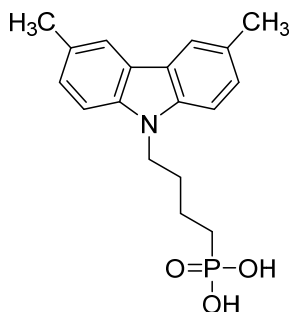
[4-(3,6-dimethyl-9*H*-carbazol-9-yl)butyl]phosphonic acid (Me-4PACz): **3b** (0.6 g, 1.55 mmol) was dissolved in anhydrous 1,4-dioxane (20 ml) under argon atmosphere and bromotrimethylsilane (2.12 ml, 15.59 mmol) was added dropwise. Reaction was stirred for 22 h at 25ºC under argon atmosphere. Afterwards, methanol (3 ml) was added and stirring continued for 3h. Finally, distilled water was added dropwise (15 ml), until solution became opaque, and it was stirred overnight. Product was filtered off, washed with water, dissolved in tetrahydrofuran (1 ml) and precipitated into *n*-hexane (15 ml). The product was filtered off and washed with *n*-hexane, to give 0.460 g (91 %) of white powder.

^{1}H NMR (400 MHz, (CD$_3$)$_2$SO): δ 7.88 (s, 2H), 7.45 (d, J = 8.3 Hz, 2H), 7.23 (d, J = 8.3 Hz, 2H), 4.34 – 4.27 (m, 2H), 2.47 (s, 6H), 1.85 – 1.76 (m, 2H), 1.58 – 1.45 (m, 4H).

^{13}C NMR (100 MHz, (CD$_3$)$_2$SO): δ 138.6, 127.0, 126.8, 122.0, 112.0, 109.0, 42.0, 29.71, 29.56, 28.1, 26.8, 21.1, 20.49, 20.45.

Anal. calcd for C$_{18}$H$_{22}$NO$_3$P, %: C 65.25, H 6.69, N 4.23, found, %: C 65.38, H 6.51, N 4.29.
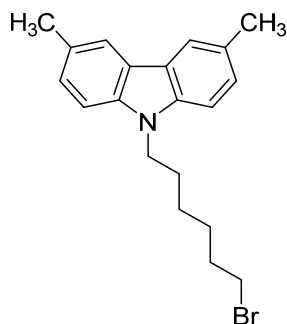
9-(6-Bromohexyl)-3,6-dimethyl-9*H*-carbazole (**2c**): **1a** (0.6 g, 3.07 mmol) was dissolved in 1,6-dibromohexane (9 ml, 58.51 mmol), tetrabuthylammonium bromide (0.148 g, 0.46 mmol) and 50% KOH aqueous solution (0.86 ml, 15.35 mmol) were added subsequently. Reaction was stirred at 60°C overnight (TLC, acetone: *n*-hexane 1:24 *v/v*). After completion of the reaction, extraction was done with dichloromethane. The organic layer was dried over anhydrous Na_2SO_4 and the solvent was distilled off under reduced pressure. The crude product was purified by column chromatography (acetone: *n*-hexane 1:249 *v/v*) to give 1.04 g (95 %) of colourless compound

^{1}H NMR (400 MHz, CDCl₃): δ 7.85 (s, 2H), 7.25 – 7.23 (m, 4H), 4.22 (t, *J* = 7.0 Hz), 3.32 (t, *J* = 6.7 Hz, 2H), 2.52 (s, 6H), 1.88 – 1.80 (m, 2H), 1.80 – 1.72 (m, 2H), 1.47 – 1.39 (m, 2H), 1.38 – 1.29 (m, 2H).

^{13}C NMR (100 MHz, CDCl₃): δ 139.1, 127.9, 126.9, 122.9, 120.4, 108.4, 43.0, 33.9, 32.7, 29.0, 28.1, 26.6, 21.5.

Anal. calcd for $C_{20}H_{24}BrN$, %: C 67.04, H 6.75, N 3.91, found, %: C 67.18, H 6.62, N 4.10.
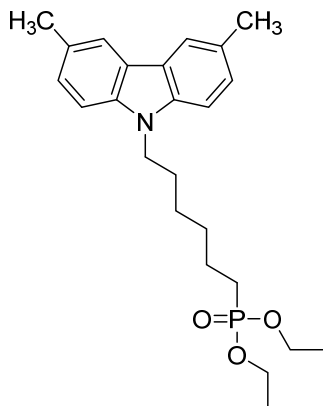
Diethyl [6-(3,6-dimethyl-9*H*-carbazol-9-yl)hexyl]phosphonate (3c): **2c** (1 g, 2.79 mmol) was dissolved in triethyl phosphite (10 ml, 58.32 mmol) and the reaction mixture was heated at reflux overnight. After reaction completion (TLC, acetone: *n*-hexane 6:19 *v/v*) the solvent was distilled off under reduced pressure. The crude product was purified by column chromatography (acetone: *n*-hexane 4:21 *v/v*) to give 0.96g (82%) of yellowish resin.

^{1}H NMR (400 MHz, CDCl₃): δ 7.84 (s, 2H), 7.25 – 7.22 (m, 4H), 4.22 (t, *J* = 7.0 Hz, 2H), 4.10 – 3.99 (m, 4H), 2.52 (s, 6H), 1.82 (p, *J* = 7.0 Hz, 2H), 1.70 – 1.59 (m, 2H), 1.59 – 1.48 (m, 2H), 1.40 – 1.31 (m, 4H), 1.28 (t, *J* = 7.0 Hz, 6H).

^{13}C NMR (100 MHz, CDCl₃): δ 139.0, 127.8, 126.8, 122.8, 120.3, 108.3, 61.50, 61.44, 43.0, 30.52, 30.36, 28.9, 26.9, 26.4, 25.0, 22.45, 22.40, 21.5, 16.6, 16.5.

Anal. calcd for $C_{24}H_{34}NO_3P$, %: C 69.37, H 8.25, N 3.37, found, %: C 69.56, H 8.13, N 3.50.
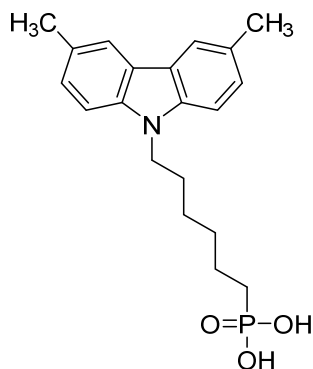
[6-(3,6-Dimethyl-9*H*-carbazol-9-yl)hexyl]phosphonic acid (Me-6PACz): **3c** (0.8 g, 1.92 mmol) was dissolved in anhydrous 1,4-dioxane (20 ml) under argon atmosphere and bromotrimethylsilane (2.5 ml, 19.25 mmol) was added dropwise. Reaction was stirred for 22 h at 25 ºC under argon atmosphere. Afterwards, methanol (3 ml) was added and stirring continued for 3h. Finally, distilled water was added dropwise (15 ml), until solution became opaque, and it was stirred overnight. Product was filtered off, washed with water, dissolved in tetrahydrofuran (2 ml) and precipitated into *n*-hexane (25 ml). The product was filtered off and washed with *n*-hexane, to give 0.580 g (84 %) of white powder.

^{1}H NMR (400 MHz, (CD$_3$)$_2$SO): δ 8.44 (br s, 2H), 7.84 (s, 2H), 7.38 (d, *J* = 8.4 Hz, 2H), 7.20 (d, *J* = 8.2 Hz, 2H), 4.25 (t, *J* = 6.9 Hz, 2H), 2.43 (s, 6H), 1.72 – 1.63 (m, 2H), 1.46 – 1.17 (m, 8H).

^{13}C NMR (100 MHz, (CD$_3$)$_2$SO): δ 138.6, 127.0, 126.8, 122.0, 120.0, 108.8, 42.2, 31.0, 29.9, 29.7, 28.4, 26.2, 22.7, 22.1, 21.0, 14.0.

Anal. calcd for C$_{20}$H$_{26}$NO$_3$P, %: C 66.84, H 7.29, N 3.90, found, %: C 66.73, H 7.47, N 3.76.

nPACz (n = 2,4,6)
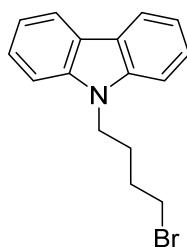
9-(4-Bromobutyl)-9*H*-carbazole (2d): **1b** (1 g, 5.98 mmol) was dispersed in toluene (13 ml). Afterwards, catalytic amount of tetrabutylammonium bromide, 50% KOH aqueous solution (13 ml) and 1,4-dibromobutane (1.428 ml, 11.96 mmol) were added. After 24h of stirring at room temperature, additional amount of 1,4-dibromobutane (1.428 ml, 11.96 mmol) was added, and the mixture was stirred at room temperature for additional 24h. After completion of the reaction (TLC, acetone:n-hexane, 3:22, v:v)., extraction was done with ethyl acetate. The organic layer was dried over anhydrous Na$_2$SO$_4$ and the solvent was distilled off under reduced pressure. The product was purified by column chromatography (*n*-hexane), to give 1.31 g (73 %) of white crystalline solid.

^{1}H NMR (400 MHz, (CD$_3$)$_2$SO): δ 8.15 (d, *J* = 7.7 Hz, 2H), 7.62 (d, *J* = 8.2 Hz, 2H), 7.45 (t, *J* = 7.7 Hz, 2H), 7.19 (t, *J* = 7.4 Hz, 2H), 4.44 (t, *J* = 6.6 Hz, 2H), 3.54 (t, *J* = 6.3 Hz, 2H), 2.00 – 1.70 (m, 4H).

^{13}C NMR (101 MHz, (CD$_3$)$_2$SO): δ 139.9, 125.7, 122.0, 120.3, 118.7, 109.2, 41.3, 34.7, 29.8, 27.2.

Anal. calcd for C$_{16}$H$_{16}$BrN, %: C 63.59, H 5.34, N 4.63, found, %: C 63.64, H 5.40, N 4.67.

65
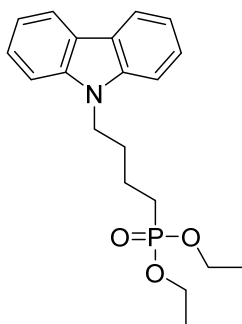
Diethyl [4-(9*H*-carbazol-9-yl)butyl]phosphonate (3d): **2d** (1.3 g, 4.3 mmol) was dissolved in triethyl phosphite (13 ml, 76 mmol) and the reaction mixture was heated at reflux for 24 h. After reaction completion (TLC, acetone:*n*-hexane, 7:18, v:v) the solvent was distilled off under reduced pressure. The crude product was purified by column chromatography (*n*-hexane; acetone:*n*-hexane, 1:4, v:v) to give 1.46 g (95%) of clear liquid.

^{1}H NMR (400 MHz, (CD$_3$)$_2$SO): δ 8.14 (d, *J* = 7.7 Hz, 2H), 7.62 (d, *J* = 8.2 Hz, 2H), 7.44 (t, *J* = 7.7 Hz, 2H), 7.19 (t, *J* = 7.4 Hz, 2H), 4.41 (t, *J* = 7.0 Hz, 2H), 3.89 (quint, *J* = 7.4 Hz, 4H), 1.96 – 1.63 (m, 4H), 1.58 – 1.39 (m, 2H), 1.13 (t, *J* = 7.0 Hz, 6H).

^{13}C NMR (101 MHz, (CD$_3$)$_2$SO): δ 140.4, 126.1, 122.5, 120.7, 119.1, 109.8, 61.24, 61.18, 42.2, 29.76, 29.60, 25.4, 24.0, 20.26, 20.21, 16.71, 16.66.

Anal. calcd for C$_{20}$H$_{26}$NO$_3$P, %: C 66.84, H 7.29, N 3.90, found, %: C 66.58, H 7.21, N 3.82.
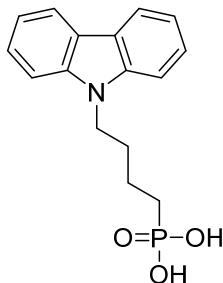
[4-(9*H*-carbazol-9-yl)butyl]phosphonic acid (4PACz): **3d** (1 g, 2.78 mmol) was dissolved in anhydrous 1,4-dioxane (30 ml) under argon atmosphere and bromotrimethylsilane (3 ml, 22.73 mmol) was added dropwise. Reaction was stirred for 24 h at 25 °C under argon atmosphere. Afterwards solvent was partially distilled off under reduced pressure, and the liquid residue was dissolved in methanol (30 ml). Next, distilled water was added dropwise (30 ml), until solution became opaque. Product was filtered off and washed with water to give 0.47 g (56 %) of white solid.

^{1}H NMR (400 MHz, (CD$_3$)$_2$SO): δ 8.14 (d, *J* = 7.7 Hz, 2H), 7.61 (d, *J* = 8.2 Hz, 2H), 7.44 (t, *J* = 7.6 Hz, 2H), 7.19 (t, *J* = 7.4 Hz, 2H), 4.39 (t, *J* = 6.9 Hz, 2H), 1.85 (quint, *J* = 7.2 Hz, 2H), 1.64 – 1.42 (m, 4H).

^{13}C NMR (101 MHz, (CD$_3$)$_2$SO): δ 140.2, 125.9, 122.2, 120.4, 118.8, 109.5, 42.2, 29.9, 29.7, 28.3, 26.9, 20.72, 20.67.

Anal. calcd for C$_{16}$H$_{18}$NO$_3$P, %: C 63.36, H 5.98, N 4.62, found, %: C 63.25, H 6.11, N 4.54.

66
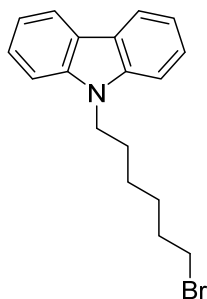
9-(6-bromohexyl)-9H-carbazole (2e): **1b** (1 g, 5.98 mmol) was dispersed in toluene (13 ml). Afterwards, catalytic amount of tetrabutylammonium bromide, 50% KOH aqueous solution (13 ml) and 1,6-dibromohexane (1.84 ml, 11.96 mmol) were added. After 24h of stirring at room temperature, additional amount of 1,6-dibromohexane (1 ml, 6.5 mmol) was added, and the mixture was stirred at room temperature for additional 24h. After completion of the reaction (TLC, acetone:*n*-hexane, 3:22, v:v)., extraction was done with ethyl acetate. The organic layer was dried over anhydrous Na_2SO_4 and the solvent was distilled off under reduced pressure. The product was purified using column chromatography (*n*-hexane), to give 1.38 g (70 %) of white crystalline solid.

^{1}H NMR (400 MHz, (CD_3)_2SO): δ 8.14 (d, *J* = 7.7 Hz, 2H), 7.59 (d, *J* = 8.2 Hz, 2H), 7.44 (t, *J* = 7.6 Hz, 2H), 7.19 (t, *J* = 7.4 Hz, 2H), 4.37 (t, *J* = 7.1 Hz, 2H), 3.46 (t, *J* = 6.6 Hz, 2H), 1.86 – 1.64 (m, 4H), 1.47 – 1.22 (m, 4H).

^{13}C NMR (101 MHz, (CD_3)_2SO) δ 139.7, 125.4, 121.8, 120.0, 118.4, 109.0, 41.9, 34.8, 31.9, 28.1, 27.0, 25.4.

Anal. calcd for $C_{18}H_{20}BrN$, %: C 65.46, H 6.10, N 4.24, found, %: C 65.52, H 6.09, N 4.26.
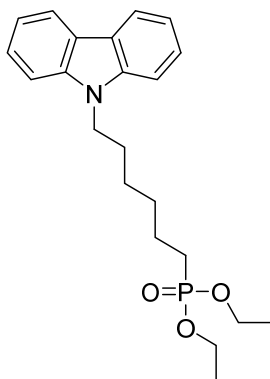
diethyl [6-(9H-carbazol-9-yl)hexyl]phosphonate (3e): **2e** (1.18 g, 3.59 mmol) was dissolved in triethyl phosphite (12 ml, 69.98 mmol) and the reaction mixture was heated at reflux for 24 h. After reaction completion (TLC, acetone:*n*-hexane, 7:18, *v/v*) the solvent was distilled off under reduced pressure. The crude product was purified by column chromatography (*n*-hexane; acetone:*n*-hexane, 1:4, *v/v*), to give 1.39 g (99%) of clear yellowish liquid.

^{1}H NMR (400 MHz, (CD_3)_2SO): δ 8.14 (d, *J* = 7.7 Hz, 2H), 7.59 (d, *J* = 8.2 Hz, 2H), 7.44 (t, *J* = 7.6 Hz, 2H), 7.19 (t, *J* = 7.4 Hz, 2H), 4.38 (t, *J* = 7.0 Hz, 2H), 4.07 – 3.94 (m, 4H), 1.79 – 1.57 (m, 6H), 1.43 – 1.23 (m, 10H).

^{13}C NMR (101 MHz, (CD_3)_2SO): δ 140.0, 125.6, 122.0, 120.2, 118.6, 109.2, 60.73, 60.67, 42.1, 29.43, 29.27, 28.2, 25.9, 25.0, 23.6, 21.95, 21.90, 16.30, 16.24.

Anal. calcd for $C_{22}H_{30}NO_3P$, %: C 68.20, H 7.80, N 3.62, found, %: C 68.33, H 7.84, N 3.68.
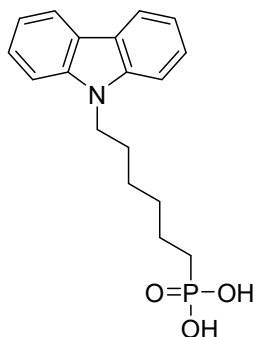
[6-(9*H*-carbazol-9-yl)hexyl]phosphonic acid (6PACz): 3e (1.4 g, 3.16 mmol) was dissolved in dry 1,4-dioxane (30 ml) under argon and bromotrimethylsilane (3 ml, 22.73 mmol) was added dropwise. Reaction was stirred for 24 h at 25 °C under argon atmosphere. Afterwards solvent was partially distilled off under reduced pressure, and the liquid residue was dissolved in methanol (30 ml). Next, distilled water was added dropwise (40 ml), until solution became opaque. Product was filtered off and washed with water to give 0.33 g (25 %) of white solid.

^{1}H NMR (400 MHz, (CD$_3$)$_2$SO): δ 8.15 (d, J = 7.7 Hz, 2H), 7.59 (d, J = 8.2 Hz, 2H), 7.45 (t, J = 7.6 Hz, 2H), 7.19 (t, J = 7.4 Hz, 2H), 4.37 (t, J = 7.1 Hz, 2H), 1.75 (quint, J = 7.2 Hz, 2H), 1.52 – 1.20 (m, 8H).

^{13}C NMR (101 MHz, (CD$_3$)$_2$SO): δ 140.0, 125.7, 122.0, 120.3, 118.6, 109.2, 42.2, 29.80, 29.64, 28.34, 28.10, 26.75, 26.15, 22.69, 22.64.

Anal. calcd for C$_{18}$H$_{22}$NO$_3$P, %: C 65.25, H 6.69, N 4.23, found, %: C 65.40, H 6.62, N 4.17.

G Publication: 27.9% Efficient Monolithic Perovskite/Silicon Tandem Solar Cells on Industry Compatible Bottom Cells

The following pages contain the publication addressed in section .

- Publication:
  Eike Köhnen, Philipp Wagner, Felix Lang, Alexandros Cruz, Bor Li, Marcel Roß, Marko Jošt, Anna B. Morales Vilches, Marko Topič, Martin Stolterfoht, Dieter Neher, Lars Korte, Bernd Rech, Rutger Schlatmann, Bernd Stannowski and Steve Albrecht. 27.9% Efficient Monolithic Perovskite/Silicon Tandem Solar Cells on Industry Compatible Bottom Cells. *Solar RRL*, 5:2100244, 2021.

- Author contribution:
  E.K. fabricated the perovskite top cell, measured the EQE, $J-V$ and UV-Vis and performed the optical simulations; P.W., A.B.M.V., L.K. and B.S. developed and fabricated the silicon bottom cell; E.K., A.B.M.V., P.W., B.S. and S.A. planned the experiments. E.K. and F.L. conducted and analyzed the PL measurements; A.C. performed the silicon single-junction solar cell simulations; M.R. conducted and analyzed the XRD measurements; E.K., M.J. ,B.L. and M.T. designed fabricated and built-up the tandem aging setup; E.K. drafted the manuscript; All authors participated in proofreading and correcting; M.T., D.N., L.K., B.R., R.S., B.S. and S.A. supervised the projects.

27.9% Efficient Monolithic Perovskite/Silicon Tandem Solar Cells on Industry Compatible Bottom Cells

Eike Köhnen, Philipp Wagner, Felix Lang, Alexandros Cruz, Bor Li, Marcel Roß, Marko Jošt, Anna B. Morales-Vilches, Marko Topič, Martin Stolterfoht, Dieter Neher, Lars Korte, Bernd Rech, Rutger Schlatmann, Bernd Stannowski,* and Steve Albrecht*

Monolithic perovskite/silicon tandem solar cells recently surpass the efficiency of silicon single-junction solar cells. Most tandem cells utilize >250 μm thick, planarized float-zone (FZ) silicon, which is not compatible with commercial production using <200 μm thick Czochralski (CZ) silicon. The perovskite/silicon tandem cells based on industrially relevant 100 μm thick CZ-silicon without mechanical planarization are demonstrated. The best power conversion efficiency (PCE) of 27.9% is only marginally below the 28.2% reference value obtained on the commonly used front-side polished FZ-Si, which are about three times thicker. With both wafer types showing the same median PCE of 27.8%, the thin CZ-Si-based devices are preferred for economic reasons. To investigate perspectives for improved current matching and, therefore, further efficiency improvement, optical simulations with planar and textured silicon have been conducted: the perovskite's bandgap needs to be increased by ≈0.02 eV when reducing the silicon thickness from 280 to 100 μm. The need for bandgap enlargement has a strong impact on future tandem developments ensuring photostable compositions with lossless interfaces at bandgaps around or above 1.7 eV.

1. Introduction

Today's photovoltaic market is dominated by crystalline silicon-based solar cell technology. With a record power conversion efficiency (PCE) of 26.7%,[1] silicon single-junction solar cells are approaching their theoretical limit of 29.4%.[2] To overcome this limit, silicon solar cells can be combined with wider bandgap materials into multijunction solar cells, where each photovoltaic active material converts a specific part of the spectrum efficiently into electrical power. With two active materials (commonly termed tandem solar cells), the theoretical PCE limit is ≈46% based on detailed balance arguments.[3] The excellent optoelectronic properties as well as the tunable bandgap and potentially low-cost fabrication make metal halide perovskites suitable candidates for the top cell material in tandem solar cells.[4–13] Only 3 years after the first realization of a p–i–n tandem solar cell by Bush et al.,[14]

E. Köhnen, Dr. P. Wagner, B. Li, M. Roß, Dr. L. Korte, Prof. S. Albrecht
Helmholtz-Zentrum Berlin für Materialien und Energie GmbH
Young Investigator Group Perovskite Tandem Solar Cells
12489 Berlin, Germany
E-mail: steve.albrecht@helmholtz-berlin.de

Dr. F. Lang, Dr. M. Stolterfoht, Prof. D. Neher
Institute of Physics and Astronomy
University of Potsdam
14476 Potsdam, Germany

Dr. A. Cruz, Dr. A. B. Morales-Vilches, Prof. R. Schlatmann,
Prof. B. Stannowski
Helmholtz-Zentrum Berlin für Materialien und Energie GmbH
PVcomB
12489 Berlin, Germany
E-mail: bernd.stannowski@helmholtz-berlin.de

Dr. M. Jošt, Prof. M. Topič
Faculty of Electrical Engineering
University of Ljubljana
Tržaška 25, 1000 Ljubljana, Slovenia

Prof. B. Rech
Helmholtz-Zentrum Berlin für Materialien und Energie GmbH
Scientific Management
12489 Berlin, Germany

Prof. B. Rech, Prof. S. Albrecht
Faculty IV – Electrical Engineering and Computer Science
Technical University Berlin
10587 Berlin, Germany

Prof. R. Schlatmann
Faculty 1 School of Engineering – Energy and Information
HTW Berlin–University of Applied Sciences
12459 Berlin, Germany

Prof. B. Stannowski
Faculty II – Mathematics, Physics, Chemistry
Beuth University of Applied Sciences Berlin
13353 Berlin, Germany

the highest scientifically reported efficiency of 29.15% is close to the theoretical limit of silicon single-junction solar cells.[15] With a certified efficiency of 29.52%, Oxford PV surpassed this limit but did not disclose any further details.[16]

These high efficiencies are achieved on rather thick front-side polished float-zone (FZ) silicon heterojunction solar cells, which are industrially not relevant for three reasons: 1) chemical–mechanical polishing (CMP) is time consuming and expensive. Therefore, it is desirable to use either chemical polishing as it is used in passivated emitter and rear cell (PERC) industry or double-side textured wafers. The latter approach is favored because such textures can be produced in a standard batch process and they provide optical advantages. Perovskite/silicon tandem processing on such wafers is addressed in recent publications.[4,9,17–21] However, solution processing of high-efficiency tandem solar cells using such textures still remains challenging due to the difficulties of processing very thin perovskite layers on micrometer-sized pyramid structures. 2) FZ-silicon is not used for PV mass production. Instead, Czochralski (CZ) silicon will remain the main method to fabricate silicon ingots,[22] mainly because of lower costs. 3) The absorption of Si for photon energies just above the bandgap, i.e., in the infrared (IR) part of the spectrum, is relatively poor. For tandem cells, however, where the top cell will absorb most of the higher energy photons, the IR response of the bottom cells is crucial.[5,23] Therefore, the bottom cell thickness in most publications on perovskite/silicon tandem solar cells is 260 to 300 μm, whereas according to current market forecasts, the industrially relevant thickness for n-type monocrystalline silicon is just 140 to 150 μm (as cut) in 2022.[24]

In this article, we demonstrate for the first time monolithic perovskite/silicon tandem solar cells based on thin non-CMP n-type CZ-silicon bottom cells. The reduced response in the IR region for thinner bottom cells will shift the optimal top cell bandgap for standard test conditions toward larger energies.

2. Solar Cells

We use (100)-oriented ≈130 μm thick (as cut) n-type CZ-silicon wafers with random pyramids on the rear side and a specified resistivity of ≈5 Ω cm. The front side of these CZ-based bottom cells was chemically polished using standard etching procedures in PERC industry but using a more aggressive treatment, removing up to 20 μm, to obtain a surface compatible with the top-cell processing.[25,26] Tandem solar cells with these type of bottom cells are termed "CZ-based." As a reference, we use (100)-oriented 280 ± 20 μm thick FZ wafers with random pyramids on the rear side, a CMP front side, and a resistivity of ≈3 Ω cm (in the following termed "FZ-based"). The front and rear side of all wafers are passivated with intrinsic amorphous silicon ((i)a-Si:H) layers. On the rear side, p-doped a-Si:H is deposited on the passivating layer. N-doped nanocrystalline silicon oxide (nc-SiO$_x$:H) optimized in refractive index for optimum NIR incoupling on the front passivating layer serves as electron-selective contact.[5] All silicon layers were deposited by plasma-enhanced chemical vapor deposition (PECVD). On top of the (n) nc-SiO$_x$:H layer, an In$_2$O$_3$-based transparent conducting oxide (TCO) is deposited, whereas the rear contact consists of a layer stack of aluminum-doped zinc oxide (AZO) and silver. More details can be found in the Materials and methods section in the Supporting Information. After processing the bottom cells, the measured thicknesses of the CZ- and FZ-based bottom cells are 100 and 280 μm, respectively. **Figure 1** shows photographs of the polished and nonpolished bottom cell front surfaces and the topography of the respective wafers acquired via confocal 3D laser scanning microscope (CLSM). For the CMP surface of the FZ silicon, horizontal artifacts appeared during acquisition
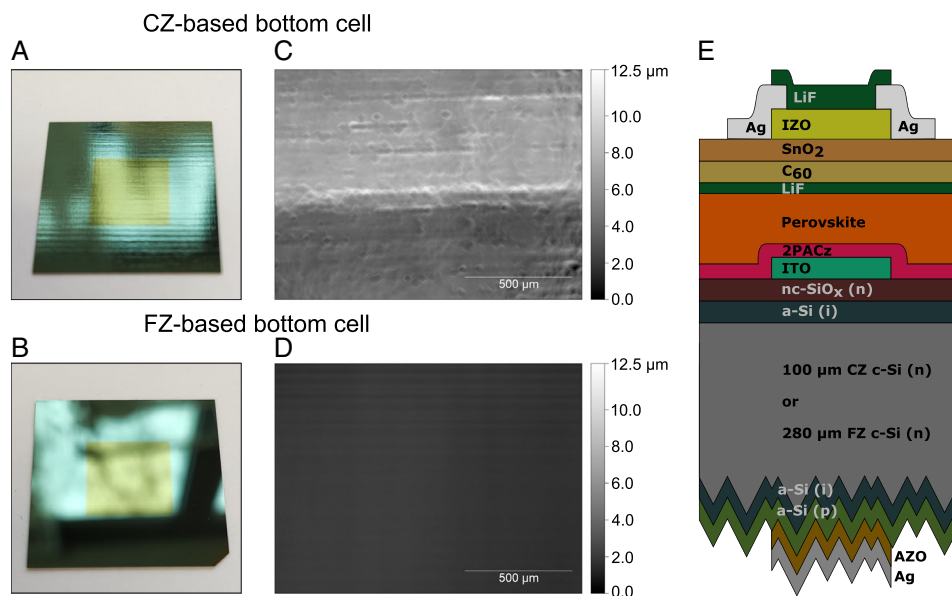
Figure 1. A,B) Photographs of the CZ-based silicon bottom cell and chemical–mechanical polished FZ-based silicon bottom cell. C,D) The topography of the CZ-based bottom cell and FZ-based bottom cell is acquired with a confocal laser scanning microscope and similar z-scalebars. E) Schematic stack of the monolithic perovskite/silicon tandem solar cell used in this work.

leading to falsified roughness values (see Figure S2, Supporting Information, for an adjusted scale). Therefore, atomic force microscopy (AFM) is used to image and analyze the surface of the FZ-based bottom cell (Figure S3, Supporting Information). The root mean square roughness values (Sq) are extracted from the areas as shown in Figure S3, Supporting Information. They amount to 1 and 736 nm for the FZ-based and CZ-based bottom cells, respectively. The maximum height values (Sz) are 9 nm and 7.7 μm for the FZ-based and CZ-based bottom cells, respectively. Although the Sz for CZ silicon is very high, the lateral dimension of the features is large enough to enable complete coverage during spin coating. This is evident for the saw mark visible for the CZ silicon in the CLSM image (Figure 1C): The step height is ≈5–6 μm (see Figure S4, Supporting Information), but since it extends over 100 μm, it should not be problematic for solution-processed perovskite layers.

To investigate the influence of the different wafer types (i.e., thickness and topography) on the optical properties, we measured reflection of the bare wafers. The reflection spectra shown in Figure S5, Supporting Information, demonstrate that the reflection for wavelengths below 950 nm is not affected by the difference in topography or thickness. For longer wavelengths, the reflection is higher for the thin CZ silicon. Less light is absorbed due to the thinner silicon. Thus, the amount of light arriving at the rear side of the cell is increased, which consequently increases the amount of light reflected at the rear side, too. For the same reason, the light reflected at the rear side of the cell is absorbed less while being transferred back in the thinner silicon bottom cell, leading ultimately to an increased outcoupling at the front side and thus reflection.

For the p–i–n top cell which is identical on both types of bottom cells (Figure 1E), a self-assembled monolayer, 2PACz, is used as a hole-selective layer (HSL). In addition to its electrical advantages, it enables conformal coverage on the nonpolished bottom cell.[27] The nominal perovskite composition is $Cs_{0.05}(MA_{0.23}FA_{0.77})_{0.95}Pb(Br_{0.23}I_{0.77})_3$ yielding a bandgap of 1.68 eV. On top of the perovskite, LiF and C_{60} are deposited via thermal evaporation and SnO_2 is deposited via atomic layer deposition. After the sputter deposition of zinc-doped indium

oxide (IZO) as transparent conductive oxide, Ag and LiF are thermally evaporated as split ring-type bus bar electrode and antireflective coating, respectively. The active area of the resultant tandem solar cells is 1 cm². A detailed description can be found in the Materials and Methods section in the Supporting Information. To monitor the process, opaque perovskite single-junction solar cells with an active area of 0.16 cm² were fabricated together with the tandem solar cells. The median performance values (10 devices) for opaque perovskite single-junctions are 78.5% for the fill factor (FF), 20.3 mA cm⁻² for the short-circuit current density (J_{SC}), 1.2 V for the open-circuit voltage (V_{OC}), and 19.3% for the PCE (see Figure S6, Supporting Information). A maximum efficiency of 19.9% with a V_{OC} of 1.21 V was obtained in this p–i–n type configuration, which is among the highest PCE and V_{OC} values for perovskite cells as typically used in two-terminal tandem solar cells.[28]

Figure 2A shows the external quantum efficiency (EQE) and reflection spectra of two-terminal (monolithic) tandem solar cell champion devices based on thin CZ and thick FZ bottom cells. In the short-wavelength range, a minor difference in reflection occurs. We account this difference to very slight variations of layer thicknesses in the front contact, leading to altered interference patterns. The difference in the long wavelength range is a result of a difference in the bottom cell thickness, as described previously. For both tandem solar cells, the EQE spectra of the perovskite subcells (top cells) are very similar. Consequently, the photogenerated current densities (J_{Ph}) under 100 mW cm⁻² AM1.5 G illumination are also similar in both perovskite subcells (19.56 and 19.44 mA cm⁻² for the CZ and FZ cells, respectively). The main difference between the tandem cells occurs in the EQEs of the silicon subcells (bottom cells). The J_{Ph} in the silicon bottom cell of the thick FZ-based tandem solar cell is 19.08 mA cm⁻². The reduced bottom cell thickness in the CZ-based tandem solar cell causes a lower response in the near-IR region leading to a reduced photogenerated current density of 17.81 mA cm⁻². Therefore, the cumulative photogenerated current density decreases from ≈38.52 to ≈37.37 mA cm⁻². As the J_{SC} of tandem solar cells is mainly determined by the J_{Ph} of the limiting subcell, a lower J_{SC} for the thin CZ-based tandem solar cell is expected. In contrast,
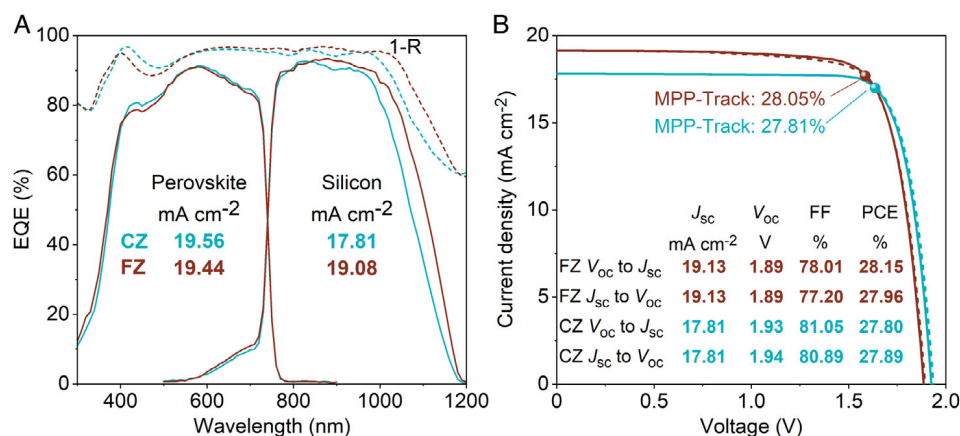
Figure 2. A) Comparison of the EQE spectra and reflection spectra (denoted as 1-R) between champion tandem solar cells based on thick FZ-silicon and thin CZ-silicon. B) J–V measurement of the tandem solar cells shown in (A) including the photovoltaic parameters and values obtained by 5 min MPP-tracking as shown in Figure S9, Supporting Information.

the current mismatch between the subcells increases. As we have reported previously, the tandem's FF is affected by the current mismatch.[7] Generally, the FF increases with larger mismatch. In addition, thinner silicon wafers lead to higher V_{OC} values due to an decreasing total recombination current density.[2] To estimate the gain in V_{OC}, we simulated silicon single-junction solar cells (illumination spectrum as in the tandem) with CZ- and FZ-silicon as used for tandem solar cells with the program Quokka3 (see Figure S7, Supporting Information, and the Materials and Methods section in the Supporting Information for more details). A V_{OC} enhancement of ≈17 mV is expected when using 100 μm CZ-silicon instead of 280 μm FZ-silicon. Even though the FF of the bottom cell also depends on the thickness and fabrication method, the simulations reveal that the configurations investigated in this work, both cell types, FZ and CZ, should deliver the same FF of 82.5% to 83% (see Figure S7, Supporting Information). Summarizing, the thinner CZ-based tandem solar cell is expected to have a lower J_{SC}, higher FF (due to larger current mismatch), and higher V_{OC}.

The J–V curves shown in Figure 2B confirm these expectations. The best reference device based on thick FZ wafers has a J_{SC} of 19.13 mA cm^{-2}, V_{OC} of 1.89 V, and FF up to 78.01% and as a result a PCE of up to 28.15%. This value is in very good agreement to our previous results for similar tandem layer stacks.[15] For the thin CZ tandem solar cell, the high FF of 80.89% partially compensates the lower J_{SC} of 17.81 mA cm^{-2}. Combined with a higher V_{OC} of 1.94 V, the PCE of this cell is 27.89%. This value is just 0.26%$_{abs}$ below the PCE of the front-side polished, thick FZ reference cell. Note that another J–V scan of the same cell led to a similar but yet slightly higher FF of 81.15% which is to the best of our knowledge the highest FF presented for perovskite/silicon tandem solar cells to date (see Figure S8, Supporting Information). The improvement of the FF per mismatch is higher than what we reported previously,[7] but as elaborated by Boccard et al., the improvement in FF depends strongly on the performance of the individual subcells.[29] Stable operation of the herein presented tandem solar cells is highlighted by 5 min maximum power point (MPP)-tracks as shown in Figure S9, Supporting Information. After 300 s MPP-tracking, PCE values of 28.05% and 27.81% are measured for the FZ- and CZ-based device, respectively, which is well in line with the J–V curve-derived efficiency. The illuminated J–V results for three CZ and four FZ tandem solar cells are summarized in Figure S10, Supporting Information. They reveal the same median PCE of 27.8% for both CZ- and FZ-based tandem solar cells. The V_{OC} improvement by 30 to 40 mV for the best devices is slightly more than expected from simulations. Therefore, we measured absolute photoluminescence of the top and bottom cell for both configurations to extract the quasi-Fermi level splitting (QFLS or implied V_{OC}).[30,31] The intensity of the laser was set to match the current density generated within each subcell under AM1.5 G illumination. The PL spectra, QFLS values, and radiative limits are shown in Figure S11, Supporting Information. For the perovskite subcell, the QFLS values are the same on both the FZ- and CZ-based tandem solar cells. They amount to ≈1.20 eV, which is consistent with the V_{OC} of the perovskite single-junction solar cells (see Figure S6, Supporting Information). The QFLS of the silicon subcell in the FZ-based tandem solar cell is ≈690 meV.

Consequently, the sum of the perovskite and silicon QFLS for the FZ-based cell is ≈1.89 eV, which is in very good agreement with its V_{OC} extracted from the J–V curve (1.90–1.91 V for this specific sample). For the CZ-based tandem cell, a QFLS of 710 meV in the Si wafer was calculated. The enhancement of ≈19 meV compared to the FZ-based cell matches well with the simulated V_{OC} enhancement of 17 mV. We find well-agreeing values of the cumulative QFLS (1.910 eV) and the measured V_{OC} (1.92–1.93 V for this sample) for the CZ-based tandem cells. Therefore, we account the previously mentioned V_{OC} improvement of up to 40 mV to a sample to sample variation.

To exclude any structural changes in the perovskite due to different surface topographies of the bottom cells, X-ray diffraction (XRD) measurements were conducted. The XRD patterns acquired for the HSL/perovskite stack deposited on the different bottom cells reveal similar crystallization of the perovskite films on both surfaces (see Figure S12, Supporting Information). We attribute the additional peak around 32.8° for the FZ-sample to stem from the In$_2$O$_3$-based recombination layer.

To analyze the effect of the bottom cell in more detail, we measured the J–V curve of the CZ-based tandem solar cell in a way that the J_{Ph} values of both subcells are equal to the respective J_{Ph} values in the FZ tandem solar cell (i.e., same mismatch conditions for CZ- and FZ-based tandem solar cells). This required to increase the illumination intensity only in the IR region of the spectrum, which can be easily done with the utilized light-emitting diode sunsimulator. In Figure S13, Supporting Information, this J–V measurement with adjusted J_{Ph} values is compared to the J–V of the FZ tandem solar cell under AM1.5G conditions. In addition to the increased V_{OC}, just a slight deviation occurs at voltages just below the MPP. The FF values of both measurements are very similar, demonstrating that the increased FF of the CZ tandem solar cell under AM1.5G conditions arises mainly from the increased current mismatch.[7]

The long-term stability of one CZ- and two FZ-based tandem solar cells (nonencapsulated) is shown in Figure S14, Supporting Information. The initial PCE values are 27.6% (CZ), 28.15% (FZ), and 27.4% (FZ). The cells were held at 25 °C in air, the relative humidity (RH) was not actively controlled. In addition to the J_{MPP}, V_{MPP}, the resulting PCE, and the normalized PCE, we show time series of the cell temperature and RH. The latter one ranges from 11% to 26%. After 1000 h continuous tracking, the cells were still performing at 67% (CZ), 70% (FZ), and 67% (FZ) of their respective initial PCE values, where the main parameter driving the reduction in PCE is J_{MPP}.

These efficient monolithic perovskite/silicon tandem solar cells demonstrate that it is not mandatory to use chemical-mechanical polishing for spin-coated perovskite films. Instead, chemical polishing as it is already deployed in industry, is sufficient for solution processing such as spin coating. Furthermore, it shows that industry relevant, almost threefold thinner CZ-silicon wafers can enable the same performance as the thick, CMP FZ-silicon wafers standardly used in lab-scale devices.

3. Optical Simulation

The reduced photogenerated current density for thinner silicon bottom cells necessitates adjustments to achieve current

matching or power matching conditions. Although the aforementioned experiment and previous reports demonstrate that the tandem solar cells are not highly sensitive to current mismatch conditions,[7,32–34] the highest PCE values might be achieved with current or power matching conditions. Moreover, there are various effects affecting the mismatch conditions, as we will discuss later. Each of the effects needs to be controlled to obtain ultimately a current or power matched tandem solar cell.

Apart from increasing the IR response of the bottom cell by optical improvements, which is not the focus of this study, current matching can be achieved by reducing the perovskite thickness and/or widening the perovskite bandgap. To shed light on this aspect, we used GenPro4 to simulate the optical performance of tandem solar cells.[35] We simulated tandem solar cells with a silicon bottom cell thickness of 100 and 280 μm. For both bottom cells, the perovskite thickness and its bandgap were varied. The lower limit of the thickness of 700 nm represents a realistic case as this thickness can be easily achieved with solution processing.[9,10,17,18,21,36–38] As the J_{Ph} saturates toward thicker films (**Figure 3**A), an upper limit of 1500 nm was chosen. For each thickness, the bandgap of the perovskite was varied by shifting the refractive index n and extinction coefficient k (measured via spectral ellipsometry for $E_g = 1.63$ eV) along the wavelength axis to cover a bandgap range of 1.63 to 1.78 eV (Figure S15, Supporting Information).[39,40] The bandgap is taken as the inflection point of the perovskite absorption edge as shown in Figure S16, Supporting Information. All other layers were kept as in the experiment. An example of simulated EQE spectra with various perovskite bandgaps is shown in Figure S17, Supporting Information. Figure 3B shows the ideal top cell bandgap $E_{g,top,matched}$ as a function of the top cell's thickness when utilizing a 280 μm and 100 μm thick silicon bottom cell (see also Table S3, Supporting Information). The photogenerated current density of the perovskite top cell $J_{Ph,Perovskite}$ increases with thicker perovskite layers. As a consequence, the photogenerated current density of

the silicon bottom cell $J_{Ph,Silicon}$ decreases with thicker perovskite layers (Figure S18, Supporting Information). Thus, for thicker perovskite layers, it is necessary to widen the top cell bandgap if current matching is desired. When increasing the thickness from 700 to 1500 nm, the top cell bandgap needs to be increased by 0.047 eV for both bottom cell thicknesses. In the best case, this would improve the V_{OC}. As evident from Table S3, Supporting Information, the matched photogenerated current density $J_{Ph,matched}$ stays almost constant. In addition, the bottom cell thickness alters current matching conditions. We found that the reduction of the bottom cell thickness from 280 to 100 μm requires to widen the top cell bandgap by 0.02 eV, regardless of the perovskite's thickness. However, simultaneously $J_{Ph,matched}$ decreases from 19.64 to 19.14 mA cm^{-2} (average values). Therefore, for a perovskite thickness of 700 nm, its bandgap needs to increase from ≈1.69 to ≈1.71 eV if the bottom cell thickness is reduced. The higher V_{OC} from both top and bottom cell together (40–50 mV) will exactly compensate the reduced J_{SC} (when assuming that $J_{Ph,matched} = J_{SC}$). Obviously, the FF of the perovskite top cells needs to remain the same regardless of the perovskite thickness to maintain the high PCE. Ultimately, a trade-off between high J_{SC} (thick silicon wafer and narrow perovskite bandgap) and high V_{OC} (thin silicon wafer and wide perovskite bandgap) needs to be made to yield the highest efficiency. Finding this optimum bottom cell thickness will be work for the future. These simulations do not include any optimization of other (e.g., contact) layer thicknesses. The adjustment of these layer thicknesses can reduce the interference patterns appearing, especially in the NIR wavelength range for the silicon subcell (see Figure S18, Supporting Information). This would require an optimization for each individual top cell bandgap and thickness.

The same simulations were performed for double-side textured tandem solar cells. As previously simulated and experimentally demonstrated,[4,6,19,20] the additional front-side texture reduces reflection and removes interference patterns, enabling higher J_{Ph} and J_{SC} values (see Figure S19, Supporting
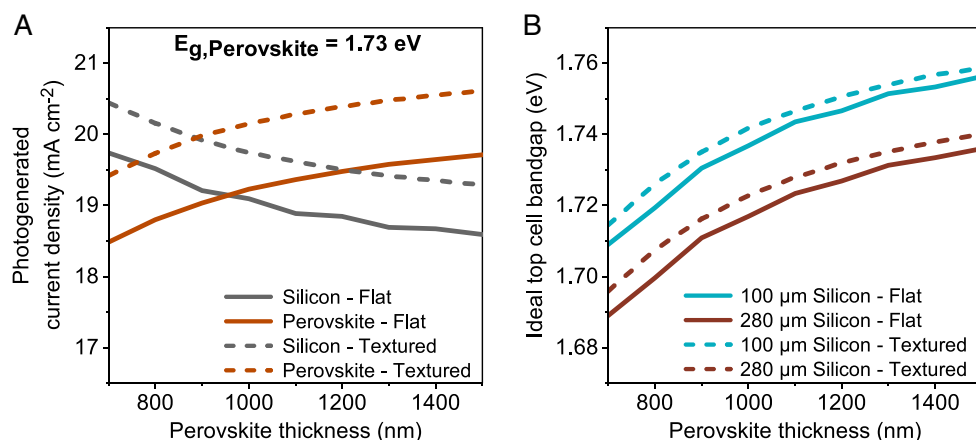
Figure 3. A) Simulated photogenerated current densities J_{ph} of perovskite/silicon tandem solar cells as a function of the perovskite thickness. The thickness of the silicon bottom cell is 100 μm and the perovskite bandgap is 1.73 eV. The rear side of the tandem cells is textured. The front side is either flat (denoted as "Flat") or textured (denoted as "Textured"). The corresponding EQE spectra are shown in Figure S18, Supporting Information. B) Ideal top cell bandgap which is needed to obtain current matching conditions as a function of the perovskite's thickness. Reducing the thickness of silicon from 280 to 100 μm increases the ideal top cell bandgap by ≈0.02 eV for both textured and flat front sides. The values including the photogenerated current density are shown in Table S3 (Flat) and Table S4 (Textured), Supporting Information.

Information, for simulated EQEs). The same trends appear as for planar devices: With thinner silicon, a larger perovskite bandgap is needed to ensure current matching conditions (See Table S4, Supporting Information and Figure 3). When reducing the silicon thickness from 280 to 100 μm, the perovskite bandgap should increase by 0.019 eV to maintain current matching at the same perovskite thickness. However, this comes along with a reduction of $J_{ph,matched}$ by $\approx$0.5 mA cm^{-2}.

Ultimately, the optimum bandgap not just depends on the thickness of the perovskite layer and the thickness of the silicon wafer. Luminescence from the perovskite top cell into the silicon bottom cell will relax the requirement for current matching conditions.[41] Furthermore, it was previously shown that higher operational temperatures and respective optical changes in top and bottom cells will lead to different optimum perovskite top cell bandgaps around 1.63 eV for highest energy yield with thick bottom cell wafers.[20] The transition from a monofacial to a bifacial tandem solar cell reduces the bandgap as well, if current matching should be maintained.[21] Therefore, the ideal device design cannot be easily derived from the performance under standard test conditions but needs to be derived for each case individually considering realistic outdoor conditions.

4. Conclusion

We demonstrated perovskite/silicon tandem solar cells based on industrially relevant silicon bottom cells, namely, 100 μm thin CZ-wafer with an industrial deployed chemical polishing for the front side and a textured rear side. For comparison, we fabricated tandem cells based on 280 μm thick FZ-wafers with a chemical–mechanical polished front side, which is standardly used in lab-scale devices. The CZ-based tandem cells have a PCE of up to 27.89%, which is just slightly below the value of 28.15% for FZ-based tandem cells. However, the median PCE of 27.8% indicates equal performance for both bottom cell types. The median V_{OC} increases from 1.89 V (max. 1.91 V) for the FZ-based cells to 1.92 V (max. 1.94 V) for the CZ-based cells, explained by the higher V_{OC} of the thin CZ bottom cell. Simultaneously, thinner silicon bottom cells present a lower EQE in the IR region, leading to a lower photogenerated current density and, thus, a lower J_{SC} (19.1 vs 17.8 mA cm^{-2}). The increased mismatch, when using an identical top cell, results in improved FF values (77.2% vs 80.9%). After 1000 h continuous MPP-tracking, the nonencapsulated cells still performed at 67% (CZ) and 67 to 70% (FZ) of their initial PCEs. We performed optical simulations to find current matching conditions for the 100 and 280 μm silicon bottom cells with planar and textured front sides. The perovskite bandgap needs to be increased by $\approx$0.02 eV when using a 100 μm thin silicon wafer instead of the commonly used thickness of 280 μm. Simultaneously, the expected J_{SC} reduces by $\approx$0.5 mA cm^{-2}. The higher V_{OC} from both top and bottom cell together (40 to 50 mV) can exactly compensate the reduction in J_{SC} for thinner wafers. Thus, to achieve highest PCE values with industrial bottom cells, the perovskite's bandgap needs to be widened to values well over 1.71 eV. The precise optimum top cell bandgap in this region is highly important, as these wide bandgap compositions are typically prone to phase segregation or are limited by nonradiative

recombination.[42,43] Therefore, this work highlights that further investigation is needed to enable highly efficient and stable wider bandgap compositions and with that, highest tandem PCE values when using industry relevant bottom cells.

5. Experimental Section

Detailed information about the fabrication and characterization is given in the Supporting Information.

Supporting Information

Supporting Information is available from the Wiley Online Library or from the author.

Conflict of Interest

The authors declare no conflict of interest.

Data Availability Statement

The data that supports the findings of this study are available in the supplementary material of this article or from the corresponding authors upon reasonable request.

[1] K. Yoshikawa, H. Kawasaki, W. Yoshida, T. Irie, K. Konishi, K. Nakano, T. Uto, D. Adachi, M. Kanematsu, H. Uzu, K. Yamamoto, *Nat. Energy* **2017**, *2*, 17032.

[2] A. Richter, M. Hermle, S. W. Glunz, *IEEE J. Photovoltaics* **2013**, *3*, 1184.

[3] A. S. Brown, M. A. Green, *Phys. E: Low-Dimensional Syst. Nanostruct.* **2002**, *14*, 96.

[4] F. Sahli, J. Werner, B. A. Kamino, M. Bräuninger, R. Monnard, B. Paviet-Salomon, L. Barraud, L. Ding, J. J. Diaz Leon, D. Sacchetto, G. Cattaneo, M. Despeisse, M. Boccard, S. Nicolay, Q. Jeangros, B. Niesen, C. Ballif, *Nat. Mater.* **2018**, *17*, 820.

[5] L. Mazzarella, Y.-H. Lin, S. Kirner, A. B. Morales-Vilches, L. Korte, S. Albrecht, E. Crossland, B. Stannowski, C. Case, H. J. Snaith, R. Schlatmann, *Adv. Energy Mater.* **2019**, *9*, 1803241.

[6] M. Jošt, E. Köhnen, A. B. Morales-Vilches, B. Lipovšek, K. Jäger, B. Macco, A. Al-Ashouri, J. Krč, L. Korte, B. Rech, R. Schlatmann, M. Topič, B. Stannowski, S. Albrecht, *Energy Environ. Sci.* **2018**, *11*, 3511.

[7] E. Köhnen, M. Jošt, A. B. Morales-Vilches, P. Tockhorn, A. Al-Ashouri, B. Macco, L. Kegelmann, L. Korte, B. Rech, R. Schlatmann, B. Stannowski, S. Albrecht, *Sustain. Energy Fuels* **2019**, *3*, 1995.

[8] B. Chen, Z. Yu, K. Liu, X. Zheng, Y. Liu, J. Shi, D. Spronk, P. N. Rudd, Z. Holman, J. Huang, *Joule* **2019**, *3*, 177.

[9] Y. Hou, E. Aydin, M. De Bastiani, C. Xiao, F. H. Isikgor, D. Xue, B. Chen, H. Chen, B. Bahrami, A. H. Chowdhury, A. Johnston, S. Baek, Z. Huang, M. Wei, Y. Dong, J. Troughton, R. Jalmood, A. J. Mirabelli, T. G. Allen, E. Van Kerschaver, M. I. Saidaminov, D. Baran, Q. Qiao, K. Zhu, S. De Wolf, E. H. Sargent, *Science* **2020**, *367*, 1135.

[10] J. Xu, C. C. Boyd, Z. J. Yu, A. F. Palmstrom, D. J. Witter, B. W. Larson, R. M. France, J. Werner, S. P. Harvey, E. J. Wolf, W. Weigand, S. Manzoor, M. F. A. M. van Hest, J. J. Berry, J. M. Luther, Z. C. Holman, M. D. McGehee, *Science* **2020**, *367*, 1097.

[11] P. S. C. Schulze, A. J. Bett, M. Bivour, P. Caprioglio, F. M. Gerspacher, Ö. Ş. Kabaklı, A. Richter, M. Stolterfoht, Q. Zhang, D. Neher, M. Hermle, H. Hillebrecht, S. W. Glunz, J. C. Goldschmidt, *Sol. RRL* **2020**, *4*, 2000152.

[12] D. Kim, H. J. Jung, I. J. Park, B. W. Larson, S. P. Dunfield, C. Xiao, J. Kim, J. Tong, P. Boonmongkolras, S. G. Ji, F. Zhang, S. R. Pae, M. Kim, S. B. Kang, V. Dravid, J. J. Berry, J. Y. Kim, K. Zhu, D. H. Kim, B. Efficient Shin, *Science* **2020**, *368*, 155.

[13] M. Jošt, L. Kegelmann, L. Korte, S. Albrecht, *Adv. Energy Mater.* **2020**, *10*, 1904102.

[14] K. A. Bush, A. F. Palmstrom, Z. J. Yu, M. Boccard, R. Cheacharoen, J. P. Mailoa, D. P. McMeekin, R. L. Z. Hoye, C. D. Bailie, T. Leijtens, I. M. Peters, M. C. Minichetti, N. Rolston, R. Prasanna, S. Sofia, D. Harwood, W. Ma, F. Moghadam, H. J. Snaith, T. Buonassisi, Z. C. Holman, S. F. Bent, M. D. McGehee, *Nat. Energy* **2017**, *2*, 17009.

[15] A. Al-Ashouri, E. Köhnen, B. Li, A. Magomedov, H. Hempel, P. Caprioglio, J. A. Márquez, A. B. Morales Vilches, E. Kasparavicius, J. A. Smith, N. Phung, D. Menzel, M. Grischek, L. Kegelmann, D. Skroblin, C. Gollwitzer, T. Malinauskas, M. Jošt, G. Matič, B. Rech, R. Schlatmann, M. Topič, L. Korte, A. Abate, B. Stannowski, D. Neher, M. Stolterfoht, T. Unold, V. Getautis, S. Albrecht, *Science* **2020**, *370*, 1300.

[16] National Renewable Energy Laboratory, Best Research-Cell Efficiency Chart, https://www.nrel.gov/pv/cell-efficiency.html (accessed: January 2021).

[17] B. Chen, Z. J. Yu, S. Manzoor, S. Wang, W. Weigand, Z. Yu, G. Yang, Z. Ni, X. Dai, Z. C. Holman, J. Huang, *Joule* **2020**, *4*, 850.

[18] A. S. Subbiah, F. H. Isikgor, C. T. Howells, M. De Bastiani, J. Liu, E. Aydin, F. Furlan, T. G. Allen, F. Xu, S. Zhumagali, S. Hoogland, E. H. Sargent, I. McCulloch, S. De Wolf, *ACS Energy Lett.* **2020**, *5*, 3034.

[19] G. Nogay, F. Sahli, J. Werner, R. Monnard, M. Boccard, M. Despeisse, F.-J. Haug, Q. Jeangros, A. Ingenito, C. Ballif, *ACS Energy Lett.* **2019**, *4*, 844.

[20] E. Aydin, T. G. Allen, M. De Bastiani, L. Xu, J. Ávila, M. Salvador, E. Van Kerschaver, S. De Wolf, *Nat. Energy* **2020**, *5*, 851.

[21] M. De Bastiani, A. J. Mirabelli, Y. Hou, F. Gota, E. Aydin, T. G. Allen, J. Troughton, A. S. Subbiah, F. H. Isikgor, J. Liu, L. Xu, B. Chen, E. Van Kerschaver, D. Baran, B. Fraboni, M. F. Salvador, U. W. Paetzold, E. H. Sargent, S. De Wolf, *Nat. Energy* **2021**, *6*, 167.

[22] International Technology Roadmap for Photovoltaic (ITRPV), 9th ed., https://itrpv.vdma.org/documents/27094228/29066965/ITRPV0Ninth0-Edition02018.pdf/23bde665-600c-4f3f-c231-fed2568f08e0 (accessed: October 2019).

[23] R. Santbergen, R. Mishima, T. Meguro, M. Hino, H. Uzu, J. Blanker, K. Yamamoto, M. Zeman, *Opt. Express* **2016**, *24*, A1288.

[24] ITRPV. International Technology Roadmap for Photovoltaic (ITRPV), 11th ed., https://itrpv.vdma.org/en/ueber-uns (accessed: June 2020).

[25] C. Kranz, S. Wyczanowski, U. Baumann, K. Weise, C. Klein, F. Delahaye, T. Dullweber, R. Brendel, *Energy Procedia* **2013**, *38*, 243.

[26] C. Kranz, S. Wyczanowski, S. Dorn, K. Weise, C. Klein, K. Bothe, T. Dullweber, R. Brendel, in *27th European Photovoltaic Solar Energy Conf. and Exhibition*, Frankfurt, Germany **2012**, pp. 557–560.

[27] A. Al-Ashouri, A. Magomedov, M. Roß, M. Jošt, M. Talaikis, G. Chistiakova, T. Bertram, J. A. Márquez, E. Köhnen, E. Kasparavičius, S. Levcenco, L. Gil-Escrig, C. J. Hages, R. Schlatmann, B. Rech, T. Malinauskas, T. Unold, C. A. Kaufmann, L. Korte, G. Niaura, V. Getautis, S. Albrecht, *Energy Environ. Sci.* **2019**, *12*, 3356.

[28] J. Tong, Q. Jiang, F. Zhang, S. B. Kang, D. H. Kim, K. Zhu, *ACS Energy Lett.* **2021**, *6*, 232.

[29] M. Boccard, C. Ballif, *ACS Energy Lett.* **2020**, *5*, 1077.

[30] M. Jošt, T. Bertram, D. Koushik, J. A. J. A. Marquez, M. A. M. A. Verheijen, M. D. M. D. Heinemann, E. Köhnen, A. Al-Ashouri, S. Braunger, F. Lang, B. Rech, T. Unold, M. Creatore, I. Lauermann, C. A. C. A. Kaufmann, R. Schlatmann, S. Albrecht, *ACS Energy Lett.* **2019**, *4*, 583.

[31] M. Stolterfoht, C. M. Wolff, J. A. Márquez, S. Zhang, C. J. Hages, D. Rothhardt, S. Albrecht, P. L. Burn, P. Meredith, T. Unold, D. Neher, *Nat. Energy* **2018**, *3*, 847.

[32] M. Meusel, R. Adelhelm, F. Dimroth, A. W. Bett, W. Warta, *Prog. Photovoltaics Res. Appl.* **2002**, *10*, 243.

[33] W. E. McMahon, K. E. Emery, D. J. Friedman, L. Ottoson, M. S. Young, J. S. Ward, C. M. Kramer, A. Duda, S. Kurtz, *Prog. Photovoltaics Res. Appl.* **2008**, *16*, 213.

[34] C. Ulbrich, C. Zahren, A. Gerber, B. Blank, T. Merdzhanova, A. Gordijn, U. Rau, *Int. J. Photoenergy* **2013**, *2013*, 1.

[35] R. Santbergen, T. Meguro, T. Suezaki, G. Koizumi, K. Yamamoto, M. Zeman, *IEEE J. Photovoltaics* **2017**, *7*, 919.

[36] B. Chen, S. Baek, Y. Hou, E. Aydin, M. De Bastiani, B. Scheffel, A. Proppe, Z. Huang, M. Wei, Y. Wang, E. Jung, T. G. Allen, E. Van Kerschaver, F. P. García de Arquer, M. I. Saidaminov, S. Hoogland, S. De Wolf, E. H. Sargent, *Nat. Commun.* **2020**, *11*, 1257.

[37] F. Xu, J. Liu, A. S. Subbiah, W. Liu, J. Kang, G. T. Harrison, X. Yang, F. H. Isikgor, E. Aydin, M. De Bastiani, S. De Wolf, *Small Sci.* **2021**, 2000044.

[38] A. Y. Alsalloum, B. Turedi, K. Almasabi, X. Zheng, R. Naphade, S. D. Stranks, O. F. Mohammed, O. M. Bakr, *Energy Environ. Sci.* **2021**, *14*, 2263.

[39] S. Albrecht, M. Saliba, J.-P. Correa-Baena, K. Jäger, L. Korte, A. Hagfeldt, M. Grätzel, B. Rech, *J. Opt.* **2016**, *18*, 064012.

[40] K. Jäger, L. Korte, B. Rech, S. Albrecht, *Opt. Express* **2017**, *25*, A473.

[41] A. R. Bowman, F. Lang, Y. Chiang, A. Jiménez-Solano, K. Frohna, G. E. Eperon, E. Ruggeri, M. Abdi-Jalebi, M. Anaya, B. V. Lotsch, S. D. Stranks, *ACS Energy Lett.* **2021**, *6*, 612.

[42] E. T. Hoke, D. J. Slotcavage, E. R. Dohner, A. R. Bowring, H. I. Karunadasa, M. D. McGehee, *Chem. Sci.* **2015**, *6*, 613.

[43] F. Peña-Camargo, P. Caprioglio, F. Zu, E. Gutierrez-Partida, C. M. Wolff, K. Brinkmann, S. Albrecht, T. Riedl, N. Koch, D. Neher, M. Stolterfoht, *ACS Energy Lett.* **2020**, *5*, 2728.

Supporting Information

27.9% Efficient Monolithic Perovskite/Silicon Tandems on industry compatible bottom cells

Eike Köhnen, Philipp Wagner, Felix Lang, Alexandros Cruz, Bor Li, Marcel Roß, Marko Jošt,

Anna B. Morales-Vilches, Marko Topič, Martin Stolterfoht, Dieter Neher, Lars Korte,

Bernd Rech, Rutger Schlatmann, Bernd Stannowski* and Steve Albrecht*

209

Materials and methods

Device fabrication

Preparation of the silicon bottom cell:

The silicon heterojunction (SHJ)-bottom cells were fabricated on two different wafer types. On the one hand a 130 µm thick saw damage etched CZ <100> n-type crystalline silicon (c-Si) wafer with a resistivity of ~5 Ω cm. On the other hand a 260 to 300 µm thick chemical mechanical polished FZ <100> n-type c-Si wafer with a resistivity of ~3 Ω cm. The front surface of the FZ wafers were left unmodified, while the front surface of the CZ wafers were chemically polished using standard etching procedures in PERC industry [1]but using a more aggressive treatment, removing up to 20µm,[2] in order to obtain a smoother surface compatible with the top cell processing. The rear surface of both wafer types were wet-chemically textured to obtain random pyramid with <111> facets in order to improve the optical response of the bottom cell in the NIR region. After a final RCA clean and a 3 minute HF dip (1% dilution in water) to strip the SiO_2 of the surface, a 5 nm thick, intrinsic (i) amorphous silicon (a-Si:H) layer was grown on both sides of the c-Si wafer in order to passivate the c-Si surface. A 5 nm thick, p-doped a-Si:H was deposited on the rear passivating layer to form the junction of the SHJ cell. On the polished front-side, a 90 nm thick, n-doped nanocrystalline silicon oxide layer (nc-SiO_x:H) with a refractive index n of 2.7 at 633 nm was used as a front surface field (FSF) of the SHJ bottom cell and intermediate layer between the top and the bottom cells. All the a- and nc-Si layers were deposited with an Applied Materials (AKT1600) plasma enhanced chemical vapor deposition (PECVD) tool. In order to contact the bottom cell a ZnO:Al/Ag layer stack was deposited on the textured back-side and a 20 nm thick commercially available In_2O_3-based TCO (nSCOT by Advanced Nano Products Co.,Ltd) was deposited on the front-side on top of the nc-SiOx:H interlayer, both depositions were DC-sputtered in an in-line sputtering tool from Leybold Optics. The contact layers of the silicon were deposited using shadow masks with an opening of 1.13×1.13 cm^2. The thickness of the silicon bottom cells (100 µm for CZ-Si and 280 µm for FZ-Si) was measured using a micrometer.

Perovskite materials:

Anhydrous DMSO (dimethyl sulfoxide), DMF (dimethylformamide) were purchased from Sigma Aldrich. Anhydrous ethanol was purchased from VWR. C_{60} (purity = 99.9 %) and lithium fluoride (purity $\geq$ 99.99 %) were purchased from Sigma Aldrich. FAI (formamidinium iodide) and MABr (methylammonium bromide) were purchased from Dyenamo. PbI_2 and $PbBr_2$ and 2PACz were bought from TCI. CsI was purchased from abcr GmbH. The ceramic 2 inch IZO (In_2O_3(90)ZnO(10)wt%) target was purchased from FHR Anlagenbau.

Preperation of the perovskite top cell:

The fabricated perovskite top cell has an inverted (p-i-n) planar structure and a layer configuration of <bottom cell>2PACz/Perovskite/LiF/C_{60}/SnO_2/IZO/Ag/LiF(ARC), where 2PACz is the hole-selective layer, LiF/C_{60} are the electron transport layer, SnO_2 is

the buffer layer and IZO (zinc doped indium oxide) is the TCO, Ag is the silver electrode and LiF(ARC) is the antireflective coating. The silicon substrates were blown with nitrogen and ethanol was spincoated at 3000 rpm to remove any dust particles. Afterwards they were treated in an UV-ozone cleaner for 10 min. 100 µl of the hole-selective material, 2PACz (1 mMol l^{-1} in anhydrous ethanol), was deposited on the substrate, spun at 3000 rpm for 30 s and annealed for 10 min at 100 °C. For the perovskite with the nominal composition $Cs_{0.05}(MA_{0.23}FA_{0.77})_{0.95}Pb(Br_{0.23}I_{0.77})_3$, whereas a PbX_2 (X=I or Br) excess of 9% was found to be beneficial, all powders (PbI_2, $PbBr_2$, FAI, MABr and CsI) were weighed in a single vial. The 1.5 mol l^{-1} solution was fabricated by adding a mixture of DMF:DMSO with a volume ratio of 4:1. Subsequently, the solution was shaked for 1 hour at 60°C. 100 µl of perovskite solution was then spread on the HSL and spun using one-step spincoating process (5s acceleration to 3500 rpm. Then 3500 rpm for 35 s). 25 s after the start of a spinning, 500 µl ethyl acetate anti-solvent drop was utilized. The films were annealed at 100 °C for 20 min. Afterwards, 1 nm LiF and 18 nm C_{60} were thermally evaporated at a rate of 0.05 and 0.15 Å s^{-1}, respectively. 20 nm SnO_2 were prepared by thermal ALD in an Arradiance GEMStar reactor. Tetrakis(dimethylamino)tin(IV) (TDMASn) was used as the Sn precursor and was held at 60 °C in a stainless steel container. Water was used as oxidant, and was delivered from a stainless steel container without intentional heating, whereas the precursor delivery manifold was heated to 115 °C. For the deposition at 80 °C, the TDMASn/purge1/H2O/purge2 times are of 1s/10s/0.2s/15s with corresponding nitrogen flows of 30sccm/90sccm/90sccm/90sccm. With this, 140 cycles leads to 20 nm tin oxide. IZO was sputtered in a Roth&Rau MicroSys 200 PVD. At a RF-power of 70 W the cells oscillated under the target to have a uniform deposition. A gas flow of 40 sccm Ar/O$_2$ (with 0.25vol% O$_2$) are used. A 100 nm thick Ag metal frame was evaporated at a rate of 1 Å s^{-1} through a shadow mask as a top contact, giving an active area of ~1 cm^2. Finally, 100 nm LiF was evaporated at a rate of 1 Å s^{-1} to serve as an anti-reflective coating.

Preparation of perovskite single junction devices

The perovskite single junction devices were fabricated very similarly to the top cell of the tandem solar cells. ITO-covered glass (Automated Research GmbH, 15 Ohm/sq sheet conductivity) was used as substrate, which was cleaned with Mucasol (2% in DI-water, substrates were brushed), DI-water, acetone and isopropanol, each for 15 minutes in an ultrasonic bath. Afterwards, the substrates were cleaned for 10 minutes in an UV-O$_3$ cleaner (FHR UVOH 150 Lab). The deposition of the 2PACz/Perovskite/LiF/C$_{60}$/SnO$_2$ layer stack is done as described in the previous section. Subsequently, 100 nm Ag are evaporated at a rate of 1 Å s^{-1}. The active area is 0.16 cm^2.

Characterization

J-V – Tandem solar cells

The tandem solar cells were measured in air under AM1.5G 1-sun-equivalent illumination with a Wavelabs Sinus-70 LED class AAA sun simulator. The cells did not experience any preconditioning. For calibration we used a slightly modified calibration route compared to Meusel *et al.*[3] We adjusted the spectrum such that for both subcells it led to the

photogenerated current densities obtained by EQE measurements. For this, we assumed that the J_{SC} of the tandem solar cell is equal to the photogenerated current density of the limiting subcell. Thus, for a silicon-limited cell, we first increased the intensity of the NIR light in order to assure a perovskite-limited cell. Subsequently, the blue wavelength region was adjusted until the J_{SC} of the perovskite-limited tandem solar cell was equal to the $J_{Ph,Perovskite}$ (calculated from EQE and AM1.5G spectrum). Finally, the intensity of the blue light was decreased until the tandem solar cell was silicon-limited again and the J_{SC} was equal to the $J_{Ph,Silicon}$. Note, that one must ensure that a change in the NIR wavelength region does not affect the photogenerated current density in the perovskite subcell and a change in the blue region does not affect the photogenerated current density in the silicon subcell. The backside of the cell was contacted with a metal vacuum chuck at 25°C, whereas the front side was contacted with two Au probes. A black laser-cut aperture mask designates the illuminated area to 1.008 cm^2. The J-V measurements were recorded using a home-built LabView software. The typical step size was 20 mV, with an integration time of 20 ms and settling time of 20 ms (250 mV/s).

J-V – Perovskite single junction solar cells

The J-V curves of single-junction cells were recorded in nitrogen atmosphere with a solar simulator (Oriel LCS-100) and Keithley 2400 source-measure unit, controlled by a custom LabView program. The intensity was calibrated to AM1.5G 1-sun-equivalent with a filtered KG3 Silicon reference solar cell, calibrated by Fraunhofer ISE (spectral mismatch is around 0.997, within the measurement error, thus no correction was applied). *J-V* scans were as performed in a 2-point-probe configuration. The typical step size was 20 mV, with an integration time of 20 ms and settling time of 20 ms (250 mV/s). The cells did not experience any preconditioning.

EQE – Tandem solar cells

The external quantum efficiency (EQE) was measured as a function of wavelength from 300 nm to 1200 nm with a step of 10 nm using a home built small spot EQE system. The beam size is 2×5 mm^2, thus smaller than the active area. When measuring perovskite top cell, infrared (850 nm) bias light was applied along with 0.6 V bias voltage to ensure a measurement in short-circuit conditions. When measuring silicon bottom cell, blue (455 nm) bias light was applied along with a bias voltage of 1 V.

Long-term stability

Monolithic non-encapsulated tandem solar cells were tracked in air at the maximum power point (MPP) with a self-constructed ageing setup. To guarantee homogenous illumination the LED-array consists of 193 LEDs, 144 of which are blue LEDs and 49 are NIR LEDs with a wavelength of 470 nm and 940 nm, respectively. With an independent tuneability of both intensities, the photocurrent of the top and bottom cell can be adjusted to increase or decrease the current mismatch as intended. The bottom cell is electrically connected to a copper block on the backside, whereas the top cell is connected with 2 pogo-pins. The cells were cooled to 25 °C using a peltier-element, while the cells were kept in place with

a vacuum pump. A black mask was used to cover the outside of the active area. The relative humidity was tracked every 15 minutes with an ISO-calibrated sensor. The current and voltage of each cell at MPP (using voltage perturbation), as well as the cell temperature was recorded every 5 minutes. To account for any measurement noise, the normalized PCE-track was normalized to the average of the first 60 minutes of the respective MPP-track. For the same reason, the final value is the average of the last 60 minutes.

Quantification of the QFLS in the perovskite and silicon sub-cells

We calculate the quasi-Fermi level splitting in the individual sub-cells by using the Shockley-Queisser equation, which links the radiative recombination density of free charges (J_{rad}) with the chemical potential per free electron-hole pair (μ) or the quasi-Fermi level splitting (QFLS) in the respective active material.[4,5]

$$J_{rad} = J_{0,rad} \exp (QFLS/k_B T), \qquad \text{(eq. S1)}$$

Here, $J_{0,rad}$ is the radiative thermal recombination current density in the dark, k_B the Boltzmann constant and T the temperature. Note that equation S1 is a simplification of Würfel's generalized Planck law, which is only valid for a QFLS that is a few $k_B T$ smaller that the bandgap $\mu < E_G - 3k_B T$.[6] If radiative recombination comes only from free charges, the radiative recombination current is identical to the photoluminescence yield times the elementary charge, that is $J_{rad} = \phi_{PL} \cdot e$. Moreover, we can define the photoluminescence quantum yield (PLQY) as the ratio of radiative to total recombination ($J_{R,tot}$), where the latter is identical to the generation current density (J_G) under open-circuit conditions (V_{OC})

$$\text{PLQY} = \frac{J_{rad}}{J_{R,tot}} = \frac{J_{rad}}{J_G} \qquad \text{(eq. S2)}$$

The QFLS is then given by

$$QFLS = k_B T \ln (\text{PLQY} * \frac{J_G}{J_{0,rad}}) \qquad \text{(eq. S3)}$$

With T = 300K and the measured PLQY values.

For a PLQY = 1, we further get the radiative limit of the QFLS (QFLS$_{rad}$) via:

$$QFLS_{rad} = k_B T \ln (\frac{J_G}{J_{0,rad}}) \qquad \text{(eq. S4)}$$

We note that equations 2 and 4 are only valid if the spectral dependence of J_{rad} is identical to $J_{0,rad}$, meaning recombination goes through the same channels regardless of the QFLS.

The parameters J_G and $J_{0,rad}$ were obtained in the following way: The generation current density J_G was approximated with the short-circuit current density of the complete solar cell. Similarly, the $J_{0,rad}$ was estimated by integrating the overlap of the external quantum efficiency of the device (EQE) with the black body spectrum ϕ_{BB} at 300 K over the energy.

$$J_{0,rad} = \int EQE\ \phi_{BB}\ d\epsilon \qquad \text{(eq. S5)}$$

with

$$\phi_{BB} = \frac{1}{4^2 \hbar^3 c^2} \cdot \frac{E^2}{\exp\left(\frac{E}{k_B T}\right) - 1} \qquad \text{(eq. S6)}$$

As shown in Figure S1.
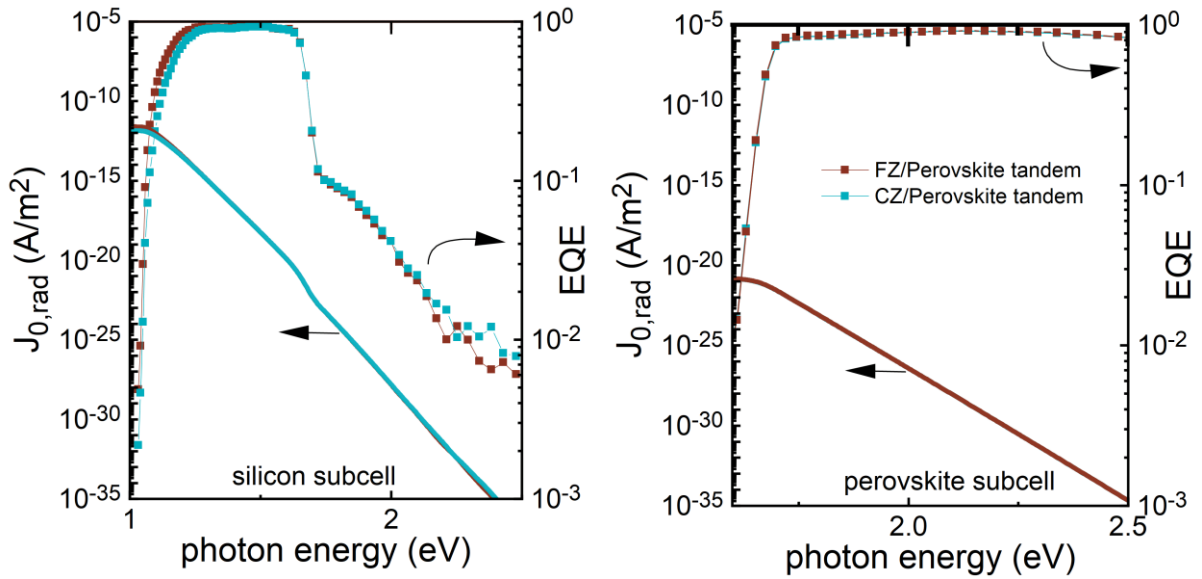
Figure S1: EQE$_{PV}$ onset of the two silicon and two perovskite subcells and their emitted spectral photon flux calculated when the device is in equilibrium with the black-body (BB) radiation of the surroundings at 300 K according to equation S5 and S6.

Table S1: Summary of the derived J_G and $J_{0,rad}$ values for the respective perovskite top and silicon bottom cells

sample	$J_{0,rad}$ perovskite subcell (A/m^2)	$J_{0,rad}$ silicon subcell (A/m^2)	J_{gen} perovskite subcell (A/m^2)	J_{gen} silicon subcell (A/m^2)
FZ	1.50E-21	2.71E-12	196	178
CZ	1.49E-21	1.56E-12	196	190

214

Absolute Photoluminescence Characterization: Photoluminescence of the perovskite top-and the silicon bottom-cell were recorded under selective excitation using a 445 nm or 808 nm CW laser from Insaneware. Both lasers were coupled through an optical fiber into an integrating sphere. The intensity of the lasers was adjusted to a one sun equivalent intensity, which matched the current density generated within each subcell (1.4×10^{17} and 1.3×10^{17} photons cm^{-2} s^{-1} for the perovskite top-and the silicon bottom-cell, respectively). The photoluminescence was then detected via a second optical fiber that coupled the output of the integrating sphere to an Andor SR393i-B spectrometer equipped with an Andor iDus silicon CCD camera and an iDus InGaAs (1.7μm) detector array. Photoluminescence from the perovskite was then measured with the silicon CCD, while the silicon bottom cell PL was measured with the InGaAs detector. The system was calibrated using a calibrated halogen lamp with specified spectral irradiance, which was shone into the integrating sphere. For each detector array, a spectral correction factor was calculated to match the detector's spectral output to the calibrated spectral irradiance of the lamp. The spectral photon density was obtained from the corrected detector signal (spectral irradiance) by division through the photon energy (hf), and the photon numbers of the excitation and emission obtained from numerical integration using Matlab. We corroborated the accuracy of derived PLQY values for the Si detector by measuring three fluorescent test samples with high specified PLQY ($\approx$ 70%) supplied from Hamamatsu Photonics, where the specified value could be accurately reproduced within a small relative error of <5%. The accuracy of PLQY values measured with the InGaAs detector was double-checked with the Si detector.

X-Ray Diffraction

For the X-ray diffraction patterns a Bruker D8 diffractometer in Bragg-Brentano geometry was used. The X-ray tube was operated at 40 mA and 40 kV acceleration voltage, emitting Cu K-alpha radiation. All X-ray diffraction patterns were recorded at room temperature using a self-constructed nitrogen filled sample holder.

Simulation of Silicon single junction solar cells

To simulate the J-V parameters of the silicon heterojunction solar cells used for bottom devices, the Quokka3 simulation tool was utilized.[7] For this purpose, typical silicon wafer absorber properties were introduced as input parameters as enlisted in Table S2. Most parameters are equal for CZ and FZ wafers in this case except for the wafer resistivity which was acquired via QSSPC measurements from the experimental wafers.[8] The obtained wafer resistivities (ρW) were of 7 and 3 Ωcm for the CZ and the FZ wafer, respectively. Apart from this parameter, the wafers differ on their electron and hole fundamental lifetime (τe, τp) which were set to 3000 and 6000 μs for the CZ and the FZ wafer, respectively. The wafer thickness was varied from 100 to 340 μm to highlight the behavior of the J-V parameters of the bottom cells in dependence of this parameter.

Table S2: Quokka3 simulations parameter settings for Silicon Heterojunction bottom solar cells based on a Czochralski and a Float Zone wafer. Parameters that were equal for both wafer types are enlisted once.

Parameter	Czochralski	Float Zone	Unit
Dimensions	2		
Unit Cell Thickness	100 - 340		µm
Unit Cell width	10000		µm
Material Group			
J_0 $n_{i\,eff}$ Type	User Constant and a Temperature		
J_0 $n_{i\,eff}$ Temperature	298.15		K
Generation Profile File	'GenProf_cSi_PST_AlbrechtsStackNK.txt'		
Auger Model	Si-Altermatt2011		
Radiative Recombination Model	Si-Nguyen		
Density of State	Si-Green1990		
Intrinsic Carrier Density Model	user-const		
Intrinsic Carier Density n_{i0}	9.65e9		cm^{-3}
Silicon Mobiylity Model	Si-Klaassen1992		
Si Band Gap Narrowing Model	Si-Schenk1998		
Doping Setting Type	dopingtype-resistivity		
Doping Type	n-type		
Doping Resistivity	7	3	Ωcm
Bulk Recombination Type	intrinsic plus SRH		
Bulk Recombination SRH Type	τ-E_t		
Bulk Recombination SRH τ_n	3000	6000	µs

Bulk Recombination SRH τ_p	3000	6000	µs
Bulk Recombination SRH τ E_t-E_i	0		eV
Electron Selective Contact			
Electron Skin Feature (i-aSi + n-aSi + TCO stack)			
Geometry Plane	front		
Geometry Shape	full		
Electrical Model Type	lumped		
R_{sh}	120		Ω
Conduction Type	n-type		
Vertical Resistivity Type	ohmic		
Vertical Resistivity	0.05		Ωcm²
Contact Recombination Type	J_0		
Contact Recombination J_0	3.1e-15		A/cm²
Electron Contact Feature			
Geometry Plane	front		
Geometry Shape	full		
Ohmic Resistivity (TCO/Metal)	1e-5		Ωcm²
Current Transport Model	ohmic		
Electron Metal Feature			
Geometry Plane	front		
Geometry Shape	full		

Polarity	n-type	
R_{sh}	1e-3	Ω
Shading Fraction	0	

Hole Selective Contact

Hole Skin Feature (i-aSi + p-aSi + TCO stack)

Geometry Plane	rear	
Geometry Shape	full	
Electrical Model Type	lumped	
R_{sh}	120	Ω
Conduction Type	p-type	
Vertical Resistivity Type	ohmic	
Vertical Resistivity	0.3	Ωcm²
Contact Recombination Type	J_0	
Contact Recombination J_0	3.1e-15	A/cm²

Contact Feature

Geometry Plane	rear	
Geometry Shape	full	
Ohmic Resistivity (TCO/Metal)	1e-5	Ωcm²
Current Transport Model	ohmic	

Hole Metal Feature

Geometry Plane	rear	

Geometry Shape	full	
Polarity	p-type	
R_{sh}	1e-3	Ω
Shading Fraction	0	
<u>External Circuit Settings</u>		
External Circuit R_s	0.2	Ωcm^2
External Circuit R_{shunt}	1e10	Ωcm^2
External Circuit Diode J_0	0	A/cm^2
External Circuit Diode Ideality	1	
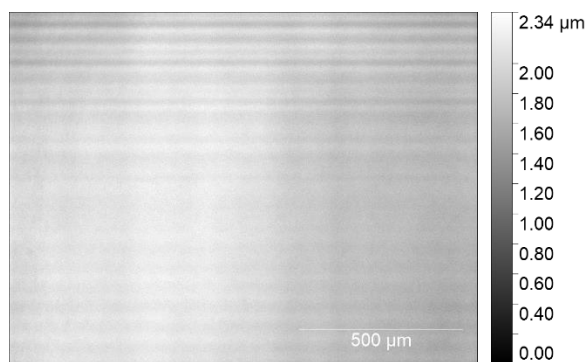
Figure S2: Confocal 3D laser scanning microscope image of the chemical-mechanical polished FZ bottom cell shown in the main text in Figure 1D with an adjusted scale. The horizontal features are artefacts generated during acquisition.

A
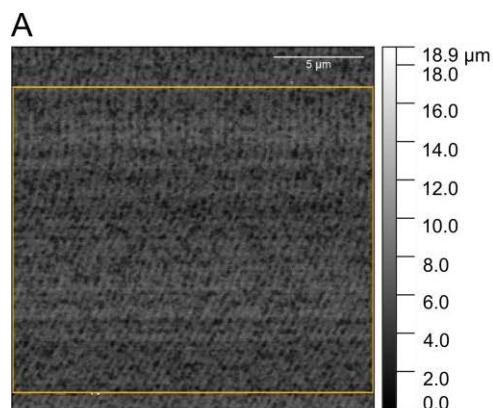
RMS roughness (Sq) = 1.257 nm
Maximum height (Sz) = 8.860 nm

B
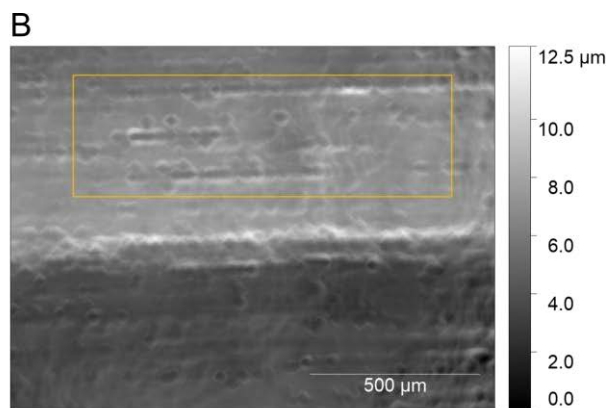
RMS roughness (Sq) = 735.881 nm
Maximum height (Sz) = 7.7260 µm

Figure S3: Surface analysis of the FZ-Si (chemical-mechanical polished) (A) and CZ-Si (chemically polished) (B) wafers. For the FZ-Si in (A), AFM is used. Due to the large feature size for the CZ-Si wafers in (B), 3D laser scanning microscopy is used to image the surface. The root mean square roughness values (Sq) and maximum height values (Sz) are extracted from the orange indicated area.

A

B
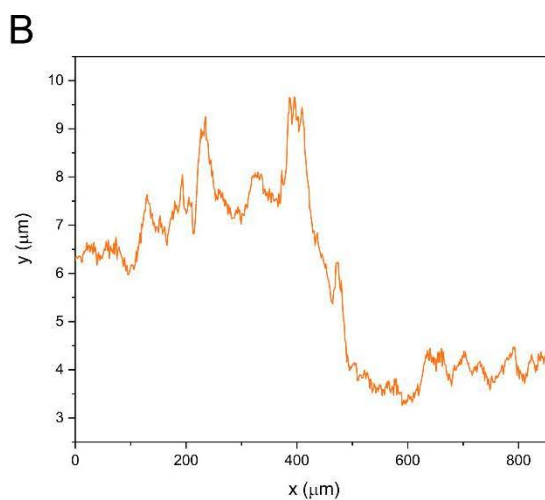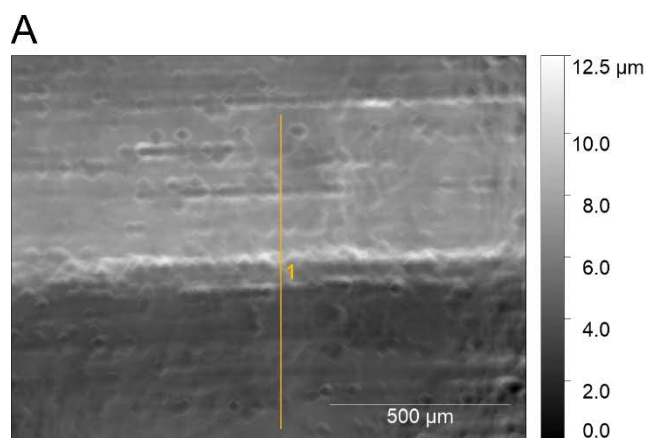
Figure S4: Profile of the saw mark of the non-polished silicon wafer. (A) is the confocal 3D laser scanning microscope image including profile line. The height profile is shown in (B). The saw mark creates a 5 to 6 µm step which ranges over approx. 100 µm.

220
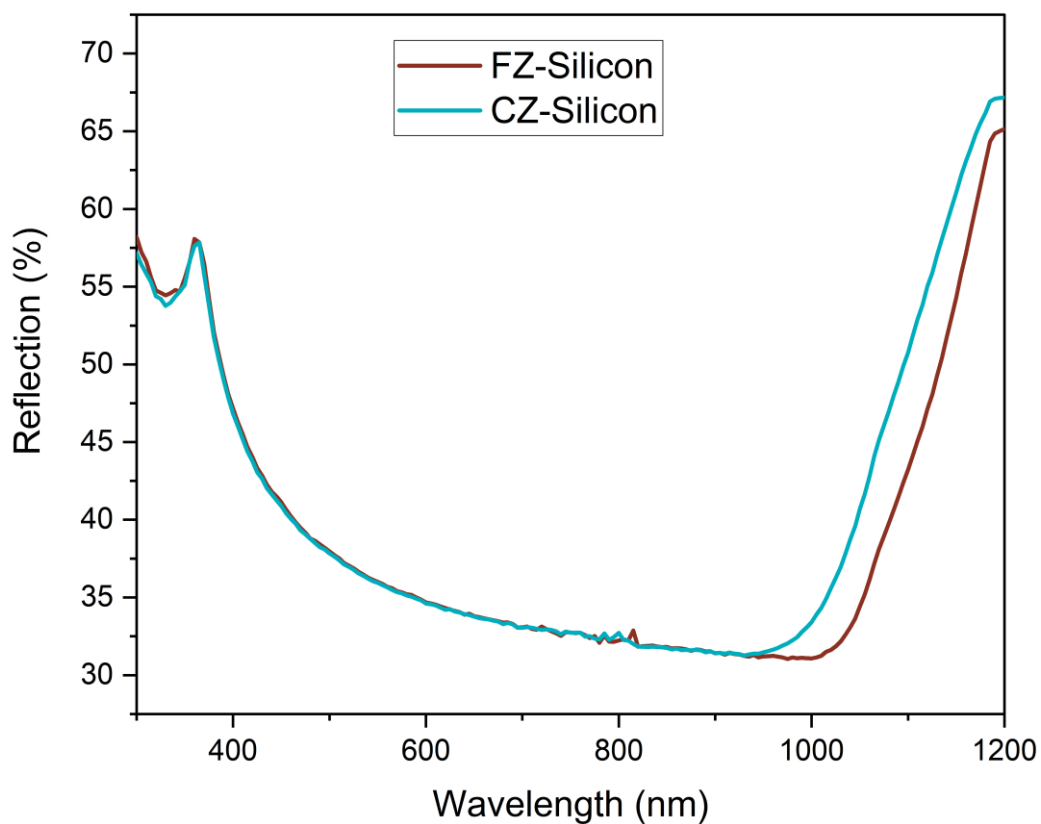
Figure S5: Reflection spectra of bare wafers. The reflection up to 950 nm for the thin, rough CZ silicon and the thick, chemical-mechanical polished FZ silicon is identical. The difference in reflection for wavelength above 950 nm is a result of different wafer thicknesses.
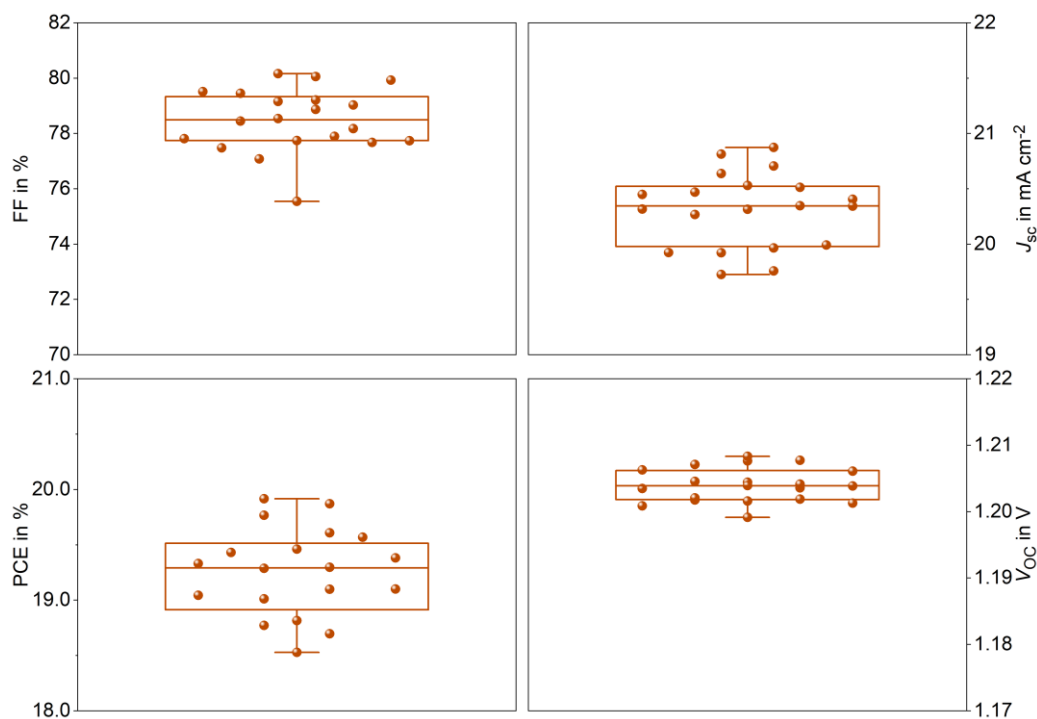
Figure S6: Statistics of opaque perovskite single-junction solar cells. The boxes indicate the 25/75 percentiles and the whiskers mark the minimum and maximum values. The line in the plots mark the respective median value.

221

13
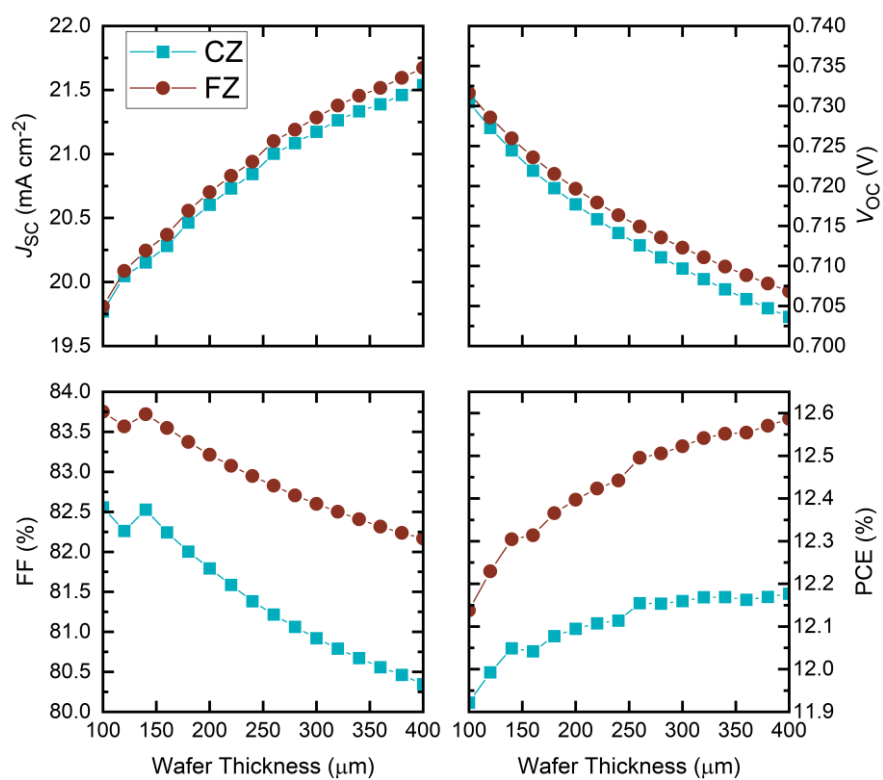
Figure S7: Quokka3 simulation of silicon single-junction solar cells made of Czochralski (CZ) and float-zone (FZ) silicon. For the current generation, the EQE of a tandem solar cell is used (i.e. around 20 mA cm^{-2}). More details can be found in the section "Materials and Methods" and in Table S2

	J_{sc} mA cm^{-2}	V_{oc} V	FF %	PCE %
V_{OC} to J_{SC}	17.83	1.92	81.15	27.78
J_{SC} to V_{OC}	17.83	1.93	80.92	27.86
V_{OC} to J_{SC}	17.81	1.93	81.05	27.80
J_{SC} to V_{OC}	17.81	1.94	80.89	27.89
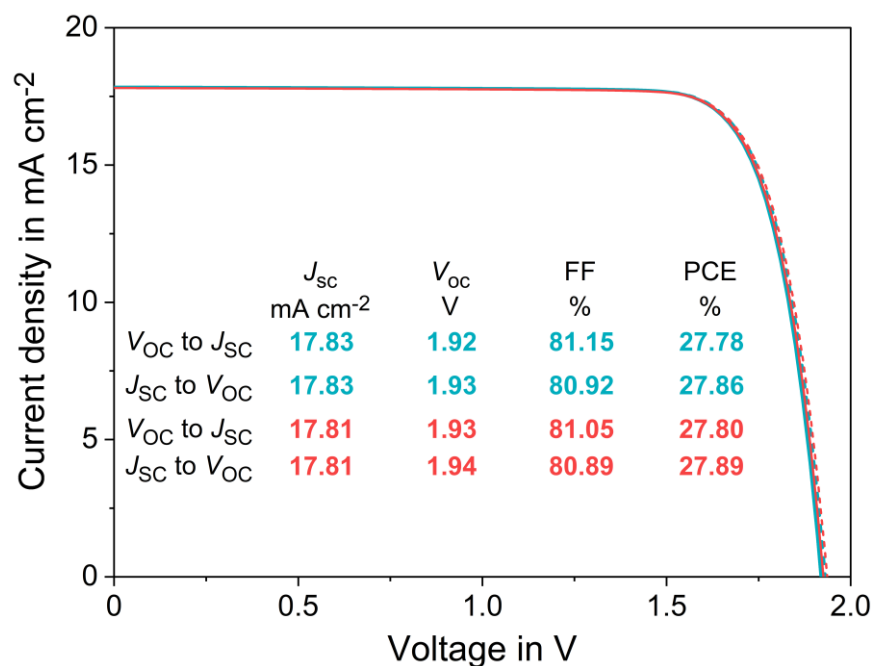
Figure S8: J-V scan of a CZ-based perovskite/tandem solar cell presenting the highest FF achieved in this work (blue curve). The J-V curve, measured immediately afterwards (red curve) presents the highest PCE measured for this tandem design (same J-V as shown in the main paper in Figure 2).
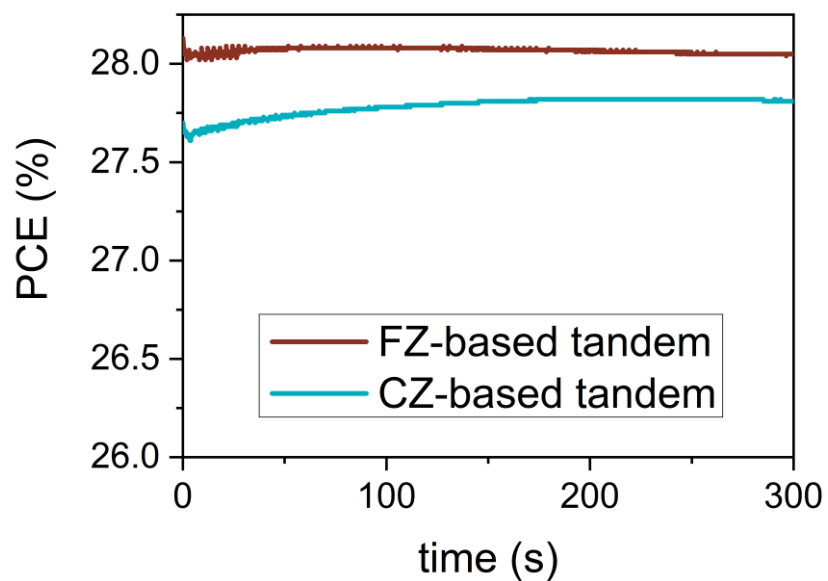
Figure S9: Maximum power point tracks of the floatzone (FZ) and czochralski (CZ) based tandem solar cells shown in the main text in Figure 2. After 300 seconds, the FZ and CZ-based tandem cells had a PCE of 28.05% and 27.81%, respectively.

223

15
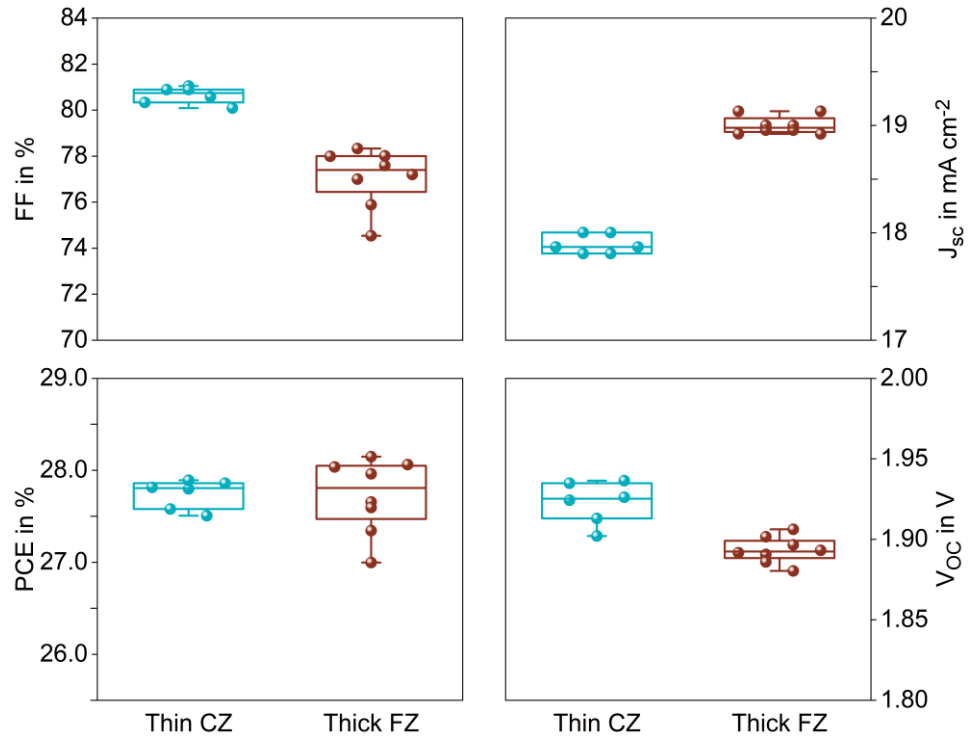
Figure S10: Statistical distribution of perovskite/silicon tandem solar cells fabricated on 100 µm thin CZ silicon with a chemically polished front side surface and 280 µm thick FZ silicon with a chemical-mechanical polished front side surface. The boxes indicate the 25/75 percentiles and the whiskers mark the minimum and maximum values. The line in the plots mark the respective median value.
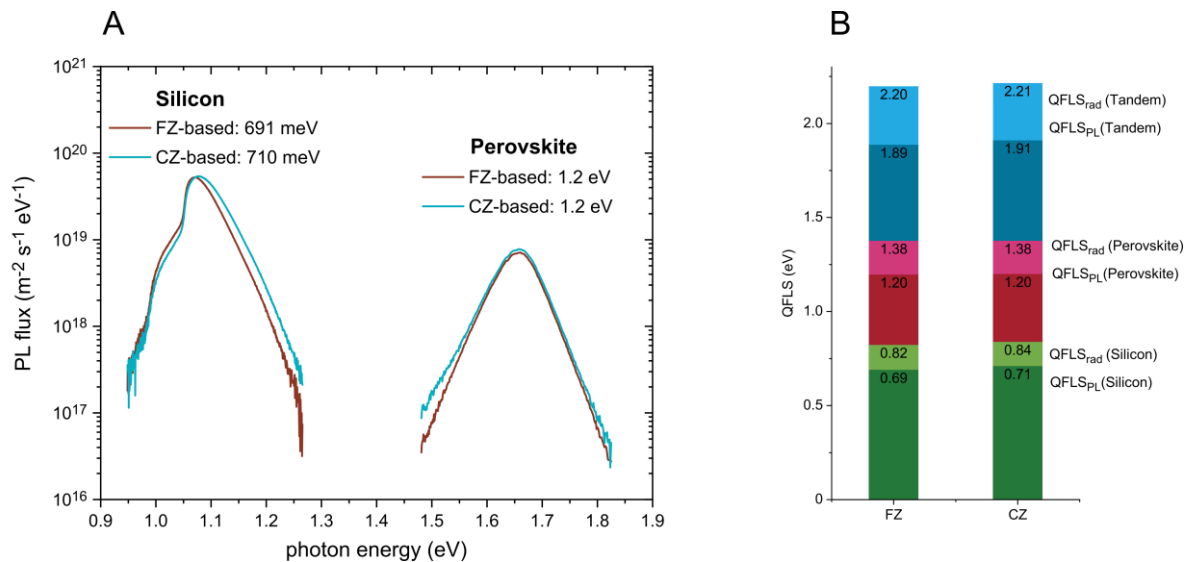
Figure S11: A) Absolute photoluminescence spectra of the perovskite and silicon subcells in FZ and CZ-based tandem solar cells. The extracted quasi fermi level splitting (QFLS) values are given in the figure. The QFLS values of the perovskite subcell are equal for CZ and FZ-based cells. In the silicon subcells, CZ-based tandem solar cells lead to an enhancement of 19 meV. Note that the generation current is adapted from the respective EQE. B) QFLS values and radiative limits of the perovskite and silicon subcells in FZ and CZ based tandem solar cells including the values for the respective tandem solar cells (sum of the subcells).
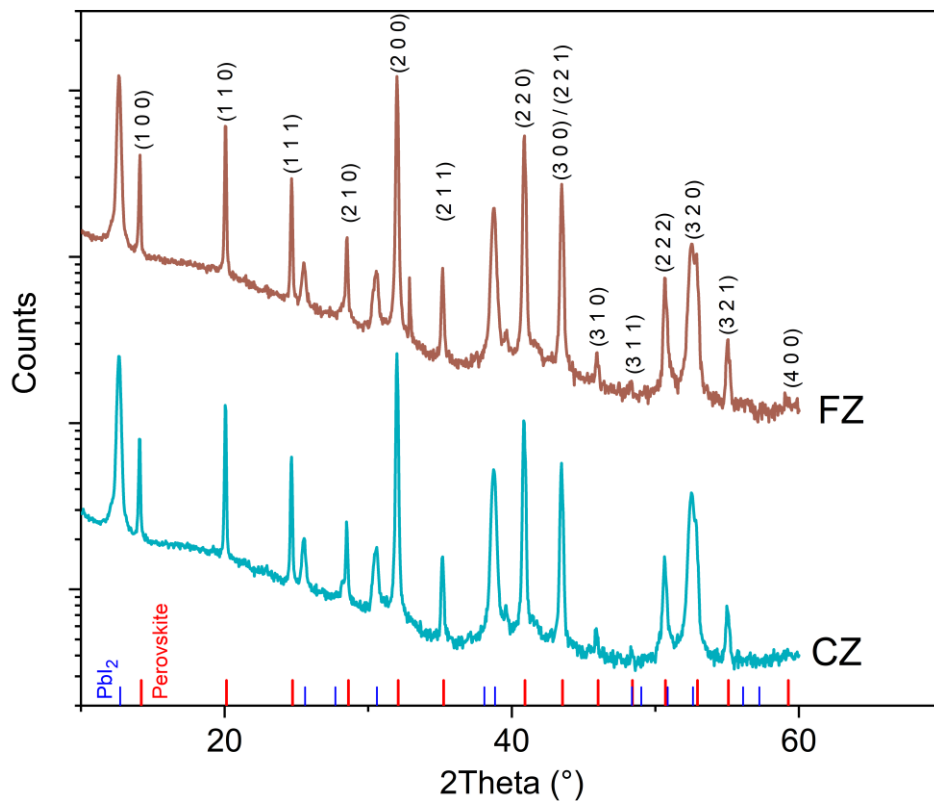
Figure S12: XRD patterns of the hole selective layer/perovskite stack deposited on bottom cells based on CZ and FZ-silicon. The blue lines indicate peak position of the PbI$_2$ and the red lines indicate peak position from the perovskite. Additionally, the orientations of the perovskite peaks are given.
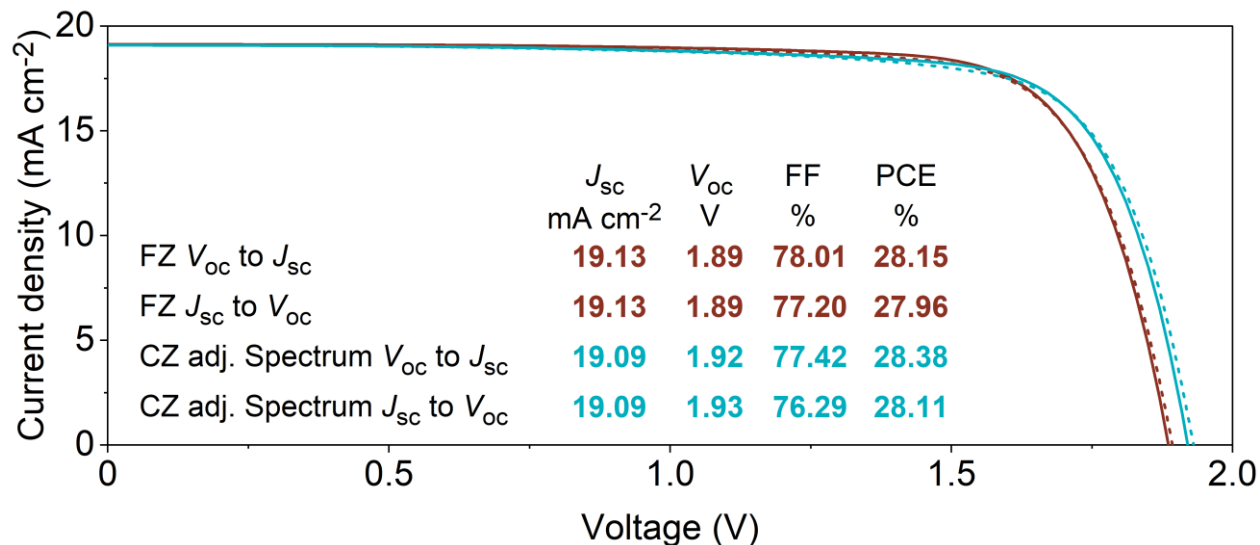
Figure S13: Comparison the thick FZ based tandem solar cell measured under AM1.5G conditions and the thin CZ-based tandem solar cells under an adjusted spectrum. For the letter, the blue and infrared part of the spectrum is adjuated in a way that the photogenerated current densities of the perovskite and silicon subcell is equal to the photogenerated current densities of the respective subcells of the FZ tandem solar cell under AM1.5G conditions. In other words, for both cells (FZ and CZ), the J_{Ph} of the perovskite subcell is 19.44 mA cm^{-2} and the J_{Ph} of the silicon subcell is 19.08 mA cm^{-2}.

	J_{sc} mA cm^{-2}	V_{oc} V	FF %	PCE %
FZ V_{oc} to J_{sc}	19.13	1.89	78.01	28.15
FZ J_{sc} to V_{oc}	19.13	1.89	77.20	27.96
CZ adj. Spectrum V_{oc} to J_{sc}	19.09	1.92	77.42	28.38
CZ adj. Spectrum J_{sc} to V_{oc}	19.09	1.93	76.29	28.11
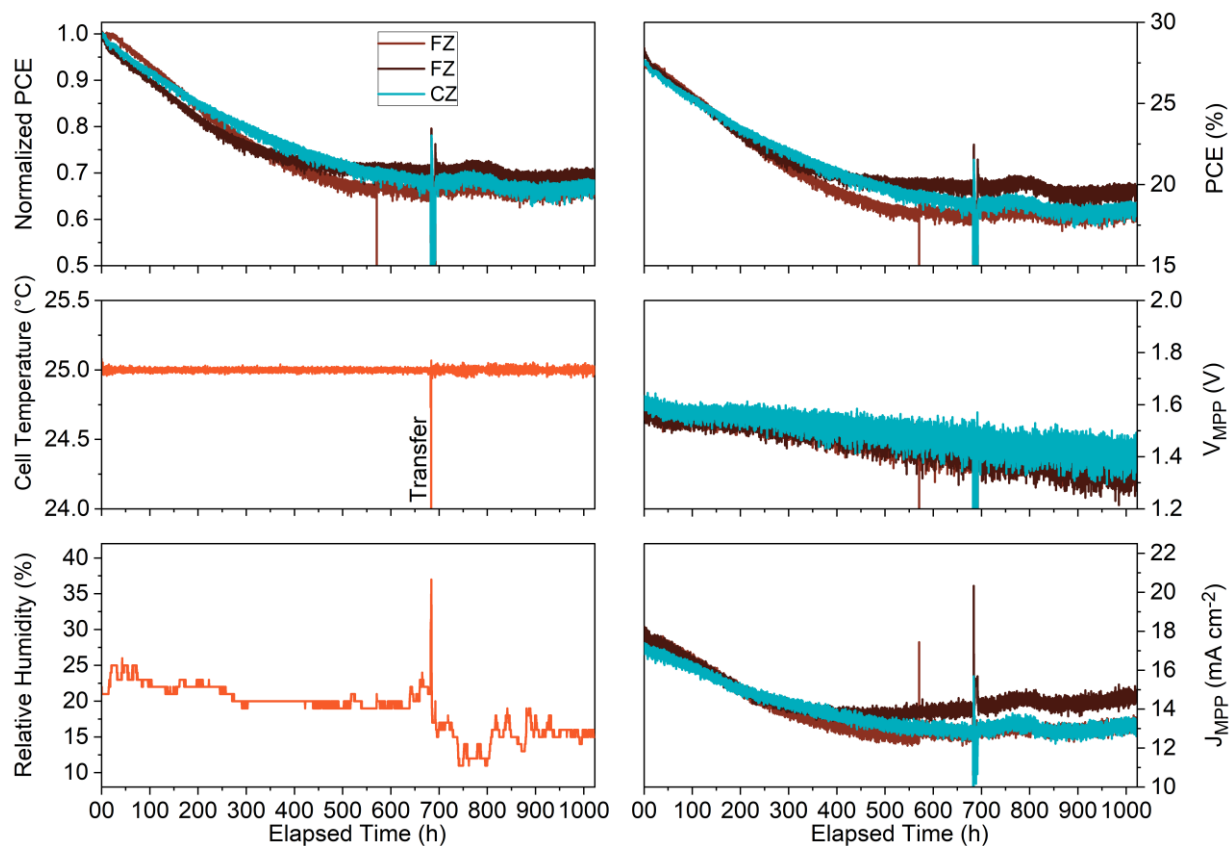
Figure S14: Long-term stability of one CZ and two FZ-based tandem solar cells under 1 sun AM1.5G conditions. The cells were continuously loaded with V_{MPP}, which was determined via voltage perturbation. The photogenerated current density in the subcells was set by adjusting the intensity of blue (470 nm) and infrared (940 nm) LEDs. The performance (V_{MPP} and J_{MPP}) was recorded every 5 minutes. During the measurement (after 680 h), the setup needed to be moved to another lab. Therefore, the measurement had to be stopped for approx. 10 min but continued immediately. More details can be found in the section "Materials and methods".

226

18
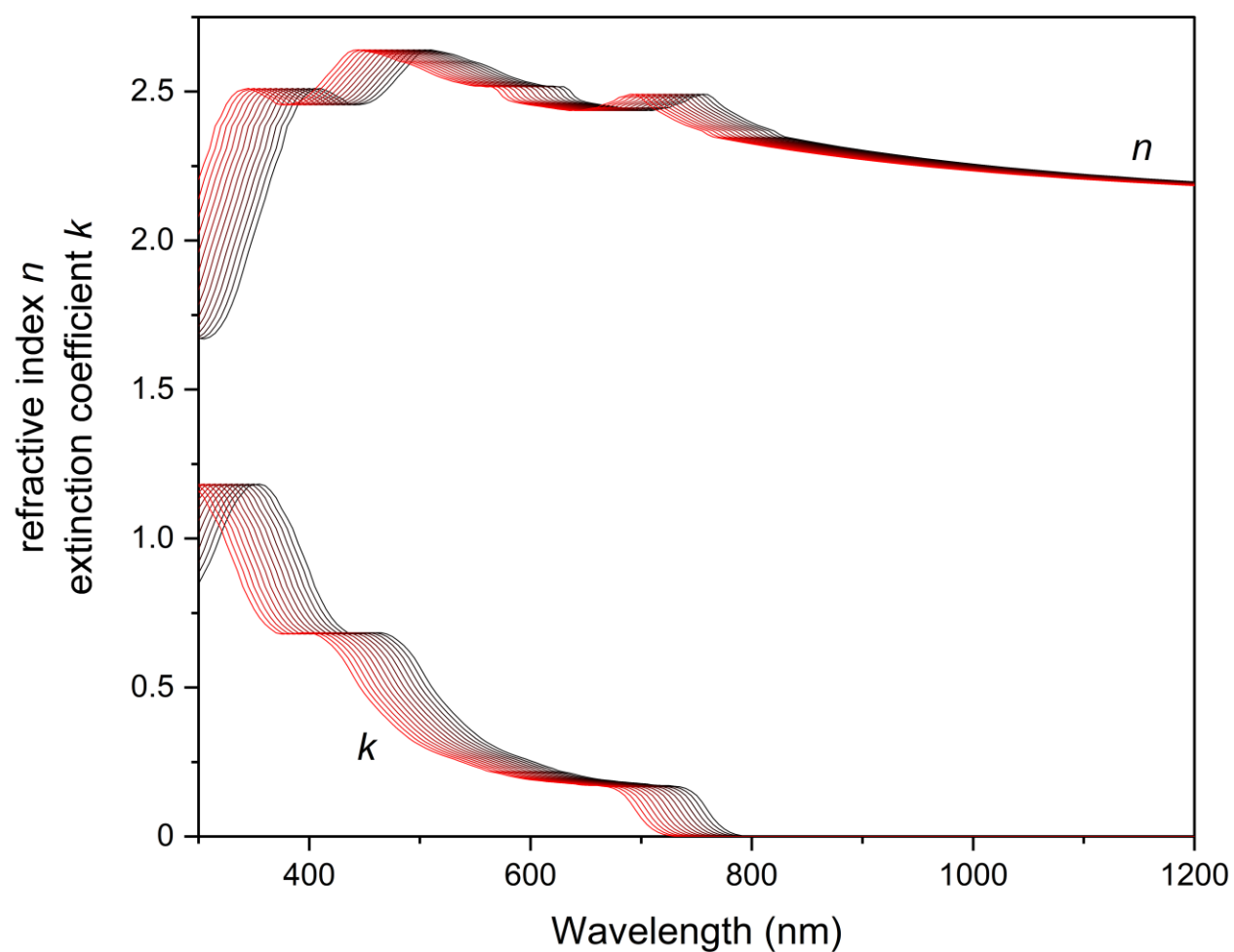
Figure S15: Optical data of the perovskite as input for optical simulations. The refractive index n and extinction coefficient k are measured via spectral ellipsometry for the lowest bandgap (black line). For wider bandgaps, the values are shifted along the x-axis towards lower wavelengths. The evaluation of the bandgap using the inflection point of the extinction coefficient k is shown in Figure S14.
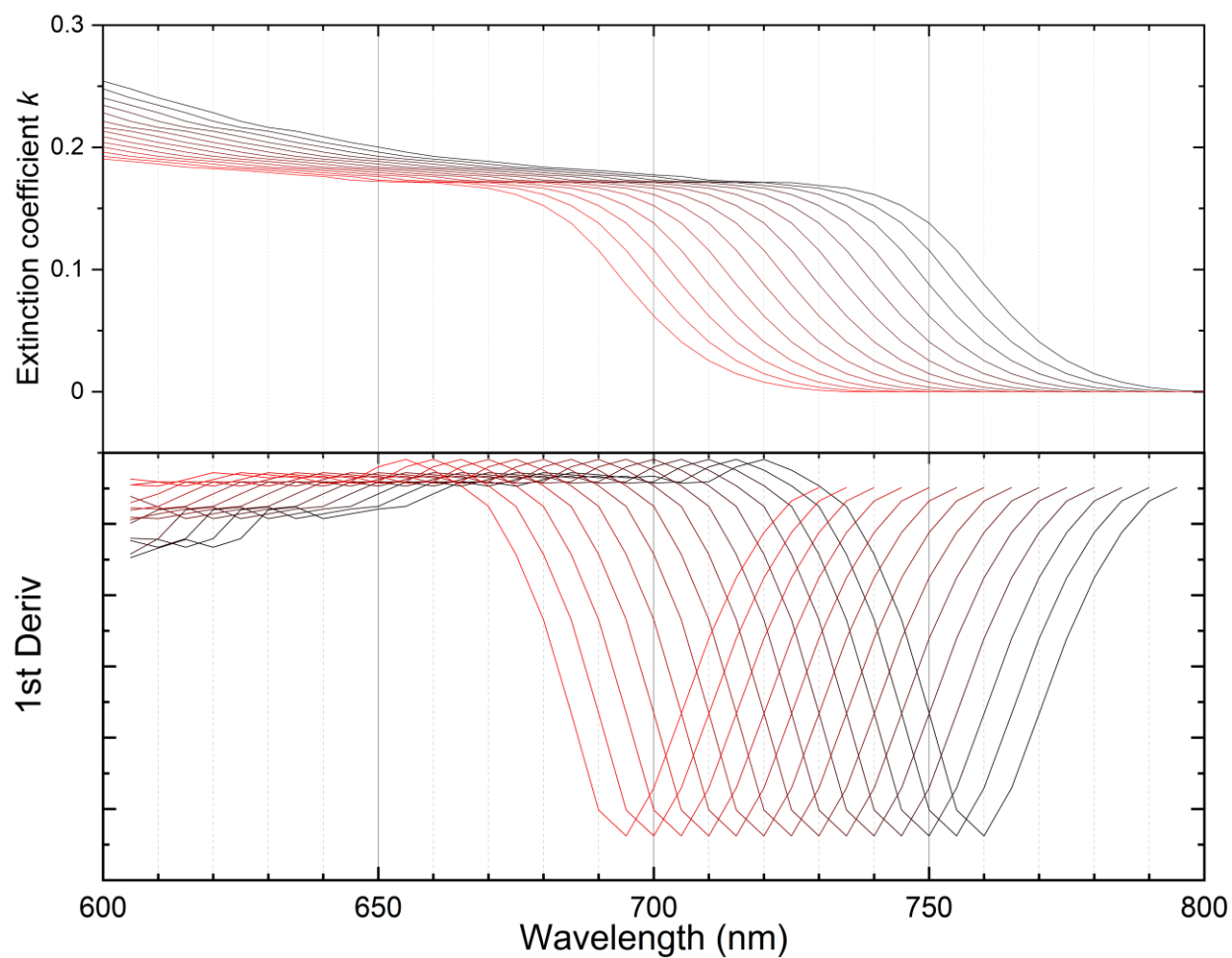
Figure S16: Evaluation of the perovskite's bandgap from the data shown in Figure S13 using the inflection point of the extinction coefficient k. The inflection points of the extinction coefficients k range from 695 nm to 760 nm which corresponds to bandgap energies of 1.78 eV to 1.63 eV.
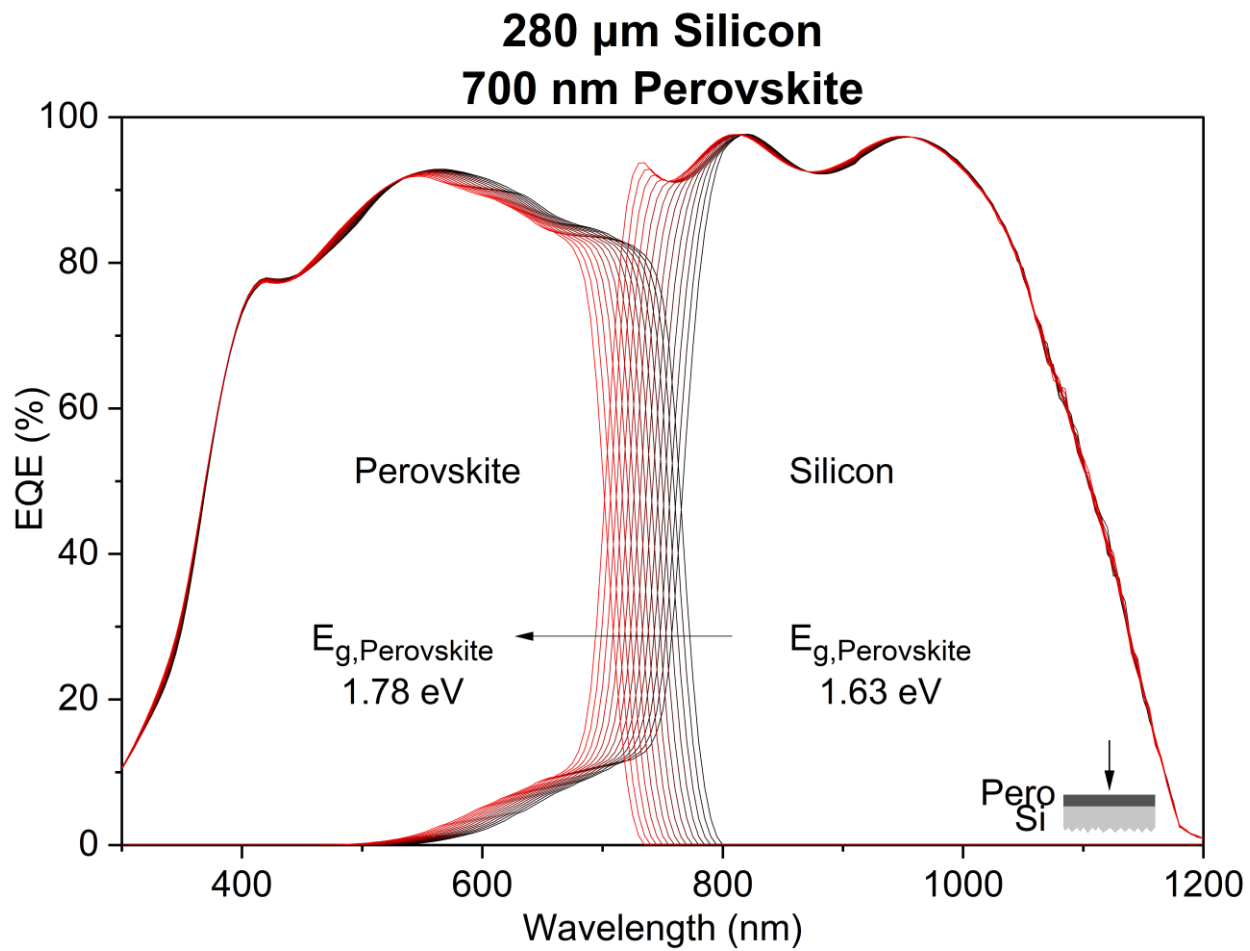
Figure S17: Simulated external quantum efficiency spectra of perovskite/silicon tandem solar cells with varying perovskite bandgap values ranging from 1.63 eV to 1.78 eV. The perovskite and silicon thicknesses are 700 nm and 280 μm, respectively. The front side is planar, whereas the rear side is textured.

Table S3: Results of optical simulations of perovskite/silicon tandem solar cells with planar front side and textured rear side. For perovskite thicknesses ranging from 700 nm to 1500 nm the ideal top cell bandgap to obtain current matching conditions ($E_{g,top,matched}$) is stated together with the corresponding current density, which is generated in both subcells ($J_{Ph,matched}$). The data were extracted for tandem solar cells with 100 µm and 280 µm thick silicon bottom cells. Additionally, the differences between the values for 280 µm and 100 µm thick silicon are calculated.

Perovskite thickness (nm)	Planar front side					
	100 µm Silicon		280 µm Silicon			
	$E_{g,top,matched}$ (eV)	$J_{Ph,matched}$ (mA cm^{-2})	$E_{g,top,matched}$ (eV)	$J_{Ph,matched}$ (mA cm^{-2})	Difference $E_{g,top,matched,100}$-$E_{g,top,matched,280}$ (eV)	Difference $J_{Ph,matched,100}$-$J_{Ph,matched,280}$ (mA cm^{-2})
700	1.709	19.094	1.689	19.591	0.020	-0.497
800	1.719	19.152	1.700	19.641	0.020	-0.490
900	1.730	19.123	1.711	19.615	0.020	-0.491
1000	1.737	19.160	1.717	19.655	0.020	-0.495
1100	1.743	19.133	1.723	19.630	0.020	-0.497
1200	1.747	19.167	1.727	19.662	0.020	-0.495
1300	1.751	19.144	1.731	19.642	0.020	-0.498
1400	1.753	19.168	1.733	19.657	0.020	-0.490
1500	1.756	19.160	1.736	19.662	0.020	-0.502
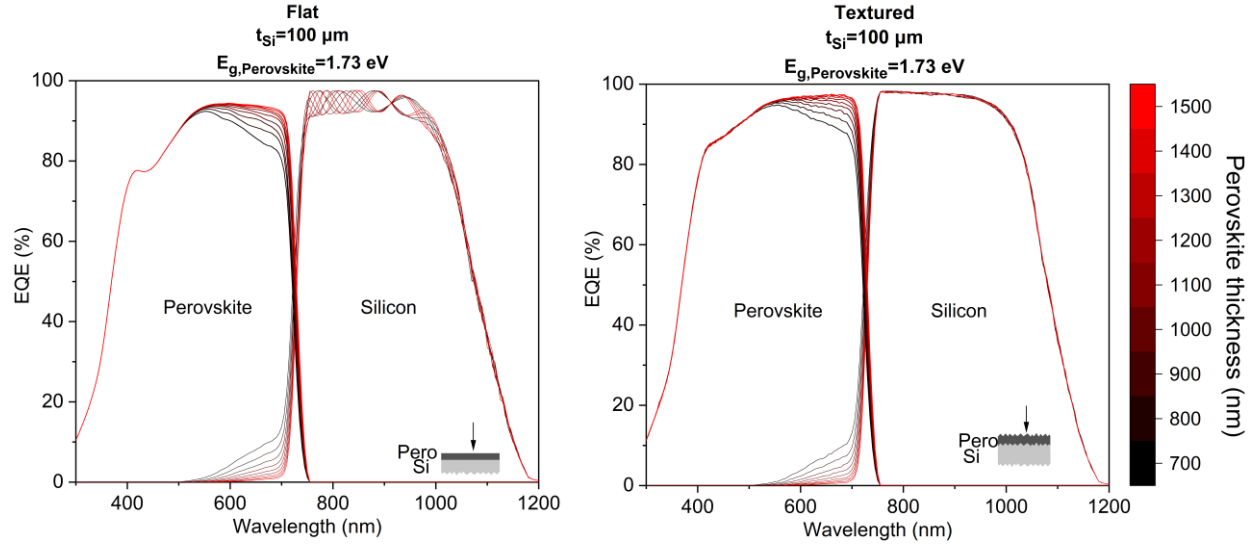
Figure S18: Simulated external quantum efficiency of perovskite/silicon tandem solar cells for a perovskite bandgap of 1.73 eV and a perovskite thickness ranging from 700 nm to 1500 nm. The rear side of the tandem cells is textured whereas the front side is either flat (left) or textured (right). The silicon bottom cell has a thickness of 100 μm
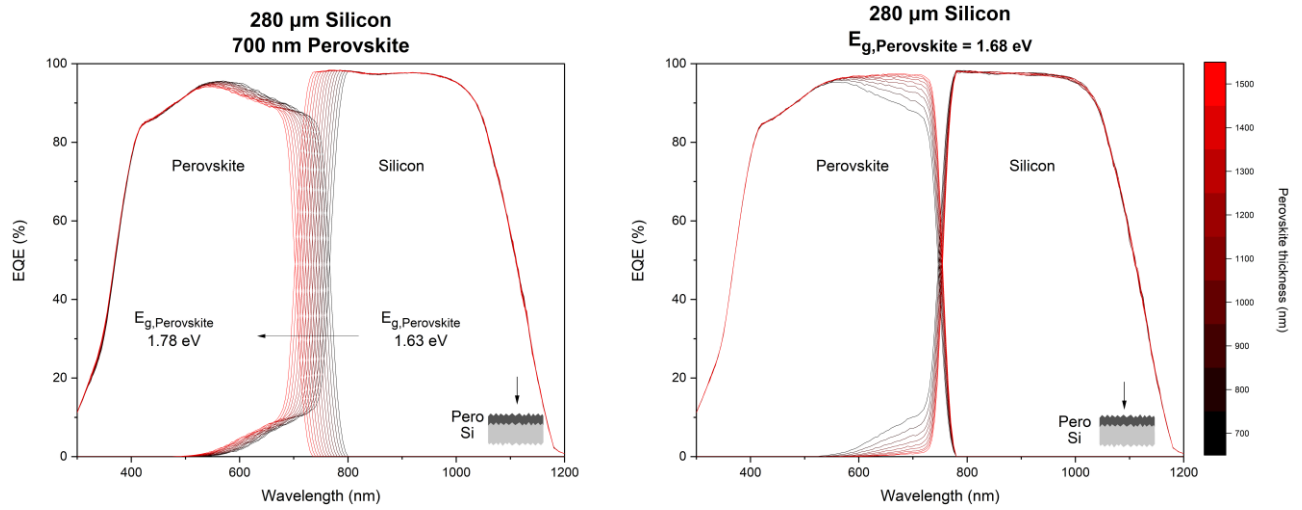
Figure S19: Optical simulations of double-side textured perovskite/silicon tandem solar cells using GenPro4. Left: Variation of the perovskite's bandgap for perovskite and silicon thicknesses of 700 nm and 280 μm, respectively. Right: Variation of the perovskite thickness for a perovskite bandgap of 1.68 eV and a silicon thickness of 280 μm

231

Table S4: Results of optical simulations of perovskite/silicon tandem solar cells with textured front and rear side. For perovskite thicknesses ranging from 700 nm to 1500 nm the ideal top cell bandgap to obtain current matching conditions ($E_{g,top,matched}$) is stated together with the corresponding current density, which is generated in both subcells ($J_{Ph,matched}$). The data were extracted for tandem solar cell with 100 μm and 280 μm thick silicon bottom cells. Additionally, the difference between the values for 280 μm and 100 μm highlights are calculated.

Perovskite thickness (nm)	Textured front side					
	100 μm Silicon		280 μm Silicon			
	$E_{g,top,matched}$ (eV)	$J_{Ph,matched}$ (mA cm^{-2})	$E_{g,top,matched}$ (eV)	$J_{Ph,matched}$ (mA cm^{-2})	Difference $E_{g,top,matched,100}$-$E_{g,top,matched,280}$ (eV)	Difference $J_{Ph,matched,100}$-$J_{Ph,matched,280}$ (mA cm^{-2})
700	1.715	19.927	1.696	20.425	0.019	0.497
800	1.726	19.946	1.708	20.439	0.018	0.493
900	1.735	19.949	1.716	20.441	0.019	0.492
1000	1.742	19.945	1.723	20.445	0.019	0.500
1100	1.747	19.954	1.728	20.446	0.019	0.492
1200	1.751	19.953	1.732	20.447	0.019	0.493
1300	1.754	19.956	1.735	20.451	0.019	0.495
1400	1.757	19.950	1.738	20.449	0.019	0.499
1500	1.759	19.961	1.740	20.449	0.019	0.488

References

[1]   Kranz, C.; Wyczanowski, S.; Baumann, U.; Weise, K.; Klein, C.; Delahaye, F.; Dullweber, T.; Brendel, R. Wet Chemical Polishing for Industrial Type PERC Solar Cells. *Energy Procedia* **2013**, *38* (0), 243–249.

[2]   Kranz, C.; Wyczanowski, S.; Dorn, S.; Weise, K.; Klein, C.; Bothe, K.; Dullweber, T.; Brendel, R. Impact of the Rear Surface Roughness on Industrial-Type PERC Solar Cells. In *27th European Photovoltaic Solar Energy Conference and Exhibition*; 2012; pp 557–560.

[3]   Meusel, M.; Adelhelm, R.; Dimroth, F.; Bett, A. W.; Warta, W. Spectral Mismatch Correction and Spectrometric Characterization of Monolithic III-V Multi-Junction Solar Cells. *Prog. Photovoltaics Res. Appl.* **2002**, *10* (4), 243–255.

[4]   Wurfel, P. The Chemical Potential of Radiation. *J. Phys. C Solid State Phys.* **1982**, *15* (18), 3967–3985.

[5]   Shockley, W.; Queisser, H. J. Detailed Balance Limit of Efficiency of P-n Junction Solar

Cells. *J. Appl. Phys.* **1961**, *32* (3), 510–519.

[6]   Würfel, P.; Würfel, U. *Physics of Solar Cells: From Basic Principles to Advanced Concepts, 3rd Edition*; Wiley-VCH Verlag GmbH & Co. KGaA, 2019.

[7]   Fell, A. A Free and Fast Three-Dimensional/Two-Dimensional Solar Cell Simulator Featuring Conductive Boundary and Quasi-Neutrality Approximations. *IEEE Trans. Electron Devices* **2013**, *60* (2), 733–738.

[8]   Sinton, R. A.; Cuevas, A. Contactless Determination of Current–Voltage Characteristics and Minority-carrier Lifetimes in Semiconductors from Quasi-steady-state Photoconductance Data. *Appl. Phys. Lett.* **1996**, *69* (17), 2510–2512.

H   Acknowledgments